Moment Redistribution in Cold-Formed Steel Purlin Systems

A thesis submitted to the Imperial College London for the degree of Doctor of Philosophy

By

Chi Hui

Department of Civil and Environmental Engineering

Imperial College London

London SW7 2AZ

United Kingdom

March 2014

ABSTRACT

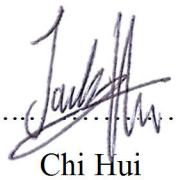
The external envelope of steel framed industrial buildings normally involves the use of purlins and rails spanning between the main hot-rolled frames to support the roofing/cladding. These purlins are typically light-gauge cold-formed steel members of complex shape for which the thinness of the material means that local instabilities will significantly influence their structural behaviour. In this thesis, the finite element (FE) method (ABAQUS) has been used to develop numerical analyses to study the buckling behaviour and degree of moment redistribution in continuous and sleeved cold-formed steel 2-span purlin systems. Five types of nonlinear FE analyses have been validated against reported physical tests: (i) continuous 2-span beams subjected to uniformly distributed load (UDL), (ii) single span beams subjected to a moment gradient, (iii) single span beams subjected to pure bending (iv) sleeved 2-span beams subjected to a UDL and (v) single span sleeved sections subjected to a moment gradient. The FE analyses were used to generate a large portfolio of new results for gravity and uplift loading for continuous and sleeved 2-span arrangements covering a wide range of cross-sections by varying the flange and web dimensions and material thickness. The effects of local and distortional buckling and limited rotational capacities for single span FE models were investigated. The 2-span FE results formed the basis for a simple modification to conventional plastic design that recognises the possibility of a reduction in moment with increasing rotation in the interior support region. The assumption of full moment redistribution for gravity loading was found to be only valid for stocky sections but not for slender sections. For uplift loading in addition to the potential reductions in moment at the interior support, limitations in the span moment due to lateral torsional buckling (LTB) for slender members were also accounted for. Based on the FE results, an α-reduction framework was established to predict the collapse load for continuous and sleeved 2-span systems. It was assumed that the cross-section or LTB resistance was

achieved in the span while a reduced cross-section resistance allowing for the post-peak fall in capacity was achieved at the interior support. The accuracy of the proposed design method was compared against elastic and full plastic design cases by considering their ultimate load carrying capacities. Whereas the elastic design method provides overly-conservative results and plastic design overestimates the capacity of slender sections, the proposed design method gave accurate predictions of the failure load with minimal scatter for all cases. The developed α-reduction framework provides a foundation for allowing the use of other purlin sections and interior support connections by inserting alternative cross-sectional moment capacity inputs obtained from several sources such as physical testing, hand calculations from design codes and FE analyses.

Declaration:

The copyright of this thesis rests with the author and is made available under a Creative Commons Attribution Non-Commercial No Derivatives licence. Researchers are free to copy, distribute or transmit the thesis on the condition that they attribute it, that they do not use it for commercial purposes and that they do not alter, transform or build upon it. For any reuse or redistribution, researchers must make clear to others the licence terms of this work.

I hereby declare that this thesis is my own work and that, to the best of my knowledge and belief, it reproduces no material previously published or written nor material which has been accepted for the award for any other degree of diploma, except where due acknowledgement has been made in the text.

Signature: …..…..……

Chi Hui

ACKNOWLEDGEMENTS

I would like to express my utmost gratitude to my supervisors; Professor L. Gardner and Professor D.A. Nethercot for all their guidance and continuous help throughout the course of this study. Their scientific knowledge and supervision have been an inspirational source of encouragement and support which made this thesis possible.

I would like to thank Ayrshire Metal Products for providing me with financial support, with special thanks to Bruce Boutell, Peter Short, Scott Reilly and David Wigley for their commercial influence and technical support.

I will always be grateful to my parents, my siblings and friends for their care and support.

Finally, I would like to thank all my fellow PhD students, research assistants and staff in the steel structures section for the technical and valuable discussions.

CONTENTS

ABSTRACT ii
ACKNOWLEDGEMENTS v
CONTENTS vi
NOMENCLATURE xi
LIST OF FIGURES xviii
LIST OF TABLES xxvii

CHAPTER 1 - INTRODUCTION

1.1 Background 1
1.2 Purlin and sheeting rail systems 2
1.3 Moment redistribution of statically indeterminate cold-formed steel beams 4
1.4 Aims and objectives 5
1.5 Outline of the thesis 6

CHAPTER 2 – LITERATURE REVIEW

2.1 Introduction 8
2.2 Material properties of cold-formed steel members 8
2.2.1 Enhancement of material properties in the corner regions 9
2.2.2 Modelling the stress-strain relationship of cold-formed steel 12
2.2.3 Residual stresses 15
2.3 Geometric imperfections in cold-formed steel members 16
2.3.1 Distribution and magnitudes of initial imperfections 19
2.4 Review of design codes and standards for cold-formed steel sections 21
2.4.1 Eurocode 3: Design of Steel Structures: Part 1-3 21

2.4.2 AISI Specification for Design of Cold-formed Steel Structural Members 22
2.4.3 Cold-formed Steel Structure Code–AS/NZ 4600:2005 23
2.5 Existing investigations into the flexural behaviour of cold-formed steel sections 23
2.5.1 Experimental investigations 24
2.5.1.1 Single span cold-formed steel bare section tests 25
2.5.1.2 Lapped connections between cold-formed steel members 27
2.5.1.3 Sleeve connections between cold-formed steel members 28
2.5.1.4 Multi-span cold-formed steel purlin systems 29
2.5.2 Numerical investigations 31
2.6 Concluding remarks 33

CHAPTER 3 – NUMERICAL MODELLING - BARE SECTIONS

3.1 Introduction 34
3.2 Finite element modelling parameters 35
3.2.1 Material modelling 35
3.2.1.1 Proposed material model for FE models 36
3.2.1.2 Estimation of 1% proof stress 37
3.2.1.3 Corner enhancements 37
3.2.1.4 Tensile coupon tests 38
3.2.2 Element type 41
3.2.3 Mesh density and aspect ratio 42
3.2.4 Modelling of common trapezoidal sheeting 42
3.2.5 Method of analysis 44
3.2.6 Imperfections 45
3.2.6.1 Initial imperfection study 46
3.3 Validation of bare section FE models 51
3.3.1 Introduction 51
3.3.2 Boundary conditions and loading 54
3.3.3 Single span tests 56
3.3.3.1 4-point and 3-point bending tests by Wang and Zhang (2009) 56
3.3.3.2 4-point bending tests conducted by Yu and Schafer (2003) 60
3.3.3.3 3-point bending tests by Bryan, Davies and Deakin (1979-1992) 64
3.3.3.4 Comparison between single span tests and FE results 67

3.3.4 2-span continuous beam tests 75
3.3.4.1 Gravity 2-span continuous beam tests 75
3.3.4.2 Uplift 2-span continuous beam tests 77
3.3.4.3 Comparison between 2-span tests and FE results 78
3.4 Concluding remarks 82

CHAPTER 4 – BARE SECTION PARAMETRIC STUDY AND DESIGN

4.1 Introduction 83
4.2 Design approach for 2-span systems 83
4.2.1 Moment redistribution 84
4.3 Parametric study – gravity loading 85
4.3.1 Outline 85
4.3.2 Influence of cross-section slenderness 89
4.3.2.1 Rotation capacity study 89
4.3.2.2 Influence of moment gradient 95
4.3.3 Reference FE models 101
4.3.4 Alpha framework 103
4.3.4.1 Stocky versus slender 2-span sections 103
4.3.4.2 Design proposal 113
4.4 Parametric study – uplift loading 122
4.4.1 Outline 122
4.4.2 Lateral torsional buckling 122
4.4.3 Reference FE models 124
4.4.4 Alpha framework 126
4.4.4.1 Stocky versus slender 2-span sections 128
4.4.4.2 Design proposal 135
4.5 Conclusions 146

CHAPTER 5 – NUMERICAL MODELLING - SLEEVED SECTIONS

5.1 Introduction 148
5.2 Definition of different type of sleeved arrangements 149
5.3 Additional finite element modelling assumptions for sleeved systems 151

5.3.1 Modification to mesh 151
5.3.2 Contact modelling 152
5.3.3 Bolt characteristics 153
5.3.4 Whiffletree and solver scheme 154
5.4 Contact modelling and artificial damping sensitivity study 156
5.5 Validation of sleeved section FE models 160
5.5.1 Introduction 160
5.5.2 Boundary conditions and loading 162
5.5.3 Single span 3-point bending sleeved tests 164
5.5.3.1 Comparison between 3-point bending sleeved tests and FE results 167
5.5.4 Full scale 2-span sleeved tests 173
5.5.4.1 Comparison between 2-span sleeved tests and FE results 177
5.6 Concluding remarks 182

CHAPTER 6 – SLEEVED SECTION PARAMETRIC STUDY AND DESIGN

6.1 Introduction 183
6.2 Design approach for 2-span sleeved systems 184
6.3 Parametric study – gravity loading 185
6.3.1 Outline 185
6.3.2 Influence of sleeve length and bolt connection details 186
6.3.3 Reference FE models 199
6.3.4 Alpha framework for gravity loading 202
6.3.4.1 Moment redistribution comparison between 2-span sleeved and continuous systems 205
6.3.4.2 Design proposal 211
6.4 Parametric study – uplift loading 219
6.4.1 Outline 219
6.4.2 Lateral torsional buckling design using EC3 for 2-span sleeved purlins 219
6.4.3 Reference FE models 220
6.4.4 Alpha framework 222
6.4.4.1 Moment redistribution behaviour 223
6.4.4.2 Design proposal 226

6.5 Conclusions 234

CHAPTER 7 – CONCLUSIONS AND SUGGESTIONS FOR FUTURE WORK

7.1 Conclusions 236
7.2 Suggestions for future work 241

REFERENCES 242
APPENDICES 254

A Raw data for bare section parametric study – gravity loading 255
B Flow diagram to calculate the critical lateral buckling moment using Eurocode 3: Part 1-3 section 10 263
C Worked example - design procedure to check for lateral torsional buckling 265
D Raw data for bare section parametric study – uplift loading 268
E End support reaction derivation for 2-span sleeved systems 277
F Raw data for sleeved section parametric study – gravity loading 279
G Raw data for sleeved section parametric study – uplift loading 285

NOMENCLATURE

α_b	Strength coefficient
α_i	Flexural rigidity ratio
$\alpha_{FE,g}$	Interior support reduction factor for bare 2-span systems subjected to gravity loading obtained from FE results
$\alpha_{design,g}$	Estimated interior support reduction factor for bare 2-span systems subjected to gravity loading
$\alpha_{FE,gs}$	Interior support reduction factor for sleeved 2-span system subjected to gravity loading obtained from FE results
$\alpha_{design,gs}$	Estimated interior support reduction factor for sleeved 2-span system subjected to gravity loading
$\alpha_{FE,u}$	Interior support reduction factor for bare 2-span system subjected to uplift loading obtained from FE results
$\alpha_{design,u}$	Estimated interior support reduction factor for bare 2-span system subjected to uplift loading
γ_g, γ_M, γ_Q	Partial load factor
γ_1	Moment resistance ratio
γ_2	Ultimate load ratio between continuous and sleeved 2-span gravity systems
γ_3	Ultimate load ratio between continuous and sleeved 2-span uplift systems
δ	Maximum vertical deflection for 2-span systems
δ_{steel}	Density of steel
δ_{water}	Density of water
Δd	Measured distortional imperfections
Δl	Measured local imperfections
ε	Engineering strain
$\varepsilon_{0.2}$	Total strain at 0.2% proof stress

$\varepsilon_{1.0}$	Total strain at 1.0% proof stress
ε_u	Ultimate strain
ε^{pl}_{true}	Logarithmic plastic strain
ε_f	Elongation before fracture
$\eta_1, \eta_2, \eta_3, \eta_4$	Coefficients to determine the buckling length of the free flange
θ	Angle of inclination of any corner
θ	Angle on the $C_{L,0}$ - $C_{D,0}$ plane
θ_1, θ_2	End rotations for rotational capacity study
θ_c	Angle of inclination of the compression lip
θ_M	Central rotation
θ_{rot}	Limiting rotation of which the moment falls back below M_y
θ_t	Angle of inclination of the tension lip
θ_y	Elastic component of rotation upon reaching M_y
κ_{rot}	Elastic component of curvature upon reaching M_y
κ_y	Limiting curvature at which the moment resistance drops back below M_y
λ_l	Relative slenderness
$\bar{\lambda}_{cr,d}$	Elastic distortional buckling cross-section slenderness
$\bar{\lambda}_{cr,l}$	Elastic local buckling cross-section slenderness
$\bar{\lambda}_{cs}$	Cross-section slenderness
$\bar{\lambda}_{cs,s}$	Cross-section slenderness for sleeved systems
$\bar{\lambda}_{cs,+ve}$	Cross-section slenderness (positive pure bending)
$\bar{\lambda}_{cs,-ve}$	Cross-section slenderness (negative pure bending)
$\bar{\lambda}_{fz}$	Relative slenderness for flexural buckling
μ	Damping factor
ν	Poisson's ratio
σ	Engineering stress
$\sigma_{0.2}$	0.2% proof stress
$\sigma_{0.2,corner}$	0.2% proof stress for corners
$\sigma_{1.0}$	1.0% proof stress
σ_t	Total stress
σ_u	Ultimate stress

σ_{true}	True stress (Cauchy Stress)
χ_{LT}	Reduction factor for lateral torsional buckling
χ_{LT1}	Reduction factor for lateral torsional buckling for design case 1
χ_{LT2}	Reduction factor for lateral torsional buckling for design case 2
a	Longitudinal distance between end support and start of the sleeve section
b	Out-to-out flange width
b_c	Out-to-out compression flange width
b_p	Effective width of the plate
b_t	Out-to-out tension flange width
c	Out-to-out lip length
d	Section depth
d	bolt diameter
d_c	Compression lip length
d_t	Tension lip length
d_0	Extension of the bolted fastening
d_1	Maximum local buckling imperfection (Schafer and Peköz, 1998b)
d_2	Maximum distortional buckling imperfection (Schafer and Peköz, 1998b)
e	Nondimensional proof stress
f_u	Material ultimate strength
f_y	Material yield strength
f_{ya}	Average yield strength
f_{yb}	Basic yield strength
f_{yc}	Material yield strength of the corner region
f_{yf}	Average yield strength for flat regions
h	Out-to-out web height
k	Average yield strength coefficient
k_p	Plate buckling factor
l_{fz}	Buckling length for the free flange
l_{fz1}	Buckling length for the free flange for design case 1
l_{fz2}	Buckling length for the free flange for design case 2
m	Strain hardening coefficient determining the sharpness of the knee of the stress-strain curve

n	Strain hardening coefficient determining the sharpness of the knee of the stress-strain curve
$n'_{0.2,1.0}$	Strain hardening coefficient representing a curve passing thought 0.2% and 1% proof stresses
q	Applied load per metre span
q_{1g}, q_{2g}, q_{3g}	Ultimate load carrying capacities for design methods 1, 2 and 3 for bare 2-span system subjected to gravity loading
q_{1u}, q_{2u}, q_{3u}	Ultimate load carrying capacities for design methods 1, 2 and 3 for bare 2-span systems subjected to uplift loading
q_{1gs}, q_{2gs}, q_{3gs}	Ultimate load carrying capacities for design methods 1, 2 and 3 for sleeved 2-span systems subjected to gravity loading
q_{1us}, $q_{2us,}$ q_{2us}, q_{4us}	Ultimate load carrying capacities for design methods 1, 2, 3 and 4 for a sleeved 2-span q_{3us} q_{4us} systems subjected to uplift loading
$q_{FE,g}$	Ultimate load carrying capacity for bare 2-span systems subjected to gravity loading obtained from the FE results
$q_{FE,u}$	Ultimate load carrying capacity for bare 2-span systems subjected to uplift loading obtained from the FE results
$q_{FE,gs}$	Ultimate load carrying capacity for sleeved 2-span systems subjected to gravity loading obtained from the FE results
$q_{FE,us}$	Ultimate load carrying capacity for sleeved 2-span systems subjected to uplift loading obtained from the FE results
$q_{h,FD}$	Lateral load
q_{ult}	Ultimate design load carrying capacity for a 2-span system
$q_{ult,FE}$	Ultimate load carrying capacity obtained from FE analysis
$q_{ult,test}$	Ultimate load carrying capacity obtained from physical tests
r_i	Internal bending radius of the corner
r_{dc}	Outer radius between compression flange and compression lip
r_{dt}	Outer radius between tension flange and tension lip
r_{hc}	Outer radius between compression flange and web
r_{ht}	Outer radius between compression flange and web
t	Steel thickness
t_{bare}	Thicknesses of the bare section
t_{cor}	Core thickness of steel
t_p	Plate thickness

t_{sleeve}	Thicknesses of the sleeve section
w	Plate width
w_p	Actual width of the plate
x	Longitudinal distance from end support
y_1, y_2, y_3, y_4	Vertical displacements at section ends
z_1, z_2, z_3, z_4	longitudinal displacements at section ends

A	Tensile coupon cross-sectional area
A_g	Gross cross-sectional area
C	Ratio of corner area to total cross-sectional area
C_D	Total rotational spring stiffness
C_{DA}	Stiffness of the connection between the sheeting and purlin
C_{DC}	Flexural stiffness of the sheeting
$C_{L,0}$	Local imperfection amplitude
$C_{D,0}$	Distortional imperfection amplitude
D_M	Vertical deflection of the midspan
D_L	Average vertical deflection of the loading points
E	Young's Modulus
E_0	Initial Young's modulus
$E_{0.2}$	Tangent modulus at 0.2% proof stress
E_{plate}	Young's Modulus for plate elements
E_{tree}	Young's Modulus for whiffletree beam elements
F_b	Force developed in the bolt
F_u	Ultimate plate capacity
I	Second moment of area of bare cross-section
I_s	Second moment of area of sleeved cross-section
K	Lateral spring stiffness
L	Span length for 2-span systems
L'	Span length for single span moment gradient FE systems
L*	Span length for single span pure bending systems
L_a	Length between anti-sagbars
L_{sleeve}	Sleeve length
L_{coupon}	Tensile coupon length

M_1	Moment capacity for single span FE models subjected to positive uniform bending
M_2	Moment capacity for single span FE models subjected to negative uniform bending
M_3	Moment capacity for single span FE models subjected to negative 3-point bending
M_4	Moment capacity for single span FE models subjected to positive 3-point bending
$M_{3sleeve}$	Moment capacity for single span FE sleeved models subjected to positive 3-point bending
$M_{4sleeve}$	Moment capacity for single span FE sleeved models subjected to negative 3-point bending
M_{coupon}	Mass of coupon
M_{cr}	Critical elastic buckling moment
$M_{cr,d}$	Critical elastic distortional buckling moment
$M_{cr,l}$	Critical elastic local buckling moment
$M_{DS,d}$	Cross-sectional moment capacity obtained from the direct strength method for distortional buckling
$M_{DS,l}$	Cross-sectional moment capacity obtained from the direct strength method for local buckling
M_{FE}	Moment capacity obtained from FE analysis
$M_{FE,noslip}$	Moment capacity obtained from FE analysis with no bolt slip
$M_{FE,slip}$	Moment capacity obtained from FE analysis with bolt slip
$M_{FE,span}$	Span moment at ultimate load from the sleeved 2-span uplift FE model
M_{span}	Span moment obtained from the 2-span FE models
$M_{support}$	Interior support obtained moment from the 2-span FE models
M_{test}	Moment capacity obtained from physical tests
M_y	Yield moment
$M_{yy}(x)$	In-plane bending moment at distance (x) from the end support
$M_{zz}(x)$	Lateral bending moment at distance (x) from the end support
N	Number of 90º bends in the cross-section
P	Applied load
P_{ult}	Ultimate load-carrying capacity
$P_{ult,model,1}$	Ultimate load-carrying capacity for case 1

$P_{ult,test}$	Ultimate load-carrying capacity obtained from physical tests
$P_{ult,FE,noslip}$	Ultimate load-carrying capacity from FE analysis with no bolt slip
$P_{ult,FE,slip}$	Ultimate load-carrying capacity from FE analysis with bolt slip
R	Rotation capacity
R	Spring support coefficient
R_1	Vertical end support reaction
R_{bare}	Rotation capacity for bare section
R_{sleeve}	Rotation capacity for sleeve section
$W_{eff,y}$	Effective section modulus of the cross-section for only bending about the y-y axis
W_{fz}	Section modulus of the free flange plus the contributing part of the web for bending about the z-z axis
W_{uw}	Weight of coupon while submerged water
W_{ow}	Weight of coupon outside the water

$\mathbf{F_v}$	Viscous damping forces
M*	Artificial mass matrix
v	Vector of nodal velocities

LIST OF FIGURES

1.1 Various shapes of cold-formed sections: (a) lipped Zed, (b) lipped channel, (c) Zeta I, (d) Zeta II and (d) hat

1.2 Typical cold-formed steel purlin systems spanning between hot-rolled frames

1.3 Roof purlin systems in common use: (a) simply supported, (b) continuous, (c) sleeved and (d) overlap

1.4 (a) Schematic of plastic collapse mechanisms and (b) typical moment-rotation curves for cold-formed steel members

2.1 Indicative stress-strain curves for cold-formed steel flat and corner regions

2.2 Typical Gardner and Ashraf (2006) modified Ramberg-Osgood stress-strain relationship for the flat and corner regions of cold-formed steel sections

2.3 Typical finite strip analysis results, showing the half-wavelengths for local, distortional and lateral-torsional buckling modes

2.4 Definition of geometric imperfections (Schafer and Peköz, 1998b) (a) Type 1: Local imperfections and (b) Type 2: Distortional imperfections

2.5 (a) Initial geometrical imperfection representation in the CD,0 -CL,0 plane and (b) 4 FE models imperfection shapes (θ = 0°, 90°, 180°, 270°) by Borges and Camotim (2010)

2.6 Stress distribution in (a) stiffened and (b) unstiffened plates

2.7 Four-point bending tests carried out by (a) Yu and Schafer (2003) and (b) Yu and Schafer (2006)

3.1 Typical stress-strain responses for cold-formed steel

3.2 Tensile coupon test using Instron 8802

3.3 Stress-strain curves for 3.0 mm thick coupons

3.4 Stress-strain curves for 1.3 mm thick coupons

3.5 Stress-strain curves for 3.0 mm thick coupons with 0.2% and 1.0% offset lines
3.6 Stress-strain curves for 1.3 mm thick coupons with 0.2% and 1.0% offset lines
3.7 Two-spring model to reprsent sheeting
3.8 Signature curve showing local and distortional buckling modes
3.9 Geometrical dimensions of Zed section for imperfection sensitivity study
3.10 Load-displacement responses for models 1-8
3.11 Imperfection mode for model 1 - inward 33 local and 5 distortional waves
3.12 Imperfection mode for model 2 - inward 33 local and 6 distortional waves
3.13 Imperfection mode for model 3 - inward 32 local and 5 distortional waves
3.14 Imperfection mode for model 4 - inward 32 local and 6 distortional waves
3.15 Imperfection mode for model 5 - outward 33 local and 5 distortional waves
3.16 Imperfection mode for model 6 - outward 33 local and 6 distortional waves
3.17 Imperfection mode for model 7 - outward 32 local and 5 distortional waves
3.18 Imperfection mode for model 8 - outward 32 local and 6 distortional waves
3.19 Definitions for cross-sectional dimensions: (a) Zed, (b) Channel, (c) Zeta I and (d) Zeta II
3.20 Test type 1 - single span 4-point (pure) bending
3.21 Test type 3 - single span 3-point bending (moment gradient)
3.22 Test type 5 - continuous 2-span test subjected to gravity UDL
3.23 Test type 6 - continuous 2-span test subjected to uplift UDL
3.24 3-point bending FE model arrangement
3.25 2-span continuous FE model arrangement
3.26 4-point (pure) bending test arrangement of Wang and Zhang (2009)
3.27 3-point bending test arrangement of Wang and Zhang (2009)
3.28 Overall view by Wang and Zhang (2009): (a) 4-point (pure) bending tests and (b) 3-point bending tests
3.29 Schematic diagram of initial geometric imperfections
3.30 Definition for cross-sectional dimension for C-sections
3.31 Overall view of testing setup by Yu and Schafer (2003)
3.32 Four-point bending arrangement (a) experimental (Yu and Schafer (2003)) and (b) FE model
3.33 Plan view for panel-to-purlin screw locations from Yu and Schafer (2003)
3.34 Notation used for the geometry for (a) C-sections and (b) Zed sections physical test conducted by Yu and Schafer (2003)

3.35 3-point bending test arrangement
3.36 Definition of cross-sectional dimensions for (a) Zeta IA and (b) Zeta IB sections
3.37 Definition of cross-sectional dimensions for Zeta II sections
3.38 Load-deformation curves from Yu and Schafer (2003) tests and FE models (Zed sections)
3.39 Load-deformation curves from Yu and Schafer (2003) tests and FE models (C-sections)
3.40 Stress profile at different load stages for Test 1 from Yu and Schafer (2003)
3.41 3-point bending load-deformation curves from Bryan and Davies (1979) and Deakin (1991a) tests and FE models (Zeta IA, Zeta IB sections)
3.42 3-point bending load-deformation curves from Davies & Deakin (1992) tests and FE models (Zeta II sections)
3.43 2-span purlin tests by Bryan, Davies and Deakin (1979-1991), (a) overview of loading arrangement and (b) Section A-A
3.44 Definition of cross-sectional dimensions for Zeta IC
3.45 Section A-A for 2-span uplift purlin tests by Bryan and Davies (1980a) and Deakin (1991a, 1991b)
3.46 Test 5 2-span gravity load-deformation curves from Bryan and Davies (1979) and FE models (Zeta IB sections)
3.47 Test 10 2-span gravity load-deformation curves from Deakin (1991b) and FE models (Zeta IB sections)
3.48 Comparison of failure modes between physical Test 7 from Bryan and Davies (1980a) and FE model
3.49 2-span uplift load-deformation curves for test 1 from Bryan and Deakin (1980a) and FE models (Zeta IB sections)
3.50 2-span uplift load-deformation curves for test 2 from Bryan and Deakin (1980a) and FE models (Zeta IB sections)

4.1 Elastic bending moment diagram (BMD) for (a) multi-span and (b) 2-span purlin systems
4.2 Idealised full moment redistribution in a 2-span system and flat topped moment-rotation relationship
4.3 Definition of cross-sectional dimensions for (a) Zeta I and (b) Zeta II sections
4.4 Definition of cross-sectional dimensions for (a) Zed and (b) channel sections

4.5 System for naming sections

4.6 Definition of rotation capacity from (a) moment-curvature response and (b) moment–rotation response

4.7 Schematic setup for 4-point bending models

4.8 Schematic setup for 3-point bending FE models

4.9 Rotation capacity versus cross-section slenderness

4.10 Typical moment-rotation responses for (a) M_3 1/150_40 and (b) M_3 Z/12514

4.11 Typical moment-curvature responses for (a) M_1 2/225_50 and (b) M_1 Z/200_25

4.12 M_1/M_y and M_3/M_y versus cross-section slenderness $\bar{\lambda}_{cs}$

4.13 Geometric dimensions for section 1/175_16

4.14 M_4 moment–rotation responses for L' = 2, 3, 4 and 5 m for 1/175_16

4.15 Stress profile at (a) ultimate load and (b) beyond ultimate load for 1/175_16 M_4 L'= 3 m

4.16 Stress profile at (a) ultimate load and (b) beyond ultimate load for 1/175_16 M_1 L^*= 4880 mm

4.17 M_3 moment–rotation responses for L' = 2, 3, 4 and 5 m for 1/175_16

4.18 Stress profile at (a) ultimate load and (b) beyond ultimate load for 1/175_16 M_3 L'= 3000 mm

4.19 Stress profile at (a) ultimate load and (b) beyond ultimate load for 1/175_16 M_2 L^*= 4880 mm

4.20 Elastic bending moment diagram (BMD) for 2-span and reference M_1 and M_3 single span purlin systems

4.21 (a) Bending moment diagram for an ideal situation of full redistribution and (b) corresponding 2/225_50 M_3 reference moment–rotation behaviour

4.22 Applied load q, Msupport and Mspan versus maximum deflection δ for 2/225_50 L = 6 m

4.23 Msupport/Mspan versus maximum vertical displacement δ for 2-span 2/225_50 L = 6 m

4.24 Deformed stress profiles for gravity 2-span 2/225_50 L = 6m FE model at (a, b) stage 1 (c, d) stage 2 and (e, f) ultimate load

4.25 Deformed stressed profile for M_1 2/225_50 L^* = 4880 mm

4.26 Deformed stressed profile for M_3 2/225_50 L' = 3000 mm

4.27 Typical moment redistribution behaviour for slender sections with corresponding reference moment–rotation behaviour

4.28 Applied load q, Msupport and Mspan versus maximum deflection δ for 2/225_14 L = 8 m

4.29 $M_{support}/M_{span}$ versus maximum vertical displacement δ for 2-span 2/225_14 L = 8 m

4.30 Deformed stress profiles for gravity 2-span 2/225_14 L= 8m FE model at (a, b) stage 1 (c, d) stage 2 and (e, f) ultimate load

4.31 Deformed stress profile for M_1 2/225_14 L^* = 4880 mm

4.32 Deformed stress profile for M_3 2/225_14 L' = 4000 mm

4.33 Support moment reduction versus cross-section slenderness

4.34 Ultimate load comparison between FE and design methods 2 and 3 against negative cross-section slenderness

4.35 Ultimate load comparison between FE and design method 3, arranged by span length

4.36 α-reduction comparison between design method and FE results

4.37 Superposition of stresses in a cold-formed section under uplift loading

4.38 Elastic bending moment diagram (BMD) for 2-span continuous beam under uplift loading, M4 (positive 3-point bending) and M2 (negative pure bending)

4.39 Applied load q, $M_{support}$ and M_{span} versus maximum vertical deflection δ for uplift 2-span 1/175_20 L = 6 m FE model

4.40 Deformed stress profiles for uplift 2-span 1/175_20 L= 6 m FE model at (a) interior support and (b) span regions at ultimate load

4.41 Comparisons between M_{span}/M_2 at ultimate load versus flexural slenderness

4.42 Applied load q, $M_{support}$ and M_{span} versus maximum vertical deflection δ for uplift 2-span 1/200_16 L = 10 m FE model

4.43 $M_{support}/M_{span}$ versus maximum vertical displacement δ for uplift 2-span 1/200_16 L = 10 m

4.44 Design load comparisons between design method and FE results against flexural slenderness

4.45 Applied load q, $M_{support}$ and M_{span} versus maximum vertical deflection δ for uplift 2-span Z/200_13 L = 10 m FE model

4.46 Deformed stress profiles for uplift 2-span Z/200_13 L= 10m FE model at (a, b) q_{ult} [$M_{support}$ = max ($M_{support}$)] and (c, d) q = q_{stage3}

4.47 Interior support moment reduction versus positive cross-section slenderness from the uplift 2-span parametric study
4.48 Ultimate load comparison between FE and design methods 2 and 3 for 2-span uplift configuration against positive cross-section slenderness
4.49 α-reduction comparison between design method and FE results
4.50 Comparison between M_{span}/M_2 for different span lengths against χ_{LT}

5.1 Bolt arrangements in sleeved sections
5.2 Bolt type definition in sleeved sections
5.3 Adjustment of web nodes to account for bolt locations
5.4 Contact definitions: (a) sleeve length, (b) master and slave surfaces and (c) 7 individual contact pairs
5.5 (a) Nonlinear spring model for bolt, (b) Typical load-displacement relationship assigned to nonlinear springs (DOF 2 and 3)
5.6 4 tier 16 point whiffletree and loading diagrams
5.7 Connection detail between whiffletree and beam (a) aligned and (b) misaligned
5.8 Geometrical dimensions for Zeta IB sleeved section for artificial damping sensitivity study
5.9 Load-displacement responses for artificial damping sensitivity study
5.10 Initial load-displacement responses for artificial damping sensitivity study
5.11 Sleeved cross-section shapes: (a) Zeta II ,(b) Zeta I and (c) Zed
5.12 Test type 7 – Single span 3-point bending (moment gradient) sleeved tests
5.13 Test type 9 – 2-span sleeved tests subjected to gravity UDL
5.14 Test type 10 – 2-span sleeved tests subjected to uplift UDL
5.15 3-point bending sleeved FE model arrangement
5.16 2-span sleeved FE model arrangement
5.17 3-point bending sleeved test arrangement
5.18 Definition of cross-sectional dimensions for (a) Zeta IB sleeved and (b) Zeta II sleeved sections
5.19 Definition of cross-sectional dimensions for (a) Z1 sleeved and (b) Z2 sleeved sections
5.20 Sleeve dimensions for 2, 3B and 4 bolt type arrangements
5.21 Ho and Chung (2006a) bolt spring models adopted for FE validation

5.22 Load-deformation curves from Bryan and Davies (1980b) Zeta IB sleeved test 2 and FE models
5.23 Load-deformation curves from Leach (1990) Zeta IB sleeved test 5A, 5B and 5C and FE models
5.24 Load-deformation curves from Davies and Deakin (1992) Zeta II sleeved test 10 and FE models
5.25 Load-deformation curves from Davies and Deakin (1992) Zeta II sleeved test 14 and FE model
5.26 Load-deformation curves from Deakin and Melbourne (1997) Z1 sleeved tests 17A and 17B and FE models
5.27 Load-deformation curves from Deakin and Melbourne (1997) Z1 sleeved test 20 and FE models
5.28 2-span sleeved gravity test arrangement by Deakin (1991a)
5.29 2-span sleeved uplift test arrangement by Deakin (1991a)
5.30 2-span sleeved purlin test arrangement
5.31 Section A-A of 2-span sleeved purlin system: (a) gravity and (b) uplift loading
5.32 Load-deformation curves from Bryan and Davies (1980b) Zeta IB 2-span gravity sleeved test 3 and FE models
5.33 Load-deformation curves from Bryan and Deakin (1989) Zeta IB 2-span gravity sleeved test 7 and FE models
5.34 Load-deformation curves from Bryan and Deakin (1989) Zeta IB 2-span uplift sleeved test 1 and FE models
5.35 Load-deformation curves from Deakin (1991a) Zeta IB 2-span uplift sleeved test 3 and FE models
5.36 Failure modes between 2-span sleeved gravity test 5 from Leach (1990) and FE model
5.37 Failure modes between 2-span sleeved uplift test 5 from Deakin (1991b) and FE model

6.1 Joint geometry for (a) sleeved and (b) lapped connections
6.2 2-span sleeved purlin arrangement
6.3 Sleeve connection details for 1/175_16 and bolt arrangement numbers
6.4 Geometric dimensions for sleeve connection for 1/175_16 for (a) bolt arrangement 2 and 3A and (b) bolt arrangement 3B, 4 and 6

6.5 Schematic setup for 3-point bending sleeved FE models

6.6 Moment-rotation responses for $M_{3sleeve}$ 1/175_16 with L_{sleeve} = 600 mm for bolt arrangements 2, 3A, 3B, 4 and 6

6.7 Moment-rotation responses for $M_{3sleeve}$ 1/175_16 with L_{sleeve} = 900 mm for bolt arrangements 2, 3A, 3B, 4 and 6

6.8 Moment-rotation responses for $M_{3sleeve}$ 1/175_16 with L_{sleeve} = 1200 mm for bolt arrangements 2, 3A, 3B, 4 and 6

6.9 Moment-rotation responses for $M_{3sleeve}$ 1/175_16 with L_{sleeve} = 1500 mm for bolt arrangements 2, 3A, 3B, 4 and 6

6.10 Moment-rotation responses for $M_{3sleeve}$ 1/175_16 with L_{sleeve} = 1800 mm for bolt arrangements 2, 3A, 3B, 4 and 6

6.11 Moment-rotation responses for $M_{3sleeve}$ 1/175_16 with L_{sleeve} = 2100 mm for bolt arrangements 2, 3A, 3B, 4 and 6

6.12 Deformed stressed profile for $M_{3sleeve}$ 1/175_16 L' = 3000 mm L_{sleeve} = 600 mm with bolt arrangement 2 at (a) ultimate load and (b) post ultimate stage

6.13 Deformed stressed profile for $M_{3sleeve}$ 1/175_16 L' = 3000 mm L_{sleeve} = 600 mm with bolt arrangement 4 at (a) ultimate load and (b) post ultimate stage

6.14 Deformed stressed profile for $M_{3sleeve}$ 1/175_16 L' = 3000 mm L_{sleeve} = 1500 mm with bolt arrangement 3A at (a) ultimate load and (b) post ultimate stage

6.15 (a) Moment resistance and (b) flexural rigidity ratios for sleeved systems against different bolt configurations and sleeve length

6.16 Rotation capacity for sleeved sections

6.17 Elastic bending moment diagram (BMD) for 2-span sleeved and reference M_1 and $M_{3sleeve}$ single span purlin systems

6.18 Definition of cross-sectional dimensions for (a) Zeta I and (b) Zeta II sleeved sections

6.19 Definition of cross-sectional dimensions for Zed sleeved sections

6.20 Definition of sleeve details for the 2-span parametric study

6.21 Applied load q, $M_{support}$ and M_{span} vs. maximum deflection δ for sleeved 2-span 1/200_16 L = 8 m FE model

6.22 $M_{3sleeve}$ and M_3 moment-rotation responses for 1/200_16 L' = 3000mm

6.23 Applied load q, $M_{support}$ and M_{span} versus maximum deflection δ for 1/200_16 L = 6 m sleeved and continuous 2-span FE models

6.24 Deformed stress profiles for 1/200_16 2-span sleeved FE model at stage 2 and ultimate load for the interior support (a, b and d, e) and span (c and f) regions

6.25 Deformed stress profiles for 1/200_16 2-span continuous FE model at stage 2 and ultimate load for the interior support (a, b and d, e) and span (c and f) regions

6.26 Support moment reduction versus cross-section slenderness

6.27 Additional load carrying capacity due to addition of sleeves γ_2 versus L/d ratio

6.28 Ultimate load comparisons between sleeved 2-span FE results and design methods 2 and 3 against negative cross-sectional slenderness

6.29 Ultimate load comparison between sleeved 2-span FE results and design method 3 by span length

6.30 Elastic bending moment diagram (BMD) for 2-span sleeved uplift, M_2 and $M_{4sleeve}$

6.31 Applied load q, $M_{support}$ and M_{span} versus maximum vertical deflection δ for uplift 2-span Z/200_13 L = 10 m FE model

6.32 Applied load q, $M_{support}$ and M_{span} versus maximum deflection δ for 1/200_13 L = 6 m sleeved and continuous 2-span uplift FE models

6.33 Deformed stress profiles for 1/200_13 2-span sleeved uplift FE model at ultimate load for the (a) interior support and (b) span regions

6.34 Additional load carrying capacity for uplift loading γ_3 versus (a) L_{sleeve}/d and (b) span length L

6.35 Normalised 2-span moments: (a) $M_{4sleeve}/M_{support}$ and (b) M_2/M_{span} versus cross-sectional slenderness

6.36 Normalised design loads against 2-span uplift sleeved FE results versus cross-section slenderness

6.37 Calculated M_{span} reduction factors for design methods 3 and 4 against $\bar{\lambda}_{fz}$

B.1 Flow diagram to calculate the critical lateral buckling moment using Eurocode 3: Part 1-3 section 10

C.1 Geometrical dimensions of the Zeta IC section

C.2 Gross properties of the free flange including the contributing web

E.1 Non-prismatic 2-span system schematic

LIST OF TABLES

2.1 Summary of single bare span bending experimental studies

2.2 Summary of multi-span bending experimental studies

3.1 Coupon test results

3.2 Imperfection study results

3.3 Summary of single span test validation

3.4 Geometry and material properties for 4-point (pure) bending tests by Wang and Zhang (2009)

3.5 Geometry and material properties for 3-point bending tests by Wang and Zhang (2009)

3.6 Measured geometry and material strength for Zed section 4-point bending tests by Yu and Schafer (2003)

3.7 Measured geometry and material strength for C-section 4-point bending tests by Yu and Schafer (2003)

3.8 3-point bending tests by Bryan and Davies (1979, 1980a), Bryan and Deakin (1989), Deakin (1991a, 1991b) and Davies and Deakin (1992)

3.9 Comparison of bending resistances obtained from FE models and 4-point bending tests by Wang and Zhang (2009)

3.10 Comparison of bending resistances obtained from FE models and 3-point bending tests by Wang and Zhang (2009)

3.11 Comparison of bending resistances obtained from FE models and pure bending tests by Yu and Schafer (2003)

3.12 Comparison of bending resistances obtain from FE models and 3-point bending tests

3.13 Summary of 2-span tests for validation study

3.14 Measured geometry and material strength for 2-span gravity tests by Deakin et al. (1979), Bryan and Davies (1979, 1980a), Bryan and Deakin (1989) and Deakin (1991a, 1991b)
3.15 Measured geometry and material strength for 2-span uplift tests by Bryan and Davies (1980a) and Deakin (1991a, 1991b)
3.16 Comparison of ultimate loads obtain from FE models and 2-span gravity tests
3.17 Comparison of ultimate loads obtain from FE models and 2-span uplift tests by Bryan and Deakin (1980a) and Deakin (1991a, 1991b)
3.18 Summary of single span and 2-span tests for validation

4.1 List of dimensions for Zeta I, Zeta II, Zed and channel sections
4.2 Rotation capacity results for M1 and M3 single span models
4.3 Comparison between M1, M2, M3 and M4 for 1/175_16
4.4 Moment comparisons between 2-span and M_1 and M_3 models for 2/225_50
4.5 Moment comparisons between gravity 2-span, M_1 and M_3 models for 2/225_14 L = 8 m
4.6 M_{span} and $M_{support}$ inputs values for Equation 4.8 for design methods 1, 2 and 3
4.7 Ultimate load comparison between 2-span FE results and design methods 1, 2 and 3 for span length L = 4 m
4.8 Ultimate load comparison between 2-span FE results and design methods 1, 2 and 3 for span length L = 6 m
4.9 Ultimate load comparison between 2-span FE results and design methods 1, 2 and 3 for span length L = 8 m
4.10 Summary of comparisons between FE results and design calculations
4.11 List of dimensions for Zeta I, Zeta II, Zed and channels sections for uplift 2-span parametric study
4.12 Moment comparisons between 2-span uplift, M_2 and M_4 models for 1/175_20 L = 6 m
4.13 Moment comparisons between 2-span uplift, M_2 and M_4 models for 1/200_16 L = 10 m
4.14 Moment comparisons between 2-span uplift, M_2 and M_4 models for Z/200_13 L = 10 m
4.15 M_{span} and $M_{support}$ inputs values for Equation 4.8 for design methods 1, 2 and 3 for uplift 2-span parametric study

4.16 Ultimate load comparison between uplift 2-span FE results and design methods 1, 2 and 3 for span length L = 4 m
4.17 Ultimate load comparison between uplift 2-span FE results and design methods 1, 2 and 3 for span length L = 6 m
4.18 Ultimate load comparison between uplift 2-span FE results and design methods 1, 2 and 3 for span length L = 8 m
4.19 Ultimate load comparison between uplift 2-span FE results and design methods 1, 2 and 3 for span length L = 10 m
4.20 Summary of proposed α-framework for uplift loading
4.21 Ultimate load comparison between design methods 1, 2 and 3 for different span lengths

5.1 Dissipated energy fraction sensitivity study results
5.2 3-point bending sleeved test details by Bryan, Davies, Deakin, Leach and Melbourne (1980-1997)
5.3 Comparison between bending resistances obtain from FE models and 3-point bending sleeved tests
5.4 Measured geometry and material strength for 2-span gravity sleeved tests by Bryan and Davies (1980b), Leach (1990), Bryan and Deakin (1989) and Deakin (1991a, 1991b)
5.5 Measured geometry and material strength for 2-span uplift sleeved tests by Bryan and Deakin (1989) and Deakin (1991a, 1991b)
5.6 Comparison of ultimate loads from FE models and 2-span gravity sleeve tests
5.7 Comparison of ultimate loads from FE models and 2-span uplift sleeve tests
5.8 FE validation summary for 3-point bending and 2-span sleeved test arrangements

6.1 Comparison between M_3 and $M_{3sleeve}$ for section 1/175_16
6.2 Flexural rigidity ratios against sleeve length
6.3 Moment resistance ratios against sleeve length
6.4 List of dimensions for Zeta I, Zeta II and Zed sections
6.5 Moment comparisons between 2-span sleeved and M_1 and $M_{3sleeve}$ FE models for 1/200_16 L = 6000 mm
6.6 M_{span} and $M_{support}$ inputs values for Equation 6.13 for design methods 1, 2 and 3

6.7 Ultimate load comparison between 2-span FE sleeved results and design methods 1, 2 and 3 for Zeta I section for span lengths L = 4, 6 and 8 m

6.8 Ultimate load comparison between 2-span FE sleeved results and design methods 1, 2 and 3 for Zeta II section for span lengths L = 6, 8, 10 and 12 m

6.9 Ultimate load comparison between 2-span FE sleeved results and design methods 1, 2 and 3 for Zed section for span lengths L = 4, 6 and 8 m

6.10 Summary of proposed α-framework for sleeved gravity loading

6.11 List of dimensions for Zeta I and Zeta II sections for 2-span sleeved uplift study

6.12 Moment comparisons between 2-span sleeved and $\chi_{LT2}M_2$ and $M_{4sleeve}$ FE models for 1/200_16 L = 6000 mm

6.13 Load ratios γ_3 for Zeta I and Zeta II cross-sections

6.14 M_{span} and $M_{support}$ inputs values for Equation 6.13 for design methods 1, 2, 3 and 4 for uplift 2-span parametric study

6.15 Ultimate load comparison between 2-span FE sleeved results and design methods 1, 2, 3 and 4 for Zeta I sections with span lengths L = 4, 6, 8 and 10 m

6.16 Ultimate load comparison between 2-span FE sleeved results and design methods 1, 2, 3 and 4 for Zeta II sections with span lengths L = 4, 6, 8 and 10 m

6.17 Ultimate load comparison between design methods 1, 2 and 3 for different span lengths

A.1 Bare Zeta I 2-span gravity FE and design methods 1, 2 and 3 results

A.2 Bare Zeta II 2-span gravity FE and design methods 1, 2 and 3 results

A.3 Bare Zed 2-span gravity FE and design methods 1, 2 and 3 results

A.4 Bare channel 2-span gravity FE and design methods 1, 2 and 3 results

D.1 Bare Zeta I 2-span uplift FE and design methods 1, 2 and 3 results

D.2 Bare Zeta II 2-span uplift FE and design methods 1, 2 and 3 results

D.3 Bare Zed 2-span uplift FE and design methods 1, 2 and 3 results

D.4 Bare channel 2-span uplift FE and design methods 1, 2 and 3 results

E.1 Sleeved Zeta I 2-span gravity FE and design methods 1, 2 and 3 results

E.2 Sleeved Zeta II 2-span gravity FE and design methods 1, 2 and 3 results

E.3 Sleeved Zed 2-span gravity FE and design methods 1, 2 and 3 results

F.1 Sleeved Zeta I 2-span uplift FE and design methods 1, 2, 3 and 4 results

F.2 Sleeved Zeta II 2-span uplift FE and design methods 1, 2, 3 and 4 results

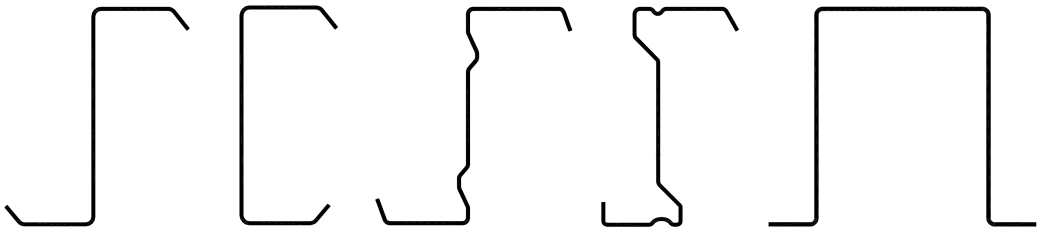
CHAPTER 1

INTRODUCTION

1.1 BACKGROUND

Cold-formed steel products are lightweight manufactured elements that are made by bending thin flat sheets of steel at room temperature into shapes suitable for a variety of uses. While cold-formed steel products for structural applications had been used as early as the 1850s in the USA and in the UK for automotive, ship building, rail and aeronautical applications, widespread usage of these members for agricultural, industrial and commercial buildings in the UK only started in the 1950s. Furthermore, cold-formed steel members have recently become more common in residential buildings. Owing to their high strength-to-weight ratio, their sections are widely used to carry loads in secondary steelwork spanning between hot-rolled main frames, but more recently, such sections have also been used as primary framing members in buildings typically up to 3 or 4 storeys in height. The emphasis of this thesis is on structural members used for buildings, with special attention on cold-formed steel purlin systems mainly used for large warehouse type buildings where the span lengths range from 4 m to 12 m.

The manufacturing process for cold-formed steel sections starts from cold-reduced hot-rolled slabs, annealed to improve ductility and flattened into thin sheets. Steel sheets for cold-forming range in thickness from 0.9 to 5 mm thick with nominal yield strengths between 280 and 550 N/mm^2. The sheets are cut into wide long strips, coiled and shipped to the fabricators. The coil of sheet steel would then be uncoiled, flattened and cold-formed into various shapes. Various organic or metal coatings are applied to prevent corrosion and weathering. Figure 1.1 shows the most common shapes used for purlin roof systems.



(a) (b) (c) (d) (e)

Figure 1.1: *Various shapes of cold-formed sections: (a) lipped Zed, (b) lipped channel, (c) Zeta I, (d) Zeta II and (d) hat*

Generally, the cold-forming process consists of either roll-forming or press-braking, where the former process tends to be used for longer members, more complex profiles and larger volume production. With short setup times for the roll forming machines and high output speeds (up to 50 m/min), it is possible to roll many different purlin shapes in a short time. Due to the cold-forming, the mechanical properties of cold-formed steel sections are different to conventional hot-rolled sections. Hot-rolled sections exhibit distinct yielding followed by a plateau and strain hardening. Cold-formed steel tends to exhibit a gradual yielding behaviour with earlier strain hardening. The cold-forming process also enhances the yield and ultimate strengths in the corner regions, though with corresponding reductions in ductility and generally a disappearance of the yield plateau.

1.2 PURLIN AND SHEETING RAIL SYSTEMS

Roof purlins account for a large proportion of the cold-formed steel usage in buildings. In the 1950s, the basic Zed and C shaped purlins were introduced in Europe. When used in conjunction with sheeting, these shapes provide high structural efficiency

and ease of construction. Figure 1.2 shows typical steel frames for industrial and commercial applications.



(a) AWS Eco Plastics' Recycling Plant (Photo: metsec.com)



(b) Storage building for WGP Group (Photo:southweststeelconstruction.co.uk)

Figure 1.2: *Typical cold-formed steel purlin systems spanning between hot-rolled frames*

Since then, competition between fabricators has led to substantial research and development in the search for more efficient cross-sectional shapes and innovative structural purlin systems exhibiting even greater efficiency. A variety of purlin systems is available to enable the designer to choose between simple inexpensive and easy to erect systems or more complex but more efficient systems. Apart from the simply supported case as shown in Figure 1.3(a), the continuous, sleeved and lapped cases - Figures 1.3(b-d) can be designed as statically indeterminate structures so as to yield higher load carrying capacities and stiffer systems.

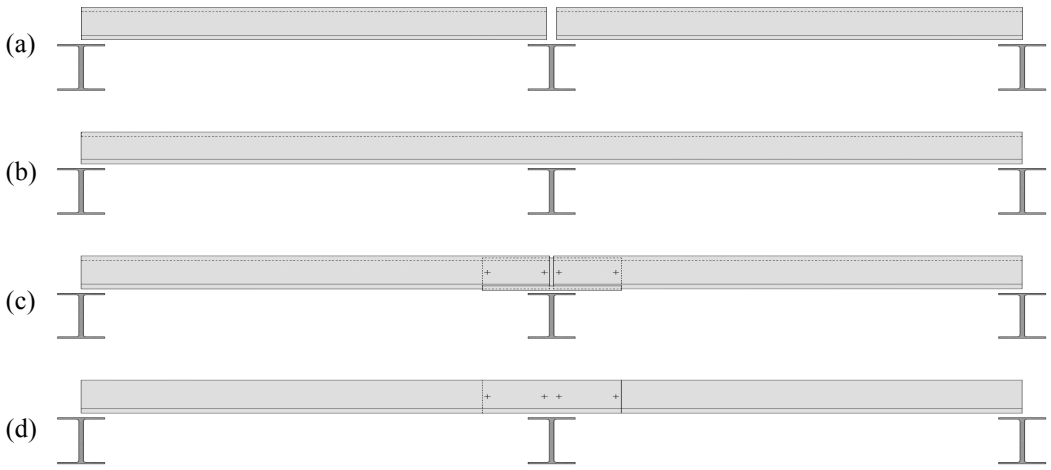


Figure 1.3: *Roof purlin systems in common use: (a) simply supported, (b) continuous, (c) sleeved and (d) overlap*

1.3 MOMENT REDISTRIBUTION OF STATICALLY INDETERMINATE COLD-FORMED STEEL BEAMS

For a statically indeterminate 2-span system, as shown in Figure 1.4(a), additional load carrying capacity can be achieved if the cross-section bending moment capacity can be maintained over large enough rotations by allowing moment redistribution and taking advantage of the unused moment capacity within the span. This principle is commonly used when designing hot rolled steelwork and has been adapted for reinforced concrete and composite construction. Prior to 1980, the inelastic reserve capacity of cold-formed steel beams was rarely considered in design since most sections comprised plates with high width-to-thickness ratios which most often exceeded the limits outlined for plastic design. This led to 2-span purlin designs being based mainly on elastic principles which only utilise the full cross-sectional moment capacity at the central support but not within the span. Figure 1.4(b) shows typical slender and stocky cold-formed steel moment-rotation responses, alongside the idealised elastic-perfectly plastic moment-rotation curve commonly assumed for plastic design. While the idealised moment-rotation model may be applicable for class 1 cross-sections (e.g. thick hot-rolled sections), it is not applicable to slender cold-formed steel members since they are usually incapable of developing rotating plastic hinges without local buckling.

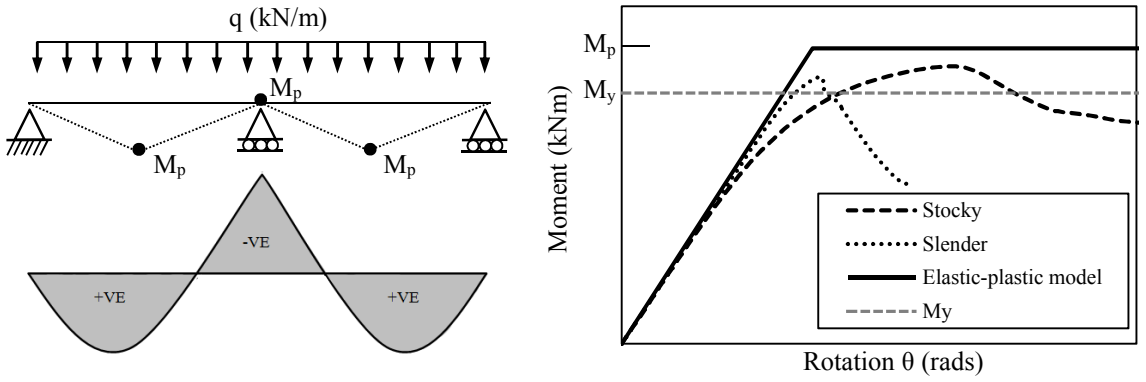


Figure 1.4: *(a) Schematic of plastic collapse mechanisms and (b) typical moment-rotation curves for cold-formed steel members*

Despite the above behaviour, Reck et al. (1975) and Yener and Peköz (1980, 1985a, 1985b) have shown that the inelastic strength reserve for cold-formed steel beams due to partial plastification of the cross-section can enable increases of up to 35% beyond

the original yield moment for many practical shapes. Thus, higher design capacities for statically indeterminate purlin systems are possible by allowing for moment redistribution, while recognising certain limitations in the moment-rotation relationships of cross-sections. The results and findings led to new design provisions in the 1980 edition of the AISI Specification which allows the use of the inelastic reserve strength of cold-formed steel members. To qualify, cold-formed steel sections must comprise stiffened compression elements without intermediate stiffeners with sufficiently low width-to-thickness ratios and the benefit was limited to a 25% gain beyond the yield moment. Yener and Peköz (1980) conducted experiments on single span beams of hat and channel sections and concluded that the inelastic flexural reserve capacity of continuous beams due to moment redistribution may be allowed for in design using the AISI Specification providing: (i) the member does not undergo lateral or torsional deformations, (ii) no corner enhancement strength is factored into the determination of the yield stress, (iii) premature web crippling at the interior support is accounted for, (iv) the system can satisfy combined shear and bending checks at the interior support and (v) reductions are made to the interior support moment capacity due to limitations of the rotation capacity. While Eurocode 1-3 recognises the potential of inelastic strength of cold-formed steel sections and the scope for moment redistribution through appropriate physical testing, direct guidance on statically indeterminate purlin systems is absent.

1.4 AIMS AND OBJECTIVES

Depending on the degree of lateral restraint, the thin open nature of cold-formed steel members makes them susceptible to local, distortional and lateral torsional buckling prior to yielding. The non-compact nature of such sections when arranged as continuous systems introduces even more complexity due to the varying scope to exploit the inelastic reserve and the degree of moment redistribution. While rough guidelines for moment redistribution in cold-formed steel systems have been identified by studies conducted at Cornell University, more recent studies on the subject have been extremely limited; a full understanding of the degree of moment redistribution in cold-formed steel 2-span systems remains elusive. While full scale testing provides useful but general information on the structural behaviour, full scale tests are costly, time consuming and provide limited detail on the buckling and moment redistribution behaviour. For example, it is difficult to recognise the controlling parameters involved with local or distortional buckling during

the testing, as it is common to report failure modes from the deformed shaped after loading. The finite element (FE) method has been shown in the present study to be able to provide accurate deformation, stress and moment profiles at different stages of the full load-displacement responses for 2-span and single span cold-formed steel systems.

In the present study, the magnitude of the reduction in interior support and span moments for 2-span cold-formed systems has been investigated and quantified. A numerical investigation of the effect of cross-sectional slenderness on the interior support moment reduction at ultimate load for cold-formed steel 2-span systems, considering both uplift and gravity loads was carried out. The aim of this thesis is to provide a robust design procedure which incorporates the potential loss of interior support moment and determines the ultimate load of such systems without the need to conduct numerous full scale physical experiments on cold-formed steel 2-span beams. The framework would be applicable for all cold-formed steel sections covering the range of span lengths commonly used in practise. Therefore, a full understanding of the initial and failure buckling behaviour as well as its moment redistribution behaviour for 2-span systems has been achieved in the present study.

1.5 OUTLINE OF THE THESIS

An introduction to cold-formed steel structural members with special reference to purlin systems has been presented in this chapter. A summary of the subjects discussed in each succeeding chapter is also presented. Chapter 2 provides a brief overview of the most relevant numerical and experimental studies on the behaviour and design of cold-formed steel sections in flexure.

Chapter 3 presents the development and validation of geometrically and materially nonlinear FE models for single and 2-span continuous cold-formed steel members subjected to a range of loading conditions. All essential features of the FE models were investigated through sensitivity studies. The numerical models have been carefully validated against over 60 existing test results.

An investigation into the degree of moment redistribution in continuous cold-formed steel beams subjected to uniformly distributed loading (UDL) is reported in Chapter 4. The validated finite element models were applied to a range of cross-sections

and span lengths to increase the pool of results to study the relationship between cross-sectional slenderness and the drop-off in moment at the interior support. These results are used to develop a design formula to estimate the post-peak reduction of the interior support moment from its initial peak, and then to use this reduced moment in conjunction with the full span moment to determine the load-carrying capacity of the system. The proposed design approach is referred to as the α (alpha) framework, with (1-α) representing the drop off in moment at the interior support at the peak system load. The validity of the proposed design method was compared against other design cases.

In Chapter 5, the developed bare section FE models from Chapter 3 were further developed to include single and 2-span sleeved arrangements. Key FE modelling parameters, including the contact definition and bolt characteristics were validated against existing physical test responses from several sources.

Chapter 6 includes a numerical study to investigate the ability of 2-span sleeved systems to generate worthwhile levels of moment redistribution through rotation of the sleeved region. The validated sleeved FE model from Chapter 5 was used to generate a portfolio of new results which formed the basis for a simple modification to conventional plastic design that recognises the possibility of a reduction in moment with increasing rotation in the sleeved region. Thus, the proposed alpha-method for the design of continuous purlin systems from Chapter 4 was extended to sleeved systems. Chapter 7 summarises the key findings and identifies potential avenues for further study.

CHAPTER 2

LITERATURE REVIEW

2.1 INTRODUCTION

This chapter reviews the most relevant literature on the buckling behaviour and design of cold-formed steel purlins, with special reference to the influence of material and geometric nonlinearities. A careful overview of the previous experimental and numerical studies covering continuous, lapped and sleeved connection details for single and multi-span cold-formed steel purlin systems has been presented.

2.2 MATERIAL PROPERTIES OF COLD-FORMED STEEL MEMBERS

Cold-forming processes such as rolling and press braking, have a significant influence on the material properties of steel. The induced plastic deformations cause an increase in yield strength, a reduction in ductility and result in the formation of residual stresses. The mechanical properties for cold-formed sections are generally determined by conducting experimental tensile and compression coupon tests. Early work by Chajes et al. (1963) included physical tests on 5 different types of carbon flat sheets by applying uniform cold stretching. It was identified that the cold-reduction process may produce

directional dependant Bauschinger effects in the steel, i.e. the mechanical properties are different under tension and compression and the steel material is anisotropic; the mechanical properties are different in the longitudinal and transverse direction after longitudinal rolling. More recently, many cold-formed steel material testing studies have been carried out including: a total of 12 compression tests by Young and Hancock (2003) and Young and Rasmussen (1998), 373 tensile coupon tests cut from press-braked channel sections and G550 sheet (f_y = 300 N/mm^2) steels by Sivakumaran (1987) and Rogers and Hancock (1997), and several tensile and compressive coupon tests by Ye and Rasmussen (2008). Rogers and Hancock (1997) identified coupons cut from the transverse direction exhibited on average a 5%, 20% and 15%, increase in Young's modulus, yield and ultimate stresses over longitudinal coupons. The Young's modulus is direction-dependent because the original random distribution of the grain develops a preferred orientation in the rolling direction. Transverse coupons were also found to exhibit the least amount of elongation before fracture. Experimental results by Ye and Rasmussen (2008) support the findings observed by Rogers and Hancock (1997). All tension and compression coupon tests mentioned exhibited different stress-strain characteristics to those of hot-rolled steel sections, showing a gradual rounded stress-strain curve with no distinct yield point, followed by strain hardening.

2.2.1 Enhancement of material properties in the corner regions

The cold-forming process plays a critical role in influencing the mechanical properties of cold-formed steel. Earliest experiential studies investigating the mechanical properties of light-gauge steel sections were conducted by Karren (1967) and Karren and Winter (1967). Karren (1967) conducted a large study comprising compressive and tensile coupon tests on 9 carbon steels, 2 of which were cold-reduced and 7 were hot-rolled. All specimens were cold-worked by either: (i) air press braking, (ii) coin press braking and (iii) cold-rolling. It was found that the yield strength of corner coupons after the cold-working process could increase by up to 70% beyond its virgin yield strength. Karren and Gohil (1975) conducted an additional 32 tensile and 6 compression coupon tests and identified that the corner enhancement was influenced by its internal corner radii r_i and steel thickness t; negligible yield strength enhancements for corners with r_i/t ratios above 60 were observed, while up to 29% in enhancement yield strength was observed for r_i/t ratios of 1.67. The percentage increase for ultimate strength was found to be less

than the increase in yield strength; the maximum ultimate strength gain was 47% above the virgin steel strength. The increase in strength was accompanied by a loss in ductility and a disappearance of the yielding plateau and strain hardening range. Karren and Winter (1967) conducted additional compression tests on compact cold-formed steel columns made up of either hat or back-to-back channel sections made from the same sheet material as those tested by Karren (1967). Variations of tensile yield and ultimate strengths in the corner regions were found to be similar to strength enhancements observed by Karren (1967), while the flat portions of the cross-section were similar to virgin steel strength. This suggests the mechanical properties in the flat regions are not highly influenced by the cold-rolling process. Many other researchers including Abdel-Rahman and Sivakumaran (1997) and Guo et al. (2007) conducted various tensile coupon tests on specimens cut from different locations from cold-formed steel sections. Both studies agreed with the increased corner property observations initially observed by Karren (1967) and Karren and Winter (1967). Abdel-Rahman and Sivakumaran (1997) also showed that the yielding behaviour of the tensile coupon tests varies depending on the steel grade by testing specimens with a range of nominal yield strengths of 228-345 N/mm^2. Some of the coupons cut from grade 33 steel (f_y = 228 N/mm^2) exhibited either a sharp or mixed yielding behaviour rather than the more common gradual yielding behaviour mostly found in cold-formed sections. Owing to the gradual yielding behaviour of the cold-formed steel, the most common approach to define the yield stress is the 0.2% offset method. Figure 2.1 shows a typical stress-strain curve for cold-formed steel for flat and corner regions. The yield point is defined by the intercept of an imaginary line with a gradient equal to the elastic Young's Modulus E at the 0.2% strain.

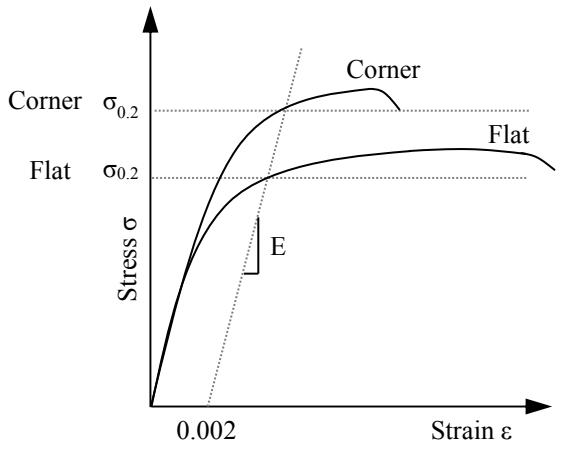


Figure 2.1: *Indicative stress-strain curves for cold-formed steel flat and corner regions*

Based on their coupon test responses, Karren (1967) presented a semi-empirical model to predict the corner yield strength enhancement as follows:

$$\frac{f_{yc}}{f_y} = \frac{B_c}{(r_i/t)^a} \tag{2.1}$$

where:

$$B_c = 3.69\left(\frac{f_u}{f_y}\right) - 0.819\left(\frac{f_u}{f_y}\right)^2 - 1.79 \tag{2.2}$$

$$a = 0.192\left(\frac{f_u}{f_y}\right) - 0.068 \tag{2.3}$$

where f_u and f_y are the ultimate and yield strength of the virgin material, f_{yc} is the yield strength of the corner region, r_i is the internal radius of the corner, and t is the material thickness. Whilst the model can be used to predict the increase in yield strength of the corner regions of cold-formed steel sections, it is not valid for areas adjacent to the corners even though increased yield strengths were identified in the adjacent regions. Based on 41 tensile coupon tests cut from cold-formed steel channel sections, Abdel-Rahman and Sivakumaran (1997) found corner enhancement ratios f_{yc}/f_y ranged between 26%-60% less than those predicted by Karren's model. They suggested continuing the use of Karren's model (Equation 2.1) but with a constant 0.6 reduction factor as follows:

$$\frac{f_{yc}}{f_y} = 0.6\left[\frac{B_c}{(r_i/t)^m}\right] \tag{2.4}$$

To obtain the full cross-section properties, Karen and Winter (1967) proposed an approximation of the full cross-section yield strength f_{yu} using a weighted average method:

$$f_{yu} = Cf_{yc} + (1-C)f_{yf} \tag{2.5}$$

where f_{yf} is the average yield strength for flat regions, C is the ratio of corner area to total cross-sectional area and f_{yc} is calculated using Equation 2.1. AISI (1996) adopted the use of Equations 2.1-2.3 and 2.5 to include the use of beneficial corner enhancement strength. The strength enhancement equations for cold-formed steel corners (Equations 2.1-2.3 and

2.5) proposed by Karren (1967) and Karren and Winter (1967) is also taken into account in EN 1993-1-3 (2006) by considering the average yield strength f_{ya} obtained by:

$$f_{ya} = f_{yb} + \left(f_u - f_{yb}\right)\frac{kNt_{cor}^2}{A_g}; \qquad \text{providing} \quad f_{ya} \le \frac{f_u + f_{yb}}{2} \tag{2.6}$$

where k is equal to 7 for roll forming or 5 for other forming methods, N is the ratio of total corner area to that of a 90º corner (providing it is less than t < 5 mm), f_{yb} is the basic yield strength, t_{cor} is the core thickness of the steel prior to cold-forming excluding any coatings and A_g is the gross cross-sectional area. Rather than adopt the discussed corner enhancement models to calculate the enhanced material properties at the corner regions for the FE models in this study, the corner enhancement strengths were determined independently by conducting several tensile coupons tests on specimens cut from representative cold-formed steel channel sections. Measured enhancements from the test program were then used directly in the FE models. Further details on the testing procedure, results and application are explained in more detail in Section 3.2.1.3.

2.2.2 Modelling the stress-strain relationship of cold-formed steel

Accurate material models to predict the stress-strain response of cold-formed steel are crucial for achieving reliable FE simulations. While various simplistic tri-linear material models for cold-formed steel have been used by researchers such as Moreyra and Peköz (1994b) and Feng et al. (2003), these do capture gradual yielding material behaviour with high accuracy. It has been most common to accurately represent the gradual yielding behaviour of cold-formed steel by a closed-formed expression initially proposed by Ramberg and Osgood (1943) and modified by Hill (1944):

$$\varepsilon = \frac{\sigma}{E_0} + 0.002\left(\frac{\sigma}{\sigma_{0.2}}\right)^n \tag{2.7}$$

where σ and ε are the engineering stress and strain respectively, E_0 is the initial Young's modulus of the material, $\sigma_{0.2}$ is the material's 0.2% proof stress and n is the power exponent that determines the sharpness of the knee of the stress-strain curve. Initially used for aluminium, the model is considered valid for all other metals with similar gradual yielding stress-strain behaviour including cold-formed steel. While Equation 2.7

is more accurate than bi-linear and tri-linear stress-strain relationships, further improvements to the basic Ramberg-Osgood expression have been proposed by numerous researchers. Modifications to the original expression have been proposed by Mirambell and Real (2000) because the original model tends to over-predict stresses beyond the 0.2% proof stress. The modified Ramberg-Osgood expression consists of two different expressions: (i) the original Ramberg-Osgood expression is unchanged for stresses up to the 0.2% proof stress and (ii) a second Ramberg-Osgood curve from the 0.2% proof stress to the material ultimate stress σ_u. The 0.2% proof stress acts as the new origin for the second Ramberg-Osgood curve, and allows for continuity at the transition point between the two expressions. Rasmussen (2003) carried out further work, and proposed the latter expression for the second stage of the two-stage model:

$$\varepsilon = \frac{\sigma - \sigma_{0.2}}{E_{0.2}} + \varepsilon_u \left(\frac{\sigma - \sigma_{0.2}}{\sigma_u - \sigma_{0.2}} \right)^m + \varepsilon_{0.2} \qquad (\sigma > \sigma_{0.2}) \qquad (2.8)$$

where $\varepsilon_{0.2}$ and ε_u are the total strain at 0.2% proof stress and ultimate strain respectively. The tangent modulus of the stress-strain curve at the 0.2% proof stress $E_{0.2}$ and corresponding exponent for the power function m are obtained as follows:

$$E_{0.2} = \frac{E_0}{1 + 0.002n/e} \qquad (2.9)$$

$$m = 1 + 3.5\frac{\sigma_{0.2}}{\sigma_u} \qquad (2.10)$$

where e is the nondimensional proof stress and is equal to $\sigma_{0.2}/E_0$. Gardner and Nethercot (2004) found two drawbacks to using the ultimate stress in the second expression for the modified Ramberg-Osgood expression. Under compression, the absence of the necking phenomenon in materials means that the ultimate stress can no longer be achieved, hence making the model invalid. Also, it has been shown that results from the strains obtained for the normal range of structural behaviour are much smaller than the ultimate strains and thus greater accuracy can be achieved by anchoring the second stage of the Ramberg-Osgood curve to the 1.0% proof stress $\sigma_{1.0}$. Gardner and Ashraf (2006) presented the final version of this proposal as:

$$\varepsilon = \frac{\sigma - \sigma_{0.2}}{E_{0.2}} + \left[\left(\varepsilon_{1.0} - \varepsilon_{0.2} \right) - \frac{\sigma_{1.0} - \sigma_{0.2}}{E_{0.2}} \right] \left(\frac{\sigma - \sigma_{0.2}}{\sigma_{1.0} - \sigma_{0.2}} \right)^{n'_{0.2,1.0}} + \varepsilon_{0.2} \quad (\sigma_{0.2} < \sigma < \sigma_u) \qquad (2.11)$$

where $n'_{0.2,1.0}$ is the strain hardening exponent for a curve passing through $\sigma_{0.2}$ and $\sigma_{1.0}$. Haidarali (2011) conducted a material model sensitivity study to identify the most suitable stress-strain relationship for cold-formed steel Zed section FE models by comparing load-displacement responses against physical tests by Yu and Schafer (2006). Four cases were considered: (i) the modified two stage Ramberg-Osgood model by Gardner and Ashraf (Equation 2.7 and 2.11), (ii) the basic Ramberg-Osgood (Equation 2.7) followed by linear hardening at a slope of E/50 at $\sigma > \sigma_{0.2}$, (iii) Basic Ramberg-Osgood (Equation 2.7) followed by flat yield plateau at $\sigma > \sigma_{0.2}$, and (iv) Linear elastic behaviour up to $\sigma_{0.2}$ followed by flat yield plateau. While it was discovered that the strain-hardening component had minimal effect on the overall bending resistance, the accuracy against the physical tests was found to be highly influenced by the stress-strain definition up to $\sigma_{0.2}$. Overall, the modified Ramberg-Osgood proposed by Gardner and Ashraf (2006) provided the best agreement. Therefore, the same material model with the same n, $n'_{0.2,1.0}$ values of 20 and 2 respectively has been used for all cold-formed steel FE models in this study. In addition, the chosen material model was extended to allow for the enhanced strength in the corners regions. Based on corner tensile coupon test results discussed in Section 3.2.1.3, an estimated increase in 0.2% proof stress for the corner regions was applied directly to the modified Gardner and Ashraf Ramberg-Osgood material model; Figure 2.2 shows typical calculated stress-strain relationships for cold-formed steel with 5 and 10% additional corner strength.

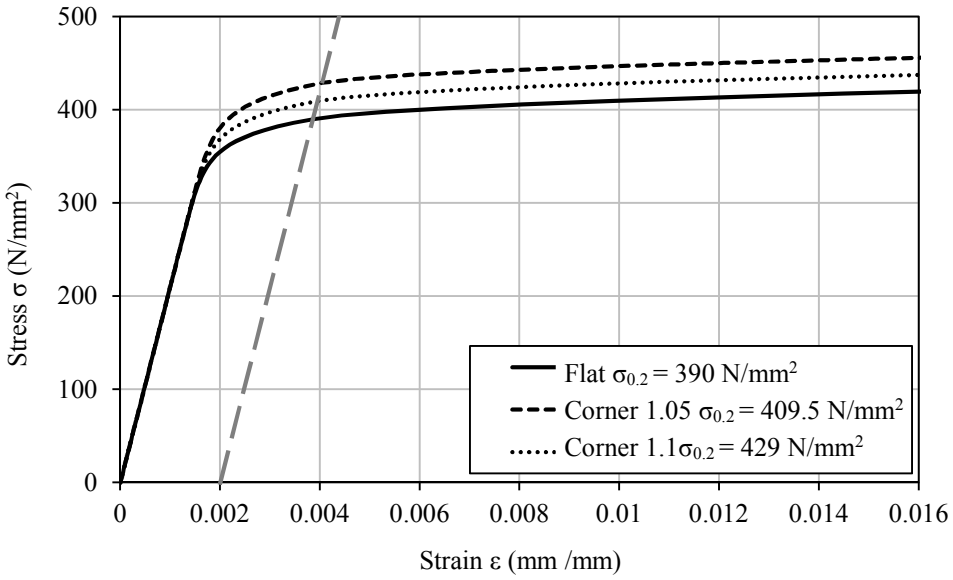


Figure 2.2: *Typical Gardner and Ashraf (2006) modified Ramberg-Osgood stress-strain relationship for the flat and corner regions of cold-formed steel sections*

2.2.3 Residual stresses

While residual stresses in hot-rolled section are mainly the result of uneven cooling, residual stresses in cold-formed steel members are induced primarily through the cold-forming process. The cold-forming process causes plastic deformation at heavily worked regions (corners and intermediate stiffeners) which are not allowed to recover due to the new permanent shape. This causes trapped longitudinal and transverse residual stresses and strains in the section which have the potential to cause premature yielding that influences the load-displacement response and the ultimate capacity of structural elements.

Measuring residual stresses in cold-formed steel sections is generally undertaken using destructive methods such as the conventional saw cutting, electrical discharge machining (EDM) destruction and hole drilling methods. Other nondestructive methods such as x-ray diffraction are also possible and are discussed in more detail by Roy et al. (1994). Weng and Peköz (1990) compared the saw cutting and EDM methods and found minor differences in results between the two techniques. Early tests by Ingvarrson (1975) on a 7.5 mm thick cold-formed steel channel section showed that corner regions of the section had higher magnitudes of residual stresses (up to $0.4f_y$) than the flat portions of

the section. Their findings were broadly verified by Weng and Peköz (1990) and Abdel-Rahman and Sivakumaran (1997).

Residual stresses in cold-formed steel members can be considered as having flexural and membrane components. Schafer and Peköz (1998b) collected surface strain results from 1975–1993 which included studies by: Ingvarrson (1975), Dat and Peköz (1980), Batista and Rodrigues (1992) and Key and Hancock (1993). For the 29 cold-formed steel specimens, Schafer and Peköz (1998b) estimated the average membrane residual stresses for rolled-formed and pressed braked sections were less than $0.1f_y$ while flexural residual stresses were found to be considerably larger ($0.2\text{-}0.5f_y$). Analytical models by Moen et al. (2008), Ingvarrson (1975) and Rondal (1987) indicated that the variation of residual stresses through the thickness is rather complex and nonlinear. Unfortunately, confirming such findings for thin plates is not straightforward as it is often not possible to verify the magnitude of residual stresses for various stages of the fabrication process. Residual stresses are often omitted in numerical models due to a lack of reliable predictive models and the occurrence of greater numerical instabilities. Also, many researchers argue that the influence of bending residual stresses is inherently present in the stress-strain behaviour of coupons cut from cold-formed sections as although the residual stresses are initially released during cutting, they straighten again upon the application of tensile loading (Jandera et al. 2008).

2.3 GEOMETRIC IMPERFECTIONS IN COLD–FORMED STEEL MEMBERS

Early research conducted by Yamaki (1959) and Timoshenko and Gere (1961) has shown that the behaviour and strength of plates and columns in compression are highly influenced by initial geometric imperfections. Imperfections in a member could include local deviations, bowing, warping and twisting. All can have a significant effect on the buckling and post-buckling behaviour of cold-formed steel sections. The influence of initial geometric imperfections on the ultimate strength is governed by their shape, distribution and magnitude. Therefore, it is crucial that the three factors are modelled accurately. An elastic buckling analysis to produce eigenmodes to use as the shapes of initial geometric imperfections is a common approach. The three most common modes of buckling in cold-formed steel beams are: (i) local buckling, (ii) distortional buckling and

(iii) lateral torsional buckling. The half-wavelength for the three modes, along with their corresponding buckling shapes are shown in Figure 2.3. The minima in Figure 2.3 represent the lowest load at which a particular buckling mode occurs. It is often the case that an eigenmode produced through FE analysis will contain a combination of buckling modes, with various numbers of half-wavelengths. Finite strip analysis enables the pure buckling models (see Figure 2.3) to be isolated.

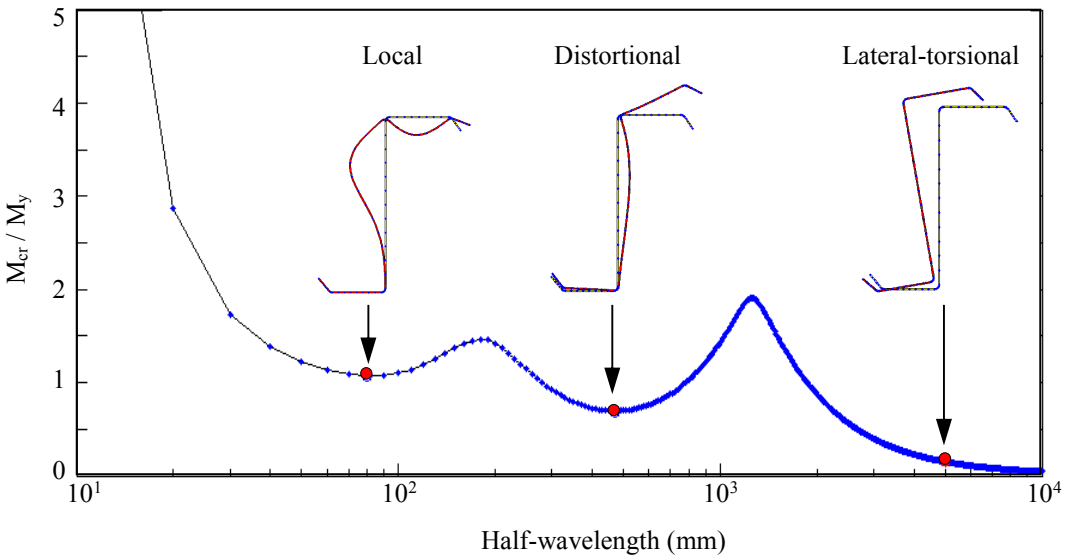


Figure 2.3: *Typical finite strip analysis results, showing the half-wavelengths for local, distortional and lateral-torsional buckling modes*

Research to determine suitable maximum geometric imperfections has been undertaken by numerous researchers such as Dawson and Walker (1972), Dat and Peköz (1980) and Mulligan and Peköz (1984). Many other researchers, including Moreyra and Peköz (1994b) and Schafer and Peköz (1998b) adopted a multiple of the thickness to represent the imperfection magnitude. Chou et al. (2000) performed finite element analysis on cold-formed lipped channel hat section columns with different imperfection amplitudes. The analyses demonstrated that a common multiplier of the plate thickness is not ideal for general application to all plates. Schafer and Peköz (1998b) classified imperfections in lipped channels into two categories (Figure 2.4) and outlined several rules of thumb to estimate the magnitude of each type of imperfection (Equation 2.12-2.14). Type 1 imperfections are defined as the maximum out-of-plane imperfection in a stiffened element (web or flange) and Type 2 imperfection are the maximum deviation of the lip/flange junction from straightness.

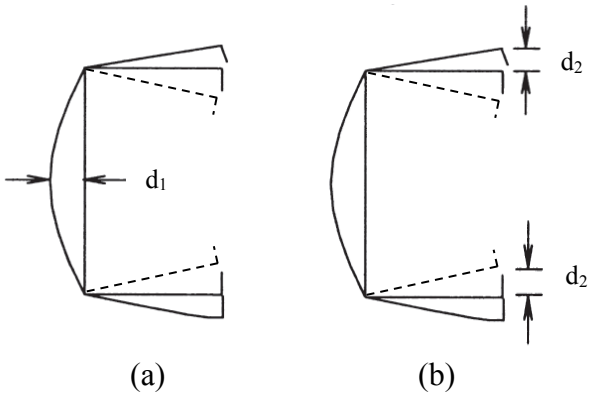


Figure 2.4: *Definition of geometric imperfections (Schafer and Peköz, 1998b) (a) Type 1: Local imperfections and (b) Type 2: Distortional imperfections*

Type 1: local imperfections

- $d_1 \approx 0.006w$ (2.12)

- $d_1 \approx 6te^{-2t}$ (2.13)

Type 2: distortional imperfections

- $d_2 = t$ (2.14)

where d_1 and d_2 are imperfection amplitude shown in Figure 2.4, w is the plate width and t is the thickness of the plate. The rule of thumb calculations for Type 1 and Type 2 imperfections are valid when $w/t < 200$ and the thickness of the plate is no more than 3 mm. Schafer and Peköz (1998b) identified that the rules of thumb do not cover the whole characterization of imperfection magnitudes. An alternative statistical approach was proposed in which the initial geometric imperfections are actually measured and the maximum imperfection magnitude is treated as a random variable. Numerically estimated cumulative distribution function (CDF) values were computed which indicated the magnitude of the imperfection based on a confidence percentage. Within their results, a 95% confidence [$P(\Delta<d) = 0.95$] corresponds to 1.35 and 3.44 for d_1/t and d_2/t respectively. Other general probabilistic approaches are discussed in Schafer et al. (1998). Haidarali (2011) conducted an imperfection magnitude study and showed that FE models with $P(\Delta < d) = 0.5$ ($d_1 = 0.34t$ and $d_2 = 0.94t$) imperfection magnitudes best agreed with the physical test responses by Yu and Schafer (2006). In addition, it was found that for every 25% increase in confidence (P = 0.25, 0.5 or 0.75), the predicted ultimate bending capacity altered by approximately 4%. This suggests that bending capacity is not highly

sensitive to the imperfection magnitude alone, for small variation in d_1 and d_2. For the present study, the imperfection magnitudes are based on representative measurements reported by Boutell and Hui (2013), which recommended imperfection magnitudes of 0.099t and 0.299t for d_1 and d_2. These values were validated by conducting a geometrical imperfection sensitivity study, which is discussed in Chapter 3.

2.3.1 Distribution and magnitudes of initial imperfections

Elastic buckling analysis to generate elastic buckling modes (eigenmodes) is the most common technique to define the shape and distribution of initial imperfections. Moreyra and Peköz (1994b) and Wang and Zhang (2009) suggested the lowest eigenmode is often selected as the shape of the initial geometry of a structure. Choosing the correct eigenmode could prove to be challenging because it is not trivial to find the critical buckling mode into which the system will be triggered. Kwon and Hancock (1991, 1993) found the effects on the behaviour of thin-walled sections to be more sensitive to the mode of imperfections rather than the amplitude of the imperfections. Yu and Schafer (2007) have shown that CUFSM (Schafer 2006) can be used to obtain the initial imperfection shapes for cold-formed steel members, CUFSM being a useful open source program that utilises the finite strip method (FSM). The adopted semi-analytical FSM provides solutions for thin walled cross-section stability and an accurate identification of the buckling modes, i.e. it is possible to identify and isolate local and distortional buckling shape solutions. The technical background, together with illustrative examples for the stability analysis of cold-formed sections, using a conventional and constrained finite strip method is presented by Schafer and Ádány (2006). Yu and Schafer (2007) and Haidarali and Nethercot (2011a) applied geometric imperfections to their FE models by scaling individual local and distortional buckling modes obtained from CUFSM with imperfection magnitudes outlined by Schafer and Peköz (1998b). Borges et al. (2007) and Borges and Camotim (2010) investigated geometrical local and distortional imperfection mode interaction for cold-formed steel lipped channel sections subjected to major axis bending by varying linear combinations of normalised pure local and distortional buckling modes. To enforce a family of 'acceptable' combinations of imperfection shapes, the local and distortional imperfection amplitudes $C_{L,0}$ and $C_{D,0}$ were normalised with their maximum corresponding imperfection amplitude and satisfying the condition shown in Equation 2.15. The combinations can be best represented in the $C_{L,0}$ -

$C_{D,0}$ plane, where the location on circle represents the corresponding amplitude for each mode, as illustrated in Figure 2.5(a). An angle θ on the $C_{L,0}$-$C_{D,0}$ plane, measuring anticlockwise and starting from the horizontal $C_{D,0}$ axis can identify the direction and magnitude of the corresponding local and distortional imperfections (see Figure 2.5(b)). It was assumed that the local and distortional buckling modes exhibit an odd number of half-waves so that the superimposed maximum displacements always occurred at the midspan. Borges et al. (2007) and Borges and Camotim (2010) suggested that the imperfection spectrum can be overly conservative if the maximum local and distortional buckling imperfection amplitudes were both unscaled. Providing the local and distortional buckling imperfections amplitudes are independent of each other, scaling both imperfection amplitudes so that it satisfies Equation 2.15 may yield more accurate results.

$$\left(C_{D,0}\right)^2 + \left(C_{L,0}\right)^2 = 1 \tag{2.15}$$

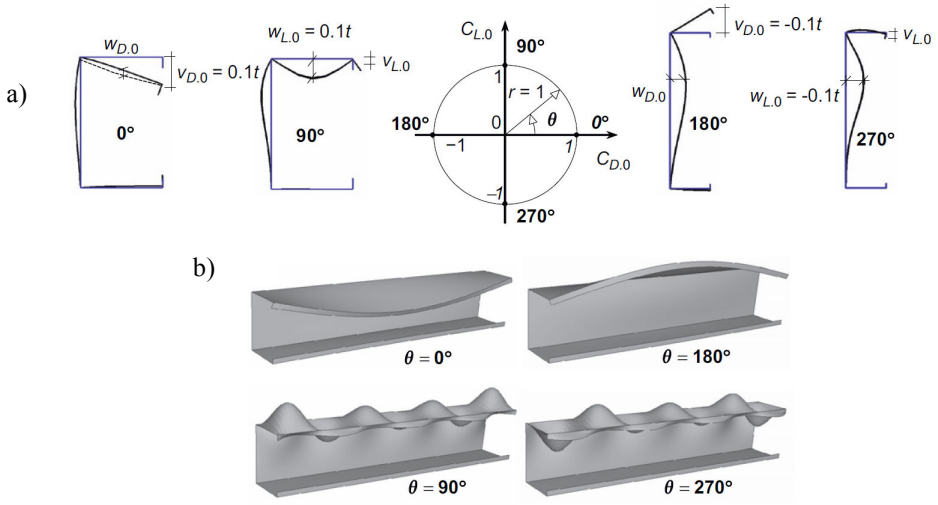


Figure 2.5: *(a) Initial geometrical imperfection representation in the $C_{D,0}$-$C_{L,0}$ plane and (b) 4 FE models imperfection shapes (θ = 0°, 90°, 180°, 270°) by Borges and Camotim (2010)*

While there are many methods for applying geometrical imperfection for thin-walled FE models, a similar method to that of Yu and Schafer (2007) and Haidarali and Nethercot (2011a) has been adopted in the present study. The finite strip software CUFSM (Schafer 2006) has been used to obtain the local and distortional buckling shapes, but scaled with imperfection magnitudes outlined earlier. The exact sinusoidal

longitudinal distribution details were further investigated in a geometrical sensitivity study detailed in Section 3.2.6.1.

2.4 REVIEW OF DESIGN CODES AND STANDARDS FOR COLD-FORMED STEEL SECTIONS

The high width-to-thickness ratios of the individual elements of cold-formed sections make them prone to buckling under compression at stress levels less than their yield strength. Determining the local buckling behaviour strength for such sections is of great importance in evaluating their ultimate capacity. Cold-formed steel members tend to achieve additional load carrying capacity after initial buckling has occurred, thus ultimate capacity normally allows for post-buckling strength. In order to optimise the structural efficiency, intermediate and edge stiffeners of sufficient dimensions are often incorporated in to the geometry of cold-formed steel sections. Furthermore, the open nature of cold-formed steel purlins makes the shape weak to twisting which makes their torsional-flexural response in columns and lateral-torsional buckling in beams an influential failure mode. There are several codes of practice for the design of cold-formed steel structures and these are discussed in the subsequent sections.

2.4.1 Eurocode 3: Design of Steel Structures: Part 1-3

The European code for the structural use of steelwork, Eurocode 3, comprises two main parts for the design of cold-formed steel members: (i) Part 1-1 (BS EN 1993-1-1:2005): General Rules and Rules for Buildings and (ii) Part 1-3 (BS EN 1993-1-3:2006): General Rules–Supplementary Rules for Cold-Formed Members and Sheeting. Eurocode 3 presents a limit state design method in which partial safety factors are applied to the resistance of cross-sections and members γ_M and to the applied external loading (permanent loads γ_G and variable loads γ_Q). The European code covers the design of cold-formed steel products with basic yield strength f_{yb} up to 700 N/mm^2 with core thickness t_{cor} not exceeding 15 mm for sheeting and members, and 4 mm for connections. The European code discretises four different classes of steel cross-sections based on their local buckling resistance: (i) ductile (class 1), (ii) compact (class 2), (iii) semi-compact (class 3) and (iv) slender (class 4). Cold-formed steel sections are generally slender. For such sections, the effective width concept is adopted in Eurocode 3 Part 1-5: Plated Structural Elements (BS EN 1993-1-5:2005) to evaluate the post-buckling strength of cold-formed

steel sections. To account for the distortional buckling of elements with edge and intermediate stiffeners, effective regions of the flange and stiffener are treated as a compression member with continuous partial restraint with spring stiffness K. Guidelines for purlins and liner trays restrained by sheeting are provided in detail. The design of 2-span continuous purlins subjected to gravity and uplift loading is covered by limiting the maximum stress in the cross-section (Clause 10.1.4.1 of EC3 Part 1-3). For gravity loading, this includes a combination of bending and axial force, whereas for uplift load, an additional lateral bending moment must also be considered to the unrestrained compression flange. Special shear and web-crippling checks which include the additional support from cleats to prevent distortion are detailed. To account for torsion, lateral bending and cross-sectional distortion when subjected to uplift, the free flange is modelled as a beam on an elastic foundation with a lateral spring K. Further details for considering lateral torsional buckling using EC3 are discussed in more detail in Section 4.4.2. Eurocode 3 1-3 also includes other design guidelines for cold-formed steel systems including: (i) stressed skin design, (ii) trapezoidal sheeting, (iii) serviceability and (iv) joint design.

2.4.2 AISI Specification for Design of Cold-Formed Steel Structural Members

The first edition of the American Iron and Steel Institute (AISI) Specification for the Design of Cold-Formed Steel Members was released in 1946 and was based largely on research on beams, studs, connections and roof decks by Prof. G Winter between 1939 and 1946. This is where the concept of "effective width" of stiffened elements was first introduced to cold-formed steel sections and remained unchanged until the revision in 1986. The 1996 edition includes both allowable stress design (ASD) and load and resistance factor design (LRFD) in one document. The specification allows the use of cold-formed steel material yield strength up to 553 N/mm^2. The first edition of the North American Specification for the Design of Cold-Formed Steel Structural Members (NAS, 2001) was jointly developed by the AISI Committee on Specifications, the Canadian Standards Association (CSA) Technical Committee on Cold-Formed Steel Structural Members and the Camara Nacional de la Industria del Hierro y del Acero (CANACERO); the NAS (2001) superseded the AISI (1996) Specification and the CSA (1994) Specification and is intended for use in Canada, Mexico and the United States. The ASD and LRFD methods are adopted in the Unites States and Mexico, while the limit state

design (LSD) method is used in Canada. In 2004, AISI issued further revisions and additions in a supplement to NAS (2001): North American Specification for the Design of Cold-Formed Steel Structural Members, 2001 (2004). The supplement introduced the Direct Strength Method (DSM) for determining the nominal axial strength of columns and flexural strength of beams for cold-formed steel structural members. The DSM provides expressions to determine the strength of cold-formed elements as a function of elastic critical loads for local, distortional and global buckling, which can be determined numerically. Major changes to the latest revision of NAS (2001), referred to as AISI S100 (2007) in the USA and CSA S136 in Canada, incorporated second-order analysis of structural systems and new guidance on distortional buckling for C and Zed-sections for flexural and compression members.

2.4.3 Cold-Formed Steel Structure Code–AS/NZS 4600:2005

The Australian / New Zealand Standard is very similar to the AISI Specification. Section 1–5 from AS/NZS 4600 (2005) consists of similar guidance to Sections A to E of the AISI Specification. Similar to EC3, AS/NZ 4600 is only available in the limit state design (LSD) format. Furthermore, AS/NZ 4600 only permits the use of cold-formed steel material with design strength up 550 N/mm^2 and thickness of no less than 0.9 mm.

2.5 EXISTING INVESTIGATIONS INTO THE FLEXURAL BEHAVIOUR OF COLD -FORMED STEEL SECTIONS

Early studies of the buckling behaviour of thin steel plates include those by Von Karman et al. (1932), where the effective width concept was proposed for the prediction of ultimate plate capacity $F_u = b_p f_y$; in which:

$$\frac{b_p}{w_p} = \sqrt{\frac{f_{ol}}{f_y}} \tag{2.16}$$

where:

$$f_{ol} = \frac{k_p \pi^2 E}{12\left(1-\upsilon^2\right)}\left(\frac{t_p}{w_p}\right)^2 \tag{2.17}$$

where t_p, w_p and b_p are the plate thickness, actual and effective width of the plate respectively, k_p is the plate buckling factor, f_y is the material yield stress, E is the modulus

of elasticity and ν is the Poisson's ratio. Figure 2.6 shows the effective stress distribution in stiffened (internal) and unstiffened (outstand) buckled plates.

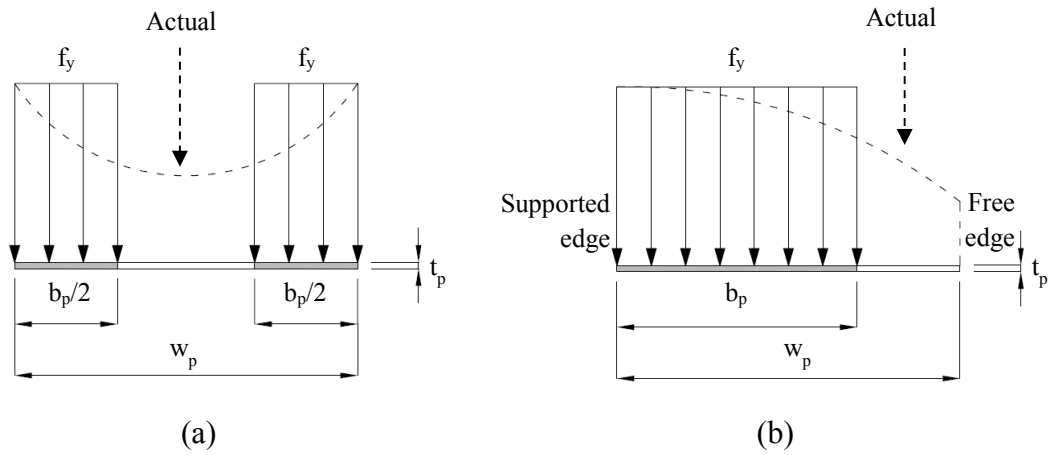


Figure 2.6: *Stress distribution in (a) stiffened and (b) unstiffened plates*

Von Karman's formula was later modified by Winter (1947) for cold-formed steel elements. As cold-formed steel members became more common for additional structural applications, the amount of literature for the buckling behaviour of cold-formed steel members increased. Relevant experimental and numerical investigations for this study have been identified in the subsequent sections.

2.5.1 Experimental investigations

Investigations conducted by experimental means are an important means of investigating the flexural behaviour of cold-formed steel members. It allows the researcher to directly investigate the buckling behaviour of cold-formed members. Unfortunately, due to the large variety of cold-formed steel shapes, dimensions and material grades, it is not economical and is very time consuming to test every possible combination. The inelastic behaviour of cold-formed sections subjected to compression has been studied by several researchers, but in comparison, fewer investigations have been carried out into the behaviour of cold-formed sections subjected to bending. The prediction of the ultimate bending capacity of cold-formed steel sections is complicated due to local, distortional, combined local/distortional buckling and potential lateral torsional buckling if the section is not adequately laterally restrained. Early studies on laterally braced beams with cold-formed steel lipped channel and Zed sections were conducted by Winter (1947), LaBoube and Yu (1978), Desmond et al. (1978, 1981) and

Elhouar and Murray (1985). Further details on single span bare sections tests from 1980 onwards are discussed in Section 2.5.1.1, whilst lapped connections, sleeved connections and multi-span testing arrangements are discussed in Section 2.5.1.2, 2.5.1.3 and 2.5.1.4 respectively.

2.5.1.1 Single span cold-formed steel bare section tests

Cold-formed steel members are generally subjected to uniformly distributed loads. Therefore, pure bending of cold-formed sections is an idealised case which rarely occurs in reality. Nevertheless, many researchers conduct pure bending tests by adopting a 4-point loading configuration, with uniform moment in the central region of the beam. Table 2.1 summarises recent single span experimental studies for cold-formed steel members subjected to bending. The highlighted studies were then used to validate the FE models, as discussed in Chapter 3.

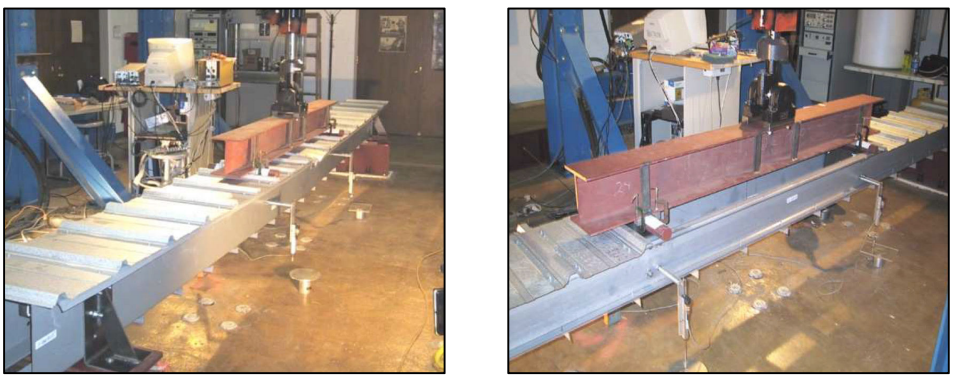
Table 2.1: *Summary of single bare span bending experimental studies*

Reference	No. of tests conducted	Testing arrangement	Section type
Bryan and Davies (1979, 1980a)* Bryan and Deakin (1989)* Deakin (1991a, 1991b)*	7	3-point bending	Zeta
Willis and Wallace (1990)	4	Pure bending	Zed/Channel
Davies and Deakin (1992)*	5	3-point bending	Zeta II
Ellifritt et al. (1992)	23	4-point pure bending	Zed/Channel
Moreyra and Peköz (1994a)	9	4-point pure bending	Channel
Papazian et al. (1994)	24	UDL- vacuum chamber	Hat
Laine and Tuomala (1999)	72	3-point bending	Zed, Zeta, Channel and Hat
Yu and Schafer (2003)*	24	4-point pure bending	Zed/Channel
Yu and Schafer (2006)	24	4-point pure bending	Zed/Channel
Nguyen et al. (2006)	30	4-point pure bending	Zed
Wang and Zhang (2009)*	6 6	4-point pure bending 3-point bending	Channel
Maduliat et al. (2012)	42	Monash pure bending**	Channel
Pham and Hancock (2013)	24	4-point pure bending	Channel SupaCee channel

* Used for validating FE models – See Chapter 3 for more details

** Further details of Monash test rig are provided in Cimpoeru (1992)

Yu and Schafer (2003) investigated the role of the web slenderness on local buckling by conducting physical four-point bending tests on various lipped C and Zed sections, as shown in Figure 2.7(a). Distortional and lateral-torsional buckling were restricted by attaching a through fastened panel on the compression flange. It was found that the location of the panel-to-purlin fastener can govern the lowest mode of buckling, which was either local or distortional buckling. The test results were compared against several design methods including: AISI (1996), CSA (1994), NAS (2001) and the Direct Strength Method (DSM). The ultimate design capacity predictions from AISI (1996), CSA (1994) and NAS (2001) were found to adequate for slender sections, but conservative for non-slender sections. Overall, the Direct Strength Method (DSM) was shown to have the best agreement with the test results for both slender and non-slender sections. Yu and Schafer (2006) investigated the effects of distortional buckling on the same cold-formed sections as Yu and Schafer (2003), as shown in Figure 2.7(b).To allow distortional buckling, the panelling located at the middle portion of the beam was removed to allow distortional half-wavelengths to develop. It was observed that distortional buckling occurred before local buckling with an average loss of 17%, compared in bending capacity to its local buckling test equivalent. Over predictions in the bending capacity by AISI (2001) and CSA (1994) Specifications for distortional buckling were illustrated, whereas Eurocode EC3-1-3 (2006) was found to be conservative.



(a) (b)

Figure 2.7: *Four-point bending tests carried out by (a) Yu and Schafer (2003) and (b) Yu and Schafer (2006)*

Wang and Zhang (2009) conducted both numerical and experimental investigations of the bending strength of cold-formed steel C-sections with various edge stiffeners. The purpose of their study was to investigate the interaction of local and

distortional buckling by conducting 6 pure bending (4-point) and 6 moment gradient (3-point) bending tests experimentally and numerically. The FE models were found to provide good agreement with the experiments. The overall moment capacity of the sections was found to be sensitive to the angle of the lip in both the FE models and the tests. Sections with upright edge stiffeners showed an 11% increase in capacity compared to the equivalent 45° inclined lipped sections, but the differences diminished as the lip length increased. For the pure bending tests, local bucking was observed near the loading point rather than the midspan and several tests exhibited distortional modes and mixed modes. The specimens subjected to 3-point bending that failed by distortional buckling exhibited an average 17% increase in moment capacity compared with the pure bending tests. For tests that failed by local buckling or mixed modes, the increase in capacity reduced to a marginal 5%. The failure mode was found to be the main reason for moment capacity increase under a moment gradient compared to pure bending. It is well known that local buckling half-wavelengths are shorter than distortional buckling half-wavelengths. Under a moment gradient, the moment varies little within a shorter half-wavelength of local buckling, but the moment varies considerably over the longer distortional half-wavelengths. Therefore, if the specimens fail by distortional buckling the bending capacity is more sensitive to the presence or not of a moment gradient.

2.5.1.2 Lapped connections between cold-formed steel members

To maintain continuity in multi-span purlin systems, a common cold-formed steel purlin arrangement is to overlap the sections over interior supports. A limited preliminary study by Robertson and Kurt (1986) indicated that the lapping process enhances the load capacity of the beam provided the lap joints were bolted tightly. Ghosn and Sinno (1995 and 1996) and Ho and Chung (2004) conducted a total number of 54 single span lapped tests on cold-formed steel Zed sections, covering web depth-to-thickness ratios (h/t) from 79 to 131 and lap-to-span lengths of 0.25 to 1.0. Theoretical deflection equations were later derived and validated against the experimental data of Ghosn (2002). Ghosn and Sinno (1995) concluded that the lapping process significantly enhanced the load carrying capacity for lap lengths less than half the span length L but additional sleeve lengths beyond 0.5L gave minimal additional load-carrying capacity. Ho and Chung (2004) suggested a minimum lap length to section depth ratio of 2.0 and 4.0 for ‘full strength’ and ‘full stiffness’ laps, respectively. Zhang and Tong (2008) conducted alternative 3-

point bending tests with one half being simply supported and one half being cantilevered and loaded at the free end. This allowed the ratio of moments between the simply supported span and the cantilever to be varied by modifying the cantilever length. From the three most recent experimental studies, it was observed that the majority of lapped connections failed in a sudden local buckling mode at the compressive flange near the end of the lapped region.

2.5.1.3 Sleeved connections between cold-formed steel members

Sleeved connections are alternative bolted joint connections to lapped arrangements. The sleeve connection is made by using an additional short cold-formed steel member that laps the two purlin ends and is bolted through the web. Unlike the studies on overlap joints discussed earlier, research on sleeved joints for cold-formed steel purlins is much more limited. Some of the earliest reported physical sleeve tests were conducted in Salford University in a study between 1980 and 1997 presented in a collection of reports: Bryan and Davies (1980b), Bryan and Deakin (1989), Leach (1990), Deakin (1991a, 1991b), Davies and Deakin (1992) and Deakin and Melbourne (1997). Of the 7 reports, 3 types of sleeve tests were conducted: (i) single span moment gradient sleeved tests ranging from spans of 2.2 m to 4 m, (ii) full 2-span sleeved beam tests subjected to gravity UDL and (iii) full 2-span sleeved beam tests subjected to uplift UDL. The results were used to form the basis of load tables. Further details on sleeve tests conducted in Salford University are given in Chapter 5. More recently, Gutierrez et al. (2011) and Ye et al. (2013) conducted a total of 28 3-point tests to investigate the flexural rigidity of cold-formed steel sleeved connections. Both studies used FE models, which were validated against their experimental results. In both studies, the load-displacement response was characterised into a series of segments; Gutierrez et al. (2011) characterised the response using three linear segments: (i) initial stiffness prior to bolt slippage, (ii) partial stiffness of the connection due to bearing of the bolts against the bolt holes and (iii) sleeve flanges yielding. Ye et al. (2013) divided the nonlinear load-deflection curves into 4 segments. An additional intermediate stage between (i) and (ii) was introduced to represent slippage of the bolts prior to bearing. The overall load-carrying capacity was found to be insensitive to the degree of bolt slip. Their findings on partial stiffness and strength of sleeve connections for systems with small lap length to depth ratios were

similar to the experimental findings on lapped joints between cold-formed steel Zed sections of Ho and Chung (2006b).

2.5.1.4 Multi-span cold-formed steel purlins systems

Despite the wide use of cold-formed roof systems in the 1970s and 80s, available literature on the physical testing of multi-span cold-formed purlins systems is relativity scarce compared to single span tests. Continuous bare and sleeved 2-span tests were conducted at the University of Salford between 1979 and 1991 for both gravity and uplift loading to provide ultimate load data for future load tables. These are reported by Deakin et al. (1979), Davies (1979), Bryan and Davies (1979, 1980a), Bryan and Deakin (1989), Leach (1990) and Deakin (1991a, 1991b). Table 2.2 summarises the readily available reported experimental studies on the multi-span purlin systems. The highlighted 2-span continuous beam tests from Table 2.2 were used for the FE model validation in Chapter 3, while the highlighted 2-span continuous beam sleeved tests were used for the FE model validation and discussed in Chapter 5.

Early work on multi-span cold-formed steel purlin lapped systems was reported by LaBoube et al. (1988) and Hancock et al. (1990). LaBoube et al. (1988) conducted 19 3-span lapped beam tests subjected to uniformly distributed uplift load by using a pressurising test chamber. Of the 19 tests, 14 were Zed sections, whilst the remaining 5 were lipped channel sections. The results confirmed that lapped lengths of one and half times the section depth were sufficient to achieve full continuity, as previously suggested by Robertson and Kurt (1986). Hancock et al. (1990) conducted an extensive test program on purlin-sheeting systems comprising of single, two and three spans Zed and channel sections subjected to uplift loading by using a vacuum chamber. The purlins were supported by 0, 1 or 2 braces per span. Results coincided with recommendations presented by LaBoube et al. (1988) where unbraced system load-carrying capacities were roughly 70% of those of braced systems. This was found to be caused by the excessive twisting in the case of the unbraced systems. The position of the screw fasteners relative to the width of flange was found to be influential in the torsional resistance and subsequent ultimate load carrying capacity.

Willis and Wallace (1990) conducted eight 3-span bare purlin tests on channel and Zed sections. The obtained results suggested that the 1986 revision of the AISI

Specification gave unconservative predictions for purlins with long lip lengths (lip lengths greater than 2.06 mm), whilst sections made up of short lip lengths of less than 2.06 mm gave higher results than predicted ones. A limitation on the edge stiffener width-to-flange ratio of 0.46 was suggested. Chung and St Quinton (1996) conducted five 2-span tests to determine whether certain cladding rail systems were adequate to provide full lateral restraint. In combination with 12 single span tests, it was found that always assuming full lateral restraint was unconservative. Increased thickness of the insulation layers yielded insufficient restraint to the purlin which can lead to lateral torsional buckling in the span.

Table 2.2: *Summary of multi-span bending experimental studies*

Reference	No. of tests conducted	Testing arrangement	Loading arrangement	Section type
Bryan and Davies (1980b)[B] Leach (1990)[B] Bryan and Deakin (1989)[B] Deakin (1991a, 1991b)[B]	9	Sleeved 2-span gravity	4p	Zeta IB
Bryan and Deakin (1989)[B] Deakin (1991a, 1991b)[B]	10	Sleeved 2-span uplift	4p	Zeta IB
Deakin et al. (1979)[A] Davies (1979)[A] Bryan and Davies (1979, 1980a)[A] Bryan and Deakin (1989)[A] Deakin (1991a, 1991b)[A]	10	Bare 2-span gravity	4p	Zeta IA Zeta IB Zeta IC
Bryan and Davies (1980a)[A] Deakin (1991a, 1991b)[A]	6	Bare 2-span uplift	4p	Zeta IB
LaBoube et al. (1988)	19	Lapped 3-span uplift	UDL[C]	Channel Zed
Hancock et al. (1990)	9 3	Lapped 3-span uplift Lapped 2-span uplift	UDL[C]	Zed
Willis and Wallace (1990)	8	Bare 3-span gravity	UDL[D]	Channel Zed
Chung and Quinton (1996)	5	Bare 2-span gravity	UDL[C]	Zed Sigma
Zhang and Tong (2008)	11	Lapped 2-span gravity	2p	Zed

2p 2 evenly spaced point loads per span
4p 4 evenly spaced point loads per span
A Used for validating bare FE models – See Chapter 3 for more details
B Used for validating sleeved FE models – See Chapter 5 for more details
C Uniform load was applied to all tests by sucking air out of a vacuum chamber
D Uniform load was applied to all tests by symmetrically placing solid concrete blocks directly above the purlins between the ribs of the decking

2.5.2 Numerical investigations

Research using numerical modelling to investigate the buckling response of cold-formed elements has emerged relatively recently. Numerical models allow researchers to investigate the buckling behaviour of cold-formed steel sections without the need to conduct a large expensive physical test study. Numerical studies for cold-formed steel members include the use of: finite element (FE) modelling, Generalised Beam Theory (GBT) and the Finite Strip Method (FSM). Where this thesis focuses predominantly on research methods using FE modelling, FSM and GBT have also been shown as accurate modelling tools to investigate the local and distortional buckling behaviour of cold-formed steel sections. Bradford and Hancock (1984) developed a nonlinear finite strip analysis of imperfect folded plate assemblies, which offered designers the ability to obtain load-carrying capacities without the need to calculate the effective widths. The FSM has been developed over the years to cover a range of cold-formed steel sections subjected to flexural and/or compression loading by: Schafer and Ádány (2006), Papangelis and Hancock (1994, 2005) and Rhodes (2002). CUFSM (Schafer, 2006) is a readily available freeware program based on the FSM that allow users to calculate the elastic buckling modes and capacities for arbitrary thin-walled sections.

Generalised Beam Theory (GBT) is an extension to conventional engineering beam theory that allows for higher order modes of deformation which involve cross-section distortion. This makes it an ideal method for solving buckling problems in cold-formed sections. One main advantage of GBT over other methods is that it can distinguish the significance of individual buckling modes for a range of loading, e.g. bending and/or axial compression. Early literature describing the principles of GBT with local and global buckling examples for cold-formed steel sections is covered by Schardt (1994), Davies and Leach (1992, 1994) and Davies et al. (1994). More recently, GBT has been further used as a tool to investigate the distortional, lateral torsional and post-buckling behaviour of cold-formed steel sections as presented by Silvestre and Camotim (2004a, 2004b).

In general, numerical studies on cold-formed steel members subjected to compression are more common than the case of bending. Loughlan et al. (2012), Borges Dinis et al. (2007), Dubina and Ungureanu (2002), Telue and Mahendran (2004) and Schafer et al. (2010) showed that FE models can capture the local and/or distortional

buckling behaviour of cold-formed column sections when subjected to axial compression. For bending, Moreyra and Peköz (1994b), Yu and Schafer (2003, 2006) and Wang and Zhang (2009) simulated the local and distortional buckling behaviour for lipped channel and Zed members using FE modelling conducted using ABAQUS. Their FE models were validated against previous experimental tests (Moreyra and Peköz (1994a), Yu and Schafer (2003, 2006) and Wang and Zhang (2009) and showed that the FE method can account for complex geometrical and material nonlinear behaviour as well as the additional rotational restraints offered by sheeting.

More recently, Haidarali and Nethercot (2011a, 2011b) developed FE models of cold-formed steel beams which accounted for geometrical and material nonlinearity for channel and Zed sections. The models were then used to investigate the local and distortional buckling behaviour of cold-formed steel Zed sections with various edge stiffener details. It was found that a transition between local, distortional and local/distortional buckling was observed by varying the lip–to–flange ratio c/b. Deviation of the edge stiffeners by no more than 20° from vertical did not affect its moment capacity, whereas the ultimate load capacity was significantly reduced as the angle decreased further. Results from the FE models were compared against design capacities obtained from Eurocode 3 (EC3). By taking into consideration local and distortional buckling using EC3, the design capacities were found to be, on average, 10% unconservative. An empirical modified buckling factor, which is dependent on the c/b, ratio was proposed to provide suitable improvements to the current EC3 method. Haidarali and Nethercot (2012) extended their work to cover Zed sections with intermediate and edge stiffeners. It was found that the moment capacity was more dependent upon its edge stiffener characteristic than the intermediate stiffener. The location of the intermediate stiffener was varied along the flange to check against design calculations using Eurocode 3 (EC3). The design loads were found to be unconservative when the intermediate stiffener was closer to the lip/flange junction. It was concluded that modifications to the Eurocode design guidelines for distortional buckling of edge stiffeners when an intermediate stiffener is also present, were needed.

2.6 CONCLUDING REMARKS

The increased popularity in using cold-formed steel products for purlin systems has seen a growth in the amount of research on the flexural behaviour of cold-formed steel purlins. Cold-formed steel permits a vast array of purlin shapes, system arrangements, connection details and steel grades, which means that the available research to cover all of these combinations is limited in some cases. For the physical testing studies reviewed in this chapter, most of these investigations evaluate currently available purlin systems, principally in terms of ultimate load-carry capacity, with comparisons to either: (i) pre-testing design assumptions (e.g. assuming full restraint or full rigidity for bolted connections) or (ii) against relevant design calculations. The review of literature in this chapter has identified that even though there is enough full scale testing data to evaluate the design capacity for the more common section types and arrangements, limited research on moment redistribution in multi-span span purlin systems exists. The lack of research in this field to cover the vastly growing portfolio of cold-formed steel sections has yet to be attained. Consequently, international standards for this area have not acknowledged the use of moment redistribution directly. The scope of the present study is to investigate the moment redistribution behaviour of continuous cold-formed steel purlin systems to enable the development of appropriate and simple design equations, which can be easily adapted to a regular full plastic design approach more commonly used in hot-rolled steel.

CHAPTER 3

NUMERICAL MODELLING – BARE SECTIONS

3.1. INTRODUCTION

Traditionally, conducting physical experiments has been the most straightforward way of developing an understanding of the structural behaviour of cold-formed steel members. Unfortunately, full-scale experimental studies tend to be costly and time consuming. With growing computational speed over the past few decades, finite element (FE) simulations have been increasingly used for research into cold-formed steel. Numerical simulations can not only capture various sources of nonlinear behaviour: large deformations, plasticity and contact compatibility, but can also provide additional information such as stresses and strains that would be more challenging to obtain from physical tests. ABAQUS (2010) was the chosen finite element (FE) software package for this study due to its widespread use, track record in solving similar problems and ability to find unstable equilibrium paths for nonlinear problems, such as those studied herein. In this chapter, finite element modelling of bare cold-formed steel sections for single span and 2-span systems is discussed in detail, and validation against the results of physical testing obtained from a range of sources is described.

3.2. FINITE ELEMENT MODELLING PARAMETERS

3.2.1. Material modelling

Prescribing an accurate representation of the material behaviour for FE analyses plays a significant role in the accuracy and validity of the results. Failure to capture such behaviour adequately would provide inherently inaccurate results.

Cold-formed steel members do not exhibit the same stress-strain characteristics as hot-rolled steel sections. The latter exhibits a distinct sharp yield point followed by a plateau and some strain hardening at large strains, whereas cold-formed steel exhibits a more gradual and rounded yielding response followed by a considerable amount of strain hardening at relatively low strains. To define the yield stress for materials with gradual yielding behaviour, the 0.2% offset method is often used. The yield point is defined by the intercept of an imaginary line with gradient equal to the elastic Young's Modulus E at the 0.2% strain; the stress value at the intercept is defined as the 0.2% proof stress $\sigma_{0.2}$. Figure 3.1 shows a typical stress-strain curve for cold-formed steel. Due to the distinct differences between hot-rolled and cold-formed steel stress-strain behaviour, adopting an elastic-perfectly plastic material model, which is commonly used for hot-rolled sections, will lead to inaccurate results. Therefore, a gradual yielding material model is needed to exploit the special material behaviour.

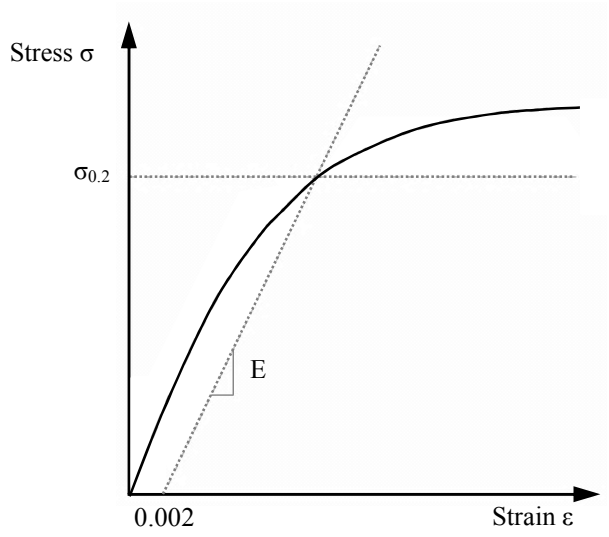


Figure 3.1: *Typical stress-strain responses for cold-formed steel*

3.2.1.1. Proposed material model for FE models

The original Ramberg-Osgood expressions suggested by Ramberg and Osgood (1943) were proposed to represent the stress-strain behaviour of aluminium. The expressions were later investigated for other gradual yielding materials by several researchers including: Hill (1944), Mirambell and Real (2000), Rasmussen (2003) and Gardner and Ashraf (2006).

Haidarali (2011) conducted a material model sensitivity study to find an appropriate stress-strain relationship for cold-formed steel by comparing numerical results using four different material models against the physical tests of Yu (2005). Of the four models considered, the strain hardening part of the stress-strain curve was found to have no significant effect on the cross-sectional bending resistance, whereas the stress-strain curve up to $\sigma_{0.2}$ was found to be influential.

Based on Haidarali's (2011) sensitivity study, the two-stage modified Ramberg-Osgood expressions proposed by Gardner and Ashraf (2006), as given by Equation 3.1 and 3.2, were chosen throughout this thesis since they best capture the yielding behaviour of cold-formed steel. The material model consists of two different expressions: the original Ramberg-Osgood expression for stresses up to the 0.2% proof stress $\sigma_{0.2}$, and a second curve from $\sigma_{0.2}$, passing through the 1.0% proof stress $\sigma_{1.0}$ and up to the ultimate tensile stress σ_u. The 0.2% proof stress acts as a new origin for the second stage of the modified Ramberg-Osgood formula, and ensures that continuity is maintained at the transition point between the two expressions.

$$\varepsilon = \frac{\sigma}{E} + 0.002\left(\frac{\sigma}{\sigma_{0.2}}\right)^{n} \qquad ; \sigma \leq \sigma_{0.2} \qquad (3.1)$$

$$\varepsilon = \frac{\sigma - \sigma_{0.2}}{E_{0.2}} + \left(\varepsilon_{1.0} - \varepsilon_{0.2} - \frac{\sigma_{1.0} - \sigma_{0.2}}{E_{0.2}}\right)\left(\frac{\sigma - \sigma_{0.2}}{\sigma_{1.0} - \sigma_{0.2}}\right)^{n'_{0.2,1.0}} + \varepsilon_{0.2} \qquad ; \sigma_{0.2} < \sigma \leq \sigma_u \qquad (3.2)$$

where σ and ε are the engineering stress and strain respectively, E is the initial Young's modulus of the material, $\varepsilon_{0.2}$ and $\varepsilon_{1.0}$ are the total strain at the 0.2% and 1.0% proof stresses and n and $n'_{0.2,1.0}$ determines the sharpness of the knee of the stress-strain curve. $E_{0.2}$ is the tangent modulus of the stress-strain curve at the 0.2% proof stress.

Knowing that large inelastic strains are expected to occur in the modelling of cold-formed steel sections, engineering stresses σ and engineering strains ε were converted into corresponding true stress (Cauchy Stress) σ_{true} and logarithmic plastic strains ε_{true}^{pl} from the following equations:

$$\sigma_{true} = \sigma(1+\varepsilon) \tag{3.3}$$

$$\varepsilon_{true}^{pl} = \ln(1+\varepsilon) - \frac{\sigma}{E} \tag{3.4}$$

3.2.1.2. Estimation of 1% proof stress

After identifying that the two-stage modified Ramberg-Osgood model by Gardner and Ashraf (2006) gave best the material model predictions against the stress-strain responses from tensile coupons tests by Yu (2005), Haidarali (2011) conducted further work to obtain the most suitable values for n, $n'_{0.2,1.0}$ and $\sigma_{1.0}$ by comparing input values against tensile coupon results by Yu (2005). It was found that $n'_{0.2,1.0}$ and $\sigma_{1.0}$ varied for different values of 0.2% proof stress $\sigma_{0.2}$; $n'_{0.2,1.0}$ ranged between 1.6 to 2.7 with an average of 2.03, while $\sigma_{1.0}/\sigma_{0.2}$ ratios decreased as $\sigma_{0.2}$ increased (ranging between 1.02 to 1.18 for the values of $\sigma_{0.2}$ considered). The strain hardening exponent n was found to be fairly consistent with values close to 20. By fixing the n' and $n'_{0.2,1.0}$ values to 20 and 2 respectively, the most representative relationship between the $\sigma_{1.0}/\sigma_{0.2}$ and $\sigma_{0.2}$ was identified, as presented in Equation 3.5. Owing to the success of the validation study of Haidarali (2011), the calculated 1% proof stresses from Equation 3.5 and the same constant n and $n'_{0.2,1.0}$ values of 20 and 2 were also adopted throughout this thesis.

$$\frac{\sigma_{1.0}}{\sigma_{0.2}} = 1.8656\sigma_{0.2}^{-0.0948} \tag{3.5}$$

3.2.1.3. Corner enhancements

The cold-forming process affects the mechanical properties of cold-formed steel. Abdel-Rahman and Sivakumaran (1997) completed various tensile coupon tests cut from different locations of cold-rolled lipped channel sections. It was found that the plastic deformation caused from the cold-forming process makes the yield and ultimate strength at the corner regions higher than the flat regions. The increase in strength is accompanied

by a loss in ductility and a disappearance of the yielding plateau. It is therefore important to capture the differing material behaviour for cold-formed steel in the FE models by allowing for corner strength enhancements. The increased yield strength due to the forming process was considered in the FE models by conducting a small sample of tensile coupon tests.

3.2.1.4. Tensile coupon tests

A total of 7 cold-formed steel tensile coupon tests were conducted to investigate the potential increase in yield and ultimate strengths between materials cut from corner and flat regions. Coupons were cut from nominal 1.3 mm and 3 mm rolled lipped C-sections with nominal yield strength of 390 N/mm^2. The tensile coupons tests were conducted using an Instron 8808 with tensile strain rates prior to the 0.2% proof stress of 0.5 mm/min and 3 mm/min beyond the 0.2% proof stress until failure (Figure 3.2). To measure accurately the applied strain, two strain gauges were attached at the middle on either side of each coupon. The axial load readings from the Instron 8802 and the two strain gauges were logged using a Datascan 7220 data acquisition system. For the corner coupons, short steel rods with radii equal to the internal radii of the curved coupons were attached at either ends of the coupon to aid clamping of the coupons during testing.

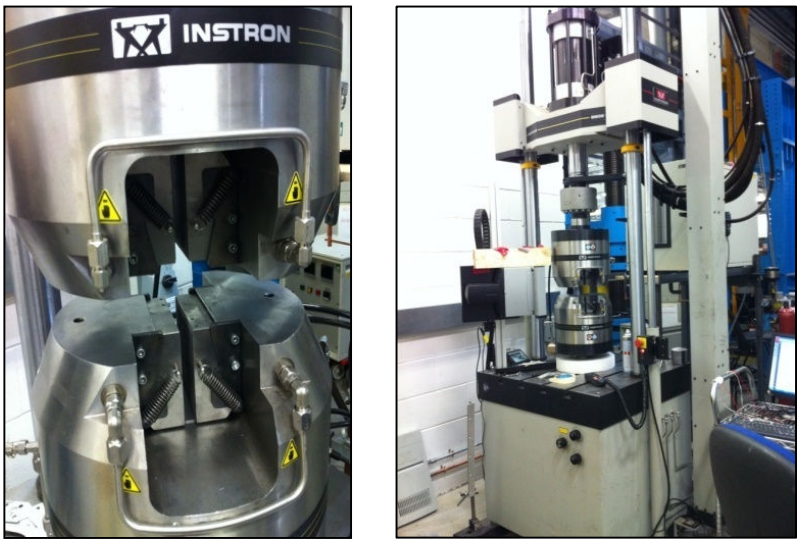


Figure 3.2: *Tensile coupon test using Instron 8802*

Flat coupon cross-sectional areas A, were calculated by multiplying the average measured width and thickness. For the corner coupons, the cross-sectional areas were calculated using Equation 3.6.

$$A = \frac{M_{coupon} \times L_{coupon}}{\delta_{steel}} \tag{3.6}$$

where M_{coupon} is the mass of each coupon, L_{coupon} is the measured length and δ_{steel} is the density of the cold-formed steel sample. The density of the cold-formed steel material was determined using Equation 3.7 by measuring the ratio of weights submerged and unsubmerged in water:

$$\delta_{steel} = \frac{\delta_{water}}{1-\left(W_{uw}/W_{ow}\right)} \tag{3.7}$$

where W_{uw} and W_{ow} are the coupon material weights measured in a tank of water (density of water δ_{water} = 1000 kg/m^3) and outside the water respectively. Table 3.1 shows the measured 0.2%, 1% proof and ultimate tensile stresses for the flat and corner coupons. Figures 3.3-3.4 show the stress-strain curves for the 3.0 mm and 1.3 mm thick coupon tests respectively. Figures 3.5 and 3.6 show the stress-strain curves at low strains to show the offset method. Due to the loss of ductility from the cold work, the 1% proof stress for several corner coupons was not reached. The elongation before fracture ε_f was found to be on average 11% and 16% lower than the equivalent 3.0 mm and 1.3 mm flat corner coupons respectively. The test shows that there is an increase in yield strength in the corner regions, ranging from 13-18%. Given the limited number of tests, the conservative strength increases used for the FE model are given by Equation 3.8 and 3.9.

$$\sigma_{0.2,corner} = 1.05\sigma_{0.2} \quad ; \quad \text{for } 0° < \theta < 90° \tag{3.8}$$

$$\sigma_{0.2,corner} = 1.10\sigma_{0.2} \quad ; \quad \text{for } 90° \leq \theta < 180 \tag{3.9}$$

where $\sigma_{0.2,corner}$ is the estimated 0.2% proof strength at corner regions, θ is internal angle of any corner and $\sigma_{0.2}$ is the 0.2% proof strength of the flat material.

Table 3.1: *Coupon test results*

Coupon #	Flat / Corner	t (mm)	$\sigma_{0.2}$ (N/mm^2)	$\sigma_{1.0}$ (N/mm^2)	σ_u (N/mm^2)	ε_f (%)
1	Flat	3.0	485	490	529	9.524
2	Flat	1.3	408	410	507	20.280
3	Corner	3.0	545	-	572	1.037
4	Corner	3.0	555	-	575	1.035
5	Corner	1.3	480	503	507	1.478
6	Corner	1.3	475	-	497	1.223
7	Corner	1.3	490	-	509	0.963

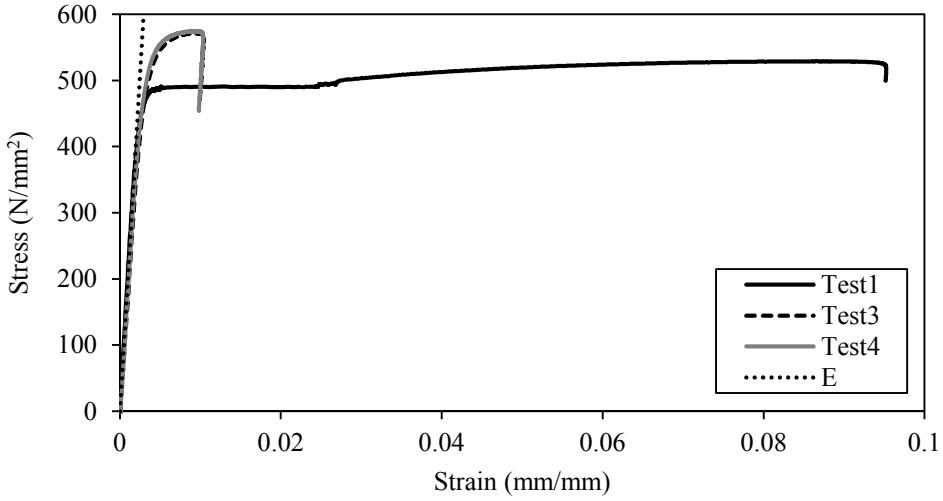


Figure 3.3: *Stress-strain curves for 3.0 mm thick coupons*

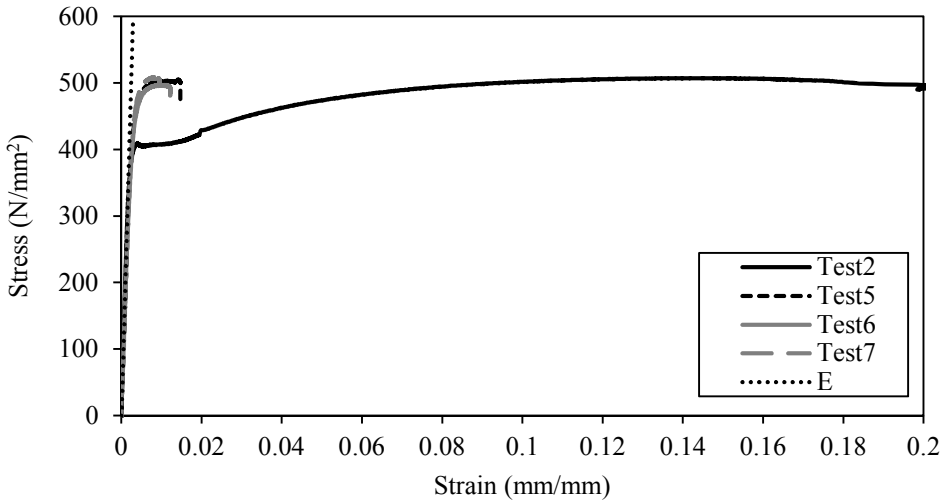


Figure 3.4: *Stress-strain curves for 1.3 mm thick coupons*

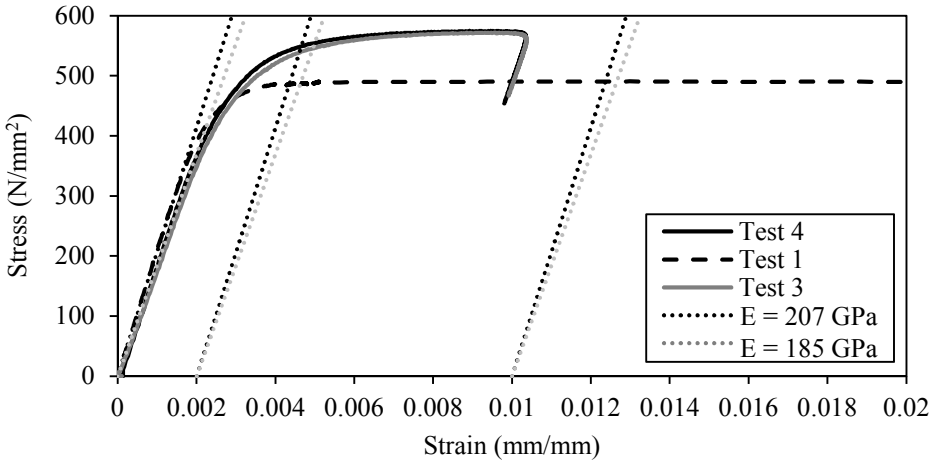


Figure 3.5: *Stress-strain curves for 3.0 mm thick coupons with 0.2% and 1.0% offset lines*

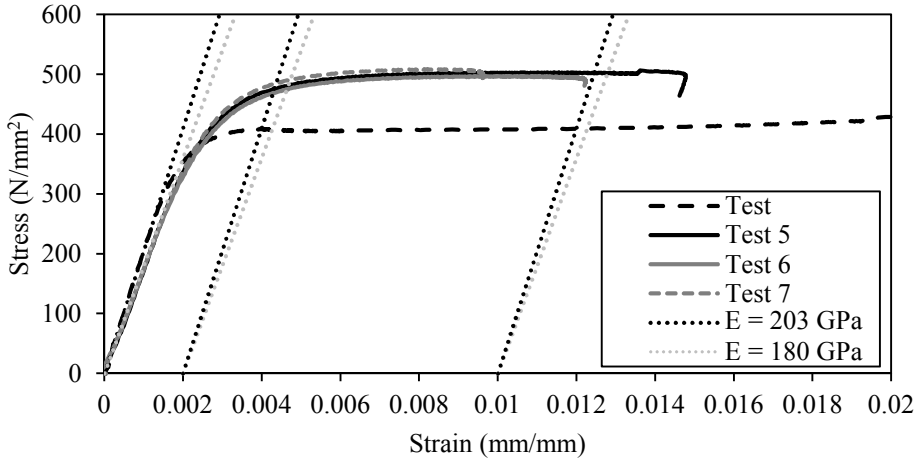


Figure 3.6: *Stress-strain curves for 1.3 mm thick coupons with 0.2% and 1.0% offset lines*

3.2.2. Element type

Owing to the fact that cold-formed steel sections are relatively thin compared to their other dimensions, shell elements were considered the ideal element choice due to their greater ability to capture local buckling more efficiently than beam elements. The general-purpose S4R elements are quadrilateral 4-node linear shell elements with reduced integration and hourglass control; they are commonly used to model thin-walled sections including cold-formed steel members (ABAQUS 2010). Previous similar numerical studies on the flexural behaviour of cold-formed steel members by Wang and Zhang (2009), Yu and Schafer (2003, 2006) and Haidarali (2011) have shown S4R elements to be highly successful in capturing the complex nonlinearities and anticipated physical behaviour. S4R elements were therefore employed throughout this study.

3.2.3. Mesh density and aspect ratio

The density of the FE model mesh is one of the important parameters that may influence the results. Invariably, increasing the mesh density is directly proportional to the computational time needed to complete the analysis. Schafer et al. (2010) investigated mesh sensitivity by modelling a typical cold-formed column section using ABAQUS for a range of meshes from coarse to fine. A finer mesh was found to be more favourable since the peak and collapse responses by adopting a coarse mesh resulted in inaccuracies. The number of elements (mesh density) from previous numerical studies on cold-formed steel varies due to the wide range of cross-sectional shapes that have been considered and the advances in computational processing power. The chosen mesh density for this study was similar to that adopted by Haidarali (2011) to model lipped Zed-sections, where a total of 55 nodes (54 elements) were used to discretise the cross-section. The validity of the chosen mesh density was shown to be adequate by Haidarali (2011) since the simulation results were in very good agreement with the results of physical tests conducted by Yu and Schafer (2003, 2006).

A similar mesh density was employed for other cross-sections; a compromise was made to allow for rectangular elements in the flat regions with moderate aspect ratios (no more than 5 to 1) without making the mesh too fine by adding unnecessary additional nodes. To minimise numerical and geometrical inaccuracy, 4 elements were used for the corners regions, and sufficient elements in the flat regions to ensure the elements remain relatively square. Substantial numbers of elements were used for intermediate stiffeners since the stiffener shape varies greatly over a short length. It was decided that 16 elements should be used to model an intermediate stiffener (a total of 4 corners resulting in 16 elements). The mesh size in the longitudinal direction was fixed at 10.2 mm for pure bending models and 10 mm for all other cases.

3.2.4. Modelling of common trapezoidal sheeting

Cold-formed steel members are widely used in large industrial buildings as intermediate members between the main structural frames and corrugated roofing. The trapezoidal decking is through fastened by screws which resist lateral, local and distortional buckling by limiting the natural half-wavelengths of all buckling modes.

Incorporating rotational and translational restraints afforded by the sheeting will ensure the FE model replicates failure modes and capacities found in practice.

A two-spring model was used to replicate the restraining behaviour of common sheeting attached to the top flange of cold-formed sections. The restraining behaviour acting on the beam offered by each fastener was modelled using 'SPRINGA' 3D linear translational spring elements. The spring vertically restrains the connected flange in both compression (bearing into sheeting) and tension (fastener pull-out). Haidarali (2011) found that the precise value of spring stiffness selected had little effect on the in-plane failure mode and section capacity, provided the spring stiffness was greater than a threshold stiffness value. The threshold value determines whether the section failure mode gets triggered by local buckling (high stiffness) or distortional buckling (low stiffness). Even though the threshold value is thought to be a function of cross-section slenderness $\bar{\lambda}_{cs}$, the linear spring stiffness was set to 5000 N/mm for both tension and compression.

Compression-only springs were also attached to the lip/flange junction between fastener locations to prevent any negative vertical displacement. These springs were modelled using 'SPRINGA' elements and assigned nonlinear stiffness values using the *SPRING, NONLINEAR command in ABAQUS. The inclusion of the nonlinear spring prevents the flange deforming upwards (into the sheeting) whilst leaving it free to deform downwards. The nonlinear spring compressive stiffness was also set to 5000 N/mm but with negligible tensile stiffness. For both types of springs, the command *EQUATION was used for each slave spring node to ensure the spring is always directly above the connected beam node, as shown in Figure 3.7. The translational and longitudinal displacements (DOF 1 and 3) of the beam node were equated to the slave spring node. The vertical displacement (DOF 2) at the web/flange junction was equated to the slave spring node to prevent additional extension of the spring due to global bending. The two-spring model approach is validated by comparing against the responses obtained from physical tests conducted by Yu and Schafer (2003) in Section 3.3.3.2.

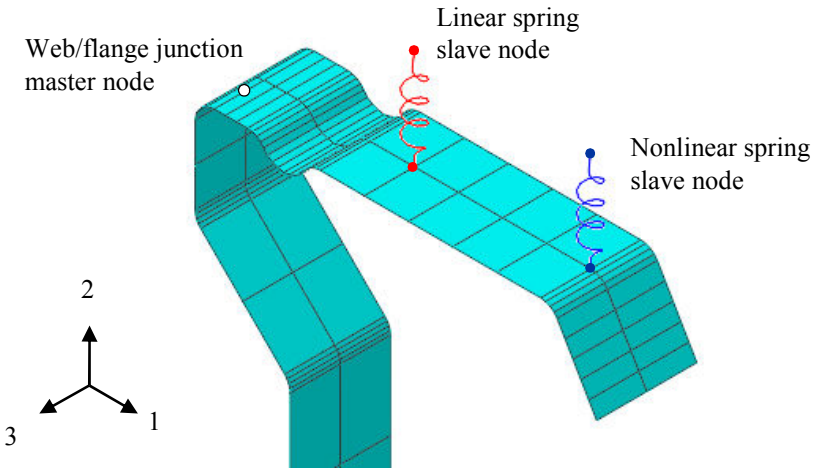


Figure 3.7: *Two-spring model to reprsent sheeting*

3.2.5. Method of analysis

The nonlinear static models of the bare cold-formed steel sections were solved using the modified Riks method by adopting the "*STATIC, RIKS" command in ABAQUS. The modified Riks method can accurately provide solutions for geometrically and materially nonlinear static problems involving unstable buckling behaviour. The modified Riks method adopts a proportional load magnitude as an additional unknown parameter by solving for the loads and displacements simultaneously. The 'arc length' is used to measure the progress of the analysis by tracking the static equilibrium path in a load-displacement space. To determine the next increment in the load-displacement response, the method adopts the Newton-Raphson algorithm to locate the next possible solution (based on a trial arc-length and load magnitude) and checks iteratively whether the new deformed state can satisfy equilibrium checks of the system. Due to introduction of finite radii of convergence from the Newton-Raphson algorithm, it is essential to limit the increment size (length of the tangent line) to prevent inaccurate results and convergence issues. Unfortunately, knowing that the increment size is problem dependent, standardising the increment size for all FE models may yield satisfactory results for one FE model, but may not for others. Instead, a rule of thumb of ensuring that at least 80 increments to reach ultimate load by manually scaling the maximum increment size was adopted. Material and geometrical nonlinearities were incorporated in the FE models through the *PLASTIC and *STEP, NLGEOM commands respectively.

3.2.6. Imperfections

The representation of initial imperfections for complex interactive buckling problems is particularly challenging. It is crucial that the distribution and magnitude of the imperfection shape are modelled accurately in the numerical analysis since the ultimate load and buckling mode can be sensitive to the imperfections. Since both local and distortional buckling are likely to occur in the FE models, the imperfection shapes were taken as the superposition of the local and distortional buckling modes, with independent imperfection amplitudes. Haidarali (2011) conducted an imperfection sensitivity study by comparing FE models against physical tests conducted by Yu (2005) with imperfections obtained using:

- An elastic buckling (Eigenmode) analysis within ABAQUS
- CUFSM (Schafer 2006) and manually distributing the imperfection shapes longitudinally with periods equal to the buckling half-wavelength.

Adopting the Eigenmode method was found to be troublesome for two reasons: (i) considerable computational time may be needed to find the pure local buckling mode and, (ii) feeding inappropriate Eigenmodes containing mixed modes rather than a superposition of pure local and distortional buckling modes gave unrealistic failure modes and bending resistances. Therefore, it was decided to generate the buckling shapes and distribution of initial imperfections manually by using CUFSM.

The finite strip software CUFSM, implements the classical finite strip method to calculate all elastic buckling modes of a simply supported thin-walled member of arbitrary cross-section. The finite strip method adopts polynomial functions and a single half-sinewave for the transverse and longitudinal shape functions respectively. CUFSM version 3.12 (Schafer 2006) within MATLAB was used for this study to obtain the pure local and distortional buckling shapes for each cross-sectional node. CUFSM provides a signature curve which gives the local and distortional buckling mode shapes along with their elastic critical loads and half-wavelengths. A typical signature curve from CUFSM showing local and distortional buckling modes is shown in Figure 3.8.

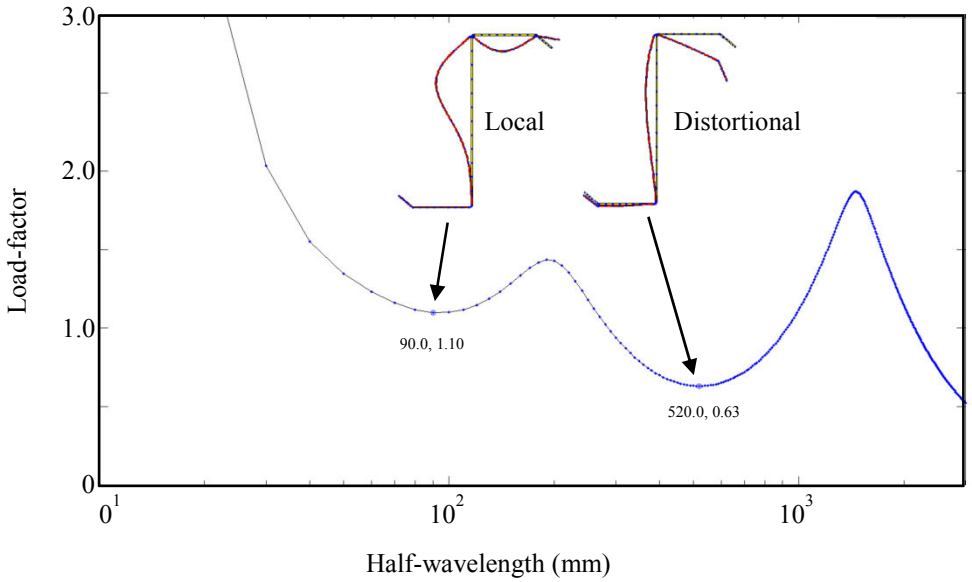


Figure 3.8: *Signature curve showing local and distortional buckling modes*

The method of creating initial imperfections was carried out in two stages: i) determine the elastic local and distortional buckling mode shapes using CUFSM by feeding in the same material properties and section dimensions as the ones used for the ABAQUS FE model and (ii), distribute the individual shapes longitudinally using sinusoidal functions with pre-assigned amplitude and direction with periods similar to the corresponding buckle half-wavelengths. The goal was to obtain the worst case imperfection spectrum based on different signs and combinations of wave numbers. Unfortunately, a standardised application for the imperfection direction and longitudinal distribution are unknown; the sign for each imperfection mode shape and the applied number of half-sign waves for the FE model were investigated in a sensitivity study to find a robust/repeatable method to obtain an initial imperfection spectrum.

3.2.6.1. Initial imperfection study

Eight identical single span gravity 3-point bending FE models were simulated with varying initial imperfection spectrums. The dimensions for the chosen Zed section are shown in Figure 3.9. The imperfection sign and number of half-sine waves were varied for this study. The imperfection amplitude was kept constant and artificially set at a high value to amplify the effect of the sign and distribution of the initial imperfection.

It was assumed that the worst case distributions for the initial imperfection were those with periods equalling the half-wavelength. However, the span length may not always be divisible by the local and distortional buckling half-wavelengths. To overcome this, the numbers of waves were rounded to nearest odd or even number. For the considered Zed section, the half-wavelength for local and distortional buckling from CUFSM were 90 mm and 520 mm respectively. For a span length L' of 3000 mm, the nearest odd and even local and distortional waves were therefore 33, 32 and 5, 6 respectively. The sign of the imperfection spectrum was also investigated by modifying the direction of deformation inwards or outwards at the midspan. Figures 3.11-3.18 shows the initial imperfections for all 8 cases.

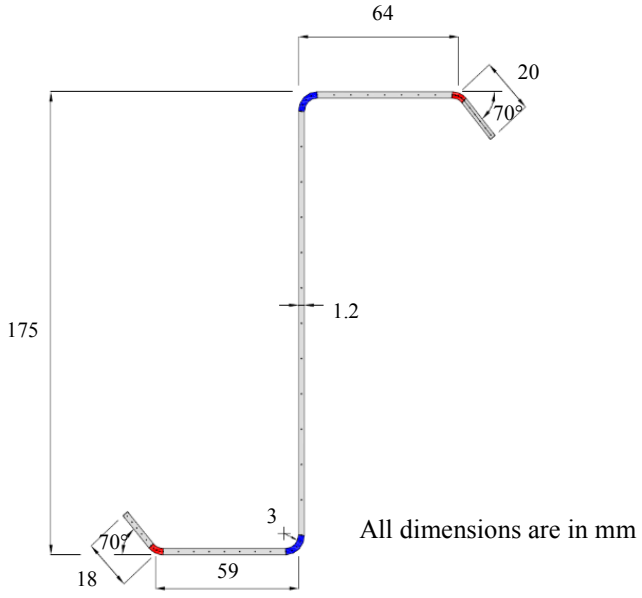


Figure 3.9: *Geometrical dimensions of Zed section for imperfection sensitivity study*

The ultimate load capacities P_{ult} and load-displacement responses from the imperfection study are shown in Table 3.2 and Figure 3.10. The ultimate load capacities for each model case was normalised against case 1, $P_{ult,model,1}$. Two main observations were noted: (i) in all cases, having an inward direction of the imperfection at midspan was always more severe than outward imperfection and (ii), generated imperfection modes with an odd amount of half sine-waves for both local and distortional buckling generally produced lower capacities than modes with even number of waves. Thus, for future FE models, the worst case imperfection would be applied by ensuring an odd number of waves for local and distortional buckling modes, and having the imperfection direction towards the neutral axis at midspan.

Table 3.2: *Imperfection study results*

Model #	Local mode direction at midspan	Distortional mode direction at midspan	No. of local waves	No. of distortional waves	P_{ult} (kN)	P_{ult} / $P_{ult,model,1}$
1	Inwards	Inwards	33	5	4.81	1.00
2	Inwards	Inwards	33	6	5.30	1.10
3	Inwards	Inwards	32	5	4.93	1.02
4	Inwards	Inwards	32	6	5.46	1.13
5	Outwards	Outwards	33	5	5.53	1.14
6	Outwards	Outwards	33	6	5.75	1.19
7	Outwards	Outwards	32	5	5.74	1.19
8	Outwards	Outwards	32	6	5.52	1.14

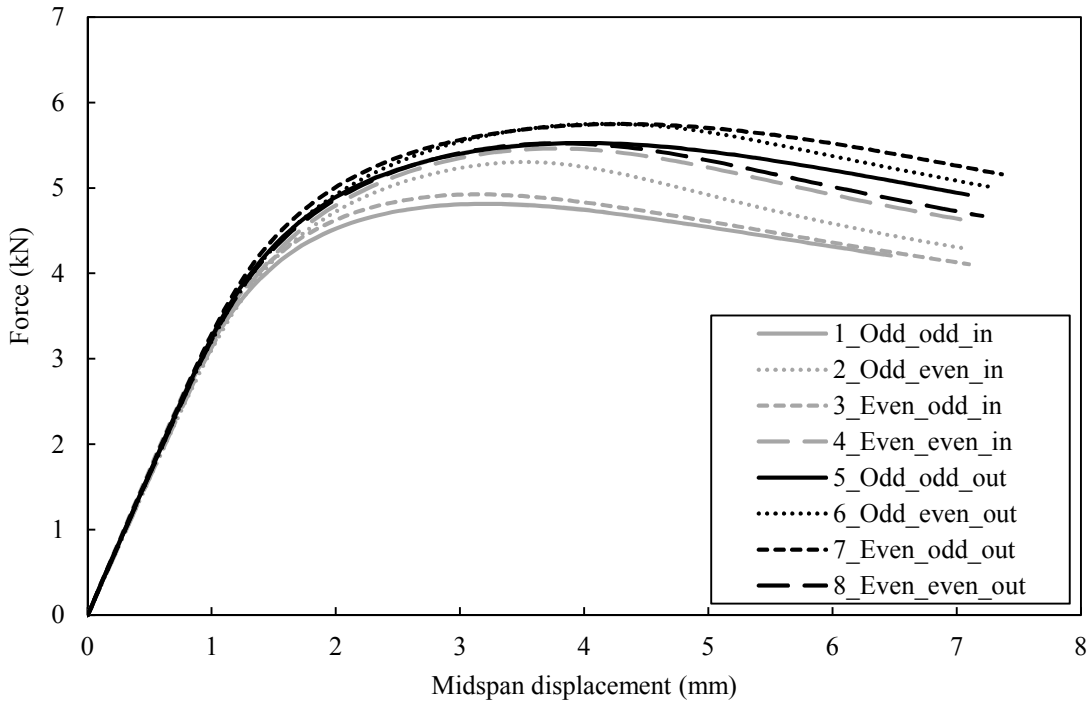


Figure 3.10: *Load-displacement responses for models 1-8*

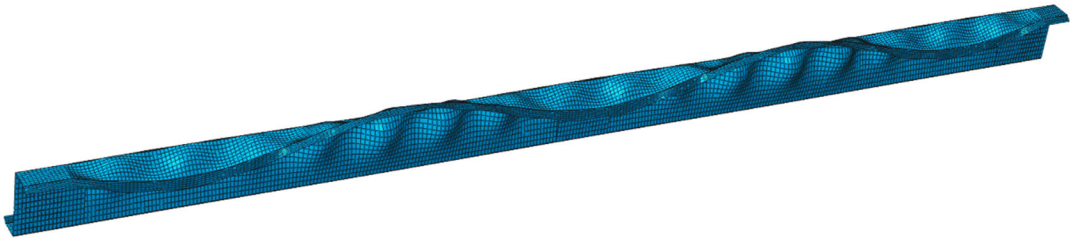


Figure 3.11: *Imperfection mode for model 1 - inward 33 local and 5 distortional waves*

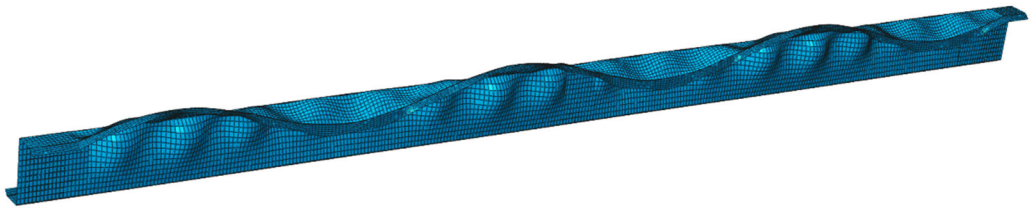


Figure 3.12: *Imperfection mode for model 2 - inward 33 local and 6 distortional waves*

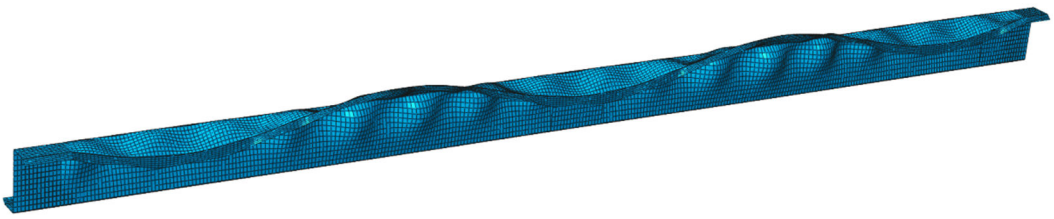


Figure 3.13: *Imperfection mode for model 3 - inward 32 local and 5 distortional waves*

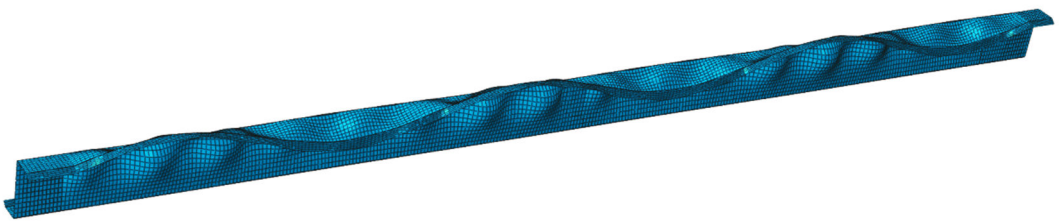


Figure 3.14: *Imperfection mode for model 4 - inward 32 local and 6 distortional waves*

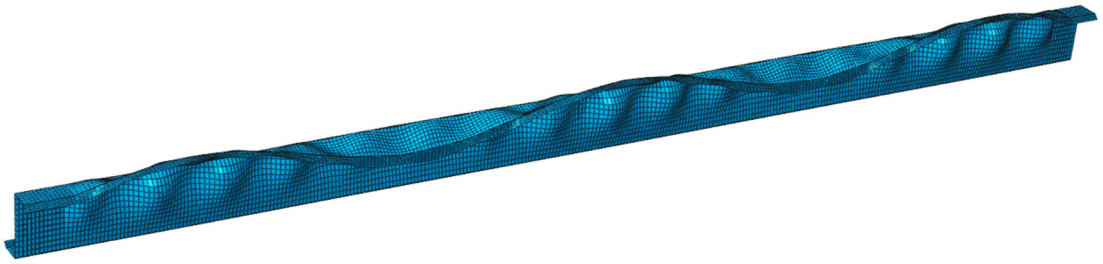


Figure 3.15: *Imperfection mode for model 5 - outward 33 local and 5 distortional waves*

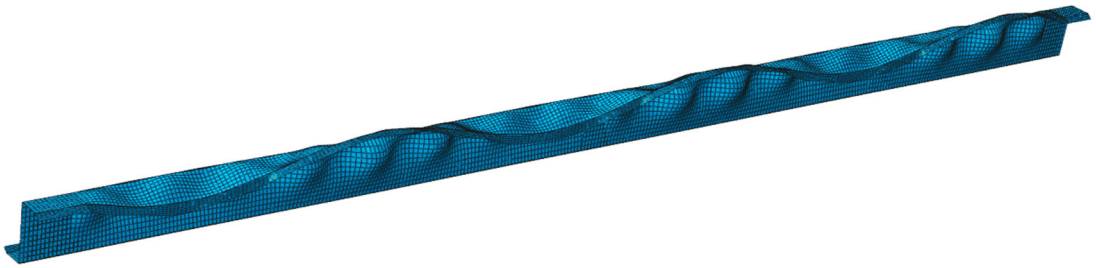


Figure 3.16: *Imperfection mode for model 6 - outward 33 local and 6 distortional waves*

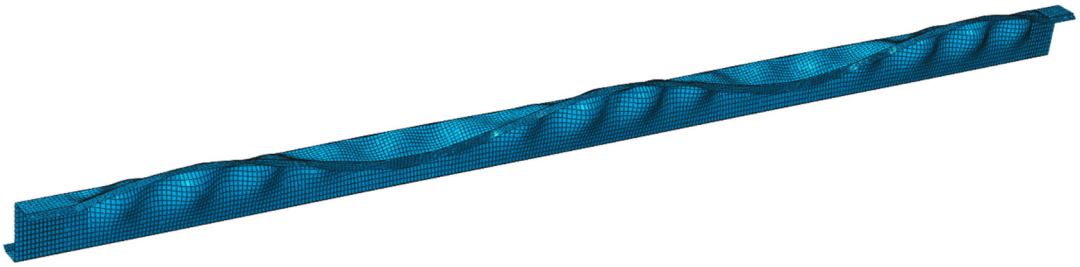


Figure 3.17: *Imperfection mode for model 7 - outward 32 local and 5 distortional waves*

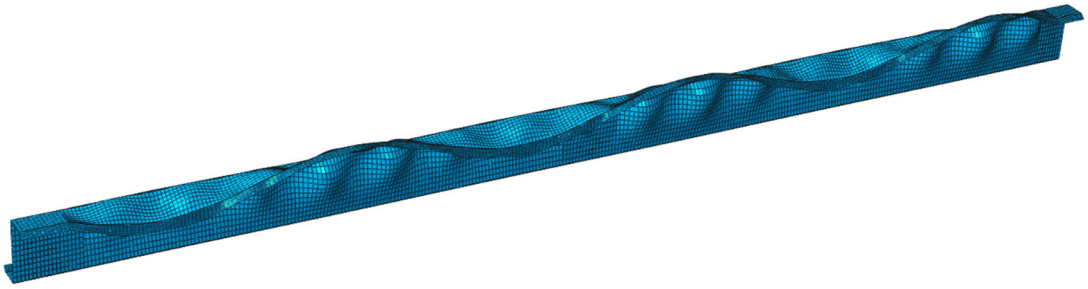
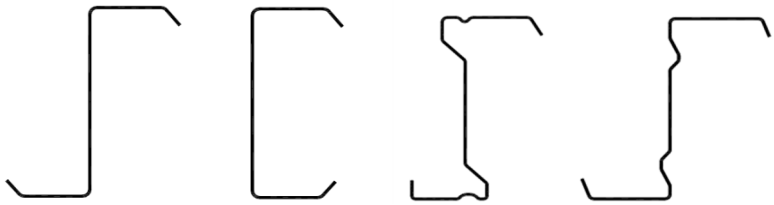


Figure 3.18: *Imperfection mode for model 8 - outward 32 local and 6 distortional waves*

3.3. VALIDATION OF BARE SECTION FE MODELS

3.3.1. Introduction

The finite element method (FEM) is a powerful technique for studying the complex interactive buckling behaviour of cold-formed steel members. However, the results from the numerical models are only meaningful if the simulations are able to capture accurately the buckling behaviour and bending capacities observed in practice (i.e. in physical experiments). In this study, the finite element package ABAQUS 6.10 (2010) has been used to develop numerical models of bare cold-formed steel sections, which have been validated against a range of single and 2-span physical tests, covering 4 sections types: lipped Zeds, lipped channels, Zeta I sections and Zeta II sections as shown in Figure 3.19. Further details on the testing arrangements for single span and 2-span tests are discussed in Section 3.3.3 and 3.3.4 respectively.



(a) (b) (c) (d)

Figure 3.19: *Definitions for cross-sectional dimensions: (a) Zed, (b) Channel, (c) Zeta I and (d) Zeta II*

A total of 6 different bare section test arrangements were considered for this thesis and are highlighted in the list below. Test type 1, 3, 5 and 6 were considered for the FE model validation study with test type 2 and 4 considered in Chapter 4. The bending moment diagram (BMD) schematics for test type 1, 3, 5 and 6 are illustrated in Figures 3.20-3.23.

Test type 1. Single span 4-point (pure bending in the central region) subjected to downwards loading

Test type 2. Single span 4-point (pure bending in the central region) subjected to upward loading

Test type 3. Single span 3-point (moment gradient) bending subjected to upward loading

Test type 4. Single span 3-point (moment gradient) bending subjected to downwards loading

Test type 5. Continuous 2-span tests subjected to a gravity UDL

Test type 6. Continuous 2-span tests subjected to a uplift UDL

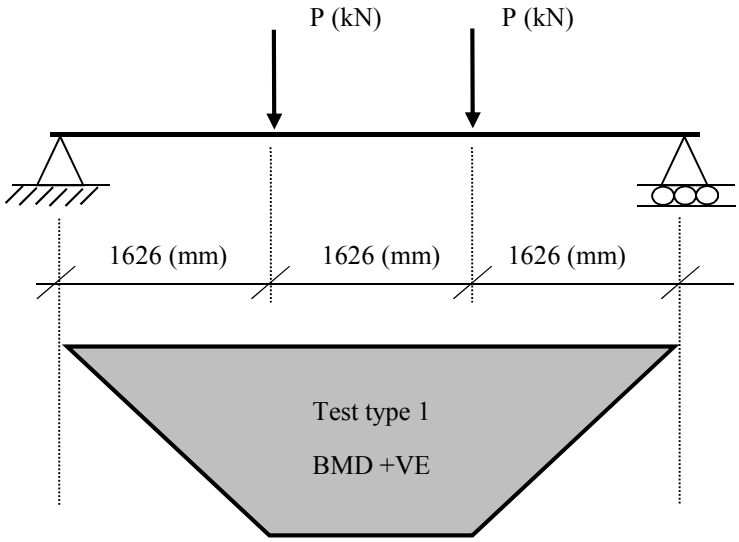


Figure 3.20: *Test type 1* **-** *single span 4-point (pure) bending*

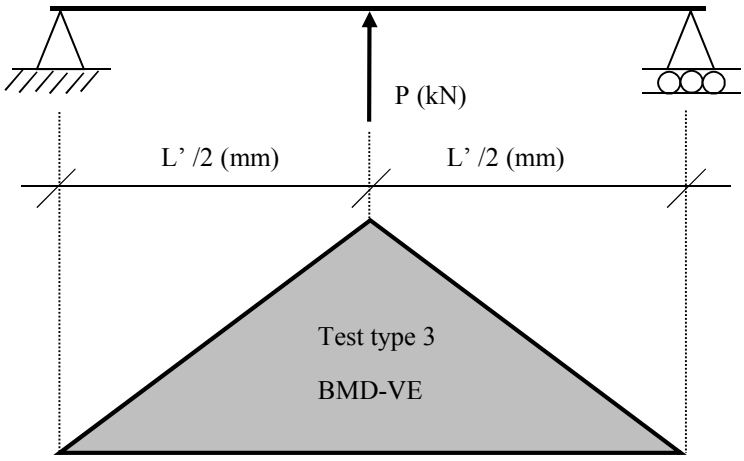


Figure 3.21: *Test type 3 - single span 3-point bending (moment gradient)*

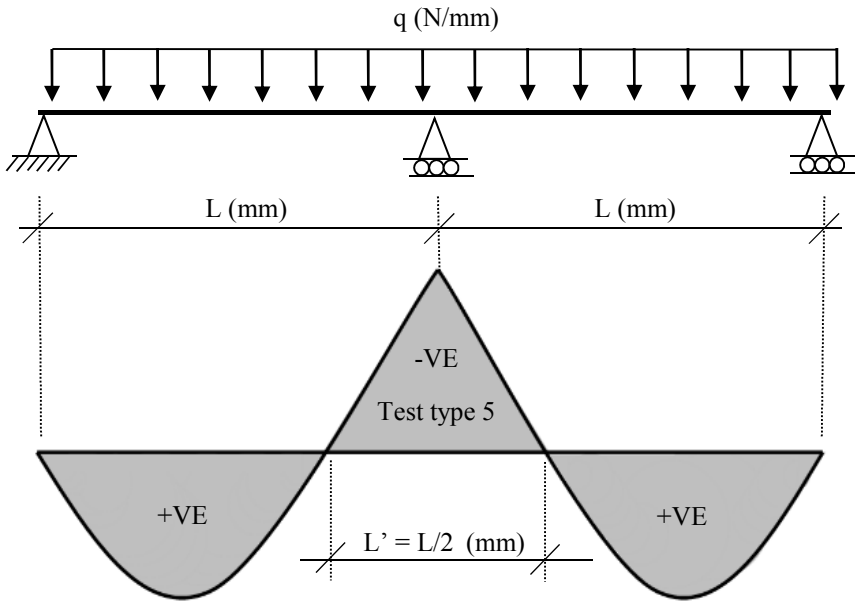


Figure 3.22: *Test type 5 - continuous 2-span test subjected to gravity UDL*

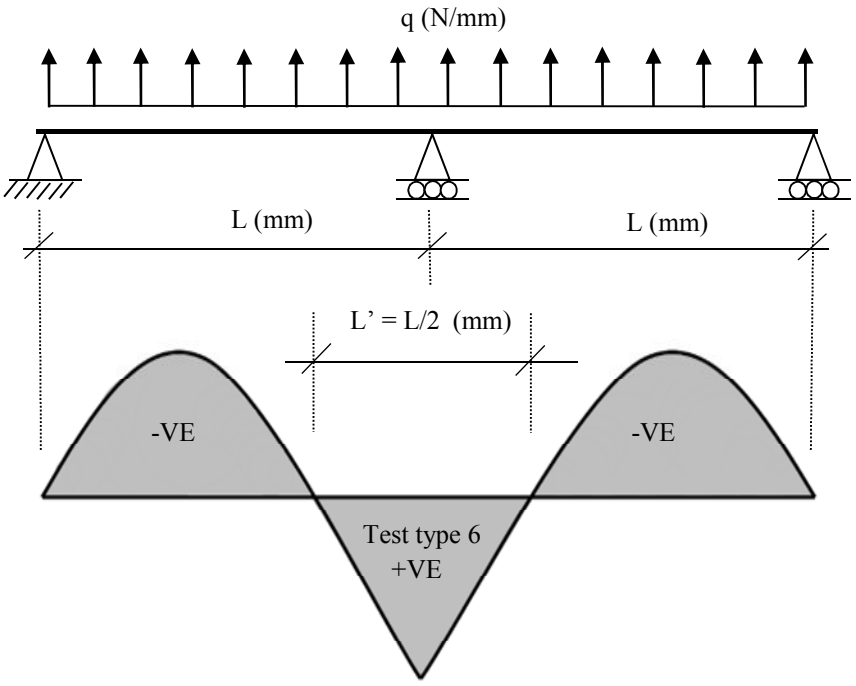


Figure 3.23: *Test type 6 - continuous 2-span test subjected to uplift UDL*

3.3.2. Boundary conditions and loading

The modelled beams were fitted with additional flat and corner plates to replicate the localised restraining effect from loading plates and cleats; the plates prevent premature buckling at locations of high concentrated loads. The plate elements were given an artificially high elastic modulus E_{plate} of 2100 GPa compared to 210 GPa for the beam section to enhance their rigidity. The flat and corner plates were modelled using S4R elements and assigned thicknesses of 6 mm and 3 mm and placed at the reaction and loading points at the web and tension web/flange junction respectively. The connecting bolts between loading plates and the beam were assumed to be 'perfect' with no bolt slip and were simulated using the *TIE command between the nodes located on the flat plate and the beam. This ensures all 6 degrees of freedom (DOF) from the beam and plate at the tie locations are equated. Lateral restraints along the beam at the web/flange junction were applied in the FE model by adding out-of-plane translational (DOF1) boundary conditions. To prevent rigid body motion longitudinal translational boundary conditions (DOF3) were applied at the midspan web nodes. Simply supported end reactions were modelled by fixing DOFs 1, 2, 5 and 6 at the tension flange nodes. For the single span tests, the load was applied through the centre of the flat stiff plates using the ABAQUS command *CLOAD. Figure 3.24 illustrates a 3-point bending FE model showing the locations of the stiff plates, translational springs and prescribed boundary conditions.

The uniformly distributed load (UDL) for the 2-span tests were modelled using a pressure load by applying the load through the smaller flat portion of the top flange using *DLOAD, as shown in Figure 3.25. In order to reduce the model size and computational cost, only one half of the continuous 2-span beam was modelled by applying appropriate boundary conditions. *BOUNDARY, ZSYMM (DOFs 3, 4 and 5 = 0) was applied at the interior support to ensure longitudinal symmetry. An initial full FE model was prepared to check the validity of the half model. Although it is recognised that this supresses anti-symmetric buckling modes, comparisons between full and half length (with symmetric boundary conditions) models yielded very similar results. This finding was also made by Theofanous and Gardner (2010). Owing to the long computational time needed for the full model, the half model was chosen to simulate all 2-span arrangements.

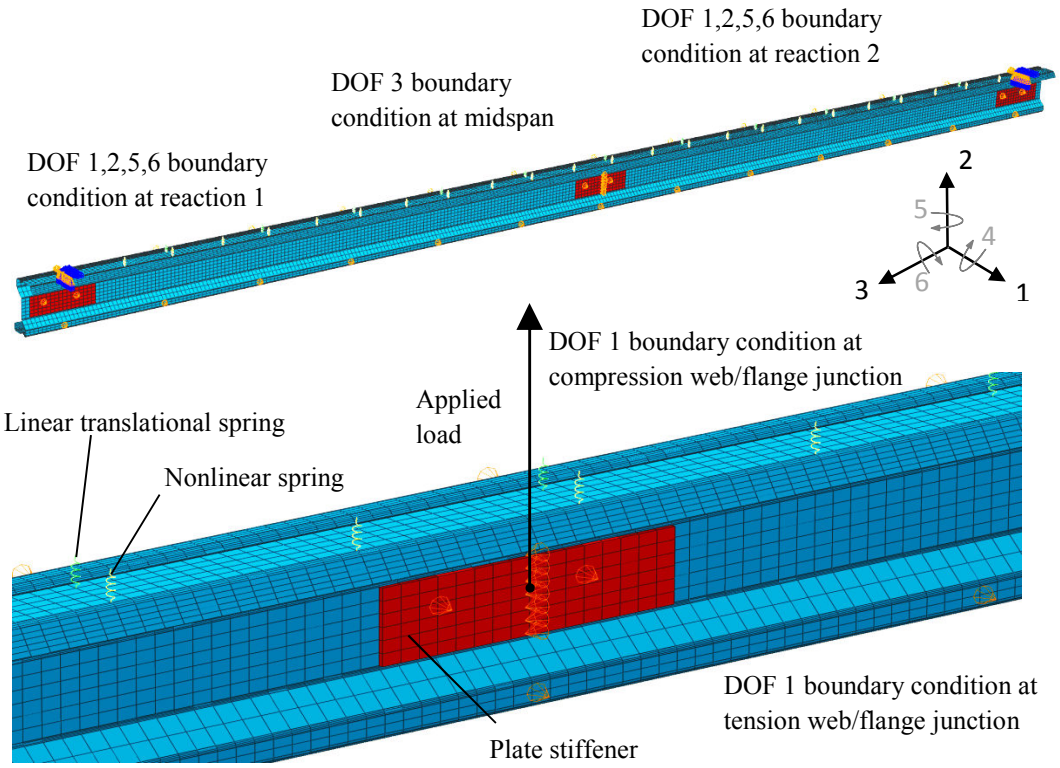


Figure 3.24: *3-point bending FE model arrangement*

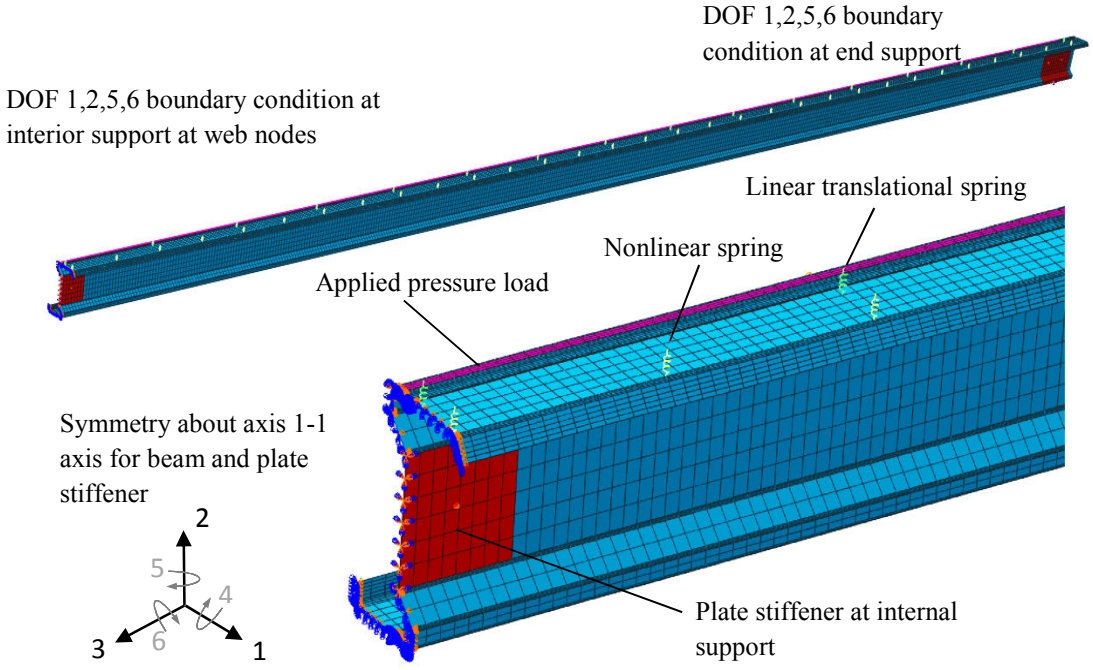


Figure 3.25: *2-span continuous FE model arrangement*

3.3.3. Single span tests

Single span pure bending and moment gradient physical tests (test type1 and 3) by Wang and Zhang (2009), Yu and Schafer (2003), Bryan and Davies (1979, 1980a), Bryan and Deakin (1989), Deakin (1991a, 1991b) and Davies and Deakin (1992) have been used to develop single span numerical models for a variety of cold-formed steel cross-sections. Table 3.3 summarises all the single span tests considered for this study. Details of each study are given in the Sections 3.3.3.1-3.3.3.4.

Table 3.3: *Summary of single span test validation*

Reference	Test type	Section Type	Number of tests
Wang and Zhang (2009)	4-point (pure) bending	C	4
Yu and Schafer (2003)	4-point (pure) bending	Zed/C	25
Wang and Zhang (2009)	3-point bending	C	4
Bryan and Davies (1979, 1980a) Bryan and Deakin (1989) Deakin (1991a, 1991b)	3-point bending	Zeta IA Zeta IB	7
Davies and Deakin (1992)	3-point bending	Zeta II	5

3.3.3.1. 4-point and 3-point bending tests by Wang and Zhang (2009)

Wang and Zhang (2009) conducted a total of 12 physical bending (6 4-point and 6 3-point bending) tests using 24 paired specimens. The study comprised of 3 types of channel sections with different edge stiffener characteristics: 90° edge stiffeners, 45° edge stiffeners and reverse lips (both 90°). Channel sections with return lips tests were not considered for this validation study; the models were validated against a total of 8 tests. Figures 3.26 and 3.27 show the 4-point (pure) bending and 3-point test arrangements for Wang and Zhang (2009) respectively. Each 4-point and 3-point bending test comprised of two nominally identical specimens which were tested in parallel. Steel plates were attached to the shear spans by fastening single row screws at 200 mm spacing at the centre of the compression flange of each section as shown in Figure 3.28.

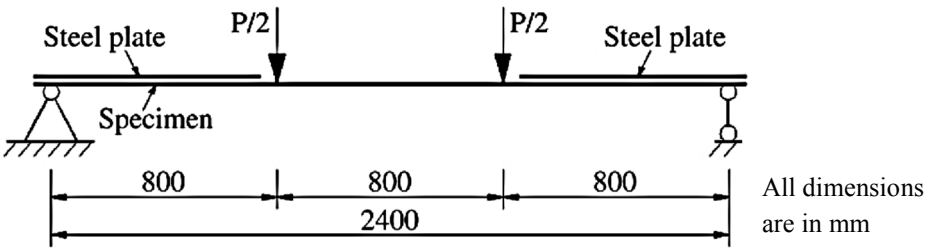


Figure 3.26: *4-point (pure) bending test arrangement of Wang and Zhang (2009)*

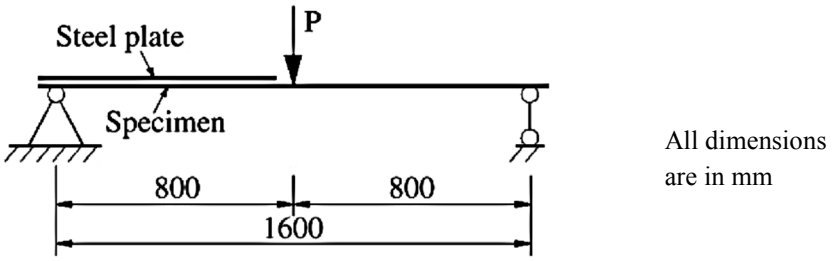
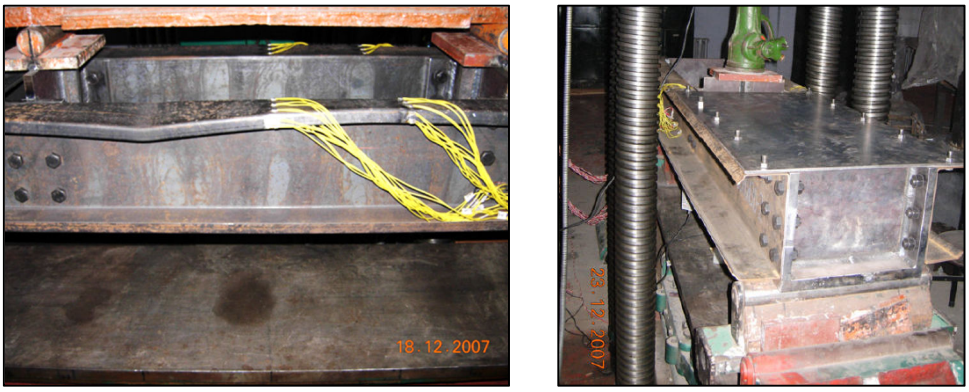


Figure 3.27: *3-point bending test arrangement of Wang and Zhang (2009)*



(a) (b)

Figure 3.28: *Overall view by Wang and Zhang (2009): (a) 4-point (pure) bending tests and (b) 3-point bending tests*

The measured local and distortional imperfections (defined as Δl and Δd respectively) for test specimens at the compression flange are defined in Figure 3.29 (Wang and Zhang, 2009). Three repeated tensile coupon tests were conducted on material extracted from the flat regions of the web, tension flange and compression flange, resulting in a total of 9 tensile coupons per section. The average yield f_y and ultimate stresses f_u, Young's Modulus E and Poisson's ratios ν for each corresponding section were averaged and applied in the FE models. The section dimensions, imperfections and material properties are shown in Tables 3.4-3.5. The notation used for the dimensions are shown in Figure 3.30.

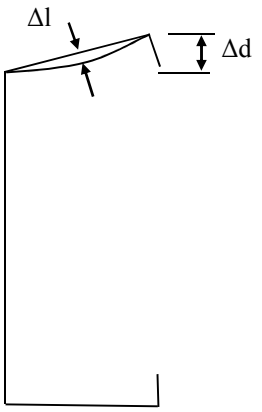


Figure 3.29: *Schematic diagram of initial geometric imperfections*

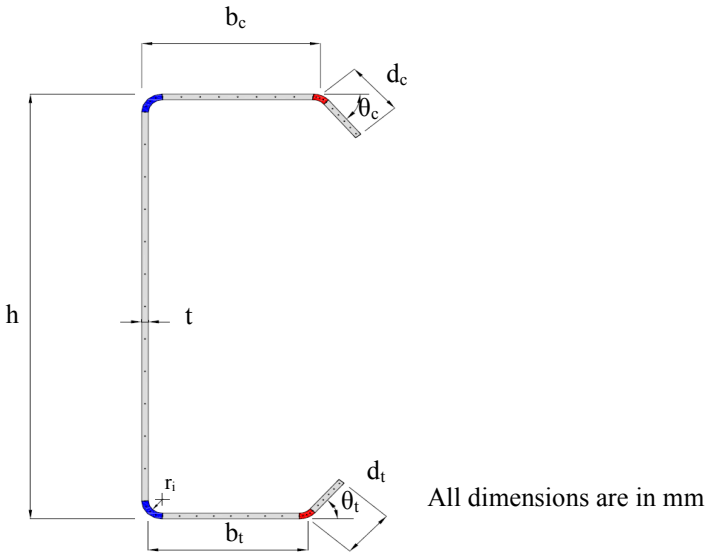


Figure 3.30: *Definition for cross-sectional dimension for C-sections*

Table 3.4: *Geometry and material properties for 4-point (pure) bending tests by Wang and Zhang (2009)*

Test #	Test label	h (mm)	b_c (mm)	d_c (mm)	θ_c (deg)	b_t (mm)	d_t (mm)	θ_t (deg)	t (mm)	f_y (N/mm^2)	f_u (N/mm^2)	E (GPa)	ν	Δl/t	Δ d/t
1	L_UH200B80d20	197.05	81.95	22.10	85.00	82.30	22.55	85.00	2.94	350.87	497.33	201.649	0.299	0.109	1.643
2	L_UH200B80d40	198.50	81.70	42.40	85.50	82.05	42.45	85.00	2.94	350.87	497.33	201.649	0.299	0.068	1.067
3	L_IH200B80d20	196.00	80.50	21.10	39.00	80.35	21.50	40.00	2.94	352.57	494.87	203.785	0.292	0.135	1.757
4	L_IH200B80d40	195.80	81.00	41.60	41.00	81.00	40.90	41.00	2.94	352.57	494.87	203.785	0.292	0.116	1.774

Table 3.5: *Geometry and material properties for 3-point bending tests by Wang and Zhang (2009)*

Test #	Test label	h (mm)	b_c (mm)	d_c (mm)	θ_c (deg)	b_t (mm)	d_t (mm)	θ_t (deg)	t (mm)	f_y (N/mm^2)	f_u (N/mm^2)	E (GPa)	ν	Δl/t	Δd/t
5	S_UH200B80d20	197.50	82.55	21.10	87.50	82.25	22.40	88.00	2.94	350.87	497.33	201.649	0.299	0.070	1.100
6	S_UH200B80d40	200.25	81.60	42.00	88.00	51.55	42.15	88.50	2.94	350.87	497.33	201.649	0.299	0.049	0.869
7	S_IH200B80d20	198.15	80.25	20.35	42.00	80.00	19.85	43.00	2.94	352.57	494.87	203.785	0.292	0.061	1.158
8	S_IH200B80d40	195.45	80.50	40.25	43.5	80.75	40.25	42.5	2.94	352.57	494.87	203.785	0.292	0.085	1.155

3.3.3.2. 4-point bending tests conducted by Yu and Schafer (2003)

Yu and Schafer (2003) conducted 25 4-point bending tests. The 5.5 m long lipped Zed section and C-section were tested in parallel, whereby the pairs of specimens were oriented in an opposed arrangement as shown in Figure 3.31. Figure 3.32 illustrates the four-point bending test arrangement against the developed FE model. Boundary conditions, element type, material definition and plate elements for the 4-point pure bending FE model were identical to the 3-point bending FE model as described in Section 3.3.2, but with an additional loading plate as opposed to the single plate.

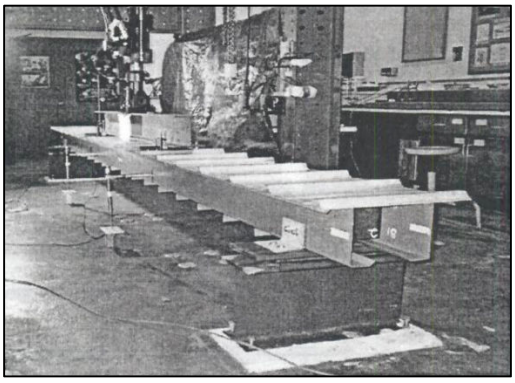


Figure 3.31: *Overall view of testing setup by Yu and Schafer (2003)*

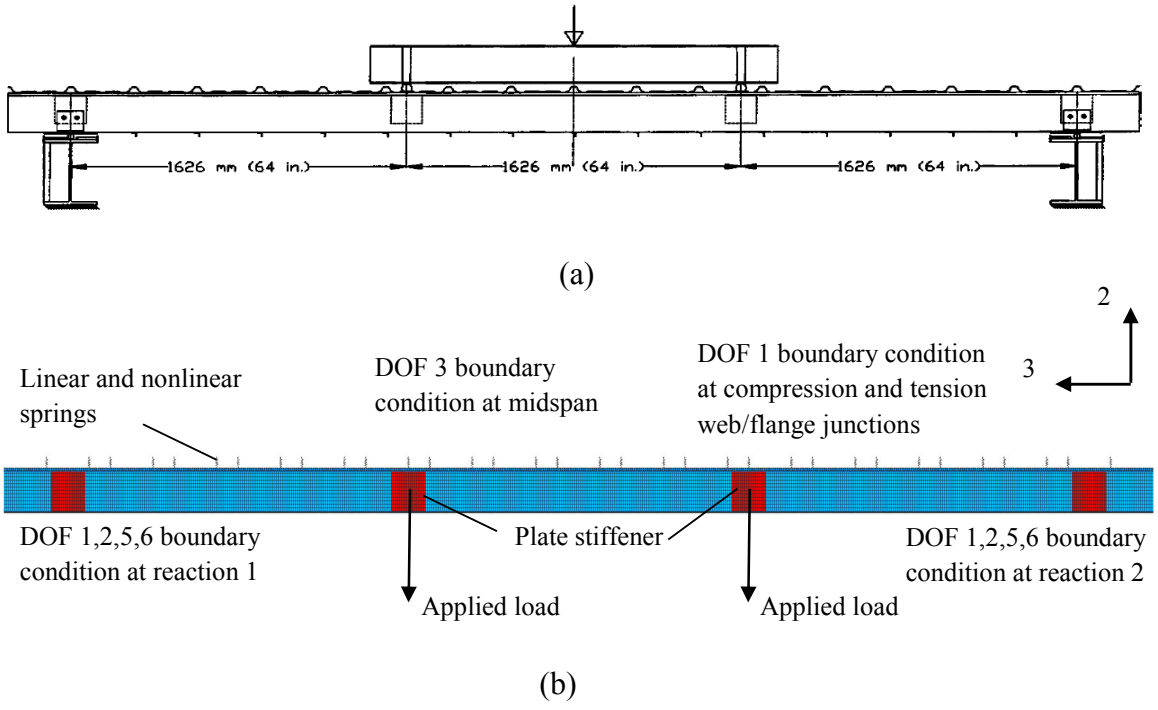


Figure 3.32: *Four-point bending arrangement (a) experimental (Yu and Schafer (2003)) and (b) FE model*

Yu and Schafer (2003) varied the panel-to-purlin fastener detail in the constant moment region to investigate the effect of bending resistance of Zed and C-sections. As shown in Figure 3.33, four different fastener details were considered:

A. Single bolt per compression flange at 304.8 mm spacing.
B. Single bolt per compression flange at alternating 203.2 mm and 101.6 mm spacing (either side of the panel rib).
C. Two bolts (38.1mm apart) per compression flange at alternating 203.2 mm and 101.6 mm spacing (either side of the panel rib).
D. Two bolts (38.1 mm apart) per compression flange at 101.6 mm spacing.

Linear translational springs which capture the pull-out and bearing restraint of the fasteners were employed in the FE models; the location and number of the fasteners were replicated in the FE analyses to ensure a similar buckling response to the physical tests. Tables 3.6 and 3.7 shows the dimensions and material strength f_y of the tested Zed and C cross-sections respectively. The notation used for the geometry for the C and Zed sections is shown in Figure 3.34(a) and 3.34(b) respectively.

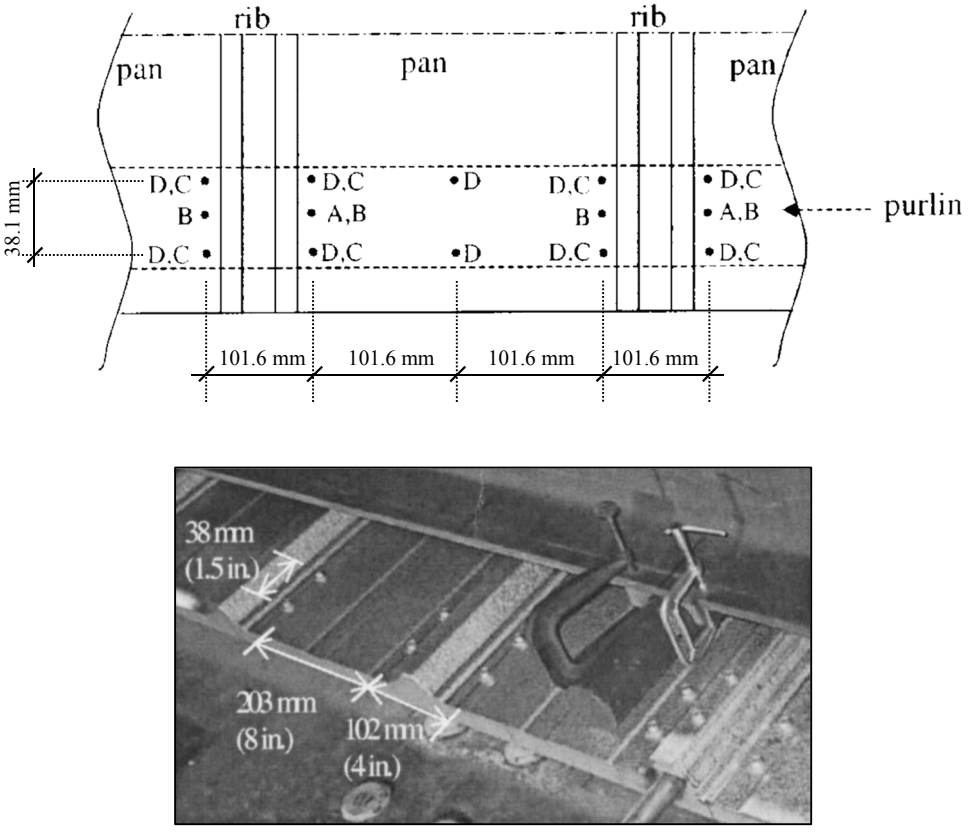


Figure 3.33: *Plan view for panel-to-purlin screw locations from Yu and Schafer (2003)*

Table 3.6: *Measured geometry and material strength for Zed section 4-point bending tests by Yu and Schafer (2003)*

Test #	Test label	Panel Type*	h (mm)	b_c (mm)	d_c (mm)	θ_c (deg)	b_t (mm)	d_c (mm)	θ_t (deg)	r_{hc} (deg)	r_{dc} (deg)	r_{ht} (deg)	r_{dt} (deg)	t (mm)	f_y (N/mm^2)
1	8.5Z120-3E2W	C	214.5	66.0	24.0	47.50	62.0	25.0	48.90	9.0	9.0	9.0	9.0	3.000	418.37
2	8.5Z105-2E1W	C	214.5	68.0	24.5	50.60	60.0	23.5	48.70	8.0	8.0	9.0	9.0	2.655	467.14
3	8.5Z092-4E2W	C	214.0	66.0	23.5	52.40	61.0	24.0	50.60	7.0	7.0	8.0	8.0	2.270	393.72
4	8.5Z082-1E2W	C	215.0	64.0	24.0	48.45	60.5	24.5	51.35	7.0	7.0	8.0	8.0	2.035	401.36
5	8.5Z073-6E5W	A	216.0	64.0	23.0	49.60	61.0	24.0	50.90	7.0	7.0	8.0	8.0	1.840	377.59
6	8.5Z073-4E3W	C	216.0	64.0	23.5	49.85	60.5	23.5	50.65	7.0	7.0	7.5	7.5	1.825	384.81
7	8.5Z073-1E2W	B	216.0	64.5	23.5	49.30	61.0	23.5	51.10	7.0	7.0	8.0	8.0	1.825	380.45
8	8.5Z065-3E1W	C	215.0	61.5	20.0	47.35	62.0	20.5	47.20	7.0	7.0	7.0	7.0	1.630	367.24
9	8.5Z059-4E3W	C	216.0	63.0	20.0	50.55	58.0	18.0	49.65	7.0	7.0	7.0	7.0	1.505	403.41
10	8.5Z059-2E1W	D	216.0	64.0	20.0	50.90	59.0	18.0	49.80	7.0	7.0	7.0	7.0	1.500	406.51
11	11.5Z092-1E2W	C	289.0	84.5	24.5	49.20	89.5	23.5	48.80	6.5	7.0	7.0	7.0	2.615	418.36
12	11.5Z082-2E1W	C	291.0	89.0	22.5	50.45	87.5	22.0	51.60	8.0	8.0	9.0	9.0	2.230	420.00
13	11.5Z073-2E1W	C	288.5	89.0	23.0	45.70	85.5	22.0	44.50	7.0	5.0	7.0	4.5	1.785	455.50

*Refer to Figure 3.33 for panel-to-beam fastener location details

Table 3.7: *Measured geometry and material strength for C-section 4-point bending tests by Yu and Schafer (2003)*

Test #	Test label	Panel Type*	h (mm)	b_c (mm)	d_c (mm)	θ_c (deg)	b_t (mm)	d_c (mm)	θ_t (deg)	r_{hc} (deg)	r_{dc} (deg)	r_{ht} (deg)	r_{dt} (deg)	t (mm)	f_y (N/mm^2)
14	8C097-2E3W	C	204.0	53.5	14.5	84.80	53.0	13.5	86.95	8.0	7.0	7.0	7.5	2.440	411.68
15	8C068-4E5W	C	203.5	52.0	13.0	83.60	52.0	13.5	87.30	7.0	6.0	6.0	6.5	1.935	350.36
16	8C068-1E2W	C	204.0	52.0	13.5	83.25	52.0	13.5	87.85	7.5	6.0	6.0	7.0	1.925	355.18
17	8C054-1E8W	C	204.0	51.5	14.0	88.50	51.5	12.5	83.50	6.0	5.5	6.0	6.0	1.385	276.64
18	8C043-5E6W	C	204.5	51.0	14.0	88.85	50.5	13.0	87.15	5.0	5.0	5.5	5.0	1.250	309.71
19	8C043-3E1W	C	204.0	51.0	14.0	89.15	50.5	13.5	86.65	5.0	5.0	6.0	5.0	1.205	315.91
20	12C068-9E5W	C	305.0	47.0	13.5	83.95	51.5	14.0	90.05	7.0	7.0	7.0	7.0	1.660	241.29
21	12C068-3E4W	C	304.5	50.5	14.0	81.55	51.0	13.5	80.35	6.5	7.0	7.0	7.0	1.700	392.46
22	10C068-2E1W	C	255.5	50.5	13.5	81.95	50.0	13.5	82.60	7.0	6.5	7.0	6.0	1.450	233.4
23	6C054-2E1W	C	153.0	51.0	14.0	86.10	51.5	13.0	90.25	5.5	6.0	6.5	6.0	1.565	251.69
24	4C054-1E2W	D	100.0	50.0	13.5	76.70	50.5	14.0	76.10	6.0	6.5	6.0	6.0	1.460	309.00
25	3.62C054-1E2W	D	93.0	50.0	12.5	78.45	50.5	11.0	83.95	6.0	6.5	6.5	6.5	1.410	223.08

*Refer to Figure 3.33 for panel-to-beam fastener location details

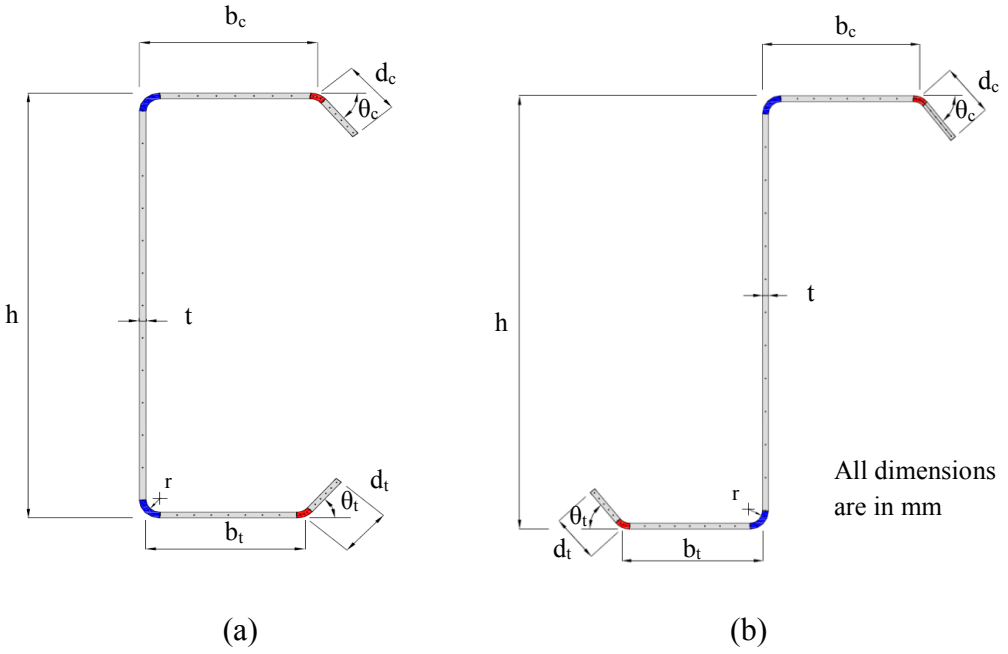


Figure 3.34: *Notation used for the geometry for (a) C-sections and (b) Zed sections physical test conducted by Yu and Schafer (2003)*

3.3.3.3. 3-point bending tests by Bryan, Davies and Deakin (1979-1992)

Bryan, Davies and Deakin conducted numerous types of physical tests on Zeta I, Zeta II and Zed cold-formed steel sections at University of Salford from 1979-1992: Bryan and Davies (1979, 1980a), Bryan and Deakin (1989), Deakin (1991a, 1991b) and Davies and Deakin (1992). The library of reports covers single span moment gradient (3-point bending) tests and full scale 2-span tests subjected to gravity and uplift UDL. 3-point bending tests are discussed in this section and 2-span tests are discussed in Section 3.3.4. The details of 3-point bending tests are summarized in Table 3.8. Each test comprised two nominally identical section pairs, with C-section ties to prevent lateral displacement as shown in Figure 3.35. The geometry of Zeta IA, Zeta IB and Zeta II section types have the nominal dimensions illustrated in Figures 3.36 and 3.37. Apart from the section measured thickness, the nominal dimensions for each section were used in the FE models since there were no reported measured geometrical dimensions.

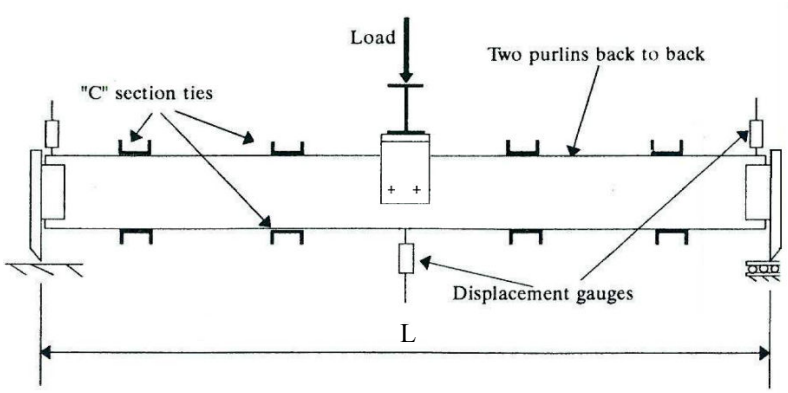


Figure 3.35: *3-point bending test arrangement*

Table 3.8: *3-point bending tests by Bryan and Davies (1979, 1980a), Bryan and Deakin (1989), Deakin (1991a, 1991b) and Davies and Deakin (1992)*

Test#	Reference	Section type*	Span (m)	Height (mm)	Thickness (mm)	f_y (N/mm^2)
1	Bryan and Davies (1979)	Zeta IA	2.4	170	1.58	306.33
2		Zeta IB	2.4	150	1.55	306.00
3		Zeta IB	1.8	150	1.55	307.30
4	Bryan and Davies (1980a)	Zeta IB	2.2	200	1.52	302.80
5	Bryan and Deakin (1989)	Zeta IB	2.6	175	1.56	311.33
6	Deakin (1991a)	Zeta IB	2.4	150	1.42	368.80
7	Deakin (1991b)	Zeta IB	3.0	200	1.33	295.00
8	Davies & Deakin (1992)	Zeta II	4.0	285	1.96	312.00
9		Zeta II	3.6	285	1.47	264.00
10		Zeta II	3.4	265	1.58	286.00
11		Zeta II	3.2	245	1.46	262.00
12		Zeta II	3.0	225	1.41	401.00

*Refer to Figures 3.36 and 3.37 for cross-sectional dimensions

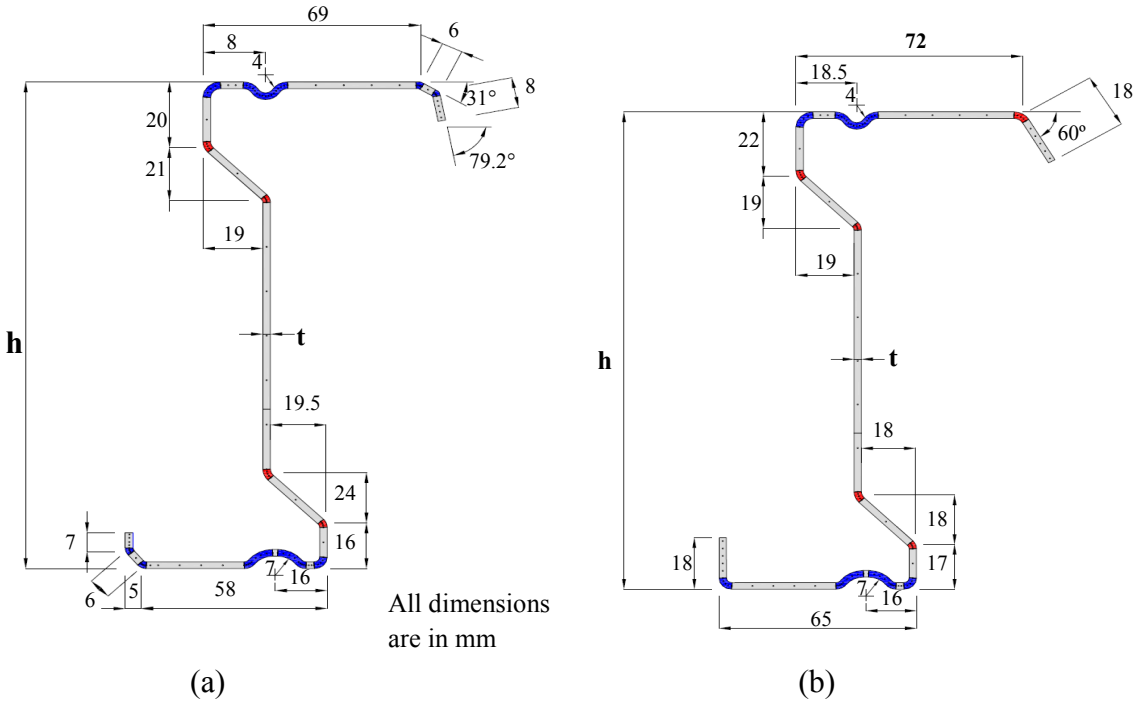


Figure 3.36: *Definition of cross-sectional dimensions for (a) Zeta IA and (b) Zeta IB sections*

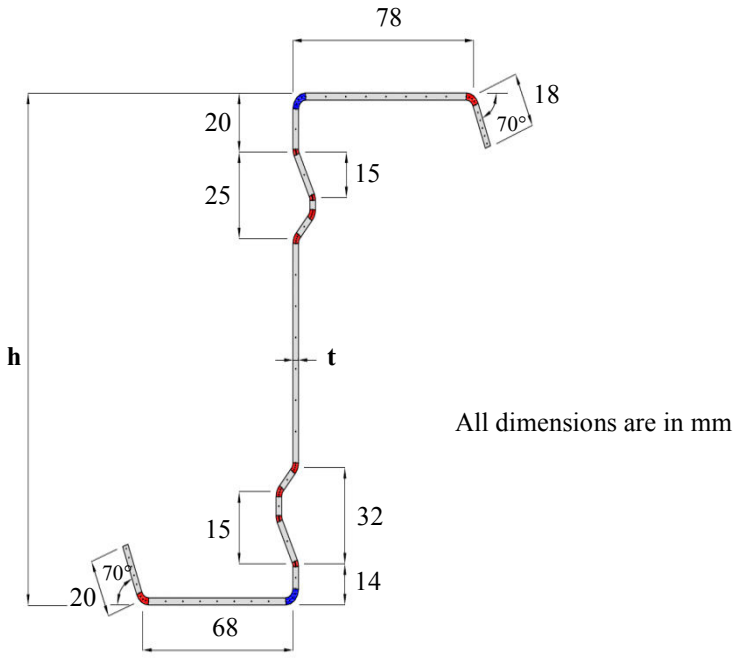


Figure 3.37: *Definition of cross-sectional dimensions for Zeta II sections*

3.3.3.4. Comparison between single span tests and FE results

The single span FE models were validated against the experimental results by Wang and Zhang (2009), Yu and Schafer (2003) and Bryan and Davies (1979, 1980a), Bryan and Deakin (1989), Deakin (1991a, 1991b) and Davies and Deakin (1992). Tables 3.9-3.12 show that the developed FE models moment capacities M_{FE} are able to accurately predict the observed ultimate bending capacities M_{test}, with average M_{FE}/M_{test} ratio of 0.99 with coefficient of variation (COV) of 0.03. For the three sets of physical tests, some variation in the amount of scatter was observed. The COV for the predictions of the Wang and Zhang (2009) 4-point bending and 3-point bending test results was only 0.020 and 0.009 respectively, whereas the Bryan, Davies and Deakin (1979-1991) and Yu and Schafer (2003) COVs were slightly higher at 0.043 and 0.055. This may be due to: (i) initial imperfection measurements were only conducted by Wang and Zhang, giving a closer representation of the initial imperfection in the FE model, (ii) apart from the measured thicknesses, no other measured dimensions were reported in tests by Bryan, Davies and Deakin (1979-1991) and it was assumed the nominal dimensions were constant for all specimens, (iii) additional complexity with panelling fixing by Yu and Schafer (2003). Nevertheless, the results from the single span validation study shows that the models are robust even if not all the input values were accurately known. The observed load-displacements responses from the FE models gave close agreement to those obtained from the tests as shown in Figures 3.38-3.39 and 3.41-3.42. While reference to the load-displacement response from Figure 3.38(a), Figure 3.40 shows the FE deformed stress-profiles for Test 1 (8.5Z120-3-E2W) for Yu and Schafer (2003) at different points of loading (labelled points A-F). At the early stages of loading, the stresses at both top and bottom flanges increase proportionally. Prior to the ultimate load, the neutral axis rises towards the compression (top) flange as the stresses reach the yield stress. Similar to findings reported by Yu (2005), local buckling was observed at the compression flange with a restricted half-wavelength close to the spacing between translational springs. This indicates the assumed material model (including corner enhancements) and cross-sectional definition (with chosen mesh density) are valid for modelling cold-formed steel sections covering a wide range of yield strengths (262-467 N/mm^2). It can be concluded that the developed FE models are able to replicate the buckling behaviour for different cross-sectional geometries, material properties and test

setup. The FE models can therefore be employed as a basis to increase the data pool of structural capacities by conducting parametric studies of the sort described in Chapter 4.

Table 3.9: *Comparison of bending resistances obtained from FE models and 4-point bending tests by Wang and Zhang (2009*)

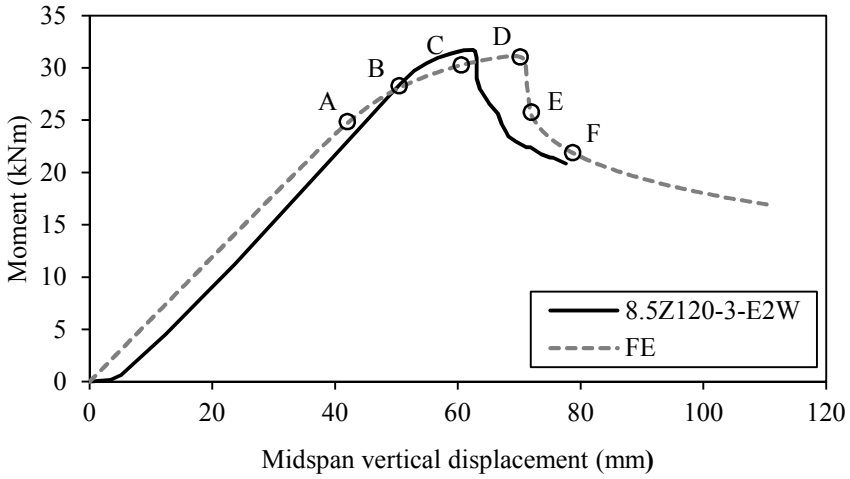
Test #	Test label	M_{test} (kNm)	M_{FE} (kNm)	M_{FE}/M_{test}
1	L_UH200B80d20	26.950	26.481	0.983
2	L_UH200B80d40	30.040	30.279	1.007
3	L_IH200B80d20	24.280	24.561	1.012
4	L_IH200B80d40	29.280	28.403	0.970
			Mean	0.993
			COV	0.020

Table 3.10: *Comparison of bending resistances obtained from FE models and 3-point bending tests by Wang and Zhang (2009)*

Test #	Test label	M_{test} (kNm)	M_{FE} (kNm)	M_{FE}/M_{test}
5	S_UH200B80d20	28.590	28.798	1.007
6	S_UH200B80d40	30.800	31.316	1.017
7	S_IH200B80d20	28.440	28.521	1.003
8	S_IH200B80d40	30.350	30.203	0.995
			Mean	1.006
			COV	0.009

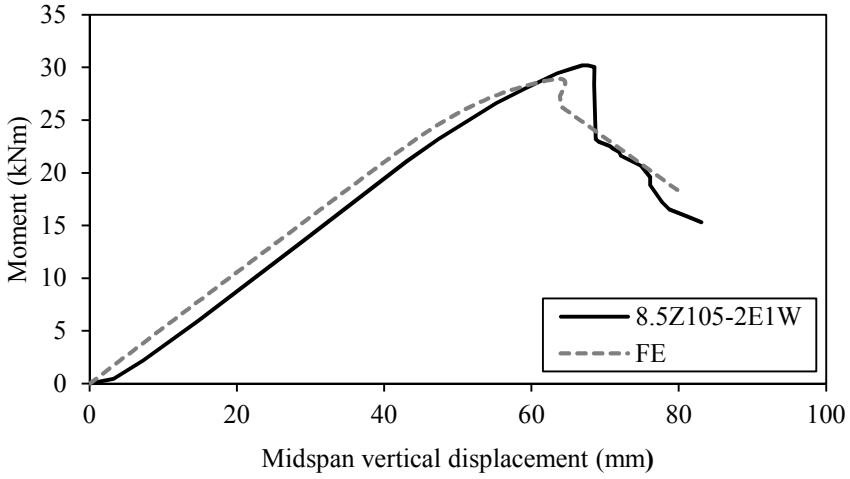
Table 3.11: *Comparison of bending resistances obtained from FE models and pure bending tests by Yu and Schafer (2003)*

Test #	Section type	Test label	M_{test} (kNm)	M_{FE} (kNm)	M_{FE}/ M_{test}
1	Zed	8.5Z120-3E2W	31.700	31.069	0.980
2	Zed	8.5Z105-2E1W	30.200	28.950	0.959
3	Zed	8.5Z092-4E2W	20.500	20.658	1.008
4	Zed	8.5Z082-1E2W	18.300	18.381	1.004
5	Zed	8.5Z073-6E5W	13.700	14.197	1.036
6	Zed	8.5Z073Z-4E3W	15.100	15.485	1.025
7	Zed	8.5Z073-1E2W	13.900	14.370	1.034
8	Zed	8.5Z065-3E1W	10.800	10.313	0.955
9	Zed	8.5Z059-4E3W	11.400	11.761	1.032
10	Zed	8.5Z059-2E1W	11.200	12.086	1.079
11	Zed	11.5Z092-1E2W	39.800	42.456	1.067
12	Zed	11.5Z082-2E1W	31.000	31.711	1.023
13	Zed	11.5Z073-2E1W	21.900	20.984	0.958
14	C	8C097-2E3W	19.500	18.544	0.951
15	C	8C068-4E5W	11.700	11.793	1.008
16	C	8C068-1E2W	11.100	11.923	1.074
17	C	8C054-1E8W	6.300	6.409	1.017
18	C	8C043-5E6W	5.800	5.628	0.970
19	C	8C043-3E1W	5.400	5.940	1.100
20	C	12C068-9E5W	11.800	11.614	0.984
21	C	12C068-3E4W	15.500	16.590	1.070
22	C	10C068-2E1W	7.900	7.320	0.927
23	C	6C054-2E1W	5.100	4.848	0.950
24	C	4C054-1E2W	3.100	3.109	1.003
25	C	3.62C054-1E2W	2.300	1.968	0.856
				Mean	1.003
				COV	0.055

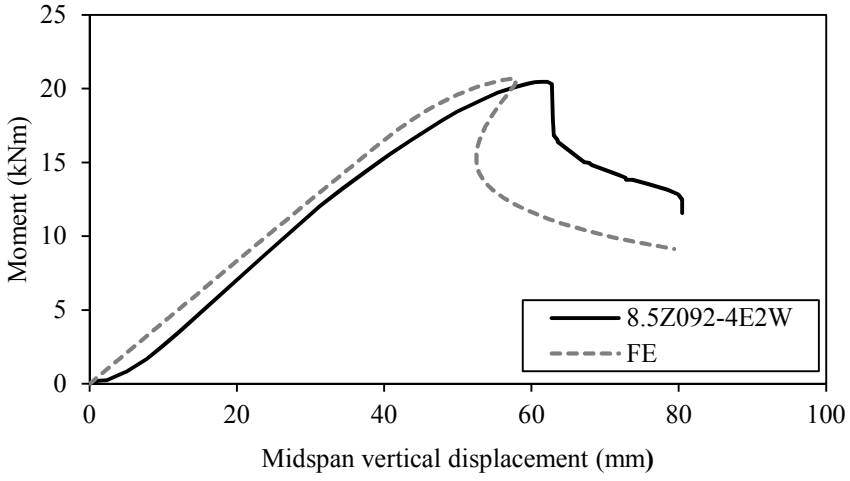


Refer to Figure 3.40 for labelled deformed stress profiles

(a) Test 1

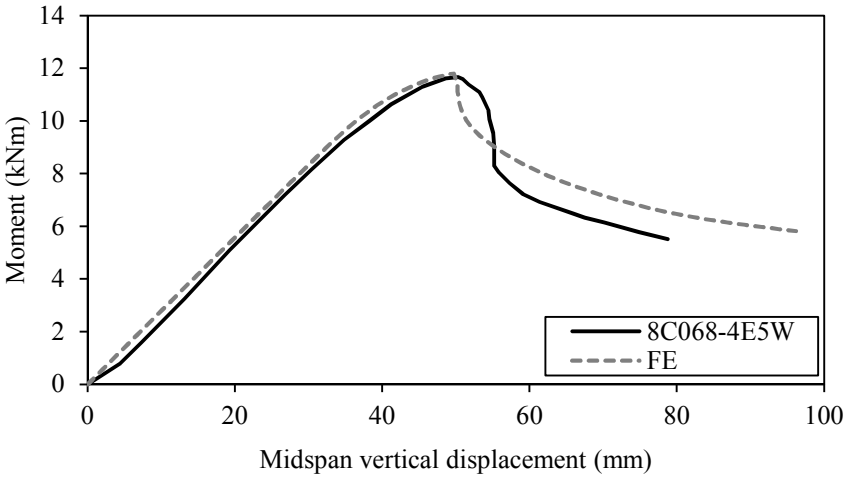


(b) Test 2

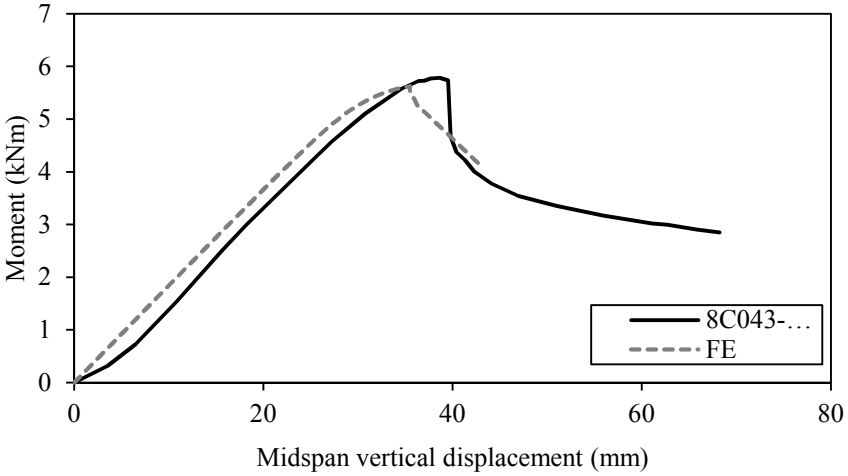


(c) Test 3

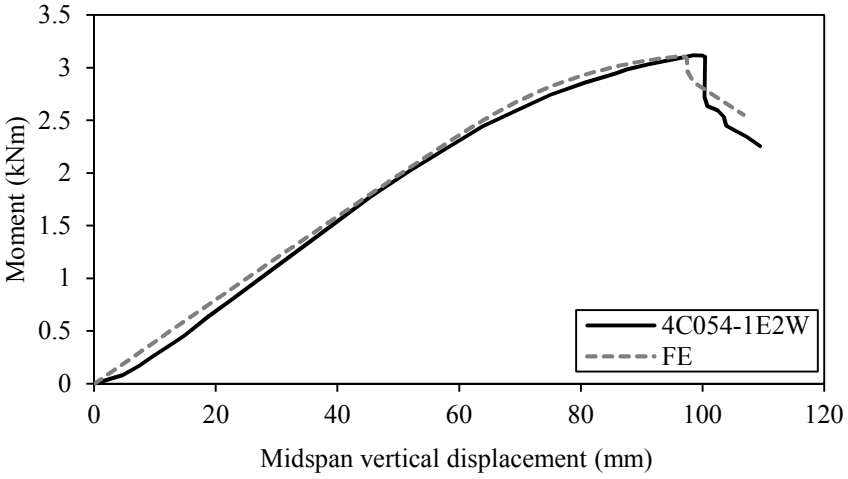
Figure 3.38: *Load-deformation curves from Yu and Schafer (2003) tests and FE models (Zed sections)*



(a) Test 15



(b) Test 18



(c) Test 24

Figure 3.39: *Load-deformation curves from Yu and Schafer (2003) tests and FE models (C-sections)*

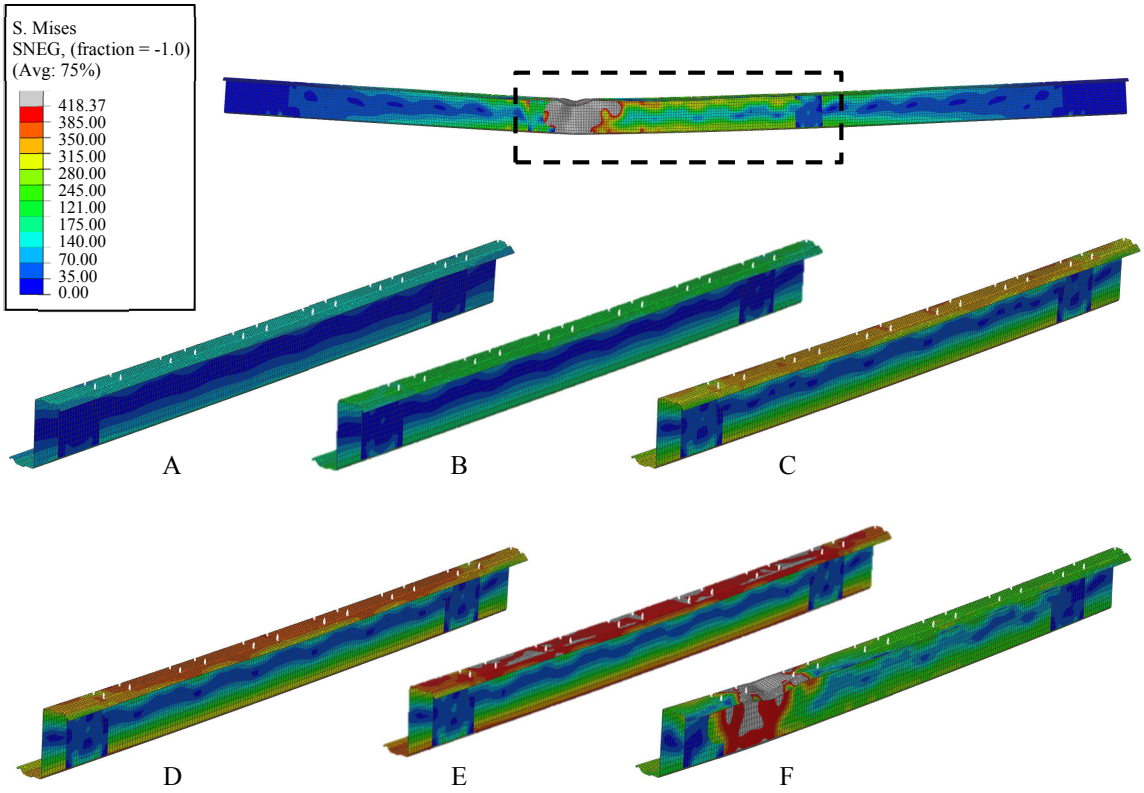
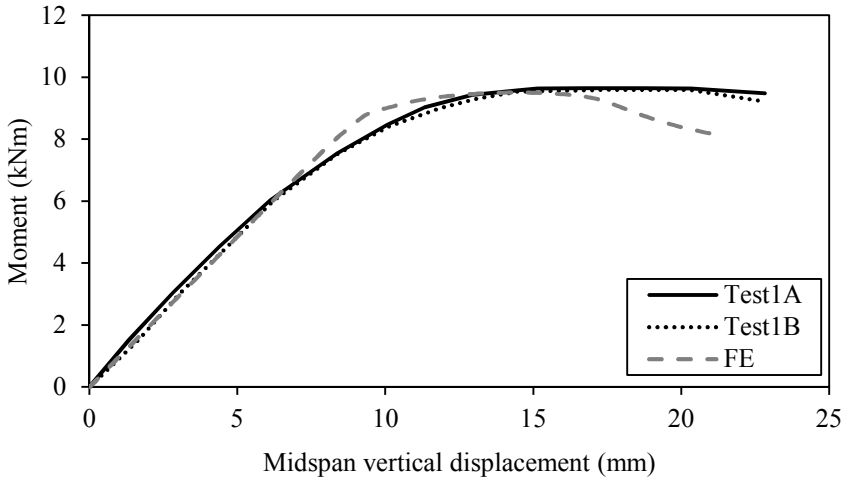


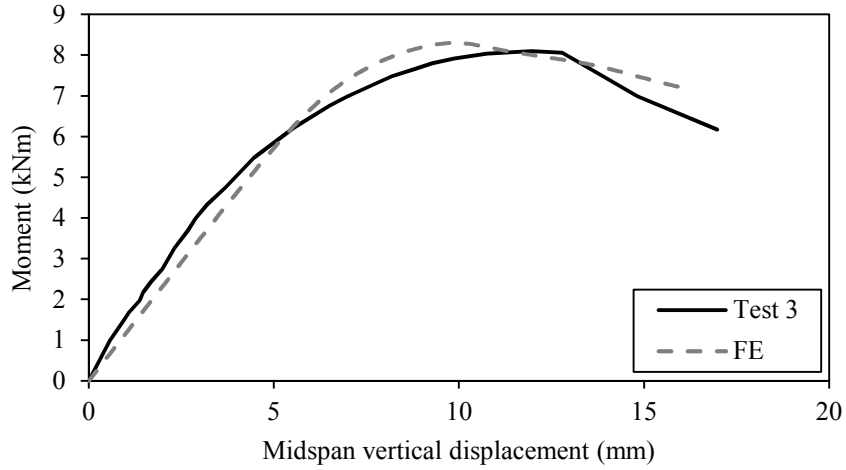
Figure 3.40: Stress profile at different load stages for Test 1 from Yu and Schafer (2003)

Table 3.12: *Comparison of bending resistances obtain from FE models and 3-point bending tests*

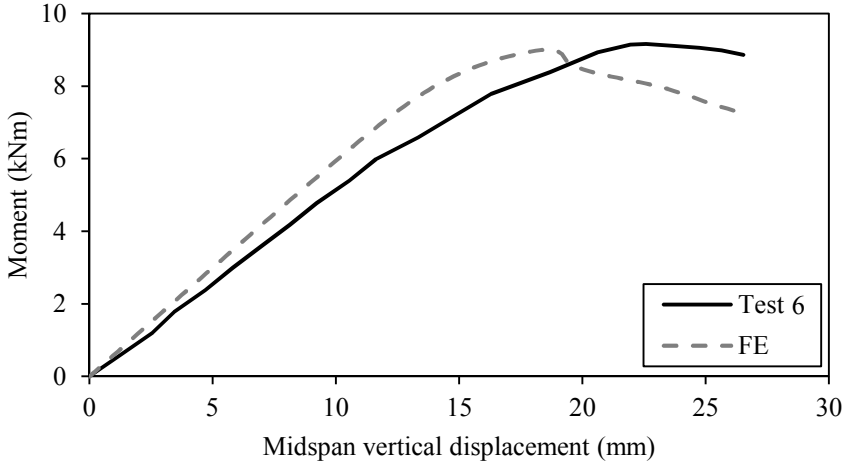
Test #	Reference	Section type	M_{test} (kNm)	M_{FE} (kNm)	M_{FE}/ M_{test}
1	Bryan and Davies (1979)	Zeta IA	9.625*	9.506	0.988
2		Zeta IB	9.300	8.580	0.923
3		Zeta IB	8.100	8.306	1.025
4	Bryan and Davies (1980a)	Zeta IB	11.275	11.825	1.049
5	Bryan and Deakin (1989)	Zeta IB	11.125	10.790	0.970
6	Deakin (1991a)	Zeta IB	9.160	9.001	0.983
7	Deakin (1991b)	Zeta IB	9.150	9.375	1.025
8	Davies and Deakin (1992)	Zeta II	24.650	24.261	0.984
9		Zeta II	13.750	13.690	0.996
10		Zeta II	16.380	16.100	0.983
11		Zeta II	12.800	12.590	0.984
12		Zeta II	14.250	14.570	1.022
*Average between 2 tests (9.60 and 9.65 kNm)				Mean	0.993
				COV	0.032



(a) Test 1

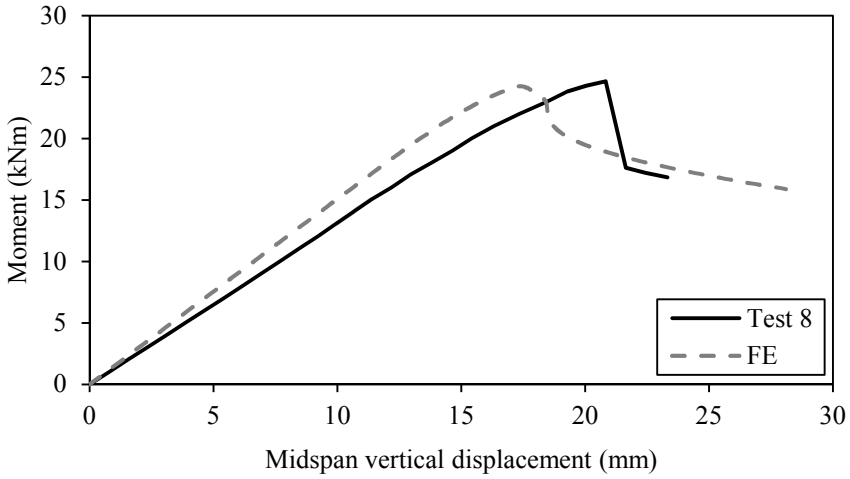


(b) Test 3

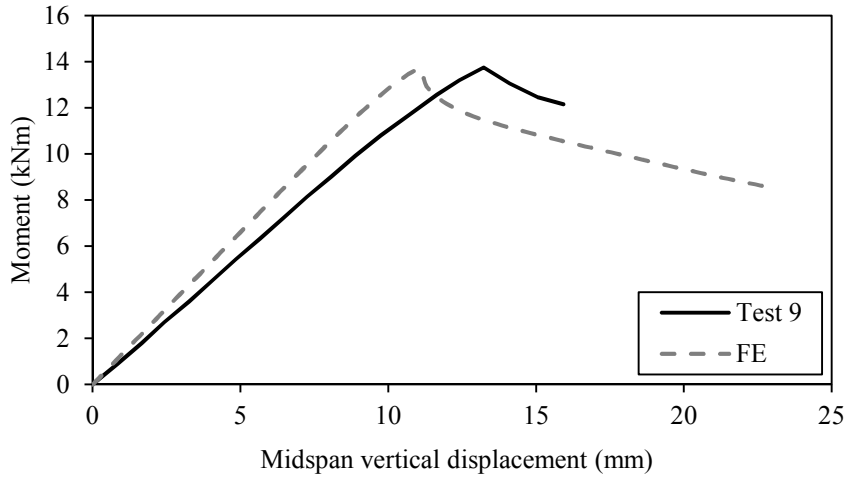


(c) Test 6

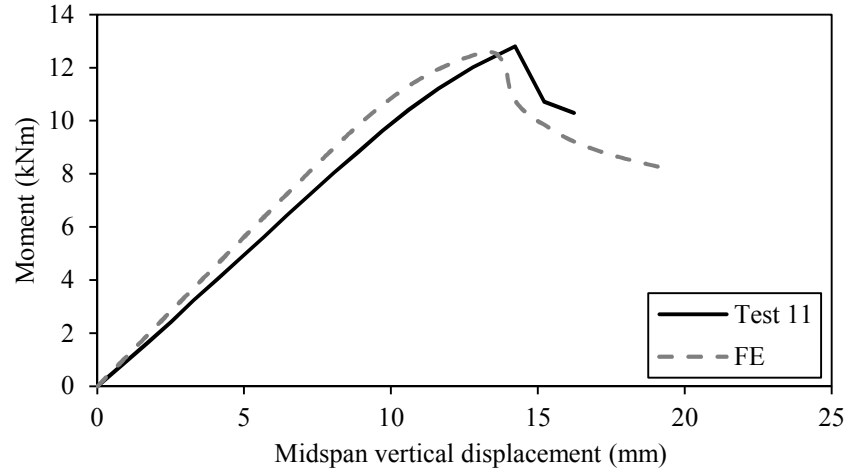
Figure 3.41: *3-point bending load-deformation curves from Bryan and Davies (1979) and Deakin (1991a) tests and FE models (Zeta IA, Zeta IB sections)*



(a) Test 8



(a) Test 9



(a) Test 11

Figure 3.42: *3-point bending load-deformation curves from Davies & Deakin (1992) tests and FE models (Zeta II sections)*

3.3.4. 2-span continuous beam tests

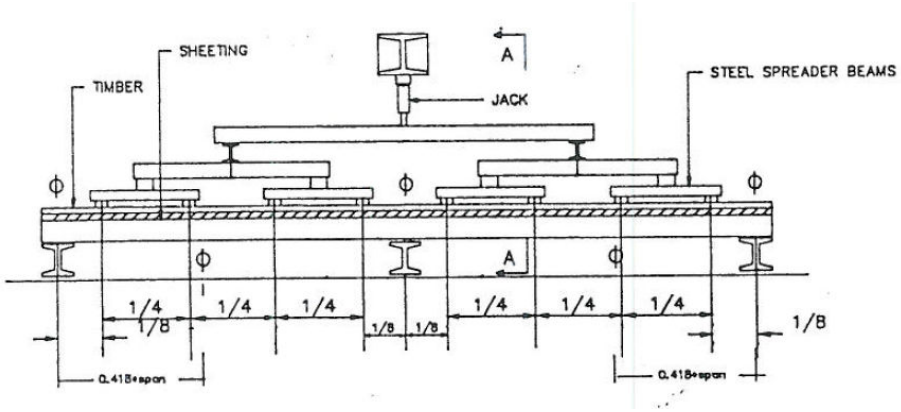
Zeta I 2-span gravity and uplift tests (test type 5 and 6) conducted by Bryan, Davies and Deakin (1979-1991) have been used to validate 2-span numerical models for a variety of cold-formed steel cross-sections. Table 3.13 summarises the 2-span tests considered for this study. 2-span gravity and uplift tests are discussed in more detail in the Sections 3.3.4.1-3.3.4.2.

Table 3.13: *Summary of 2-span tests for validation study*

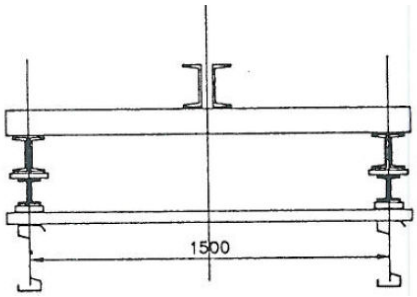
Reference	Test type	Section Type	Number of tests
Deakin et al. (1979) Bryan and Davies (1979,1980a) Bryan and Deakin (1989) Deakin (1991a, 1991b)	2-span gravity	Zeta IA Zeta IB Zeta IC	10
Bryan and Davies (1979) Deakin (1991a, 1991b)	2-span uplift	Zeta IB	6

3.3.4.1. Gravity 2-span continuous tests

Bryan, Davies and Deakin (1979-1991) conducted 10 Zeta I 2-span tests subjected to a gravity UDL. The purlins were tested in pairs (1.5 m apart) in an opposed arrangement with corrugated sheeting attached to the top flanges. Spaced at 200 mm centres, Tek self-drilling screws were used to fasten the corrugated sheeting to the purlins. The purlins were supported off cleats which were bolted to universal beam rafters. The UDL was replicated by a central hydraulic jack with spreader beams to create 4 point loads in each span as shown in Figure 3.43. Three different types of Zeta I sections were tested: Zeta IA and Zeta IB, which were described in Section 3.3.3.3, and are illustrated in Figure 3.36, and Zeta IC, which is new to this study, and is detailed in Figure 3.44. Apart from the section measured thickness, the nominal dimensions for each section were used in the FE models since there were no reported measured geometrical dimensions. The geometrical dimensions and measured yield strengths are shown in Table 3.14.



(a)



(b)

Figure 3.43: *2-span purlin tests by Bryan, Davies and Deakin (1979-1991), (a) overview of loading arrangement and (b) Section A-A*

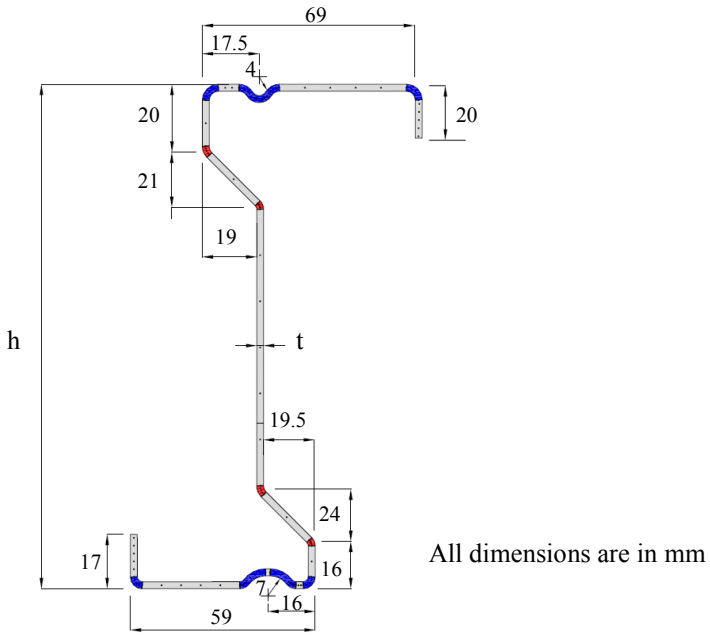


Figure 3.44: *Definition of cross-sectional dimensions for Zeta IC*

Table 3.14: *Measured geometry and material strength for 2-span gravity tests by Deakin et al. (1979), Bryan and Davies (1979, 1980a), Bryan and Deakin (1989) and Deakin (1991a, 1991b)*

Test #	Reference	Section type*	Span (m)	Height (mm)	Thickness (mm)	f_y (N/mm^2)
1	Deakin et al. (1979)	Zeta IA	6.0	170	1.58	306.33
2		Zeta IC	6.0	170	1.58	311.80
3	Bryan and Davies (1979)	Zeta IB	5.5	125	1.45	306.00
4		Zeta IB	6.0	150	1.55	307.30
5		Zeta IB	6.0	175	1.50	302.70
6		Zeta IB	7.5	200	1.52	302.80
7	Bryan and Davies (1980a)	Zeta IB	7.5	200	1.94	334.90
8	Bryan and Deakin (1989)	Zeta IB	6.5	175	1.56	311.33
9	Deakin (1991a)	Zeta IB	6.0	150	1.42	368.80
10	Deakin (1991b)	Zeta IB	7.5	200	1.33	295.00

*Refer to Figures 3.36(a), 3.36(b) and 3.43 for cross-sectional dimension details

3.3.4.2. Uplift 2-span continuous beam tests

Bryan and Davies (1980a) and Deakin (1991a, 1991b) conducted 6 Zeta IB 2-span tests subjected to an uplift UDL. The test arrangement was similar to that used previously by the same authors but with the specimens and sheeting flipped upside-down and loaded downwards. The purlins were tested in pairs (1.5 m apart) in an opposed arrangement with corrugated sheeting attached to the bottom flanges as shown in Figure 3.45. Spaced at 200 mm centres, 6.0 mm diameter bolts were used to fasten the corrugated sheeting to the purlins. The UDL was replicated by a central hydraulic jack with spreader beams to create 4 point loads in each span as shown in Figure 3.43(a) and 3.45. The geometrical dimensions and yield strengths for each specimen are shown in Table 3.15. Apart from the section measured thickness, the nominal dimensions for each section were used in the FE models since there were no reported measured geometrical dimensions. The nominal geometrical dimensions for the tested sections are shown in Figure 3.36(b). Even though anti-sagbars are commonly installed in practice to allow for easier construction and provide additional lateral restraint to the purlin system, anti-sagbars are not considered in the parametric study in Chapter 4. The effects of the anti-sagbar are simulated in the FE

model by adding lateral restraint (DOF 1) at the same location on the web and longitudinal spacing as the tests.

Table 3.15: *Measured geometry and material strength for 2-span uplift tests by Bryan and Davies (1980a) and Deakin (1991a, 1991b)*

Test #	Reference	Section type[A]	Span (m)	No. sagbars[B]	Height (mm)	Thickness (mm)	f_y (N/mm^2)
1	Bryan and Davies (1980a)	Zeta IB	5.5	0	125	1.45	306.00
2		Zeta IB	6.0	0	150	1.55	307.30
3		Zeta IB	7.5	0	200	1.52	302.80
4	Deakin (1991a)	Zeta IB	6.0	0	150	1.42	386.80
5	Deakin (1991b)	Zeta IB	7.5	1	200	1.33	295.00
6		Zeta IB	7.5	2	200	1.33	295.00

A Refer to Figure 3.36(b) for cross-sectional dimension details
B Number of evenly spaced sagbars per span

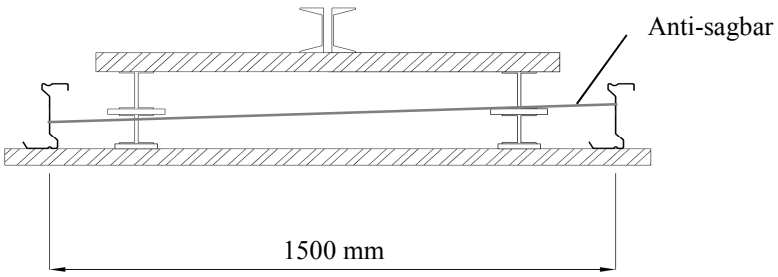


Figure 3.45: *Section A-A for 2-span uplift purlin tests by Bryan and Davies (1980a) and Deakin (1991a, 1991b)*

3.3.4.3. Comparison between 2-span tests and FE results

A total of 16 continuous 2-span FE models under gravity and uplift loading were validated against physical tests by Deakin et al. (1979), Bryan and Deakin (1979, 1980a), Bryan and Deakin (1989) and Deakin (1991a, 1991b). Tables 3.16 and 3.17 show that ultimate loads from the FE method ($q_{ult,FE}$) can accurately predict the ultimate test loads $q_{ult,test}$ with minimal scatter. The mean and COV values for 2-span gravity and uplift are 1.013, 1.015 and 0.030, 0.028, respectively. The load-displacement responses from the FE models also show good correlation with the physical experiments, as shown in Figures 3.46-3.47 and 3.49-3.50. This suggests that the FE model can accurately capture the moment redistribution behaviour of a 2-span system. The failure modes also correlate

well with the observed failure modes. Distortional buckling of the compression (bottom) flange was observed first at the interior support, and final failure of the system was governed by local/distortional buckling in the span region at the compression (top) flange, as shown in Figure 3.48. Knowing the definition of cross-section geometry, material modelling, mesh density and other FE parameters have been previously validated for single span tests in Section 3.3.3, and following successful validation against the 2-span continuous beam tests it may be concluded that the 2-span FE model is sufficiently robust to carry out further simulations using varying input parameters to create a larger library of 2-span results.

Table 3.16: *Comparison of ultimate loads obtain from FE models and 2-span gravity tests*

Test #	Reference	Section type*	$q_{ult,test}$	$q_{ult,FE}$	$q_{ult,FE}/q_{ult,test}$
1	Deakin et al. (1979)	Zeta IA	2.668	2.688	1.007
2		Zeta IC	2.920	3.007	1.030
3	Bryan and Davies (1979)	Zeta IB	2.178	2.215	1.017
4		Zeta IB	2.631	2.771	1.054
5		Zeta IB	2.933	2.900	0.989
6		Zeta IB	2.153	2.167	1.006
7	Bryan and Davies (1980a)	Zeta IB	3.006	3.117	1.037
8	Bryan and Deakin (1989)	Zeta IB	2.449	2.370	0.968
9	Deakin (1991a)	Zeta IB	2.569	2.696	1.050
10	Deakin (1991b)	Zeta IB	1.654	1.610	0.973
				Mean	1.013
*Refer to Figures 3.36(a), 3.36(b) and 3.42 for cross-sectional dimension details				COV	0.030

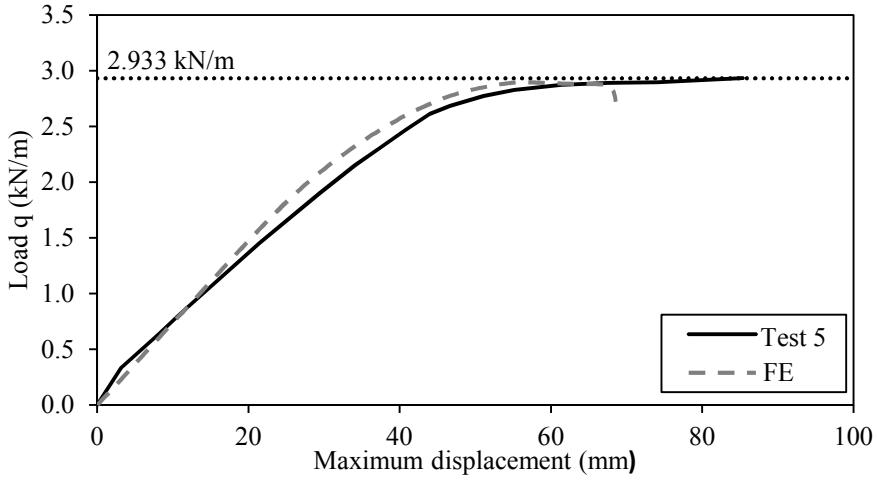


Figure 3.46: *Test 5 2-span gravity load-deformation curves from Bryan and Davies (1979) and FE models (Zeta IB sections)*

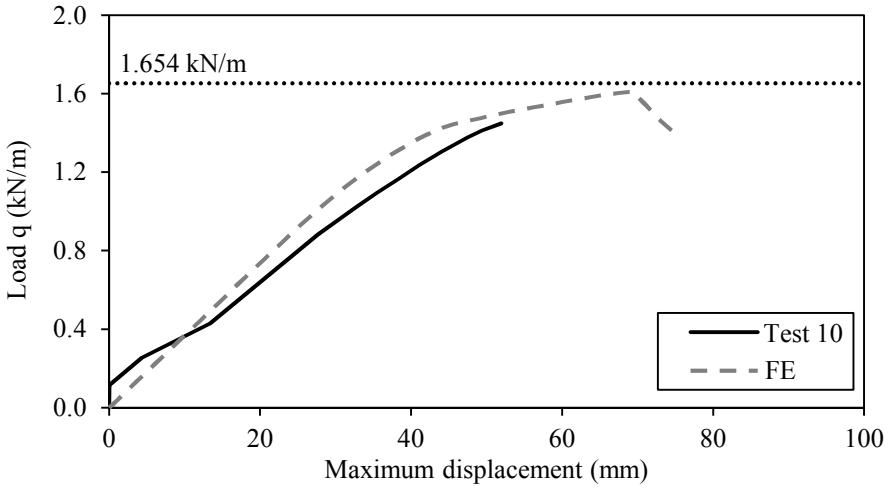


Figure 3.47: *Test 10 2-span gravity load-deformation curves from Deakin (1991b) and FE models (Zeta IB sections)*

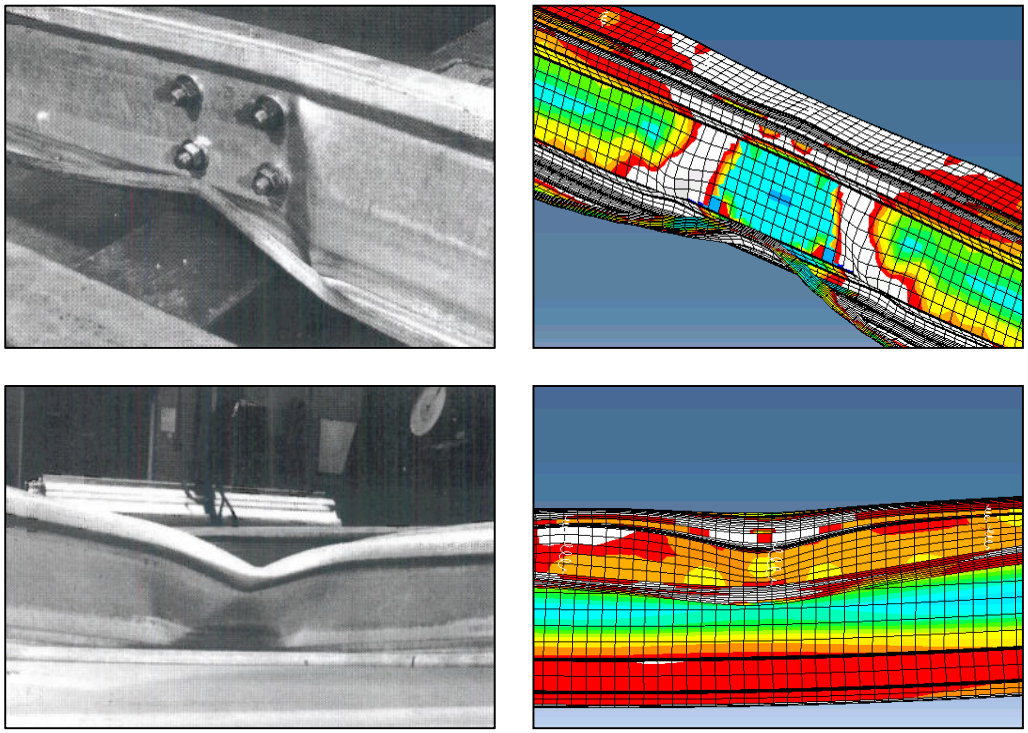


Figure 3.48: *Comparison of failure modes between physical Test 7 from Bryan and Davies (1980a) and FE model*

Table 3.17: *Comparison of ultimate loads obtain from FE models and 2-span uplift tests by Bryan and Deakin (1980a) and Deakin (1991a, 1991b)*

Test #	Reference	Section type*	$q_{ult,test}$	$q_{ult,FE}$	$q_{ult,FE}/q_{ult,test}$
1	Bryan and Deakin (1980a)	Zeta IB	2.451	2.496	1.007
2		Zeta IB	2.410	2.445	1.030
3		Zeta IB	2.013	2.102	1.017
4	Deakin (1991a)	Zeta IB	2.503	2.620	1.054
5	Deakin (1991b)	Zeta IB	1.526	1.488	0.989
6		Zeta IB	1.569	1.553	1.006
*Refer to Figures 3.36b for cross-sectional dimension details				Mean	1.015
				COV	0.028

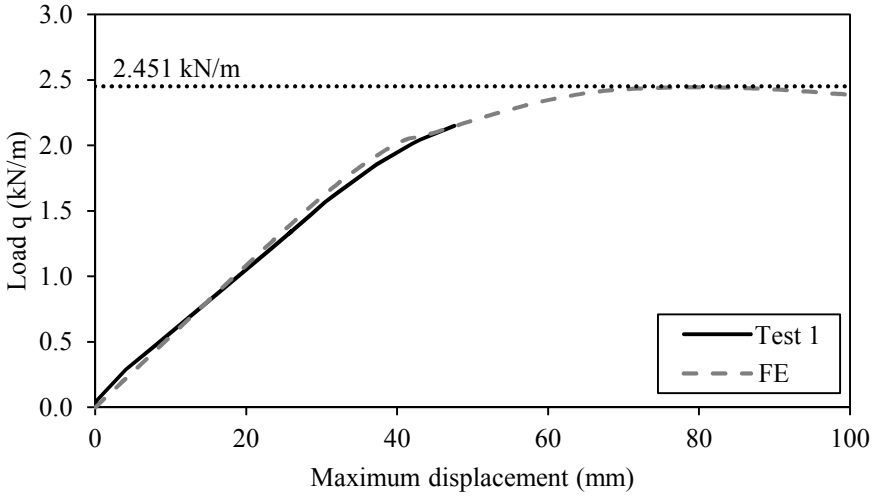


Figure 3.49: *2-span uplift load-deformation curves for test 1 from Bryan and Deakin (1980a) and FE models (Zeta IB sections)*

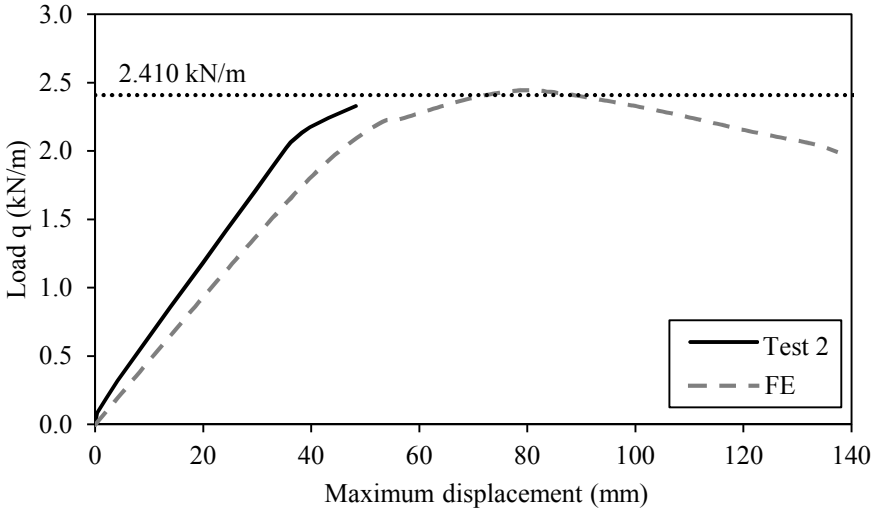


Figure 3.50: *2-span uplift load-deformation curves for test 2 from Bryan and Deakin (1980a) and FE models (Zeta IB sections)*

3.4. CONCLUDING REMARKS

In this chapter, four FE models comprising single and 2-span bending test arrangements have been developed using the ABAQUS package. Numerical analyses including material and geometrical nonlinearities have been performed. Important FE modelling parameters such as corner enhancements, a two-spring model for attached sheeting and initial imperfection were all incorporated into the numerical models. Using results from previous experiments, the FE models were validated by ensuring the ultimate capacity, initial stiffness and failure modes all correlated well with the reported values and photographs. Table 3.18 provides a summary of all the validated single and 2-span continuous FE models.

Table 3.18: *Summary of single span and 2-span tests for validation*

Reference	Test type	Section Type	No. of tests	Mean	COV
Wang and Zhang (2009)	4-point (pure) bending	C	4	0.993	0.020
Yu and Schafer (2003)	4-point (pure) bending	Zed/C	25	1.003	0.055
Wang and Zhang (2009)	3-point bending	C	4	1.006	0.009
Bryan and Davies (1979, 1980a) Bryan and Deakin (1989) Deakin (1991a, 1991b)	3-point bending	Zeta IA Zeta IB	7	0.995	0.043
Davies and Deakin (1992)	3-point bending	Zeta II	5	0.994	0.017
Bryan and Davies (1979, 1980a) Bryan and Deakin (1989) Deakin (1991a, 1991b)	2-span gravity	Zeta IA Zeta IB Zeta IC	10	1.013	0.030
Deakin et al. (1979) Deakin (1991a, 1991b)	2-span uplift	Zeta IB	6	1.015	0.028

CHAPTER 4

BARE SECTION PARAMETRIC STUDY AND DESIGN

4.1. INTRODUCTION

In this chapter, the validated bare section FE models developed in Chapter 3 are extended to study the degree of moment redistribution in 2-span continuous cold-formed steel systems subjected to gravity and uplift loading by means of parametric studies. Zeta I, Zeta II, Zed and channel cross-sections covering a wide range of slenderness values were investigated. The results from the parametric study were then used to propose design equations.

4.2. DESIGN APPROACH FOR 2-SPAN SYSTEMS

Figure 4.1 illustrates a typical multi-span purlin system (Figure 4.1(a)) with equal spans broken down into individual 2-span systems (Figure 4.1(b)). A design based on elastic principles, as shown in Figure 4.1(b), would utilise the full cross-sectional moment capacity at the internal support but not within the span. However, due to the statically indeterminate nature of the 2-span system, there is the potential to use a greater proportion (possibly all) of the unused moment capacity within the span by allowing the

redistribution of moments. The principle is commonly used when designing hot rolled steelwork; it has been adapted for reinforced concrete construction, composite construction and cold-formed steel construction by recognising certain limitations in the moment-rotation relationships of cross-sections and accepting that full redistribution may not be possible.

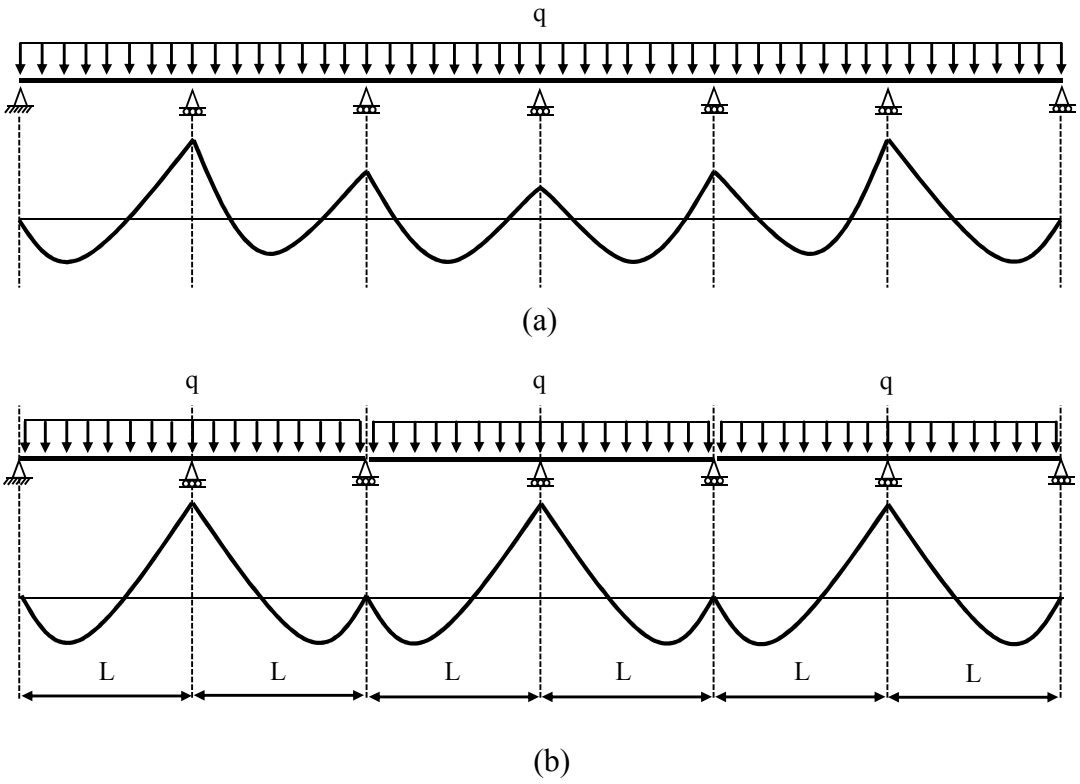


Figure 4.1: *Elastic bending moment diagram (BMD) for (a) multi-span and (b) 2-span purlin systems*

4.2.1. Moment redistribution

Given the ideal situation of full plastic redistribution of moments, the bending moment at the interior support, $M_{support}$ and within the span, M_{span} both reach their full cross-sectional capacities because the moment-rotation relationship for the support region is such that no significant drop off in capacity occurs before rotations develop sufficiently to allow the span moment to reach its capacity. For such cases, it is common for the designer to adopt an idealised elastic-perfectly plastic (flat topped) moment-rotation relationship as demonstrated in Figure 4.2.

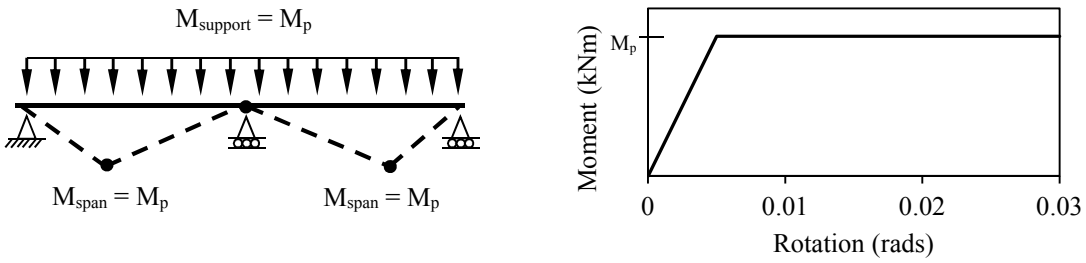


Figure 4.2: *Idealised full moment redistribution in a 2-span system and flat topped moment-rotation relationship*

However, due to the high width-to-thickness ratios of the constituent elements, cold-formed steel purlins are susceptible to local instabilities like local and/or distortional buckling. Thus the design issue for cold-formed steel construction is that the moment-rotation behaviour may differ from the ideal arrangement detailed in Figure 4.2. Should this be the case, i.e. attaining full capacity within the span is accompanied by a reduction in interior support moment, then appropriate allowance must be made.

4.3. PARAMETRIC STUDY – GRAVITY LOADING

4.3.1. Outline

The in-plane bending behaviour of cold-formed steel cross-sections was investigated by conducting single span parametric studies, as discussed in Section 4.3.2. The developed FE models were then used to study the degree of moment redistribution for cold-formed steel continuous 2-span purlin systems by analysing 2-span FE models using ABAQUS (2010). 25 cross-sections covering Zeta I, Zeta II, Zed and channel cross-sections types were chosen for this study and are detailed in Figure 4.3-4.4. The section height h, top flange width b_c, bottom flange width b_t and thickness t were varied to cover a large cross-section slenderness range. The location and dimensions of the intermediate stiffeners in the flanges and web for the Zeta I and Zeta II sections were kept constant. Excluding the Zeta I intermediate stiffeners, the internal radii for all cross-sections were kept constant at 3 mm. For each cross-section shape, the top and bottom lip lengths and lip angles were unchanged. The key dimensions for all 4 sections are tabulated in Table 4.1. The cross-section slenderness $\overline{\lambda}_{cs}$ is defined as the square root of ratio of the elastic yield moment M_y and the elastic critical buckling moment M_{cr}:

$$\bar{\lambda}_{cs} = \sqrt{\frac{M_y}{M_{cr}}} \tag{4.1}$$

where M_{cr} is the lesser of the elastic critical local buckling moment $M_{cr,l}$ or elastic critical distortional buckling moment $M_{cr,d}$. By applying pure bending to the cross-section about the x-x axis, $M_{cr,l}$ and $M_{cr,d}$ were computed using CUFSM (Schafer 2006) by extracting the 1st and 2nd minimum critical loads from the signature curve. Positive bending (b_c in compression) and negative bending (b_t in compression) were analysed using two separate cases to obtain the positive and negative cross-section slenderness values $\bar{\lambda}_{cs,+ve}$ and $\bar{\lambda}_{cs,-ve}$ respectively.

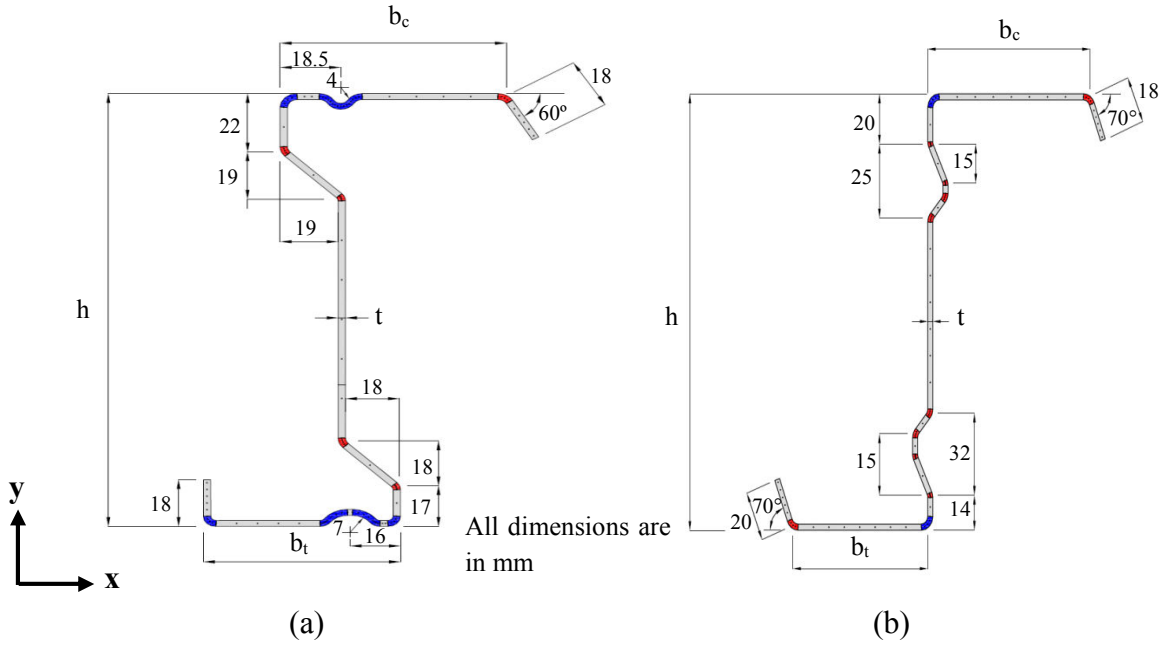


Figure 4.3: *Definition of cross-sectional dimensions for (a) Zeta I and (b) Zeta II sections*

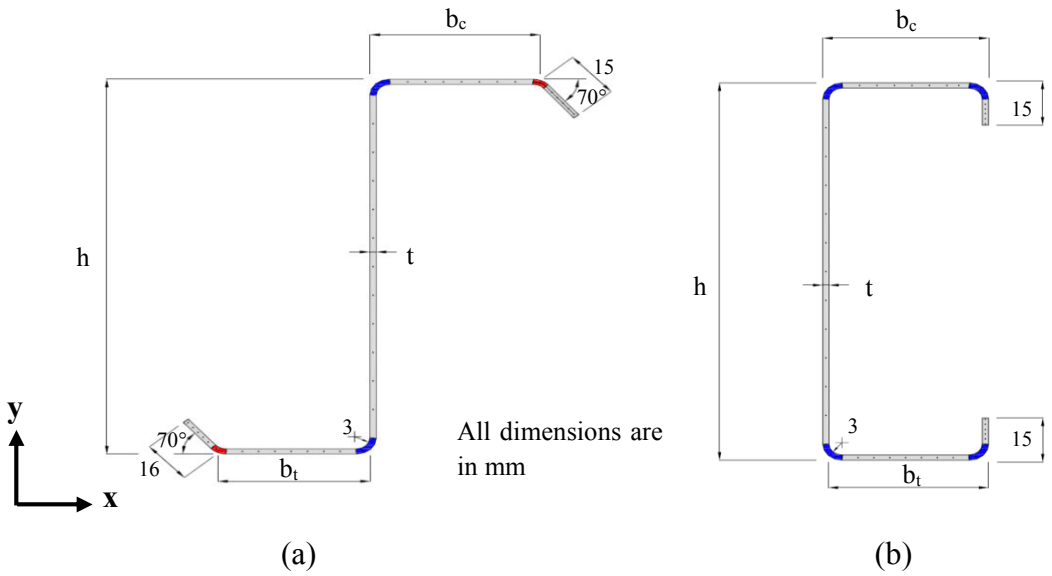


Figure 4.4: *Definition of cross-sectional dimensions for (a) Zed and (b) channel sections*

Figure 4.5 presents a typical cold-formed steel section label. The left box describes the section type: (1) Zeta I, (2) Zeta II, (Z) Zed and (C) channels. The central numbers define the nominal height h of the cross-section in mm and the right box describes the nominal thickness t in mm times 10.

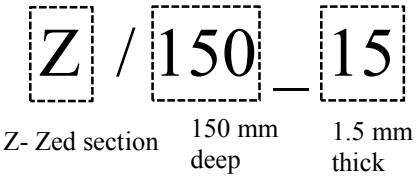


Figure 4.5: System for naming sections

Table 4.1: *List of dimensions for Zeta I, Zeta II, Zed and channel sections*

Section Type[A]	Section Reference	Top flange b_c (mm)	Bottom flange b_t (mm)	Height h (mm)	Thickness t (mm)	$\overline{\lambda}_{cs,+ve}$	$\overline{\lambda}_{cs,-ve}$
Zeta I	1/150_50	72	65	150	5.0	0.617	0.455
Zeta I	1/150_40	72	65	150	4.0	0.811	0.528
Zeta I	1/150_30	72	65	150	3.0	0.832	0.632
Zeta I	1/125_20	72	65	125	2.0	0.950	0.631
Zeta I	1/200_25	72	65	200	2.5	0.976	0.716
Zeta I	1/125_13	60	50	125	1.3	1.042	0.849
Zeta I	1/175_16	72	65	175	1.6	1.083	0.923
Zeta I	1/200_16	72	65	200	1.6	1.084	0.930
Zeta I	1/200_13	72	65	200	1.3	1.220	1.046
Zeta II	2/225_50	78	68	225	5.0	0.590	0.541
Zeta II	2/225_40	78	68	225	4.0	0.691	0.634
Zeta II	2/225_35	78	68	225	3.5	0.757	0.694
Zeta II	2/225_30	78	68	225	3.0	0.762	0.768
Zeta II	2/285_30	78	68	285	3.0	0.832	0.818
Zeta II	2/225_25	78	68	225	2.5	0.855	0.863
Zeta II	2/285_25	78	68	285	2.5	0.936	0.945
Zeta II	2/285_20	78	68	285	2.0	1.056	1.087
Zeta II	2/225_14	78	68	225	1.4	1.205	1.195
Zeta II	2/245_15	78	68	245	1.5	1.195	1.225
Zeta II	2/265_15	78	68	265	1.5	1.233	1.252
Zed	Z/125_20	55	45	125	2.0	0.778	0.700
Zed	Z/200_25	58	49	200	2.5	0.806	0.760
Zed	Z/125_14	55	45	125	1.4	0.957	0.865
Zed	Z/155_15	58	49	155	1.5	1.016	0.934
Zed	Z/170_14	58	49	170	1.4	1.087	1.009
Zed	Z/200_13	58	49	200	1.3	1.202	1.140
C	C/127_20	65	65	127	2.0	0.857	0.866
C	C/127_18	65	65	127	1.8	0.911	0.920
C	C/200_20	65	65	200	2.0	0.968	0.975
C	C/170_18	65	65	170	1.8	0.979	0.988
C	C/140_16	65	65	140	1.6	0.996	1.006
C	C/127_15	65	65	127	1.5	1.010	1.020
C	C/155_15	65	65	155	1.5	1.061	1.070
C	C/185_15	65	65	185	1.5	1.117	1.126
C	C/200_15	65	65	200	1.5	1.147	1.155

A - Refer to Figures 4.3 and 4.4 for cross-section details

4.3.2. Influence of cross-section slenderness

Eurocode 3 places cross-sections in discrete behavioural classes based upon their susceptibility to local buckling. Class 1 and class 2 cross-sections can reach their full plastic bending moment with moderate to large deformation and rotation capacities. These cross-sections can therefore be used in plastic design. Class 3 cross-sections are limited by local and/or distortional buckling and cannot attain their full plastic moment capacity; the bending moment resistance is limited to the elastic yield moment. Class 4 cross-sections are limited by local and/or distortional buckling in the elastic range. Cold-formed steel members tend to be classified as either class 3 or 4 due to their high width-to-thickness ratios and are thus susceptible to local instabilities such as local and distortional buckling. To investigate the influence of the change in section slenderness and effect of applying a moment gradient to cold-formed steel sections, 35 cross-sections, listed in Table 4.1, were simulated using numerical models and discussed in a series of single span studies in the subsequent sections.

4.3.2.1. Rotation capacity study

A series of single span pure positive bending (test type 1) and moment gradient (test type 3), with L' = 3000 mm, FE models were simulated using ABAQUS (2010) to investigate the rotation capacities of all 25 cross-sections listed in Table 4.1. The rotation capacity R was determined using two commonly adopted methods by evaluating either their moment-curvature relationship or moment-rotation behaviour. For pure bending cases (test type 1 and 2), the former of the two methods was adopted, and rotation capacity was defined as:

$$R = \frac{\kappa_{rot}}{\kappa_y} - 1 \tag{4.2}$$

where κ_y is evaluated as M_y/EI and κ_{rot} is the limiting curvature at which the moment resistance drops back below M_y as shown in Figure 4.6 (a).

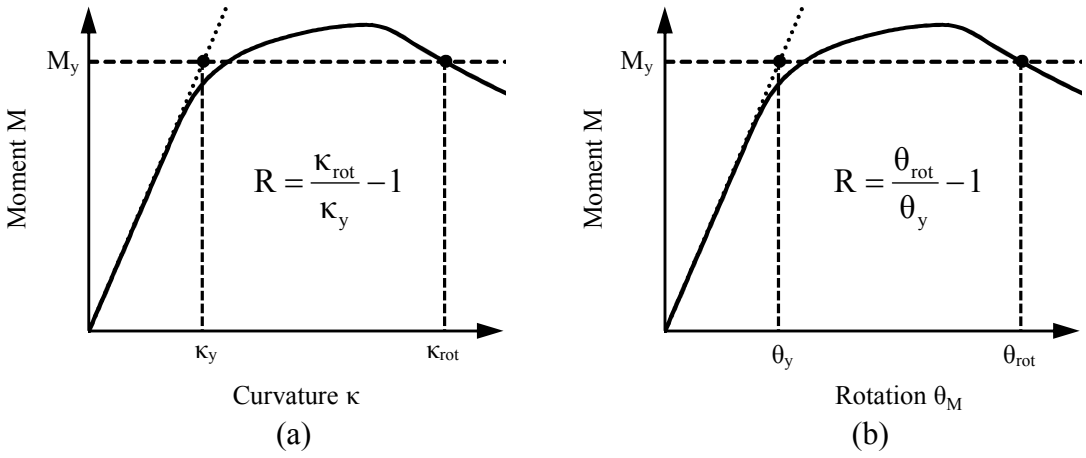


Figure 4.6: *Definition of rotation capacity from (a) moment-curvature response and (b) moment–rotation response*

The average curvature within the central pure bending region $L^*/3$ was evaluated using Equation 4.3, which is based on the assumption that the deformed shape of the pure bending region represents a segment of a circle of radius r as schematically shown in Figure 4.7.

$$\kappa = \frac{1}{r} = \frac{8(D_M - D_L)}{4(D_M - D_L)^2 + (L^*/3)^2} \tag{4.3}$$

where D_L and D_M are defined as the average vertical deflections of the two loading points and midspan respectively. The length of central region $L^*/3$ was fixed for all M_1 cases as 1.626 m.

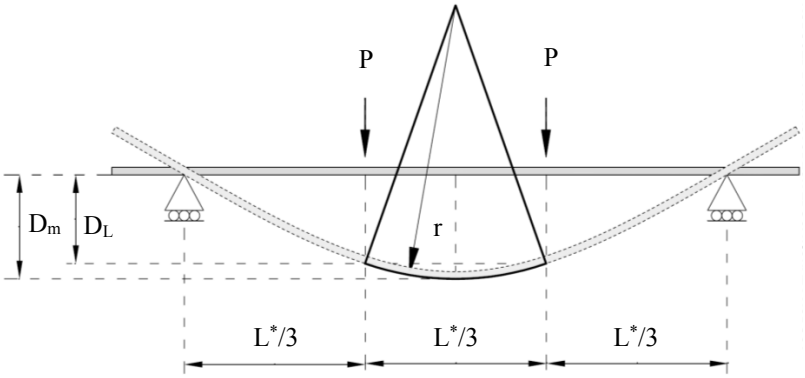


Figure 4.7: *Schematic setup for 4-point bending models*

For moment gradient cases (test type 3 and 4), the definition for rotation capacity R is based on the moment-rotation behaviour and is defined as:

$$R = \frac{\theta_{rot}}{\theta_y} - 1 \tag{4.4}$$

where θ_y is the rotation upon reaching M_y and θ_{rot} is the limiting rotation at which the moment falls back below M_y as shown in Figure 4.6(b). From Figure 4.8 it can be seen that the central rotation θ_M is defined as the summation of the end rotations θ_1 and θ_2. The end rotations θ_1 and θ_2 were calculated from longitudinal and vertical displacements from the top and bottom web/flange junctions using Equation 4.5, where symbols are defined in Figure 4.8.

$$\theta_M = \theta_1 + \theta_2 \begin{cases} \theta_1 = \tan^{-1}\left(\dfrac{z_1 - z_2}{d - (y_2 - y_1)}\right) \\ \theta_2 = \tan^{-1}\left(\dfrac{z_3 - z_4}{d - (y_4 - y_3)}\right) \end{cases} \tag{4.5}$$

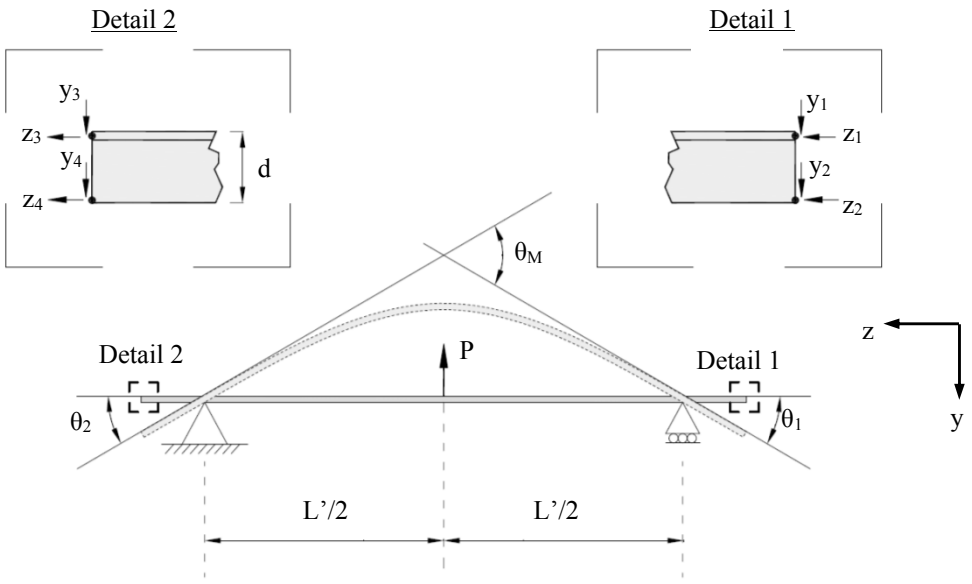


Figure 4.8: *Schematic setup for 3-point bending FE models*

Results from the rotational capacity study are presented in Table 4.2. It is clear from Figure 4.9 that the rotational capacity R falls significantly as the cross-section slenderness $\bar{\lambda}_{cs}$ increases. Of the 35 cross-sections listed in Table 4.1, it was found that

many sections were class 4 sections where M_1 or M_3 capacities was less than M_y. Figures 4.10 and 4.11 show the different moment-rotation or moment-curvature behaviour between typical relatively stocky sections (2/225_50 and 1/150_40) and slender sections (Z/125_14 and Z/200_25). It is clear that the more stocky sections can maintain their moment capacity beyond M_y over large rotations, whereas in contrast, the more slender sections show a fall after reaching a peak value.

The direct strength method (DSM) (Schafer and Peköz 1998a) uses elastic buckling solutions for the entire cross-section and provides strength curves for local and distortional buckling separately. Depending on the elastic local or distortional bucking cross-section slenderness $\bar{\lambda}_{cr,l}$ and $\bar{\lambda}_{cr,d}$, the cross-sectional bending resistance for local and distortional buckling is determined using Equations 4.6 and 4.7 respectively (AISI S100-2007). For the cross-sections listed in Table 4.1, it was found that $M_{cr,l}$ was always greater than $M_{cr,d}$. Graphs of M_1/M_y and M_3/M_y versus $\bar{\lambda}_{cs}$ with comparisons against Equation 4.6 and 4.7 were plotted in Figure 4.12. For pure bending cases, M_1/M_y consistently gave slightly higher results than Equation 4.7. The difference between Equation 4.7 and M_1/M_y is thought to be due to the springs on the compression flange of the sections, simulating the sheeting and the corner enhancements. For moment gradient cases, M_3/M_y consistently gave higher results than M_1/My and Equation 4.7. In general, the M_1 and M_3 results agree well with Equations 4.6 and 4.7.

$$M_{DS,l} = \begin{cases} M_y & \text{if } \bar{\lambda}_{cr,l} = \sqrt{M_y / M_{cr,l}} \le 0.776 \\ \left(1 - 0.15\left(\frac{M_{cr,l}}{M_y}\right)^{0.4}\right)\left(\frac{M_{cr,l}}{M_y}\right)^{0.4} M_y & \text{if } \bar{\lambda}_{cr,l} = \sqrt{M_y / M_{cr,l}} > 0.776 \end{cases} \quad (4.6)$$

$$M_{DS,d} = \begin{cases} M_y & \text{if } \bar{\lambda}_{cr,d} = \sqrt{M_y / M_{cr,d}} \le 0.673 \\ \left(1 - 0.22\left(\frac{M_{cr,d}}{M_y}\right)^{0.5}\right)\left(\frac{M_{cr,d}}{M_y}\right)^{0.5} M_y & \text{if } \bar{\lambda}_{cr,d} = \sqrt{M_y / M_{cr,d}} > 0.673 \end{cases} \quad (4.7)$$

Table 4.2: *Rotation capacity results for M_1 and M_3 single span models*

Section Reference	M_y (kNm)	M_1 (kNm)	M_3 (kNm)	R	
				$M_{1,\ L^* = 4.88\ m}$	$M_{3,\ L' = 3.00\ m}$
1/150_50	28.939	32.914	-37.616	3.196	7.003
1/150_40	23.210	26.576	-29.698	2.312	4.762
1/150_30	17.492	19.806	-21.221	1.836	2.183
1/125_20	8.015	8.965	-9.704	1.230	1.689
1/200_25	21.804	24.096	-26.247	0.997	1.167
1/125_13	5.324	5.383	-5.958	0.430	0.612
1/175_16	11.883	11.524	-12.652	-	0.345
1/200_16	14.233	13.852	-15.042	-	0.296
1/200_13	11.641	10.544	-11.851	-	0.102
2/225_50	49.806	56.021	-59.360	2.119	6.353
2/225_40	40.578	43.828	-48.279	1.126	2.440
2/225_35	35.827	38.505	-41.777	1.110	1.728
2/225_30	30.986	32.289	-35.226	0.712	1.149
2/285_30	43.005	45.035	-49.656	0.662	0.660
2/225_25	26.054	26.096	-29.176	0.372	0.653
2/285_25	36.125	36.278	-41.971	0.313	0.679
2/285_20	29.130	27.499	-28.510	-	-
2/225_14	14.877	11.939	-13.682	-	-
2/245_15	17.869	14.814	-16.910	-	-
2/265_15	19.905	16.481	-17.833	-	-
Z/125_20	7.312	7.485	-8.296	0.591	0.672
Z/200_25	17.996	18.428	-19.892	0.581	0.696
Z/125_14	5.181	4.844	-5.379	-	0.163
Z/155_15	7.740	7.169	-7.713	-	0.120
Z/170_14	8.199	7.241	-7.716	-	-
Z/200_13	9.531	8.681	-8.416	-	-
C/127_20	8.769	8.460	-9.308	-	0.287
C/127_18	7.940	7.401	-8.159	-	0.162
C/200_20	15.935	15.193	-16.578	-	0.218
C/170_18	11.601	10.824	-11.632	-	0.109
C/140_16	8.047	7.130	-7.755	-	-
C/127_15	6.675	5.706	-6.357	-	-
C/155_15	8.632	7.358	-8.979	-	0.050
C/185_15	10.898	9.234	-10.075	-	-
C/200_15	12.098	10.047	-10.855	-	-

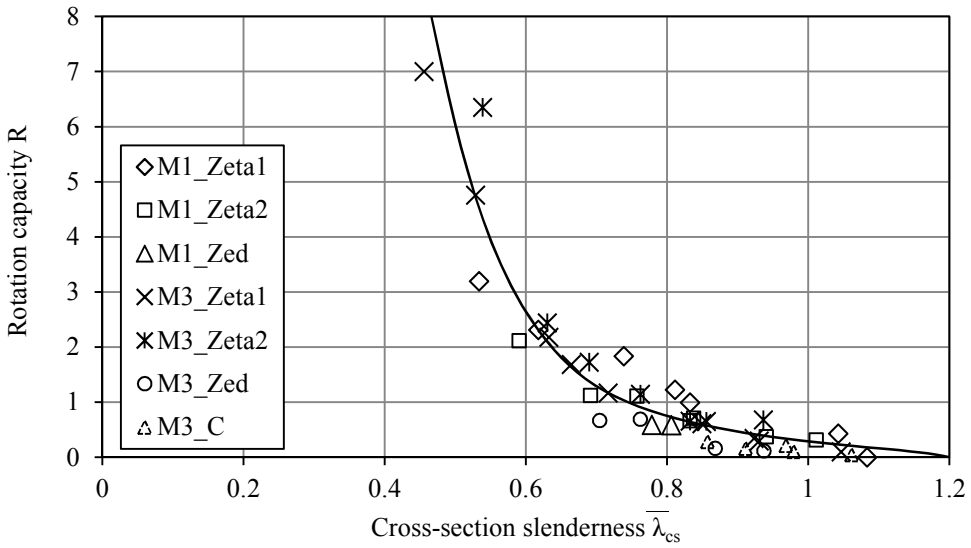


Figure 4.9: *Rotation capacity versus cross-section slenderness*

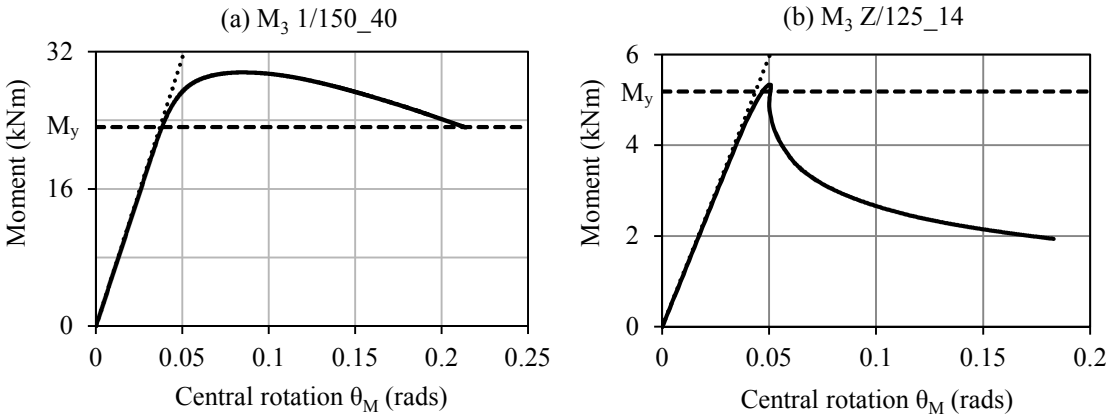


Figure 4.10: *Typical moment-rotation responses for (a) M_3 1/150_40 and (b) M_3 Z/12514*

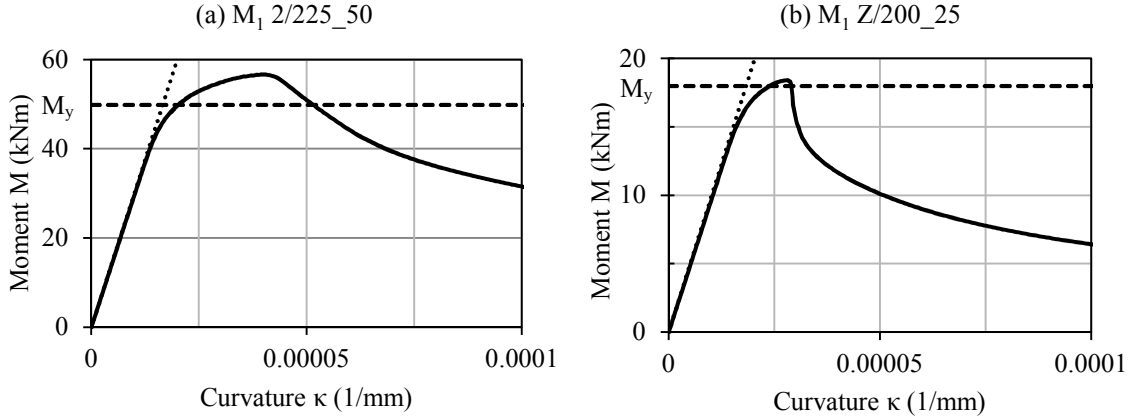


Figure 4.11: *Typical moment-curvature responses for (a) M_1 2/225_50 and (b) M_1 Z/200_25*

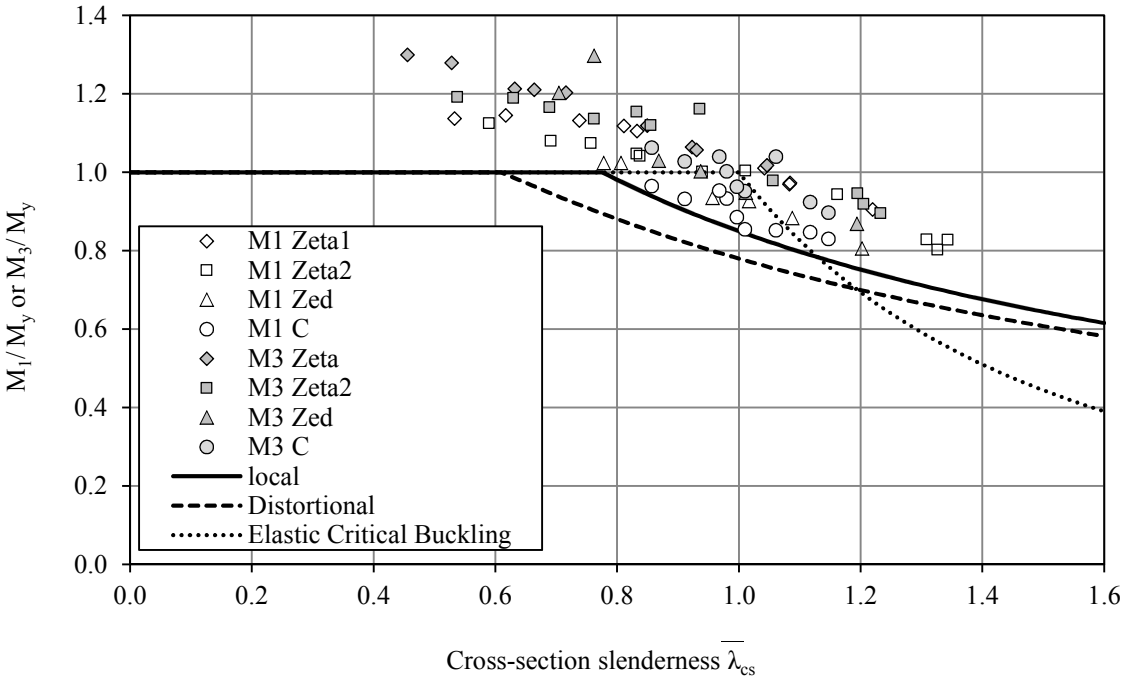


Figure 4.12: *M_1/M_y and M_3/M_y versus cross-section slenderness* $\bar{\lambda}_{cs}$

4.3.2.2. Influence of moment gradient

A study to investigate the effect of moment gradient on the in-plane bending behaviour of cold-formed steel Zeta I sections was conducted. A series of Zeta I 1/175_16 sections was simulated using the validated single span FE models discussed in Chapter 3 by applying: (i) positive pure bending (test type 1), (ii) positive linear moment gradient with L' ranging from 2 to 5 m (test type 4), (iii) negative pure bending (test type 2) and (iv) negative linear moment gradient with L' ranging from 2 to 5 m (test type 3). The geometric dimensions for 1/175_16 are detailed in Figure 4.13. All FE models for this study adopted the same compound Ramberg-Osgood material model as given by Equations 3.1 and 3.2 (Gardner and Ashraf, 2006). The described two-spring model from Section 3.2.4 was placed on to the top flange with a constant spring spacing of 250 mm. As described in Section 3.2.6.1, the standardised method for applying initial geometrical imperfections was adopted for all FE models within this study. The Young's modulus and 0.2% proof stress of 210 GPa and 390 N/mm^2 was adopted throughout this study.

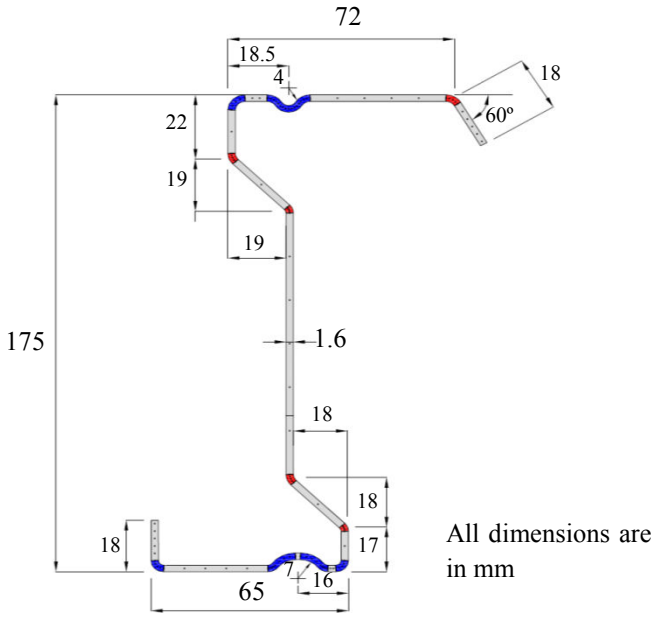


Figure 4.13: *Geometric dimensions for section 1/175_16*

The ultimate moment capacities M_{ult} from the study are shown in Table 4.3. Figure 4.14 presents the moment-rotation responses for the positive moment gradient cases (L' = 2, 3, 4 and 5 m). The stress-profiles at ultimate load and during the post-ultimate stage for positive pure bending (M_1) and moment gradient L = 3m (M_4) are shown in Figure 4.15 and 4.16 respectively. It was observed that the failure modes for both cases were dominated by distortional buckling at the compression (top) flange. The location of distortional buckling was near the central point load for the 3-point bending cases (largest bending moment and shear) and within the central region for 4-point bending cases. The observed distortional buckling half-wavelength from the FE results differed from the computed elastic restraint-free (i.e. no sheeting) distortional half-wavelength (624 mm) from the CUFSM analysis. The effect of the two-spring model was to force the distortional buckling mode to buckle downwards over a constrained longitudinal length approximating to the spring spacing of 250 mm, thus resulting in higher load-carrying capacities. As the magnitude of the moment gradient increased, the ultimate strength for the M_4 cases compared to the M_1 case increased from 5.6% to 12.6%. As the moment gradient decreases, the ultimate load reduced by approximately 2% per metre span. It is clear that the effect of the moment gradient would provide an average of 10% additional load carrying capacity to its pure bending counterpart. Figures 4.17-4.19 illustrate stress profiles and moment-rotation responses from the FE models subjected to negative pure bending and linear moment gradients. For the negative bending

cases, the lack of sheeting (2-spring model) on the bottom flange gave distortional buckling failure modes with half-wavelengths approximately equal to 500 mm, which were close to the computed elastic distortional half-wavelength of 615.5 mm from CUFSM. It was found that the moment capacities for positive and negative bending for like-for-like FE models were similar, generally within 3%. The fact that the negative bending moment capacities were as high as those with the compression flange restrained by sheeting, may be attributed to a combination of (i) a shorter compressive flange, (ii) a more effective compressive lip angle (90º as opposed to 70º) and (iii) a more effective (larger) compressive intermediate stiffener. The effect on the ultimate load caused by the magnitude of the moment gradient was greater for positive bending cases than negative bending cases. It is thought the restraining behaviour from the sheeting for positive bending cases magnified the effect of the moment gradient.

Table 4.3: *Comparison between M_1, M_2, M_3 and M_4 for 1/175_16*

Section #	Test type	Description		Span length L' or L* (mm)	M_{ult} (kNm)	M_4/M_1 or M_3/M_2
1/175_16	1	Positive pure bending	M_1	4880	11.524	-
1/175_16	4	Positive moment gradient	M_4	2000	12.976	1.126
1/175_16	4	Positive moment gradient	M_4	3000	12.643	1.097
1/175_16	4	Positive moment gradient	M_4	4000	12.367	1.073
1/175_16	4	Positive moment gradient	M_4	5000	12.167	1.056
1/175_16	2	Negative pure bending	M_2	4880	-11.525	-
1/175_16	3	Negative moment gradient	M_3	2000	-12.300	1.067
1/175_16	3	Negative moment gradient	M_3	3000	-12.652	1.098
1/175_16	3	Negative moment gradient	M_3	4000	-12.696	1.101
1/175_16	3	Negative moment gradient	M_3	5000	-12.59	1.092

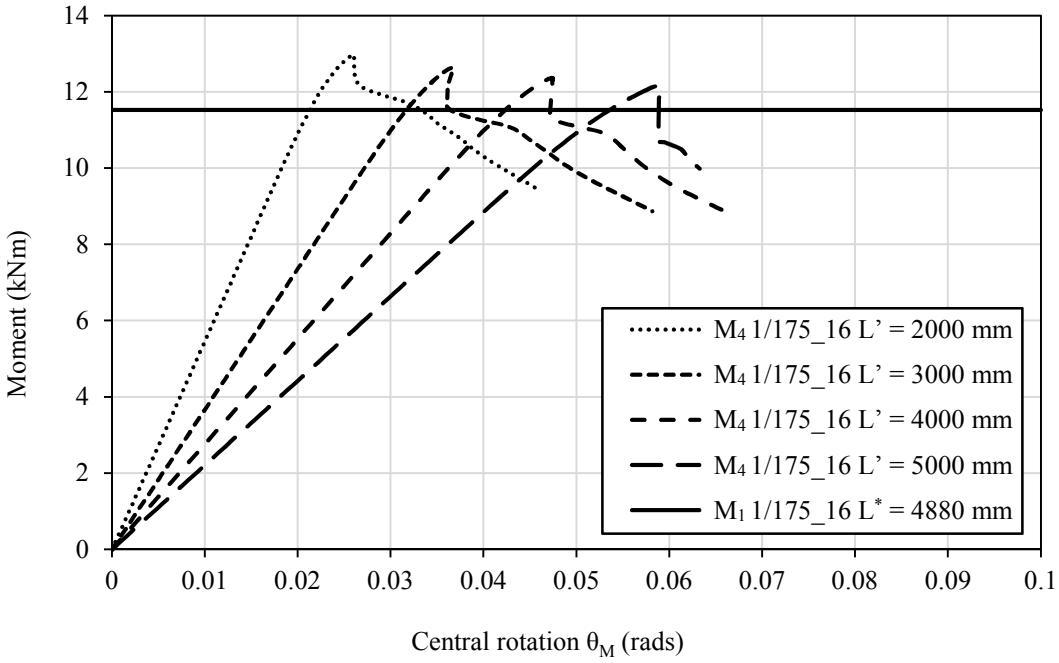
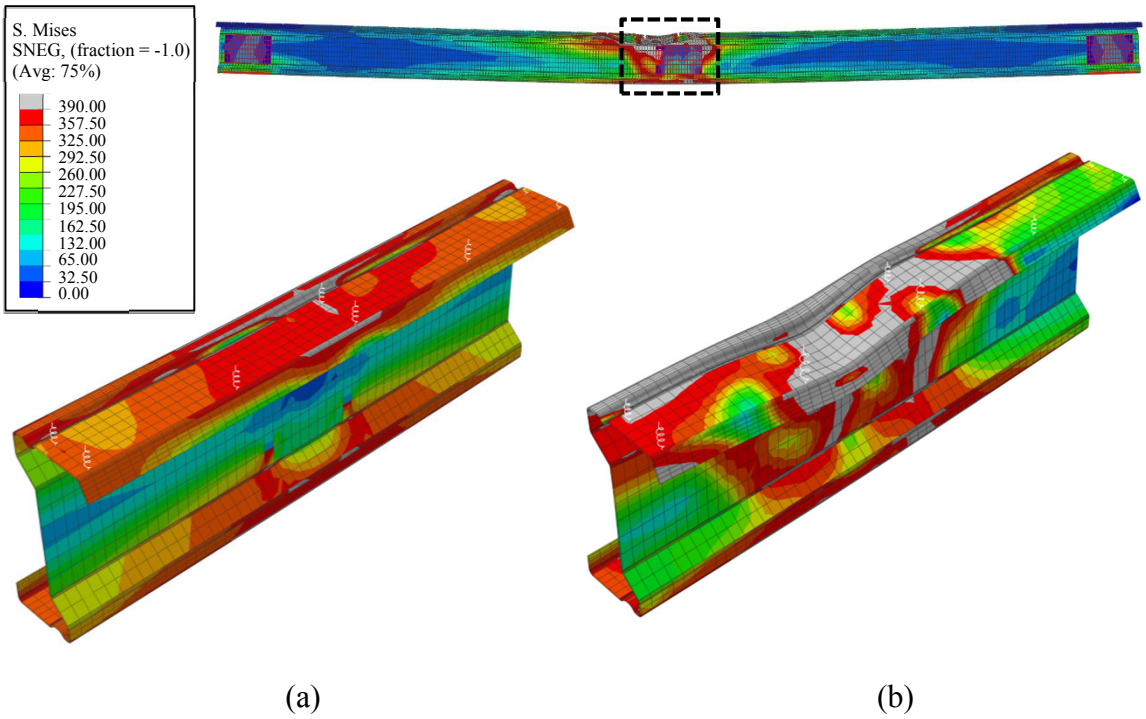


Figure 4.14: *M_4 moment–rotation responses for L' = 2, 3, 4 and 5 m for 1/175_16*



(a) (b)

Figure 4.15: *Stress profile at (a) ultimate load and (b) beyond ultimate load for 1/175_16 M_4 L'= 3 m*

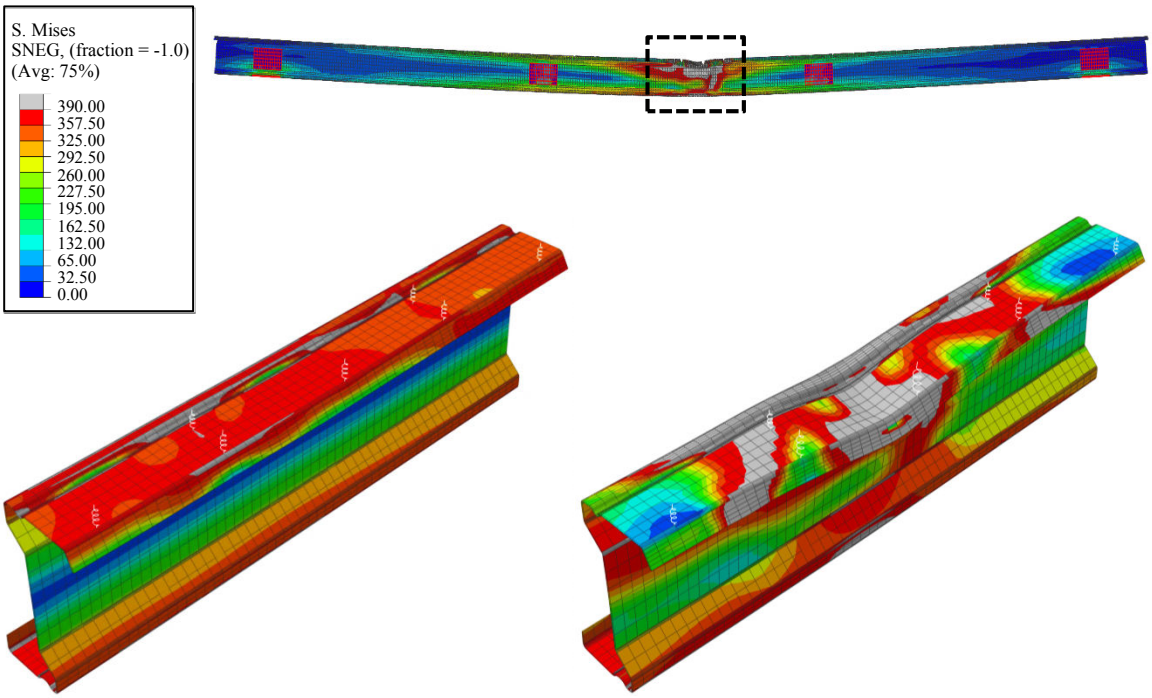


Figure 4.16: *Stress profile at (a) ultimate load and (b) beyond ultimate load for 1/175_16 M_1 L^*= 4880 mm*

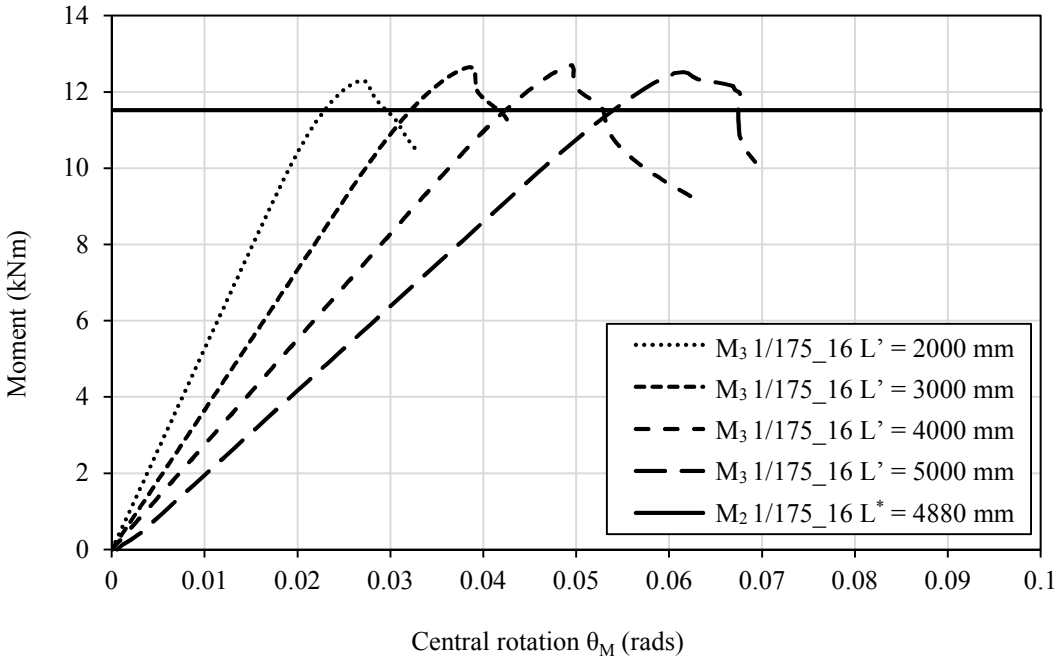
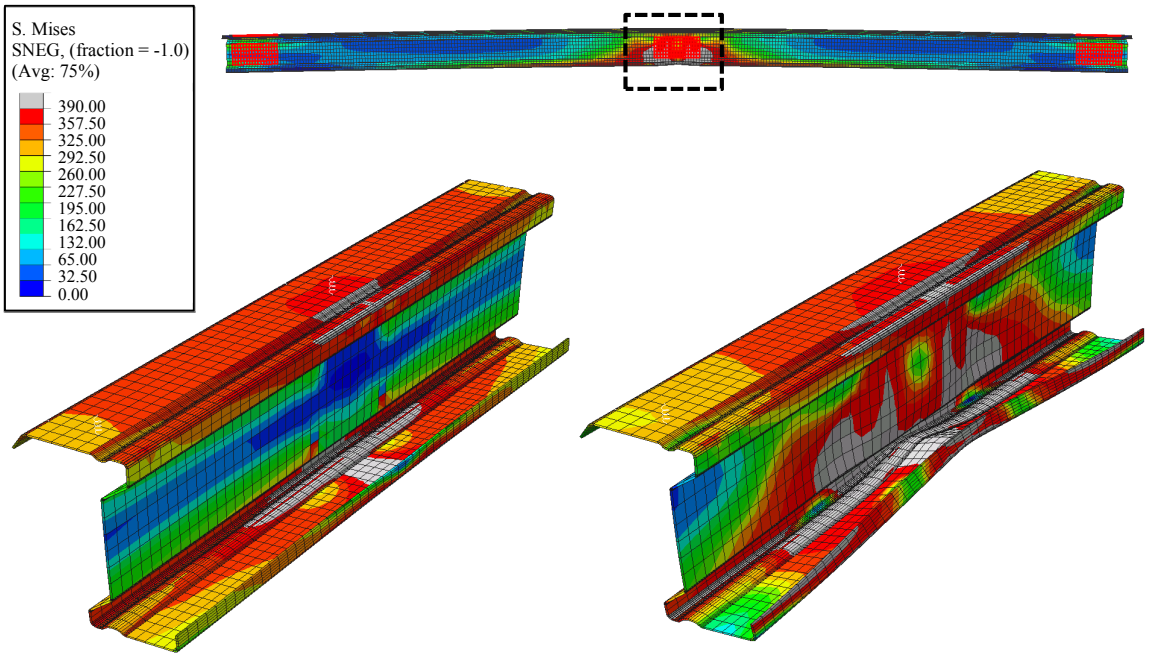
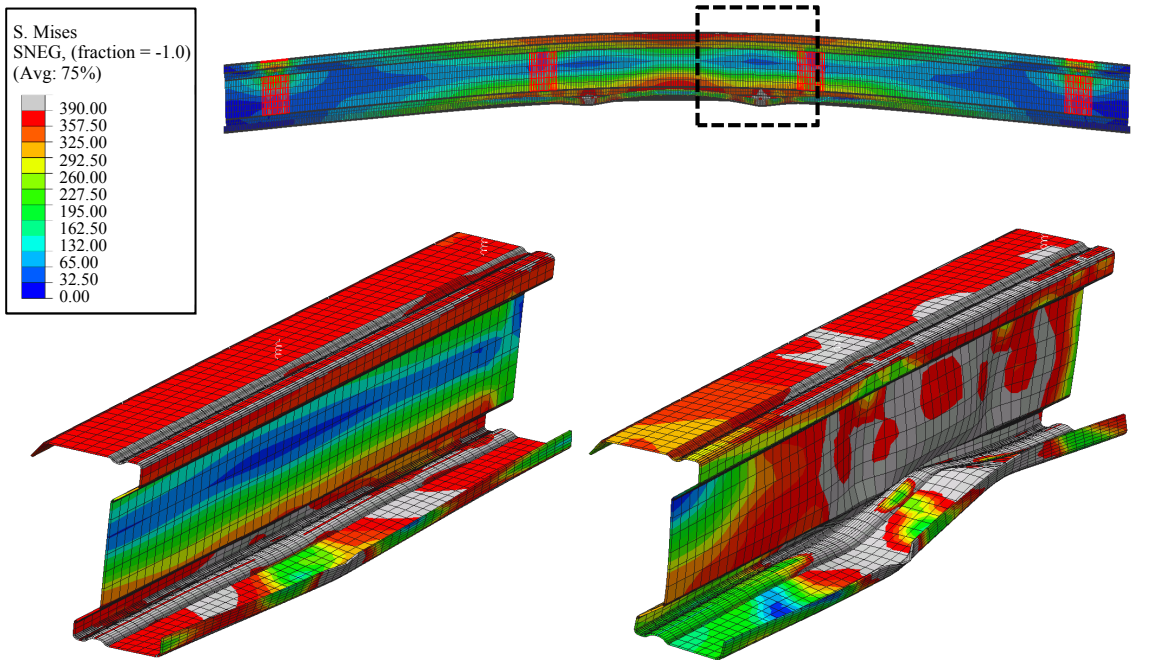


Figure 4.17: *M_3 moment–rotation responses for L' = 2, 3, 4 and 5 m for 1/175_16*



(a) (b)

Figure 4.18: *Stress profile at (a) ultimate load and (b) beyond ultimate load for 1/175_16 M_3 L'= 3000 mm*



(a) (b)

Figure 4.19: *Stress profile at (a) ultimate load and (b) beyond ultimate load for 1/175_16 M_2 L^*= 4880 mm*

4.3.3. Reference FE Models

The ultimate design load carrying capacity q_{ult} for a 2-span system with equal spans subjected to a UDL can be determined, from equilibrium, by solving for q in Equation 4.8, providing the values of interior support moment $M_{support}$ and span moment M_{span} at q_{ult} are known.

$$M_{span} = \frac{\left(qL^2 + 2M_{support}\right)^2}{8qL^2} \tag{4.8}$$

The largest sagging (positive) bending moment in the span region is located, in the case of elastic behaviour, at 3L/8 from the end support, where L is the length of each (equal) span, whereas the largest hogging (negative) moment is located at the interior support. M_{span} and $M_{support}$ can be rewritten using Equation 4.9 and 4.10 as:

$$M_{span} = \frac{3R_1L}{8} - \frac{9qL^2}{128} \tag{4.9}$$

$$M_{support} = R_1L - \frac{qL^2}{2} \tag{4.10}$$

where R_1 is the vertical end support reaction and q is the applied UDL. R_1 has an elastic magnitude of 3qL/8; thus the elastic M_{span} and $M_{support}$ values are $9qL^2/128$ and $-qL^2/8$ respectively.

To study the buckling behaviour and degree of moment redistribution for each continuous purlin system subjected to gravity loading, two additional single span FE models were analysed to provide useful reference moment values for $M_{support}$ and M_{span}: (i) the largest sagging moment M_{span} from the 2-span FE models was compared with a single span FE model subjected to uniform positive bending M_1 (test type 1) and (ii) the largest hogging moment $M_{support}$ from the 2-span FE models was compared to the maximum moment from a single span FE model subjected to 3-point negative bending M_3 (test type 3). Figure 4.20 illustrates how the reference single span FE models are related to the 2-span gravity FE model.

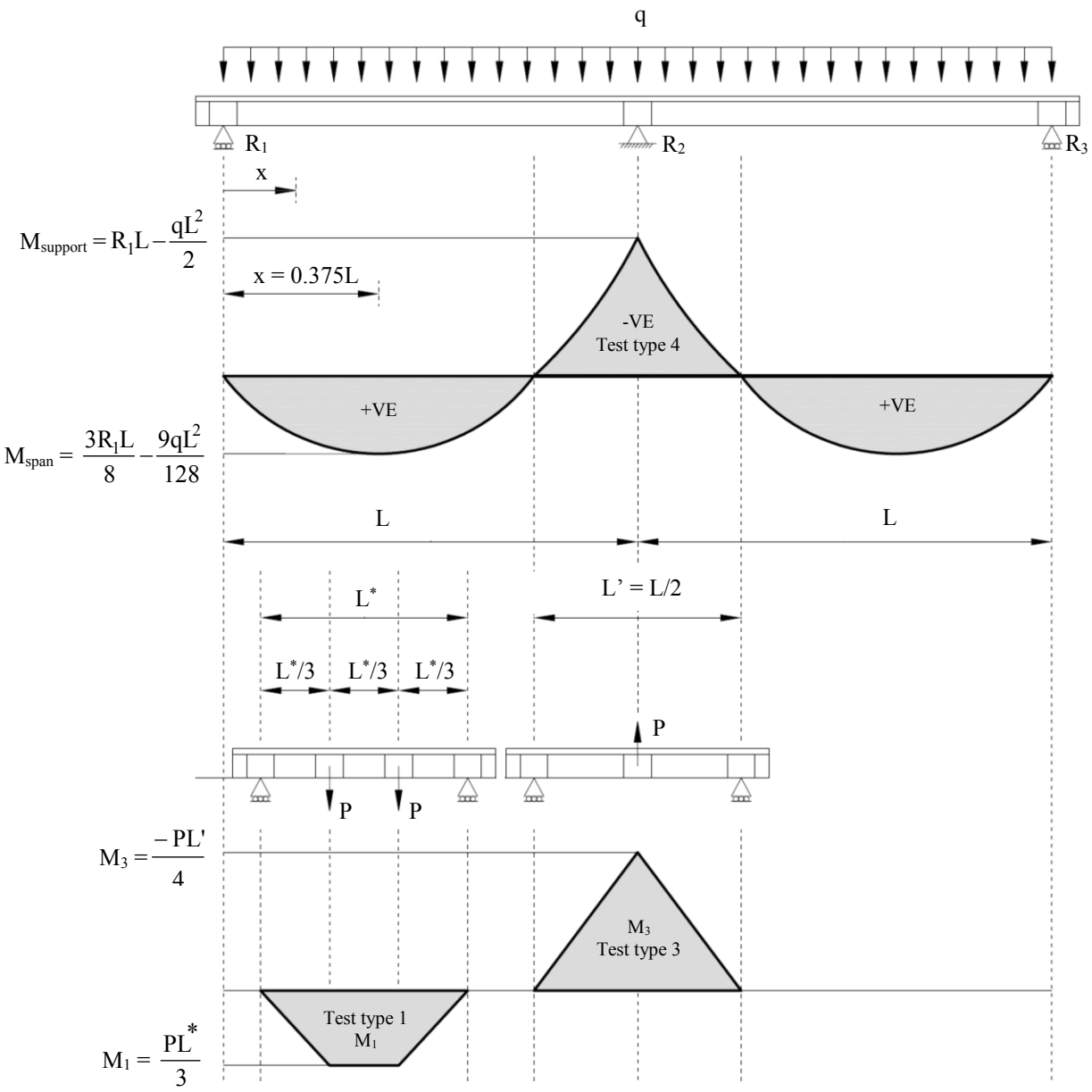


Figure 4.20: *Elastic bending moment diagram (BMD) for 2-span and reference M_1 and M_3 single span purlin systems*

The effect of the beneficially sharp parabolic moment gradient in the interior support region of the 2-span system was accounted in test type 3 with an approximate linear moment gradient; the beam length for type 3 test was made the same as the hogging region length from the 2-span models L'. The span length for pure bending L^* (test type 1) was kept constant for all section types at 4880 mm with loading points at $L^*/3$ and $2L^*/3$. This ensured the 1626.67 mm constant moment region was of sufficient length to allow for local and/or distortional buckling to freely develop.

4.3.4. Alpha framework

To investigate the degree of moment redistribution in continuous 2-span purlin arrangements subjected to gravity loading, a large range of sections, featuring 35 Zeta I, Zeta II, Zed and channel sections, listed in Table 4.1, were analysed using the validated FE models described in Chapter 3. For each cross-section, three 2-span models with 4, 6 and 8 m spans were analysed. For each 2-span FE model, two additional single span reference FE models described in Section 4.2.4 were also simulated. In total, the study comprised 245 FE analyses. The same boundary conditions, element types, corner enhancements, plate stiffener locations and material properties, mesh density and two-spring model described in Chapter 3 were adopted as a basis for the FE models used for this parametric study. Apart from the different geometric dimensions tabulated in Table 4.1, the Young's modulus E, 0.2% proof stress $\sigma_{0.2}$ and fastener spacing (spacing of the translational springs) were kept constant at 210 GPa, 390 N/mm^2 and 250 mm respectively. All FE models for this study adopted the same compound Ramberg-Osgood material model as given by Equations (3.1) and (3.2) and assumed $\sigma_{1.0}$ is proportional to $\sigma_{0.2}$ by applying Equation (3.5). The geometrical imperfections for the FE models were applied by manually fitting the local and distortional buckling shapes from CUFSM into the individual sagging and hogging regions in a harmonic manner with periods equalling their individual half-wave lengths. The imperfection magnitudes were kept constant at 0.229t and 0.099t for distortional and local buckling respectively. The modified Riks method was the chosen solver scheme in ABAQUS (2010).

4.3.4.1. Stocky versus slender 2-span sections

The continuous 2-span 2/225_50-L=6 m FE model illustrates the typical behaviour for stocky arrangements. The chosen system accords closely with the ideal situation given by plastic theory, with full moment redistribution. The schematic bending moment diagram, M_3 moment-rotation response and 2-span results are shown in Figure 4.21(a), 4.21(b) and Table 4.4 respectively. Figure 4.22 shows the M_{span}, $M_{support}$ and applied load q responses against the maximum vertical displacement. The 2-span moment and load-displacement responses obtained from the FE analysis can be discretized into 4 stages:

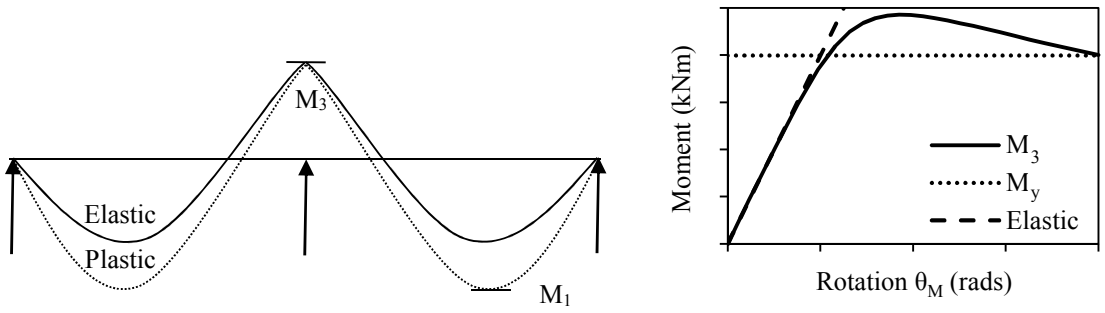
Stage 1. Elastic behaviour of the system.

Stage 2. Inelastic behaviour of the system up to $M_{support}$ reaching its peak value.

Stage 3. Redistribution of moments from the interior support to the span.

Stage 4. Post-ultimate behaviour of the system

In the initial phase of loading (stage 1), the 2-span system behaves elastically and M_{span} and $M_{support}$ increase proportionally, with the $M_{support}/M_{span}$ ratio of 16/9. The system enters stage 2 following first yield, after which inelastic behaviour occurs where M_{span} and $M_{support}$ are no longer directly proportional. It is evident in Figure 4.23 that $M_{support}/M_{span}$ starts to reduce from 16/9, as M_{span} increases at a faster rate than $M_{support}$. Figure 4.24(a) depicts signs of first yielding at the bottom (compression) flange located at the support region, whilst the cross-section in the span region is still elastic (Figure 4.24(b)). The extent of stage 2 was found to be dependent on the rotation capacity at the support, as approximated by its corresponding M_3 moment-rotation response shown in Figure 4.21(b); i.e. for stocky arrangements, stage 2 is prolonged since $M_{support}$ can continue to sustain load under increasing deformations. Owing to the redundancy of the 2-span system, the ultimate load is not reached at the end of stage 2. The deformed shape and stress profiles in the support and span regions at the end of stage 2 are presented in Figures 4.24(c) and (d), where distortional buckling was observed in the support region, while the cross-section in the span region remained relatively undeformed. As the load increased further through stage 2 ($q = 0.945q_{ult}$), the adequate rotation capacity at the interior support ensured $M_{support}$ plateaus as the applied load and subsequent displacements (and rotations) increased. The additional applied load in stage 3 onwards was transferred predominantly directly into the span. Apart from increased distortional buckling displacements, as shown in Figure 4.24(e), no significant changes in buckling behaviour were observed at the interior support from the end of stage 2. Figures 4.25 and 4.26 presents the stress profiles and buckling modes for the corresponding single span 2/225_50 M_1 and M_3 FE models respectively. By comparing buckling shapes and moment capacities between the 2-span, M_1 and M_3 FE models in Figures 4.24(e, f), 4.25-4.26 and Table 4.4, it is clear that the single span reference FE models can provide relevant moment capacity comparisons, in addition to replicating the same governing buckling failure modes. The failure of the system occurs when M_{span} tends towards its corresponding moment capacity, as approximated by M_1 (M_{span}/M_1 at $q_{ult} = 0.98$). Stage 4 is the post-ultimate stage of the system and illustrates the system collapse mechanism.



(a) (b)

Figure 4.21: *(a) Bending moment diagram for an ideal situation of full redistribution and (b) corresponding 2/225_50 M_3 reference moment–rotation behaviour*

Table 4.4: *Moment comparisons between 2-span and M_1 and M_3 models for 2/225_50*

Stage	Applied load q (kN/m)	M_{span} (kNm)	$M_{support}$ (kNm)	M_1 (kNm)	M_3 (kNm)	M_{span}/M_1	$M_{support}/M_3$
2	$q = 0.945q_{ult}$	53.225	-66.893	56.021	-59.36	0.950	1.127
3	$q = q_{ult}$	55.612	-62.907			0.993	1.060

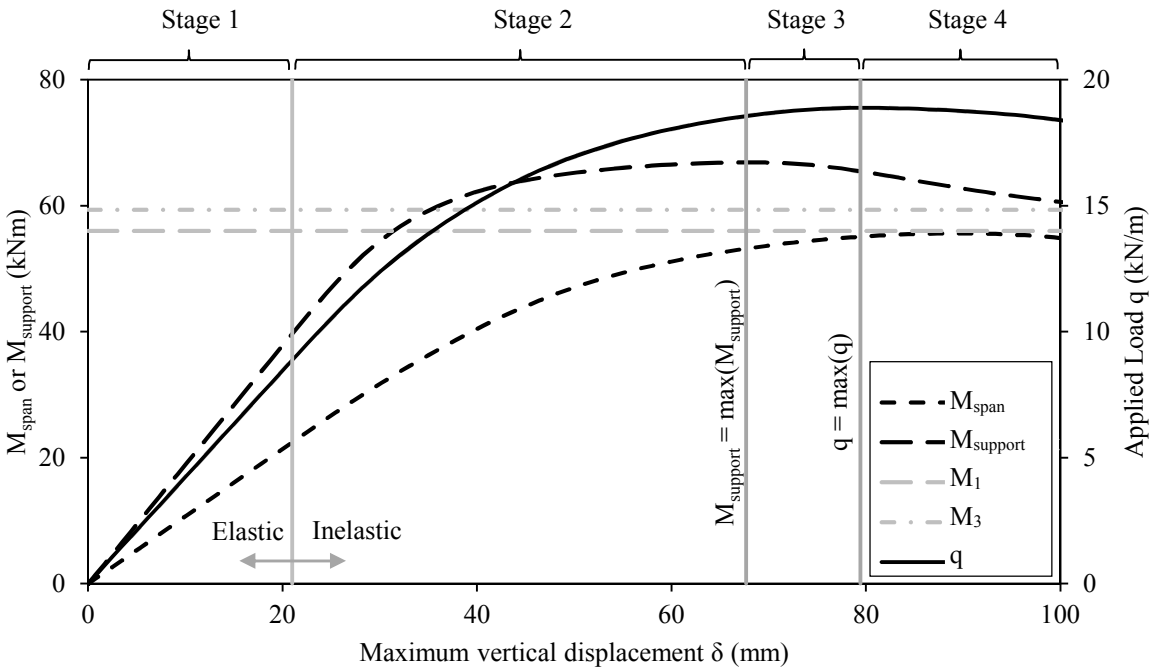


Figure 4.22: *Applied load q, $M_{support}$ and M_{span} versus maximum deflection δ for 2/225_50 L = 6 m*

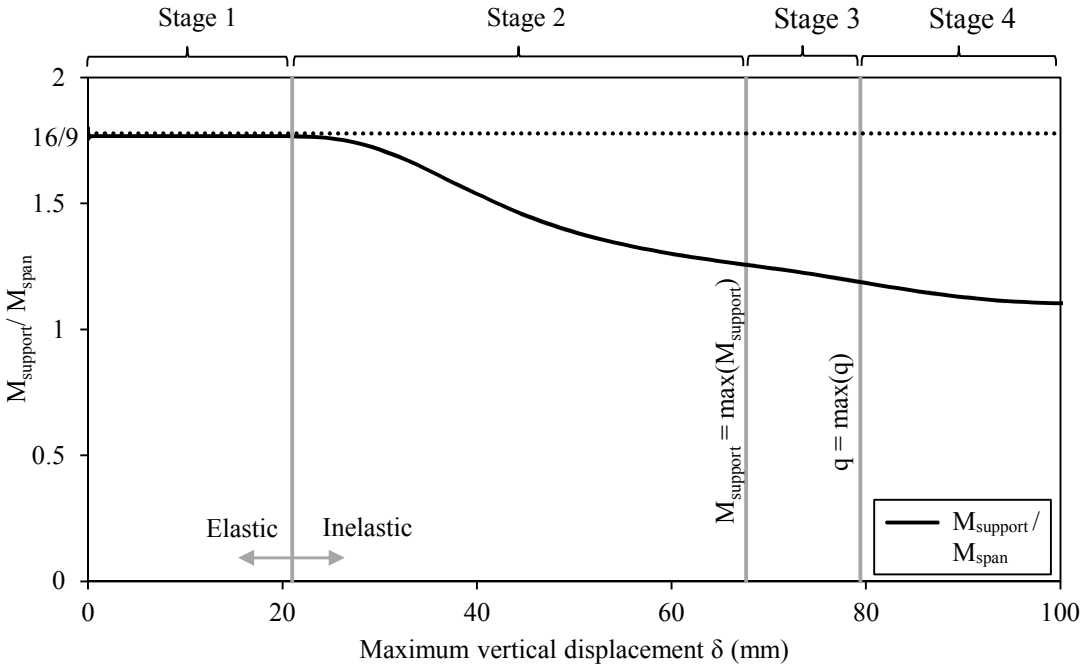


Figure 4.23: *$M_{support}/M_{span}$ versus maximum vertical displacement δ for 2-span 2/225_50 L* = 6 m

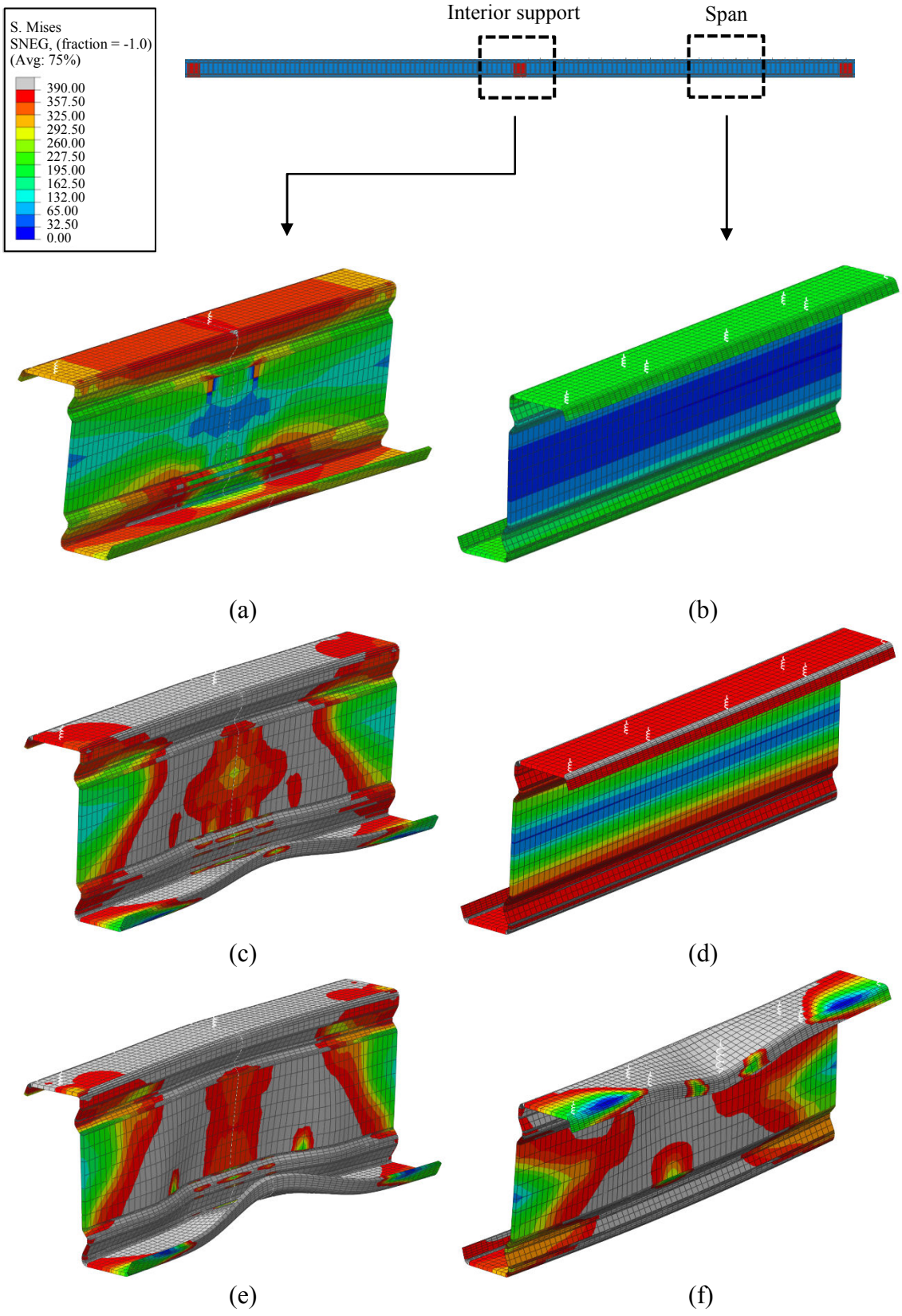


Figure 4.24: *Deformed stress profiles for gravity 2-span 2/225_50 L = 6m FE model at (a, b) stage 1 (c, d) stage 2 and (e, f) ultimate load*

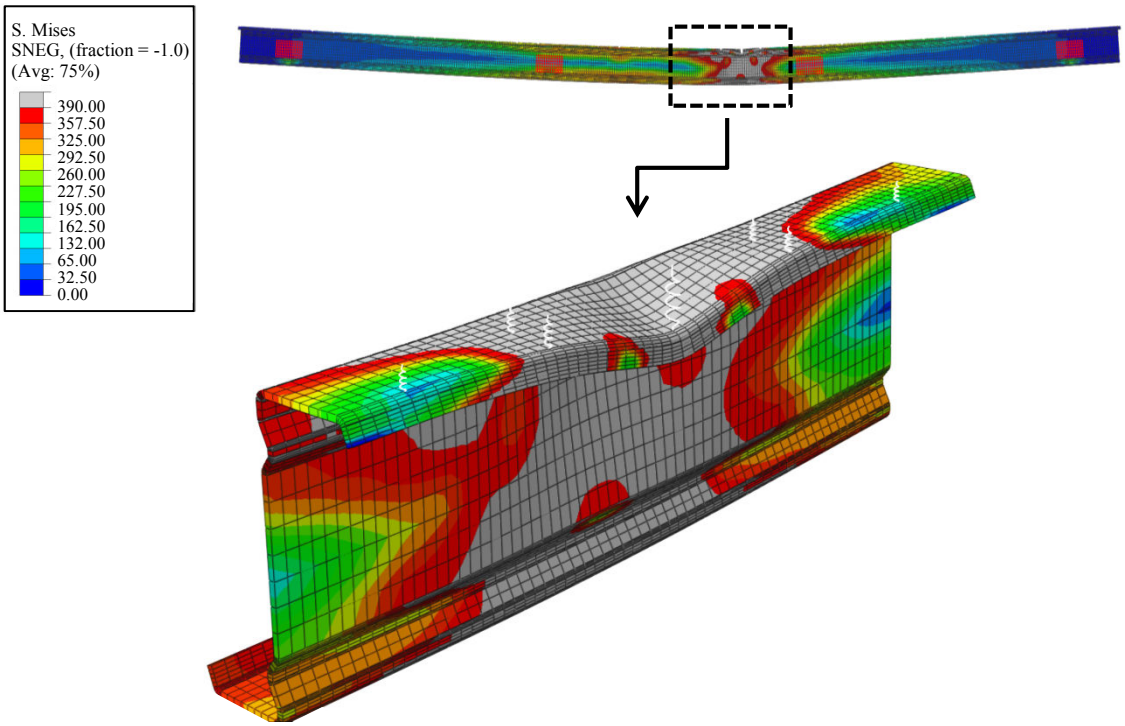


Figure 4.25: *Deformed stressed profile for M_1 2/225_50 L^* = 4880 mm*

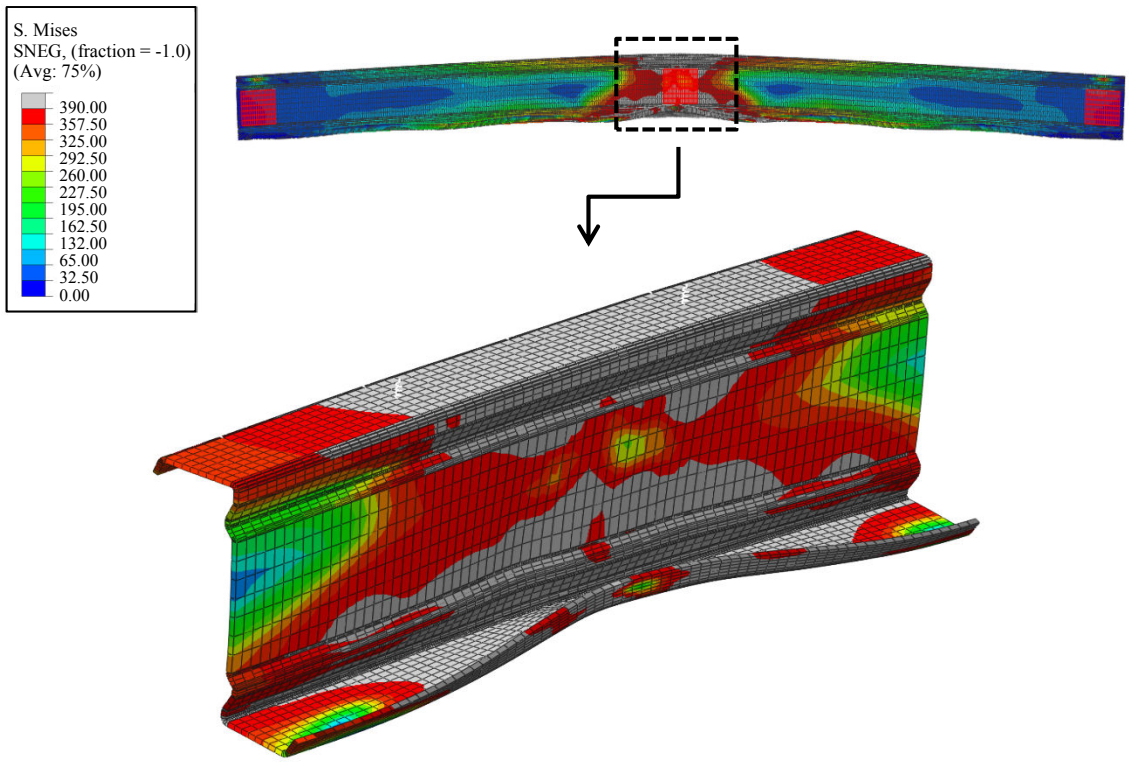


Figure 4.26: *Deformed stressed profile for M_3 2/225_50 L' = 3000 mm*

The moment redistribution behaviour for slender cross-sections was found to be rather different from stocky arrangements. Section 2/225_14 L = 8 m was chosen as an example to illustrate the typical moment redistribution behaviour for slender sections. The schematic bending moment diagram, representative M_3 moment-rotation response and 2-span results are illustrated in Figure 4.27(a), 4.27(b) and Table 4.5 respectively. The applied load q, M_{span}, $M_{support}$ and $M_{support}/M_{span}$ against maximum vertical displacement relationships are plotted in Figures 4.28 and 4.29. The extent of stages 1 and 2 for the chosen slender cross-section was found to cover a shorter range than those observed for stocky cross-sections. In contrast to the stocky section which showed a more gradual response up to its peak moment, the interior support moment-rotation relationship for the slender cross-section reached its moment capacity much earlier. The shorter displacement range of stage 1 and 2 for slender cases resulted in low M_{span}/M_1 ratios at the end of stage 2 that led to a prolonged stage 3. $M_{support}$ for such cases tends to unload quickly after reaching the maximum moment (Figure 4.27(b)). Figure 4.29 illustrates a sharper fall in $M_{support}/M_{span}$ during stage 3 as compared to stocky sections (Figure 4.23). Thus, a significant change in stiffness at the end of stage 2 is related to the loss of stiffness at the interior support. Figures 4.31 and 4.32 shows that the corresponding reference M_1 and M_3 single span deformed stress profiles are similar to those observed at the span region and interior support of the 2-span system respectively (Figure 4.30). The slender section achieved an additional 16% more load carrying capacity after $M_{support}$ reached its peak value as opposed to 5% from the stocky sections shown in Figure 4.22. By comparing $M_{support}/M_3$ ratios at q_{ult} between the stocky and slender sections using Tables 4.4 and 4.5, it can be seen that the M_{span} moment for the slender section was reduced by approximately 40% from its original cross-sectional capacity whereas no change for the stocky section was observed.

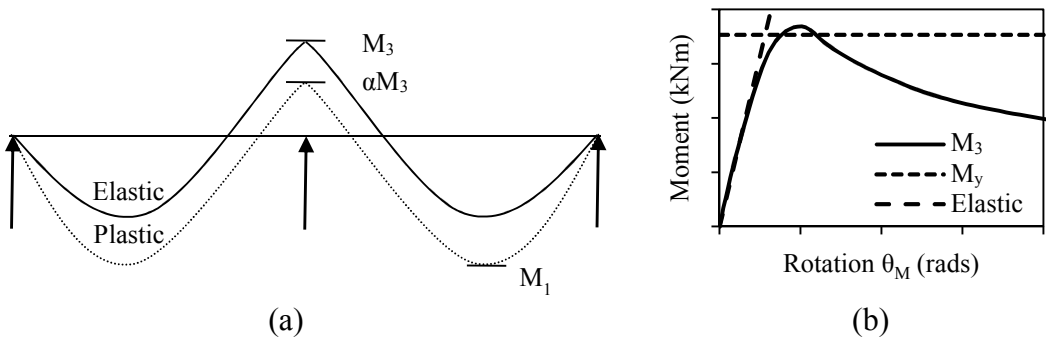


Figure 4.27: *Typical moment redistribution behaviour for slender sections with corresponding reference moment–rotation behaviour*

Table 4.5: *Moment comparisons between gravity 2-span, M_1 and M_3 models for 2/225_14*

L = 8 m

Stage	Applied load q (kN/m)	M_{span} (kNm)	$M_{support}$ (kNm)	M_1 (kNm)	M_3 (kNm)	M_{span}/M_1	$M_{support}/M_3$
2	1.673	7.951	-13.530	11.939	-13.270	0.666	1.020
3	1.936	11.570	-7.870			0.970	0.593

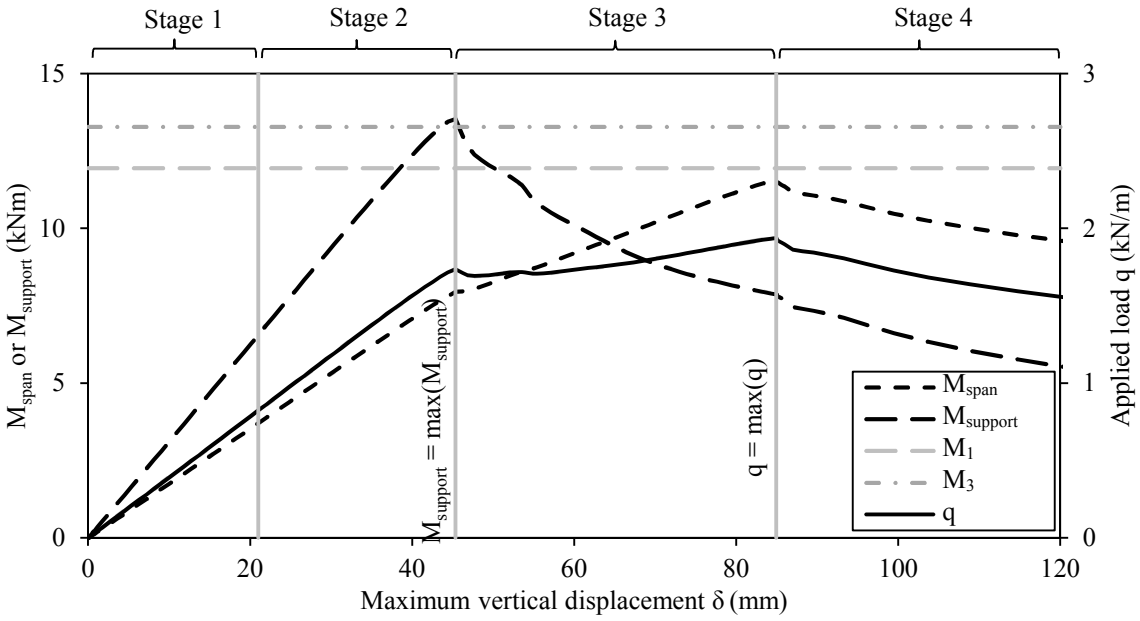


Figure 4.28: *Applied load q, $M_{support}$ and M_{span} versus maximum deflection δ for 2/225_14*

L = 8 m

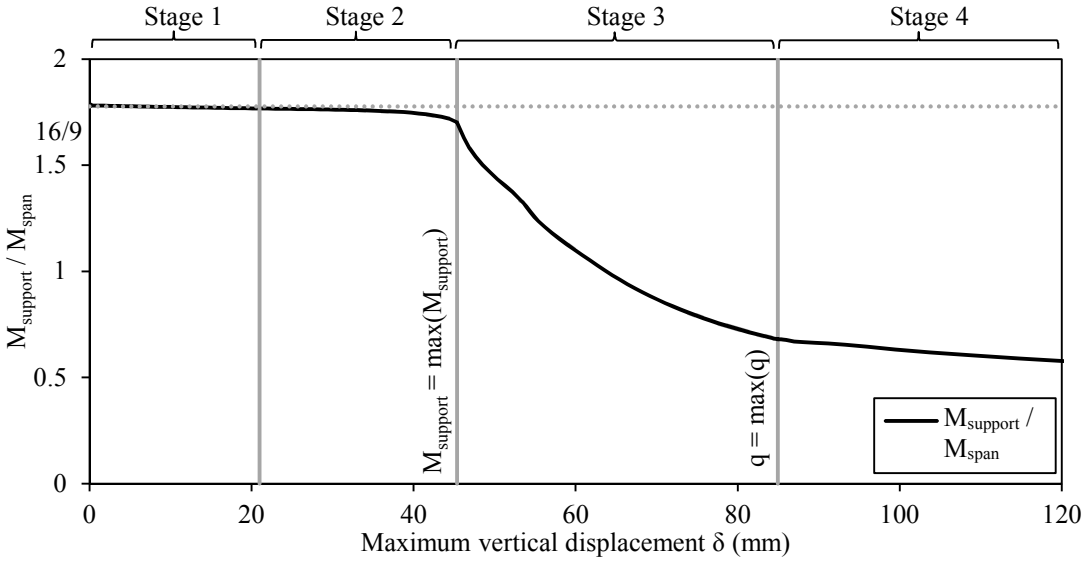


Figure 4.29: *$M_{support}/M_{span}$ versus maximum vertical displacement δ for 2-span 2/225_14*

L = 8 m

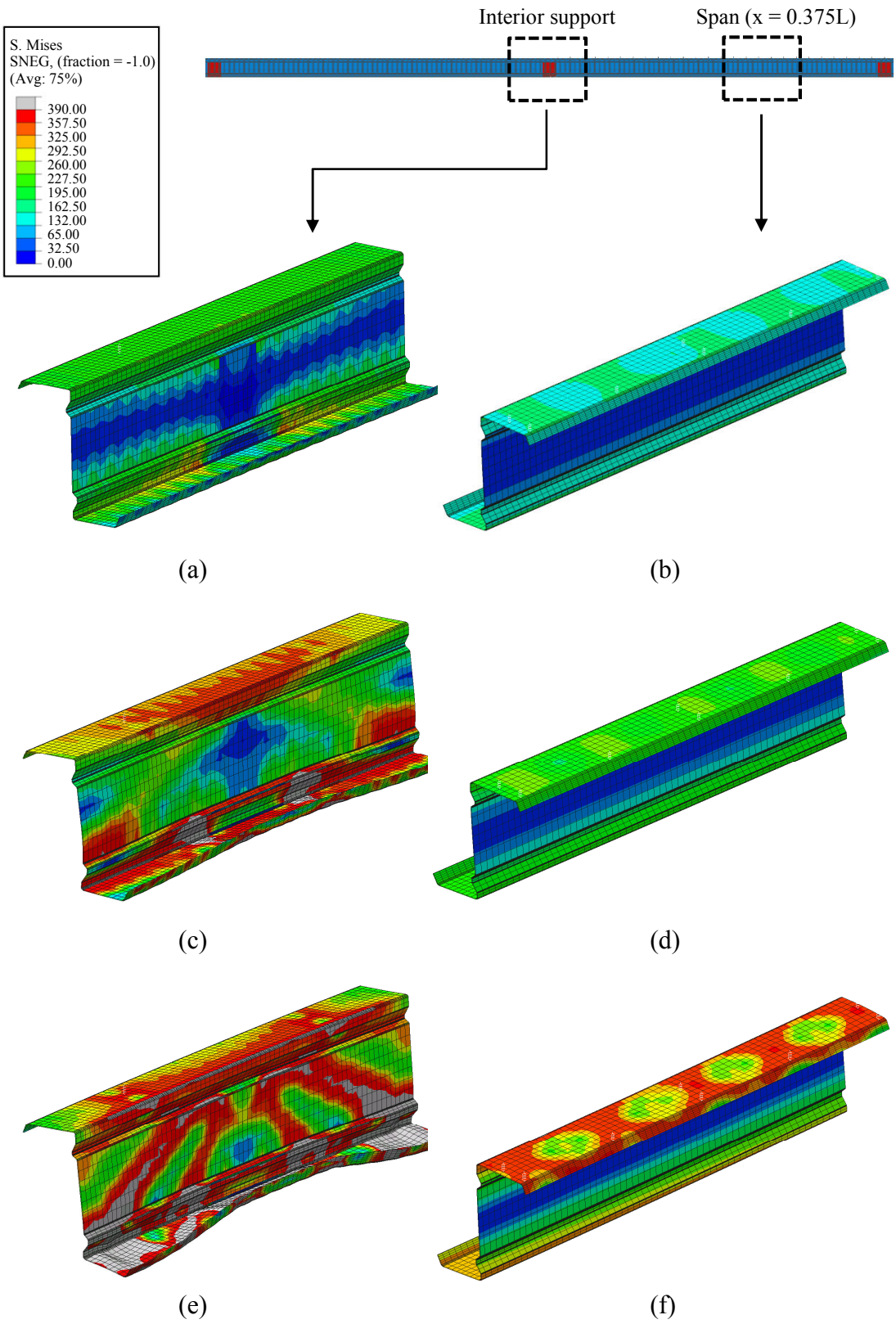


Figure 4.30: *Deformed stress profiles for gravity 2-span 2/225_14 L= 8m FE model at (a, b) stage 1 (c, d) stage 2 and (e, f) ultimate load*

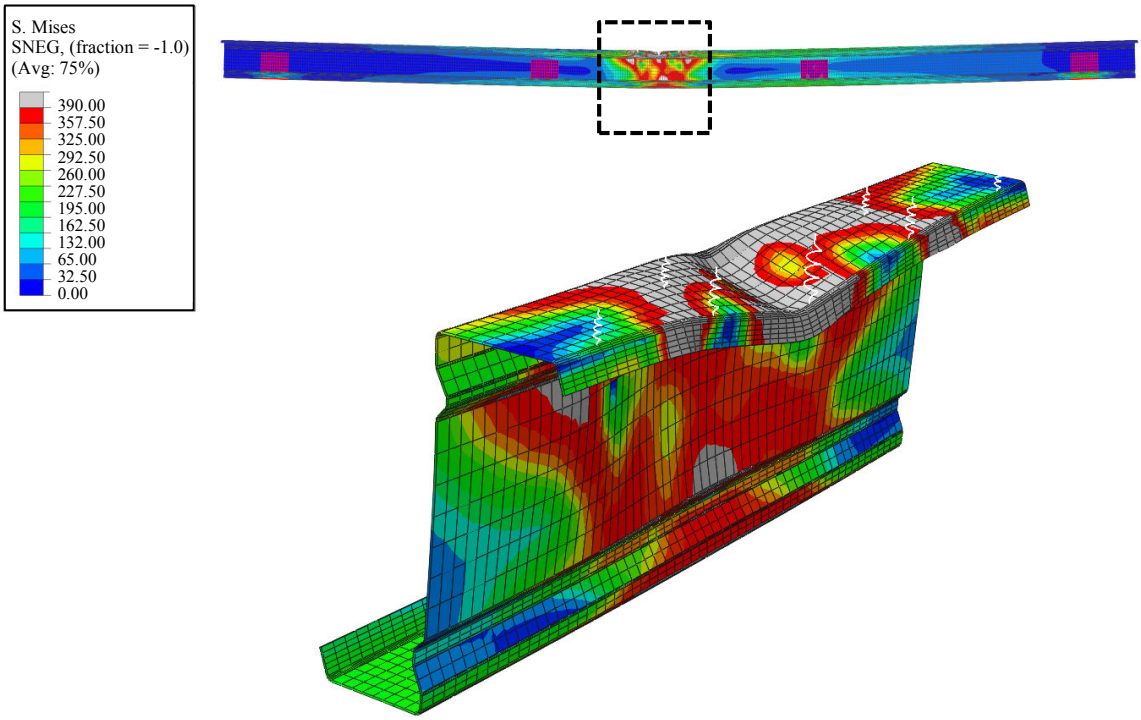


Figure 4.31: *Deformed stress profile for M_1 2/225_14 L^* = 4880 mm*

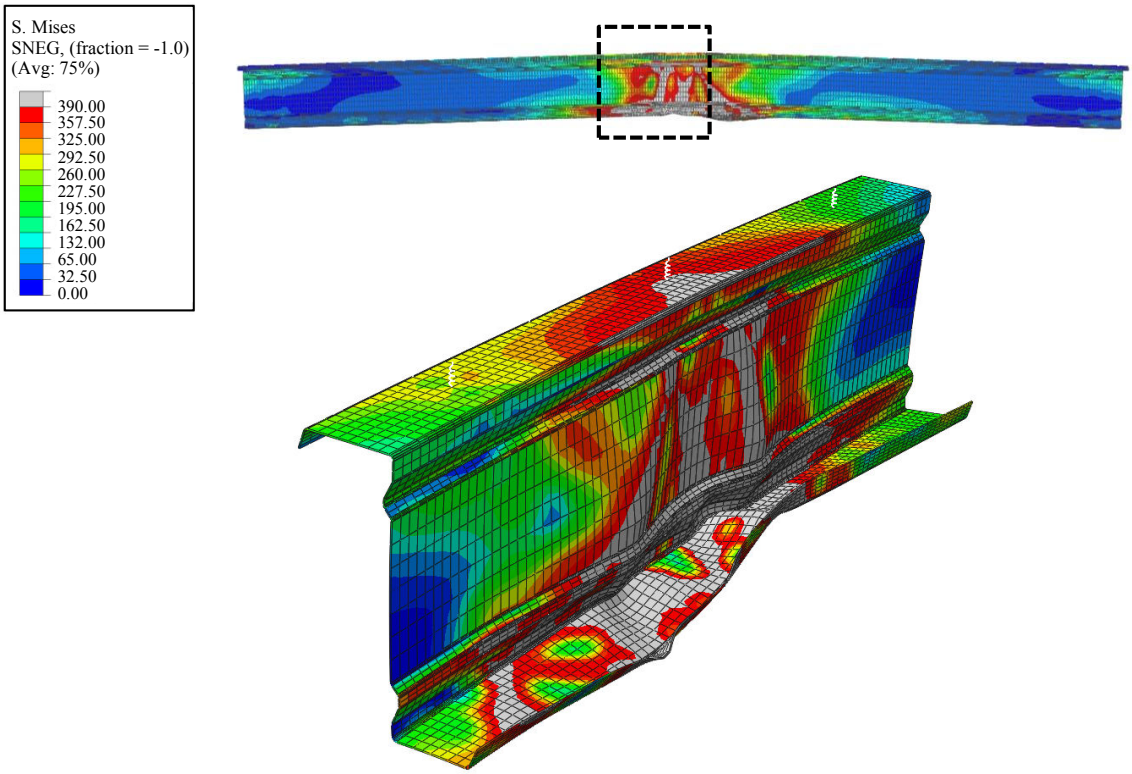


Figure 4.32: *Deformed stress profile for M_3 2/225_14 L' = 4000 mm*

4.3.4.2. Design Proposal

To quantify the drop-off in support moment for each 2-span model at ultimate load, the moment in the support region at the collapse load of the system was compared with the maximum moment from the corresponding reference moment gradient FE model. A reduction factor for gravity loading, $\alpha_{FE,g}$ is defined as the ratio of $M_{support}$ to M_3 as shown in Equation 4.11. $\alpha_{FE,g} = 1$ corresponds to full redistribution with no drop-off in support moment.

$$\alpha_{FE,g} = \frac{M_{support}}{M_3} \qquad 0 \le \alpha_{FE,g} \le 1 \qquad (4.11)$$

Understanding that the amount of interior support moment reduction is also influenced by the span length L, a single design equation $\alpha_{design,g}$ for all cross-sections is proposed to estimate $\alpha_{FE,g}$:

$$\alpha_{design,g} = \left[0.7 - 0.0045\left(\frac{L}{d}\right)\right]\bar{\lambda}_{cs,-ve}^{\left[-0.003\left(\frac{L}{d}\right)-1.4\right]} \quad \text{but} \le 1 \qquad (4.12)$$

where d is the depth of the section and $\bar{\lambda}_{cs,-ve}$ is the negative cross-section slenderness as defined in Equation 4.1. The design equation for the interior support moment reduction (Equation 4.12) was determined using the iterative Generalised Reduced Gradient (GRG2) algorithm within the Microsoft Excel add-in solver. The chosen GRG2 algorithm adopts a forward difference scheme that determines the rate of change of numerous variables independently and checks its sensitivity against a desired target. In this case, the variables were the coefficients in Equation 4.12 and the target was to minimise the coefficient of variation (COV) of the mean ratio between load-capacities obtained from design calculations and FE results. The chosen form of Equation 4.12 allowed the spacing and gradient of the family of curves to be independently directly proportional to L/d. Further details of the GRG2 algorithm are presented in Flystra et al. (1998). As shown in Figure 4.33, the $\alpha_{FE,g}$ values for all cross-sections from the FE results are plotted against the negative cross-section slenderness $\bar{\lambda}_{cs,-ve}$. $\bar{\lambda}_{cs,-ve}$ was chosen because the cross-section at the interior support is subjected to a hogging moment where the bottom flange is in compression. The results were classified into their respective span-to-depth ratios ranging

from L/d of 10 to 60. Figure 4.33 shows that higher L/d ratios tend to yield lower $\alpha_{FE,g}$ values than shorter spans for the same section.

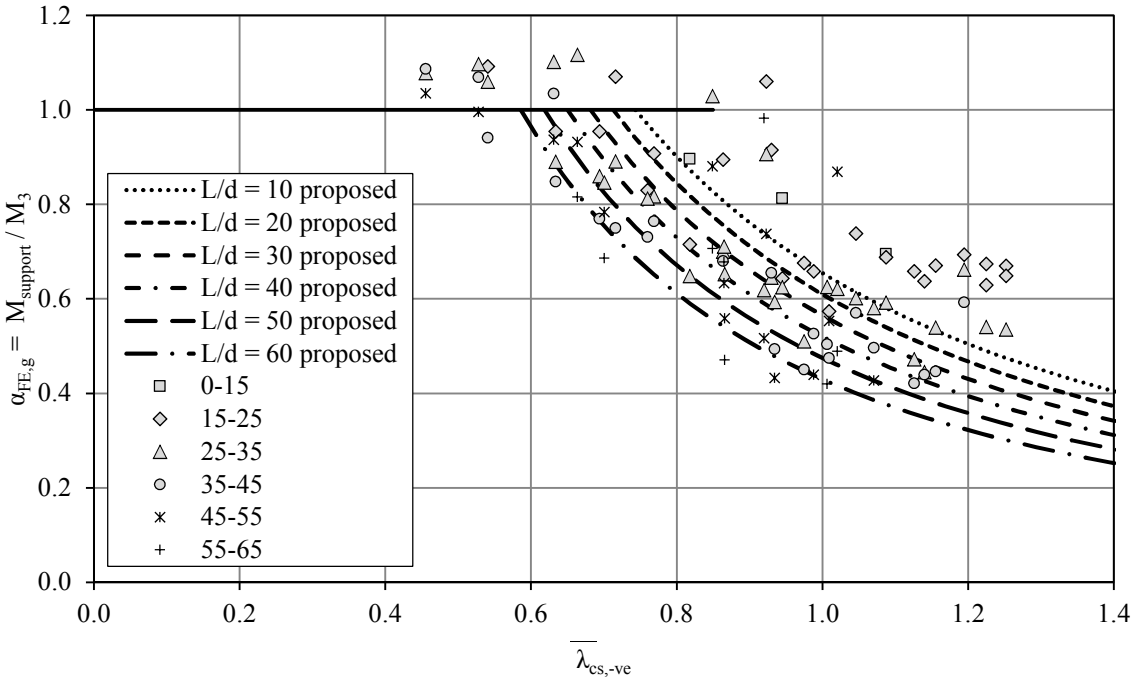


Figure 4.33: *Support moment reduction versus cross-section slenderness*

The ultimate loads q from the FE models were compared with capacity predictions from three design methods:

Method 1. Elastic design – Considers failure of the system once the interior support moment reaches its peak.

Method 2. Plastic design – Assumes full plastic redistribution, with M_3 at the interior support and M_1 in the span.

Method 3. Proposed design method – makes allowance for redistribution, but also for the reduced interior support moment at ultimate load by utilising $\alpha_{design,g}M_3$ at the interior support and M_1 in the span.

The corresponding ultimate loads for each design method (1, 2 and 3) for gravity loading are defined as q_{1g}, q_{2g} and q_{3g} respectively. The bending moment values for M_{span} and $M_{support}$ to use in Equation 4.8 for each design method are shown in Table 4.6. For design method 1, an elastic ratio of 0.5625 was used to calculate the span moment once the interior support moment reaches its maximum value of M_3. For full plastic

redistribution (design method 2), no reduction was applied to M_3 for $M_{support}$, and it was assumed that M_{span} always reaches M_1. To incorporate the potential loss of interior support moment by calculating $\alpha_{design,g}$ using Equation 4.12 into Equation 4.8, design method 3 replaces the span and support moments with M_1 and $\alpha_{design,g}M_3$ respectively.

Table 4.6: *M_{span} and $M_{support}$ inputs values for Equation 4.8 for design methods 1, 2 and 3*

	Design method	M_{span}	$M_{support}$	Equation (4.8)
1	Elastic design	$0.5625M_3$	M_3	$0.5625M_3 = \frac{\left(q_{1g}L^2 + 2M_3\right)^2}{8q_{1g}L^2}$
2	Full plastic redistribution	M_1	M_3	$M_1 = \frac{\left(q_{2g}L^2 + 2M_3\right)^2}{8q_{2g}L^2}$
3	New proposed method	M_1	$\alpha_{design,g}M_3$	$M_1 = \frac{\left(q_{3g}L^2 + 2\alpha_{design,g}M_3\right)^2}{8q_{3g}L^2}$

Comparisons between ultimate loads obtained from design methods 1, 2 and 3 and the 2-span FE results $q_{FE,g}$ for 4, 6 and 8 m spans are shown in Tables 4.7-4.9 respectively. Table 4.10 summarises the ultimate load comparisons for design methods 1, 2 and 3 for each cross-section shape, including the average and coefficient of variation (COV) of the predictions. The raw results from the continuous gravity 2-span study are tabulated in Appendix A. It is of interest to note that as sections become more slender so the value of $M_{support}$ at maximum system load falls further from its peak. Thus the design calculation based on design method 2 overestimates capacity for these slender sections. The extent of the overestimations is illustrated in Figure 4.34 where the failure loads using design methods 2 and 3 are compared against the FE results. For stocky sections, design methods 2 and 3 yield identical failure loads since $\alpha_{design,g}$ equalled unity. For 2-span arrangements with $\alpha_{design,g} < 1$, differences in $q_{2,g}$ and $q_{3,g}$ were found to be significant. Design method 2 consistently overestimated the collapse load, and estimations became more erroneous as the sections become more slender. Even though on average $q_{2,g}$ is already 12% higher than $q_{FE,g}$, the inclusion of stocky sections masks its poor ability to accurately predict the load-carrying capacity for slender sections. This is evident between cross-sectional shapes; the average design load overestimation for Zeta I sections was only 3%, whereas for channel sections the overprediction was much higher at 23%. This is because the considered channel sections were more slender than the Zeta I

sections ($\bar{\lambda}_{cs,-ve}$ ranged from 0.866-1.155 for channels opposed to Zeta I sections, where $\bar{\lambda}_{cs,-ve}$ ranged from 0.455-1.046). The overprediction for some cases was as high as 31%. Alternatively, by only considering slender sections ($\alpha_{design,g} < 1$), the average $q_{2,g}/q_{FE,g}$ increased to 1.15. In contrast, designing the system based on elastic principles (design method 1) gave highly conservative results; the average $q_{1,g}/q_{FE}$ for all cross-sections was 0.823. The conservative results for all arrangements can be explained by the fact that all results showed additional load capacity once $M_{support}$ reached its peak. One case obtained an additional 32% more load from when $M_{support}$ was at is maximum.

Figures 4.35 and 4.36 compare $q_{3,g}/q_{FE,g}$ and $\alpha_{design,g}/\alpha_{FE,g}$ ratios against $\bar{\lambda}_{cs-ve}$ respectively. Even though the accuracy for $\alpha_{design,g}$ tends to decrease for slender sections in Figure 4.36, the effect on the accuracy of the predicted ultimate load was minimal for these cases. This is mainly due to ultimate load calculation using Equation 4.8 being less sensitive to $\alpha_{design,g}M_3$ than M_1. For example, a 5% difference in estimation for $\alpha_{FE,g}M_3$ only yields a 1.5% reduction in design-ultimate load, whereas design-ultimate load changes by 3.5% for the same 5% difference in estimation for M_1. Figures 4.34 and 4.35 shows there were no significant patterns to suggest certain span lengths or section types perform poorly. This is illustrated in Table 4.10 with a mean ratio of $q_{3,g}/q_{FE,g}$ equalling unity and low scatter (COV < 0.050), with few results overpredicted and none by more than 9.4% as shown in Figure 4.35. In general, the α-framework provides a robust method for calculating the 2-span collapse load for all 4 cross-section types and covering both slender and stocky sections. Thus, the inclusion of the $\alpha_{design,g}$ factor as obtained from Equation 4.12 permits the safe use of the plastic redistribution for the range of cross-sections and span lengths covered.

The α-framework can potentially be extended to alternative cold-formed steel cross-sections and arrangements. Even though only Zeta I, Zeta II, Zed and channel sections have been analysed in this study, it is expected that Equation 4.7 could still be applied to other cold-formed steel sections because it incorporates the cross-section slenderness. The proposed method is also not strictly limited to moment input values obtained from FE analyses. The design procedure has the potential to be extended to cover a wider range of spans and support moment capacities obtained from various sources. A source of input moment values could include a mixture of: (i) physical testing, (ii) design calculations or (iii) numerical, including FE, calculations.

Table 4.7: *Ultimate load comparison between 2-span FE results and design methods 1, 2 and 3 for span length L = 4 m*

Section reference	$q_{FE,g}$ (kN/m)	$q_{1,g}$ (kN/m)	$q_{2,g}$ (kN/m)	$q_{3,g}$ (kN/m)	$q_{1,g}/q_{FE,g}$	$q_{2,g}/q_{FE,g}$	$q_{3,g}/q_{FE,g}$
1/150_50	23.603	18.533	24.860	24.860	0.785	1.053	1.053
1/150_40	20.966	15.105	20.132	20.132	0.720	0.960	0.960
1/150_30	15.289	10.795	14.809	14.809	0.706	0.969	0.969
1/125_20	6.951	5.022	6.760	6.760	0.722	0.973	0.973
1/200_25	18.535	13.154	18.025	17.986	0.710	0.972	0.970
1/125_13	4.030	2.911	4.015	3.613	0.722	0.996	0.896
1/175_16	8.694	6.150	8.561	7.617	0.707	0.985	0.876
1/200_16	9.965	7.632	10.392	9.251	0.766	1.043	0.928
1/200_13	7.020	5.950	7.969	6.788	0.848	1.135	0.967
2/225_50	43.983	29.725	41.544	41.544	0.676	0.945	0.945
2/225_40	34.429	25.571	33.479	33.479	0.743	0.972	0.972
2/225_35	29.856	22.085	29.253	29.253	0.740	0.980	0.980
2/225_30	24.578	18.591	24.560	23.848	0.756	0.999	0.970
2/285_30	32.346	24.729	33.750	32.180	0.765	1.043	0.995
2/225_25	19.606	15.051	19.861	18.372	0.768	1.013	0.937
2/285_25	25.193	20.283	27.340	24.649	0.805	1.085	0.978
2/285_20	17.570	14.385	20.305	17.577	0.819	1.156	1.000
2/225_14	7.860	7.022	9.144	7.557	0.893	1.163	0.962
2/245_15	9.741	8.593	11.295	9.305	0.882	1.160	0.955
2/265_15	10.106	8.506	12.121	10.090	0.842	1.199	0.998
Z/125_20	5.109	4.217	5.655	5.560	0.825	1.107	1.088
Z/200_25	12.780	9.952	13.739	13.362	0.779	1.075	1.046
Z/125_14	3.188	2.684	3.640	3.284	0.842	1.142	1.030
Z/155_15	4.760	3.878	5.348	4.754	0.815	1.123	0.999
Z/170_14	4.855	3.902	5.395	4.695	0.804	1.111	0.967
Z/200_13	5.449	4.176	5.738	4.836	0.766	1.053	0.887
C/127_20	5.569	4.884	6.440	5.798	0.877	1.157	1.041
C/127_18	4.790	4.237	5.620	4.950	0.885	1.173	1.033
C/200_20	9.396	8.282	11.360	10.048	0.881	1.209	1.069
C/170_18	6.746	6.022	8.144	7.117	0.893	1.207	1.055
C/140_16	4.423	3.957	5.361	4.618	0.895	1.212	1.044
C/127_15	3.552	3.147	4.282	3.656	0.886	1.205	1.029
C/155_15	4.478	4.529	5.719	4.800	1.011	1.277	1.072
C/185_15	5.478	4.976	6.880	5.810	0.908	1.256	1.060
C/200_15	5.925	5.406	7.482	6.288	0.912	1.263	1.061

Table 4.8: *Ultimate load comparison between 2-span FE results and design methods 1, 2 and 3 for span length L = 6 m*

Section reference	$q_{FE,g}$ (kN/m)	$q_{1,g}$ (kN/m)	$q_{2,g}$ (kN/m)	$q_{3,g}$ (kN/m)	$q_{1,g}/q_{FE,g}$	$q_{2,g}/q_{FE,g}$	$q_{3,g}/q_{FE,g}$
1/150_50	11.615	8.359	11.100	11.100	0.720	0.956	0.956
1/150_40	9.175	6.599	8.900	8.900	0.719	0.970	0.970
1/150_30	6.627	4.716	6.547	6.547	0.712	0.988	0.988
1/125_20	2.933	2.157	2.973	2.880	0.735	1.014	0.982
1/200_25	7.767	5.833	8.005	7.840	0.751	1.031	1.009
1/125_13	1.725	1.324	1.797	1.565	0.768	1.042	0.907
1/175_16	3.759	2.812	3.838	3.347	0.748	1.021	0.890
1/200_16	4.227	3.343	4.598	4.039	0.791	1.088	0.955
1/200_13	3.092	2.634	3.537	2.975	0.852	1.144	0.962
2/225_50	18.886	13.191	18.455	18.455	0.698	0.977	0.977
2/225_40	14.304	10.729	14.612	14.612	0.750	1.022	1.022
2/225_35	12.229	9.284	12.777	12.760	0.759	1.045	1.043
2/225_30	10.117	7.828	10.733	10.254	0.774	1.061	1.014
2/285_30	13.609	11.035	15.018	14.134	0.811	1.104	1.039
2/225_25	7.962	6.484	8.740	7.965	0.814	1.098	1.000
2/285_25	10.868	9.327	12.283	10.913	0.858	1.130	1.004
2/285_20	8.079	6.336	9.000	7.715	0.784	1.114	0.955
2/225_14	3.543	3.041	4.030	3.296	0.858	1.137	0.930
2/245_15	4.334	3.758	4.994	4.072	0.867	1.152	0.940
2/265_15	4.719	3.963	5.464	4.474	0.840	1.158	0.948
Z/125_20	2.171	1.844	2.500	2.374	0.849	1.152	1.093
Z/200_25	5.666	4.420	6.105	5.823	0.780	1.078	1.028
Z/125_14	1.351	1.195	1.619	1.415	0.885	1.198	1.047
Z/155_15	1.994	1.714	2.373	2.063	0.860	1.190	1.035
Z/170_14	2.009	1.715	2.389	2.041	0.853	1.189	1.016
Z/200_13	2.160	1.870	2.557	2.119	0.866	1.184	0.981
C/127_20	2.403	2.069	2.819	2.470	0.861	1.173	1.028
C/127_18	2.070	1.813	2.468	2.118	0.876	1.192	1.023
C/200_20	4.100	3.684	5.050	4.391	0.898	1.232	1.071
C/170_18	2.910	2.585	3.581	3.077	0.888	1.230	1.057
C/140_16	1.899	1.723	2.368	1.994	0.908	1.247	1.050
C/127_15	1.600	1.413	1.909	1.584	0.883	1.193	0.990
C/155_15	1.994	1.995	2.535	2.081	1.001	1.271	1.044
C/185_15	2.407	2.239	3.069	2.545	0.930	1.275	1.057
C/200_15	2.637	2.412	3.329	2.755	0.915	1.263	1.045

Table 4.9: *Ultimate load comparison between 2-span FE results and design methods 1, 2 and 3 for span length L = 8 m*

Section reference	$q_{FE,g}$ (kN/m)	$q_{1,g}$ (kN/m)	$q_{2,g}$ (kN/m)	$q_{3,g}$ (kN/m)	$q_{1,g}/q_{FE,g}$	$q_{2,g}/q_{FE,g}$	$q_{3,g}/q_{FE,g}$
1/150_50	6.451	4.709	6.247	6.247	0.730	0.968	0.968
1/150_40	5.020	3.570	4.946	4.946	0.711	0.985	0.985
1/150_30	3.598	2.676	3.693	3.620	0.744	1.026	1.006
1/125_20	1.576	1.229	1.679	1.555	0.780	1.065	0.986
1/200_25	4.165	3.241	4.486	4.298	0.778	1.077	1.032
1/125_13	0.913	0.730	1.005	0.847	0.800	1.100	0.927
1/175_16	2.007	1.587	2.161	1.845	0.791	1.077	0.919
1/200_16	2.327	1.873	2.583	2.231	0.805	1.110	0.959
1/200_13	1.763	1.474	1.987	1.646	0.836	1.127	0.934
2/225_50	10.246	7.416	10.379	10.379	0.724	1.013	1.013
2/225_40	7.904	5.874	8.151	8.151	0.743	1.031	1.031
2/225_35	6.617	5.250	7.199	7.057	0.793	1.088	1.066
2/225_30	5.557	4.408	6.039	5.668	0.793	1.087	1.020
2/285_30	7.484	6.172	8.433	7.834	0.825	1.127	1.047
2/225_25	4.423	3.560	4.880	4.380	0.805	1.103	0.990
2/285_25	5.995	5.031	6.818	6.002	0.839	1.137	1.001
2/285_20	4.414	3.558	5.060	4.292	0.806	1.146	0.972
2/225_14	1.936	1.659	2.245	1.819	0.857	1.160	0.939
2/245_15	2.368	2.103	2.805	2.261	0.888	1.185	0.955
2/265_15	2.569	2.215	3.068	2.487	0.862	1.194	0.968
Z/125_20	1.177	1.038	1.407	1.285	0.882	1.195	1.092
Z/200_25	3.041	2.486	3.434	3.210	0.817	1.129	1.055
Z/125_14	0.767	0.663	0.906	0.768	0.864	1.182	1.001
Z/155_15	1.074	0.959	1.332	1.132	0.893	1.241	1.054
Z/170_14	1.148	0.957	1.341	1.124	0.834	1.168	0.979
Z/200_13	1.184	1.040	1.433	1.171	0.879	1.211	0.990
C/127_20	1.314	1.157	1.583	1.344	0.881	1.205	1.022
C/127_18	1.056	1.021	1.389	1.155	0.966	1.315	1.094
C/200_20	2.258	2.017	2.817	2.414	0.893	1.248	1.069
C/170_18	1.633	1.452	2.013	1.695	0.889	1.233	1.038
C/140_16	1.074	0.967	1.331	1.093	0.901	1.239	1.018
C/127_15	0.881	0.760	1.059	0.860	0.863	1.202	0.976
C/155_15	1.077	0.961	1.358	1.113	0.892	1.260	1.033
C/185_15	1.372	1.243	1.720	1.404	0.906	1.253	1.023
C/200_15	1.477	1.331	1.862	1.521	0.901	1.260	1.030

Table 4.10: *Summary of comparisons between FE results and design calculations*

Section type	No. of 2-span FE models	$q_{1,g} / q_{FE,g}$		$q_{2,g} / q_{FE,g}$		$q_{3,g} / q_{FE,g}$	
		MEAN	COV	MEAN	COV	MEAN	COV
Zeta I	27	0.758	0.059	1.032	0.057	0.960	0.043
Zeta II	33	0.801	0.069	1.090	0.064	0.987	0.036
Zed	18	0.838	0.046	1.152	0.046	1.022	0.050
C	27	0.904	0.040	1.232	0.031	1.032	0.025
All	105	0.823	0.086	1.122	0.084	1.000	0.049

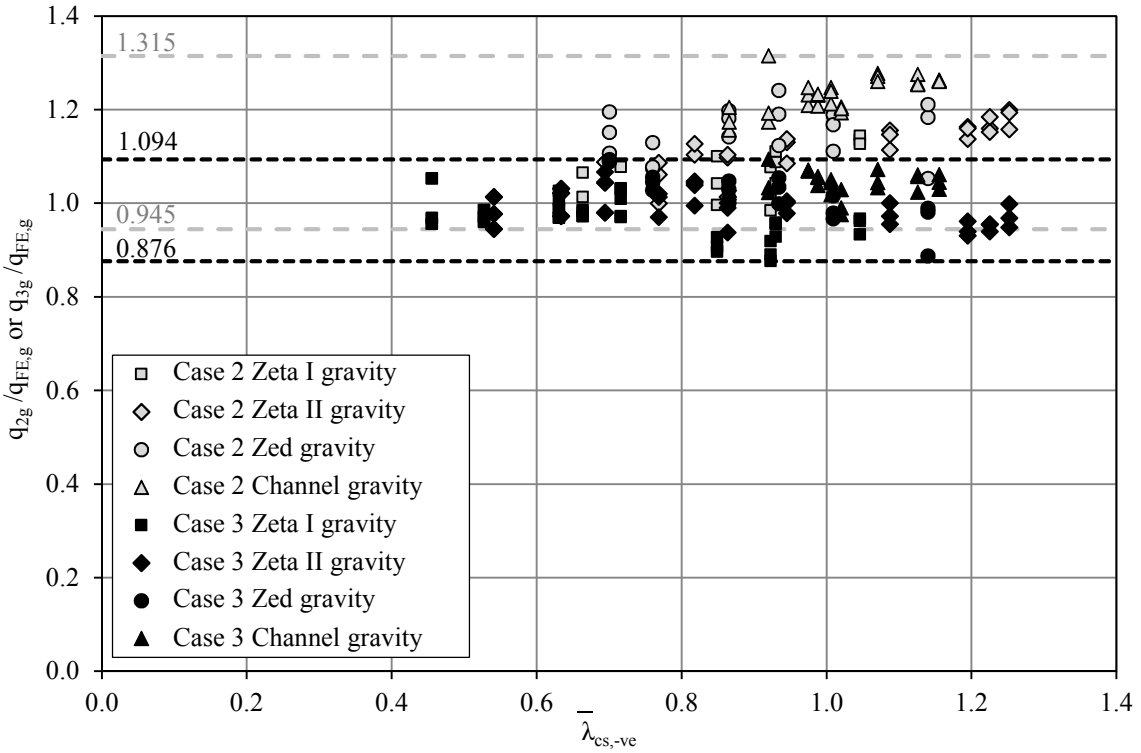


Figure 4.34: *Ultimate load comparison between FE and design methods 2 and 3 against negative cross-section slenderness*

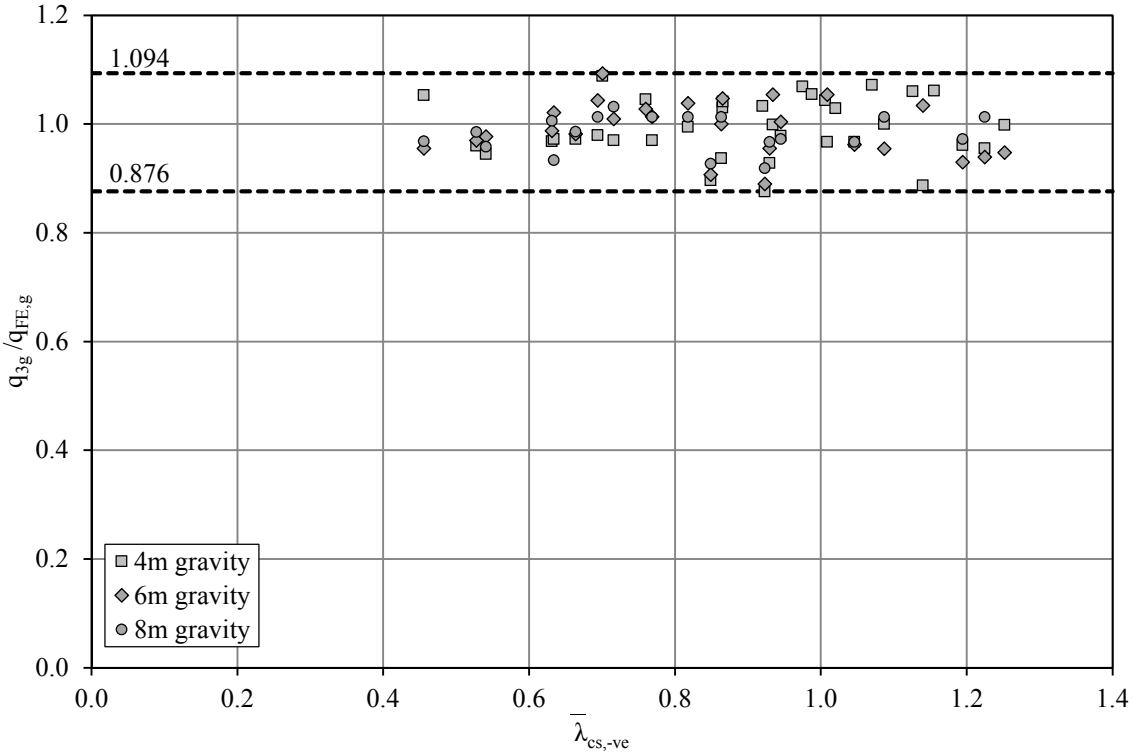


Figure 4.35: *Ultimate load comparison between FE and design method 3, arranged by span length*

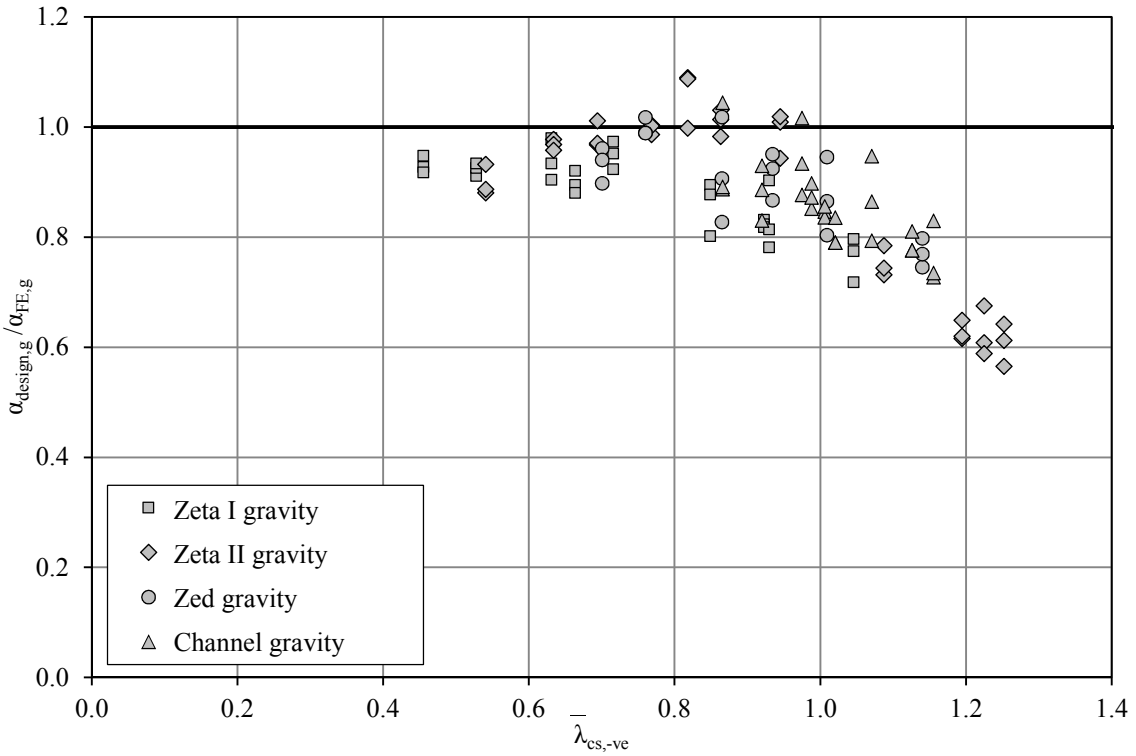


Figure 4.36: *α-reduction comparison between design method and FE results*

4.4. PARAMETRIC STUDY – UPLIFT LOADING

4.4.1. Outline

Cold-formed steel purlins when loaded in the plane of the web may twist and deflect laterally, as well as vertically, if adequate horizontal restraints are not provided. Open cold-formed steel members tend to have low torsional rigidity and lateral stiffness and are therefore prone to lateral torsional buckling (LTB). Multi-span purlin systems generally have sheeting or cladding attached to the top flange that provides lateral restraint to the member. Anti-sagbars are also generally installed during the erection stage to prevent the purlins twisting prior to installation and to provide lateral restraint to the bottom flange under uplift conditions. For gravity loading, the free compression flange in the hogging region tends to be short enough to avoid any LTB. Hence it is safe to design the purlin systems based on their cross-section capacities in conjunction with the α-framework discussed in Section 4.3.4.2. For uplift loading cases, the long unsupported compressive bottom flange in the span region would mean LTB is more prevalent. Additional checks are therefore required to ensure the horizontal bending moments associated with the free compressive flange are also satisfied.

4.4.2. Lateral torsional buckling

The behaviour for purlin systems subjected to uplift loading has never been directly addressed in the British Standards. Eurocode 3 Part 1-3 (2006) provides a method which enables the designer to evaluate the ultimate load capacity of a purlin system subjected to uplift loading. The method is based on work done by Sokol (1988) who considered the unsupported compression flange as a beam on an elastic foundation to represent LTB. The method adopts lateral linear spring with stiffness K that represents and replaces the rotational stiffness C_D offered by the sheeting. The free flange of the purlin is treated as a compression member subjected to a non-uniform axial force, (varying with the bending moment) with continuous lateral restraint of stiffness K. The procedure to check whether the section can meet the total load demands requires the total stress σ_t to be less than the yield strength f_y. Provided the purlin is subjected to bending only with no axial force, the total stress σ_t can be determined from Equation 4.13.

$$\sigma_t = \frac{1}{\chi_{LT}} \frac{M_{yy}(x)}{W_{eff,y}} + \frac{M_{zz}(x)}{W_{fz}} \tag{4.13}$$

where M_{yy} (x) and M_{zz} (x) are the in-plane bending and lateral bending moments at distance (x) from the end support respectively. $W_{eff,y}$ is the effective section modulus of the cross-section for bending about the y-y axis only and W_{fz} is the section modulus of the free flange plus the contributing part of the web for bending about the z-z axis. χ_{LT} is the reduction factor for lateral torsional buckling. Figure 4.37 shows the superposition of stresses and instructs the designer to take either 1/5 of the section height h for Z and channel sections or 1/6 for Zeta or Sigma sections as part of the contribution to the free flange.

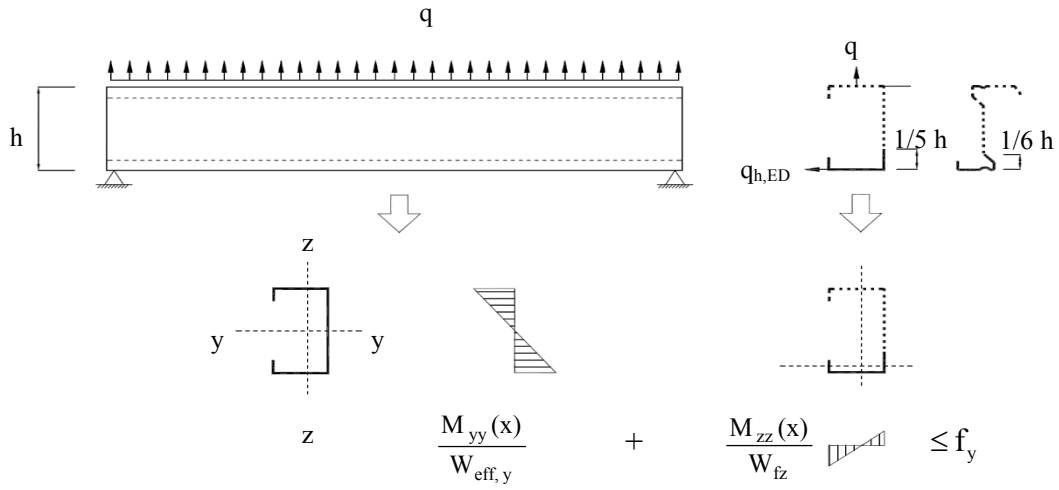


Figure 4.37: *Superposition of stresses in a cold-formed section under uplift loading*

To determine the largest vertical uplift load q that can be sustained with allowance for LTB, the method adopts an iterative method with increasing trial load increments so that Equation 4.13 still holds. An additional equivalent lateral load $q_{h,ED}$ is calculated for each vertical trial load which is based on a the coefficient of the spring support R. The method comprise of 9 main parts which involve determining:

1. $W_{eff,y}$ using the effective width method given in EN 1993-1-5:2006, with additional checks for distortional buckling using EN 1993-1-3:2006.
2. W_{fz} by assuming the free flange is fully effective.
3. M_{yy} using the current trial load.
4. $q_{h,FD}$ and M_{zz} by calculating the spring support coefficient R.

5. The lateral spring stiffness K by calculating the lateral stiffness corresponding to rotational stiffness between the joint between the sheeting and purlin K_A. K_A is a function of the rotational spring stiffness C_D. C_D is the summation of the stiffness of the connection between the sheeting and purlin C_{DA} and the flexural stiffness of the sheeting C_{DC}.
6. The equivalent lateral load and moment $q_{h,Ed}$ and $M_{fz,ED}$ by calculating R. To accommodate the presence of anti-sagbars, R is a function of the length between anti-sagbars La.
7. The lateral torsional buckling length l_{fz} by choosing the corresponding set of η values from Table 10.2b and distance between anti-sagbars L_a. η_1 to η_4 are coefficients that depend on the number of anti-sagbars.
8. χ_{LT} by using the buckling curves in EN 1993-1-1:2005 with a relative slenderness for flexural buckling $\bar{\lambda}_{fz}$ as calculated using EN 1993-1-3:2006 and lateral torsional buckling length l_{fz}.
9. The buckling resistance using Equation 4.13. If valid, increase the vertical trial load and repeat steps 1-9.

The 9 step design procedure to check for lateral torsional buckling in the span is summarised by the flowchart in Appendix B. A detailed worked example also is presented in Appendix C.

4.4.3. Reference FE models

To study the buckling behaviour and level of redistribution in cold-formed steel continuous purlins systems subjected to uplift loading, two additional single span FE models were developed to provide reference moment values, which were then compared against M_{span} and $M_{support}$ from the 2-span FE models. By extracting the applied load and end reaction forces, M_{span} and $M_{support}$ from the 2-span uplift models were calculated using Equations 4.7 and 4.8 respectively. Figure 4.38 illustrates how the reference single span FE models are related to the 2-span uplift FE model. The largest sagging moment $M_{support}$ was compared against the maximum moment in the single span FE model subjected to positive 3-point bending M_4 (test type 4). To account for a potential reduction of moment capacity due to lateral torsional buckling, M_{span} was compared against a reduced negative pure bending moment capacity $\chi_{LT}M_2$, where χ_{LT} is the reduction factor for lateral torsional buckling using EN 1993-1-3:2006 and EN 1993-1-1:2005 as discussed in

Section 4.4.2 and M_2 is the moment resistance obtained from the single span FE model subjected to negative pure bending (test type 2). Considering the cross-sections listed in Table 4.11, additional assumptions for calculating χ_{LT} using the 9 step procedure outlined in Section 4.4.2 includes:

- C_{DA} was taken as 3739 Nmm/mm for all cross-section types, based on physical testing by Leach (1992).
- C_{DC} was neglected since the total rotational spring stiffness C_D was assumed to be mainly influenced by the value of C_{DA}.

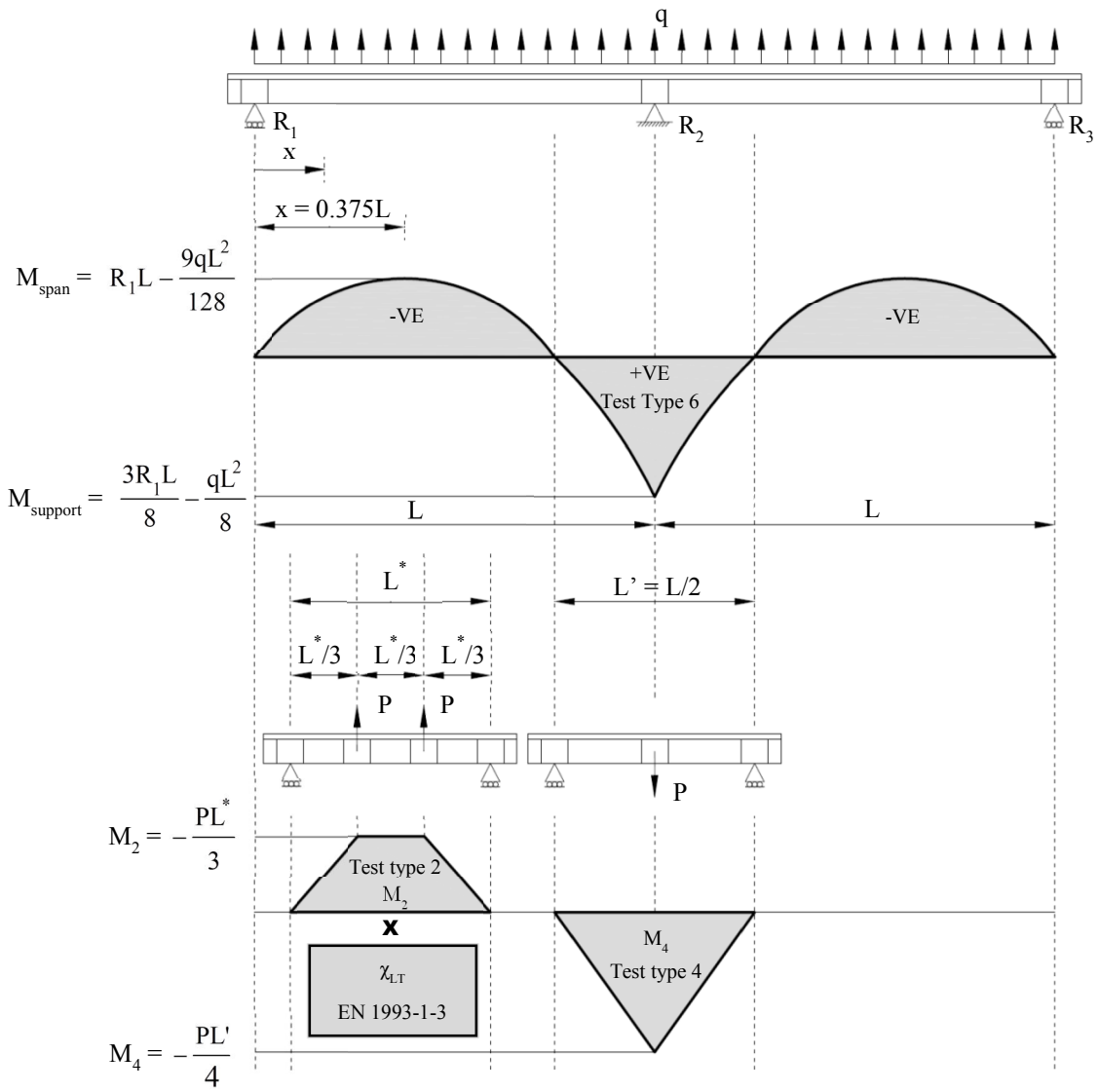


Figure 4:38: *Elastic bending moment diagram (BMD) for 2-span continuous beam under uplift loading, M_4 (positive 3-point bending) and M_2 (negative pure bending)*

4.4.4. Alpha framework

To study the degree of moment redistribution for cold-formed steel continuous 2-span purlin systems subjected to uplift UDL, 30 cross-sections including Zeta I, Zeta II, Zed and channel shapes and 4, 6, 8 and 10 m equal spans were simulated using the validated FE models described in Chapter 3. Unlike the 2-span gravity loading study discussed in Section 4.3, which covered 4, 6 and 8 m span lengths, additional 10 m span FE models were included in the uplift study to cover more globally slender purlin systems which may be governed by LTB. The chosen section types covered a large range of cross-section slenderness ($0.617 < \bar{\lambda}_{cs,+ve} < 1.233$) as shown in Table 4.11. The parametric study for uplift loading comprised 150 single span FE models discussed in Section 4.3.2 and 120 continuous 2-span FE models.

Zeta I, Zeta II, Zed and channel cross-sections types were chosen for this study and are illustrated in Figures 4.3 and 4.4. The section height h, top flange b_c, bottom flange b_t and nominal thickness t were varied to cover a large ranged cross-section slenderness. The location and dimensions of the intermediate stiffeners in the flanges and web for the Zeta I and Zeta II sections were kept constant relative to their distance to flange/web junctions. For each cross-sectional shape, the top and bottom lip lengths, and lip angles were also kept constant. The key dimensions for all 4 sections are given in Table 4.11.

Table 4.11: *List of dimensions for Zeta I, Zeta II, Zed and channels sections for uplift 2-span parametric study*

Section Type[A]	Section Reference	Top flange b_c (mm)	Bottom. flange b_t (mm)	Height h (mm)	Thickness t (mm)	$\bar{\lambda}_{cs,+ve}$
Zeta I	1/150_30	72	65	150	3.0	0.617
Zeta I	1/125_20	72	65	125	2.0	0.811
Zeta I	1/200_25	72	65	200	2.5	0.832
Zeta I	1/175_20	72	65	175	2.0	0.950
Zeta I	1/150_19	72	65	150	1.9	0.976
Zeta I	1/125_13	60	50	125	1.3	1.042
Zeta I	1/175_16	72	65	175	1.6	1.083
Zeta I	1/200_16	72	65	200	1.6	1.084
Zeta I	1/200_13	72	65	200	1.3	1.220
Zeta II	2/225_30	78	68	225	3.0	0.762
Zeta II	2/285_30	78	68	285	3.0	0.832
Zeta II	2/225_25	78	68	225	2.5	0.855
Zeta II	2/285_25	78	68	285	2.5	0.936
Zeta II	2/285_20	78	68	285	2.0	1.056
Zeta II	2/225_14	78	68	225	1.4	1.205
Zeta II	2/245_15	78	68	245	1.5	1.195
Zeta II	2/265_15	78	68	265	1.5	1.233
Zed	Z/125_20	55	45	125	2.0	0.778
Zed	Z/200_25	58	49	200	2.5	0.806
Zed	Z/125_14	55	45	125	1.4	0.957
Zed	Z/155_15	58	49	155	1.5	1.016
Zed	Z/170_14	58	49	170	1.4	1.087
Zed	Z/200_13	58	49	200	1.3	1.202
C	C/127_20	65	65	127	2.0	0.857
C	C/127_18	65	65	127	1.8	0.911
C	C/200_20	65	65	200	2.0	0.968
C	C/127_15	65	65	127	1.5	1.010
C	C/155_15	65	65	155	1.5	1.061
C	C/185_15	65	65	185	1.5	1.117
C	C/200_15	65	65	200	1.5	1.147

A - Refer to Figures 4.3 and 4.4 for cross-section details

4.4.4.1. Stocky versus slender 2-span sections

The degree of moment redistribution for each 2-span uplift FE model was found to be influenced by its LTB behaviour. Stocky cross-sections at short spans showed similar moment redistribution traits to that of stocky sections for gravity loading. To illustrate such behaviour, results obtained from an uplift 2-span 1/175_20 L = 6 m FE model are presented. Figure 4.39 shows the $M_{support}$, M_{span} and load-vertical deflection response with the same discretised stages of the response outlined in Section 4.3.4.1. Table 4.12 compares M_{span}, $M_{support}$ and their reference single span moment values. Localised distortional buckling was first observed at the interior support compression flange as shown in Figure 4.40 (a), with translational springs restricting the distortional buckling half-wavelength to the 250 mm spring spacing. The additional restraint offered by the sheeting at the top flange meant the interior support moment-rotation characteristic tends to be more ductile and more beneficial for moment redistribution at stage 3, for uplift loading as opposed to gravity loading. Differences between the moment redistribution behaviour of stocky sections for uplift and gravity cases were identified during stage 3 of the load-displacement response. For the stocky cross-section considered, the rotation capacity at the interior support allowed $M_{support}$ to be maintained at large enough rotations to enable M_{span} to increase. For gravity loading, the lateral restraint offered by the sheeting, attached to the top flange, allowed the cross-section in the span region to reach its pure bending in-plane capacity. This was not the case for uplift loading. The change in the bending direction, with compression acting at the free unrestrained flange in the span, permitted the cross-section to lateral deflect as shown in Figure 4.40(b), thus limiting the ability of M_{span} to reach its in-plane cross-sectional capacity, designated as M_2. This was found to be common for all 2-span uplift arrangements. Figure 4.41 illustrates the shortfall in M_{span}/M_2, which tends to be greater for longer spans.

Table 4.12: *Moment comparisons between 2-span uplift, M_2 and M_4 models for 1/175_20 L = 6 m*

Stage	Applied load q (kN/m)	M_{span} (kNm)	$M_{support}$ (kNm)	M_2 (kNm)	M_4 (kNm)	M_{span}/M_2	$M_{support}/M_4$
2	4.118	-10.886	17.301	-15.175	16.663	0.717	1.038
3	4.680	-13.789	15.789			0.908	0.948

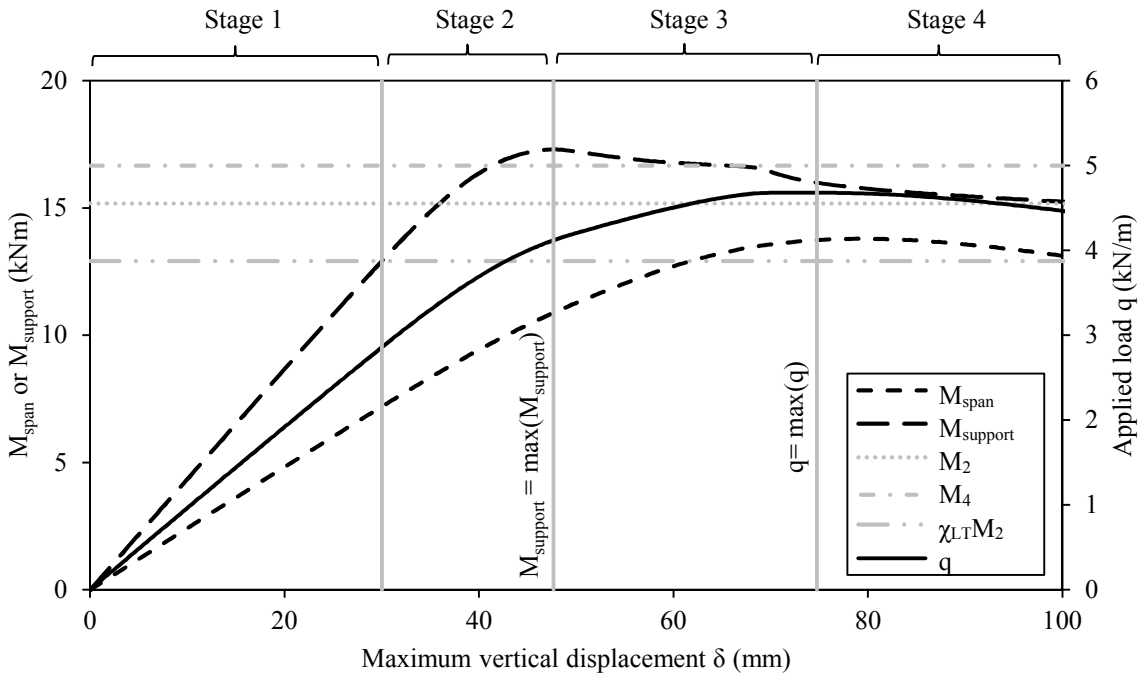


Figure 4.39: *Applied load q, $M_{support}$ and M_{span} versus maximum vertical deflection δ for uplift 2-span 1/175_20 L = 6 m FE model*

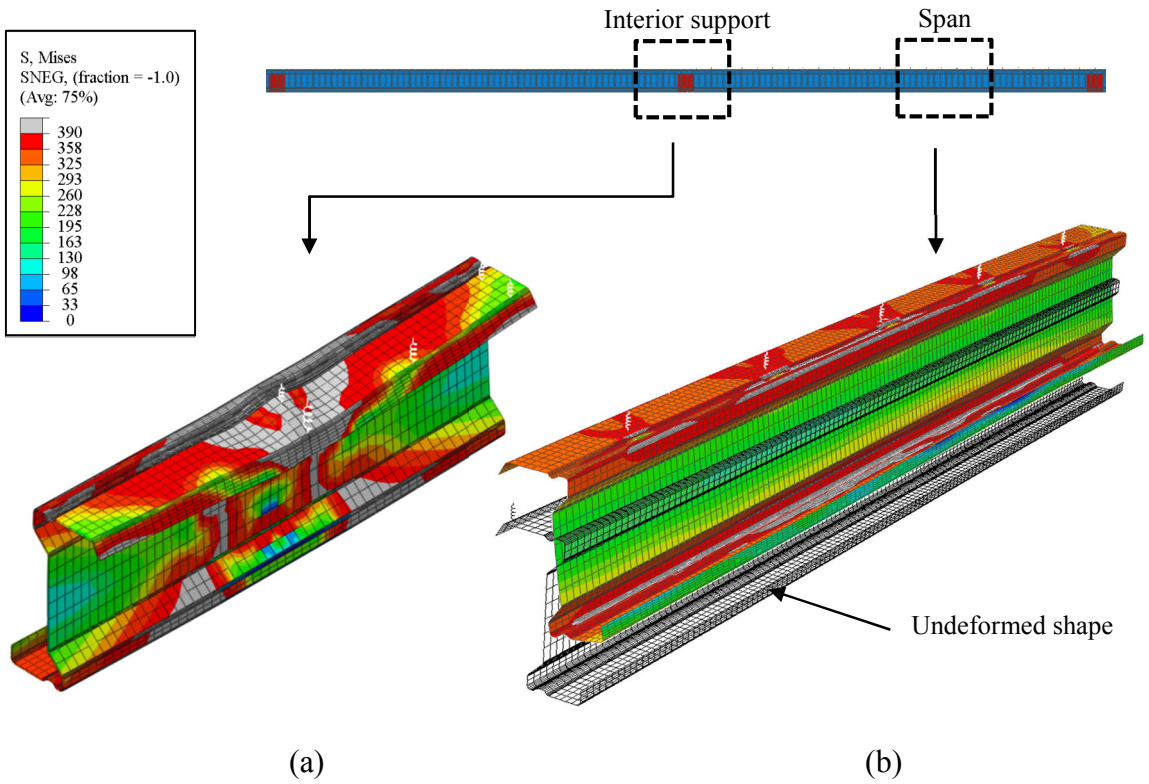


Figure 4.40: *Deformed stress profiles for uplift 2-span 1/175_20 L= 6m FE model at (a) interior support and (b) span regions at ultimate load*

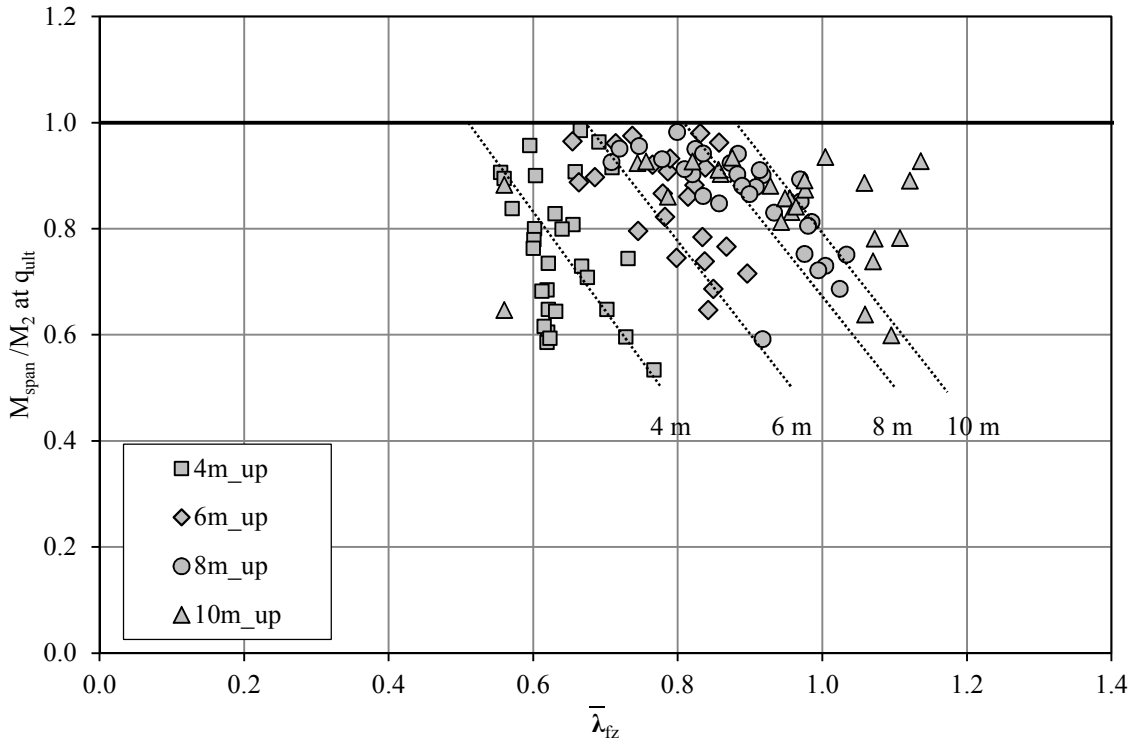


Figure 4.41: *Comaprisons between M_{span}/M_2 at ultimate load versus flexural slenderness*

Figure 4.42 and Table 4.13 show the M_{span}, $M_{support}$ and load-displacement response and tabulated results for 1/200_16 L = 10m. The chosen FE model shows typical moment redistribution behaviour for slender 2-span uplift systems; i.e. $M_{support}$ redistributes the moment into the span region after reaching a peak value, but at the expense of a reducing $M_{support}$. Differences in moment redistribution behaviour when compared against sections with low cross-section slenderness were identified during stage 3. After $M_{support}$ reached its peak value, a sudden fall in load was observed due to a rapidly reducing $M_{support}$ and a slowly increasing M_{span}. Figure 4.43 illustrates the change in the $M_{support}/M_{span}$ ratio at the initial phase of stage 3. At larger displacements ($\delta \approx 120$ mm), the reduction in $M_{support}$ became more gradual and allowed the system to slowly take additional load. The slow rate of additional load carrying capacity after this point was dependent on the stability of the LTB mode; the extent of stage 3 and the amount of additional load from the end of stage 2 q_{stage2} was influenced by its LTB resistance. The lack of lateral restraints at the compressive flange in the span region caused the system to eventually fail by LTB as shown in Figure 4.46(d). Figure 4.44 compares the ratio of q_{stage2}/q_{ult} against all FE uplift 2-span results and shows the ratio generally decreases as the slenderness increases.

For 2-span systems with flexural slenderness $\bar{\lambda}_{fz}$ greater than approximately 1.2, a detrimental impact of LTB in the span meant the system's ability to redistribute moments from the support into the span to provide additional load carrying capacity was not possible. Only three cases, with longer spans, fall under this category: Z/20013 L=10m, Z/20013 L=10m and Z/20013 L=10m. To illustrate the change in moment redistribution behaviour, the uplift 2-span Z/200_13 L= 10m FE model load-displacement response, results and FE stress plots are shown in Figures 4.45-4.46 and Table 4.14 respectively. Similar uplift systems comprising slender cross-sections, a sudden loss in interior support moment was observed after $M_{support}$ reached its peak value. The lack of ability for the span to take an additional load beyond q_{stage2} suggested these three arrangements are governed by LTB in the span with no scope for moment redistribution. The design load should therefore be based on when $M_{support}$ reached its peak value.

Table 4.13: *Moment comparisons between 2-span uplift, M_2 and M_4 models for 1/200_16 L = 10 m*

Stage	Applied load q (kN/m)	M_{span} (kNm)	$M_{support}$ (kNm)	M_2 (kNm)	M_4 (kNm)	M_{span}/M_2	$M_{support}/M_4$
2	1.203	-8.553	14.793	-13.779	15.489	0.481	0.955
3	1.251	-11.321	8.881			0.822	0.573

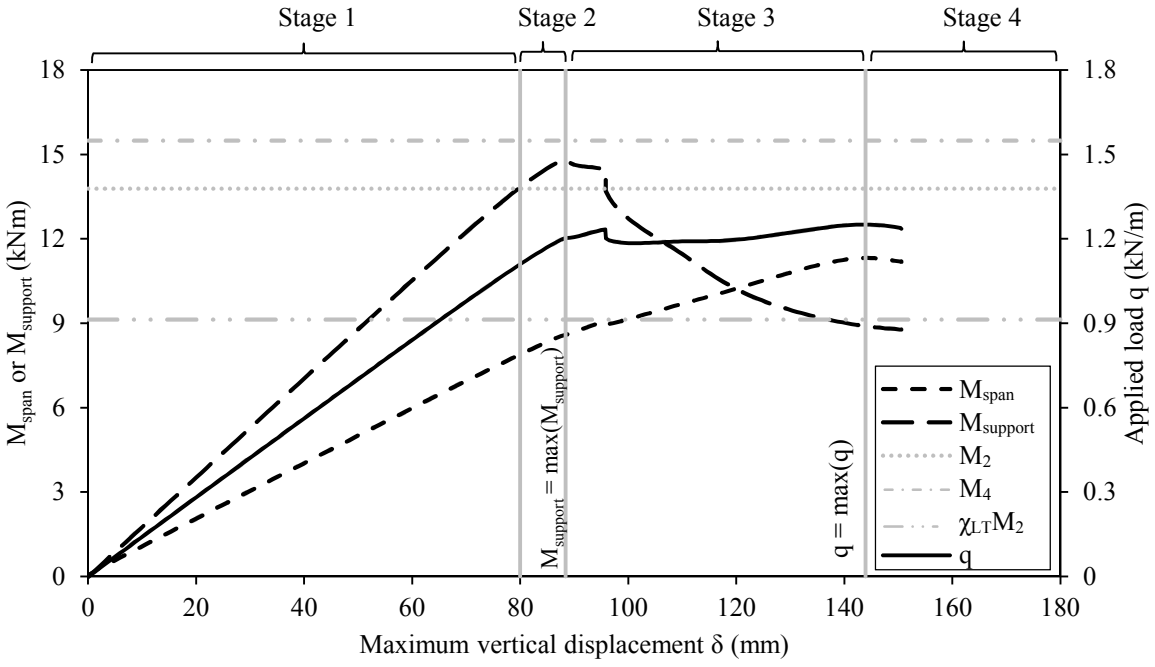


Figure 4.42: *Applied load q, $M_{support}$ and M_{span} versus maximum vertical deflection δ for uplift 2-span 1/200_16 L = 10 m FE model*

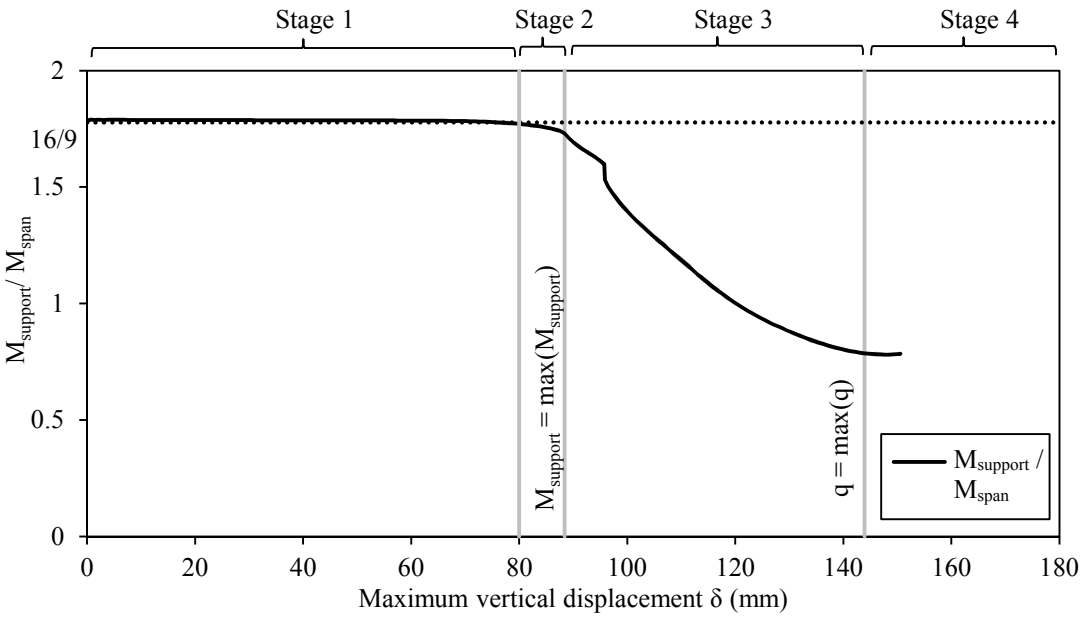


Figure 4.43: $M_{support}/M_{span}$ versus maximum vertical displacement δ for uplift 2-span 1/200_16 L = 10 m

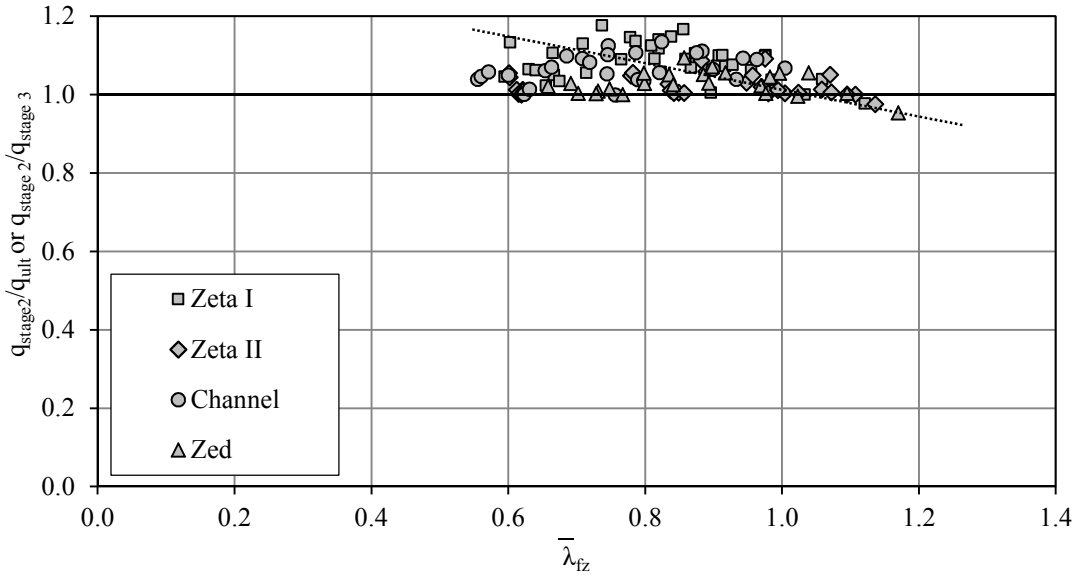


Figure 4.44: *Design load comparisons between design method and FE results against flexural slenderness*

Table 4.14: *Moment comparisons between 2-span uplift, M_2 and M_4 models for Z/200_13 L = 10 m*

Stage	Applied load q (kN/m)	M_{span} (kNm)	$M_{support}$ (kNm)	M_2 (kNm)	M_4 (kNm)	M_{span}/M_2	$M_{support}/M_4$
2 (q_{ult})	0.637	-4.424	8.000	-7.51	7.91	0.589	1.011
4	0.609	-5.255	4.773			0.700	0.603

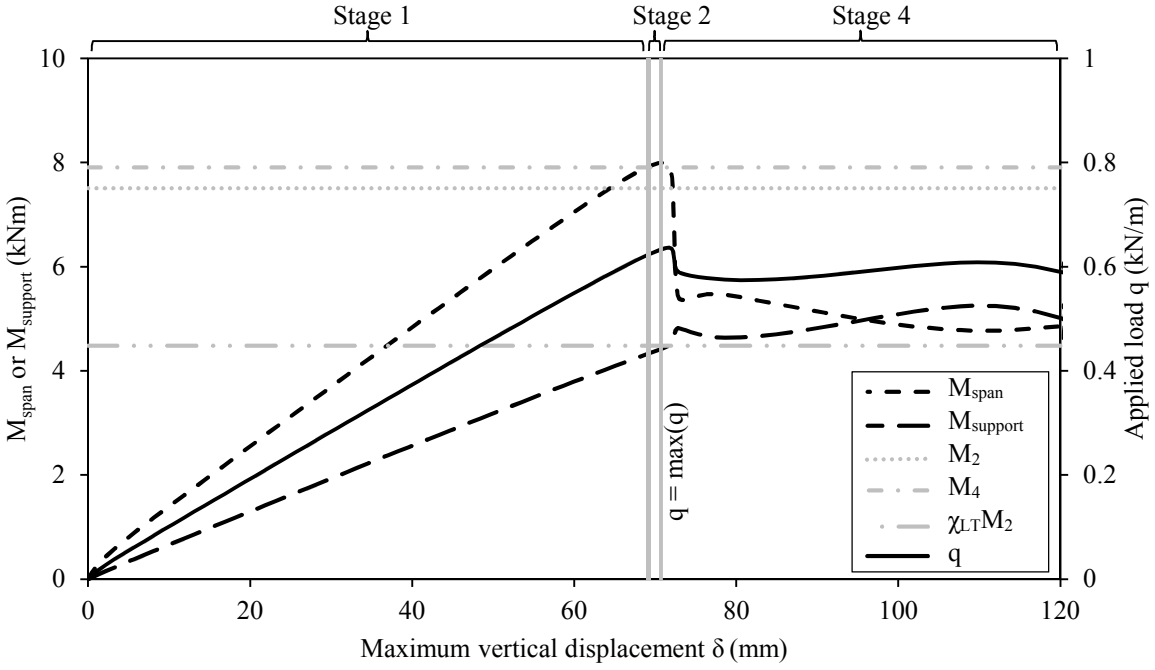


Figure 4.45: *Applied load q, $M_{support}$ and M_{span} versus maximum vertical deflection δ for uplift 2-span Z/200_13 L = 10 m FE model*

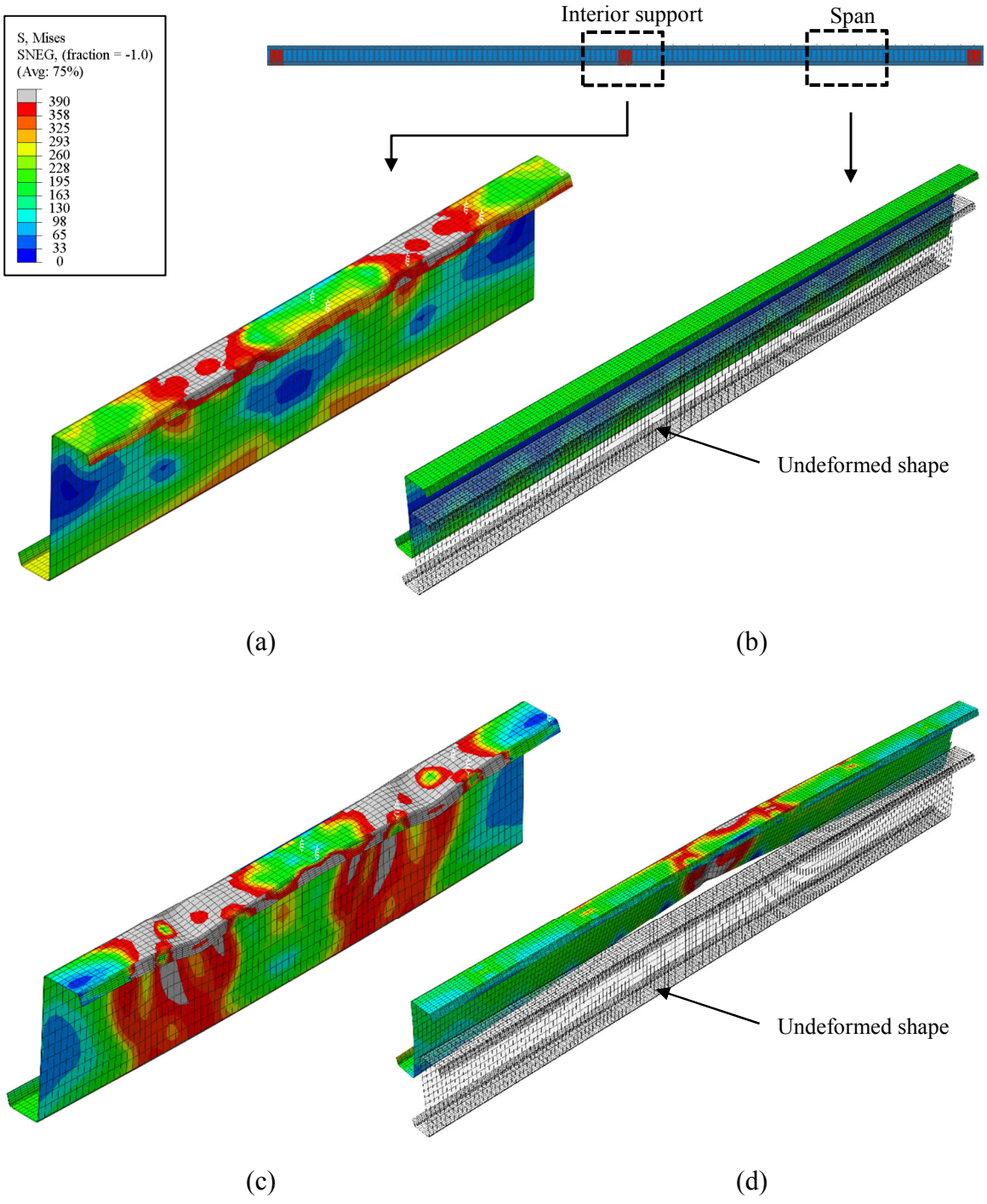


Figure 4.46: Deformed stress profiles for uplift 2-span Z/200_13 L= 10m FE model at (a, b) q_{ult} [$M_{support}$ = max ($M_{support}$)] and (c, d) q = q_{stage3}

4.4.4.2. Design Proposal

Arrangements in which both cross-section (λ_{cs}) and member (λ_{fz}) slenderness was below 1.2 showed signs of moment distribution with varying interior support moment reduction at ultimate load. For such cases, a reduction factor $\alpha_{FE,u}$ is defined as the ratio of $M_{support}$ and M_4 at q_{ult} as shown in Equation 4.14. With full redistribution providing the upper bound, $\alpha_{FE,u}$ is limited to unity.

$$\alpha_{FE,u} = \frac{M_{support}}{M_4} \qquad 0 \le \alpha_{FE,u} \le 1 \qquad (4.14)$$

The interior support moment reduction value $\alpha_{FE,u}$ for all cross-sections from the 2-span uplift FE results are plotted against the positive cross-section slenderness $\bar{\lambda}_{cs,+ve}$ in Figure 4.47. $\bar{\lambda}_{cs,+ve}$ was chosen because the cross-section at the interior support is subjected to a sagging moment where the top flange is in compression. The results were classified into their respective span-to-depth ratios ranging from stocky arrangements of 10 to slender arrangements above 75. Figure 4.47 shows that slender arrangements tends to yield lower $\alpha_{FE,u}$ values than stocky arrangements of the same cross-section. Equation 4.15 is proposed to estimate $\alpha_{FE,u}$. The coefficients that make up Equation 4.15 were determined using the same procedure previously described in Section 4.3.4.2.To avoid additional effects on Equation 4.15 due to discrepancies between χ_{LT} and M_{span}/M_2, Equation 4.15 was optimised using on the actual value of M_{span} from the FE analysis rather than $\chi_{LT}M_2$.

$$\alpha_{design,u} = \left[0.868 - 0.0049\left(\frac{L}{d}\right)\right]\bar{\lambda}_{cs,+ve}^{\left[-0.001\left(\frac{L}{d}\right)-0.5\right]} \qquad \text{but} \le 1 \qquad (4.15)$$

where L is the length of each span, d is the depth of the section and $\bar{\lambda}_{cs,+ve}$ is the positive cross-section slenderness as defined in Equation 4.1.

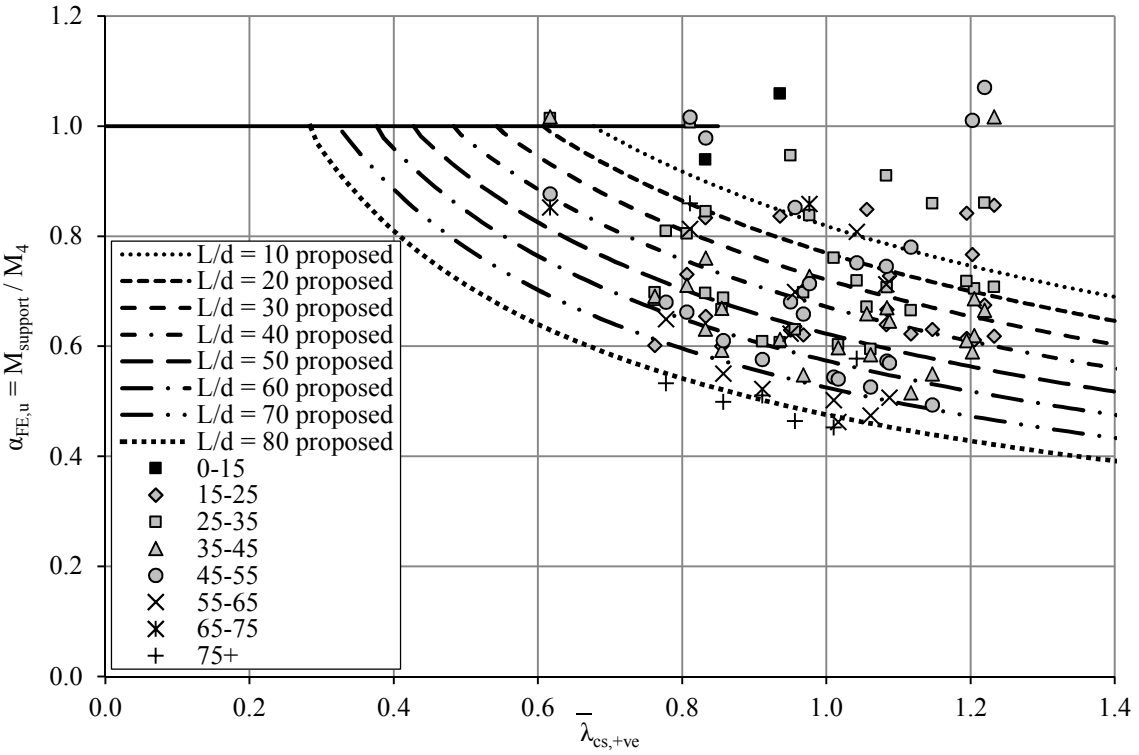


Figure 4.47: Interior support moment reduction versus positive cross-section slenderness from the uplift 2-span parametric study

The ultimate loads from uplift 2-span uplift FE analyses $q_{FE,u}$ were compared against results obtained from three design methods:

Method 1. Elastic design – Considers failure of the system once the interior support reached its moment capacity.

Method 2. Comparative α-framework design method – allows for moment redistribution by using the M_{span} value from the 2-span FE model at q_{ult} with a reduced interior support moment M_3 by calculating $\alpha_{design,u}$ using Equation 4.15.

Method 3. Proposed α-framework design method – allows for moment redistribution by estimating the influence of LTB in the span by calculating χ_{LT} using EC3 and a reduced interior support moment by calculating $\alpha_{design,u}$ using Equation 4.15.

The design loads for uplift loading for design methods 1, 2 and 3 are defined as q_{1u} and q_{2u} and q_{3u} respectively. In order to compute the design load for each design

method, the modified input values for M_{span} and $M_{support}$ for Equation 4.8 are outlined in Table 4.13. For design method 1, an elastic ratio of 0.5625 was used to calculate the equivalent span moment M_4. It was assumed for design method 1 that $M_{support}$ always reached its moment capacity M_4 before the span failed by LTB and that the span moment is in its elastic range when $M_{support}$ reaches its peak value. For the comparative design method 2, the span moment at ultimate load from the 2-span uplift FE model $M_{FE,span}$ was used to replace M_{span}, whilst $M_{support}$ was replaced by $\alpha_{design,u}M_4$ by using Equation 4.15 and its single span reference value M_4. This ensures that design method 2 is solely dependent on the prediction of the reduced interior support moment $\alpha_{design,u}M_4$. For design method 3, the same $\alpha_{design,u}M_4$ is used for $M_{support}$, whilst M_{span} was replaced with $\chi_{LT}M_2$, where χ_{LT} was calculated using EC3 based on the assumptions discussed in Section 4.4.2 and 4.2.3 and M_2, its negative pure bending moment capacity (test type 2).

Table 4.15: *M_{span} and $M_{support}$ inputs values for Equation 4.8 for design methods 1, 2 and 3 for uplift 2-span parametric study*

	Design method	M_{span}	$M_{support}$	Equation (4.8)
1	Elastic design	$0.5625M_4$	M_4	$0.5625M_4 = \frac{\left(q_{1u}L^2 + 2M_4\right)^2}{8q_{1u}L^2}$
2	Comparative α-framework method	$M_{FE,span}$	$\alpha_{design,u}M_4$	$M_{FE,span} = \frac{\left(q_{2u}L^2 + 2\alpha_{design,u}M_4\right)^2}{8q_{2u}L^2}$
3	Proposed α-framework method	$\chi_{LT}M_2$	$\alpha_{design,u}M_4$	$\chi_{LT}M_2 = \frac{\left(q_{3u}L^2 + 2\alpha_{design,u}M_4\right)^2}{8q_{3u}L^2}$

Comparison between ultimate load obtained from design methods 1, 2 and 3 and uplift 2-span FE results for 4, 6, 8 and 10 m spans are shown in Table 4.16-4.19. The raw results from the continuous uplift 2-span study are tabulated in detail in Appendix D. Table 4.20 summarises the ultimate load comparisons for design methods 1, 2 and 3 for each cross-section shape including the mean and COV values. Designing the system based on elastic principles using design method 1 was found to be consistently over conservative with an average of $q_{1,u}/q_{FE,u}$ of 0.921, with some cases as low as 0.743.

The highly conservative design procedure may initially seem substantial, but when compared against the elastic design method for gravity loading, results for uplift loading were closer to the FE results (average $q_{1,g}/q_{FE,g} = 0.823$ as opposed to $q_{1,u} / q_{FE,u}$ of 0.921). The difference between the elastic design methods for uplift and gravity loading against their corresponding FE results was due their moment redistribution behaviour (which leads to the system's ability to attain a high load capacity). Gravity loaded cases generally achieved a prolonged moment redistribution stage than uplift cases since all deflections were in-plane, whereas for uplift loading, the effect of LTB limited the spans ability reach its in-plane bending capacity. In contrast, no FE uplift results reached full moment redistribution; (where both M_{span} and $M_{support}$ reached their moment capacities M_2 and M_4). This suggested a full plastic design would always be unconservative, even for arrangements with sections at short spans.

Figure 4.48 shows a comparison between failure loads obtained using design methods 2 and 3 and the FE results. The discrepancy between design method 2 and FE results was purely based on the accuracy of estimating $\alpha_{FE,u}$ using Equation 4.15 because the actual M_{span} value at q_{ult} from the 2-span FE models were used to determine $q_{2,u}$. Figure 4.49 compares the relationship for $\alpha_{design,u}/\alpha_{FE,u}$ against flexural slenderness $\bar{\lambda}_{fz}$. In general, $\alpha_{design,u}$ estimated $\alpha_{,FE,u}$ with moderate accuracy with a mean $\alpha_{design,u}/\alpha_{FE,u} = 0.978$, but in some cases under-predicts $\alpha_{FE,u}$ by much as 40%. Large discrepancies between $\alpha_{design,u}$ and $\alpha_{FE,u}$ were caused by the M_4 inability to accurately represent the peak value of $M_{support}$. Nevertheless, design method 2 provided the closest agreement to the FE results with an average mean of 0.970 and low scatter (COV = 0.05) with largest unconservative predictions of 12% and lowest conservative predictions in ultimate design load of 5%.

For design method 3, if the calculated χ_{LT} values can predict the effect of the LTB by matching M_{span}/M_2 for all arrangements, the design load predictions between design methods 2 and 3 would be coincident. Unfortunately, this was not the case. Figure 4.50 compared M_{span}/M_2 for 4, 6, 8 and 10 m spans against the calculated χ_{LT} curve from EN 1993-1-1 (2005). It is clear from the Figure 4.50 that χ_{LT} was found to be unconservative for 4 m spans, while 6, 8 and 10 m span comparisons followed the predicted χ_{LT} trend, but with a consistent overprediction of approximately 15%. The inaccuracy in calculating χ_{LT}

to estimate the reduction in moment capacity for LTB resulted in a lower $q_{u,3}/q_{FE,u}$ mean of 0.946 than results obtained from design method 2.

Predicting the reduced moment in the span using χ_{LT} only yielded a 2.7% reduction in average design loads between methods 2 and 3, but unfortunately, an increase in scatter (COV of 0.109) was also observed. The difference between design methods 2 and 3 could be further investigated by reviewing the discretised results in Table 4.21. By only considering 4 m sections, the large unconservative estimations of χ_{LT} for design method 3 resulted in an increase in average $q_{3,u}/q_{FE,u}$ of 1.062. Meanwhile, the conservative estimations of χ_{LT} for the 6, 8 and 10 m 2-span systems (see Figure 4.50) resulted in average design loads reductions of 2.4%, 8.9% and 10.2% to those obtained from the equivalent design method 2 cases. If design load predictions for design method 3 for 6, 8 and 10m were only considered, the overall average for $q_{3,u}/q_{FE,u}$ would reduce by 4% to 0.906. In general, the proposed design method 3 gave improvements in design loads over the elastic design method 1 of 8.3%.

For multi-span purlin systems subjected to uplift loading, shortfalls in design predictions using EC3 compared to the results from physical tests have already been identified by many authors including Leach and Robinson (1993). They found on average the design loads were 20-25% more conservative than their physical test results. A potential average design load prediction improvement of 2.7% for design method 3 can be gained if χ_{LT} can accurately represent the moment reduction in the span (M_{span}/M_2). Potential areas to improve the Eurocode 3 Part 1-3 (2006) method for calculating the LTB design load resistance for cold-formed sections with sheeting could include:

- Less conservative predictions for the buckling length of the free flange l_{fz} by considering alternative coefficients η_1, η_2, η_3 and η_4 in Table 10.2(b) in Eurocode 3 Part 1-3 (2006).
- Adopt buckling curve ‘a’ ($\alpha_{LT} = 0.21$) rather than curve ‘b’ as recommended in Clause 10.1.4.2) in Eurocode 3 Part 1-3 (2006).

Table 4.16: Ultimate load comparison between uplift 2-span FE results and design methods 1, 2 and 3 for span length L = 4 m

Section Reference	$q_{FE,u}$ (kN/m)	$q_{1,u}$ (kN/m)	$q_{2,u}$ (kN/m)	$q_{3,u}$ (kN/m)	$q_{1,u} / q_{FE,u}$	$q_{2,u} / q_{FE,u}$	$q_{3,u} / q_{FE,u}$
1/150_30	14.545	11.080	14.195	13.800	0.762	0.976	0.949
1/125_20	6.748	5.026	6.265	5.808	0.745	0.928	0.861
1/200_25	15.348	12.945	14.445	15.461	0.843	0.941	1.007
1/175_20	10.113	8.522	9.304	9.883	0.843	0.920	0.977
1/150_19	7.879	6.502	7.467	7.557	0.825	0.948	0.959
1/125_13	3.689	3.026	3.448	3.308	0.820	0.935	0.897
1/175_16	7.123	6.488	6.759	7.345	0.911	0.949	1.031
1/200_16	8.030	7.615	7.580	8.688	0.948	0.944	1.082
1/200_13	5.886	5.770	5.518	6.446	0.980	0.937	1.095
2/225_30	20.517	18.931	20.606	22.554	0.923	1.004	1.099
2/285_30	26.785	26.153	26.104	29.991	0.976	0.975	1.120
2/225_25	16.047	14.845	15.791	17.637	0.925	0.984	1.099
2/285_25	20.417	18.624	18.644	22.594	0.912	0.913	1.107
2/285_20	13.950	12.011	11.906	15.857	0.861	0.853	1.137
2/225_14	6.816	6.605	6.196	7.604	0.969	0.909	1.116
2/245_15	8.076	8.263	7.160	9.377	1.023	0.887	1.161
2/265_15	8.536	9.235	7.590	10.238	1.082	0.889	1.199
Z/125_20	5.064	4.910	4.933	4.864	0.904	0.974	0.960
Z/200_25	11.342	4.266	10.911	11.657	0.919	0.962	1.028
Z/125_14	3.304	8.550	3.188	2.522	1.030	0.965	0.763
Z/155_15	4.023	3.183	4.163	4.347	0.921	1.035	1.081
Z/170_14	3.779	4.080	3.714	4.266	0.991	0.983	1.129
Z/200_13	3.756	5.152	3.864	4.464	1.061	1.029	1.189
C/127_20	5.430	5.591	5.503	5.632	1.105	1.013	1.037
C/127_18	4.639	4.265	4.701	4.849	0.842	1.013	1.045
C/200_20	8.299	10.719	8.340	9.534	0.945	1.005	1.149
C/127_15	3.455	2.707	3.442	3.711	0.819	0.996	1.074
C/155_15	4.115	4.057	4.025	4.581	1.008	0.978	1.113
C/185_15	4.855	3.920	5.143	5.726	1.037	1.059	1.179
C/200_15	5.057	4.130	4.921	6.214	1.100	0.973	1.229

A - Refer to Figures 4.3 and 4.4 for cross-section details

Table 4.17: Ultimate load comparison between uplift 2-span FE results and design methods 1, 2 and 3 for span length L = 6 m

Section Reference	$q_{FE,u}$ (kN/m)	$q_{1,u}$ (kN/m)	$q_{2,u}$ (kN/m)	$q_{3,u}$ (kN/m)	$q_{1,u} / q_{FE,u}$	$q_{2,u} / q_{FE,u}$	$q_{3,u} / q_{FE,u}$
1/150_30	6.425	4.775	6.107	5.662	0.743	0.951	0.881
1/125_20	2.837	2.154	2.545	2.371	0.759	0.897	0.836
1/200_25	6.877	5.728	6.683	6.261	0.833	0.972	0.910
1/175_20	4.680	3.703	4.293	4.003	0.791	0.917	0.855
1/150_19	3.523	2.822	3.414	3.084	0.801	0.969	0.876
1/125_13	1.573	1.328	1.483	1.336	0.844	0.942	0.849
1/175_16	3.178	2.810	3.075	2.939	0.884	0.968	0.925
1/200_16	3.780	3.360	3.410	3.451	0.889	0.902	0.913
1/200_13	2.591	2.511	2.405	2.515	0.969	0.928	0.970
2/225_30	9.549	8.065	9.364	9.079	0.845	0.981	0.951
2/285_30	11.672	11.358	11.830	11.960	0.973	1.013	1.025
2/225_25	7.066	6.709	7.185	7.210	0.949	1.017	1.020
2/285_25	9.126	9.294	8.924	9.377	1.018	0.978	1.028
2/285_20	6.314	6.908	6.181	6.785	1.094	0.979	1.075
2/225_14	3.550	2.891	3.499	3.010	0.814	0.986	0.848
2/245_15	3.502	3.667	3.287	3.720	1.047	0.939	1.062
2/265_15	3.775	4.089	3.537	4.039	1.083	0.937	1.070
Z/125_20	2.171	2.111	2.184	2.015	0.875	1.006	0.928
Z/200_25	5.206	1.841	5.166	4.697	0.885	0.992	0.902
Z/125_14	1.374	3.775	1.265	1.184	0.962	0.920	0.862
Z/155_15	1.825	1.414	1.859	1.748	0.897	1.019	0.958
Z/170_14	1.758	1.795	1.755	1.694	0.935	0.998	0.964
Z/200_13	1.750	2.241	1.788	1.725	1.015	1.021	0.986
C/127_20	2.413	2.476	2.453	2.319	1.042	1.017	0.961
C/127_18	2.081	1.893	2.123	1.996	0.872	1.020	0.959
C/200_20	3.924	4.667	4.083	3.871	0.896	1.041	0.987
C/127_15	1.576	1.160	1.605	1.533	0.844	1.018	0.972
C/155_15	1.920	1.740	1.951	1.870	0.953	1.016	0.974
C/185_15	2.208	1.686	2.257	2.300	0.959	1.022	1.042
C/200_15	2.376	1.782	2.361	2.493	1.018	0.994	1.049

A - Refer to Figures 4.3 and 4.4 for cross-section details

Table 4.18: Ultimate load comparison between uplift 2-span FE results and design methods 1, 2 and 3 for span length L = 8 m

Section Reference	$q_{FE,u}$ (kN/m)	$q_{1,u}$ (kN/m)	$q_{2,u}$ (kN/m)	$q_{3,u}$ (kN/m)	$q_{1,u} / q_{FE,u}$	$q_{2,u} / q_{FE,u}$	$q_{3,u} / q_{FE,u}$
1/150_30	3.373	2.653	3.256	2.997	0.787	0.965	0.888
1/125_20	1.479	1.224	1.369	1.257	0.827	0.925	0.850
1/200_25	3.801	3.218	3.741	3.285	0.847	0.984	0.864
1/175_20	2.426	2.037	2.380	2.092	0.839	0.981	0.862
1/150_19	1.857	1.549	1.771	1.621	0.834	0.953	0.873
1/125_13	0.874	0.730	0.780	0.694	0.835	0.892	0.794
1/175_16	1.863	1.546	1.757	1.523	0.830	0.943	0.817
1/200_16	1.996	1.852	1.951	1.767	0.928	0.978	0.885
1/200_13	1.500	1.460	1.385	1.288	0.973	0.924	0.859
2/225_30	5.189	4.630	5.356	4.798	0.892	1.032	0.925
2/285_30	6.674	6.260	6.886	6.136	0.938	1.032	0.919
2/225_25	4.035	3.607	4.110	3.724	0.894	1.019	0.923
2/285_25	5.115	5.006	5.170	4.753	0.979	1.011	0.929
2/285_20	3.728	3.670	3.502	3.391	0.985	0.939	0.910
2/225_14	1.679	1.623	1.592	1.534	0.966	0.948	0.913
2/245_15	2.001	2.018	1.912	1.876	1.008	0.956	0.938
2/265_15	2.226	2.251	2.025	2.020	1.011	0.910	0.908
Z/125_20	1.198	1.165	1.177	1.060	0.909	0.983	0.885
Z/200_25	2.738	1.018	2.765	2.439	0.900	1.010	0.891
Z/125_14	0.817	2.080	0.755	0.679	0.925	0.924	0.832
Z/155_15	1.030	0.763	1.044	0.918	0.863	1.014	0.891
Z/170_14	1.004	0.984	1.007	0.884	0.894	1.002	0.881
Z/200_13	0.995	1.263	1.002	0.882	0.983	1.007	0.886
C/127_20	1.282	1.344	1.292	1.229	0.983	1.008	0.958
C/127_18	1.130	1.037	1.140	1.056	0.866	1.009	0.934
C/200_20	2.248	2.527	2.337	2.022	0.923	1.039	0.899
C/127_15	0.885	0.654	0.885	0.805	0.801	1.000	0.910
C/155_15	1.101	0.979	1.111	0.979	0.951	1.010	0.890
C/185_15	1.285	0.954	1.321	1.202	0.950	1.029	0.936
C/200_15	1.368	1.007	1.393	1.281	1.012	1.018	0.936

A - Refer to Figures 4.3 and 4.4 for cross-section details

Table 4.19: Ultimate load comparison between uplift 2-span FE results and design methods 1, 2 and 3 for span length L = 10 m

Section Reference	$q_{FE,u}$ (kN/m)	$q_{1,u}$ (kN/m)	$q_{2,u}$ (kN/m)	$q_{3,u}$ (kN/m)	$q_{1,u} / q_{FE,u}$	$q_{2,u} / q_{FE,u}$	$q_{3,u} / q_{FE,u}$
1/150_30	2.125	1.669	2.009	1.813	0.785	0.945	0.853
1/125_20	0.955	0.764	0.842	0.754	0.800	0.881	0.790
1/200_25	2.553	2.050	2.293	1.984	0.803	0.898	0.777
1/175_20	1.472	1.328	1.444	1.272	0.902	0.980	0.864
1/150_19	1.254	1.017	1.109	0.989	0.811	0.885	0.789
1/125_13	0.504	0.469	0.474	0.416	0.930	0.940	0.826
1/175_16	1.155	0.973	1.079	0.912	0.843	0.934	0.790
1/200_16	1.251	1.239	1.248	1.068	0.991	0.998	0.854
1/200_13	0.944	0.878	0.919	0.908	0.930	0.974	0.962
2/225_30	3.265	2.892	3.311	2.886	0.886	1.014	0.884
2/285_30	4.181	4.014	4.370	3.673	0.960	1.045	0.879
2/225_25	2.521	2.332	2.604	2.259	0.925	1.033	0.896
2/285_25	3.208	3.140	3.315	2.816	0.979	1.033	0.878
2/285_20	2.411	2.422	2.336	2.024	1.004	0.969	0.840
2/225_14	1.050	1.009	1.023	0.899	0.961	0.974	0.857
2/245_15	1.239	1.238	1.210	1.093	0.999	0.977	0.882
2/265_15	1.374	1.379	1.364	1.388	1.004	0.993	1.010
Z/125_20	0.729	0.742	0.721	0.639	0.921	0.990	0.877
Z/200_25	1.684	0.639	1.700	1.473	0.971	1.009	0.875
Z/125_14	0.463	1.303	0.449	0.434	0.918	0.969	0.937
Z/155_15	0.641	0.495	0.652	0.552	0.913	1.017	0.861
Z/170_14	0.638	0.635	0.628	0.528	0.936	0.985	0.828
Z/200_13	0.637	0.790	0.631	0.636	0.878	0.991	0.999
C/127_20	0.806	0.866	0.800	0.746	0.982	0.993	0.925
C/127_18	0.658	0.656	0.647	0.639	0.900	0.983	0.971
C/200_20	1.419	1.607	1.391	1.216	0.954	0.980	0.857
C/127_15	0.542	0.411	0.536	0.490	0.888	0.989	0.904
C/155_15	0.678	0.622	0.682	0.594	0.969	1.005	0.877
C/185_15	0.900	0.599	0.785	0.719	0.939	0.873	0.799
C/200_15	0.882	0.633	0.900	0.770	0.994	1.020	0.872

A - Refer to Figures 4.3 and 4.4 for cross-section details

Table 4.20: Summary of proposed α-framework for uplift loading

Section type	No. of 2-span FE models	$q_{1,u} / q_{FE,u}$		$q_{2,u} / q_{FE,u}$		$q_{3,u} / q_{FE,u}$	
		MEAN	COV	MEAN	COV	MEAN	COV
Zeta I	36	0.852	0.081	0.942	0.032	0.891	0.089
Zeta II	32	0.965	0.070	0.973	0.051	0.988	0.107
Zed	24	0.935	0.079	0.992	0.029	0.933	0.105
C	28	0.947	0.065	1.004	0.032	0.980	0.104
All	120	0.921	0.088	0.975	0.045	0.946	0.109

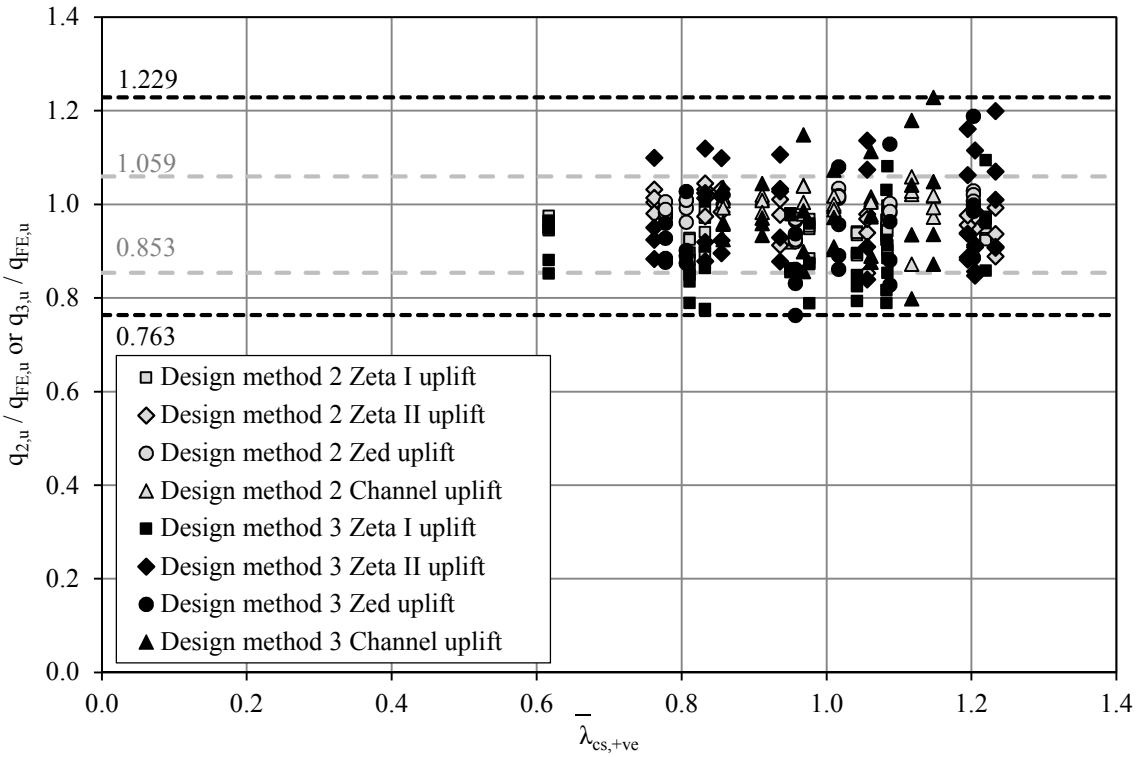


Figure 4.48: Ultimate load comparison between FE and design methods 2 and 3 for 2-span uplift configuration against positive cross-section slenderness

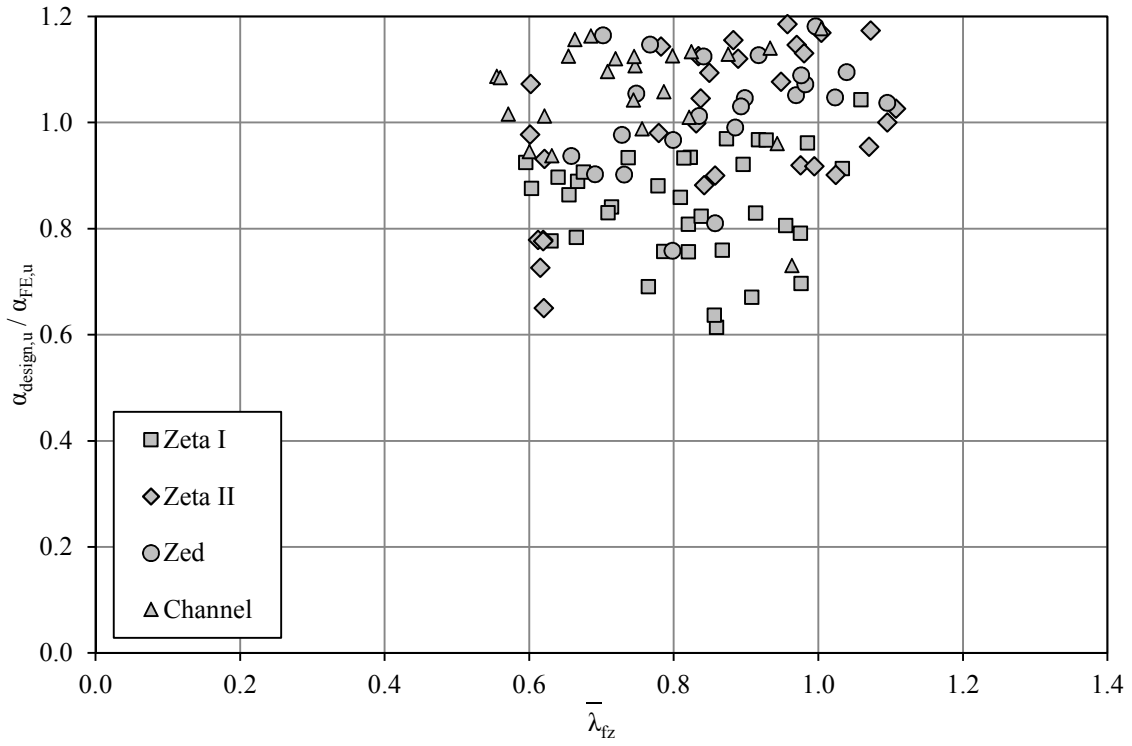


Figure 4.49: α-reduction comparison between design method and FE results

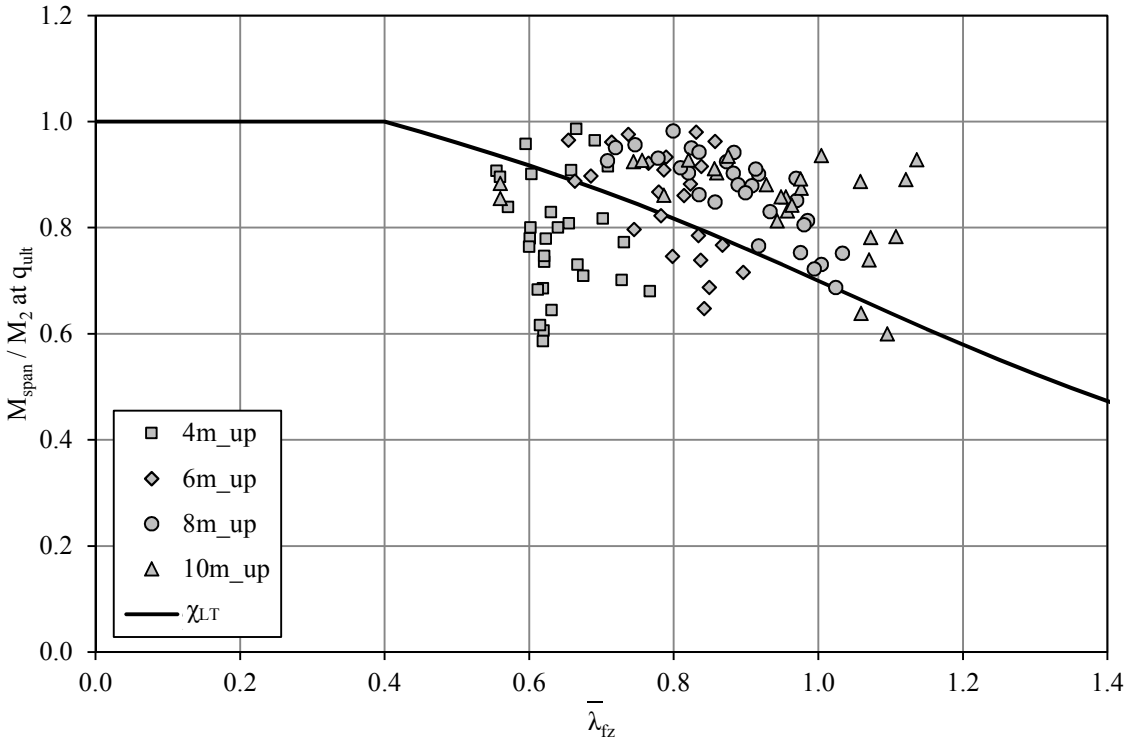


Figure 4.50: Comparison between M_{span}/M_2 for different span lengths against χ_{LT}

Table 4.21: Ultimate load comparison between design methods 1, 2 and 3 for different span lengths

Span L (m)	$q_{1,u} / q_{FE,u}$		$q_{2,u} / q_{FE,u}$		$q_{3,u} / q_{FE,u}$	
	MEAN	COV	MEAN	COV	MEAN	COV
4.0	0.934	0.104	0.963	0.049	1.062	0.099
6.0	0.916	0.103	0.979	0.041	0.955	0.075
8.0	0.911	0.073	0.982	0.042	0.893	0.042
10.0	0.923	0.069	0.976	0.046	0.874	0.068
All	0.921	0.088	0.975	0.045	0.946	0.109

4.4.5. Conclusions

The moment redistribution behaviour for continuous 2-span purlins subjected to gravity and uplift loading has been investigated herein by means of parametric studies using the previously validated FE models discussed in Chapter 3. For the gravity loading, a study consisting of 245 FE models for Zeta I, Zeta II, Zed and channel cross-sections has been conducted for 4, 6 and 8 m equal spans to evaluate the loss of moment at the central support in two-span continuous beams upon reaching the collapse load of the system from its peak moment capacity. The results from the study shows 2-span systems made up of slender sections at large spans could lose up to 50% of their maximum support moment at ultimate load due to a sharp loss of moment at the interior support, whereas, stocky sections can achieve full moment redistribution, since no significant reduction in the central support capacity is observed at system failure. A design formula is proposed to estimate the amount of moment redistribution for a 2-span purlin system by calculating a reduction value, $\alpha_{design,g}$ for the interior support moment at failure. The revised interior moment can be applied directly with the plastic mechanism approach of EC3. For the range of sections considered, the design approach of assuming full redistribution with the full interior support moment (i.e. $\alpha_{design,g}$ =1) was found to be unconservative by 12% on average and up to 60% for the more slender sections. Alternatively, the design approach based on elastic principles was found to be highly conservative by 17.7% on average. However, adopting the proposed design approach gives an average ratio of design load to FE results of $q_{3,g}/q_{FE,g}$ equal to unity and with a greatly reduced scatter (COV =0.049 compared to 0.084 for full moment redistribution).

For continuous 2-span uplift systems, a parametric study consisting of 270 FE models has been conducted to evaluate the loss of moment at the central support from its peak moment capacity and the limiting effect of LTB in the span. A design formula has been proposed to estimate the amount of moment redistribution for continuous uplift systems by calculating reduction values, $\alpha_{design,u}$ and χ_{LT} for the interior support and span moments at failure. The parametric study showed that the method of estimating the reduction factor for lateral torsional buckling χ_{LT} in Eurocode 3 Part 1.3 is rather conservative. Comparative design models have shown that a 2.9% potential increase in average design loads is possible providing χ_{LT} can accurately predict the LTB resistance moment in the span at failure. For the range of sections considered, the elastic design approach was found to be overly conservative by an average 12%. However, adopting the modified design approach gives 2.5% improved predictions (mean = 0.937) compared to the elastic design with modest scatter (COV = 0.11).

CHAPTER 5

NUMERICAL MODELLING – SLEEVED SECTIONS

5.1. INTRODUCTION

Cold-formed sleeved purlin systems are an alternative choice to purely continuous members since they generally provide additional load carrying capacity. Full scale testing has been the most common way of investigating the structural behaviour of such systems. In the present study, numerical modelling is undertaken. ABAQUS 6.10 (2010) was the chosen FE software package since it can capture the buckling behaviour of cold-formed steel bare purlins as discussed in Chapters 3 and 4 and has the potential to capture complex contact interactions and subsequent failure modes for the sleeved systems. In this chapter, additional finite element modelling parameters to those of the bare FE models discussed in Chapter 3 are explained in detail, so as to expand the study single and 2-span sleeved arrangements. For the range of cold-formed steel section types considered, several sleeved system models were validated against physical test results from the literature.

5.2. DEFINITION OF DIFFERENT TYPE OF SLEEVED ARRANGEMENTS

Typical cold-formed steel sleeved systems comprise bolted connections that tie an additional sleeve section to two adjoining members through pre-cut bolt holes in the web. The bolts holes are normally 2 mm larger than the bolt diameters. The sleeve is generally located over the interior support to utilise the extra cross-sectional capacity gain at the region of largest bending moment. For the Zeta I, Zeta II and Zed sections considered in this study, intermediate stiffener corner radii and flange lengths were made different in the top and bottom flanges in order that the bare section can be used as a sleeve section by it rotating by 180º and fitting inside itself. Figure 5.1 shows 3 different sleeve sections with defined vertical bolt locations. For this study, 5 different bolt arrangements were considered and are illustrated in Figure 5.2:

- Bolt arrangement 2 – Single row of 2 bolts per purlin
- Bolt arrangement 3A – Single row of 3 bolts per purlin
- Bolt arrangement 3B – Two rows of bolts: 1 top and 2 bottom
- Bolt arrangement 4 – Two rows of 2 bolts per purlin
- Bolt arrangement 6 – Two rows of 3 bolts per purlin

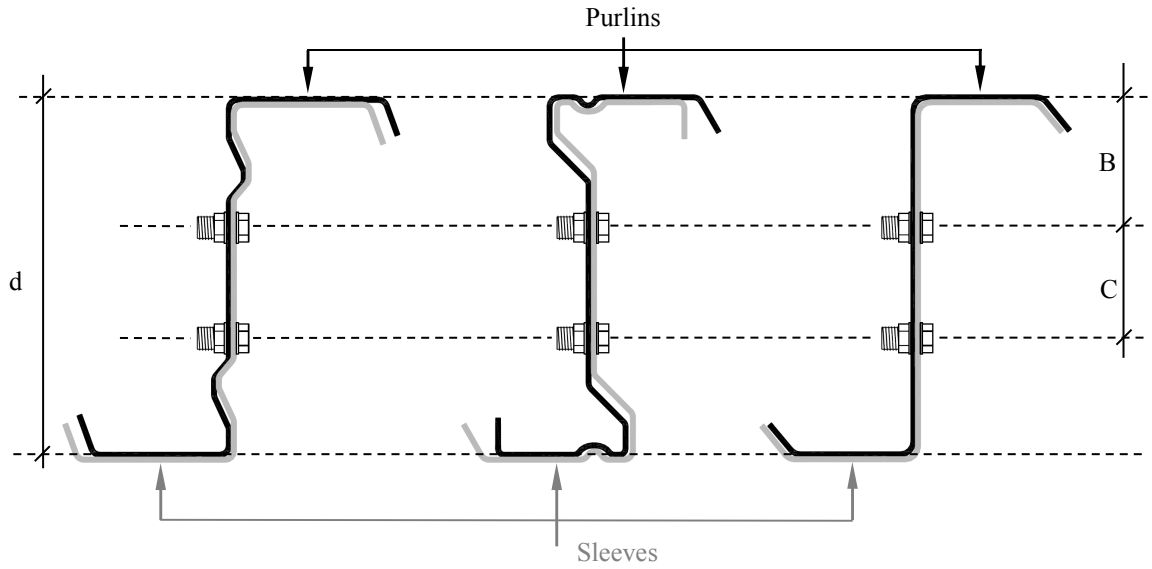


Figure 5.1: *Bolt arrangements in sleeved sections*

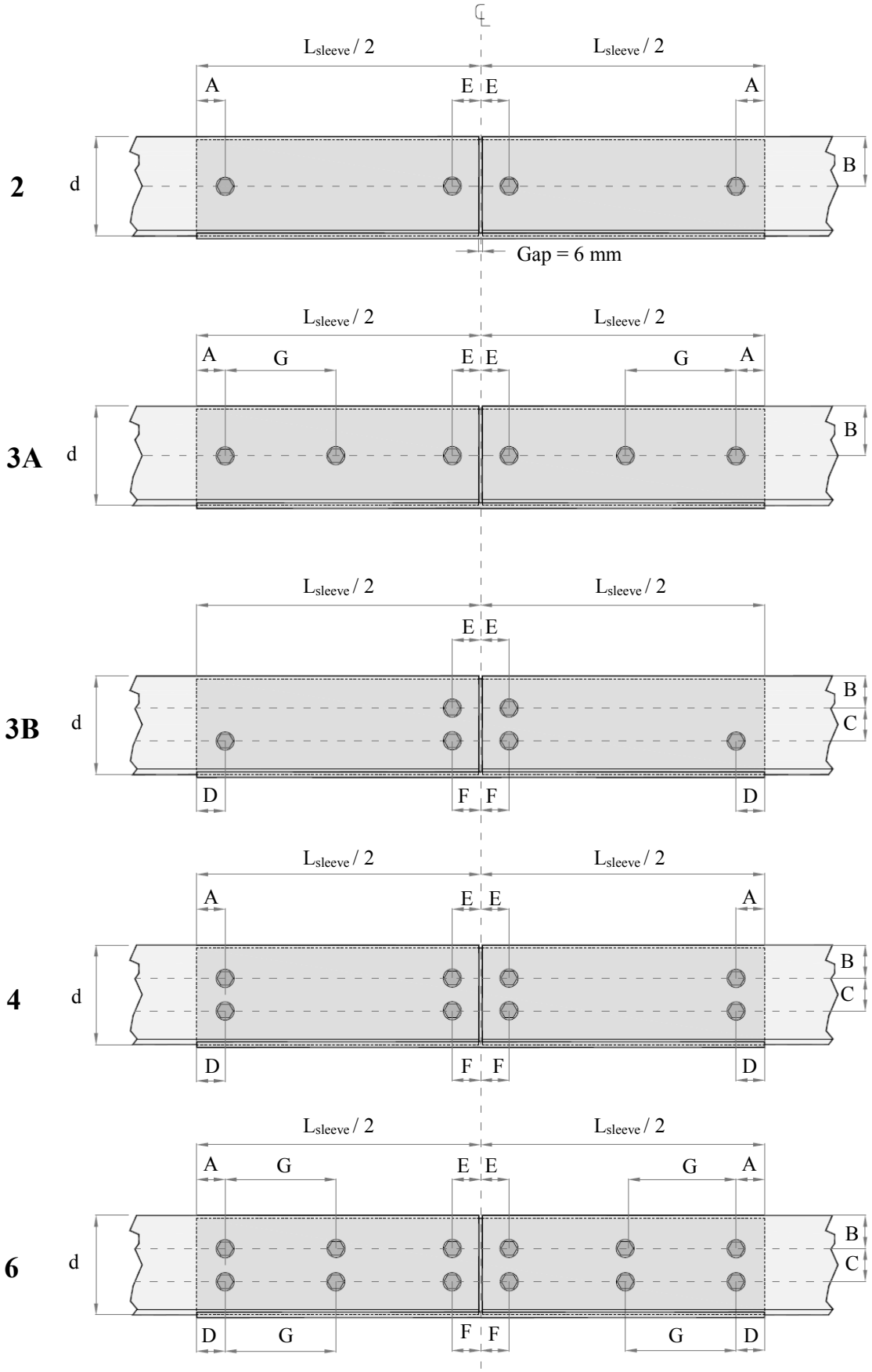


Figure 5.2: *Bolt type definition in sleeved sections*

5.3. ADDITIONAL FINITE ELEMENT MODELLING ASSUMPTIONS FOR SLEEVED SYSTEMS

The gradual yielding material model of Gardner and Ashraf (2006) and corner enhancements for the cold-formed steel sleeve section was kept the same as for the bare section. The sleeve section was also modelled using S4R elements and has the same number of nodes and mesh density as the bare section. To ensure that the sleeve and beam outer surfaces are initially touching (no separation or overclosure), the sleeve centreline co-ordinates were offset by ($t_{sleeve}/2 + t_{bare}/2$), where t_{sleeve} and t_{bare} are the thicknesses of the sleeve and bare sections respectively. The bare section geometrical imperfections (summation of local and distortional buckling modes from CUFSM with a longitudinal harmonic distribution with periods equalling their respective half-wavelengths) were transferred so that the imperfect centrelines of the sleeve and beam sections were parallel.

5.3.1. Modification to mesh

The mesh density and element aspect ratios for the bare systems were shown to be adequate by successful validation as discussed in Section 3.2.3. However, for sleeved systems the sleeve and beam section web nodes were moved to locations that match the bolt detailing as shown in Figures 5.1 and 5.2. The two-spring model used to replicate the restraining effect offered by typical trapezoidal sheeting was successfully validated against the load-displacement responses from Yu and Schafer (2003) in Section 3.3.3.2; fastened tap-in screws within the overlapping sleeve region would penetrate both sections and therefore provide additional restraint to the sleeve section. The sleeve flange node locations were modified to ensure vertical alignment between the master spring and the sleeve flange nodes so that appropriate constraints could be applied to replicate the transfer of restraint from the springs to the sleeve section. To prevent the adjacent element aspect ratios from increasing beyond 1 in 5 and so as to provide a uniform mesh surface for contact modelling, the adjacent elements in the web and flange(s) were made as square as possible by dividing the spacing of the adjacent nodes equally as shown in Figure 5.3.

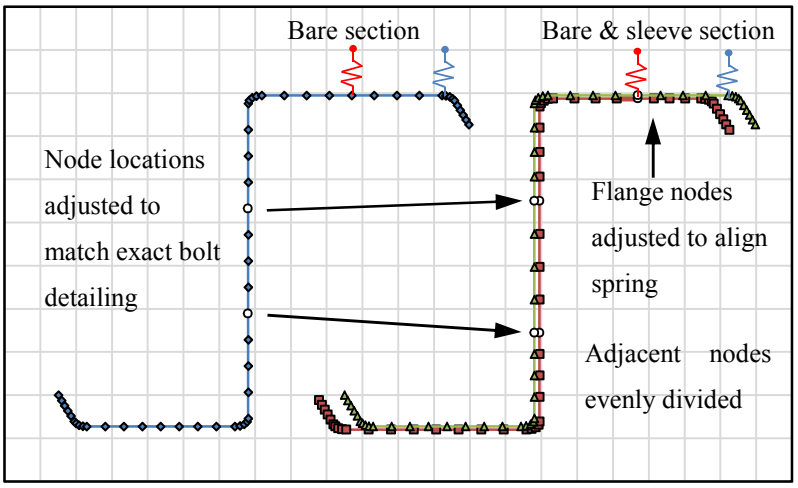


Figure 5.3: *Adjustment of web nodes to account for bolt locations*

5.3.2. Contact modelling

Hard-contact surface-to-surface contact definition was used to model contact behaviour between the sleeve and bare sections. The "*CONTACT PAIR" command in ABAQUS was used to constrain each flat surface pair (flanges and web surfaces from the sleeve and bare sections). The sleeve and beam surfaces were considered as the master and slave surfaces respectively and are shown in Figures 5.4(a) and 5.4(b). The ABAQUS command "*SURFACE BEHAVIOUR, PRESSURE-OVERCLOSURE = HARD" was used to define a "hard" pressure-overclosure relationship. To avoid unnecessarily long computation times, only the elements in the overlapping region were considered for contact modelling. Initial FE analyses indicated the edge stiffeners never came into contact and were therefore removed in the contact definition. Corner elements were also removed from the contact modelling because it tended to lead to numerical instabilities. To further reduce the computational times, the contact region was divided into separate individual flat region contact pairs. For example, Zeta I sections comprises 7 pairs: (1) top flange, (2-6) 5 individual flat web regions and (7) bottom flange, which are highlighted in Figure 5.4(c). The Coulomb friction coefficient μ was fixed at 0.3 with a default slip tolerance of 0.005. To prevent any initial overclosures (regardless of magnitude) between the contact surfaces after applying initial geometrical imperfections, the ADJUST=0.0 parameter was used with the *CONTACT PAIR command which moves any slave nodes that are penetrating the master (sleeve) surface to a position that lies on the contact master surface.

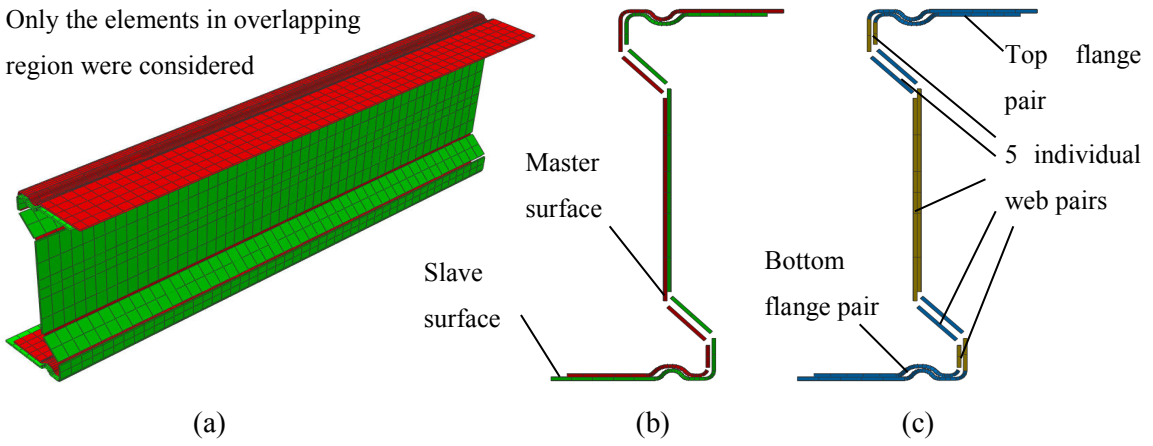


Figure 5.4: *Contact definitions: (a) sleeve length, (b) master and slave surfaces and (c) 7 individual contact pairs*

5.3.3. Bolt characteristics

Sleeved or lapped cold-formed steel systems with bolted connections are commonly used in practice. Modelling of bolts using solid C3D8I elements and applying contact interaction to adjacent sleeve and bare sections for cold-formed steel sleeved systems have been investigated by Gutierrez et al. (2011). In the present study, for improved numerical stability, the bolts were modelled by nonlinear springs with representative load-extension bearing deformation characteristics, adopted from the work of Ho and Chung (2006a). The proposed force-displacement curves were based on measured load-extension curves from 12 lap shear tests. A normalized load-extension relationship which covers different bolt diameters, cold-formed steel strip thicknesses and steel grades was developed and is given by:

$$F_b = \alpha_b dtf_u \tag{5.1}$$

where F_b, d, t, and f_u are the force developed in the bolt (N), the bolt diameter (mm), the thickness of the steel strip (mm) and the design tensile strength of the steel strip (N/mm^2). The strength coefficient α_b is defined in 3 stages by Equation 5.2. Stage 1 covers the load-extension response (up to 0.02 mm) which represents the slippage of the bolt thread, stage 2 represents the bolt slipping within the bolt hole, and stage 3 characterises the bearing behaviour of the bolt against the bolt hole.

$$\alpha_b = \begin{cases} 30d_0 & \text{for } d_0 \le 0.02 \text{ mm} \\ 1.25(d_0 - 0.02) + 0.6 & \text{for } 0.02 < d_0 \le 0.4 \text{ mm} \\ 0.85\ln\left(\dfrac{d_0 - 0.05}{0.35}\right) + 1.075 & \text{for } 0.4 < d_0 \le 3.0 \text{ mm} \end{cases} \quad (5.2)$$

where d_0 is defined as the extension of the bolted fastening and is limited for extensions up to 3 mm. Nonlinear springs were used to connect sleeve and bare section nodes, as shown in Figure 5.5(a). The in-plane and longitudinal displacements (DOF 2 and 3) were constrained using the nonlinear spring characteristics defined by Equations 5.1 and 5.2, in both tension and compression, as shown in Figure 5.5(b). The out-of-plane displacement (DOF1) for the connecting bolt node pairs were assumed tied and equated using the *EQUATION command. The rotations (DOF 4, 5 and 6) were free and bolt node rotations were assumed to be independent from each other in the section and sleeve.

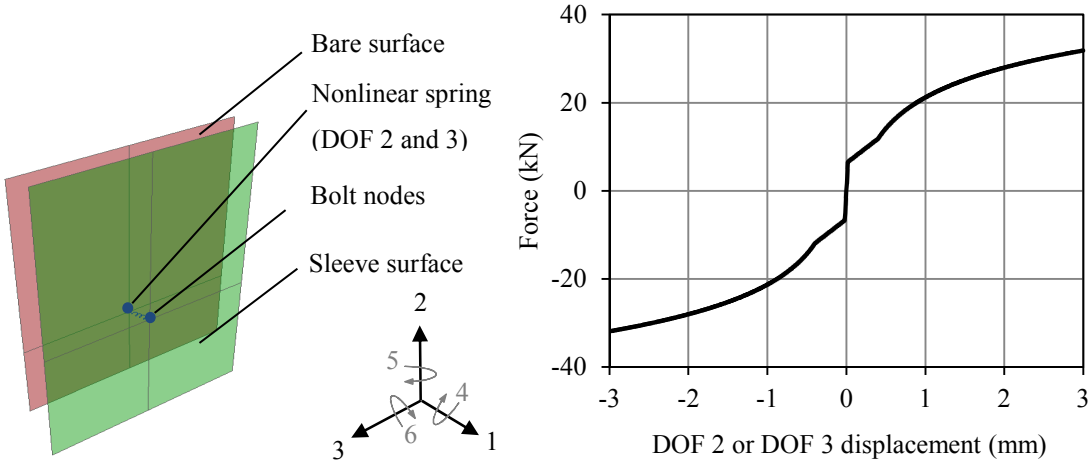


Figure 5.5: *(a) Nonlinear spring model for bolt, (b) Typical load-displacement relationship assigned to nonlinear springs (DOF 2 and 3)*

5.3.4. Whiffletree and solver scheme

The validated 2-span bare section models described in Chapter 3 adopted the modified Riks solution method (*STATIC, RIKS) and simulated a UDL by applying a pressure load on the top flange. An initial 2-span sleeved FE model with similar pressure loading and solver scheme showed the modified Riks method generally performs well in

the initial stages of loading, but fails to produce a full load-displacement response due to convergence issues caused by physical contact between the beam and sleeve surfaces.

Since ABAQUS does not allow the use of the modified Riks method with the stabilization damping algorithm and with the exact longitudinal deflection distribution for a general static displacement-control solver solution scheme unknown, an alternative approach to the modelling of the 2-span sleeved sections was sought. To overcome the FE modelling difficulties, a 4 tier whiffletree beam system was modelled to distribute the applied load from a single loading point at the top of the whiffletree to the beam. The 4 tier whiffletree provides 16 evenly spaced point loads which can accurately simulate a UDL; the difference in bending moment from the UDL case is no more than 1%. This enables the use of the general static solver with artificial stabilization (*STATIC, STABILIZE) by applying a displacement at the top of the whiffletree. Figure 5.6 shows a typical 2-span sleeve FE model with a 4 tier whiffletree and loading diagram comprising evenly spaced 16 point loads rather than a UDL.

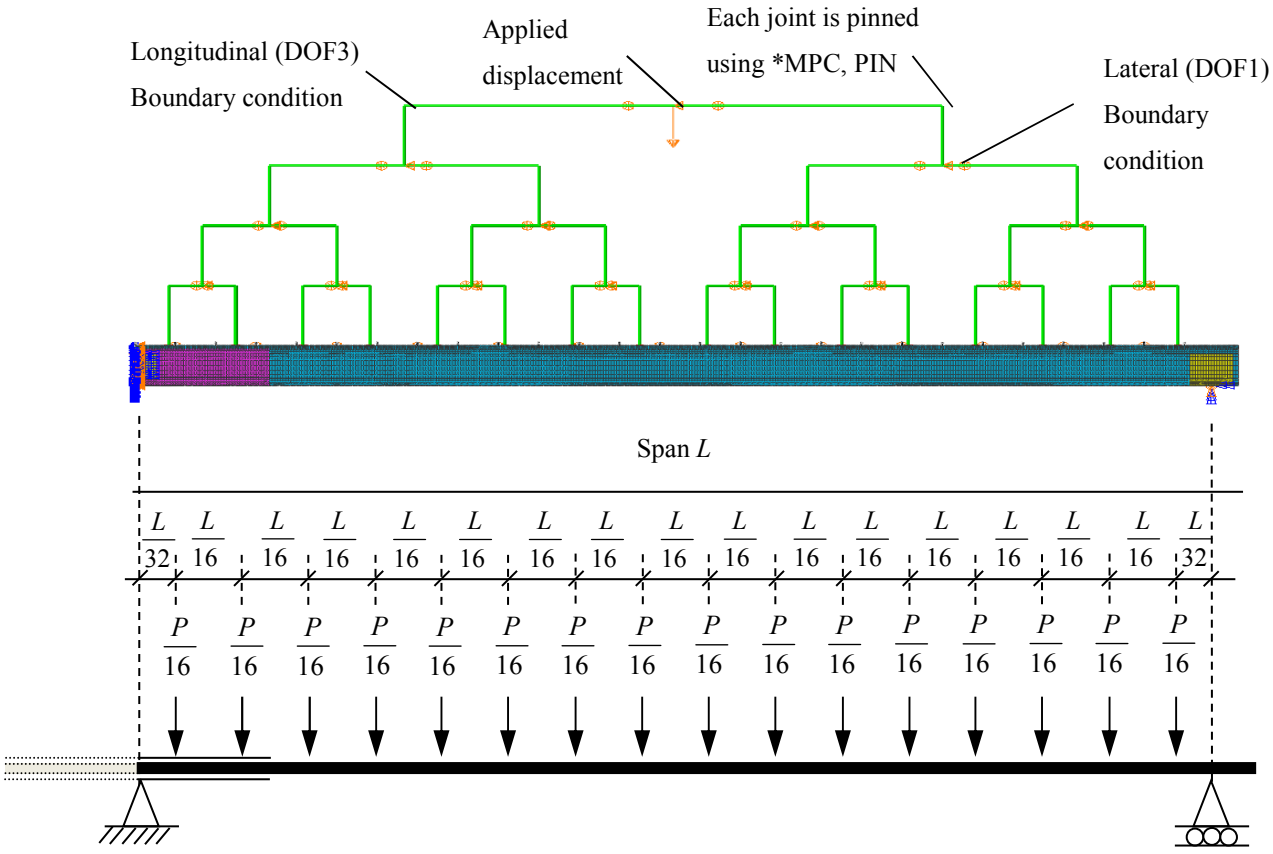


Figure 5.6: *4 tier 16 point whiffletree and loading diagrams*

To minimise bending within the whiffletree, 3-dimensional B31 beam elements were chosen and assigned an artificially high Young's modulus E_{tree} = 2100 GPa with a circular cross-section of 200 mm diameter. All whiffletree beam joints were pinned (*MPC, PIN) to ensure the applied loads were evenly distributed through each tier of the whiffletree and onto the cold-formed members. Owing to the fixed lengths of the whiffletree elements, the bottom tier of the whiffletree did not always align with the longitudinal beam mesh spacing of 10 mm. Additional horizontal B31 beams were therefore modelled to bridge the last tier of the whiffletree to the beam shell elements. Depending on whether or not the total span of the system is divisible by 320 mm, the rods were either 40 or 30 mm in length to accommodate the misalignment. The ends of the horizontal beams were pinned with the beam nodes. Figure 5.7 illustrates the two connection detail cases between the last tier of the whiffletree, connecting rod and the beam.

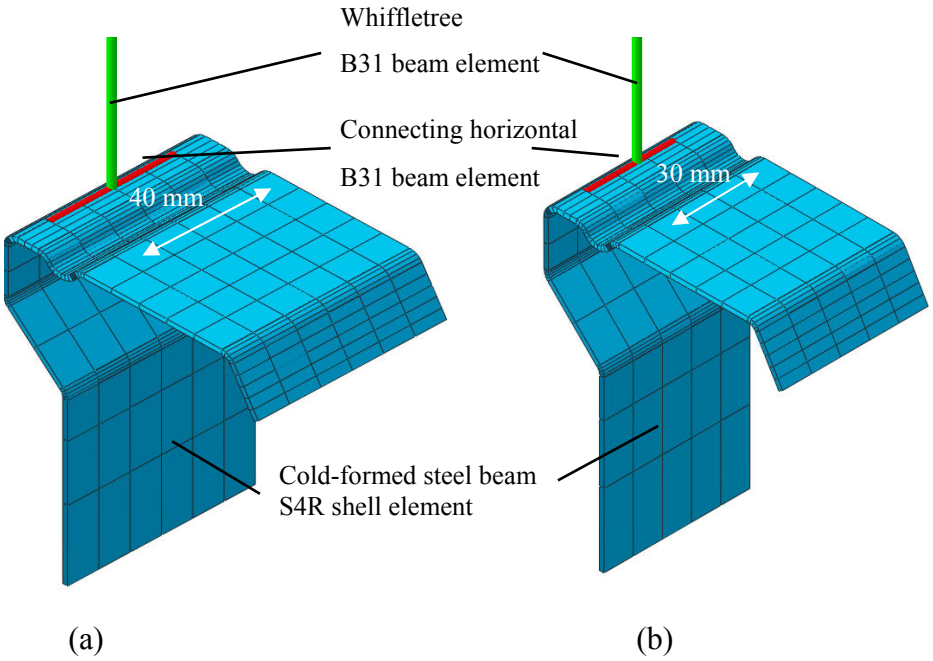


Figure 5.7: *Connection detail between whiffletree and beam (a) aligned and (b) misaligned*

5.4. CONTACT MODELLING AND ARTIFICIAL DAMPING SENSITIVITY STUDY

The general static solver with artificial stabilization (*STATIC, STABILIZE) was used for the FE contact models; initial simulations enabled full load-deformation responses to be captured beyond the ultimate load, which the modified Riks method failed

to produce. By adopting the stabilization solution scheme, additional viscous damping forces $\mathbf{F_v}$ are added to the global equilibrium equations of the system and are defined as:

$$\mathbf{F_v} = \mu \mathbf{M^* v} \tag{5.3}$$

where μ is the damping factor, $\mathbf{M^*}$ is an artificial mass matrix calculated with unit density and $\mathbf{v}$ is the vector of nodal velocities. The damping factor for any increment is calculated by extrapolating the dissipated and strain energy based on a fixed dissipated energy fraction, which has a default value of 2×10^{-4}. Since the amount of damping required is section and system dependant, there is no guarantee that the default dissipated energy is optimal. An artificial damping sensitivity study was conducted to find an optimum value for the range of cold-formed steel sleeved systems considered for this study. Finding an optimal dissipated energy fraction is nontrivial because the computational time required and risk of numerical non-convergence will increase if the amount of damping is reduced. Eleven Zeta 1B sleeved FE models with dimensions shown in Figure 5.8 (sleeve dimensions are the same as the beam) were simulated with varying dissipated energy fractions, initial step sizes, contact modelling properties and solver schemes. A total of 11 cases were considered as listed in Table 5.1.

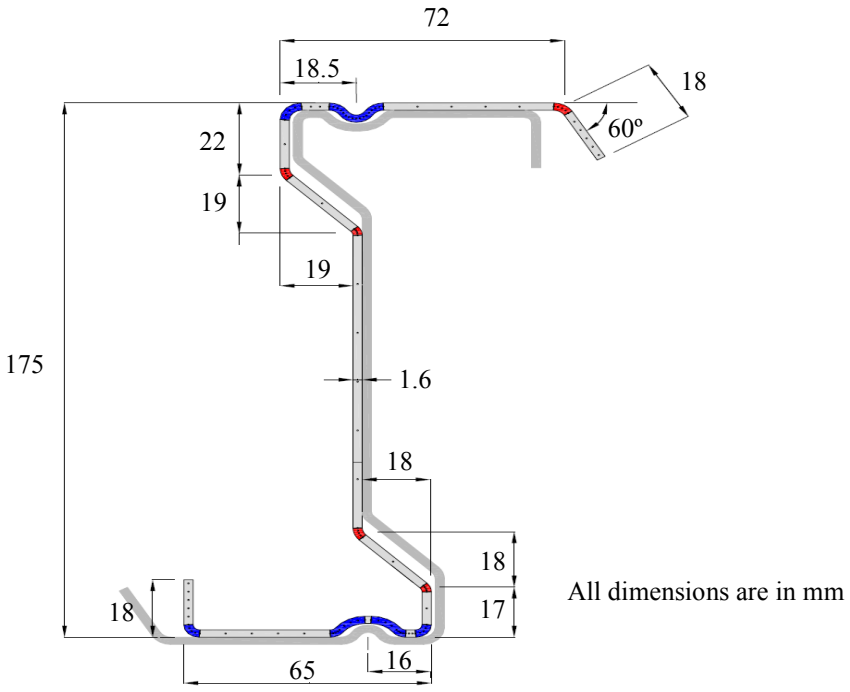


Figure 5.8: *Geometrical dimensions for Zeta IB sleeved section for artificial damping sensitivity study*

The results and load-displacement responses from the artificial damping study are shown in Table 5.1 and Figure 5.9 respectively. Hard contact FE models with contact properties defined in Section 5.3.2 gave initial satisfactory results since the ultimate loads and stiffness lies between the upper tied (7) and lower no contact (8) cases. The modified Riks method (UDL was applied using a pressure load) was used for comparing solver solution methods since it has been successfully validated for single and 2-span bare systems in Chapter 3. Despite the modified Riks method (case 6) failing to produce a full response due to non-convergence, it does provide a reliable load-displacement response for comparison. By comparing the responses with different dissipated energy fractions with case 6, the elastic stiffness and ultimate load-carrying capacity P_{ult} was found to be insensitive to the dissipated energy fraction providing the value is less than 5×10^{-4}; an increase in damping caused an increased initial stiffness and ultimate load. However, the initial stages of the FE model (1st and 2nd increments) gave over estimations of stiffness with responses roughly parallel to the modified Riks results method thereafter. Figure 5.10 illustrates that the magnitude of the initial overestimation (which leads to an overestimate in ultimate capacity) was due to large values of the dissipated energy fractions and initial step sizes. In severe cases, the initial stiffness was overestimated by a factor of 3. To avoid numerical non-convergence and ensuring reliable results without exhaustive computational times, the dissipated energy fraction was set to 0.0001 with small initial step size of 0.002 for the 2-span FE sleeved models.

Table 5.1: *Dissipated energy fraction sensitivity study results*

Case #	Contact definition	Solver type	Dissipated energy fraction	Initial step size	P_{ult} (kN)	P_{ult} / $P_{ult,test1}$
1	Hard contact	*Static, stabilize	0.00020	0.0050	23.769	1.000
2	Hard contact	*Static, stabilize	0.00005	0.0050	23.437	0.986
3	Hard contact	*Static, stabilize	0.00010	0.0050	23.642	0.995
4	Hard contact	*Static, stabilize	0.00050	0.0050	24.041	1.011
5	Hard contact	*Static, stabilize	0.00100	0.0050	25.267	1.063
6	Hard contact	*Static, riks	-	0.0050	N/A**	N/A**
7	Tied	*Static	-	0.0050	27.595	1.161
8	No Contact	*Static	-	0.0050	21.864	0.920
9	Hard contact	*Static, stabilize	0.00010	0.0020	23.291	0.980
10	Hard contact	*Static, stabilize	0.00010	0.0100	24.041	1.011
11	Hard contact	*Static, stabilize	0.00010	0.0200	24.023	1.011

** Failed to produce an ultimate load due to non-convergence

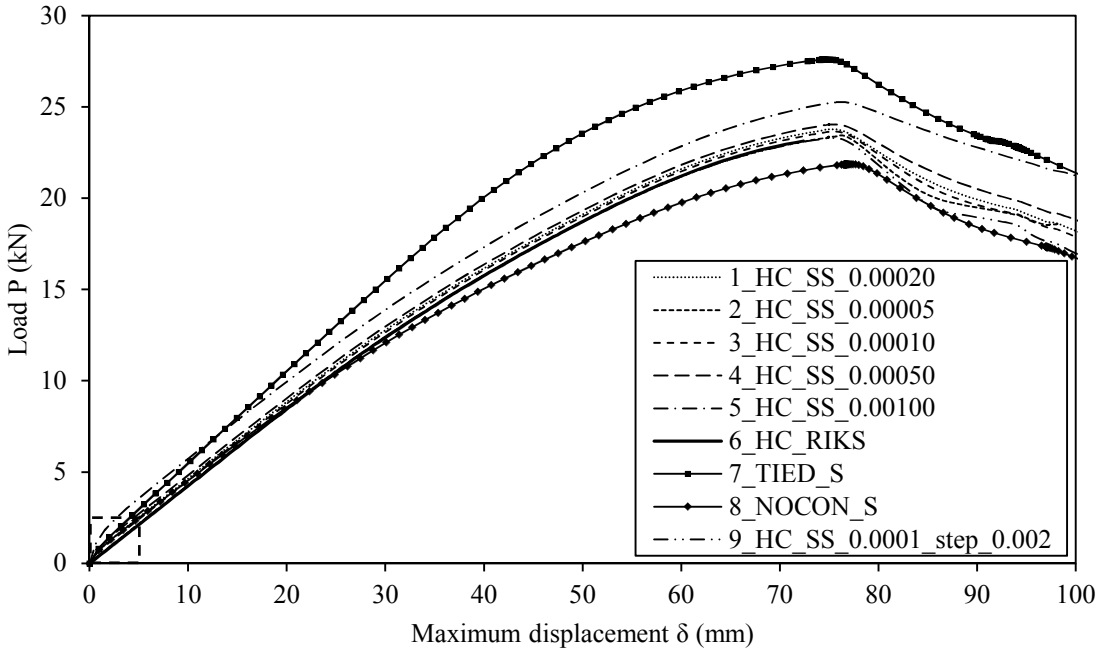


Figure 5.9: *Load-displacement responses for artificial damping sensitivity study*

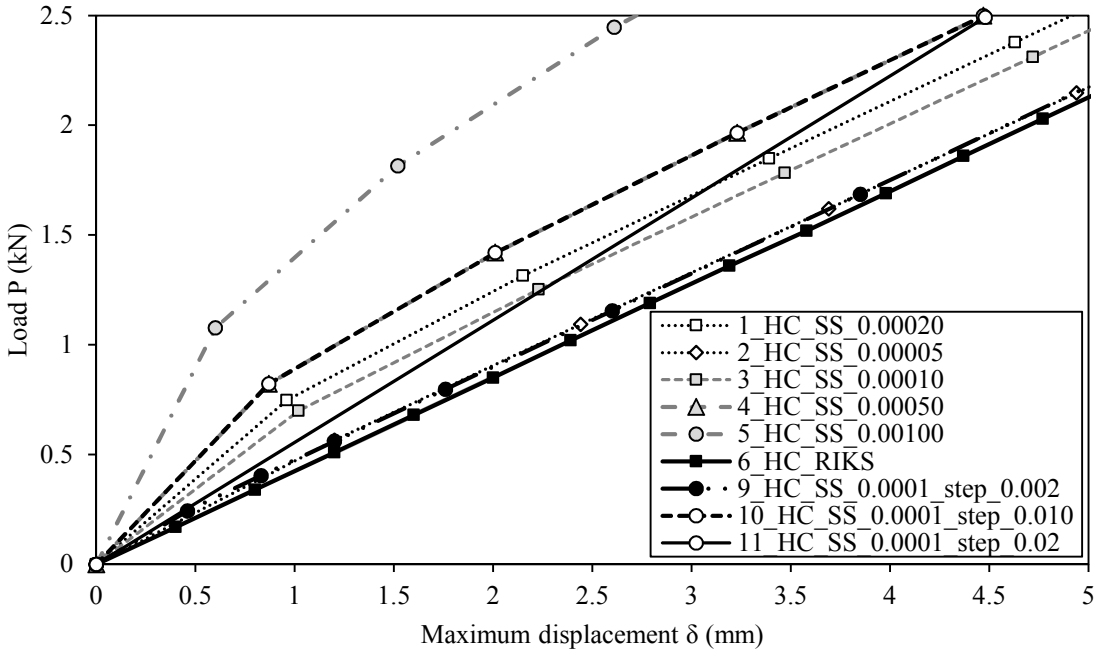
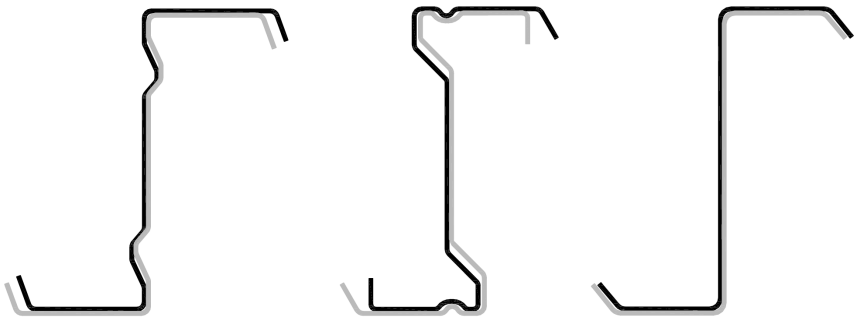


Figure 5.10: *Initial load-displacement responses for artificial damping sensitivity study*

5.5. VALIDATION OF SLEEVED SECTION FE MODELS

5.5.1. Introduction

As discussed in Chapter 3, tests on a total of 61 cold-formed steel bare single and 2-span systems have been successfully simulated using the finite element package ABAQUS 6.10 (2010). To extend the range of cold-formed steel system types considered, experiments on single and 2-span sleeved sections have been gathered and used to validate additional numerical models for Zeta I, Zeta II and Zed sections, as shown in Figure 5.11. The additional sleeved models will only be reliable providing the simulations can not only capture the buckling behaviour and load carrying capacity of the system, but also model the contact and bolt interactions which are not present within the previous cold-formed steel bare system models.



(a) (b) (c)

Figure 5.11: *Sleeved cross-section shapes: (a) Zeta II ,(b) Zeta I and (c) Zed*

Three additional test arrangements featuring sleeved (Test type 7, 9, 10) were considered for the FE model validation study and are illustrated in Figures 5.12-5.14:

Test type 7.	Single span 3-point bending (moment gradient) sleeved tests subjected to uplift loading
Test type 8.	Single span 3-point bending (moment gradient) sleeved tests subjected to downward loading
Test type 9.	2-span sleeved tests subjected to a gravity UDL
Test type 10.	2-span sleeved tests subjected to an uplift UDL

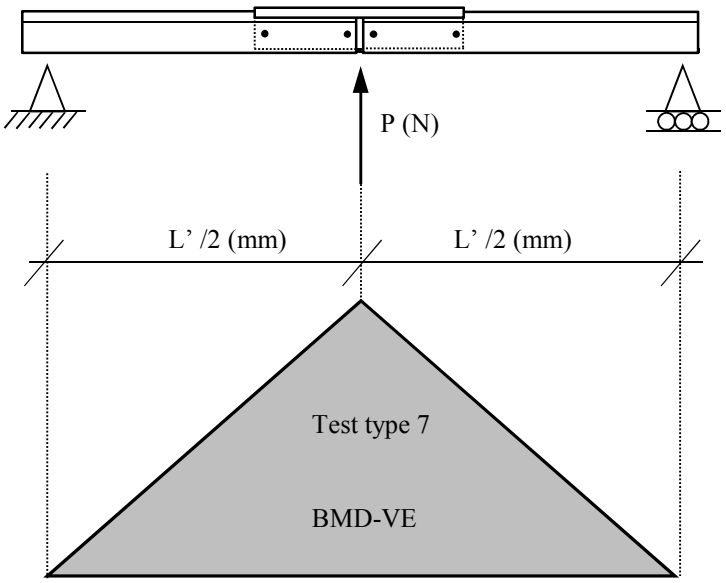


Figure 5.12: *Test type 7 – Single span 3-point bending (moment gradient) sleeved tests*

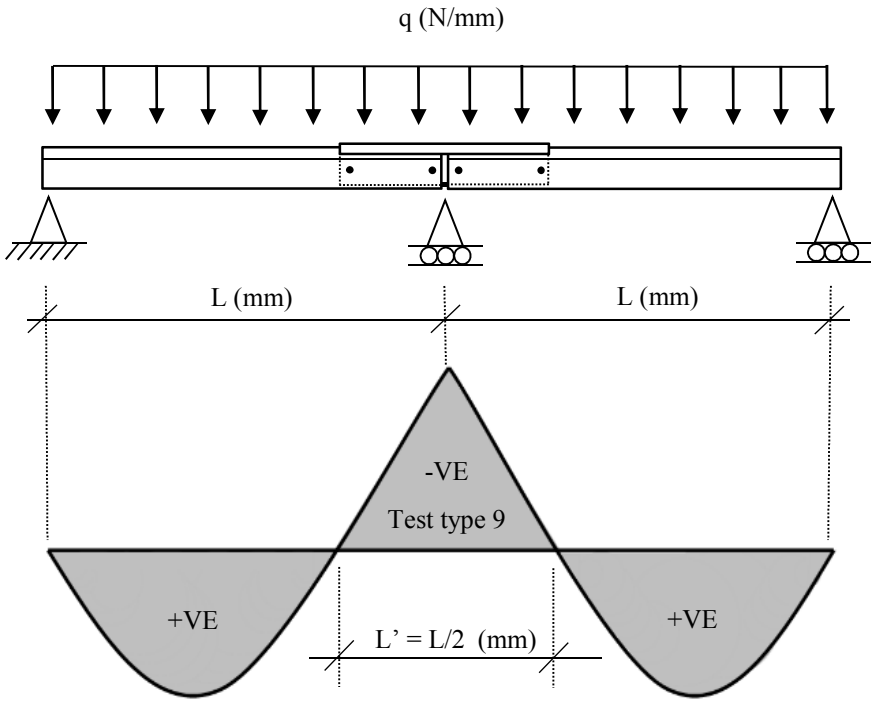


Figure 5.13: *Test type 9 – 2-span sleeved tests subjected to gravity UDL*

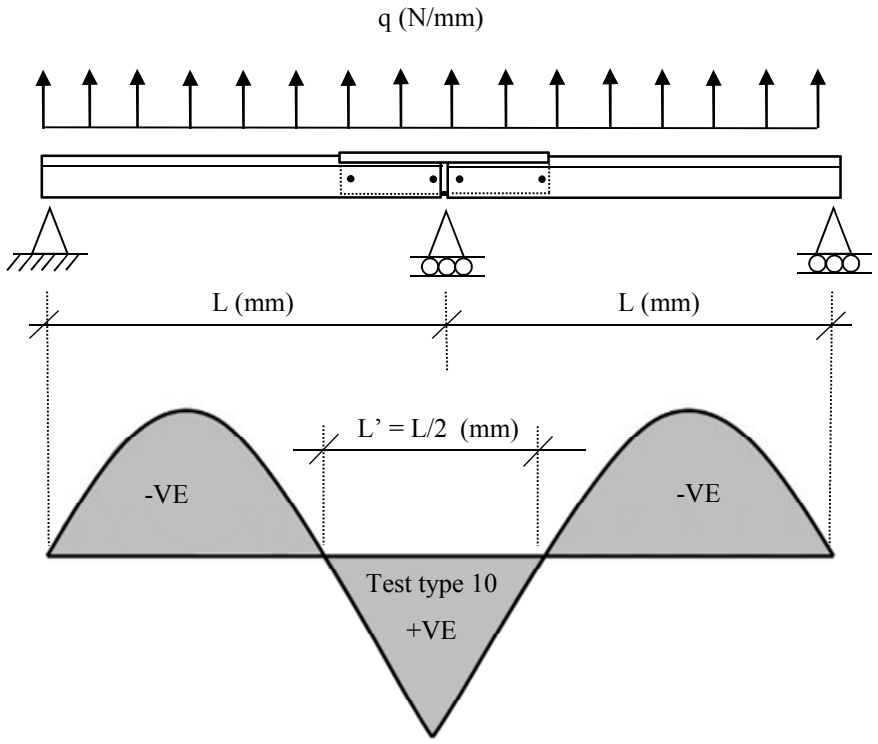


Figure 5.14: *Test type 10 – 2-span sleeved tests subjected to uplift UDL*

5.5.2. Boundary conditions and loading

Similar stiff corner and flat plates from the previous models were also employed in the sleeved FE models to replicate localised stiffening effect from loading plates and cleats; connections between the plates and the beam were not changed. Lateral restraints at the web/flange junctions were applied at a longitudinal spacing equal to the 250 mm linear spring spacing. Additional lateral restraint(s) in the overlapped sleeve region were applied as out-of-plane translational (DOF1) boundary conditions. The master linear spring nodes on the beam in the overlapped sleeve region were tied to pre-adjusted sleeve nodes using the *MPC, TIED command. Bolts that physically tie the sleeve and beam together were modelled in the FE analyses by connecting nonlinear springs between pre-adjusted web beam and sleeve nodes; the nonlinear springs were assigned the bearing load-extension properties defined by Equations 5.1 and 5.2 in the vertical and longitudinal direction only (DOF2 and 3). The lateral displacements of the bolt node pairs were equated with each other by using the *EQUATION command. Longitudinal translational boundary conditions (DOF 3) were applied at the midspan sleeve web nodes to prevent rigid body motion. Simply supported end conditions (restraining DOF 1, 2, 5 and 6) were applied at the tension flange of the beam; the internal support was modelled by applying

boundary conditions (restraining DOF 1, 2, 5 and 6) at the web nodes in the sleeved section at midspan. For single span sleeve tests, the ABAQUS command *CLOAD was used to apply the load through the centre of the loading plate and adopting the general static displacement control solver with artificial damping. Figure 5.15 shows a 3-point bending sleeve FE model (test type 7) illustrating the locations of the stiff plates, translational springs, prescribed boundary conditions and additional tie constraints to the sleeve section.

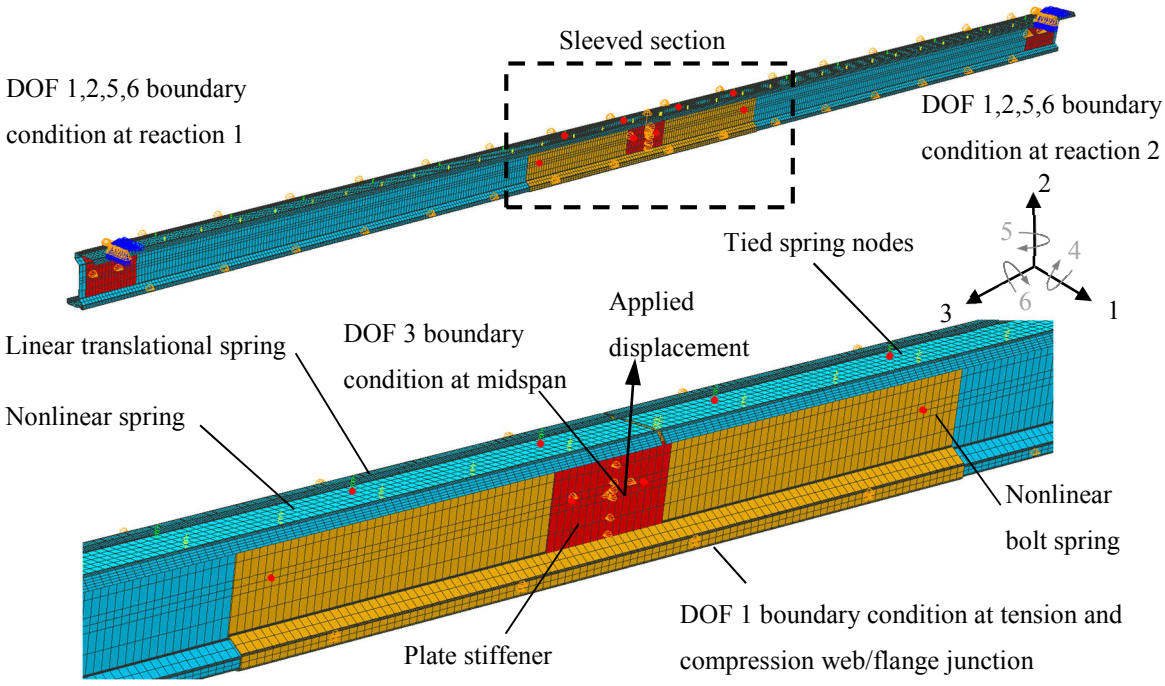


Figure 5.15: *3-point bending sleeved FE model arrangement*

The UDL for the 2-span sleeve tests was approximated by modelling a 4 tier whiffletree system as described in section 5.3.4 and shown in Figure 5.16; a vertical displacement was applied through the central position of the top tier of the whiffletree using the *BOUNDARY, direction, magnitude command. To ensure the whiffletree translates only in the vertical direction, lateral and longitudinal boundary conditions (DOF1) and (DOF3) were applied to the whiffletree beam nodes. Similar to the 2-span continuous beam models as described in section 3.3.2, only half of the 2-span sleeved system was modelled by applying longitudinal symmetry boundary conditions at the midspan sleeve and plate nodes using the *BOUNDARY, ZSYMM command (DOFs 3, 4 and 5 = 0). Initial half and full 2-span continuous FE models were found to give very similar load-displacement responses.

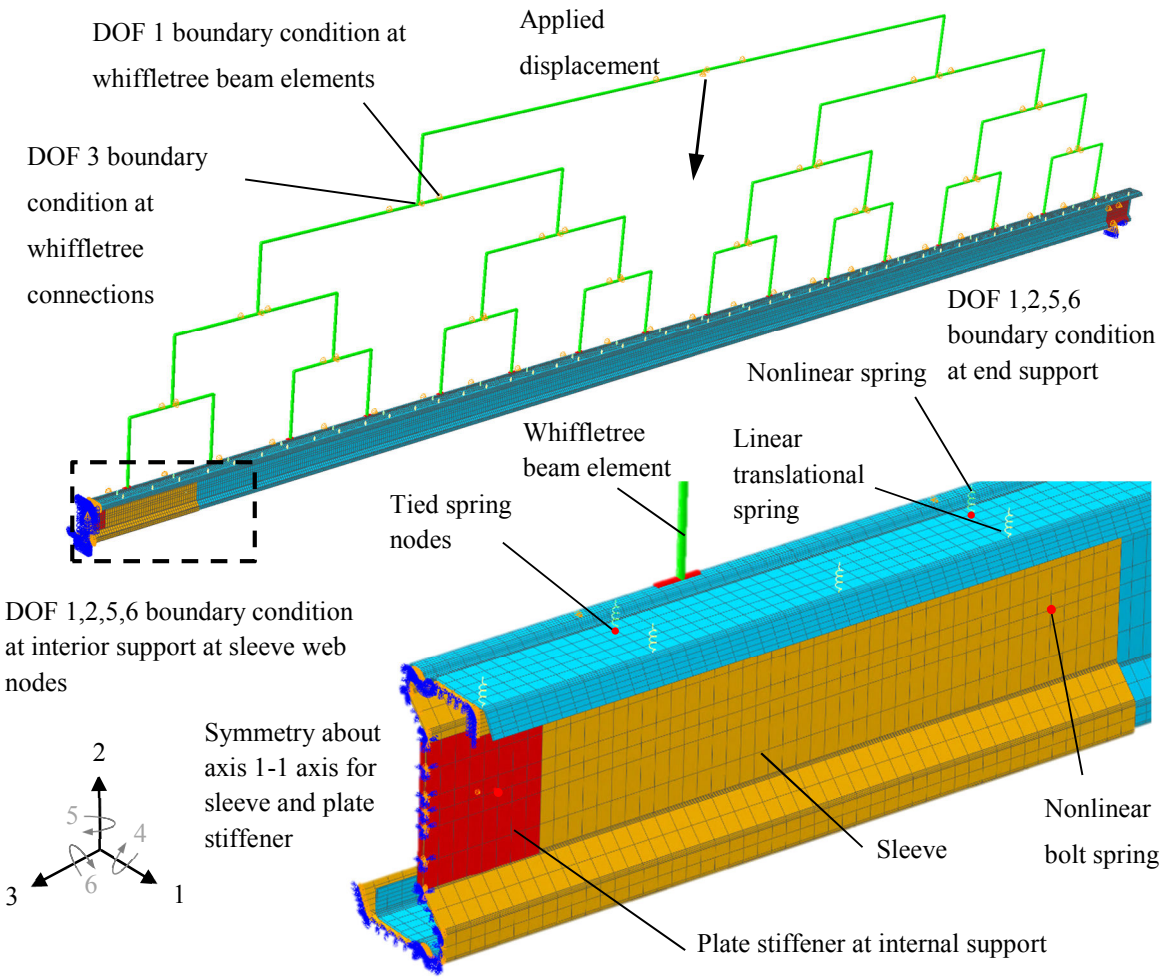


Figure 5.16: *2-span sleeved FE model arrangement*

5.5.3. Single span 3-point bending sleeved tests

Bryan and Davies (1980b), Leach (1990), Bryan and Deakin (1989), Davies and Deakin (1992), Deakin (1991a, 1991b) and Davies and Melbourne (1997) conducted a series 3-point bending sleeved tests for Zeta IB, Zeta II, Z1 and Z2 cold-formed steel sections at the University of Salford between 1979-1991. Details of the 3-point bending sleeved tests are summarized in Table 5.2. For each physical experiment, two nominally identical specimens were tested in pairs, with C-section ties to minimize lateral displacement, as shown in Figure 5.17. The nominal geometrical dimensions for the Zeta IB, Zeta II, Z1 and Z2 sections are shown in Figures 5.18 and 5.19. The sleeve dimensions were assumed to be the same as the purlins, but rotated by 180° in order for the sleeve to fit inside the section. The bolt arrangements are defined in Figure 5.20. Unfortunately, only the section thicknesses were reported; nominal dimensions for other lengths and corner radii were assumed for the FE sleeve models.

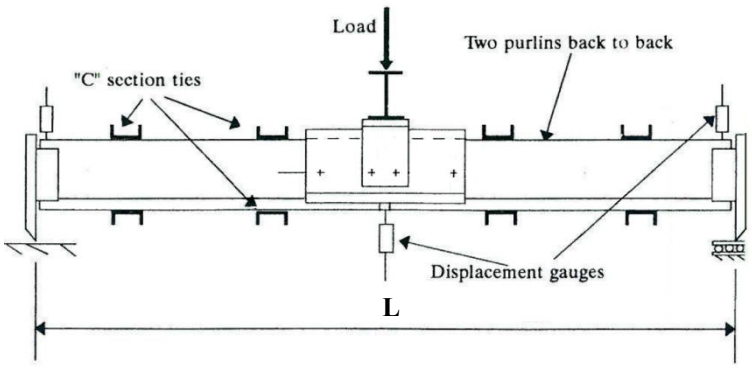


Figure 5.17: *3-point bending sleeved test arrangement*

Table 5.2: *3-point bending sleeved test details by Bryan, Davies, Deakin, Leach and Melbourne (1980-1997)*

Test #	Reference	Section Type[A]	Span L' (m)	Sleeve length[B] (m)	Bolt type[B]	Height h (mm)	Thickness t (mm)	f_y (N/mm^2)
1	Bryan and Davies (1980b)	Zeta IB	2.20	0.68	2	125	1.45	304.70
2		Zeta IB	2.40	0.80	2	150	1.55	304.70
3		Zeta IB	2.20	0.96	2	175	1.50	304.70
4		Zeta IB	3.00	0.98	3B	200	1.52	304.70
5	Leach (1990)	Zeta IB	3.60	1.00	3B	225	1.69	321.47
6		Zeta IB	4.00	1.00	3B	250	1.83	321.50
7	Bryan and Deakin (1989)	Zeta IB	2.60	0.98	2	175	1.56	311.33
9	Deakin (1991a)	Zeta IB	2.40	0.82	2	150	1.42	386.80
8	Deakin (1991b)	Zeta IB	3.00	1.00	3B	200	1.33	295.00
10	Davies and Deakin (1992)	Zeta II	4.00	1.00	3B	285	1.96	312.00
11		Zeta II	4.00	1.00	4	285	1.96	312.00
12		Zeta II	4.00	1.16	4	285	1.96	312.00
13		Zeta II	3.60	1.00	4	285	1.47	264.00
14		Zeta II	3.40	0.94	4	265	1.58	286.00
15		Zeta II	3.20	0.90	4	245	1.46	262.00
16		Zeta II	3.00	0.84	4	225	1.41	401.00
17	Deakin and Melbourne (1997)	Z1	4.00	0.96	4	300	2.46	305.60
18		Z1	2.60	0.56	4	140	1.82	354.60
19		Z1	2.60	0.56	4	140	1.31	352.80
20		Z2	2.40	0.56	4	125	1.27	364.20

A - Refer to Figures 5.18 and 5.19 for cross–sectional dimension details
B - Refer to Figure 5.20 for sleeve details

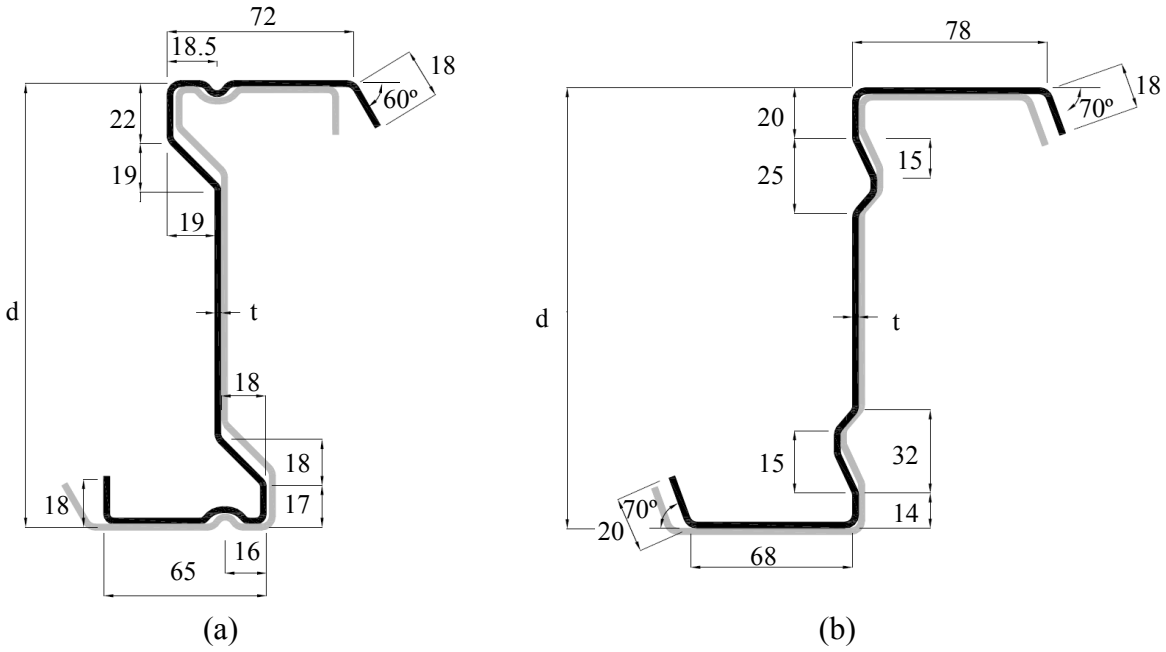


Figure 5.18: *Definition of cross-sectional dimensions for (a) Zeta IB sleeved and (b) Zeta II sleeved sections*

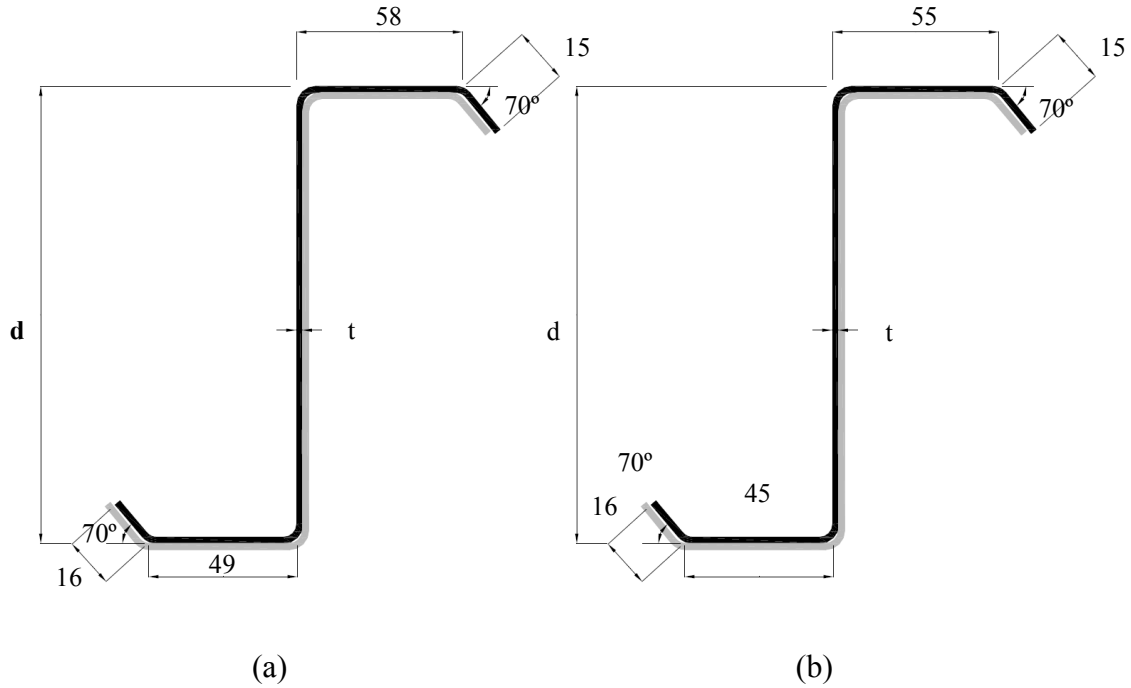


Figure 5.19: *Definition of cross-sectional dimensions for (a) Z1 sleeved and (b) Z2 sleeved sections*

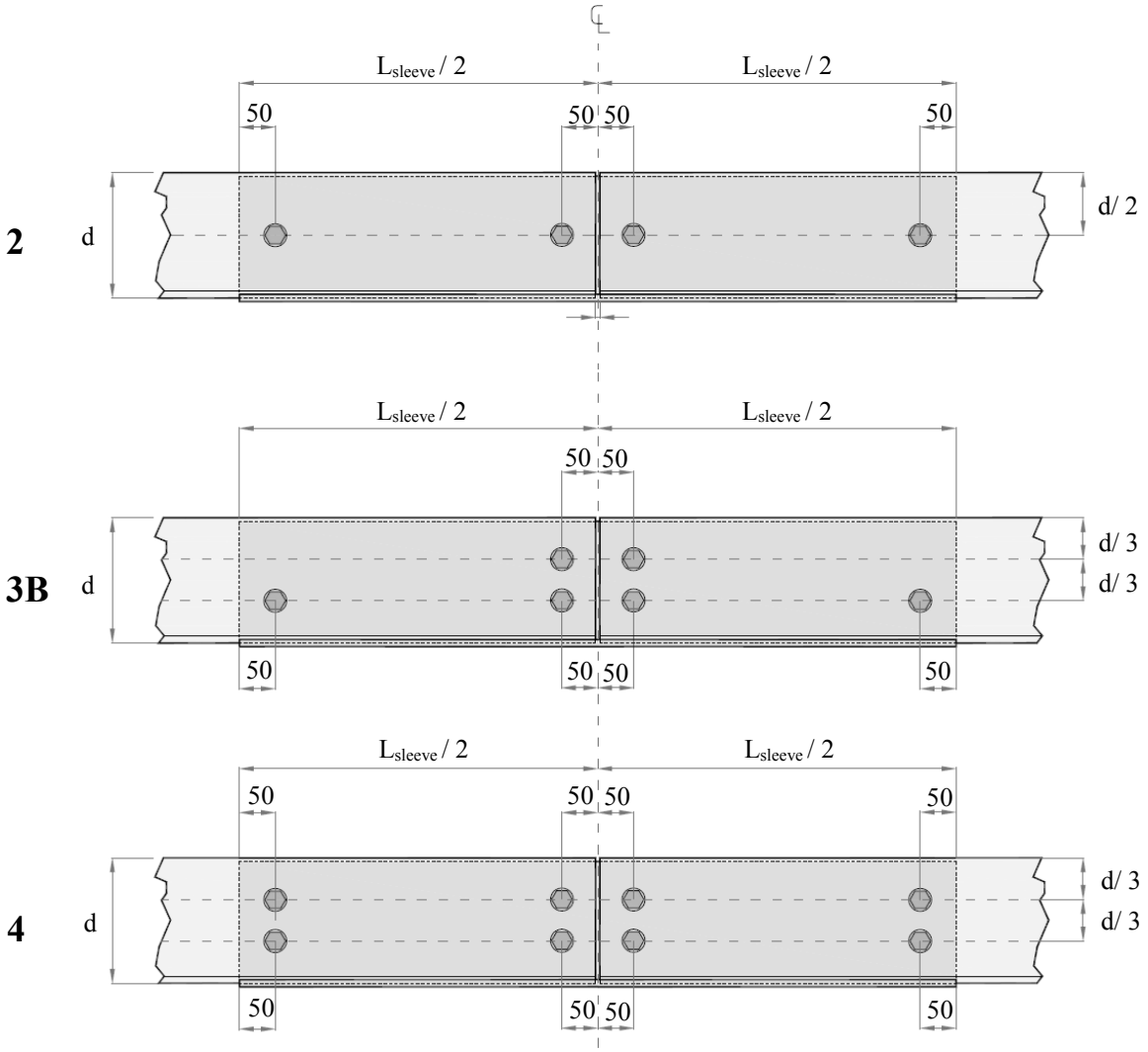


Figure 5.20: *Sleeve dimensions for 2, 3B and 4 bolt type arrangements*

5.5.3.1. Comparison between 3-point bending sleeved tests and FE results

A total of 34 (20 tests with 14 repeated) physical 3-point bending sleeved tests presented in table 5.2 were used to validate to two sets of 20 FE models with different bolt spring characteristics:

1. 'No slip' FE sleeved models with bearing only spring load-extension values calculated by Equation 5.1 and 5.2.
2. 'Slip' FE sleeve models with similar spring load-extension values but with an additional 1 mm offset to account for 1 mm clearance around the bolts.

Figure 5.21 illustrates the difference between the typical spring load-extension responses. Table 5.3 shows how the developed FE 'no slip' and 'slip' models can closely predict the observed ultimate bending capacities, with average FE/test ratio of 1.003 and 0.981 with corresponding COVs of 0.071 and 0.079 respectively. The modest scatter between the FE and test results can be explained by: (i) initial imperfection measurements were not reported and predicted values were used in the FE models, (ii) only cross-sectional thicknesses and material yield strengths were reported, resulting in the use of nominal geometrical dimensions and sleeve details for FE sleeve models, (iii) scatter between repeated physical test results were observed even though the test setup and section details were nominally identical and (iv) lack of reported bolt detailing such as bolt tightness (applied torque) and exact bolt position within each bolt hole. Figures 5.22-5.27 compare sample load-displacement responses between the physical tests and 'slip' and 'no slip' FE models. The initial stiffness for all FE models matched closely with those from the physical tests, but a sudden loss of stiffness due to bolt slippage in the physical test was not always closely replicated in the 'slip' FE models. The 'slip' FE models show signs of stiffness changes as illustrated in Figure 5.26, but this often occurred at a different position compared to the physical test. The magnitude and timing of the slip is largely dependent on the applied torque and the position of the bolts within the bolt holes which, as explained earlier, were not reported. It was concluded the 'slip' FE model can accurately simulate the sleeve-purlin slip interaction providing accurate load-extension spring properties were used. Knowing the amount of slip varies for each physical test, standardizing a suitable model for future FE models was deemed inappropriate. Considering the ultimate loads were insensitive between the 'slip' and 'no slip' FE cases, the 'no slip' spring model was chosen for future models due to simplicity.

The developed FE sleeve models were able to simulate the sleeve-purlin interaction using contact modelling and buckling behaviour for different cross-sectional geometries, material properties, bolt arrangements and test setup, though the full load-deformation history was not consistently accurately captured. The FE models can therefore be employed to increase the range of results covering a wider selection of sections geometries, bolt locations and sleeve arrangements by conducting parametric, studies as described in Chapter 6.

Table 5.3: *Comparison between bending resistances obtain from FE models and 3-point bending sleeved tests*

Test #	Reference	Section type*	$M_{FE,noslip}$ (kNm)	$M_{FE,slip}$ (kNm)	M_{test} (kNm)	$M_{FE,noslip}$ / M_{test}	$M_{FE,slip}$ / M_{test}
1	Bryan and Davies (1980b)	Zeta IB	-4.57	-4.63	-4.95	0.92	0.93
2		Zeta IB	-7.27	-7.08	-7.05	1.03	1.00
3		Zeta IB	-7.87	-7.58	-7.50	1.05	1.01
4		Zeta IB	-12.03	-12.19	-12.75	0.94	0.96
5A	Leach (1990)	Zeta IB	-16.29	-16.32	-17.90	0.91	0.91
5B					-17.46	0.93	0.93
5C					-16.49	0.99	0.99
5D					-17.20	0.95	0.95
6A		Zeta IB	-18.75	-18.76	-17.13	1.09	1.10
6B					-17.58	1.07	1.07
6C					-15.58	1.20	1.20
6D					-17.13	1.09	1.10
7A	Byran and Deakin (1989)	Zeta IB	-10.50	-9.91	-10.86	0.97	0.91
7B					-10.73	0.98	0.92
7C					-11.12	0.94	0.89
8A	Deakin (1991a)	Zeta IB	-7.67	-7.44	-8.71	0.88	0.85
8B					-8.53	0.90	0.87
9A	Deakin (1991b)	Zeta IB	-9.14	-9.19	-8.82	1.04	1.04
9B					-8.09	1.13	1.14
10	Davies and Deakin (1992)	Zeta II	-18.13	-17.85	-17.25	1.05	1.03
11		Zeta II	-20.41	-19.48	-20.60	0.99	0.95
12		Zeta II	-22.61	-22.14	-23.88	0.95	0.93
13		Zeta II	-11.36	-11.23	-11.84	0.96	0.95
14		Zeta II	-14.28	-13.65	-13.81	1.03	0.99
15		Zeta II	-10.52	-10.27	-10.52	1.00	0.98
16		Zeta II	-10.64	-10.10	-10.61	1.00	0.95
17A	Deakin and Melbourne (1997)	Z1	-29.64	-28.95	-27.71	1.07	1.04
17B					-29.40	1.01	0.98
18A		Z1	-6.35	-5.90	-6.11	1.04	0.97
18B					-6.99	0.91	0.84
19A		Z1	-3.83	-3.78	-3.90	0.98	0.97
19B					-3.80	1.01	0.99
20A		Z2	-3.23	-3.07	-3.09	1.05	0.99
20B					-3.09	1.05	0.99
* Refer to Figures 5.18-5.19 for cross–sectional dimension details					Mean	1.003	0.981
					COV	0.071	0.079

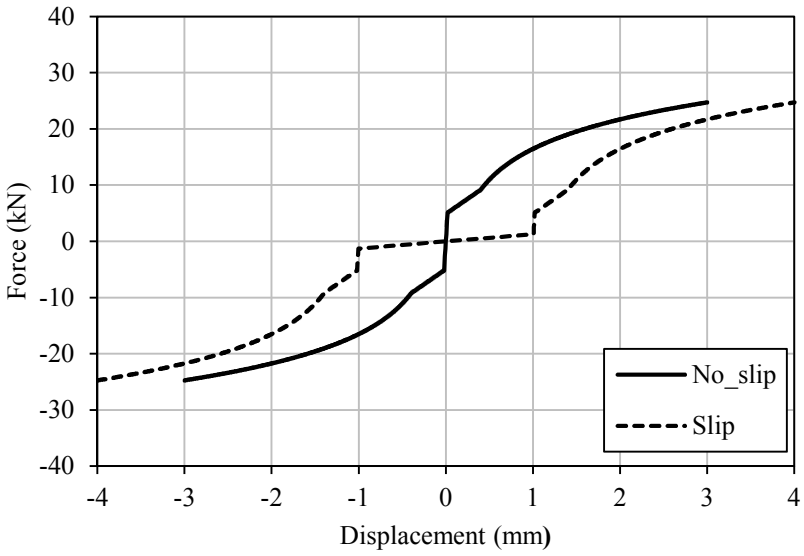


Figure 5.21: *Ho and Chung (2006a) bolt spring models adopted for FE validation*

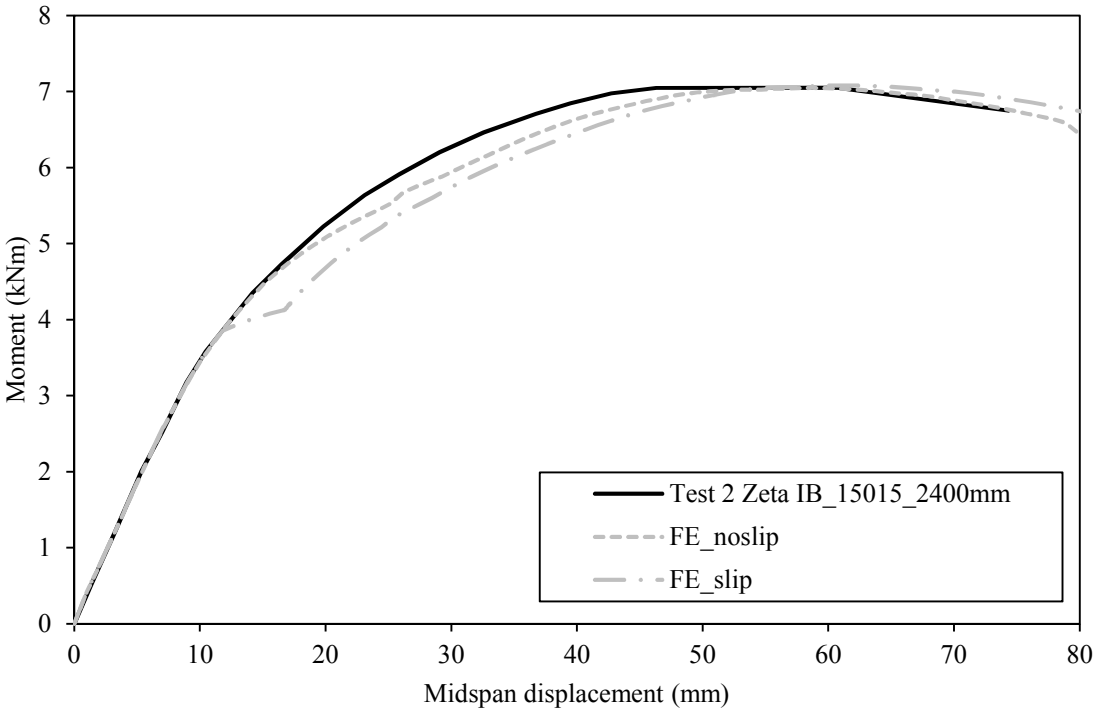


Figure 5.22: *Load-deformation curves from Bryan and Davies (1980b) Zeta IB sleeved test 2 and FE models*

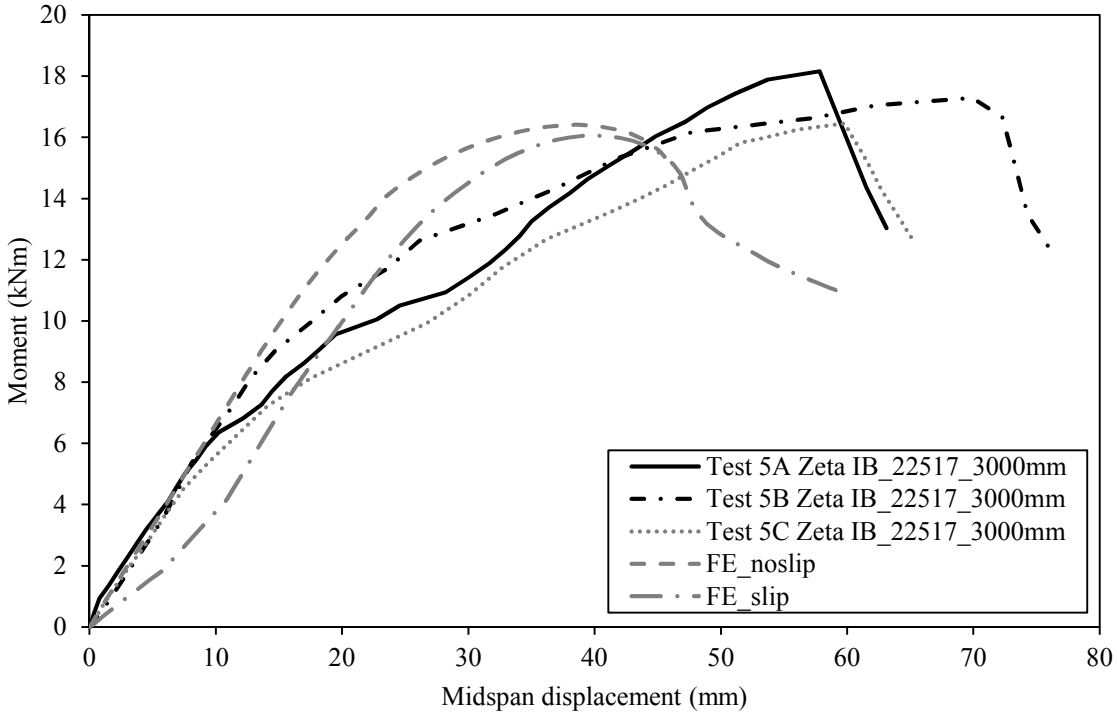


Figure 5.23: *Load-deformation curves from Leach (1990) Zeta IB sleeved test 5A, 5B and 5C and FE models*

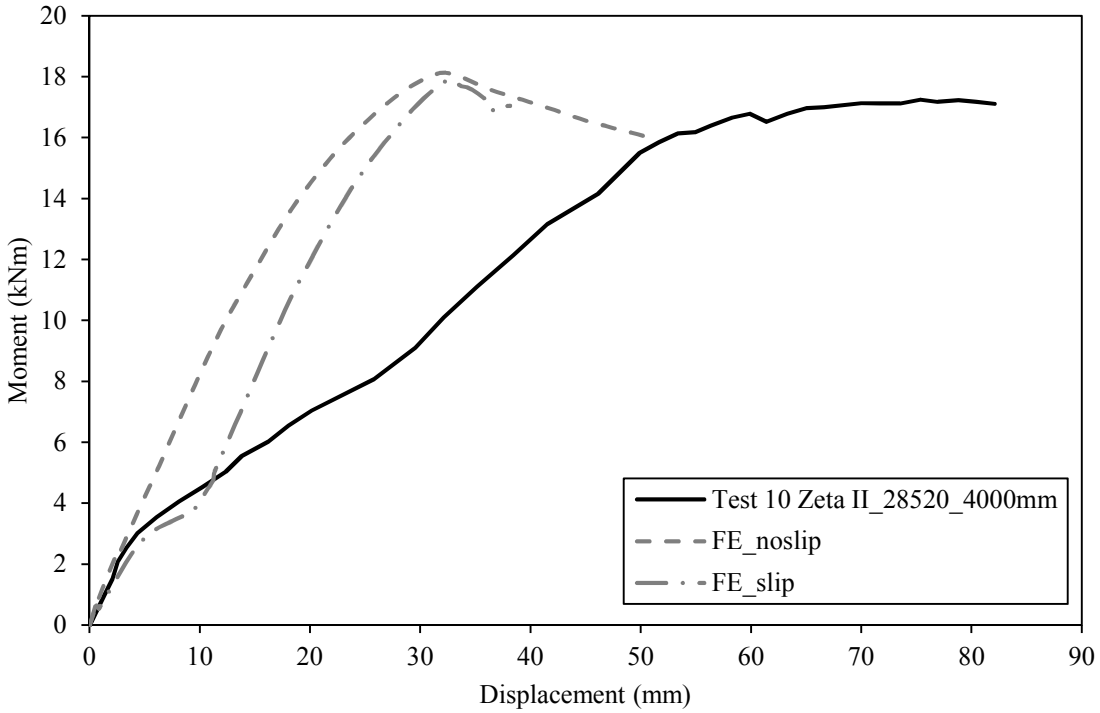


Figure 5.24: *Load-deformation curves from Davies and Deakin (1992) Zeta II sleeved test 10 and FE models*

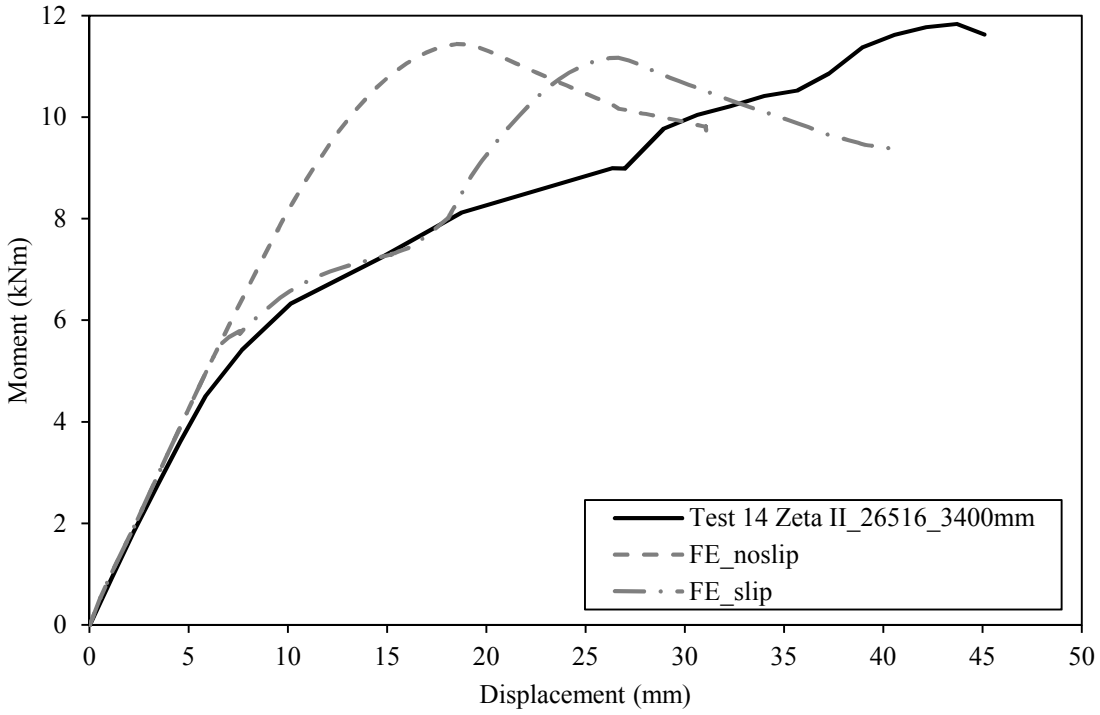


Figure 5.25: *Load-deformation curves from Davies and Deakin (1992) Zeta II sleeved test 14 and FE model*

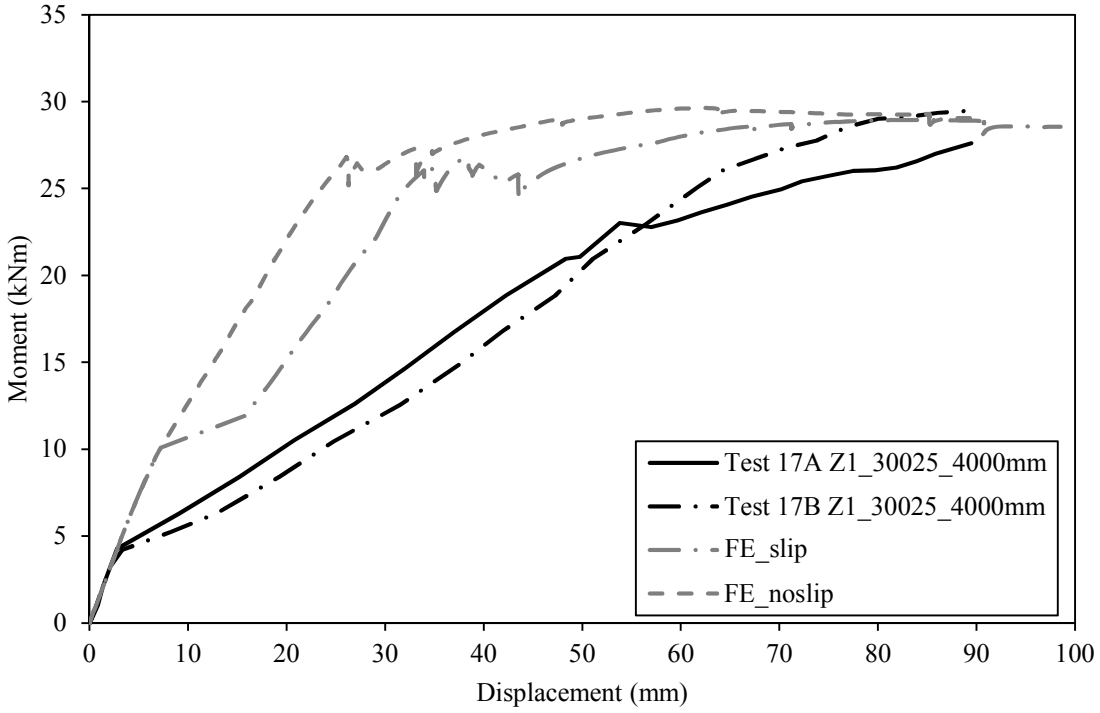


Figure 5.26: *Load-deformation curves from Deakin and Melbourne (1997) Z1 sleeved tests 17A and 17B and FE models*

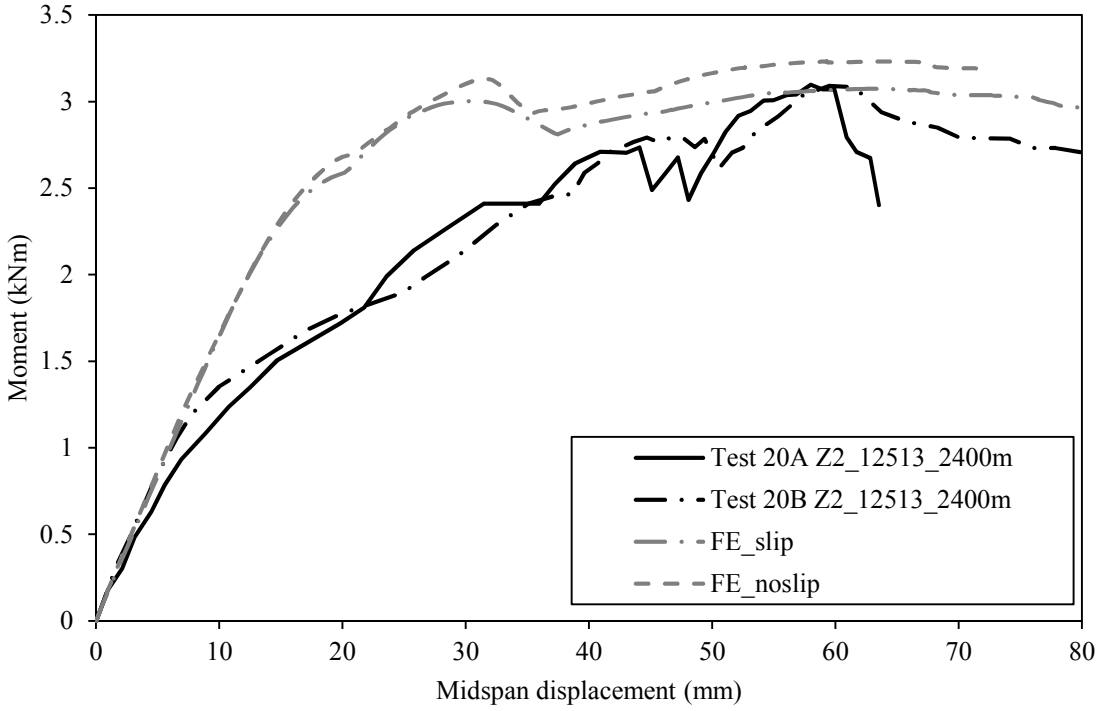


Figure 5.27: *Load-deformation curves from Deakin and Melbourne (1997) Z1 sleeved test 20 and FE models*

5.5.4. Full scale 2-span sleeved tests

Bryan and Davies (1980b), Leach (1990), Bryan and Deakin (1989), Deakin (1991a, 1991b) conducted a total of 9 gravity and 6 uplift Zeta I full scale 2-span sleeved tests subjected to a UDL at the University of Salford from 1980–1991. Figures 5.28 and 5.29 shows the general gravity and uplift 2-span setup respectively. The purlins were supported off cleats which were bolted to universal beam rafters. The system was loaded by a central hydraulic jack with spreader beams to create 4 equally spaced point loads for each span, to replicate a UDL, as illustrated in Figure 5.30. The purlins were tested in pairs and spaced 1.5 m apart with corrugated sheeting attached to the top flanges using Tek self-drilling screws at 200 mm centres. As shown in Figure 5.31, the last tier of spreader beams were vertically aligned with the purlins for the gravity tests, whereas for the uplift cases, the system was tested upside down and spreader beams placed inwards so that the purlins were free at the bottom flange. Zeta IB sections were the only section type tested in this study with geometrical dimensions shown in Figure 5.18(a). The sleeve sections have the same dimensions as the purlins and were rotated by 180º in order to slot the sleeves inside the purlins. Figure 5.20 shows the 2 and 3B bolt configurations used for

this study. Similar to the single span study discussed in Section 5.3.3, only thicknesses and yield strengths were reported and are shown in Table 5.4 and 5.5 for gravity and uplift tests respectively. Anti-sagbars were fitted for the uplift tests at the centre of the web with equal longitudinal spacing depending on the number of sagbars fitted.

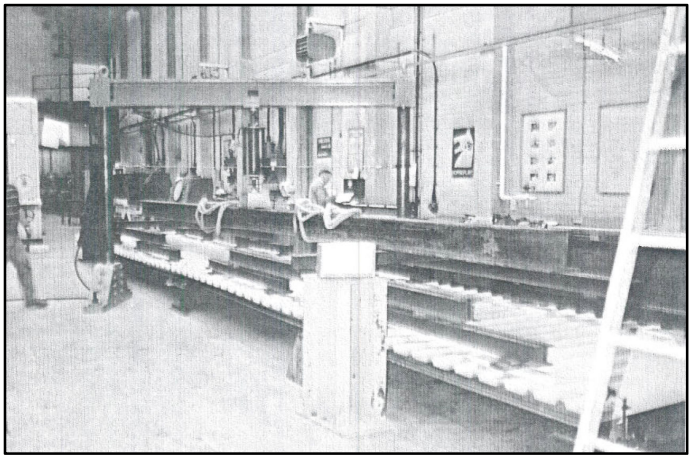


Figure 5.28: *2-span sleeved gravity test arrangement by Deakin (1991a)*

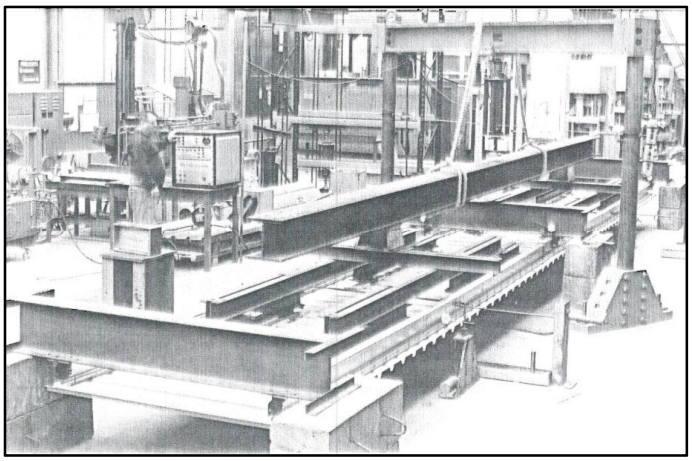


Figure 5.29: *2-span sleeved uplift test arrangement by Deakin (1991a)*

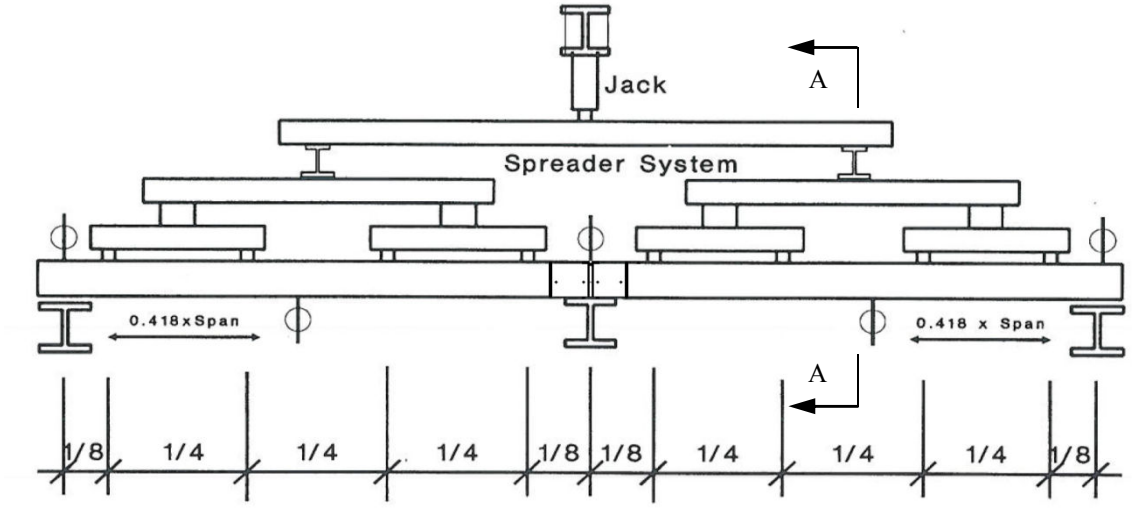
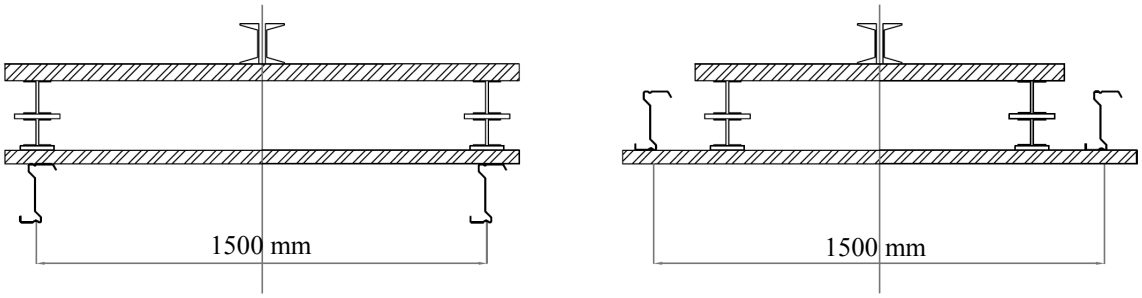


Figure 5.30: *2-span sleeved purlin test arrangement*



(a) (b)

Figure 5.31: *Section A-A of 2-span sleeved purlin system: (a) gravity and (b) uplift loading*

Table 5.4: *Measured geometry and material strength for 2-span gravity sleeved tests by Bryan and Davies (1980b), Leach (1990), Bryan and Deakin (1989) and Deakin (1991a, 1991b)*

Test #	Reference	Section Type[A]	Span L (m)	Sleeve length[B] L_{sleeve} (m)	Bolt type[B]	Depth d (mm)	Thickness t (mm)	f_y (N/mm^2)
1	Bryan and Davies (1980b)	Zeta IB	5.50	0.68	2	125	1.45	304.70
2		Zeta IB	6.00	0.80	2	150	1.55	304.70
3		Zeta IB	6.00	0.96	2	175	1.50	304.70
4		Zeta IB	7.50	0.98	3B	200	1.52	304.70
5	Leach (1990)	Zeta IB	9.00	1.00	3B	225	1.69	321.47
6		Zeta IB	10.00	1.00	3B	250	1.83	321.50
7	Bryan and Deakin (1989)	Zeta IB	6.50	0.98	2	175	1.56	311.33
8	Deakin (1991a)	Zeta IB	6.00	0.82	2	150	1.42	386.80
9	Deakin (1991b)	Zeta IB	7.50	1.00	3B	200	1.33	295.00

A Refer to Figures 5.18 and 5.19 for cross–sectional dimension details
B Refer to Figures 5.1 and 5.2 for sleeve details

Table 5.5: *Measured geometry and material strength for 2-span uplift sleeved tests by Bryan and Deakin (1989) and Deakin (1991a, 1991b)*

Test #	Reference	Section Type[A]	Span L (m)	Sleeve length[B] L_{sleeve} (m)	Bolt type[B]	No. of Anti-Sagbars[c]	Depth d (mm)	Thickness t (mm)	f_y (N/mm^2)
1	Bryan and Deakin (1989)	Zeta IB	6.50	0.98	2	0	175	1.56	311.30
2		Zeta IB	6.50	0.98	2	1	175	1.56	311.30
3	Deakin (1991a)	Zeta IB	6.00	0.82	2	0	150	1.42	386.80
4		Zeta IB	6.00	0.82	2	1	150	1.42	386.80
5	Deakin (1991b)	Zeta IB	7.50	1.00	3B	2	200	1.33	295.00
6		Zeta IB	7.50	1.00	3B	1	200	1.33	295.00

A Refer to Figures 5.18 and 5.19 for cross–sectional dimension details
B Refer to Figures 5.1 and 5.2 for sleeve details
C Number of evenly spaced sagbars per span

5.5.4.1. Comparison between 2-span sleeved tests and FE results

Two sets of 15 2-span gravity and uplift sleeved FE models were validated against 15 physical tests by Bryan and Davies (1980b), Leach (1990), Byran and Deakin (1989) and Deakin (1991a, 1991b). Similar 'no slip' and 'slip' spring characterises from the 3-point bending sleeved models (discussed in Section 5.4.3) were simulated for the 2-span sleeved models to check the sensitivity of the ultimate load and general flexural behaviour. For the 2-span sleeved gravity case, Table 5.6 compares ultimate load carrying capacities between physical tests and both sets of FE models. The FE models can accurately predict the ultimate load from physical testing; the mean and COV values for the 'slip' and 'no slip' gravity cases are 0.970 and 0.068 and 0.963 and 0.056 respectively. Table 5.7 compares ultimate load carrying capacities between 2-span sleeve uplift tests, 'no slip' and 'slip' FE models; the mean and COV values for the 'slip' and 'noslip' uplift cases are 1.002 and 0.056 and 0.990 and 0.060 respectively. The 'slip' FE cases consistently yield lower capacities than the 'no slip' cases, with small variations in stiffness, as shown in Figures 5.32-5.35. The differences in ultimate loads between the two FE cases were found to be generally small. Since the 'slip' case was more troublesome to implement due to uncertainty of bolt locations within their bolt holes, opting for the 'n oslip' case was again deemed more favourable due to its simplicity.

The contact interaction between the sleeve and the purlin was accurately simulated in the FE models since the interactive buckling modes in the sleeve region were similar to those photographed in the physical tests and confirmed in Figures 5.36 and 5.37. The contact interaction caused the web in the sleeve section to buckle outwards in conjunction with distortional buckling of the compression flange at the interior support. The change in stiffness in the load-displacement responses showed that the FE models can capture the moment redistribution behaviour, as shown in Figures 5.32-5.35. The final failure mode of the system was accurately captured by the FE models; the buckling mode in the span region was either local/distortional buckling (see Figure 5.36) or lateral torsional buckling for the uplift cases (see Figure 5.37).

Single span 3-point bending sleeved tests were validated in Section 5.5.3, and shown to be able suitable modelling modelling parameters for the additional sleeve sections including definition of the cross-section geometry, material modelling, mesh density, bolt model and contact interaction. Additional FE modelling parameters for the

2-span sleeve systems covering 4 tier whiffletree dimensions with adequate material beam properties and connections, magnitude of energy dissipation and change of solver type have been successfully validated for 2-span sleeved Zeta I sections. The FE sleeved models can therefore be used to carry out further simulations with a range of varying input parameters to extend the pool of FE results, including covering different bolt arrangements, section sizes and sleeve and test dimensions.

Table 5.6: *Comparison of ultimate loads from FE models and 2-span gravity sleeve tests*

Test #	Reference	P_{ult,FE_noslip} (kN)	P_{ult,FE_slip} (kN)	$P_{ult,test}$ (kN)	$P_{ult,FE,noslip}$ / $P_{ult,test}$	$P_{ult,FE,slip}$ / $P_{ult,test}$
1	Bryan and Davies (1980b)	12.402	12.310	14.140	0.877	0.871
2		15.703	15.679	16.981	0.925	0.923
3		18.973	18.958	19.504	0.973	0.972
4		18.742	18.903	19.854	0.944	0.952
5	Leach (1990)	21.563	21.174	22.605	0.954	0.937
6		22.573	22.853	24.251	0.931	0.942
7	Byran and Deakin (1989)	18.408	18.368	18.338	1.004	1.002
8	Deakin (1991a)	17.086	17.043	16.716	1.022	1.020
9	Deakin (1991b)	15.416	14.655	13.992	1.102	1.047
				Mean	0.970	0.963
				COV	0.068	0.056

Table 5.7: *Comparison of ultimate loads from FE models and 2-span uplift sleeve tests*

Test #	Reference	P_{ult,FE_noslip} (kN)	P_{ult,FE_slip} (kN)	$P_{ult,test}$ (kN)	$P_{ult,FE,noslip}$ / $P_{ult,test}$	$P_{ult,FE,slip}$ / $P_{ult,test}$
1	Bryan and Deakin (1989)	15.157	15.031	15.296	0.991	0.983
2		15.078	14.827	16.483	0.915	0.900
3	Deakin (1991a)	13.383	13.260	13.579	0.986	0.977
4		13.440	13.130	13.557	0.991	0.968
5	Deakin (1991b)	11.510	11.492	10.812	1.065	1.063
6		10.491	10.367	9.858	1.064	1.052
				Mean	1.002	0.990
				COV	0.056	0.060

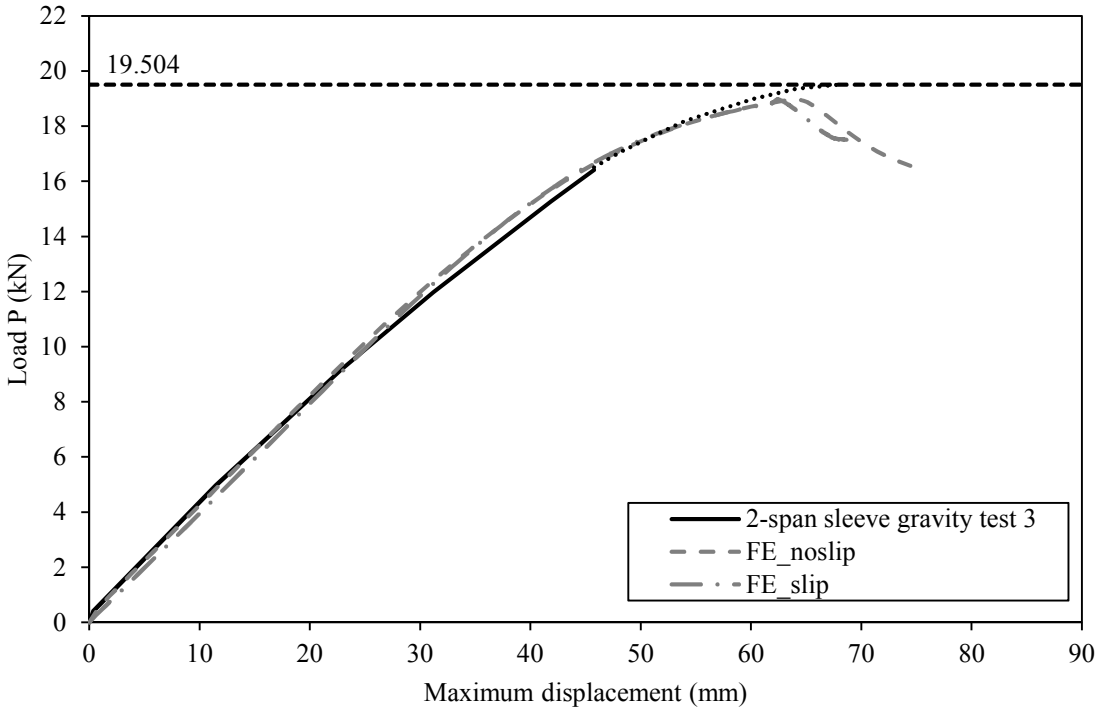


Figure 5.32: *Load-deformation curves from Bryan and Davies (1980b) Zeta IB 2-span gravity sleeved test 3 and FE models*

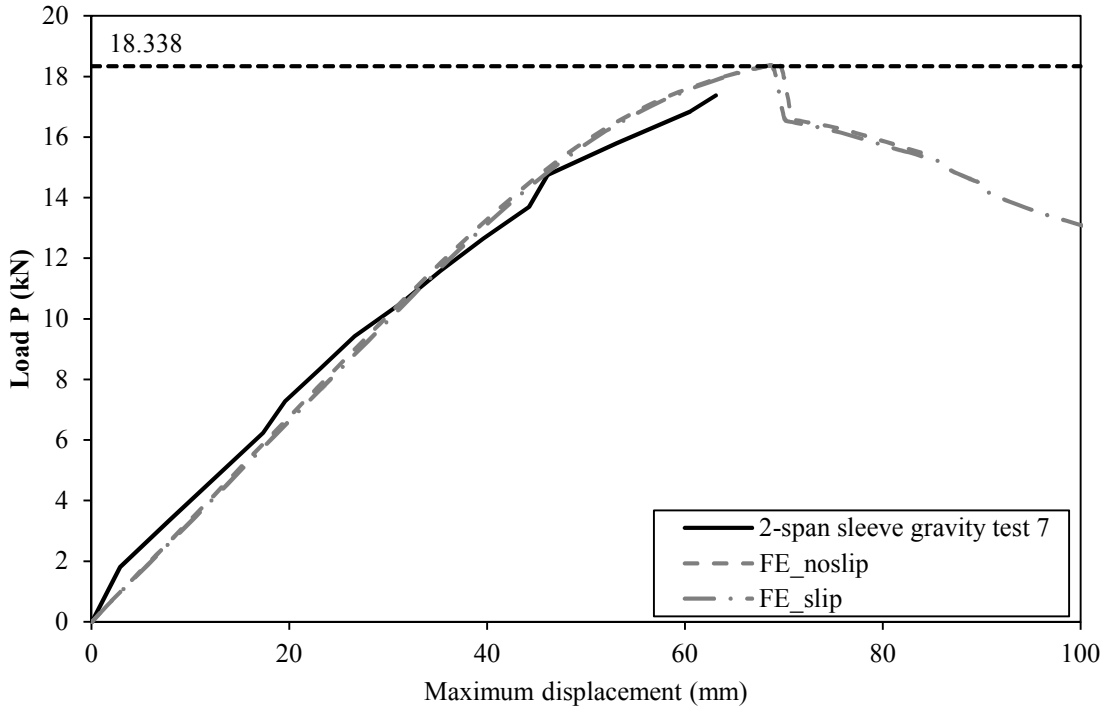


Figure 5.33: *Load-deformation curves from Bryan and Deakin (1989) Zeta IB 2-span gravity sleeved test 7 and FE models*

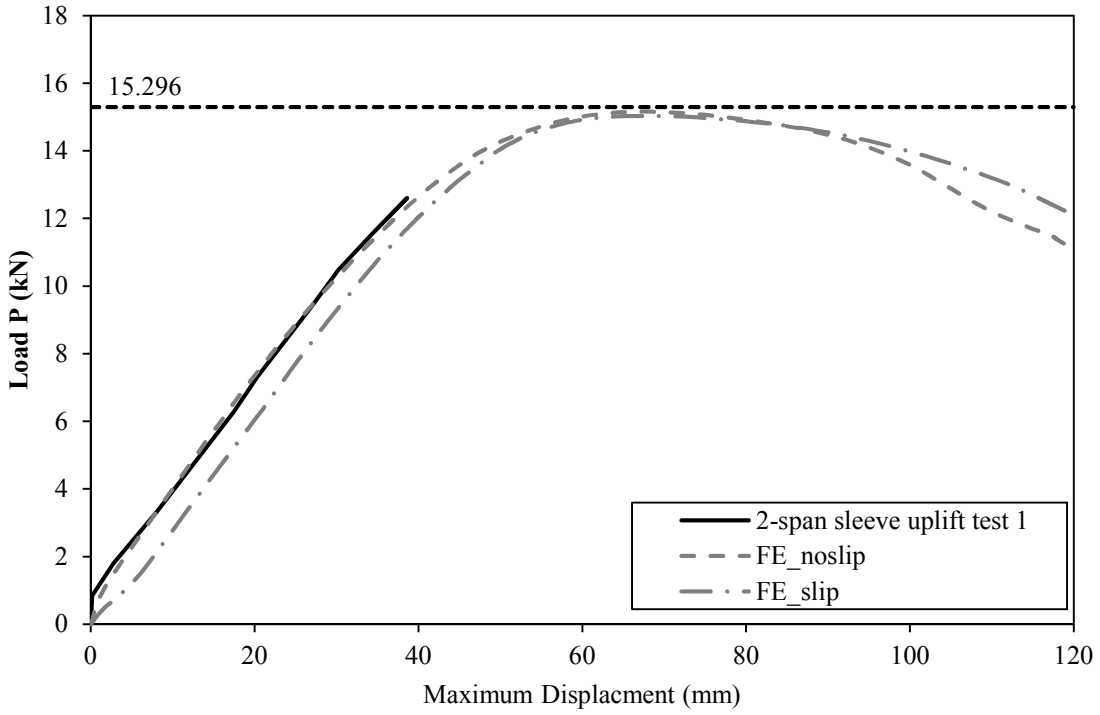


Figure 5.34: *Load-deformation curves from Bryan and Deakin (1989) Zeta IB 2-span uplift sleeved test 1 and FE models*

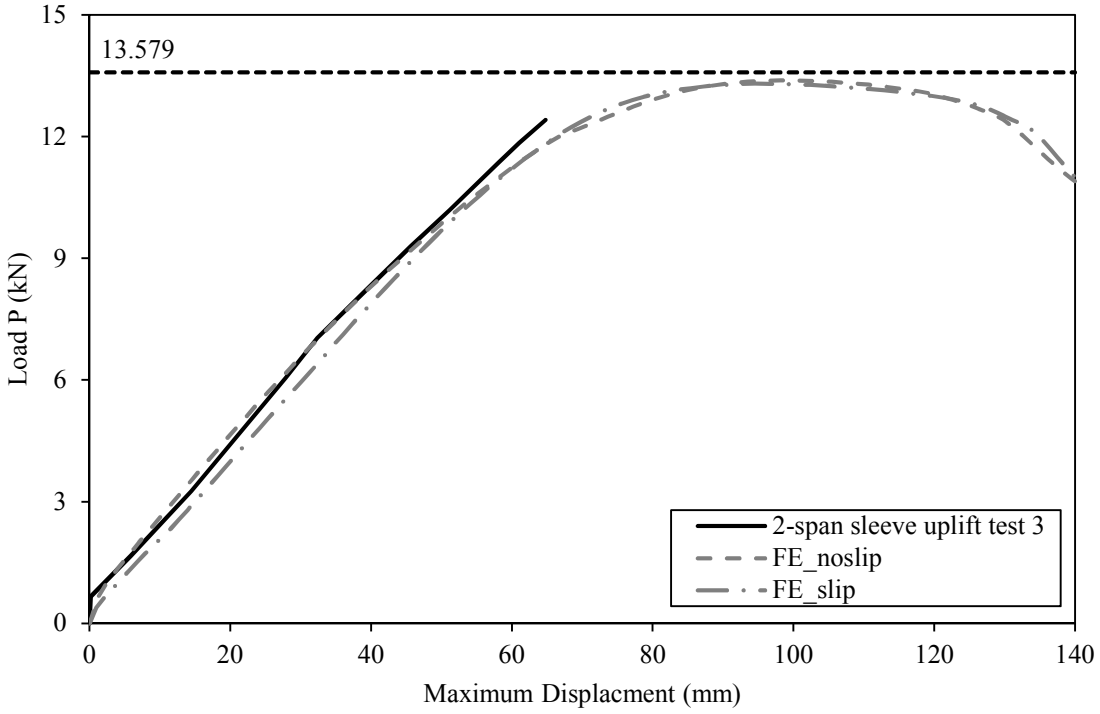


Figure 5.35: *Load-deformation curves from Deakin (1991a) Zeta IB 2-span uplift sleeved test 3 and FE models*

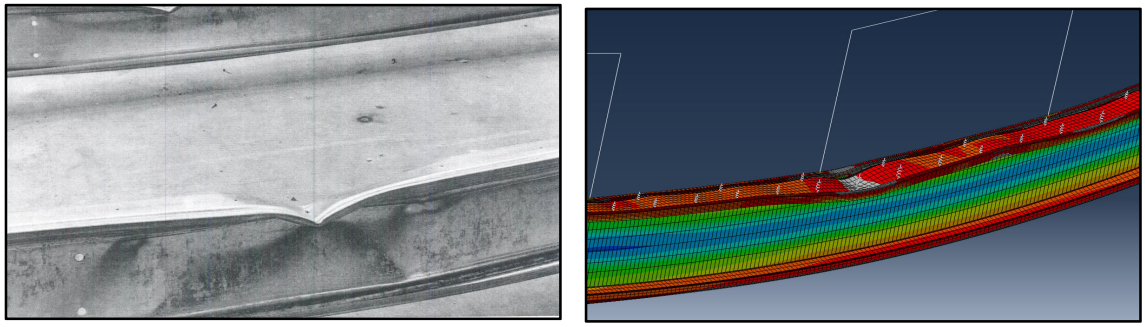


Figure 5.36: *Failure modes between 2-span sleeved gravity test 5 from Leach (1990) and FE model*

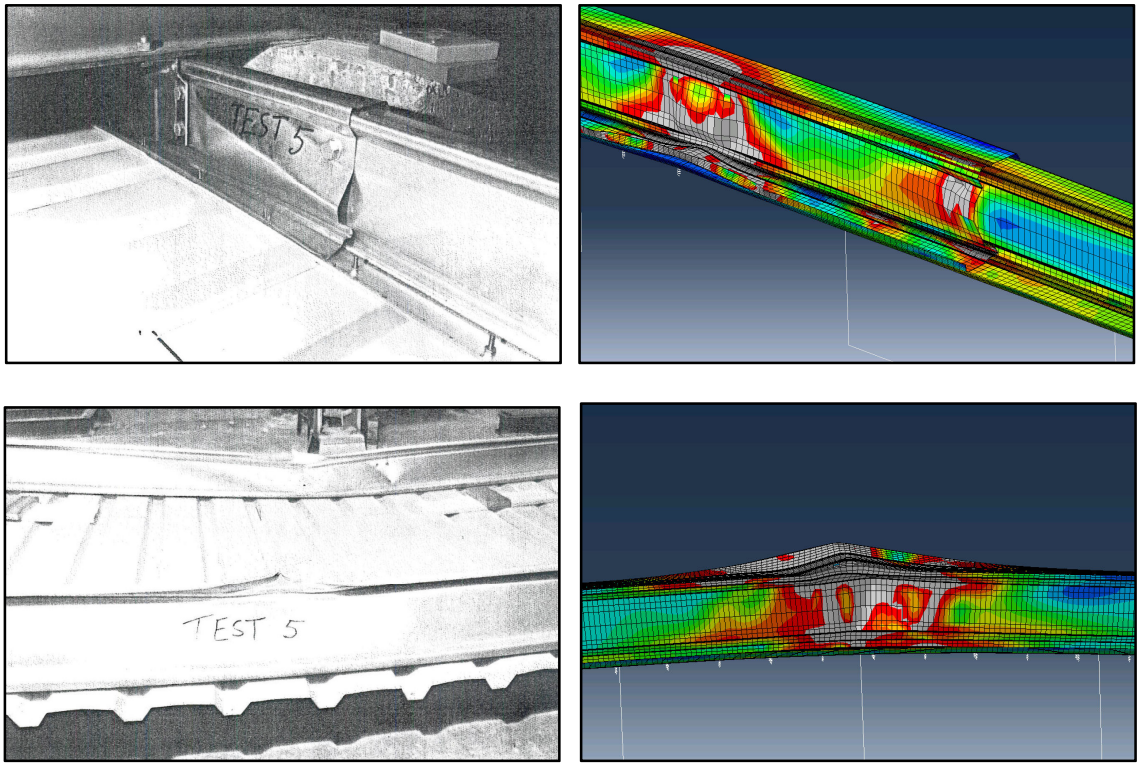


Figure 5.37: *Failure modes between 2-span sleeved uplift test 5 from Deakin (1991b) and FE model*

5.6. CONCLUDING REMARKS

In this chapter, three sleeved FE models including 3-point bending and 2-span arrangements subjected to gravity and uplift loading have been developed and validated against existing tests. Additional FE modelling parameters beyond those required for the bare sections discussed in Chapter 3, including sleeve material definitions and contact interactions and a nonlinear spring model to replicate the bolt connection, were all incorporated into the numerical models. Difficulties in simply modifying the solver type and loading application for 2-span systems were overcome by modelling a 4 tier whiffletree system that can distribute the loads from a single point load, and be solved using a static displacement control solver scheme with artificial damping. The FE models were validated against a total of 49 physical sleeve tests in terms of ultimate load carrying capacity, initial stiffness and failure models. Table 5.8 presents a summary of all validated sleeved models.

Table 5.8: *FE validation summary for 3-point bending and 2-span sleeved test arrangements*

Reference	Test type	Section Type	Number of tests	Mean	COV
Bryan and Davies (1980b) Leach (1990) Byran and Deakin (1989) Deakin (1991a, 1991b) Davies and Deakin (1992) Deakin and Melbourne (1997)	Test type – 7 3-point bending sleeve - no bolt slip	Zeta IB Zeta II Z1 / Z2	20 (14 repeats) 34 total	1.003	0.071
Bryan and Davies (1980b) Leach (1990) Byran and Deakin (1989) Deakin (1991a, 1991b)	Test type – 9 2-span gravity sleeved – no bolt slip	Zeta IB	9	0.970	0.068
Bryan and Deakin (1989) Deakin (1991a, 1991b)	Test type – 10 2-span uplift sleeved – no bolt slip	Zeta IB	6	1.002	0.056

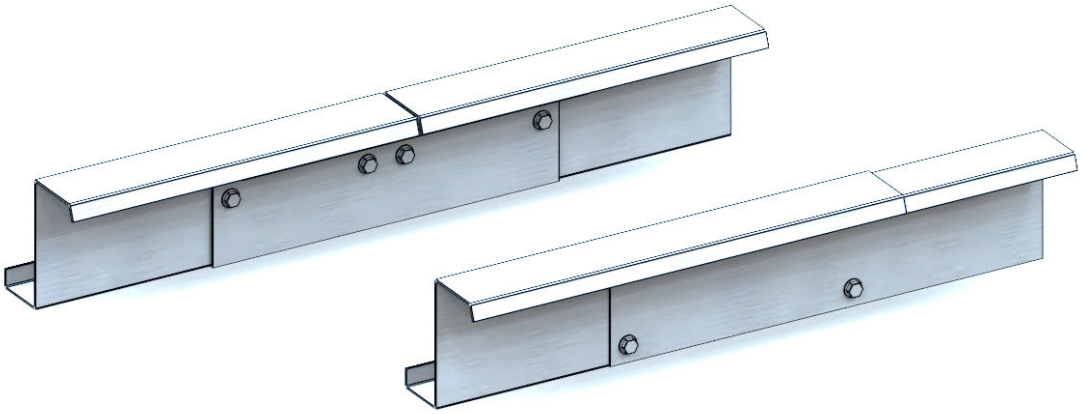
CHAPTER 6

SLEEVED SECTION PARAMETRIC STUDY AND DESIGN

6.1. INTRODUCTION

Cold-formed steel systems with lapped or slotted sleeved connections are alternatives to continuous 2-span purlin systems and exhibit different degrees of continuity (Figure 6.1), as introduced in Chapter 5. Lapped connections comprise two overlapped members with bolts connecting their webs. Sleeved connections utilise an additional section that covers the two adjoining members, with bolts connecting at their webs. Both connection types are highly favourable in practice since both types of connection are generally strategically placed over an interior support to provide additional moment and rotational capacities where the bending moments are at their largest, thus improving the overall structural efficiency. Sleeved and lapped systems tend to also provide quicker transportation and ease of construction compared with continuous purlin arrangements, owing to the shorter lengths and simpler purlin-rafter connections.

In this chapter, the validated sleeved section FE models developed in Chapter 5 have been extended to study the amount of moment redistribution for 2-span cold-formed steel sleeved systems subjected to gravity and uplift loading by means of parametric studies. A range of Zeta I, Zeta II and Zed cross-sections, sleeve lengths and span lengths and bolt arrangements were investigated to cover a wide range of purlin arrangements. The results from the parametric study were then used to propose design equations.



(a) (b)

Figure 6.1: *Joint geometry for (a) sleeved and (b) lapped connections*

6.2. DESIGN APPROACH FOR 2-SPAN SLEEVED SYSTEMS

For any statically-indeterminate 2-span system including those with sleeve arrangements shown in Figure 6.2, a design based on elastic principles would assume failure of the system once the cross-sectional moment capacity at the interior support $M_{support}$ is reached. However, allowing for redistribution of moments in the system by exploiting the unused moment capacity within the span M_{span} could result in a more efficient design. Full plastic redistribution can be achieved if the bending moment at the interior support, $M_{support}$ can be maintained through sufficiently large rotations that the moment in the span, M_{span} can develop into its full cross-sectional capacity. While the moment and rotation capacities for bare cold-formed steel members are limited by local and/or distortional buckling, determining the moment and rotational capacities for sleeved connections also requires knowledge of additional factors such as the connections. The flexural rigidity and strength of the sleeved connections are related to the cross-section geometry, sleeve length and bolt characteristics. Revision to the plastic mechanism

approach of EN 1993-1-3 (2006) can be made by recognising certain limitations in the interior support moment-rotation relationships and accepting that full redistribution may not be possible. In this case, some allowance must be made to the full plastic design procedure to ensure safe design.

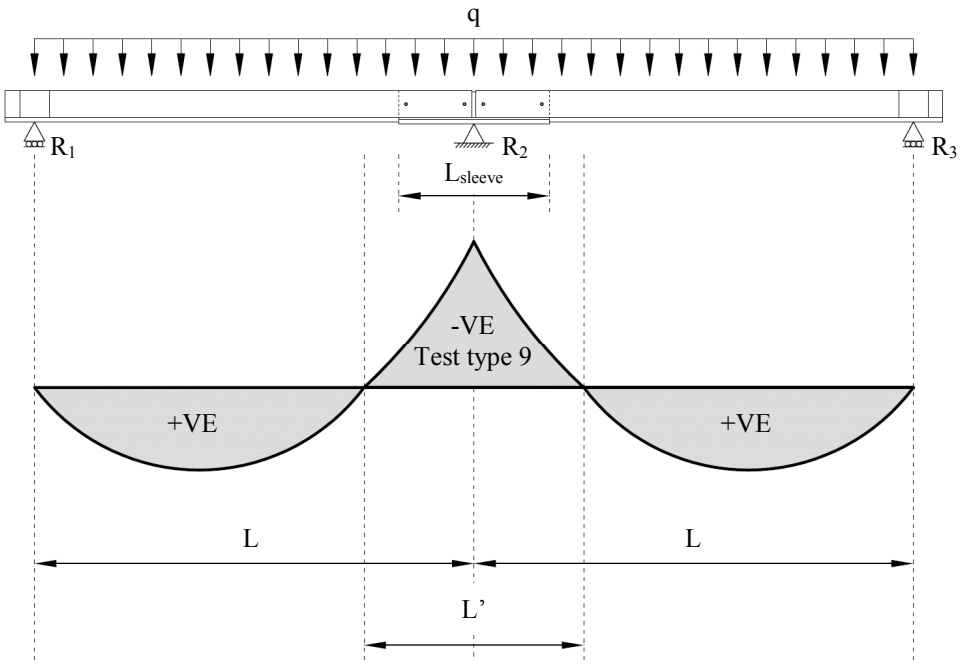


Figure 6.2: *2-span sleeved purlin arrangement*

6.3. PARAMETRIC STUDY – GRAVITY LOADING

6.3.1. Outline

In Section 6.3.2, the in-plane bending behaviour for cold-formed steel cross-sections with sleeved connections is investigated by conducting a single span parametric study. The developed FE models are then used to study the degree of moment redistribution for cold-formed steel 2-span sleeved purlin systems by analysing the results of 2-span FE models, developed using ABAQUS (2010). Zeta I, Zeta II and Zed cross-section types were chosen for the 2-span sleeved study. In general, the cross-section geometry for Zeta I and Zeta II comprised different top and bottom web and flange stiffener dimensions so that an identical section can be used as the sleeve. By ensuring the top and bottom flange lengths are not coincident and lip angles were off vertical, a sleeve section could be rotated by 180° so that it could fit inside itself. This allowed the use of

self-tapping screws for the sheeting and web bolts to be connected through both sleeve and purlin members. The section height h, top flange b_c, bottom flange b_t and nominal thickness t were varied to cover a large cross-sectional slenderness. A range of sleeve lengths L_{sleeve} and bolt configurations for the sleeve connection were considered. The location and dimensions of the intermediate stiffeners in the flanges and web for Zeta I and Zeta II sections were kept constant. Excluding the Zeta I intermediate stiffeners, the internal radii for all cross-sections were kept constant at 3 mm. For each cross-sectional shape, the top and bottom lip lengths and lip angles were unchanged. The bare cross-sectional slenderness $\bar{\lambda}_{cs}$ was defined as the square root of the ratio of the yield strength to the elastic buckling stress obtained from CUFSM (2006). For sleeved sections, the cross-sectional slenderness $\bar{\lambda}_{cs,s}$, was approximated by assuming the cross-section had double thickness (t_{sleeve} = 2t), which modifies the cross-sectional slenderness by a factor of about $1/\sqrt{2}$.

$$\bar{\lambda}_{cs,s} = \frac{1}{\sqrt{2}}\sqrt{\frac{M_y}{M_{cr}}} \tag{6.1}$$

6.3.2. Influence of sleeve length and bolt connection details

A series of moment gradient sleeved FE models (test type 7) covering a range of sleeve lengths from 600 mm to 2100 mm were simulated using ABAQUS 6.10 to investigate the rotational capacities for sleeved connections. The results were also compared against a bare section moment-rotation response subjected to the same loading conditions. A Zeta I 1/175_16 section was chosen for the study with a fixed span length L' of 3000 mm. The five different sleeve details for each bolt arrangement are illustrated in Figure 6.3, whilst Figure 6.4 shows the Zeta I 1/175_16 geometrical dimensions considered for this study. Similar to the rotation capacity study for bare sections discussed in Section 4.3.2.1, the definition for rotation capacity R is based on the moment-rotation behaviour:

$$R = \frac{\theta_{rot}}{\theta_y} - 1 \tag{6.2}$$

where θ_y is the elastic component of rotation upon reaching M_y and θ_{rot} is the limiting rotation at which the moment falls back below M_y. From Figure 6.5 it can be seen that the

central rotation θ_M is defined as the summation of the end rotations θ_1 and θ_2. θ_1 and θ_2 were calculated from longitudinal (z_1, z_2, z_3 and z_4) and vertical displacement (y_1, y_2, y_3 and y_4) measurements from the top and bottom web/flange junctions, separated by a distance d, from the FE analysis.

$$\theta_M = \theta_1 + \theta_2 \begin{cases} \theta_1 = \tan^{-1}\left(\dfrac{z_1 - z_2}{d - (y_2 - y_1)}\right) \\ \theta_2 = \tan^{-1}\left(\dfrac{z_3 - z_4}{d - (y_4 - y_3)}\right) \end{cases} \tag{6.3}$$

Whereas θ_y is straightforward to calculate for systems comprising a uniform cross-section ($\theta_y = M_yL/2EI$), this cannot be said for non-prismatic systems. The effective elastic stiffness of the sleeved system is difficult to determine using analytical methods due to the large number of unknown factors including: (i) the nonlinear restraint offered by the bolts which included bolt slip and bearing of the bolts, (ii) the contact interaction between the sleeve and bare section (normal and tangential friction) and (iii) the effectiveness of the sheeting. Nevertheless, a simplified approach to account for the change in stiffness offered by the additional sleeve section was assumed by introducing a single effective second moment of area for the sleeve region I_s. I_s was assumed to be constant over the entire length of the sleeve region and includes the stiffness of the connection. This permitted integration of the moment relationship expressed in terms of the distance from the end support x, into two separate parts: (i) from the end support to the edge of the sleeved section defined as length a and (ii) from the start of the sleeved region the midspan, defined a length (L'/2-a). By applying boundary conditions and enforcing continuity at the start of the sleeved region, the individual rotation and deflection relationships for the sleeved and bare sections could be obtained. The calculations are shown in Equations 6.4-6.11. The elastic moment-rotational tangent could then be derived by expressing the double end rotation in terms of midspan moment (PL/4) as stated in Equation 6.12. θ_y could then be easily deduced by substituting M_y into Equation 612.

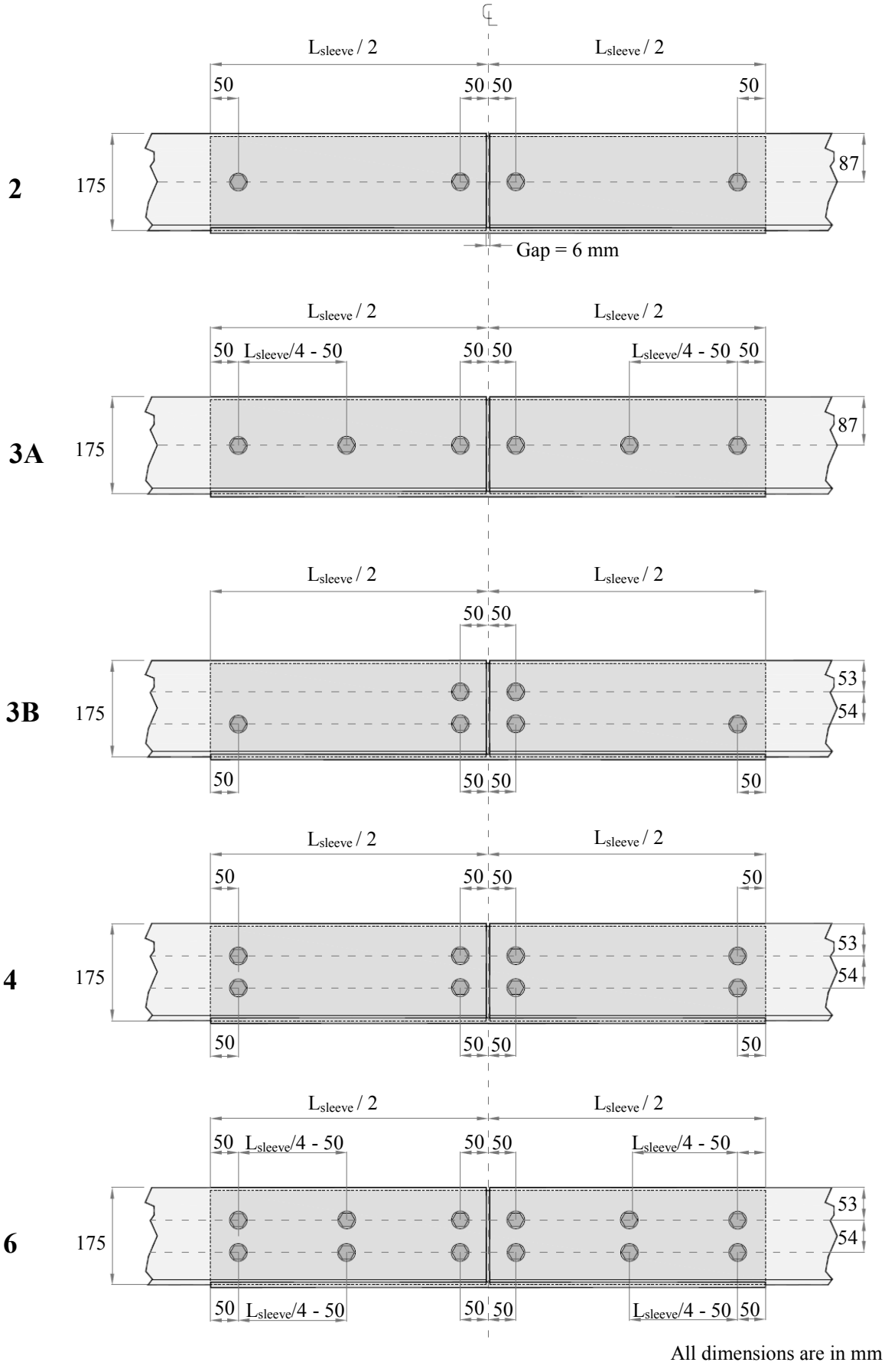


Figure 6.3: *Sleeve connection details for 1/175_16 and bolt arrangement numbers*

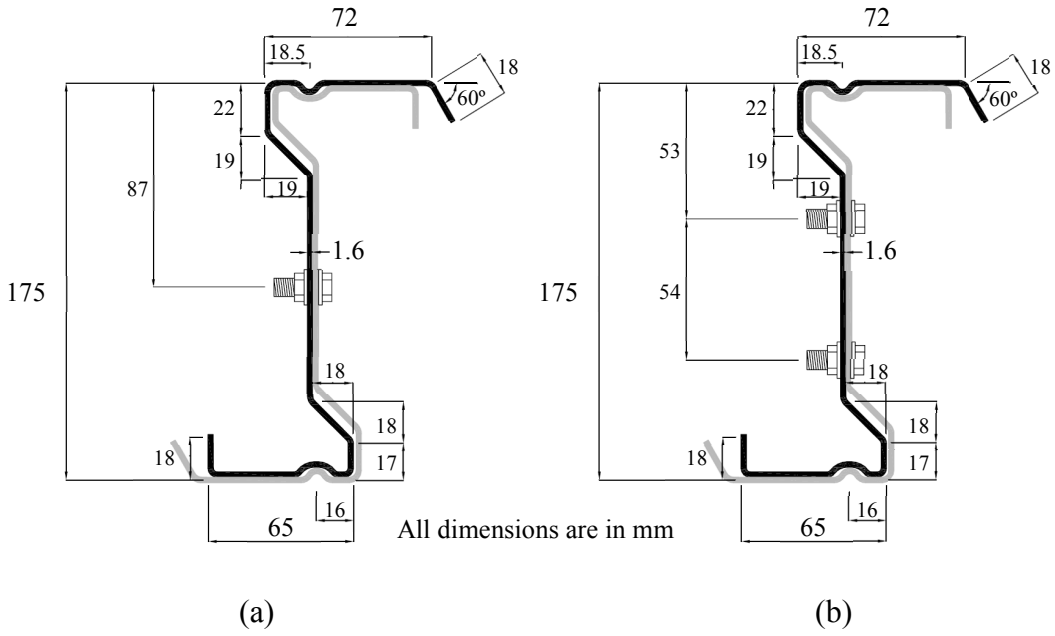


Figure 6.4: *Geometric dimensions for sleeve connection for 1/175_16 for (a) bolt arrangement 2 and 3A and (b) bolt arrangement 3B, 4 and 6*

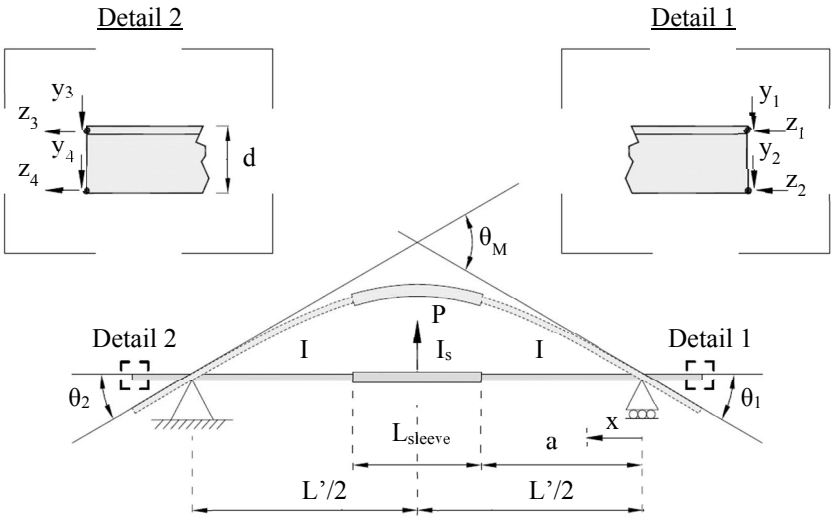


Figure 6.5: *Schematic setup for 3-point bending sleeved FE models*

Let the distance from the end support to the edge of the sleeve:

$$a = \frac{L' - L_{sleeve}}{2} \tag{6.4}$$

For $0 \le x \le a$

$$EIv'' = -\frac{Px}{2} \tag{6.5}$$

$$EIv' = -\frac{Px^2}{4} + A_1 \tag{6.6}$$

$$EIv = -\frac{Px^3}{12} + A_1x + B_1 \tag{6.7}$$

For $a \le x \le L'/2$

$$EI_sv'' = -\frac{Px}{2} \tag{6.8}$$

$$EI_sv' = -\frac{Px^2}{4} + A_2 \tag{6.9}$$

$$EI_sv = -\frac{Px^3}{12} + A_2x + B_2 \tag{6.10}$$

Applying boundary conditions to find constants A_1, A_2, B_1 and B_2:

i) $v(x = 0) = 0$ $\quad \therefore B_1 = 0$

ii) $v'(x = L'/2) = 0$ $\quad \therefore A_2 = \frac{PL'^2}{16}$

iii) $v'(x = a)$ using (6.3) = $v'(x = a)$ using (6.6) $\quad \therefore A_1 = \frac{Pa^2}{4} + \frac{PL'^2I}{16I_s} - \frac{Pa^2I}{4I_s}$

iv) $v(x = a)$ using (6.4) = $v(x = a)$ using (6.7) $\quad \therefore B_2 = \frac{Pa^3I_s}{6I} - \frac{Pa^3}{6}$

Therefore the maximum deflection at $x = L'/2$ using Equation 6.7 is

$$v_{max} = v(x = L'/2) = \frac{PL'^3}{48EI_s} + \frac{Pa^3}{6EI} - \frac{Pa^3}{6EI_s} \tag{6.11}$$

The sum of the two end rotations, expressed in terms of applied moment M through Equation 6.3 then becomes:

$$2\theta = \theta_M = M\left(\frac{2a^2}{L'EI} + \frac{L'}{2EI_s} - \frac{2a^2}{LEI_s}\right) \tag{6.12}$$

In order to quantify the stiffness and strength enhancement of the sleeved connections against bending, the initial effective flexural rigidity and moment resistance ratios α_i and γ_1 are defined as:

$$\alpha_i = \frac{(EI_s)_{05}}{EI} \tag{6.13}$$

$$\gamma_1 = \frac{M_{3sleeve}}{M_3} \tag{6.14}$$

where $M_{3sleeve}$ and M_3 are the maximum moment resistance from the single span FE analysis for test type 7 and 3 respectively. $(EI_s)_{05}$ is the initial effective flexural rigidity of the sleeved connection at 5% of the total load from the FE results. I_s was back calculated using Equation 6.12 by equating the $0.05M_{3sleeve}$ and its corresponding θ_M rotation. EI is the calculated flexural rigidity of the continuous section. It should be noted that all moment resistances are evaluated at the midspan (L'/2 = 1500 mm) for direct comparison.

Results from the sleeved rotation capacity study are presented in Table 6.1, with moment-rotation responses for each bolt arrangement and sleeve length illustrated in Figures 6.6-6.11. For sleeved systems with sleeve lengths of 600 mm ($L_{sleeve}/d \approx 3.5$), the initial slopes of the moment-rotation curves shown in Figure 6.6 were found to be more flexible than the equivalent continuous case (α_i less than unity). This was due to a discontinuity of load paths in the sleeved region. The lack of continuity meant that the systems with short sleeve lengths were more dependent on their bolt configurations; the beneficial effect of changing the bolt arrangements from a single row (bolt arrangement 2 and 3A) to two bolt rows (bolt arrangement 3B, 4 and 6) reduces the relative rotation between the sleeve and beam during bending. For example, an additional 3% in load carrying capacity as observed by increasing the number of bolts from 2 to 4, and a further 7.8% by introducing an additional 2 internal bolts, moving to bolt arrangement 6 from bolt arrangement 4. Figures 6.12 and 6.13 show the deformed stress profiles for L_{sleeve} = 600 mm for bolt arrangement 2 and 4 respectively. Local buckling was observed at the midspan of the sleeve section for both models and was also found to be a common failure mode for longer sleeve lengths. The lack of continuity meant that the moment resistance ratios for all models with L_{sleeve} of 600 mm were less than unity. As the sleeve length increases, the additional normal force between the sleeve and beam flanges due to an increased contact surface area meant that the connections 'lock' at lower relative rotations between the beam and sleeve sections. Significant loss of stiffness was observed for FE models with L_{sleeve} greater than 900 mm in the post-ultimate range. Due to the large rotations (and deflections), the buckling behaviour of the sleeve and beam flanges and

webs meant the sections were no longer in direct contact. Figure 6.14 illustrates the stress profiles for FE model with $L_{sleeeve}$ = 1500 mm and bolt arrangement 3A, and shows rotations between the sleeve and beam were less apparent than for models with sleeve lengths of 600 mm.

Tables 6.2-6.3 and Figure 6.15 show the relationship between α_i and γ_1 against L_{sleeve}/d for all bolt configurations. It was found that the increase in sleeve length was linearly proportional to the flexural rigidity ratio α_i. It was discovered that an L_{sleeve}/d ratio of approximately 8 ensured full flexural rigidity equal to that of the continuous case (α_i = 1). The moment capacity of the sleeved connection was also found to be highly sensitive for sleeve lengths shorter than L_{sleeve}/d ratios below 5, though full strength sleeves (γ_1 = 1) were observed for L_{sleeve}/d ratios of 3.5. The increase in moment capacity of L_{sleeve}/d ratios between 5 and 10 was roughly linearly proportional but diminishes beyond ratios of 10. The findings accord closely with the results of the lapped connection tests by Ho and Chung (2004), who suggested 'full stiffness' and 'full capacity' lap length-to-section depth ratios of 4 and 2 respectively. In general, the bolt arrangements were found to have less influence on the initial flexural rigidity and moment capacity than the change in sleeve length did. Minor improvements in moment capacity were observed by changing bolt arrangements from 1 single row to 2 rows. On average, bolt arrangements 4 and 6 gave 2.5 and 3 % higher moment capacities than bolt arrangements 2 and 3A respectively. The differences in the results between models with bolt arrangements 3B and 4 were minimal since the bolt at the free end of the sleeve for the bolt arrangements 3B cases was located in the compression part of the web. The rotation capacities for sleeved sections R_{sleeve} were calculated using Equations 6.2 and 6.12. Figure 6.16 shows that the sleeve connection provides a much greater rotation capacity than the bare section R_{bare}; this was found to increase roughly linearly with sleeve length. Further rotation capacity gains were observed for increases in the number of bolt rows from 1 to 2.

Table 6.1: *Comparison between M_3 and $M_{3sleeve}$ for section 1/175_16*

Test type	Description	Span length L' (m)	Sleeve length L_{sleeve} (m)	Bolt type[A]	M_3 or $M_{3sleeve}$ (kNm)	$M_{3sleeve}/M_3$ γ_1
3	Bare section - moment gradient	3.00	-	-	-12.652	-
7	Sleeved section - moment gradient	3.00	0.60	2	-10.173	0.804
7	Sleeved section - moment gradient	3.00	0.60	3A	-10.252	0.811
7	Sleeved section - moment gradient	3.00	0.60	3B	-10.325	0.816
7	Sleeved section - moment gradient	3.00	0.60	4	-10.411	0.823
7	Sleeved section - moment gradient	3.00	0.60	6	-11.256	0.890
7	Sleeved section - moment gradient	3.00	0.90	2	-12.567	0.993
7	Sleeved section - moment gradient	3.00	0.90	3A	-13.037	1.030
7	Sleeved section - moment gradient	3.00	0.90	3B	-13.154	1.040
7	Sleeved section - moment gradient	3.00	0.90	4	-13.307	1.052
7	Sleeved section - moment gradient	3.00	0.90	6	-14.017	1.108
7	Sleeved section - moment gradient	3.00	1.20	2	-13.732	1.085
7	Sleeved section - moment gradient	3.00	1.20	3A	-14.263	1.127
7	Sleeved section - moment gradient	3.00	1.20	3B	-14.316	1.132
7	Sleeved section - moment gradient	3.00	1.20	4	-14.354	1.135
7	Sleeved section - moment gradient	3.00	1.20	6	-14.462	1.143
7	Sleeved section - moment gradient	3.00	1.50	2	-14.539	1.149
7	Sleeved section - moment gradient	3.00	1.50	3A	-14.832	1.172
7	Sleeved section - moment gradient	3.00	1.50	3B	-14.785	1.169
7	Sleeved section - moment gradient	3.00	1.50	4	-14.924	1.180
7	Sleeved section - moment gradient	3.00	1.50	6	-14.813	1.171
7	Sleeved section - moment gradient	3.00	1.80	2	-15.029	1.188
7	Sleeved section - moment gradient	3.00	1.80	3A	-15.147	1.197
7	Sleeved section - moment gradient	3.00	1.80	3B	-15.017	1.187
7	Sleeved section - moment gradient	3.00	1.80	4	-15.027	1.188
7	Sleeved section - moment gradient	3.00	1.80	6	-15.028	1.188
7	Sleeved section - moment gradient	3.00	2.10	2	-15.325	1.211
7	Sleeved section - moment gradient	3.00	2.10	3A	-15.264	1.206
7	Sleeved section - moment gradient	3.00	2.10	3B	-15.187	1.200
7	Sleeved section - moment gradient	3.00	2.10	4	-15.204	1.202
7	Sleeved section - moment gradient	3.00	2.10	6	-15.172	1.199

A Refer to Figure 6.3 for bolt connection details

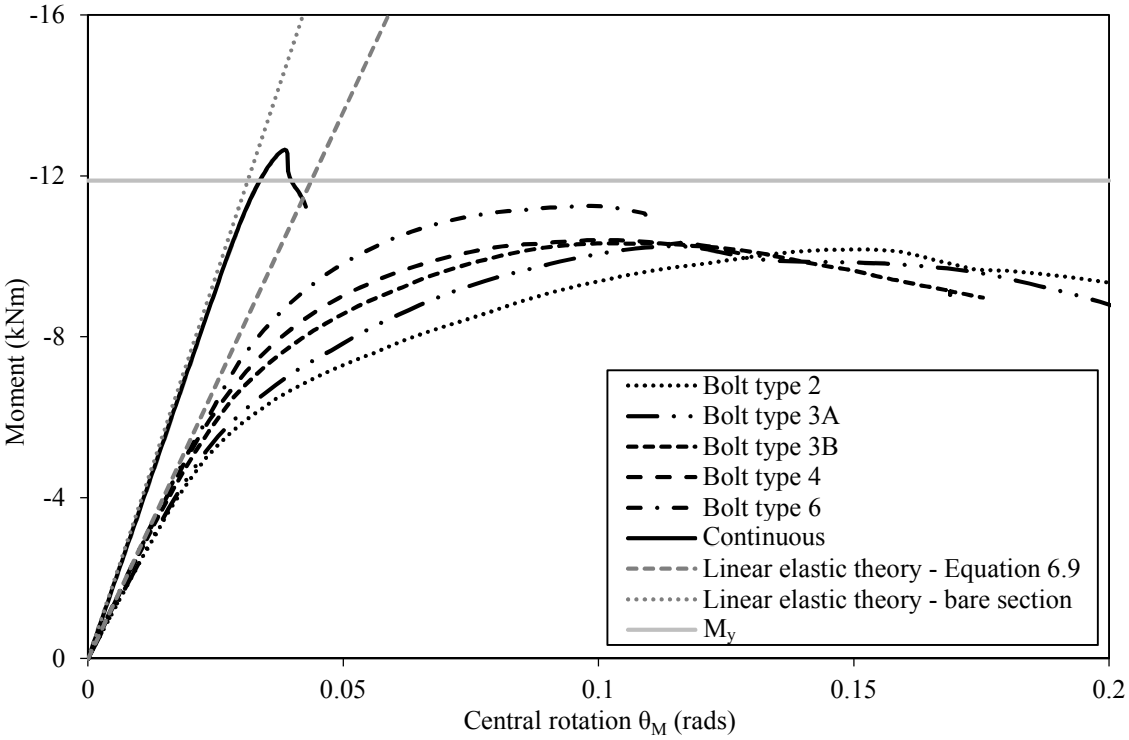


Figure 6.6: *Moment-rotation responses for $M_{3sleeve}$ 1/175_16 with L_{sleeve} = 600 mm for bolt arrangements 2, 3A, 3B, 4 and 6*

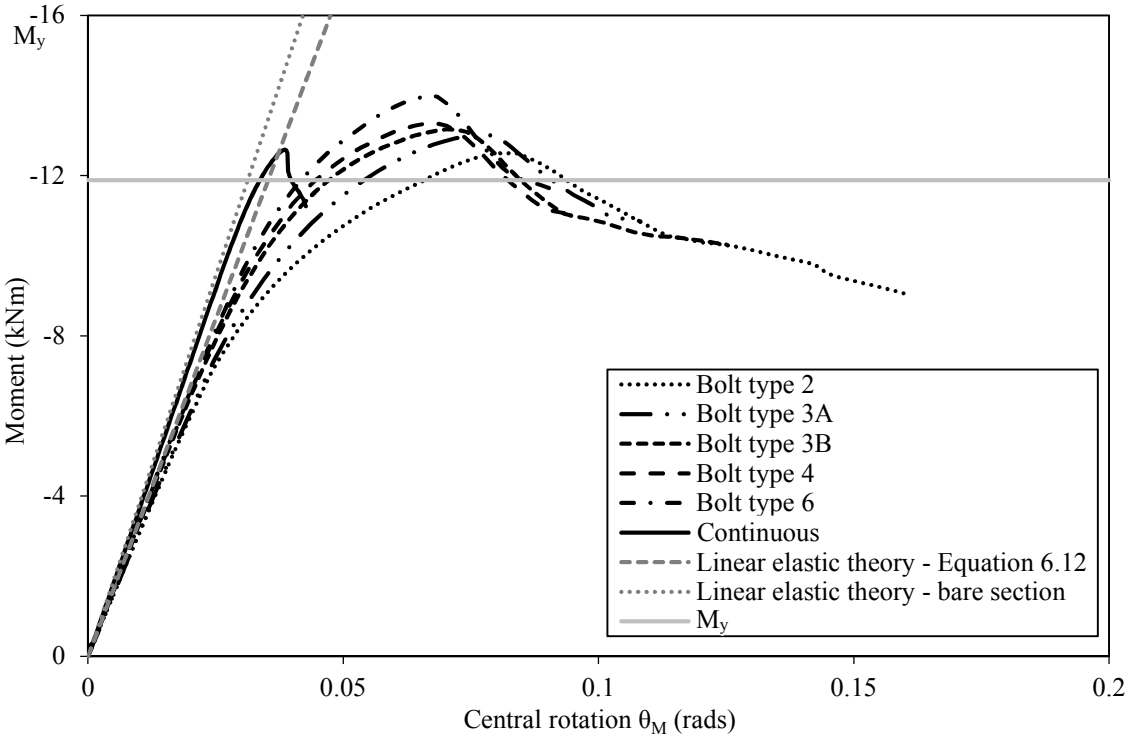


Figure 6.7: *Moment-rotation responses for $M_{3sleeve}$ 1/175_16 with L_{sleeve} = 900 mm for bolt arrangements 2, 3A, 3B, 4 and 6*

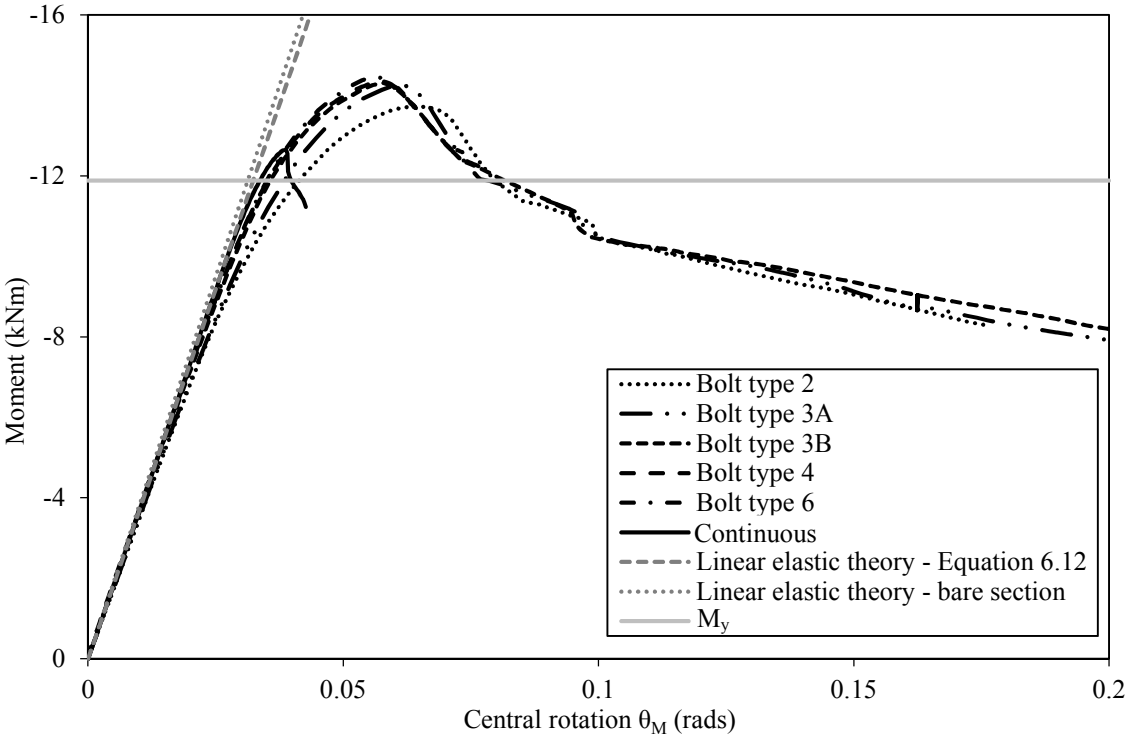


Figure 6.8: *Moment-rotation responses for $M_{3sleeve}$ 1/175_16 with L_{sleeve} = 1200 mm for bolt arrangements 2, 3A, 3B, 4 and 6*

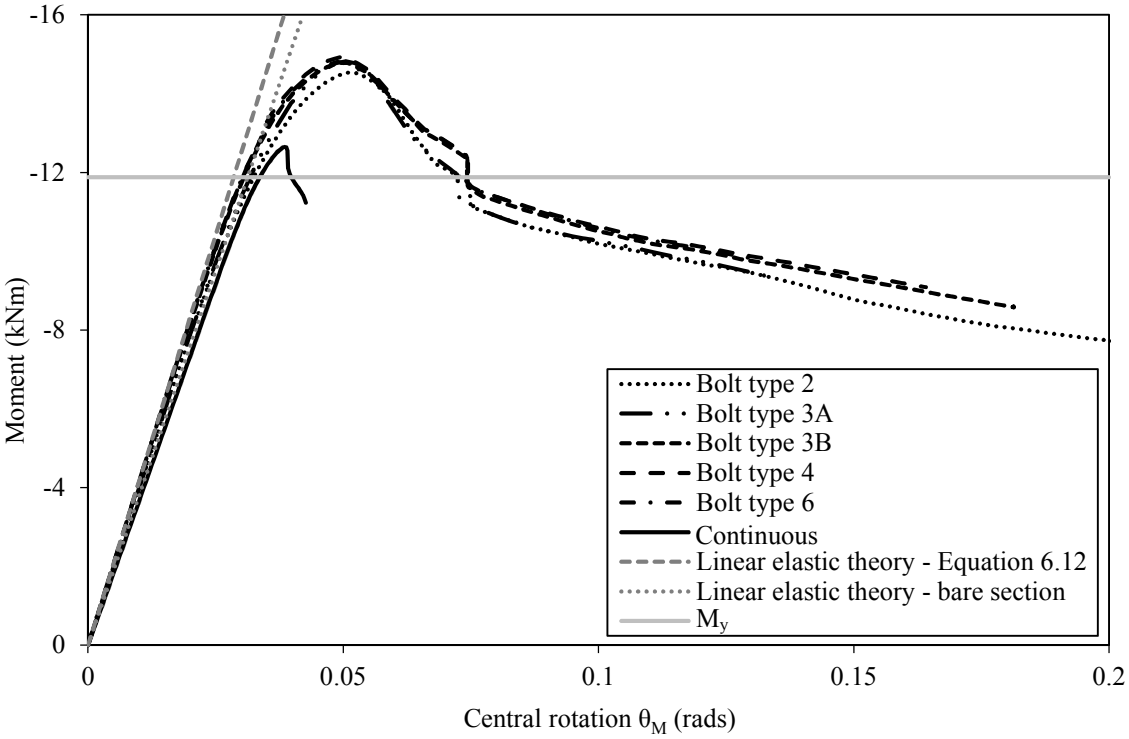


Figure 6.9: *Moment-rotation responses for $M_{3sleeve}$ 1/175_16 with L_{sleeve} = 1500 mm for bolt arrangements 2, 3A, 3B, 4 and 6*

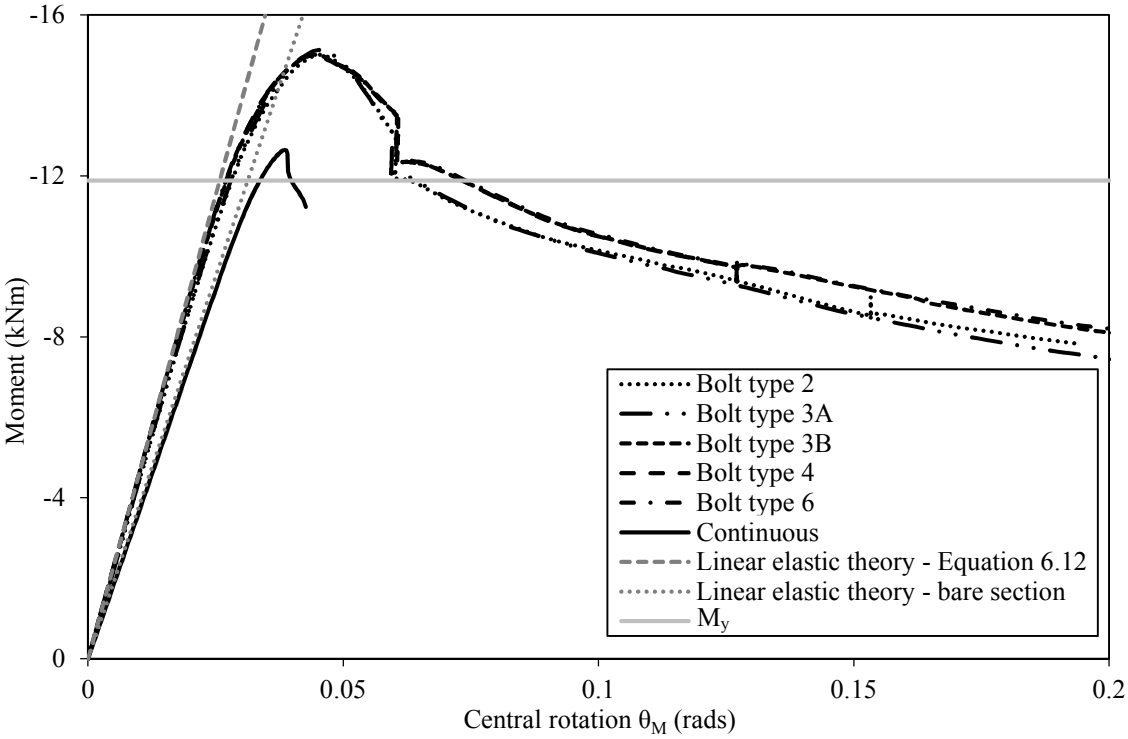


Figure 6.10: *Moment-rotation responses for $M_{3sleeve}$ 1/175_16 with L_{sleeve} = 1800 mm for bolt arrangements 2, 3A, 3B, 4 and 6*

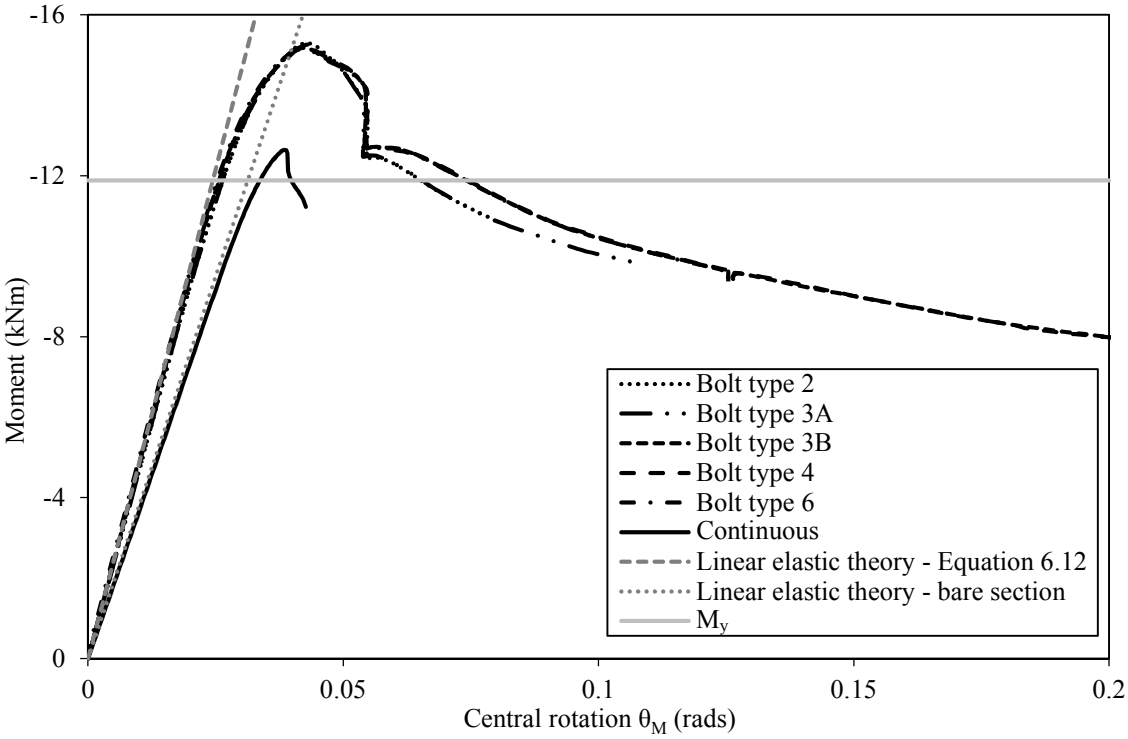


Figure 6.11: *Moment-rotation responses for $M_{3sleeve}$ 1/175_16 with L_{sleeve} = 2100 mm for bolt arrangements 2, 3A, 3B, 4 and 6*

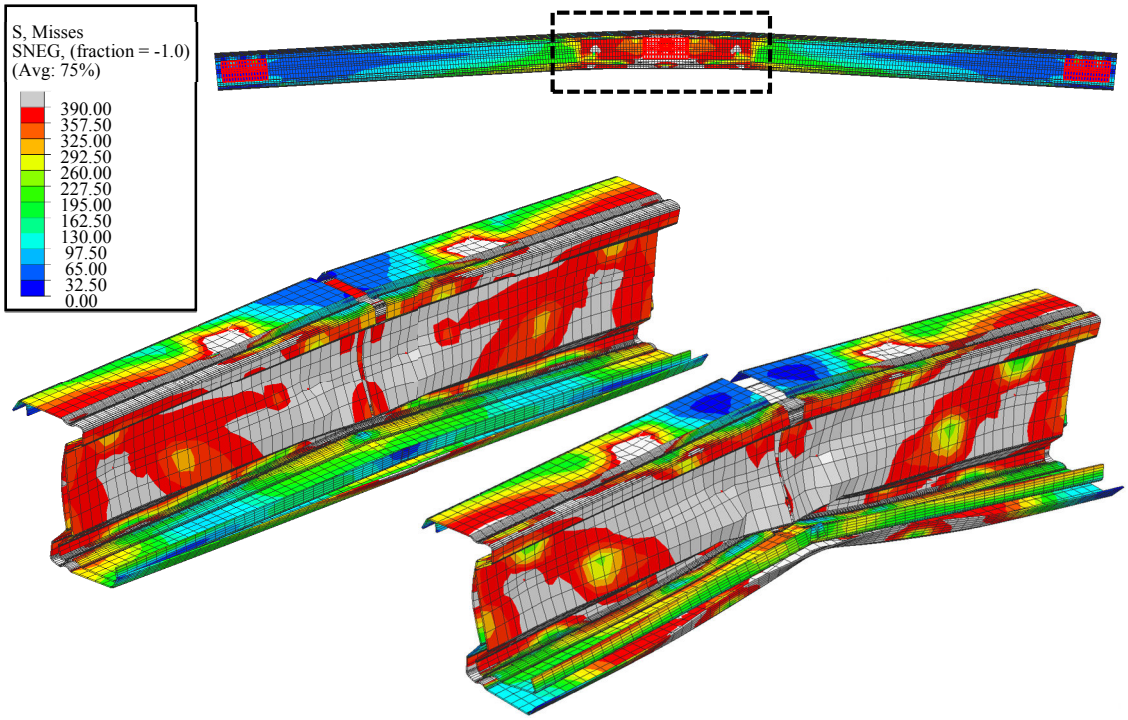


Figure 6.12: *Deformed stressed profile for $M_{3sleeve}$ 1/175_16 L' = 3000 mm L_{sleeve} = 600 mm with bolt arrangement 2 at (a) ultimate load and (b) post ultimate stage*

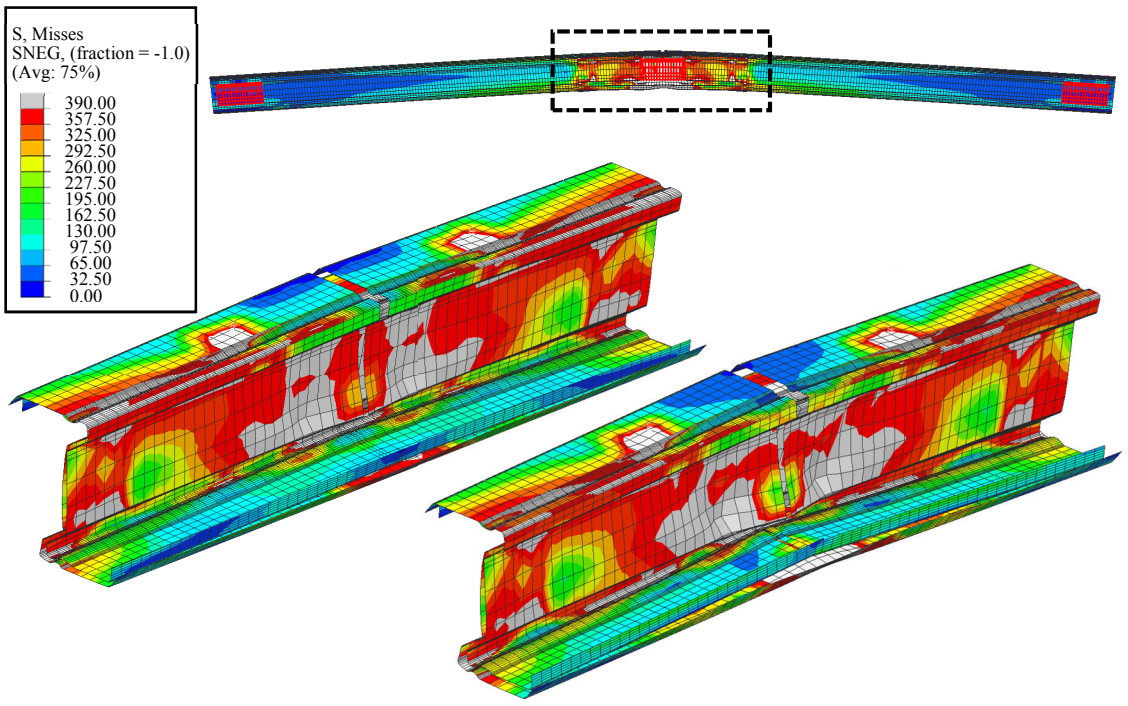


Figure 6.13: *Deformed stressed profile for $M_{3sleeve}$ 1/175_16 L' = 3000 mm L_{sleeve} = 600 mm with bolt arrangement 4 at (a) ultimate load and (b) post ultimate stage*

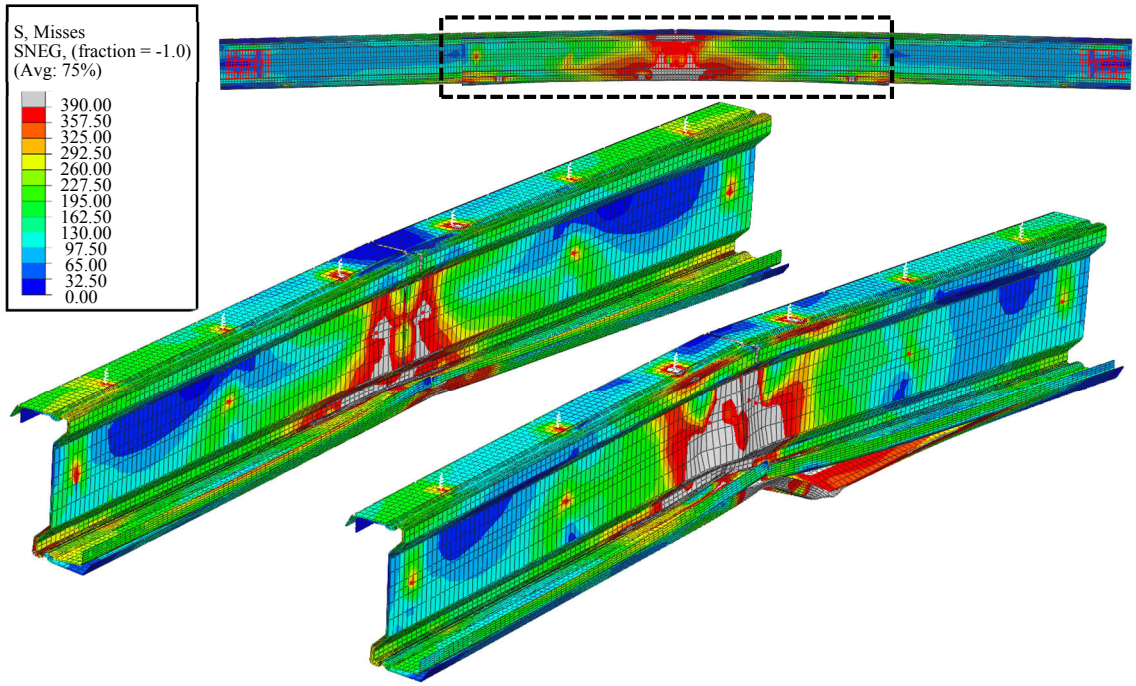


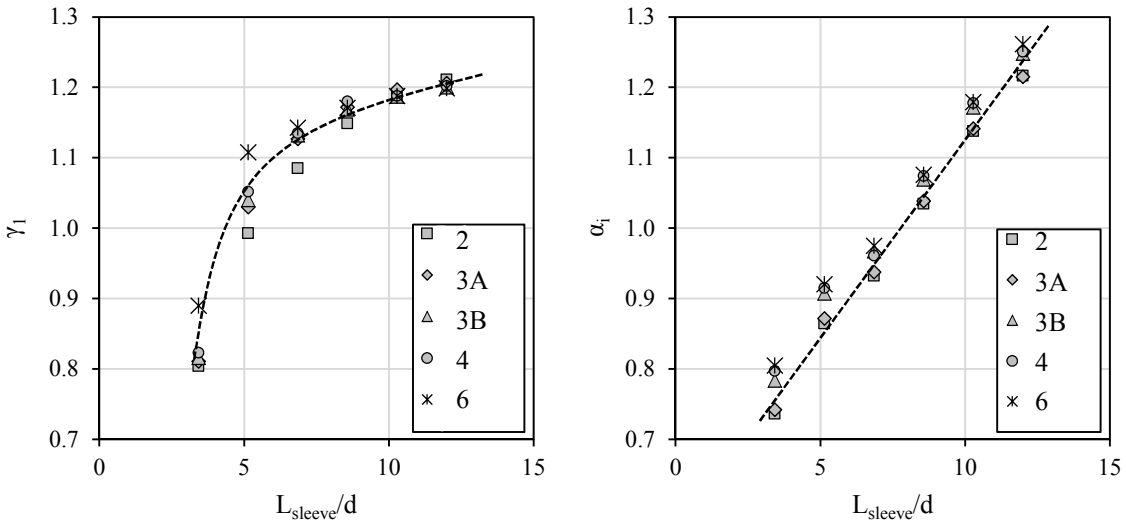
Figure 6.14: *Deformed stressed profile for $M_{3sleeve}$ 1/175_16 L' = 3000 mm L_{sleeve} = 1500 mm with bolt arrangement 3A at (a) ultimate load and (b) post ultimate stage*

Table 6.2: *Flexural rigidity ratios against sleeve length*

Bolt arrangement / L_{sleeve}/d	α_i				
	2	3A	3B	4	6
3.429	0.736	0.742	0.784	0.797	0.805
5.143	0.865	0.872	0.907	0.915	0.921
6.857	0.932	0.938	0.967	0.961	0.975
8.571	1.035	1.039	1.069	1.074	1.076
10.286	1.138	1.142	1.172	1.178	1.179
12.000	1.216	1.215	1.248	1.251	1.262

Table 6.3: *Moment resistance ratios against sleeve length*

Bolt arrangement / L_{sleeve}/d	γ_1				
	2	3A	3B	4	6
3.429	0.804	8.110	0.816	0.823	0.890
5.143	0.993	1.030	1.040	1.052	1.108
6.857	1.085	1.127	1.132	1.135	1.143
8.571	1.149	1.172	1.169	1.180	1.171
10.286	1.188	1.197	1.187	1.188	1.188
12.000	1.211	1.206	1.200	1.202	1.199



(a) Moment resistance ratio *(b) Flexural rigidity ratio*

Figure 6.15: (a) *Moment resistance and (b) flexural rigidity ratios for sleeved systems against different bolt configurations and sleeve length*

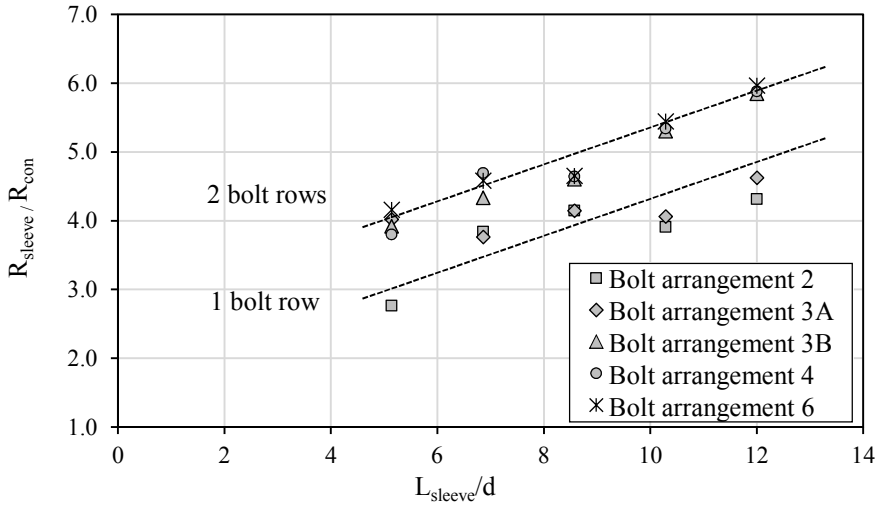


Figure 6.16: *Rotation capacity for sleeved sections*

6.3.3. Reference FE models

To study the buckling behaviour and amount of moment redistribution for each sleeved purlin system subjected to 16 evenly spaced gravity point loads, two additional single span FE models were analysed to provide useful reference moment values for $M_{support}$ and M_{span}: (i) The largest sagging moment M_{span} was compared with a single span FE model subjected to uniform bending M_1 (test type 1) and (ii) the largest hogging

moment $M_{support}$ was compared to the maximum moment in the single span sleeved FE model subjected to 3-point bending M_3 (test type 7). Figure 6.17 illustrates how the reference FE models are related to the gravity 2-span FE model. The largest sagging bending moment in the span region is elastically located at a distance 11L/32 from the end support, whereas the largest hogging moment is located at the interior support (x = L). M_{span} and $M_{support}$ were calculated by extracting the end support reaction R_1 from the 2-span sleeved FE model and applying Equations 6.10 and 6.11.

$$M_{span} = \frac{11R_1L}{32} - \frac{15PL}{256} \tag{6.10}$$

$$M_{support} = R_1L - \frac{PL}{2} \tag{6.11}$$

where P is the total applied load per span (= qL) and L is the length of each span. Unlike the continuous bare 2-span cases discussed in Chapter 4, where R_1 has an elastic magnitude of 3qL/8, R_1 for the 2-span sleeved systems is also dependent on L_{sleeve} and the effective stiffness of the connection detail. For similar reasons to that of the single span sleeve study discussed in the previous section, the 2-span sleeved system could be evaulated into two parts with different stiffness values of EI and EI_s. The full calcualtions are given in Appendix E. The elastic relationship for R_1 for sleeved systems could therefore be determined as follows:

$$R_1 = \frac{3}{8}\left[\frac{I(a/L) - I\left(L^3/a^3\right) - I_s(a/L)}{I - I_s - I\left(L^3/a^3\right)}\right]qL \tag{6.12}$$

The ultimate design load carrying capacity for a 2-span sleeved system q_{ult} with equal spans subjected to 16 evenly spaced point loads (16p) can be estimated by solving for q in Equation 6.13 providing the interior support moment $M_{support}$ and span moment M_{span} at q_{ult} are known.

$$M_{span} = \frac{\left(qL^2 + 2M_{support}\right)^2}{8qL^2} \tag{6.13}$$

The effect of the beneficially shaped parabolic moment diagram in the 2-span system was accounted for in test type 7 with an approximate linear moment gradient. For

simplicity, the beam length for the test type 7 equalled 0.5L, which is approximately the length of the hogging region from the 2-span models.

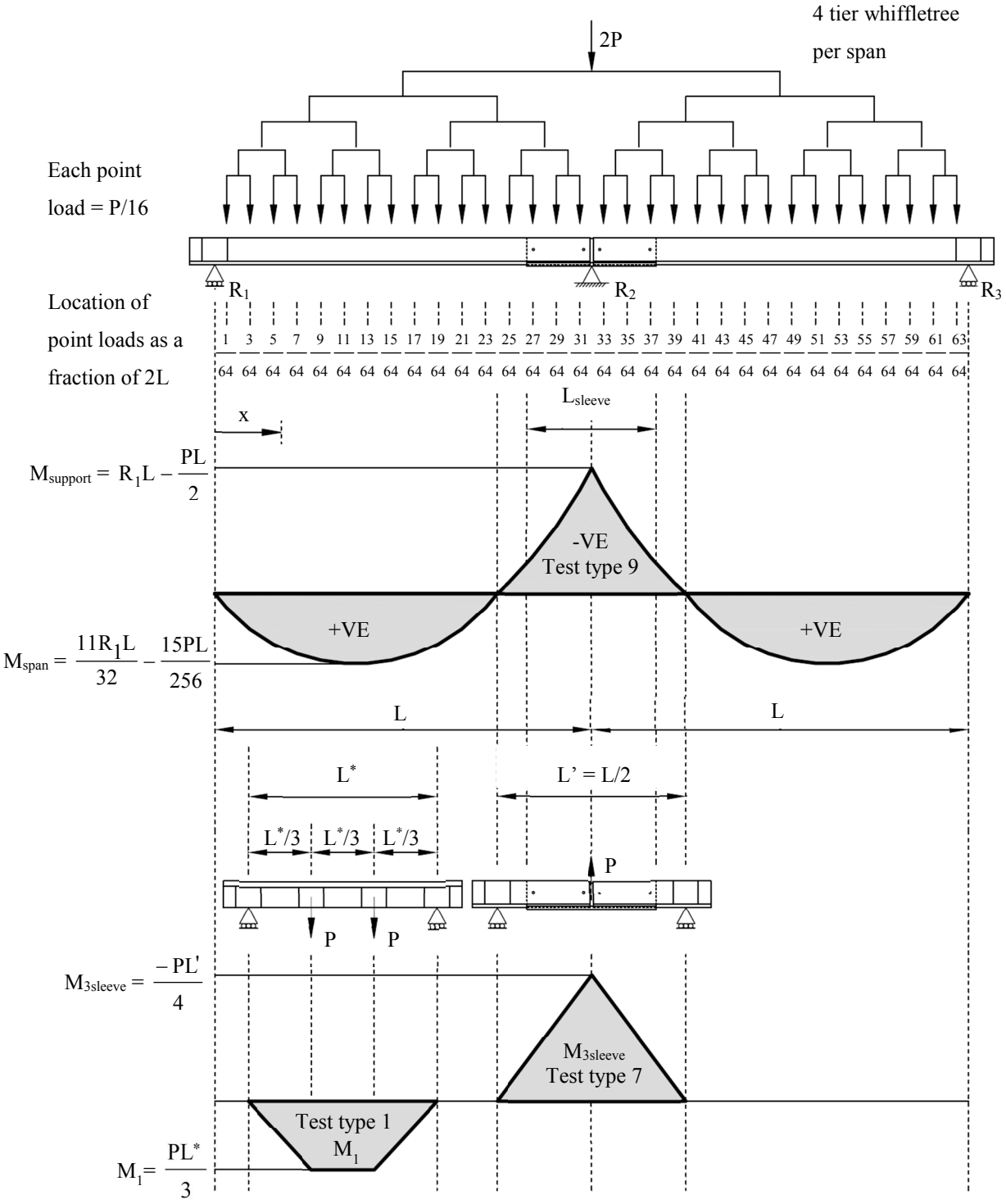


Figure 6.17: *Elastic bending moment diagram (BMD) for 2-span sleeved and reference M_1 and $M_{3sleeve}$ single span purlin systems*

6.3.4. Alpha framework for gravity loading

To investigate the degree of moment redistribution in 2-span sleeved purlin arrangements subjected to uniformly distributed gravity loading, parametric studies covering a total of 20 Zeta I, Zeta II and Zed sections, illustrated in Figures 6.18 and 6.19, were carried out using ABAQUS 6.10. Section depths and material thicknesses ranging from 125 mm to 200 mm and 1.0 mm to 2.5 mm were analysed to cover sections commonly used in practice. The parametric study comprised purlin systems with bolt arrangement 2, 3B and 4 sleeved connections and sleeve lengths ranging from 700 mm to 1000 mm, as shown in Figure 6.20. A full list of the geometrical dimensions and sleeve details is presented in Table 6.4. For the Zeta I and Zed cross-sections, three 2-span models subjected to 16 evenly spaced point loads by modelling a 4 tier whiffletree for span lengths of 4 m, 6 m and 8 m were simulated. To cover a larger span-to-depth ratio ranging from 20 to 64, 2-span sleeve models for Zeta II were analysed for span lengths of 6 m, 8 m, 10 m and 12 m. For each 2-span FE model, two additional single span reference FE models described in Section 6.3.3 were also simulated. In total, the study comprised 151 FE analyses. The same FE modelling assumptions discussed in Chapter 5 were adopted as a basis for the FE models used for this parametric study including: boundary conditions, S4R shell elements, 5 and 10% corner enhancements, plate stiffeners at loading points, 10 mm longitudinal mesh density, two-spring model for the sheeting, nonlinear springs to model the bolt connections and hard surface to surface contact definition for test type 7 and 9.

Apart from different geometrical dimensions tabulated in Table 6.1, the Young's modulus, 0.2% proof stress $\sigma_{0.2}$ and fastener spacing (spacing of the translational springs) were kept constant at 210 GPa, 390 N/mm^2 and 250 mm respectively. All FE models for this study adopted the same compound Ramberg-Osgood material model as given by Equations 3.1 and 3.2 (Gardner and Ashraf 2006) and assumed $\sigma_{1.0}$ to be proportional to $\sigma_{0.2}$ by applying Equation 3.5. The geometrical imperfections for the FE models were applied by manually fitting the local and distortional buckling shapes from CUFSM into the individual sagging and hogging regions in a harmonic manner with periods equalling their individual half-wave lengths. The imperfections for the sleeve were interpolated from the neighbouring beam so that the imperfect geometry for the sleeve and beam sections was made parallel. The imperfection magnitudes were kept constant at 0.229t

and 0.099t for distortional and local buckling respectively. The 2-span sleeved and test type 7 FE analyses were conducted using the general static solver with artificial stabilization (*STATIC, STABILIZE) by applying a displacement at the top of the whiffletree, whilst the modified Riks method was adopted for the reference single span analyses test (type 1).

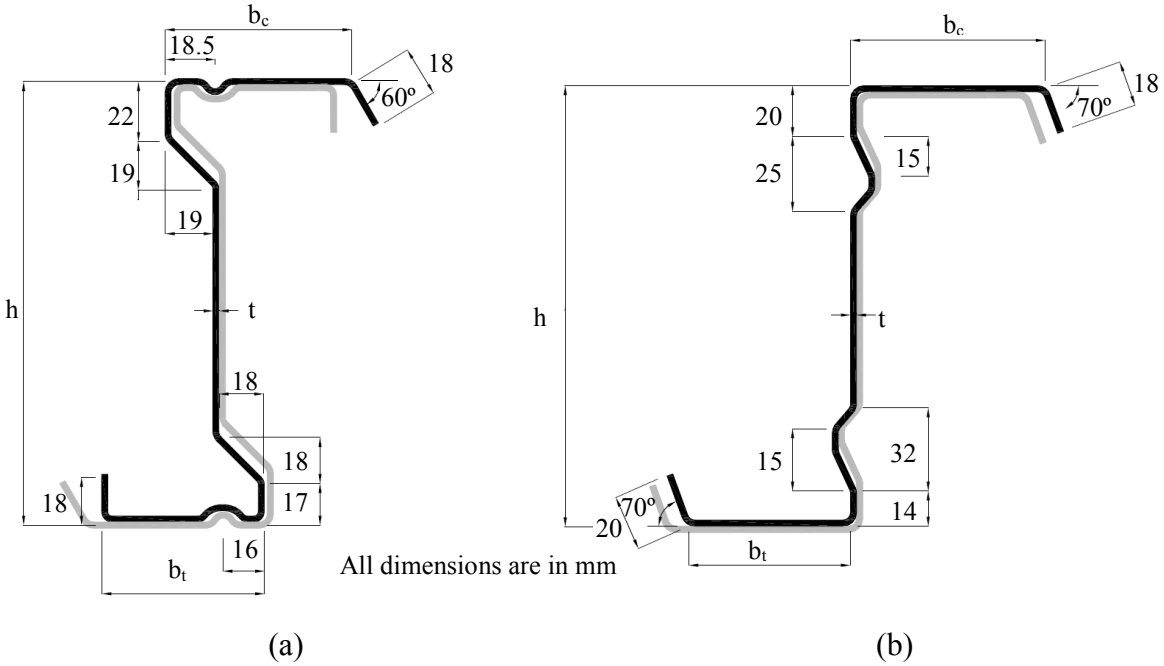


Figure 6.18: *Definition of cross-sectional dimensions for (a) Zeta I and (b) Zeta II sleeved sections*

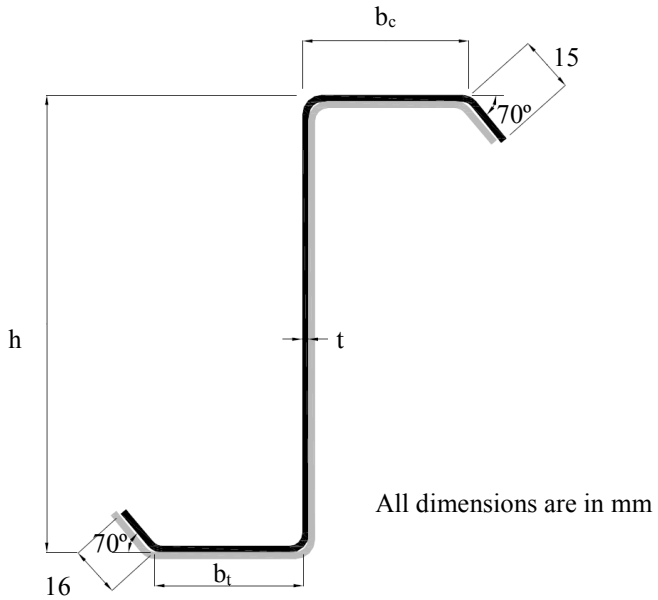


Figure 6.19: *Definition of cross-sectional dimensions for Zed sleeved sections*

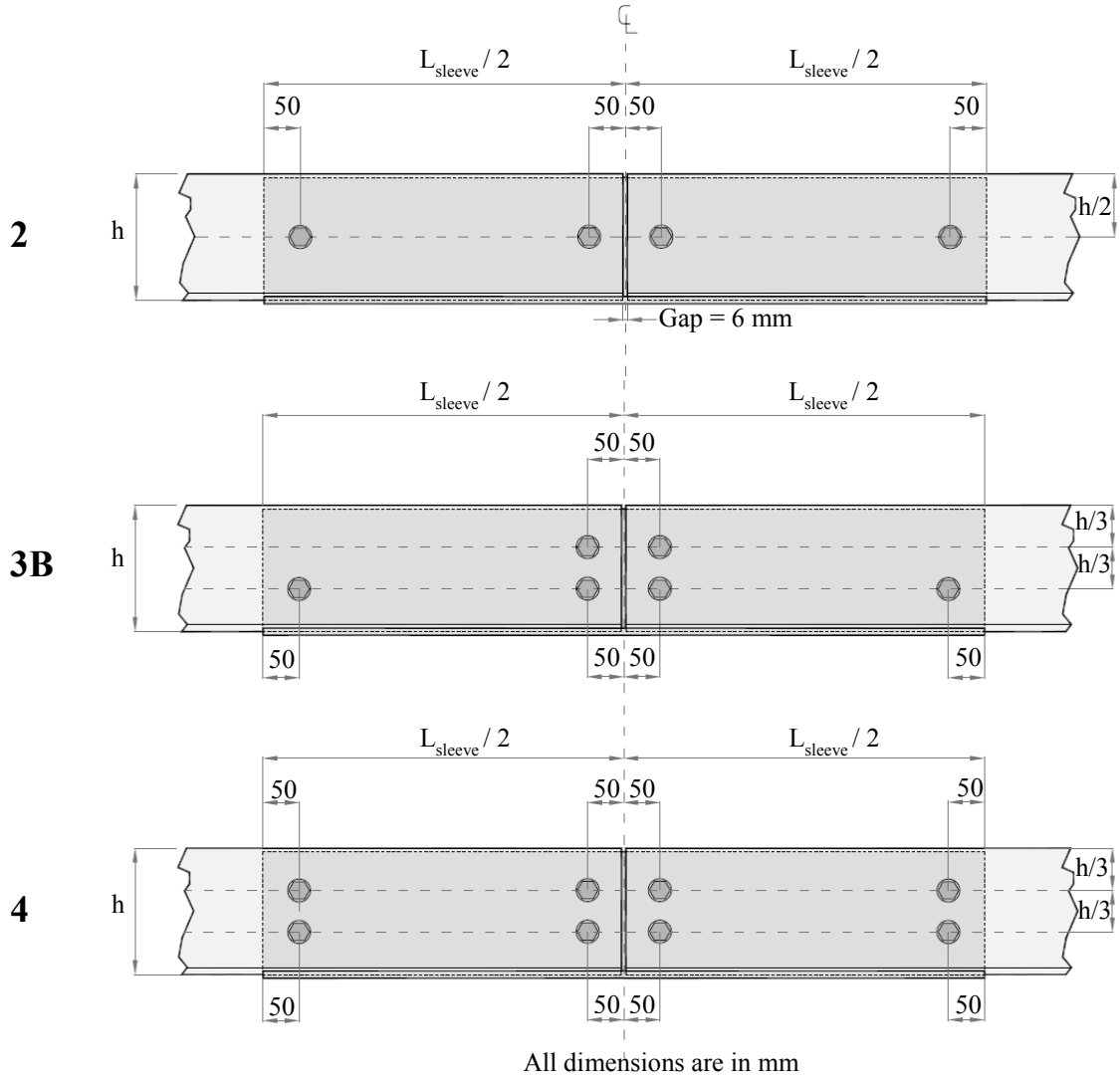


Figure 6.20: *Definition of sleeve details for the 2-span parametric study*

Table 6.4: *List of dimensions for Zeta I, Zeta II and Zed sections*

Section Type[A]	Section reference	Bolt type[B]	Sleeve length L_{sleeve} (mm)	Top flange b_c (mm)	Bottom flange b_t (mm)	Height h (mm)	Thickness t (mm)	$\overline{\lambda}_{cs,s,-ve}$
Zeta I	1/125_20	2	700	60	50	125	2.0	0.469
Zeta I	1/125_16	2	700	60	50	125	1.6	0.508
Zeta I	1/125_13	2	700	60	50	125	1.3	0.600
Zeta I	1/175_16	2	980	72	65	175	1.6	0.653
Zeta I	1/200_16	3B	1000	72	65	200	1.6	0.657
Zeta I	1/150_15	2	820	72	65	150	1.5	0.672
Zeta I	1/200_13	3B	1000	72	65	200	1.3	0.739
Zeta I	1/175_10	2	980	72	65	175	1.0	0.848
Zeta II	2/225_25	4	860	78	68	225	2.5	0.610
Zeta II	2/285_25	4	1000	78	68	285	2.5	0.668
Zeta II	2/285_20	4	1000	78	68	285	2.0	0.769
Zeta II	2/225_14	4	860	78	68	225	1.4	0.845
Zeta II	2/245_15	4	900	78	68	245	1.5	0.866
Zeta II	2/265_15	4	960	78	68	265	1.5	0.885
Zed	Z/125_20	4	700	55	45	125	2.0	0.495
Zed	Z/200_25	4	700	58	49	200	2.5	0.537
Zed	Z/125_14	4	700	55	45	125	1.4	0.612
Zed	Z/155_15	4	700	58	49	155	1.5	0.661
Zed	Z/170_14	4	700	58	49	170	1.4	0.713
Zed	Z/200_13	4	700	58	49	200	1.3	0.806

A Refer to Figures 6.18 and 6.19 for cross-sectional dimension details

B Refer to Figure 6.20 for bolt details

6.3.4.1. Moment redistribution comparison between 2-span sleeved and continuous systems

The 2-span 1/200_16 L = 6m FE model was chosen as an example to illustrate the typical moment redistribution behaviour for slender sleeved arrangements. By using Equation 6.1, the chosen section has a sleeved cross-sectional slenderness value $\overline{\lambda}_{cs,s,-ve}$ of 0.657, which is typical of the more slender cross-sections in this study. The applied load q, M_{span} and $M_{support}$ versus vertical displacement relationships, as well as tabulated results, are given in Figure 6.21 and Table 6.5 respectively. The (approximately) uniform applied load q was calculated by dividing the point load at the top of the whiffletree P by its span length. The 2-span moment and load-displacement responses obtained from the

FE analysis were evaluated using the same 4 discretized stages outlined in the continuous 2-span study in Section 4.3.4.1. Observation of the sleeve response indicated that the system behaved in a similar fashion to the slender continuous arrangements since the interior support moment reduced before the ultimate load of the system was reached. Thus, designing such a sleeve system assuming full moment redistribution and no drop-off in capacity could lead to unsafe design.

To study further the moment redistribution, the behaviour of chosen example sleeved section was compared against the continuous 1/200_16 L = 6m 2-span FE model previously considered in the 2-span parametric study of Chapter 4. The corresponding single span moment-rotation M_3 and $M_{3sleeve}$, and 2-span moment-displacement responses are compared in Figures 6.22 and 6.23. Figures 6.24 and 6.25 show the different deformed stress plots for the sleeve and continuous 2-span arrangements at designated load levels. It should be noted that both load and moment-displacement responses were evaluated for the same vertical deflection for direct comparison. The initial stages of loading for the sleeved case, the span and support regions exhibited the anticipated elastic response. Unlike the continuous 2-span cases, where peak interior support moment was estimated by single span reference capacity M_3, the additional moment capacity offered by the sleeved connection at the interior support meant $M_{support}$ from the 2-span sleeve system was able to attain a higher bending moment at the end of stage 2. It is clear from Table 6.5 and Figure 6.21 that the moment capacity from single span sleeved connection $M_{3sleeve}$ can accurately predict this largest support moment; the mean value of $M_{support}/M_{3sleeve}$ at the end of stage 2 was found to be 0.979. Differences between the 2-span sleeved and continuous cases were found by comparing their interior support moment reductions at ultimate load. Since the bare 1/200_16 cross-section is slender in nature ($\bar{\lambda}_{cs,-ve}$ of 0.930) with a limited rotation capacity at the support region, the value of the interior support moment at ultimate load for the continuous case was found to be relatively low at $0.645M_3$. In comparison, $M_{support}$ from the sleeved system only reduced to $0.91M_{3sleeve}$. This smaller reduction was due to a higher rotation capacity, as shown in Figure 6.21. Comparing deformed stress plots at the interior support for the sleeved and continuous beams (Figures 6.24 and 6.25 a, b, d and e), it can be seen that the deformations and rotations at the sleeve were restricted by contact of the sleeve and beam flanges and webs, whereas for the continuous case, the flanges and compressive parts of the web attract large stresses which triggered localised softening sooner. The change of the interior

support condition from continuous to a sleeved connection did not change the buckling mode in the span region; local/distortional buckling in the span was common for both 2-span arrangements as shown in Figures 6.24 and 6.25 c and f. Since all sleeve connections in the 2-span parametric study comprise of L_{sleeve}/d ratios of at least 5.5, 5.6 and 3.5 for bolt arrangements 2, 3B and 4 respectively, the sleeved 2-span systems consistently gave a lower $M_{support}$ reduction at ultimate load compared to the continuous case.

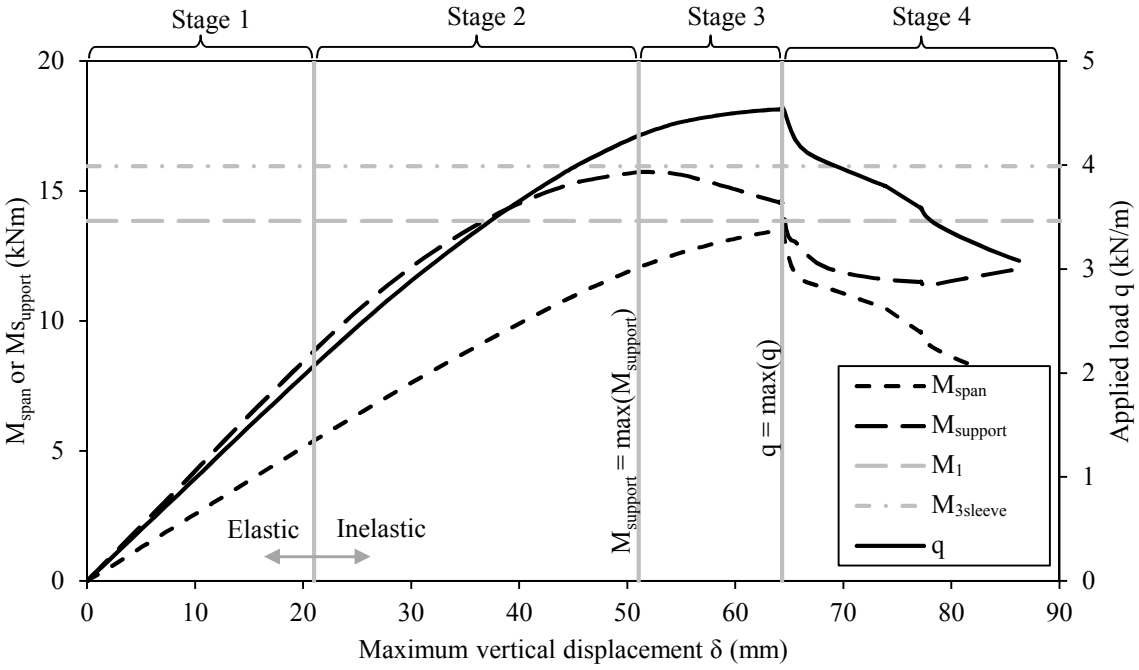


Figure 6.21: *Applied load q, $M_{support}$ and M_{span} vs. maximum deflection δ for sleeved 2-span 1/200_16 L = 8 m FE model*

Table 6.5: *Moment comparisons between 2-span sleeved and M_1 and $M_{3sleeve}$ FE models for 1/200_16 L = 6000 mm*

Stage	Applied load q (kN/m)	M_{span} (kNm)	$M_{support}$ (kNm)	M_1 (kNm)	$M_{3sleeve}$ (kNm)	M_{span}/M_1	$M_{support}/M_{3sleeve}$
2	4.286	12.148	-15.734	13.852	-15.958	0.877	0.986
3	4.535	13.487	-14.577			0.974	0.913

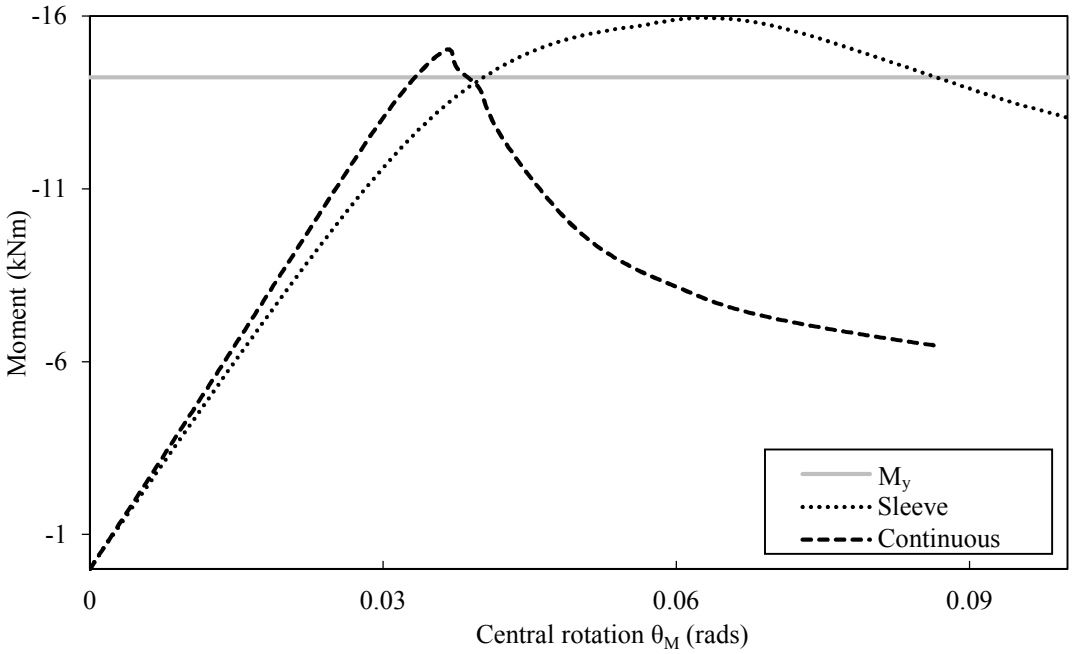


Figure 6.22: *$M_{3sleeve}$ and M_3 moment-rotation responses for 1/200_16 L' = 3000mm*

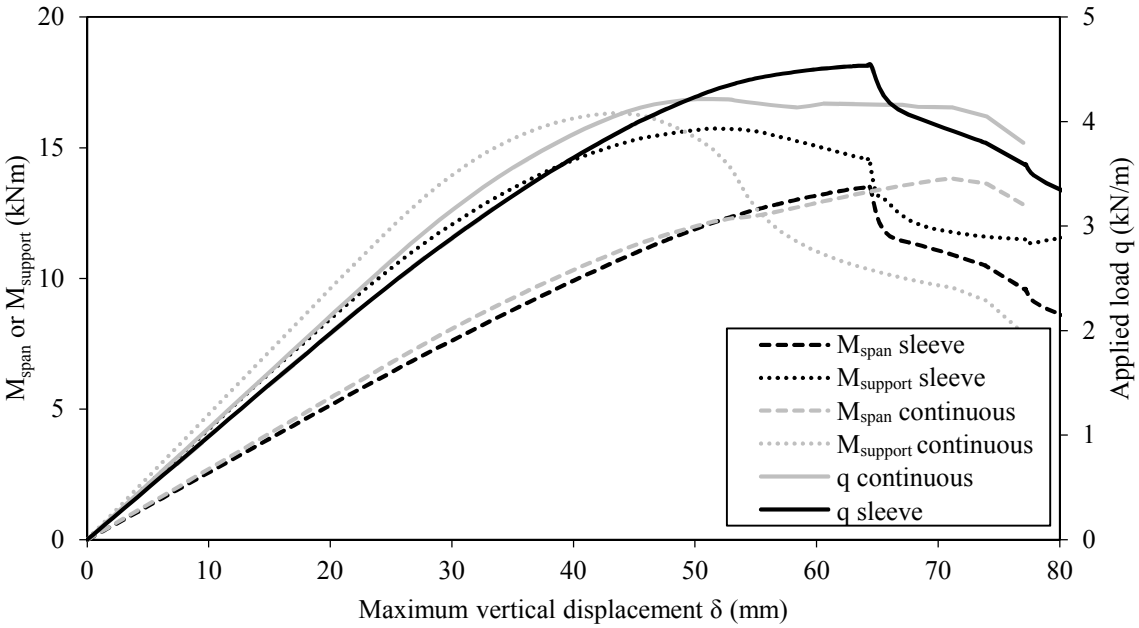


Figure 6.23: Appli*ed load q, $M_{support}$ and M_{span} versus maximum deflection δ for 1/200_16 L = 6 m sleeved and continuous 2-span FE models*

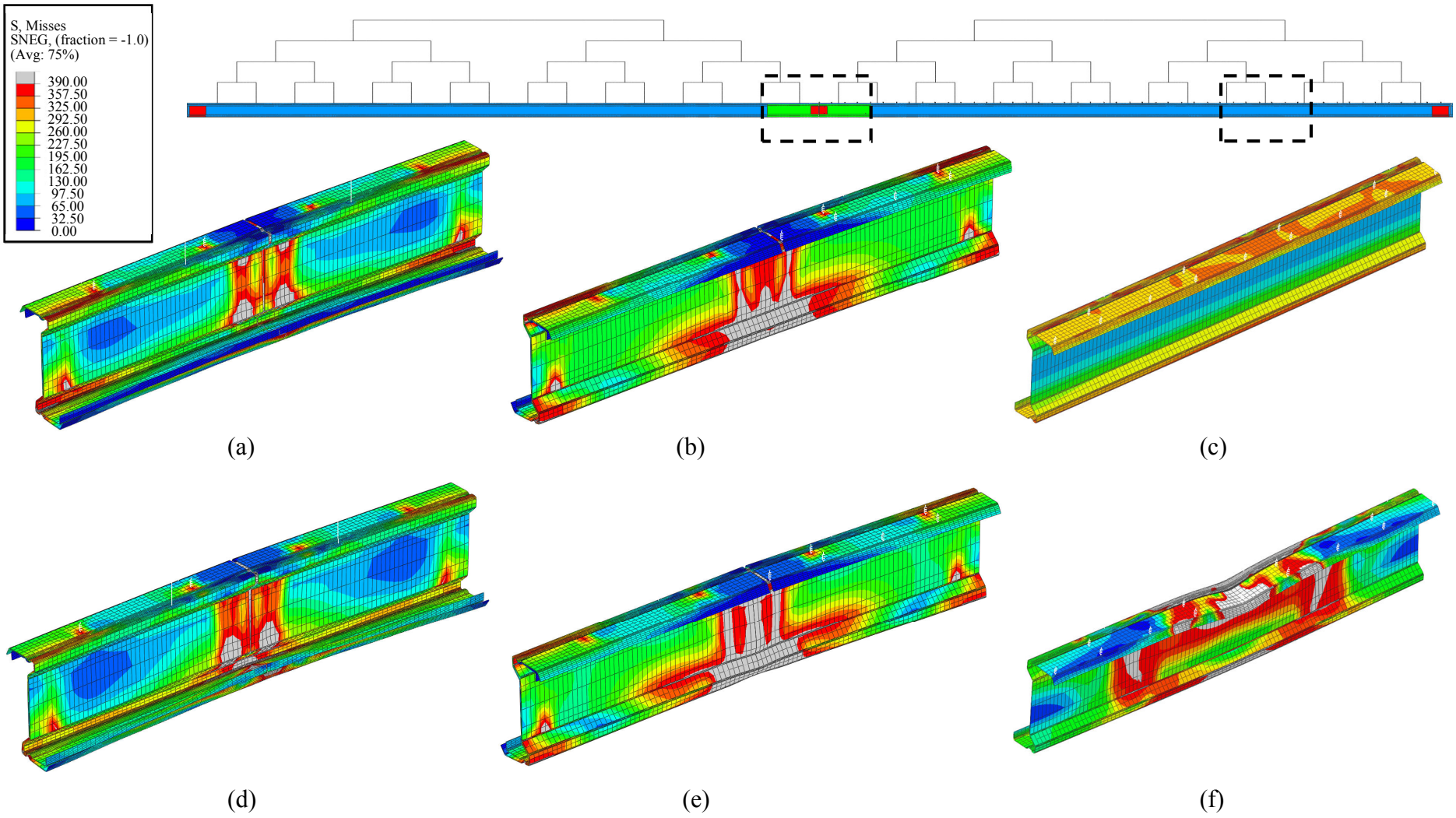


Figure 6.24: *Deformed stress profiles for 1/200_16 2-span sleeved FE model at stage 2 and ultimate load for the interior support (a, b and d, e) and span (c and f) regions*

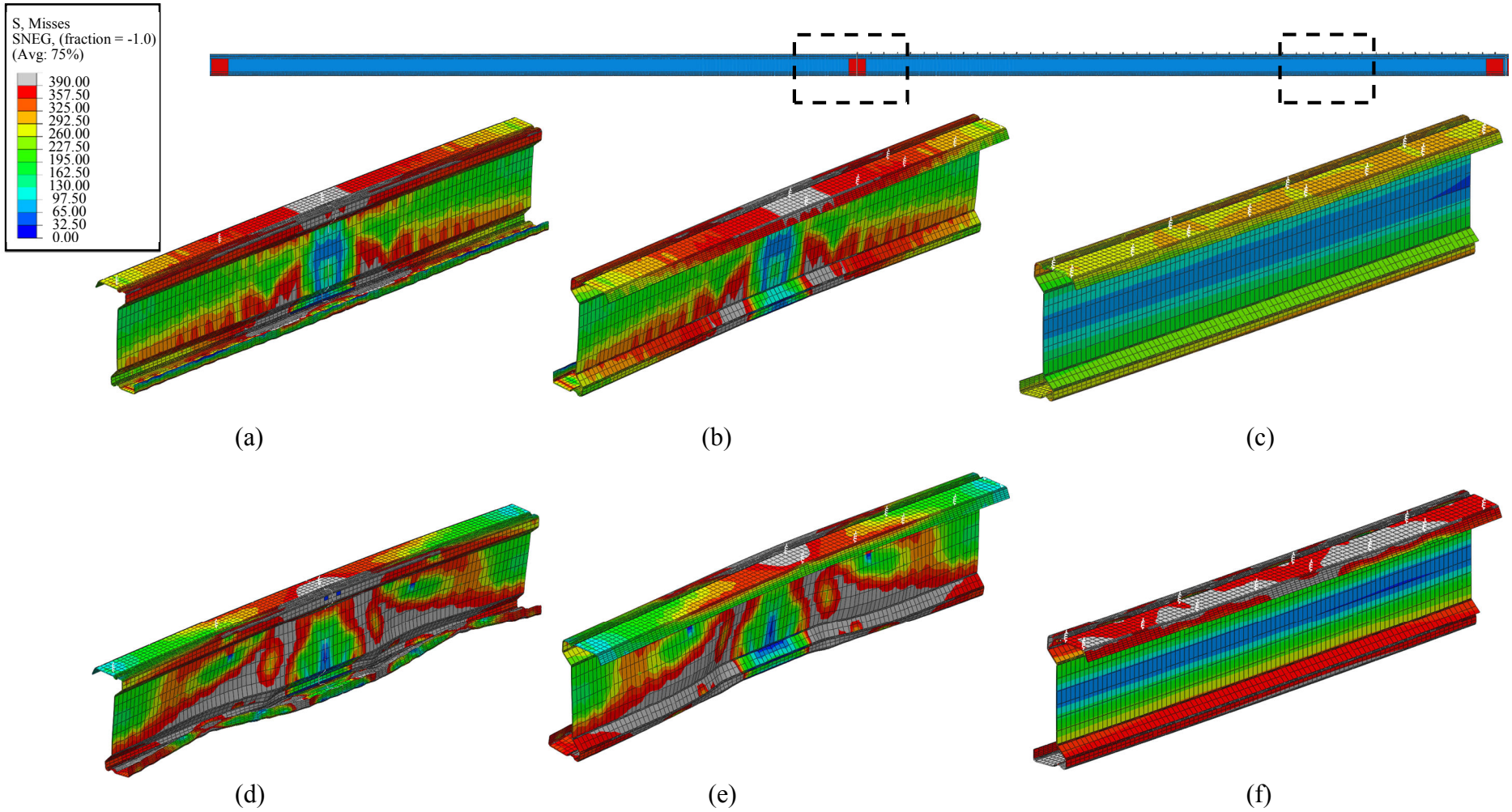


Figure 6.25: *Deformed stress profiles for 1/200_16 2-span continuous FE model at stage 2 and ultimate load for the interior support (a, b and d, e) and span (c and f) regions*

6.3.4.2. Design Proposal

To quantify the reduction in support moment for each 2-span sleeved model, the moment at the support region at ultimate load was compared with the maximum moment from the reference single span sleeved FE model subject to a moment gradient $M_{3sleeve}$. A reduction factor for gravity loading for sleeve arrangements, $\alpha_{FE,gs}$ is defined as the ratio of $M_{support}$ and $M_{3sleeve}$ at ultimate load and is given by Equation 6.14, with full redistribution providing the upper bound of unity.

$$\alpha_{FE,gs} = \frac{M_{support}}{M_{3sleeve}} \qquad 0 \leq \alpha_{FE,gs} \leq 1 \qquad (6.14)$$

As shown in Figure 6.26, the $\alpha_{FE,gs}$ values for all cross-sections from the FE sleeved results are plotted against the negative cross-sectional slenderness $\bar{\lambda}_{cs,-ve}$ using Equation 6.1. Figure 6.26 also included results from the continuous 2-span arrangements subjected to gravity loading described in Section 4.3.4.2. $\bar{\lambda}_{cs,-ve}$ was chosen because the cross-section at the interior support is subjected to a hogging moment where the bottom flange is in compression. The results were classified into their respective span-to-depth ratios ranging from L/d of 10 to 60. Similar to the findings of the continuous 2-span study described in Chapter 4, higher L/d ratios tend to yield higher reduction values than shorter spans for the same section. Since the estimation of the interior moment reduction for continuous 2-span systems is dependent on the cross-section slenderness and span-to-depth ratio, the same equation to estimate $\alpha_{FE,gs}$ for continuous 2-span systems is proposed for sleeve systems, provided the sleeved cross-sectional slenderness is calculated using Equation 6.1:

$$\alpha_{design,gs} = \left[0.7 - 0.0045\left(\frac{L}{d}\right)\right]\bar{\lambda}_{cs,s,-ve}^{\left[-0.003\left(\frac{L}{d}\right)-1.4\right]} \quad \text{but} \quad \alpha_{design,gs} \leq 1 \qquad (6.15)$$

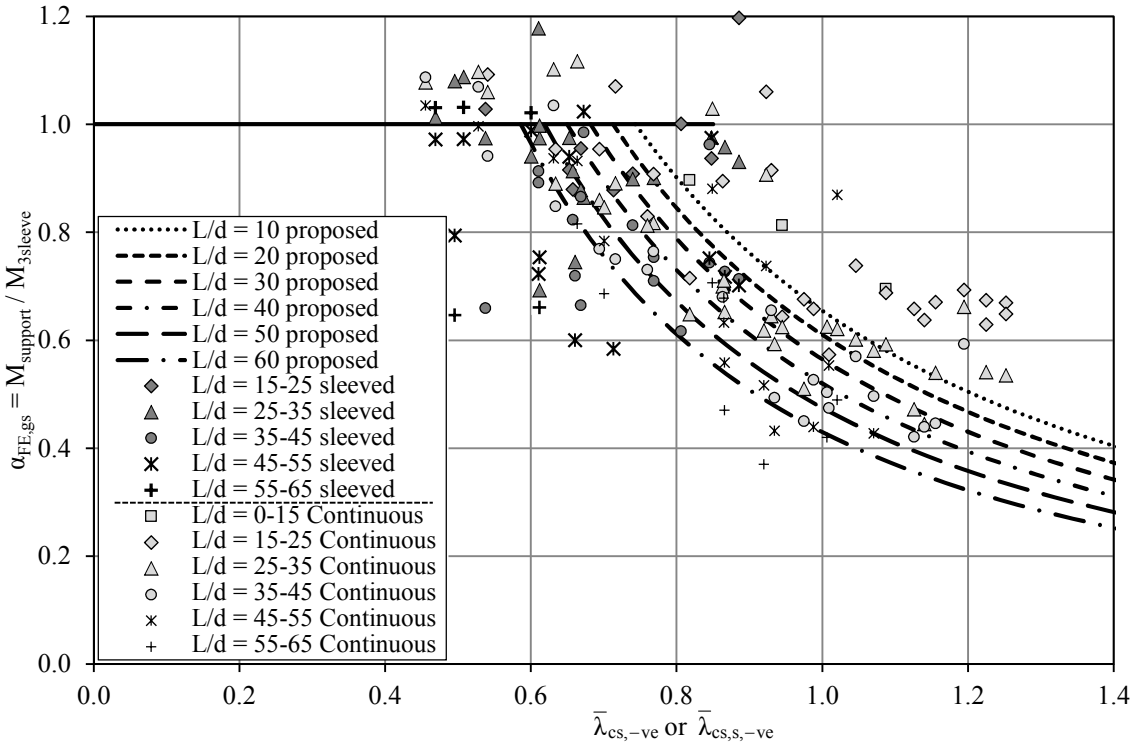


Figure 6.26: *Support moment reduction versus cross-section slenderness*

In order to quantify the additional load carrying capacity of 2-span sleeved systems $q_{FE,gs}$ in comparison to equivalent continuous 2-span systems under gravity UDL, an ultimate load ratio γ_2 is defined as:

$$\gamma_2 = \frac{q_{FE,gs}}{q_{FE,g}} \tag{6.16}$$

The ultimate loads from the FE analyses $q_{FE,gs}$ were compared against the same three design methods outlined in Section 4.3.4.2. Each design method utilised a combination of single span reference values, in conjunction with Equation 6.13. The corresponding ultimate loads from design methods 1, 2 and 3 for 2-span sleeved systems subjected to gravity loading are defined as q_{1gs}, q_{2gs} and q_{3gs} respectively. The input values for M_{span} and $M_{support}$ to be used in Equation 6.13 for each design method are shown in Table 6.6. For design method 1, elastic behaviour is assumed and hence $M_{support}$ was taken as $M_{3sleeve}$ while M_{span} was taken as $0.5625M_{3sleeve}$. For full plastic redistribution (design method 2), no reduction was applied to the $M_{3sleeve}$ for $M_{support}$, and it was assumed that M_{span} reaches M_1. To incorporate the potential loss of interior support moment by calculating $\alpha_{design,gs}$ (Equation 6.15) method 3 replaces the span and support moments with M_1 and $\alpha_{design,g}M_{3sleeve}$ respectively.

Table 6.6: *M_{span} and $M_{support}$ inputs values for Equation 6.13 for design methods 1, 2 and 3*

	Design method	M_{span}	$M_{support}$	Equation 6.13
1	Elastic design	$0.5625M_{3sleeve}$	$M_{3sleeve}$	$0.5625M_{3sleeve} = \frac{\left(q_{1gs}L^2 + 2M_{3sleeve}\right)^2}{8q_{1gs}L^2}$
2	Full plastic redistribution	M_1	$M_{3sleeve}$	$M_1 = \frac{\left(q_{2gs}L^2 + 2M_{3sleeve}\right)^2}{8q_{2gs}L^2}$
3	New proposed method	M_1	$\alpha_{design,gs}M_{3sleeve}$	$M_1 = \frac{\left(q_{3gs}L^2 + 2\alpha_{design,g}M_{3sleeve}\right)^2}{8q_{3gs}L^2}$

For the chosen range of sleeve lengths and bolt configurations in this study, on most occasions, the sleeve connection provided a superior interior support rotation capacity compared to the equivalent continuous 2-span case. Figure 6.27 illustrates the variation of ultimate load ratio γ_2 with L/d. On average, the additional load carrying capacity was found to be 6% with minimal scatter though in some cases γ_2 was as high as 18%. In general, the sleeved 2-span systems can attain higher interior support moments and extend the degree of moment redistribution enabling higher ultimate loads. To account for the additional strength from the sleeved connection and allow the use of the same design equation to estimate the interior support moment reduction factor from the continuous 2-span case, the cross-sectional slenderness for sleeve systems was reduced by a constant factor of $1/\sqrt{2}$ as defined in Equation 6.1.

Comparisons between ultimate loads predicted by design methods 1, 2 and 3 and the sleeved 2-span FE results for Zeta I, Zeta II and Zed cross-sections are shown in Table 6.7-6.9 respectively. Table 6.10 summarises the ultimate load comparisons for design methods 1, 2 and 3 for each cross-section shape including the mean prediction and coefficient of variation (COV). Full results from the gravity sleeved 2-span study are tabulated in detail in Appendix F. Differences between design predictions $q_{2,gs}$ and $q_{3,gs}$ were only observed for a small number of slender sleeved sections since many had no interior support reduction ($\alpha_{design,gs} = 1$) at ultimate load. Thus, the design calculation based on method 2 over-estimates capacity for these slender sections. The extent of the

overestimates is illustrated in Figure 6.28 where the failures loads using design method 2 and 3 are compared to the FE results. For stocky sections, the two design methods yield identical failure loads since $\alpha_{design,gs}$ equalled unity, whilst differences in $q_{2,gs}$ and $q_{3,gs}$ were found to be more significant as the sections became more slender. Overall, design method 2 overestimates the design load by approximately 3.8% with a largest overestimation of 14.5%, whilst design method based 3 reduces the overall over-prediction in design load to 0.5%. The overall improvement by adopting the proposed design method was masked by a large number of stockier sleeved sections. Figure 6.29 compares q_{3gs} and FE results for different span lengths and shows how the accuracy of design method 3 increases for 10 and 12 metre spans. For example, by only considering results for Zeta II which included many arrangements with L/d ratios in excess of 40, the average design load overestimation for method 2 of 2.9% fell by 5.6% which equates to a conservative $q_{3,gs}/q_{FE,gs}$ ratio of 0.973. In general, the same α-reduction method has been shown to be also applicable for calculating the sleeved 2-span collapse load for slender and stocky sections, provided the single span reference FE models outlined in Section 6.3.3 are used. Thus, inclusion of the $\alpha_{design,g}$ correction as obtained from Equation 6.15 permits the safe use of limited plastic redistribution for the range of cross-sections, spans and sleeve lengths covered.

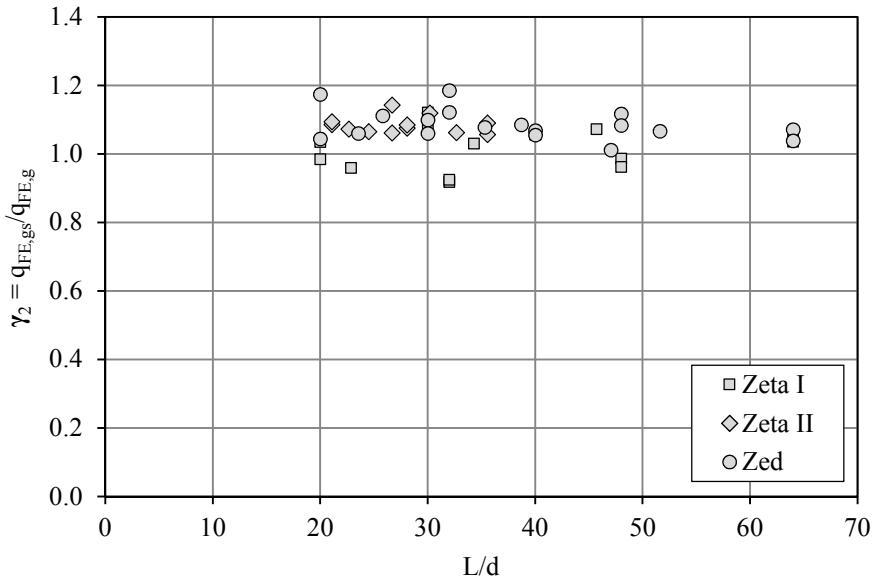


Figure 6.27: *Additional load carrying capacity due to addition of sleeves γ_2 versus L/d ratio*

Table 6.7: *Ultimate load comparison between 2-span FE sleeved results and design methods 1, 2 and 3 for Zeta I section for span lengths L = 4, 6 and 8 m*

Section reference	Span length (m)	$q_{FE,gs}$ (kN/m)	$q_{FE,g}$ (kN/m)	$q_{1,gs}$ (kN/m)	$q_{2,gs}$ (kN/m)	$q_{3,gs}$ (kN/m)	$q_{1,gs}/q_{FE,gs}$	$q_{2,g}/q_{FE,gs}$	$q_{3,gs}/q_{FE,gs}$	$q_{3,gs}/q_{FE,g}$
1/125_20	4.0	6.381	6.951	4.660	6.607	6.607	0.730	1.036	1.036	0.918
1/125_16	4.0	4.915	-	3.287	4.983	4.983	0.669	1.014	1.014	-
1/125_13	4.0	3.723	4.030	2.414	3.803	3.803	0.649	1.022	1.022	0.924
1/175_16	4.0	8.337	8.694	6.500	8.709	8.709	0.780	1.045	1.045	0.959
1/200_16	4.0	9.804	9.965	7.960	10.530	10.530	0.812	1.074	1.074	0.984
1/150_15	4.0	6.321	-	4.484	6.379	6.379	0.709	1.009	1.009	-
1/200_13	4.0	7.260	7.020	5.800	7.906	7.778	0.799	1.089	1.071	1.034
1/175_10	4.0	4.101	-	3.212	4.331	4.002	0.783	1.056	0.976	-
1/125_20	6.0	2.891	2.933	2.030	2.919	2.919	0.702	1.010	1.010	0.986
1/125_16	6.0	4.915	-	1.463	2.216	2.216	0.673	1.019	1.019	-
1/125_13	6.0	1.659	1.725	1.060	1.684	1.684	0.639	1.015	1.015	0.962
1/175_16	6.0	3.871	3.759	2.873	3.864	3.864	0.742	0.998	0.998	1.030
1/200_16	6.0	4.535	4.227	3.546	4.684	4.684	0.782	1.033	1.033	1.073
1/150_15	6.0	2.827	-	1.973	2.827	2.786	0.698	1.000	0.985	-
1/200_13	6.0	3.464	3.092	2.587	3.518	3.392	0.747	1.016	0.979	1.120
1/175_10	6.0	1.944	-	1.443	1.931	1.745	0.742	0.993	0.898	-
1/125_20	8.0	1.647	1.576	1.139	1.641	1.641	0.691	0.996	0.996	1.045
1/125_16	8.0	1.242	-	0.813	1.242	1.242	0.655	1.000	1.000	-
1/125_13	8.0	0.946	0.913	0.591	0.945	0.927	0.625	0.999	0.980	1.036
1/175_16	8.0	2.152	2.007	1.614	2.173	2.140	0.750	1.010	0.994	1.073
1/200_16	8.0	2.458	2.327	1.994	2.634	2.620	0.811	1.072	1.066	1.056
1/150_15	8.0	1.599	-	1.100	1.586	1.517	0.688	0.992	0.949	-
1/200_13	8.0	1.863	1.763	1.449	1.976	1.867	0.778	1.061	1.002	1.057
1/175_10	8.0	1.074	-	0.801	1.082	0.956	0.745	1.007	0.891	-

Table 6.8: *Ultimate load comparison between 2-span FE sleeved results and design methods 1, 2 and 3 for Zeta II section for span lengths L = 6, 8, 10 and 12 m*

Section reference	Span length (m)	$q_{FE,gs}$ (kN/m)	$q_{FE,g}$ (kN/m)	$q_{1,gs}$ (kN/m)	$q_{2,gs}$ (kN/m)	$q_{3,gs}$ (kN/m)	$q_{1,gs}/q_{FE,gs}$	$q_{2,g}/q_{FE,gs}$	$q_{3,gs}/q_{FE,gs}$	$q_{3,gs}/q_{FE,g}$
2/225_25	6.0	9.102	7.962	5.590	8.360	8.360	0.614	0.919	0.919	1.143
2/285_25	6.0	11.797	10.868	7.896	11.676	11.676	0.669	0.990	0.990	1.086
2/285_20	6.0	8.843	8.079	5.272	8.544	8.290	0.596	0.966	0.938	1.094
2/225_14	6.0	3.761	3.543	2.186	3.664	3.418	0.581	0.974	0.909	1.061
2/245_15	6.0	4.616	4.334	2.708	4.545	4.221	0.587	0.985	0.914	1.065
2/265_15	6.0	5.064	4.719	2.989	5.046	4.670	0.590	0.997	0.922	1.073
2/225_25	8.0	4.824	4.423	3.144	4.703	4.703	0.652	0.975	0.975	1.091
2/285_25	8.0	6.450	5.995	4.442	6.568	6.568	0.689	1.018	1.018	1.076
2/285_20	8.0	4.787	4.414	2.966	4.806	4.609	0.619	1.004	0.963	1.085
2/225_14	8.0	2.047	1.936	1.229	2.061	1.896	0.601	1.007	0.926	1.057
2/245_15	8.0	2.516	2.368	1.523	2.557	2.345	0.606	1.016	0.932	1.062
2/265_15	8.0	2.875	2.569	1.681	2.838	2.598	0.585	0.987	0.904	1.119
2/225_25	10.0	2.972	-	2.012	3.010	3.010	0.677	1.013	1.013	-
2/285_25	10.0	4.117	-	2.843	4.203	4.197	0.690	1.021	1.019	-
2/285_20	10.0	2.859	-	1.898	3.076	2.914	0.664	1.076	1.019	-
2/225_14	10.0	1.242	-	0.787	1.319	1.196	0.633	1.062	0.963	-
2/245_15	10.0	1.499	-	0.975	1.636	1.482	0.650	1.092	0.989	-
2/265_15	10.0	1.657	-	1.076	1.657	1.657	0.649	1.657	1.657	-
2/225_25	12.0	1.978	-	1.397	2.090	2.087	0.706	1.057	1.055	-
2/285_25	12.0	2.674	-	1.974	2.919	2.872	0.738	1.092	1.074	-
2/285_20	12.0	2.003	-	1.318	2.136	1.999	0.658	1.067	0.998	-
2/225_14	12.0	0.850	-	0.546	0.916	0.819	0.643	1.078	0.963	-
2/245_15	12.0	1.041	-	0.677	1.136	1.016	0.651	1.092	0.976	-
2/265_15	12.0	1.145	-	0.747	1.262	1.128	0.653	1.102	0.986	-

Table 6.9: *Ultimate load comparison between 2-span FE sleeved results and design methods 1, 2 and 3 for Zed section for span lengths L = 4, 6 and 8 m*

Section reference	Span length (m)	$q_{FE,gs}$ (kN/m)	$q_{FE,g}$ (kN/m)	$q_{1,gs}$ (kN/m)	$q_{2,gs}$ (kN/m)	$q_{3,gs}$ (kN/m)	$q_{1,gs}/q_{FE,gs}$	$q_{2,g}/q_{FE,gs}$	$q_{3,gs}/q_{FE,gs}$	$q_{3,gs}/q_{FE,g}$
Z/125_20	4.0	6.053	5.109	4.357	5.714	5.714	0.720	0.944	0.944	1.185
Z/200_25	4.0	14.998	12.780	11.693	14.470	14.470	0.780	0.965	0.965	1.174
Z/125_14	4.0	3.575	3.188	2.464	3.547	3.547	0.689	0.992	0.992	1.121
Z/155_15	4.0	5.291	4.760	3.629	5.242	5.242	0.686	0.991	0.991	1.112
Z/170_14	4.0	5.146	4.855	3.672	5.297	5.260	0.714	1.029	1.022	1.060
Z/200_13	4.0	5.689	5.449	3.811	5.583	5.314	0.670	0.982	0.934	1.044
Z/125_20	6.0	2.425	2.171	1.937	2.539	2.539	0.798	1.047	1.047	1.117
Z/200_25	6.0	6.225	5.666	5.197	6.431	6.431	0.835	1.033	1.033	1.099
Z/125_14	6.0	1.463	1.351	1.095	1.576	1.576	0.748	1.077	1.077	1.083
Z/155_15	6.0	2.163	1.994	1.613	2.330	2.320	0.746	1.077	1.073	1.085
Z/170_14	6.0	2.165	2.009	1.632	2.354	2.284	0.754	1.088	1.055	1.077
Z/200_13	6.0	2.288	2.160	1.694	2.481	2.320	0.740	1.085	1.014	1.059
Z/125_20	8.0	1.260	1.177	1.089	1.428	1.428	0.864	1.133	1.133	1.071
Z/200_25	8.0	3.247	3.041	2.923	3.617	3.617	0.900	1.114	1.114	1.068
Z/125_14	8.0	0.796	0.767	0.616	0.887	0.861	0.773	1.113	1.081	1.038
Z/155_15	8.0	1.145	1.074	0.907	1.310	1.268	0.793	1.145	1.108	1.066
Z/170_14	8.0	1.161	1.148	0.918	1.324	1.254	0.790	1.140	1.080	1.011
Z/200_13	8.0	1.249	1.184	0.953	1.396	1.281	0.763	1.118	1.026	1.055

Table 6.10: *Summary of proposed α-framework for sleeved gravity loading*

Section type	Span lengths	No. of 2-span sleeved FE models	$q_{1,g}/q_{FE,g}$		$q_{2,g}/q_{FE,g}$		$q_{3,g}/q_{FE,g}$	
			MEAN	COV	MEAN	COV	MEAN	COV
Zeta I	4–8 m	24	0.725	0.078	1.024	0.028	1.003	0.045
Zeta II	6–12 m	24	0.642	0.065	1.029	0.050	0.973	0.048
Zed	4–8 m	18	0.765	0.080	1.060	0.061	1.038	0.056
All		66	0.706	0.103	1.038	0.052	1.005	0.060

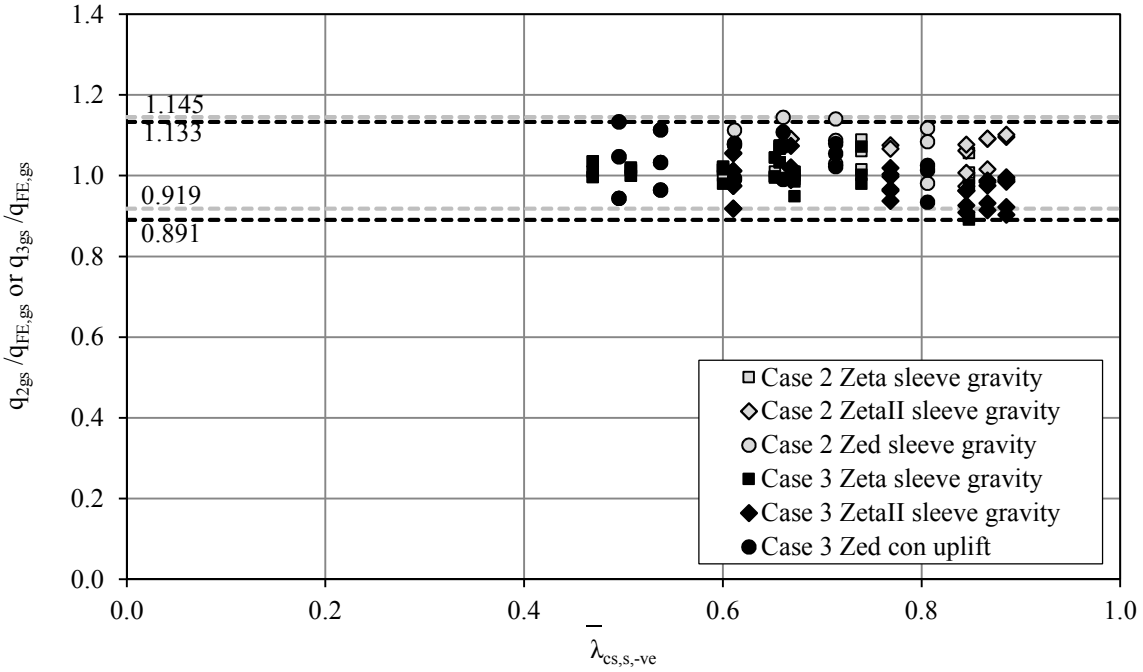


Figure 6.28: *Ultimate load comparisons between sleeved 2-span FE results and design methods 2 and 3 against negative cross-sectional slenderness*

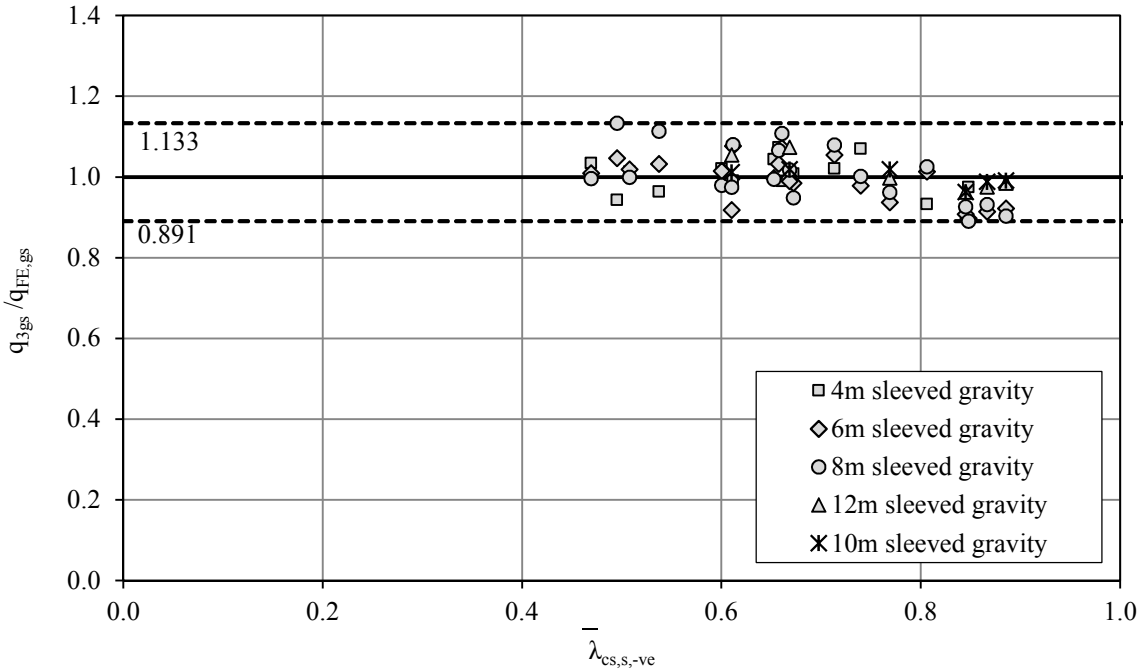


Figure 6.29: *Ultimate load comparison between sleeved 2-span FE results and design method 3 by span length*

6.4. PARAMETRIC STUDY–UPLIFT LOADING

6.4.1. Outline

To extend the alpha-reduction framework for uplift loading beyond continuous 2-span purlin systems, the moment redistribution behaviour for sleeved arrangements was investigated by means of parametric studies. Comparisons between the response of continuous and sleeved arrangements shows that sleeved connections offer greater rotational capacity that would potentially increase ultimate load carrying capacity. The results from the parametric studies are employed to propose a design equation for sleeved 2-span purlin systems

6.4.2. Lateral torsional buckling design using EC3 for 2-span sleeved purlins

Eurocode 3 Part 1-3 (2006) provides a method to evaluate the ultimate load capacity of a continuous cold-formed steel 2-span purlin system subjected to uplift loading, including limited guidance on sleeved arrangements. The method is set out in clause 10.1.3.4. Since it is difficult to quantify the level of continuity for sleeved (and lapped) connections, EC3 recommends the use of physical testing to determine the flexural stiffness, moment-rotation behaviour and moment capacity of the sleeved or lapped part. Essentially, the design for uplift of 2-span sleeved arrangements is similar to that of continuous systems: (i) check the internal support region under shear and bending and (ii) check for lateral instability in the span by calculating the buckling resistance of the free flange. The method for determining the lateral torsional buckling length of the free flange l_{fz} is covered in more detail for continuous 2-span arrangements than sleeved systems. Guidelines to allow the use of the same design procedure for sleeved systems are only valid for 2-span sleeved systems that are considered to be fully continuous. For other cases, the buckling length needs to be determined by other means or adopting less favourable η_1, η_2, η_3 and η_4 coefficient values of 0.694, 5.45, 1.27 and -0.168 respectively (Clause 10.1.4.2(3)). While Appendix B and C describes the procedure for determining the lateral torsional buckling resistance in more detail, opting for the alternative η coefficients tends to provide longer buckling lengths (generally between 10%-30% longer) in comparison to a continuous beam of identical cross-section and span length with no anti-sagbars. The longer buckling lengths obtained from the alternative method

would mean an increase in relative slenderness λ_1 and greater reductions for lateral torsional buckling $\chi_{LT,}$ thus reducing the maximum load carrying capacity.

6.4.3. Reference FE models

The bending moments in the span and at the interior support region for each 2-span sleeved FE model subject to 16p uplift loading were compared against individual representative moment capacities obtained from simulating additional single span FE models. Figure 6.30 illustrates how $M_{support}$ and M_{span} from the 2-span models relate to the results from the reference single span FE models. To account for the beneficially sharp sagging bending moment diagram at the interior support, $M_{support}$ was compared against a representative moment capacity for a single span sleeved FE model subjected to a linear moment gradient $M_{4sleeve}$ (test type 8). Similar to the continuous 2-span FE models in Chapter 4, M_{span} from the sleeved 2-span FE model was compared against $\chi_{LT}M_2$ to allow for a potential reduction for lateral torsional buckling in the span region, where χ_{LT} is the reduction factor for lateral torsional buckling obtained using EN 1993-1-3(2006) and EN 1993-1-1(2005) as discussed in Section 4.4.2 and M_2 is the pure hogging bending moment resistance obtained from the single span FE model under uplift conditions (test type 2). For the cross-sections listed in Table 6.11, additional assumptions for calculating χ_{LT} using the 9 step procedure outlined in Section 4.4.2 include:

- The stiffness of the connection between the sheeting and purlin C_{DA} was taken as 3739 Nmm/mm for all cross-section types, based on the results of physical testing (Leach 1992).
- The flexural stiffness of the sheeting C_{DC} was neglected since the total rotational spring stiffness C_D was assumed to be mainly influenced by the value of C_{DA}.
- The length between anti-sag bars L_a was assumed to be equal to the span length L.
- EN 1993-1-1(2006) permits the use of 2 design methods to determine χ_{LT}, but does not explicitly state when which case should be used. Therefore both cases were investigated in this study (defined as χ_{LT1} and χ_{LT2}). Case 1 is the original design procedure from EN 1993-1-1(2001), while Case 2 (new to the 2006 Specification) follows Clause 10.1.4.2(3) by adopting η_1, η_2, η_3 and η_4 coefficients from Table 10.2(b). Thus, the buckling length for design case 1 and 2 (l_{fz1} and l_{fz2}) was calculated through expressions given in Equations 6.17 and 6.18.

- Case 1 $$l_{fz1} = 0.7L\left[1+13.1\left(\frac{81}{256}R\right)^{1.6}\right]^{-0.125} \quad (6.17)$$

- Case 2 $$l_{fz2} = 0.596L\left(1+2.33R^{1.15}\right)^{-0.192} \quad (6.18)$$

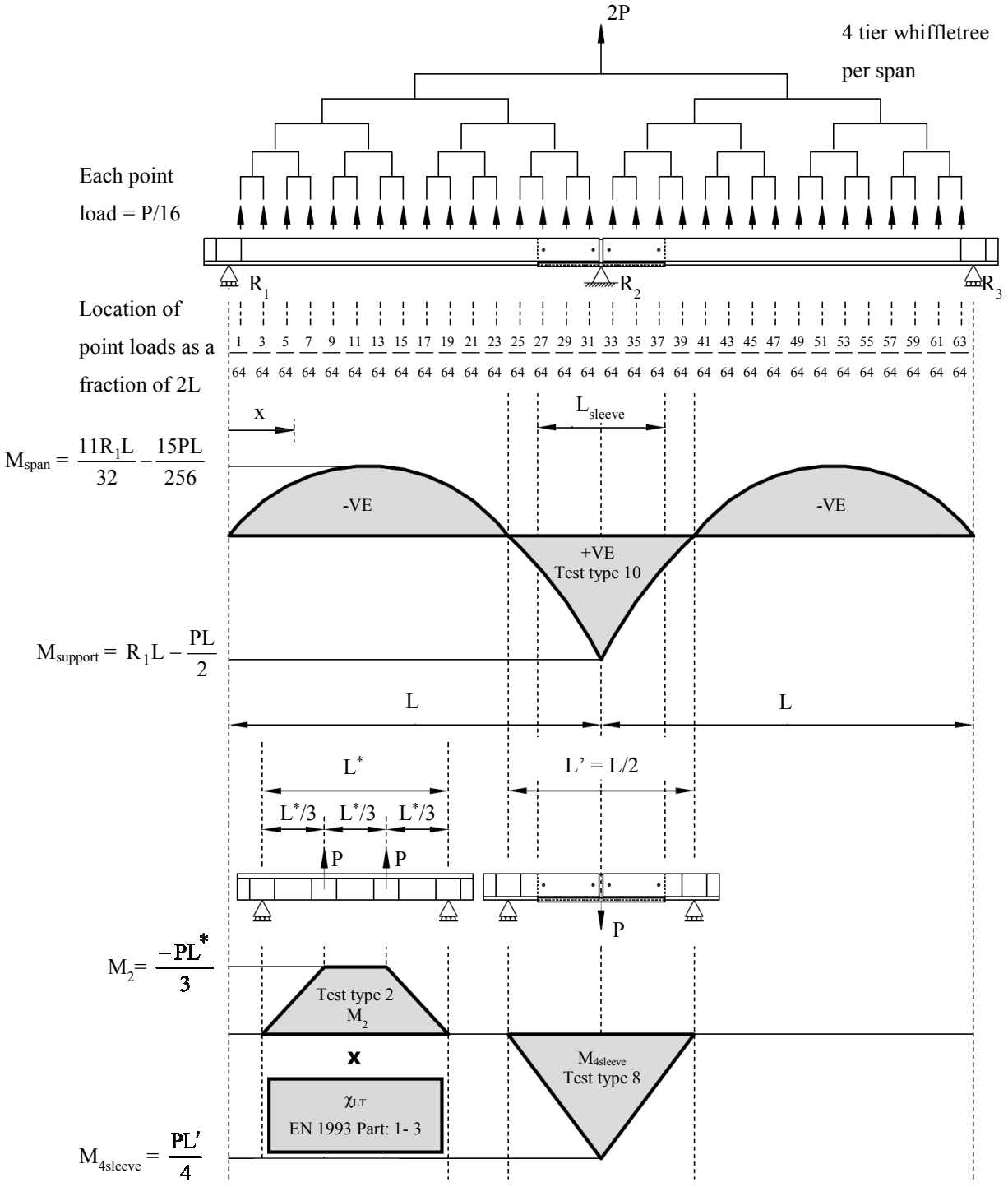


Figure 6.30: *Elastic bending moment diagram (BMD) for 2-span sleeved uplift, M_2 and $M_{4sleeve}$*

6.4.4. Alpha framework

To extend the alpha framework for 2-span purlin systems subjected to uniformly distributed uplift loading to account for the sleeved systems described in Section 6.4.3, 11 Zeta I and Zeta II cross-sections with 4, 6, 8, 10 m equal spans were simulated using the validated FE 2-span sleeve models described in Chapter 5. Longer span lengths were considered in this study to investigate the limiting effect of LTB for very slender purlin arrangements. By varying section height h, top flange width b_c, bottom flange width b_t and nominal thickness t, a modest range of sleeved sections with cross-section slenderness of 0.690-1.195 was covered to account for typical purlin arrangements commonly used in practice. Of the 88 sleeved 2-span and single span FE models, identical sleeve connections for bolt arrangements 2, 3B and 4 to that of the gravity 2-span study were considered. The geometrical definition for Zeta I and Zeta II and sleeve details are the same as the gravity 2-span alpha framework study and are illustrated in Figures 6.18 and Figure 6.20 respectively. The list of key cross-sections for this study is given in Table 6.11.

Table 6.11: *List of dimensions for Zeta I and Zeta II sections for 2-span sleeved uplift study*

Section Type[A]	Section Reference	Bolt type[B]	Sleeve length L_{sleeve} (mm)	Top flange b_c (mm)	Bottom flange b_t (mm)	Height h (mm)	Thickness t (mm)	$\bar{\lambda}_{cs,s,+ve}$
Zeta I	1/150_19	2	820	60	50	125	2.0	0.690
Zeta I	1/125_13	2	700	60	50	125	1.3	0.737
Zeta I	1/175_16	2	980	72	65	175	1.6	0.766
Zeta I	1/200_16	3B	1000	72	65	200	1.6	0.767
Zeta I	1/200_13	3B	1000	72	65	200	1.3	0.862
Zeta I	1/175_10	2	980	72	65	175	1.0	0.997
Zeta II	2/285_25	4	1000	78	68	285	2.5	0.747
Zeta II	2/225_14	4	860	78	68	225	1.4	0.852
Zeta II	2/245_15	4	900	78	68	245	1.5	0.845
Zeta II	2/265_15	4	960	78	68	265	1.5	0.872
Zeta II	2/265_10	4	960	78	68	265	1.0	1.195

A Refer to Figure 6.18 for cross-sectional details

B Refer to Figure 6.20 for bolt connection details

6.4.4.1. Moment redistribution behaviour

It was understood previously in Chapter 4 that the applied load (and subsequent q_{ult}) of any 2-span system was influenced by the interaction and magnitude of the rotation and moment capacities of the span and support regions. With L_{sleeve}/d ratios ranging from 3.5-6 considered in this study, the moment and rotation capacities of the sleeved connection at the interior support were generally about 10% and 300% higher, respectively, than the continuous case comprising the same cross-section. The improved performance of the sleeved connection showed similarities in behaviour to that of the stocky continuous cases subject to uplift loading, whilst minimal behavioural differences were observed for the span regions as the cross-section remained unchanged in the span. Figure 6.31 shows the M_{span}, $M_{support}$ and load-displacement response for the sleeved 2-span FE model with an 1/200_13 section and L = 6m. Tabulated results are given in Table 6.12. The chosen FE model shows typical moment redistribution behaviour for all sleeved 2-span purlin systems.

Although the sleeve connection offers superior rotation capacity, the initial stiffness may be less than that of the continuous case. This is due to a combination of the discontinuity in the main member over the internal support and local bolt movements between the sleeve and beam sections. The result is that the load-deformation response departs earlier from linearity an the extent of stage 1 is shorter than for the continuous cases. The extent of stage 2 for sleeved systems was found to be highly dependent on the rotation capacity at the interior support, with the sleeved system generally exhibit a prolonged stage 2, as the span moment increases steadily until LTB failure. All sleeved arrangements eventually failed by LTB in the span, with no interior support reduction. Table 6.12 shows how the reference single span moment $M_{4sleeve}$ and $\chi_{LT2}M_2$ provided similar failure moments to those observed in the 2-span systems. The deformed stress profiles for the chosen FE sleeved example at ultimate load are illustrated in Figure 6.33. With no change to the span or cross-sectional shape between the continuous and sleeved cases, the LTB failure modes for all sleeved systems were found to be similar (Figure 6.33(b)). Figure 6.32 compares the load and moment-displacement responses for the sleeved and continuous arrangements. Coincident displacement readings allowed for direct comparisons. The inferior rotation capacity offered by the continuous 2-span case forced the interior support moment to reduce at a lower ultimate load than that of the sleeved system.

Table 6.12: *Moment comparisons between 2-span sleeved and $\chi_{LT2}M_2$ and $M_{4sleeve}$ FE models for 1/200_16 L = 6000 mm*

Stage	Applied load q (kN/m)	M_{span} (kNm)	$M_{support}$ (kNm)	$\chi_{LT2}M_2$ (kNm)	$M_{4sleeve}$ (kNm)	$M_{span}/\chi_{LT2}M_2$	$M_{support}/M_{4sleeve}$
q_{ult}	2.746	-7.682	10.829	-7.080	12.07	1.085	0.897

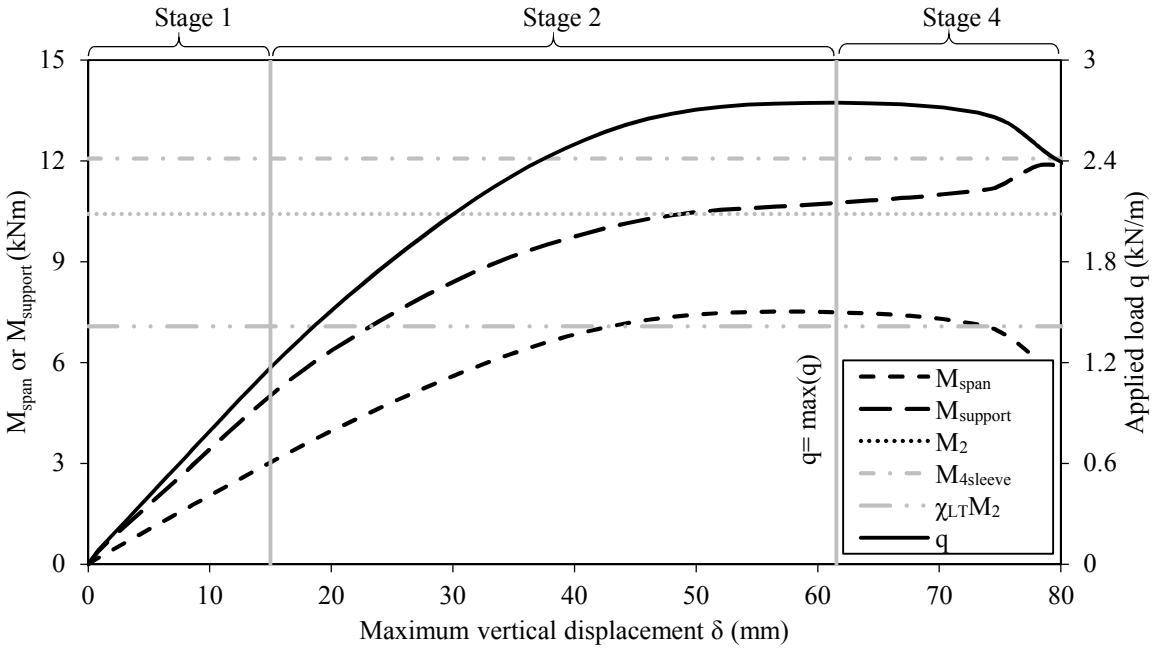


Figure 6.31: *Applied load q, $M_{support}$ and M_{span} versus maximum vertical deflection δ for uplift 2-span Z/200_13 L = 10 m FE model*

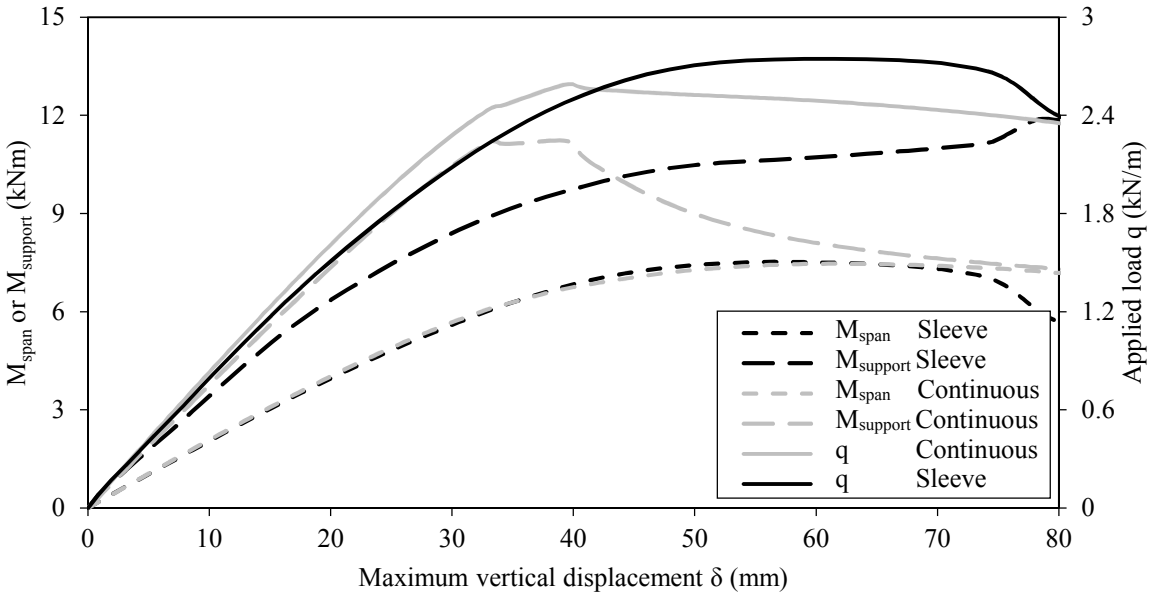


Figure 6.32: *Applied load q, $M_{support}$ and M_{span} versus maximum deflection δ for 1/200_13 L = 6 m sleeved and continuous 2-span uplift FE models*

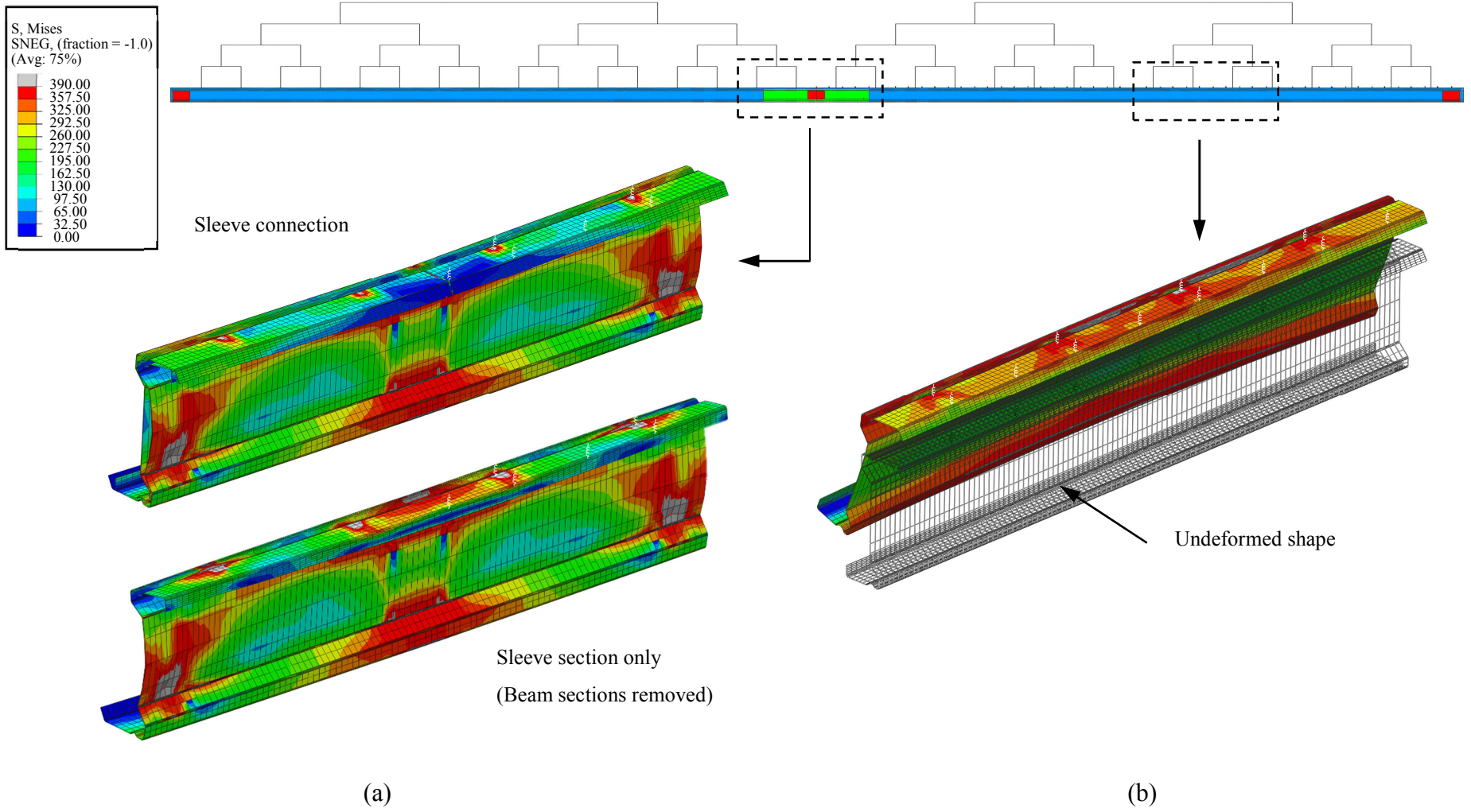


Figure 6.33: *Deformed stress profiles for 1/200_13 2-span sleeved uplift FE model at ultimate load for the (a) interior support and (b) span regions*

6.4.4.2. Design Proposal

In this section, the results obtained from the parametric studies are used as a basis for 2-span load capacity design equations by substituting a combination of calculated moment capacity values for the support and span regions. Four design methods with different assumptions were considered, of which one is recommended.

For the range of sleeved 2-span arrangements considered in this thesis, which comprised sections with $\overline{\lambda}_{cs,s,+ve}$ ranging from 0.690 to 1.195, L_{sleeve}/d ranging from 3.5 to 5.6 and span lengths up to 10 m, all 2-span sleeved purlin arrangements described in Section 6.4.4.1 showed limited moment redistribution behaviour. The span moments all reached their LTB moment capacities at ultimate load, while no interior support moment reduction was observed. Thus, the potential moment reduction at the interior support for sleeved systems subjected to uplift loading $\alpha_{FE,us}$ is fixed at unity for all cases, regardless of $\overline{\lambda}_{cs}$. Where applicable, the additional load carrying capacity obtained from sleeved 2-span FE models subjected to 16 evenly spaced uplift point loads $q_{FE,us}$ compared with the a continuous 2-span case loaded with a UDL is defined as an ultimate load ratio γ_3 as:

$$\gamma_3 = \frac{q_{FE,us}}{q_{FE,u}} \tag{6.19}$$

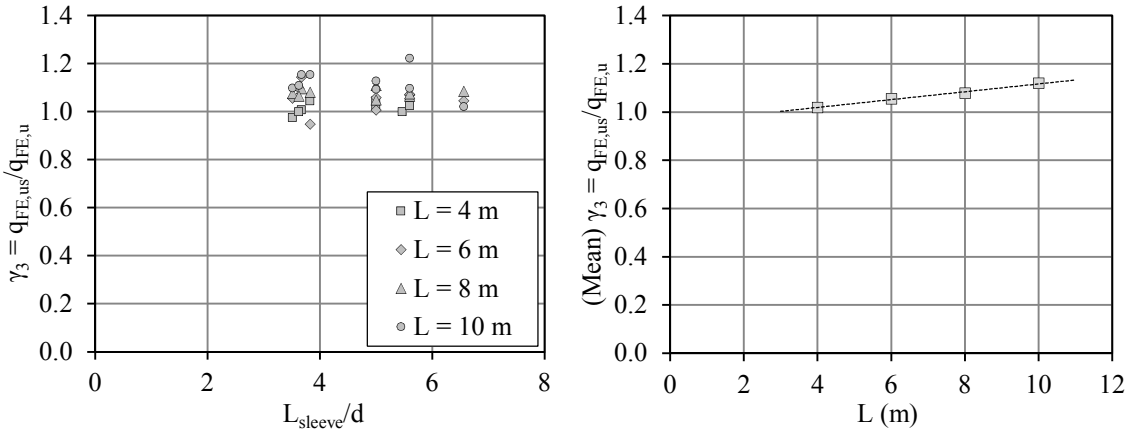
For the range of Zeta I and Zeta II cross-sections and bolt arrangements considered in this study, modifying the interior support from a continuous to a sleeved connection provided a range of additional load carrying capacities. Table 6.13 shows the γ_3 ratios for Zeta I and Zeta II sections for different span lengths.

Table 6.13: *Load ratios γ_3 for Zeta I and Zeta II cross-sections*

	γ_3			
Section	Span length L (m)			
reference	4.0	6.0	8.0	10.0
1/150_19	1.000	1.046	1.086	1.022
1/125_13	1.041	1.070	1.066	1.097
1/175_16	1.026	1.072	1.075	1.223
1/200_16	1.026	1.007	1.110	1.129
1/200_13	1.045	1.060	1.049	1.093
Mean	1.028	1.051	1.077	1.113

	γ_3			
Section	Span length L (m)			
reference	4.0	6.0	8.0	10.0
2/285_20	0.977	1.057	1.076	1.099
2/225_14	1.046	0.949	1.082	1.155
2/245_15	1.009	1.144	1.096	1.155
2/265_15	1.000	1.097	1.066	1.109
Mean	1.008	1.062	1.080	1.130

It can be seen from Figure 6.34 that γ_3 is insensitive to an increase in L_{sleeve}/d ratio, but is influenced by its 2-span length L. As previously observed in Section 6.3.2, since all 2-span L_{sleeve}/d ratios ranged from 3.5-6.5, the sleeved connection was able to provide improved interior support moment capacities to those of the continuous case. Since the lateral torsional buckling moment at failure was found to be similar for both sleeved and continuous beams, the change in γ_3 was predominantly influenced by the additional rotation and moment capacity offered by the sleeved connection at the interior support. Figure 6.34(b) shows that the average γ_3 ratio for Zeta I and Zeta II sections for 4-10 m spans increases almost linearly from 1.019 to 1.120. The increase in γ_3 can be explained by: (i) $M_{support}$ for sleeved cases tends to be approximately 10% higher than the equivalent continuous cases and (ii) $M_{support}$ reduced at ultimate load for continuous 2-span cases with long span lengths, whereas for sleeved cases, $M_{support}$ was always maintained even at large rotations. Since the increase in moment capacity between $M_{4sleeve}$ and M_4 was found to be insensitive to its single span length L', the influence on γ_3 of its moment capacity increase was therefore insensitive to the overall 2-span length L. This is not the case for higher rotation capacities at the interior support. While sleeved connections tend to offer approximately 3 times more rotation capacity than the equivalent continuous case, the high rotation demands at the interior support for the longer span lengths would cause $M_{support}$ for continuous cases to reduce up to 50% from its original maximum moment capacity. Thus, as the span length increases, the reduction at the interior support increases resulting in greater differences between the $q_{FE,u}$ and $q_{FE,us}$.



(a) (b)

Figure 6.34: Additional load carrying capacity for uplift loading γ_3 versus (a) L_{sleeve}/d and (b) span length L

The ultimate loads from 2-span uplift FE analyses $q_{FE,us}$ were also compared against results obtained from four design possibilities:

Method 1. Elastic design – Considers failure of the system once the interior support reached its moment capacity.

Method 2. Comparative design method – Full moment redistribution by using the M_{span} value from the 2-span FE model at q_{ult} with an unscaled interior support moment $M_{4sleeve}$ ($\alpha_{design,us} = 1$).

Method 3. Proposed design method 1 – Full moment redistribution by estimating the influence of LTB in the span by calculating χ_{LT1} within EC3 and an unscaled interior support moment $M_{4sleeve}$ ($\alpha_{design,us} = 1$).

Method 4. Proposed design method 2 – Full moment redistribution by estimating the influence of LTB in the span by calculating χ_{LT2} within EC3 and an unscaled interior support moment $M_{4sleeve}$ ($\alpha_{design,us} = 1$).

The design loads for uplift loading for methods 1, 2, 3 and 4 are defined as q_{1us} and $q_{2us,}$ $q_{3us,}$ and q_{4us} respectively. In order to compute the design load for each design method, the modified input values for M_{span} and $M_{support}$ for Equation 6.13 are given in Table 6.14. For design method 1, an elastic reduction value of 0.5625 was applied to $M_{4sleeve}$. It was assumed for method 1 that $M_{support}$ always reached its moment capacity $M_{4sleeve}$ before the span failed by LTB and that the span moment is in its elastic range when $M_{support}$ reaches its peak value. For the comparative design method 2, the span moment at ultimate load from the sleeved 2-span uplift FE model $M_{FE,span}$ was used to replace M_{span}, whilst $M_{support}$ was replaced by its moment gradient single span reference value $M_{4sleeve}$ with no reduction ($\alpha_{design,us} = 1$). This ensures that the accuracy of design method 2 is purely dependent on the prediction of the reduced interior support moment $M_{4sleeve}$. For methods 3 and 4, the $M_{support}$ value was replaced by $M_{4sleeve}$ at the interior support, whilst M_{span} was substituted with either $\chi_{LT1}M_2$ or $\chi_{LT2}M_2$, where χ_{LT1} and χ_{LT2} were calculated using EC3 based on the different assumptions discussed in Sections 6.3.3 and 6.4.3. M_2 is the negative pure bending moment capacity obtained from a test type 2 FE model.

Table 6.14: *M_{span} and $M_{support}$ inputs values for Equation 6.13 for design methods 1, 2, 3 and 4 for uplift 2-span parametric study*

	Design Method	M_{span}	$M_{support}$	Equation (6.13)
1	Elastic design	$0.5625M_{4sleeve}$	$M_{4sleeve}$	$0.5625M_{4sleeve} = \frac{\left(q_{1us}L^2 + 2M_{4sleeve}\right)^2}{8q_{1us}L^2}$
2	Comparative design method with no LTB error	$M_{FE,span}$	$M_{4sleeve}$	$M_{FE,span} = \frac{\left(q_{2us}L^2 + 2M_{4sleeve}\right)^2}{8q_{2us}L^2}$
3	Proposed design method 1	$\chi_{LT1}M_2$	$M_{4sleeve}$	$\chi_{LT1}M_2 = \frac{\left(q_{3us}L^2 + 2M_{4sleeve}\right)^2}{8q_{3us}L^2}$
4	Proposed design method 2	$\chi_{LT2}M_2$	$M_{4sleeve}$	$\chi_{LT2}M_2 = \frac{\left(q_{4us}L^2 + 2M_{4sleeve}\right)^2}{8q_{4us}L^2}$

Comparisons between ultimate loads predicted by each design method 1, 2, 3, 4 and uplift 2-span sleeved FE results for 4, 6, 8 and 10 m spans are shown in Table 6.15 and 6.16. The raw results from the uplift 2-span sleeved study for each cross-section are tabulated in detail in Appendix G. Table 6.17 summarises the ultimate load comparisons for design method 1, 2, 3 and 4 for each cross-section shape including the mean predictions and COV values.

Designing a 2-span system based on design method 1 was found to be highly conservative with an average $q_{1,us}/q_{FE,us}$ ratio of 0.891. Figure 6.35(a) illustrates the accuracy of $M_{4sleeve}/M_{support}$ at q_{ult}. While there is noticeable scatter, the ability of $M_{4sleeve}$ to predict the interior support moment was considered satisfactory since 32 of the 44 cases method 1 was predominantly caused by the conservative estimation of the span moment at failure. Figure 6.35(b) shows how assuming a constant elastic ratio of $0.5625M_{4sleeve}$ is highly conservative for all cases. Significant load differences were found for stockier sections ($\bar{\lambda}_{cs,s,+ve} < 0.8$). These were less influenced by lateral torsional buckling, which resulted in the most conservative design load of approximately $0.7q_{FE,us}$. Thus, significant improvements to the design method can be achieved if the reduction factor for $M_{4sleeve}$ is more representative of M_{span}, rather than fixing the reduction value for $M_{4sleeve}$ to 0.5625.

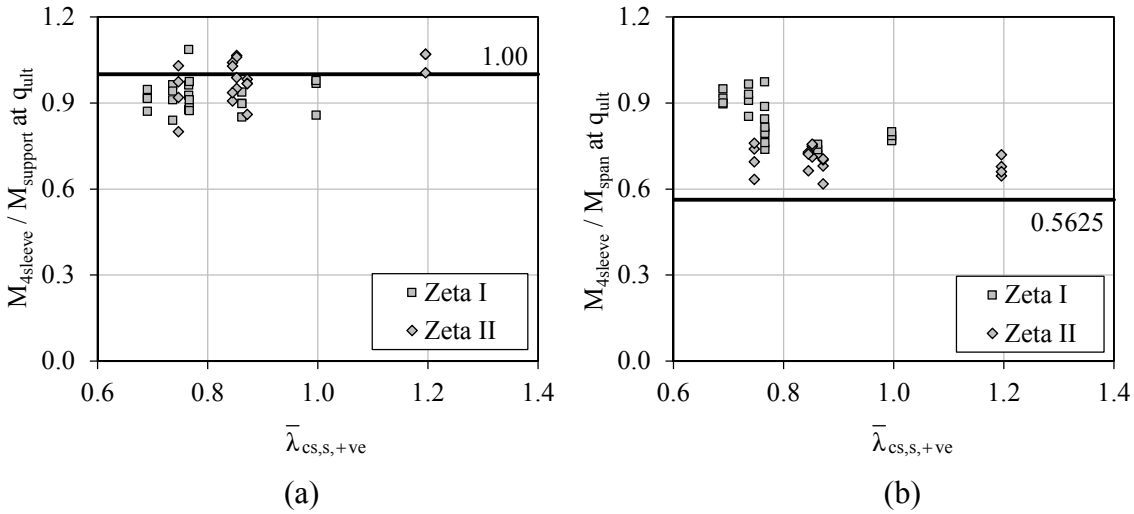


Figure 6.35: *Normalised 2-span moments: (a) $M_{4sleeve}/M_{support}$ and (b) M_2/M_{span} versus cross-sectional slenderness*

Figure 6.36 compares the accuracy of the failure loads obtained from design methods 2, 3, and 4 with respect to $\bar{\lambda}_{cs,s,+ve}$. Design method 2 provided results with the least scatter and an average design load prediction of 1.007. The accuracy of design method 2 was purely dependant on the accuracy of $M_{4sleeve}$ for $M_{support}$ at q_{ult} since the actual span moment from the 2-span FE model $M_{FE,span}$ was used in determining the ultimate load. Not only does design method 2 support the findings for the design method 1, that $M_{4sleeve}$ can accurately model the maximum value of $M_{support}$, design method 2 also provides an insight towards the most optimal outcome for an alternative design process which incorporates different estimated lateral torsional buckling factors.

Design methods 3 and 4 incorporated calculated χ_{LT} values using EN 1993-1-3 with different assumptions when determining the buckling length l_{fz}. Design loads based on design method 3 were found to be on average 11% lower than design method 4 purely because the calculated buckling length was consistently overpredicted when compared to the FE results. Figure 6.37 compares the FE M_{span}/M_2 results against $\bar{\lambda}_{fz}$ for design methods 3 and 4 for 4, 6, 8 and 10 m spans, with reference to the χ_{LT} curve. As expected, the FE results show a gradual falling trend of M_{span}/M_2 for more slender sections, but modest scatter was observed. Similar to findings from the continuous 2-span uplift study discussed in Chapter 4, design method 4 tends to predict the shortfall in the span moment capacity for the 6, 8, and 10 m spans with reasonable accuracy but was unconservative for 4 m spans. This can best be illustrated by comparing the mean $q_{4,us}/q_{FE,us}$ ratios. While the

4 m spans yields an average unconservative results of 17%, considering design method 4 for 6, 8 and 10 m separately reduces the overall mean $q_{4,us}/q_{FE,us}$ ratio from 1.005 to 0.950 with a COV of falling to 0.076. Even though not all avenues for calculating the buckling length using EN 1993-1-3 were considered in this study, the large variability in design loads between designs methods 3 and 4 suggests that the current EC3 method can be enhanced by improving the calculation for l_{fz}. Nevertheless, the current design method using EC3 to the calculate the l_{fz} design based on design method 4 is suggested as this method gave the best conservative design-to-FE load ratios of 0.950 for span lengths of 6-10m.

Table 6.15: *Ultimate load comparison between 2-span FE sleeved results and design methods 1, 2, 3 and 4 for Zeta I sections with span lengths L = 4, 6, 8 and 10 m*

Section reference	Span length L (m)	$q_{FE,us}$ (kN/m)	$q_{1,us}$ (kN/m)	$q_{2,us}$ (kN/m)	$q_{3,us}$ (kN/m)	$q_{4,us}$ (kN/m)	$q_{1,us}/q_{FE,us}$	$q_{2,us}/q_{FE,us}$	$q_{3,us}/q_{FE,us}$	$q_{4,us}/q_{FE,us}$
1/150_19	4.00	7.879	6.424	8.107	7.672	8.223	0.815	1.029	0.974	1.044
1/125_13	4.00	3.841	2.686	3.678	3.302	3.555	0.699	0.958	0.860	0.926
1/175_16	4.00	7.310	6.621	7.579	7.334	8.155	0.906	1.037	1.003	1.116
1/200_16	4.00	8.242	7.781	8.529	8.379	9.600	0.944	1.035	1.017	1.165
1/200_13	4.00	6.153	6.158	6.482	6.267	7.355	1.001	1.054	1.019	1.195
1/175_10	4.00	3.676	3.594	3.855	3.443	4.192	0.978	1.049	0.937	1.140
1/150_19	6.00	3.684	2.811	3.724	3.289	3.461	0.763	1.011	0.893	0.940
1/125_13	6.00	1.683	1.162	1.692	1.398	1.480	0.690	1.006	0.831	0.880
1/175_16	6.00	3.408	2.900	3.459	3.104	3.366	0.851	1.015	0.911	0.988
1/200_16	6.00	3.806	3.555	3.905	3.568	3.967	0.934	1.026	0.937	1.042
1/200_13	6.00	2.746	2.631	2.835	2.570	2.934	0.958	1.032	0.936	1.068
1/175_10	6.00	1.654	1.479	1.659	1.356	1.650	0.894	1.003	0.820	0.998
1/150_19	8.00	2.017	1.564	2.039	1.797	1.881	0.775	1.011	0.891	0.932
1/125_13	8.00	0.932	0.646	0.924	0.759	0.801	0.694	0.991	0.815	0.859
1/175_16	8.00	2.003	0.616	2.005	1.686	1.801	0.807	1.001	0.842	0.899
1/200_16	8.00	2.216	1.913	2.221	1.901	2.067	0.863	1.002	0.858	0.933
1/200_13	8.00	1.574	1.509	1.627	1.398	1.547	0.958	1.034	0.888	0.983
1/175_10	8.00	0.943	0.839	0.950	0.731	0.867	0.890	1.008	0.775	0.919
1/150_19	10.00	1.282	0.995	1.287	1.124	1.175	0.777	1.004	0.877	0.917
1/125_13	10.00	0.553	0.409	0.555	0.471	0.498	0.739	1.003	0.852	0.900
1/175_16	10.00	1.412	1.022	1.361	1.046	1.112	0.724	0.964	0.741	0.787
1/200_16	10.00	1.412	1.273	1.465	1.199	1.289	0.901	1.038	0.849	0.912
1/200_13	10.00	1.032	0.941	1.048	0.857	0.933	0.912	1.016	0.831	0.904
1/175_10	10.00	0.612	0.532	0.612	0.450	0.526	0.868	1.000	0.735	0.859

Table 6.16: *Ultimate load comparison between 2-span FE sleeved results and design methods 1, 2, 3 and 4 for Zeta II sections with span lengths L = 4, 6, 8 and 10 m*

Section reference	Span length L (m)	$q_{FE,us}$ (kN/m)	$q_{1,us}$ (kN/m)	$q_{2,us}$ (kN/m)	q_{3us} (kN/m)	$q_{4,us}$ (kN/m)	$q_{1,us}/q_{FE,us}$	$q_{2,g}/q_{FE,us}$	$q_{3,g}/q_{FE,us}$	$q_{4,us}/q_{FE,us}$
2/285_20	4.00	13.625	15.166	14.662	15.550	18.332	1.113	1.076	1.141	1.345
2/225_14	4.00	7.128	6.495	7.128	7.164	8.375	0.911	1.000	1.005	1.175
2/245_15	4.00	8.148	8.105	8.416	8.736	10.296	0.995	1.033	1.072	1.264
2/265_15	4.00	8.538	9.163	8.901	9.509	11.329	1.073	1.042	1.114	1.327
2/265_10	4.00	4.739	4.478	4.613	4.533	5.537	0.945	0.973	0.956	1.168
2/285_20	6.00	6.674	6.714	6.871	6.351	7.438	1.006	1.030	0.952	1.114
2/225_14	6.00	3.369	2.865	3.279	2.948	3.404	0.850	0.973	0.875	1.010
2/245_15	6.00	4.006	3.582	3.938	3.568	4.175	0.894	0.983	0.891	1.042
2/265_15	6.00	4.142	3.996	4.160	3.804	4.549	0.965	1.004	0.918	1.098
2/265_10	6.00	2.289	1.957	2.111	1.702	2.194	0.855	0.922	0.743	0.958
2/285_20	8.00	4.012	3.832	4.040	3.447	3.894	0.955	1.007	0.859	0.971
2/225_14	8.00	1.816	1.609	1.834	1.591	1.780	0.886	1.010	0.876	0.980
2/245_15	8.00	2.193	2.033	2.232	1.930	2.181	0.927	1.018	0.880	0.995
2/265_15	8.00	2.373	2.275	2.398	2.054	2.360	0.959	1.010	0.865	0.995
2/265_10	8.00	1.149	1.117	1.118	0.906	1.110	0.972	0.973	0.788	0.967
2/285_20	10.00	2.649	2.405	2.608	2.119	2.336	0.908	0.985	0.800	0.882
2/225_14	10.00	1.213	1.027	1.180	0.985	1.080	0.847	0.973	0.812	0.890
2/245_15	10.00	1.431	1.281	1.411	1.188	1.312	0.895	0.986	0.831	0.917
2/265_15	10.00	1.524	1.456	1.539	1.272	1.419	0.955	1.009	0.834	0.931
2/265_10	10.00	0.723	0.699	0.719	0.552	0.646	0.967	0.995	0.764	0.893

Table 6.17: *Ultimate load comparison between design methods 1, 2 and 3 for different span lengths*

Span length L (m)	$q_{1,us} / q_{FE,us}$		$q_{2,us} / q_{FE,us}$		$q_{3,u} / q_{FE,us}$		$q_{4,u} / q_{FE,us}$	
	MEAN	COV	MEAN	COV	MEAN	COV	MEAN	COV
4.0	0.944	0.121	1.026	0.034	1.009	0.079	1.170	0.103
6.0	0.878	0.105	1.000	0.032	0.882	0.071	1.013	0.069
8.0	0.881	0.102	1.006	0.015	0.849	0.047	0.948	0.046
10.0	0.863	0.096	0.997	0.021	0.811	0.058	0.890	0.044
All	0.891	0.109	1.007	0.028	0.888	0.106	1.005	0.128

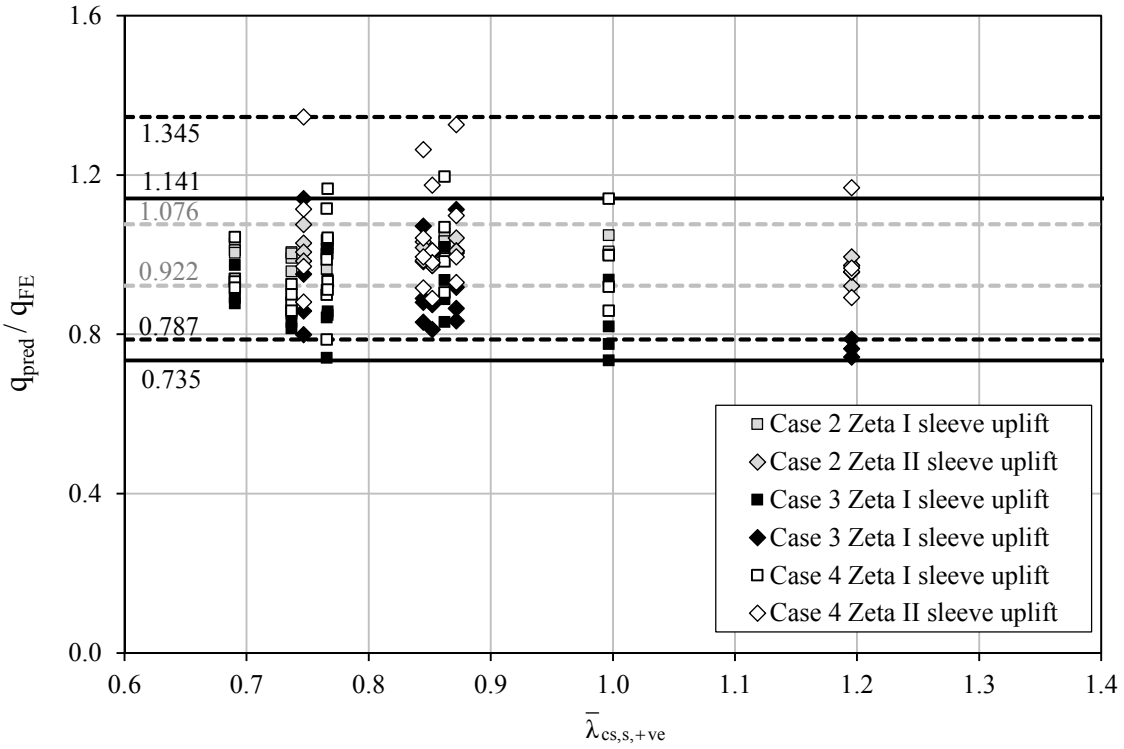


Figure 6.36: *Normalised design loads against 2-span uplift sleeved FE results versus cross-section slenderness*

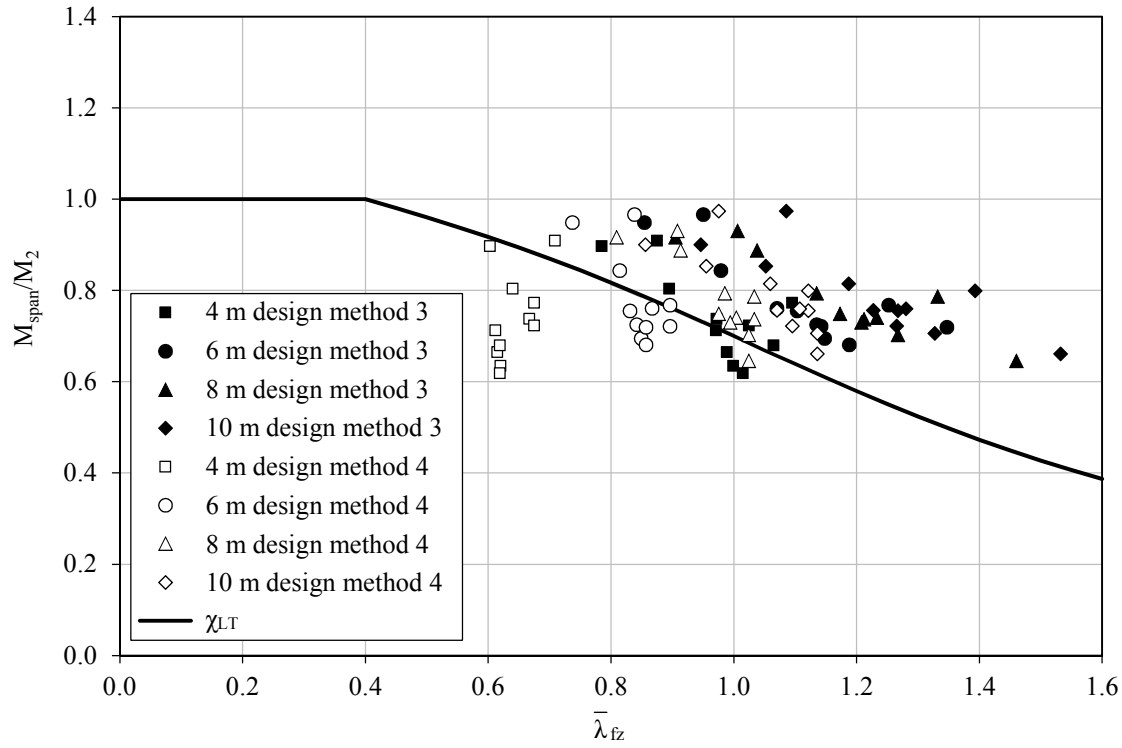


Figure 6.37: *Calculated M_{span} reduction factors for design methods 3 and 4 against $\bar{\lambda}_{fz}$*

6.5. CONCLUSIONS

The stiffness, strength and rotation capacities of sleeved connections in cold-formed purlins were investigated through a single span parametric study by varying the sleeve length and bolt configurations. Sleeve connections with at least L_{sleeve}/d ratios of 3.5 and 8 gave connections which offered full strength and full stiffness, relative to continuous sections, sleeve connections respectively. The nonlinear behaviour of the bolts and improved buckling resistance of the combined sleeve and beam sections increased the rotation capacity of sleeved connections to be approximately 3 times that of the continuous case.

The moment redistribution behaviour of sleeved 2-span purlin systems subjected to gravity and uplift loading was also investigated by means of parametric studies using the validated FE models outlined in Chapter 5. For gravity loading, a study comprising Zeta I, Zeta II and Zed cross-sections has been conducted over a range of 4-12 m spans to evaluate the potential loss of interior support moment at ultimate load. The results from the study showed that sleeved systems offer greater scope for moment redistribution compared to the equivalent continuous 2-span cases with less interior support moment reduction. For slender sleeved sections at long span lengths, where rotation demands are at their highest, moment reductions at the support were observed down to approximately 85% of the in-plane moment capacity. The existing design formula for continuous cases for gravity loading given in Chapter 4 was found to be suitable to predict the loss of the interior support moment in sleeved systems. The design method for sleeved arrangements gave results that matched with the FE results with an average $q_{3,gs}/q_{FE,gs}$ of 1.005 and a COV value of 0.060. Adopting full redistribution or elastic design was found to be unconservative by 3.8% or highly conservative by 29% respectively.

A parametric study for sleeved systems subjected to uplift loading was also conducted to extend the alpha-reduction framework beyond continuous cold-formed steel purlins. The study comprised Zeta I and Zeta II sections covering span lengths of 4-10 m with L_{sleeve}/d ratios ranging from 3.5-5.6. For the cases considered, it was found that the sleeve connections' superior rotation capacity allowed the system to redistribute the moment into the span without loss of interior support moment. An additional comparative design study has shown that a potential increase in average design loads is possible

providing χ_{LT} can accurately predict the reduced LTB moment in the span at failure. By enforcing no reduction at the interior support ($\alpha_{design,us}$ = 1), 2 design methods were considered. Since the current EC3 offers alternative methods for calculating the lateral torsional buckling length l_{fz}, large differences between reduction factors for LTB and design loads were observed. For the range of sleeved arrangements considered, the elastic design approach was found to be conservative by 11%. However, adopting the proposed design approach gives a design-to-FE load ratio of either 0.888 or 1.005, depending upon the design assumptions made.

CHAPTER 7

CONCLUSIONS AND SUGGESTIONS FOR FURTHER WORK

7.1 CONCLUSIONS

Cold-formed steel purlin systems are commonly used to support the roof and wall cladding in industrial buildings. Currently, they are designed using a mix of relatively simple theory and empirical data, largely because of the complexity of the structural actions involved. Accurate and adequately validated finite element modelling has, however, been shown to have the potential to provide more fundamental understanding of behaviour as well as the facility to generate detailed information on the response of individual members. Its extension to cover systems and the utilisation of the findings as the basis for a more appropriate design treatment has formed the core of the work reported in this thesis. In particular, it is investigated whether higher load carrying capacities for statically indeterminate systems may be possible by recognising the redistribution of moments and making suitable allowance for the limitations in the moment-rotation relationship of thin-walled cross-sections. While some guidelines for moment redistribution in cold-formed steel systems have been available in the AISI

Specification since 1980, direct guidance on statically indeterminate purlin systems using EC3 without appropriate physical testing remains elusive. The objective of this research was to comprehensively understand the moment redistribution behaviour of 2-span purlin systems subjected to gravity and uplift loading, and develop design formulae to estimate the post-peak reduction of interior support moment from its initial peak at ultimate load. This allowed the use of the reduced moment at the interior support in conjunction with the full span moment or lateral torsional buckling moment for uplift loading to determine the load-carrying capacity of the system. The review of the previous studies on cold-formed steel purlin systems in Chapter 2 showed that limited research into the moment redistribution behaviour had been carried out since the 1980s. Instead, the approach of many studies of multi-span cold-formed steel purlin systems was predominantly focused on the buckling failure modes and ultimate load carrying capacities. The approach employed in this thesis was to initially use reliable, representative physical test results for validating numerical models, and then used to generate a portfolio of new results which formed the basis for new design formulae.

The finite element (FE) method using ABAQUS (2010) has been shown to be able to accurately capture the buckling behaviour of cold-formed steel beams. In Chapter 3, finite element modelling techniques for cold-formed steel sections have been explained in detail. The lateral and translation restraints offered by sheeting have been simulated by modelling a 2-spring model consisting of: (i) a linear spring with large spring stiffness to represent the bearing and pull-out force of typical screws and (ii) compression only springs located at the lip/flange junction to prevent upward buckling into the sheeting. The chosen spring model was validated against physical test responses generated by Yu and Schafer (2003). The average ultimate load comparison and COV value against the test results of Yu and Schafer (2003) were 1.006 and 0.055 respectively. A superposition of pure local and distortional buckling modes obtained from the finite strip software CUFSM (Schafer 2006) and manually distributing the imperfection shapes longitudinally with periods equal to the half-wavelength was taken as the geometrical imperfections for the FE models. Based on results from an initial geometrical imperfection study, the chosen longitudinal imperfection spectrum (worst case) was based on an odd number of local and distortional buckling waves with imperfection directions towards the neutral axis. Cold-formed steel material behaviour was modelled using the modified Ramberg-Osgood model proposed by Gardner and Ashraf (2006). Based on a small sample of

representative corner tensile coupon tests results, an increase in 0.2% proof stress of 5 and 10% relative to that of the flat regions of the cross-section were employed in the corner regions. The 1% proof stress $\sigma_{1.0}$ was estimated using a relationship between the 0.2% proof stress $\sigma_{0.2}$ and $\sigma_{1.0}$ proposed by Haidarali (2011), which was implemented directly in the modified Ramberg-Osgood material model. For continuous Zed, Zeta, Zeta II and channel purlin members, three types of nonlinear finite element analyses were validated against a total of 61 reported physical tests including: (i) continuous two-span beams subjected to a UDL, (ii) single span beams subjected to a central point load producing a moment gradient and (iii) single span beams subjected to two equal point loads producing a central region under pure bending. The developed materially and geometrically nonlinear FE models were able to capture full load-deformation responses including the spread of yielding, buckling modes and ultimate load-carrying capacity. Observed cross-section instabilities included local buckling and distortional buckling, while global instability (lateral torsional buckling) was also observed for 2-span systems subjected to uplift loading.

For continuous 2-span systems subjected to gravity loading, a parametric study consisting of 245 FE models for Zeta, Zeta II, Zed and C-sections covering a wide range of cross-section slenderness has been conducted. For each 2-span FE model, the reduction in central support moment from its peak moment capacity upon reaching the collapse load of the system was evaluated against additional single span reference moment capacities. The results from the study showed that 2-span systems made up of stocky sections can achieve full moment redistribution, since no significant reduction in the central support capacity was observed at system failure. Conversely, slender sections at large spans could lose up to 50% of their maximum support moment at the ultimate load due to a sharp loss of moment at the interior support. The design approach of assuming full redistribution (no interior support moment reduction, $\alpha_{design,g}$ =1) was found to be unconservative by 12% on average and up to 27% for the more slender sections. Alternatively, the design approach based on elastic principles was found to be highly conservative by 22% on average. In order to estimate the reduction of the interior support moment at failure, a design formula based on the span length and cross-section slenderness was proposed so that the revised interior moment can be applied directly with the plastic mechanism approach of EC3. The proposed design approach showed an average design-to-FE results of unity with a low scatter (COV = 0.049).

A parallel parametric study consisting of 270 FE models has been conducted for continuous 2-span purlin systems subjected to uplift loading. Lateral torsional buckling (LTB) was observed in the span for all cases. The loss of moment at the central support from its peak moment capacity and the limiting effect of LTB in the span upon reaching the collapse load have been evaluated. Similar to the parametric study for gravity loading, greater interior support moment reduction was observed for slender sections and long span lengths compared to stockier arrangements. The beneficial effect of the sheeting at the interior support in conjunction with lateral torsional buckling observed in the span region meant the relationship between interior support moment reduction against span length and cross-section slenderness differed to the case of gravity loading; an alternative design formula has been proposed to estimate the amount of moment redistribution for continuous systems subjected to uplift loading. The parametric study showed that the method of estimating the reduction factor for lateral torsional buckling χ_{LT} using Eurocode 3 Part 1.3 was rather conservative. Comparative design models have shown that a 2.7% potential increase in average design loads is possible providing χ_{LT} can accurately predict the shortfall in moment in the span at failure. Nevertheless, adopting the proposed design approach gives 8.3% improved predictions (mean =0.945) compared to elastic design.

The moment redistribution behaviour for 2-span purlin systems was also extended to account for systems with sleeve connections at the interior support. Chapter 5 describes additional FE modelling techniques for two further FE sleeved models including: (i) single span sleeved beam subjected to a linear moment gradient, (ii) 2-span sleeved arrangements subjected to either gravity or uplift UDL. Additional FE modelling parameters beyond those required for the bare sections included sleeve material definitions, contact interactions and a nonlinear spring model to replicate the bolted connections. For 2-span cases, difficulties due to non-convergence were overcome by changing the solver type to displacement control with artificial damping and applying displacements through an evenly spaced 4 tier 16 point whiffletree. An initial damping sensitivity study showed that results coincided with the modified Riks method (used for continuous cases) providing the dissipated energy fraction was set to 1×10^{-4}. A total of 49 physical sleeved tests were used to validate two sets of FE models with: (i) no bolt slip and (ii) 1 mm bolt slip. Both sets of FE models were found to agree well with the physical tests which exhibited similar ultimate load capacities, failure models and initial stiffness;

the average ultimate load ratio between physical tests and FE models was 0.991. FE models that allowed for bolt slip yielded only marginal differences in load capacity.

The elastic stiffness, ultimate load and rotation capacities for sleeved connections were investigated in an initial single span study by varying the sleeve length to section depth ratio for 5 different bolt configurations. In general, it was found that sleeve connections with sleeve to section depth ratios of at least 3.5 and 8 respectively provided full stiffness and strength connections. The rotation capacities of sleeve sections were generally 3 times greater than the equivalent continuous case.

The 2-span moment redistribution behaviour study for continuous members was extended to sleeved arrangements by means of additional parametric studies. For gravity loading, a total of 152 FE models covering of Zeta I, Zeta II and Zed cross-sections for a range of 4-12 m spans were simulated. The higher moment and rotation capacities offered by the sleeve connection resulted in greater scope for moment redistribution compared to the equivalent continuous 2-span case, thus providing higher ultimate load capacities of approximately 10%. Interior support moment reduction was observed for slender arrangements but was less severe than for the continuous systems. The previously proposed design equation for continuous 2-span cases subjected to gravity loading was found to be suitable in predicting the reduction in interior support moment at the collapse load, provided reduced cross-section slenderness values were used; the average design-to-FE ultimate load gave results close to unity and modest scatter, with a mean of 1.005 and COV of 0.060.

A fourth 2-span parametric study was conducted to examine the moment redistribution behaviour of sleeved systems subjected to uplift loading. The study comprised Zeta I and Zeta II sections covering span lengths of 4-10 m with L_{sleeve}/d ratios ranging from 3.5-5.6. For the cases considered, it was found that the enhanced rotation capacity offered by the sleeved connection allowed the system to distribute the moment into the span without a loss of interior support moment, with the span region eventually failing by LTB. The presence of the sleeved connection resulted in an average of 7% increase in load carrying capacity compared to the equivalent continuous case. A similar design method to that of the continuous 2-span uplift case was proposed. Improvements to the design method by considering alternative approaches to determining the reduction factor for lateral torsional buckling were outlined.

Generally, the investigations in this thesis have provided an in-depth understanding into the buckling and moment redistribution behaviour of single and 2-span continuous and sleeved beams. Design proposals for each (continuous and sleeved) 2-span system and covering both gravity and uplift loading were made. The framework allows the collapse loads of indeterminate systems to be calculated based on cross-section moment capacities derived from previously conducted physical tests, design codes or analytical and numerical models. In general, designing the collapse load for purlins systems using the proposed framework has consistently shown significant improvements against the elastic design method. While any improvements in load table values are welcome for cold-formed steel purlin fabricators (even by a few percent), the revised methods provide an opportunity for greater structural efficiency and material savings.

7.2 SUGGESTIONS FOR FUTURE WORK

The findings of this thesis provide a sound basis for extending the investigation on moment redistribution behaviour of cold-formed steel systems. While this thesis covered the 4 most common section types (Zed, channel, Zeta I and Zeta II) and span lengths used in practice, further investigations on the suitability of alternative cross-sections can be checked against the proposed design methods. This can be investigated with the finite element models developed in this study. In addition, the validated FE models can be used as a tool to investigate the most optimal cross-section and sleeve details, e.g. varying the internal stiffener locations or changing bolt details.

To develop the moment redistribution design method further, alternative purlins systems should be also investigated. These could include: 2-span overlapped systems with varying bolt connections, systems made up of compound cross-sections (such as back-to-back channel sections) and systems with different cleat, anti-sagbar and sheeting arrangements.

While the proposed design method for 2-span purlins system is only valid for equal span lengths, extending the portfolio of design cases to allow 2-span purlin systems comprising unequal spans and 3 or 4-span systems should be investigated by conducting further parametric studies. Further variables worthy of investigation include different load combinations and off-centred lapped or sleeve arrangements.

REFERENCES

ABAQUS. (2010). ABAQUS Version 6.10. Pawtucket, USA: Hibbitt, Karlsson & Sorensen, Inc.

Abdel-Rahman, N. and Sivakumaran, K. S. (1997). Material properties models for analysis of cold-formed steel members. *Journal of Structural Engineering*. **123(9)**, 1135-1143.

American Iron Steel Institute (AISI). (1996). Specification for the Design of Cold-Formed Steel Structural Members. American Iron and Steel Institute, Washington, D.C.

American Iron Steel Institute (AISI). (2004). Commentary on Appendix 1: Design of Cold-Formed steel Structural Members with the Direct Strength Method. American Iron and Steel Institute, Washington, D.C.

American Iron Steel Institute (AISI). (2007). Specification for the Design of Cold-Formed Steel Structural Members. American Iron and Steel Institute, Washington, D.C.

Batista E. M. and Rodrigues, F. C. (1992). Residual stresses measurements on cold formed profiles. *Experimental techniques.* **16(5)**, 25-29.

Borges Dinis, P., Camotim, D. and Silvestre, N. (2007). FEM-based analysis of the local-plate/distortional mode interaction in cold-formed steel lipped channel columns. *Computers and Structures*. **85(19-20)**, 1461–1474.

Borges Dinis, P. and Camotim, D. (2010). Local/distortional mode interaction in cold-formed steel lipped channel beams. *Thin-Walled Structures*. **48 (10-11)**, 771 –785.

Boutell, B. and Hui, C. (2013). Imperfections used in finite element analysis. *Imperial College London Report for Ayrshire Metal Products*, Ref. **A3**. Imperial College London.

Bradford, M. A. and Hancock, G. (1984). Elastic interaction of local and lateral buckling in beams. *Thin-Walled Structures*. **2 (1)**, 1–25.

Bryan, E. R. and Davies, J. M. (1979). Design basis of Zeta purlins: Part 1. *Department of Civil Engineering Report.* Ref. no. **80/132**, University of Salford.

Bryan, E. R. and Davies, J. M. (1980a). Design basis of Zeta purlins: Part 2. *Department of Civil Engineering Report.* Ref. no. **80/135**. University of Salford.

Bryan, E. R. and Davies, J. M. (1980b). Design basis of Zeta purlins: Part 3. *Department of Civil Engineering Report.* Ref. no. **80/138**. University of Salford.

Bryan, E. R. and Deakin, W. H. (1989). Tests and design of 175mm deep continuous and sleeved Zeta purlins. *Department of Civil Engineering Report.* Ref. no. **J287**. University of Salford.

Canadian Standards Association (CSA). (1994). Cold-formed Steel Structural Members. S136-94. Canadian Standards Association, Ontario, Canada.

Chajes, A., Britvec, S. J. and Winter, G. (1963). Effects of cold-straining on structural steel sheets. *Journal of the Structural Division, ASCE*. **89(ST2)**, 1-32.

Chou, S. M., Chai, G. B. and Ling, L. (2000). Finite element technique for design of stub columns. *Thin-Walled Structures*. **37(2)**, 97-112.

Chung, K.F. and St Quinton, D. (1996). Structural performance of modern roofs with thick over-purlin insulation – experimental investigation. *Journal of Constructional Steel Research*. **40(1)**, 17-38.

Cimpoeru, S. J. (1992). The modelling of the collapse during roll-over of bus frames consisting of square thin-walled tubes. *PhD Thesis*. Monash University, Melbourne.

CUFSM. (2006). CUFSM Version 3.12, Schafer, B. W. Department of Civil Engineering, Johns Hopkins University. http://www.ce.jhu.edu/bschafer/cufsm/

Dat, D. T. and Peköz, T. (1980). The strength of cold-formed steel columns. *Department of Structural Engineering Report.* Report no. **80-4**. Cornell University, Ithaca, New York.

Dawson, R. G., and Walker, A. C. (1972). Post-buckling of geometrically imperfect plates. *Journal of the Structural Division, ASCE.* **98(1)**: 75-94.

Davies, J. M. (1979). Prototype purlins supplementary tests and analysis. *Department of Civil Engineering Report.* Ref. no. **79/130**. University of Salford

Davies, J. M. and Deakin, W. H. (1992). Sleeve tests on Zeta II purlins. *Department of Civil Engineering Report.* Ref. no. **SJ498**. University of Salford

Davies, J. M. and Leach, P. (1992). Some applications of generalized beam theory. *Proceedings of the Eleventh International Specialty Conference on Cold-Formed Steel Structures.* University of Missouri-Rolla, St Louis, MO. 479-501.

Davies, J. M. and Leach, P. (1994). First-order generalised beam theory. *Journal of Constructional Steel Research*. **31(2-3)**, 187-220.

Davies, J. M., Leach, P. and Heinz. D. (1994). Second-order generalised beam theory. *Journal of Constructional Steel Research*. **31(2-3)**, 221-241.

Deakin, W. H., Bryan, E. R. and Davies, J. M. (1979). Bending tests on prototype purlins. *Department of Civil Engineering Report.* Ref. no. **79/120**. University of Salford

Deakin, W. H. (1991a). Tests and design of 150mm deep continuous and sleeved Zeta purlins rolled from Z35 material. *Department of Civil Engineering Report.* Ref. no. **SJ450**. University of Salford

Deakin, W. H. (1991b). Tests and design of 200mm deep x 1.4mm thick continuous and sleeved Zeta purlins. *Department of Civil Engineering Report.* Ref. no. **SJ457**. University of Salford

Deakin, W. H. and Melbourne, C. (1997). Report prepared for Ayrshire Metal Products (Daventry) Ltd: Sleeve tests on cold rolled purlins. *Department of Civil Engineering Report.* Ref. no. **SJ683**. University of Salford

Desmond, T. P., Peköz, T. and Winter, G. (1978). Local and overall buckling of cold formed compression members. *Department of Structural Engineering Report.* Cornell University, Ithaca, New York.

Desmond, T. P., Peköz, T. and Winter, G. (1981). Edge stiffeners for thin-walled members. *Journal of the Structural Division, ASCE*. **107(ST2)**, 329-354.

Dubina, D. and Ungureanu, V. (2002). Effect of imperfections on numerical simulation of instability behaviour of cold-formed steel members. *Thin-Walled Structures.* **40(3)**, 239-262

Elhouar, S. and Murray, T. M. (1985). Adequacy of proposed AISI effective width specification provisions for Z- and C- purlin design. *Fears Structural Engineering Laboratory Research Report*. Report no. **FSEL/MBMA 85-04**. University of Oklahoma, OK.

Ellifritt, D., Sputo, T. and Haynes, J. (1992). Flexural capacity of discretely braced C's and Z's. *Proceedings of the Eleventh International Specialty Conference on Cold-Formed Steel Structures.* University of Missouri-Rolla, St Louis, MO. 109-129.

EN 1993-1-3. (2005). Eurocode 3: Design of Steel Structures – Part 1-1: General Rules and Rules for Buildings. *CEN*.

EN 1993-1-3. (2006). Eurocode 3: Design of Steel Structures – Part 1-3: General rules – Supplementary Rules for Cold Formed Members and Sheeting. *CEN*.

EN 1993-1-5. (2006). Eurocode 3: Design of Steel Structures – Part 1-5: Plated Structural Elements. *CEN*.

Feng, M., Wang, Y. C. and Davies, J. M. (2003). Structural behaviour of cold-formed thin-walled short steel channel columns at elevated temperature. Part 2: Design calculation and numerical analysis. *Thin-walled structures.* **41(6)**, 571-594.

Fylstra, D., Lasdon, L., Watson, J. and Waren, A. (1998). Design and use of the Microsoft Excel Solver. *Interfaces*. **28(5)**, 29-55.

Gardner, L. and Ashraf, M. (2006). Structural design for non-linear metallic materials. *Engineering Structures.* **28(6)**, 926-934.

Gardner, L. and Nethercot, D. A. (2004). Numerical modelling of stainless steel structural components - a consistent approach. *Journal of Structural Engineering.* **130(10)**, 1586-1601.

Ghosn, A. A. (2002). Deflection of nested cold-formed steel Z-section beams. *Journal of Structural Engineering, ASCE.* **128(11)**, 1423-1428.

Ghosn, A. A. and Sinno, R. R. (1995). Governing stresses in Z-purlin lap joints. *Journal of Structural Engineering, ASCE.* **121(12)**, 1735-1741.

Ghosn, A. A. and Sinno, R. R. (1996). Load capacity of nested, laterally braced, cold-formed steel Z-section beams. *Journal of Structural Engineering, ASCE.* **122(8)**, 968-971.

Guo, Y-J., Zhu, A-Z., Pi, Y-L and Tin-Loi, F. (2007). Experimental study on compressive strengths of thick-walled cold-formed sections. *Journal of Constructional Steel Research*. **63(5)**, 718-723.

Gutierrez, R., Loureiro, A., Lopez, M. and Moreno, A. (2011). Analysis of cold-formed purlins with slotted sleeve connections. *Thin-Walled Structures.* **49(12)**, 883-841.

Haidarali, M. R. (2011). Local and distortional buckling behaviour of cold-formed steel Z section beams. *PhD thesis*. Imperial College London, UK.

Haidarali, M. R. and Nethercot, D.A. (2011a). Finite element modelling of cold-formed steel beams under local buckling or combined local/distortional buckling. *Thin-Walled Structures.* **49(12)**, 1554-1562.

Haidarali, M. R. and Nethercot, D.A. (2011b). Local and distortional buckling of cold-formed steel beams with edge-stiffened flanges. *Journal of Constructional Steel Research*. **73**, 31-42.

Haidarali, M. R. and Nethercot, D.A. (2012). Local and distortional buckling of cold-formed steel beams with both edge and intermediate stiffeners in their compression flanges. *Thin-Walled Structures.* **54**, 106-112.

Hancock, G. J., Celeban, M., Healy, C., Georgiou, P. N. and Ings, N. L. (1990). Tests of purlins with screw fastened sheeting under wind uplift. *Proceedings of the Tenth International Specialty Conference on Cold-Formed Steel Structures.* University of Missouri-Rolla, St Louis, MO. 393-419.

Hill, H. N. (1944). Determination of stress-strain relations from the "offset" yield strength values. *Technical note no. 927. National advisory Committee for Aeronautics, Washington, D.C.*

Ho, H. C. and Chung, K. F. (2004). Experimental investigation into the structural behaviour of lapped connections between cold-formed steel Z sections. *Thin-Walled Structures.* **42(7)**, 1013-1033.

Ho, H. C. and Chung, K. F. (2006a). Analytical prediction on deformation characteristics of lapped connections between cold-formed steel Z sections. *Thin-Walled Structures.* **44(1)**, 115-130.

Ho, H. C. and Chung, K. F. (2006b). Structural behavior of lapped cold-formed steel Z sections with generic bolted configurations. *Thin-Walled Structures.* **44(4)**, 466-480.

Ingvarsson, L. (1975) Cold forming residual stresses, effect of buckling. *Proceedings of the Third International Specialty Conference on Cold-Formed Steel Structures.* University of Missouri-Rolla, St Louis, MO. 85-119.

Jandera, M., Gardner, L. and Machacek, J. (2008). Residual stresses in cold-rolled stainless steel hollow sections. *Journal of Constructional Steel Research*. **64(11)**, 1255-1263.

Karren, K. W. (1967). Corner properties of cold-formed steel shapes. *Journal of the Structural Division, ASCE*. **93(ST1)**, 401-432.

Karren, K. W. and Gohil M. M. (1975). Strain hardening and aging in cold-formed steel. *Journal of the Structural Division, ASCE*. **101(ST1)**, 187-200.

Karren, K. W. and Winter, G (1967). Effects of cold-forming on light-gage steel members. *Journal of the Structural Division, ASCE*. **93(ST1)**, 433-469.

Key, P. W. and Hancock, G. J. (1993). A theoretical investigation of the column behaviour of cold-formed square hollow sections. *Thin-Walled Structures.* **16(1-4),** 31-64.

Kwon, Y. B. and Hancock, G. J. (1991). A nonlinear elastic spline finite strip analysis for thin-walled sections. *Thin-Walled Structures.* **12(4)**, 295-319.

Kwon, Y. B. and Hancock, G. J. (1993). Post-buckling analysis of thin-walled channel sections undergoing local and distortional buckling. *Journal of Computers and Structures*. **49(3)**, 507-516

LaBoube, R. A., Golovin, M., Montague, D. J., Perry, D. C. and Wilson, L. L. (1988). Behavior of continuous span purlin systems. *Proceedings of the Ninth International Specialty Conference on Cold-Formed Steel Structures.* University of Missouri-Rolla, St Louis, MO. 191-203.

LaBoube, R. A. and Yu, W. W. (1978). Structural behavior of beams webs subjected to combination of bending stress. *Civil Engineering Study Structural Series*. Report. no. **78-1**. University of Missouri-Rolla, St Louis, MO.

Laine, M. and Tuomala, M. (1999). Testing and design of gravity-loaded steel purlins restrained by sheeting. *Journal of Constructional Steel Research*. **49(2)**, 129-138.

Leach, P. (1990). Testing of 225 dp and 250 dp sleeved Zeta purlin systems. *Department of Civil Engineering Report.* Ref. no. **J397**. University of Salford

Leach, P. (1992). Small-scale testing on Zeta II purlins according to Eurocode 3: Part 1.3 – to obtain rotational restrain factors. *Department of Civil Engineering Report.* Ref. no. S**J534-A**. University of Salford

Leach, P. and Robinson, P. (1993). The behaviour of purlins subject to wind uplift (an assessment of EC3: Part 1.3). *The Structural Engineer*. **71(14)**, 250-252

Loughlan, J., Yidris, N. and Jones, K. (2012). The failure of thin-walled lipped channel compression members due to coupled local-distortional interactions and material yielding. *Thin-Walled Structures*. **61**, 14-21.

Maduliat, S., Bambach, M. R. and Zhao, X. L. (2012). Slenderness limits for cold-formed channel sections in bending by experimental methods. Journal of Constructional Steel Research. **76**, 75-82.

Mirambell, E. and Real, E. (2000). On the calculation of deflections on structural stainless steel beams: an experimental and numerical investigation. *Journal of Constructional Steel Research*. **54(1)**, 109-133.

Moen, C. D., Igusa, T. and Schafer, B. W. (2008). Prediction of residual stresses and strains in cold-formed steel members. *Thin-Walled Structures.* **46(11)**, 1274-1289.

Moreyra, M. E. and Peköz, T. (1994a). Experiments on lipped channel flexural members. *Proceedings of the Twelfth International Specialty Conference on Cold-Formed Steel Structures.* University of Missouri-Rolla, St Louis, MO. 41-56.

Moreyra, M. E. and Peköz, T. (1994b). Finite element studies on lipped channel flexural members. *Proceedings of the Twelfth International Specialty Conference on Cold-Formed Steel Structures.* University of Missouri-Rolla, St Louis, MO. 57-74.

Mulligan, G. P. and Peköz, T. (1984). Locally buckled thin-walled columns. *Journal of Structural Engineering, ASCE.* **110(11)**, 2635-2654.

Nguyen, N. T. B., Fung, T. C. and Young, B. (2006). Strength and behavior of cold-formed steel Z-sections subjected to major axis bending. *Journal of Structural Engineering, ASCE.* **132(10)**, 1632-1640.

North American Specification (NAS). (2001). North American Specification for the design of cold-formed steel structural members. American Iron and Steel Institute, Washington, D.C.

Papangelis, J. P. and Hancock, G. (1994). Computer analysis of thin-walled structural members. *Computers and Structures.* **56(1)**, 157-176.

Papangelis, J. P. and Hancock, G. (2005). Computer analysis and design of cold-formed purlins. 1*0th International Conference on Civil, Structural and Environmental Engineering Computing,* UK.

Papazian, R. P., Schuster, R. M. and Sommerstein, M. (1994). Multiple stiffened deck profiles. *Proceedings of the Twelfth International Specialty Conference on Cold-Formed Steel Structures.* University of Missouri-Rolla, St Louis, MO. 217-228.

Pham, C. H. and Hancock, G. J. (2013). Experimental investigation and direct strength design of high-strength, complex C-sections in pure bending. *Journal of Structural Engineering*, *ASCE*. **139(11)**, 1842-1852.

Ramberg, W. and Osgood, W. R. (1943). Description of stress-strain curves by three parameters. *Technical Note No. 902. National Advisory Committee for Aeronautics. Washington, D.C.*

Rasmussen, K. J. R. (2003). Full-range stress-strain curves for stainless steel alloys. *Journal of Constructional Steel Research*. **59(1)**, 47-61.

Reck, H. P., Pekoz, T. and Winter, G. (1975). Inelastic strength of cold-formed steel beams. *Journal of the Structural Division, ASCE*. **101(ST11)**, 2193-2203.

Rhodes, J. (2002). Post-buckling analysis of light gauge members using finite strips. *16h International Specialty Conference on Cold-Formed Steel Structures.* Orlando, Florida, 53-67

Robertson, G. W. and Kurt, C. (1986). Behavior of nested Z-shaped purlins. *Proceedings of the Eighth International Specialty Conference on Cold-Formed Steel Structures.* University of Missouri-Rolla, St Louis, MO. 95-110.

Rogers, C. A. and Hancock, J. G. (1997). Ductility of G550 sheet steels in tension. *Journal of Structural Engineering, ASCE.* **123(12)**, 1586-1594.

Rondal, J. (1987). Residual stresses in cold-rolled profiles. *Construction and Building Materials.* **1(3),** 150-164.

Roy, G., Mohamedien, M. A. and Polyzois, D. (1994). Residual stresses in cold formed steel sections. *Proceedings of the Twelfth International Specialty Conference on Cold-Formed Steel Structures.* University of Missouri-Rolla, St Louis, MO. 691-703.

Schafer B. W. and Ádány, S. (2006). Buckling analysis of cold-formed steel members using CUFSM: conventional and constrained finite strip methods. *18th International Specialty Conference on Cold-Formed Steel Structures.* Orlando, Florida, 39-54

Schafer, B. W., Grigoriu, M. and Peköz, T. (1998). A probabilistic examination of the ultimate strength of cold-formed steel elements. *Thin-Walled Structures.* **31(4)**, 271-288.

Schafer, B. W., Li, Z. and Moen, C. D. (2010). Computational modelling of cold-formed steel. *Thin-Walled Structures.* **48(10-11)**, 752-762.

Schafer, B. W. and Peköz, T. (1998a). Direct strength prediction of cold-formed steel members using numerical elastic buckling solutions. *Proceedings of the Fourteenth International Specialty Conference on Cold-Formed Steel Structures.* University of Missouri-Rolla, St Louis, MO. 691-703.

Schafer, B. W. and Peköz, T. (1998b). Computational modeling of cold-formed steel: characterizing geometric imperfection and residual stresses. *Journal of Constructional Steel Research*. **47(3)**, 193-210.

Schardt, R. (1994). Lateral torsional and distortional buckling of channel- and hat-sections. *Journal of Constructional Steel Research.* **31(2-3)**, 243-265.

Silvestre, N. and Camotim, D. (2004a). Distortional buckling formulae for cold-formed steel C and Z-section members part I-derivation. *Thin-Walled Structures.* **42(11)**, 1567-1597.

Silvestre, N. and Camotim, D. (2004b). Distortional buckling formulae for cold-formed steel C and Z-section members part II-validation and application. *Thin-Walled Structures.* **42(11)**, 1599-1629.

Sivakumaran, K. S. (1987). Analysis for local buckling capacity of cold-formed steel sections with web opening. *Computers and Structures.* **26(1/2)**, 275-282.

Sokol, L. (1998). Flexion laterole de la semelle intérieure des pannes en Z ou C. Contruction Metalique. **1**.

Standards Australia and the Australian Institute of Steel Construction (AS/NZS). (2005). AS/NZS 4600: 2005 Cold-Formed Steel Structures.

Telue, Y. and Mahendran, M. (2004). Behaviour and design of cold-formed steel wall frames lines with plasterboard on both sides. *Engineering Structures.* **26(5)**, 567-579.

Theofanous, M and Gardner, L. (2010). Experimental and numerical studies of lean duplex stainless steel beams. *Journal of Constructional Steel Research.* **66(6)**, 816-825.

Timoshenko, S. P. and Gere, J. M. (1961).Theory of Elastic stability, 2nd ed. Mcgraw Hill, New York.

Wang, H. and Zhang, Y. (2009). Experimental and numerical investigation on cold-formed steel C-section flexural members. *Journal of Constructional Steel Research.* **65(5)**, 1225-1235.

Weng, C. C. and Peköz, T. Residual stresses in cold-formed steel members. *Journal of Structural Engineering*, *ASCE*. **116(6)**, 1611-11625.

Willis, C. T. and Wallace, B. (1990). Behaviour of cold-formed steel purlins under gravity loading. *Journal of Structural Engineering*, *ASCE*. **116(8)**, 2061-2069.

Winter, G. (1959). Cold-formed light-gage steel construction. *Journal of the Structural Division, ASCE*. **85**, 151-171

Von Karman, T., Sechler, E. E. and Donnell, L. H. (1932). The strength of thin plates in compression. *Transactions of ASCE*. **54**, 53-57.

Yamaki, N. (1959). Postbuckling behaviour of rectangular plates with small initial curvature loaded in edge compression, *Journal of Applied* Mechanics, ASME. **26**, 407-414

Ye, J. and Rasmussen, K. J. R. (2008). Compression strength of unstiffened elements in cold-reduced high strength steel. *Journal of Structural Engineering*, *ASCE*. **134(2)**, 189-197.

Ye, W., Wang, C. J., Mynors, D. J., Kibble, K. A., Morgan, T. and Cartwright, B. (2013). Load-deflection behaviour of sleeved joints in modified Z purlin system. *Thin-Walled Structures.* **73**, 318-328.

Yener, M. and Peköz, T. (1980). Inelastic load carrying capacity of cold-formed steel beams. *Proceedings of the Fifth International Specialty Conference on Cold-Formed Steel Structures.* University of Missouri-Rolla, St Louis, MO. 145-174.

Yener, M. and Peköz, T. (1985a). Partial stress redistribution in cold-formed steel. *Journal of Structural Engineering*, *ASCE*. **111(6)**, 1169-1186.

Yener, M. and Peköz, T. (1985a). Partial moment redistribution in cold-formed steel. *Journal of Structural Engineering*, *ASCE*. **111(6)**, 1187-1203.

Young, B. and Hancock, G. J. (2003). Compression tests of channels with inclined simple edge stiffeners. *Journal of Structural Engineering*, *ASCE*. **129(10)**, 1403-1411.

Young, B. and Rasmussen, K. J. R. (1998). Tests of fix-ended plain channel columns. *Journal of Structural Engineering, ASCE.* **124(2)**, 131-139.

Yu, C. (2005). Distortional buckling of cold-formed steel members in bending. *PhD thesis*. John Hopkins University, Baltimore, MD.

Yu, C. and Schafer, B. W. (2003). Local buckling tests on cold-formed steel beams. *Journal of Structural Engineering, ASCE.* **129(12)**, 1596-1606.

Yu, C. and Schafer, B. W. (2006). Distortional buckling tests on cold-formed steel beams. *Journal of Structural Engineering, ASCE.* **132(4)**, 515-528.

Yu, C. and Schafer, B. W. (2007). Simulation of cold-formed steel beams in local and distortional buckling with applications to the direct strength method. *Journal of Constructional Steel Research*. **63(5)**, 581-590.

Zhang, L. and Tong, G. (2008). Moment resistance and flexural rigidity of lapped connections in multi-span cold formed Z purlin systems. *Thin-Walled Structures.* **46(5)**, 551-560.

APPENDICES

Tables A.1-A.4, D.1-D.4, F.1-F.3 and G.1-G.2 presents the raw data for the 2-span bare and sleeved FE parametric studies outlined in the Chapter 4 and 6. The first of the two rows for each 2-span FE result in the M_{span} and $M_{support}$ columns show the moment values at the start of stage 2 ($M_{support}$ reaches its peak), whilst the second row show the final span and support moments at ultimate load.

APPENDIX A: RAW DATA FOR BARE SECTION PARAMETRIC STUDY – GRAVITY LOADING

Table A.1: *Bare Zeta I 2-span gravity FE and design methods 1, 2 and 3 results*

Section #	Span	$q_{FE,g}$	M_{span}	$M_{support}$	M_{span} / M_1 Stage 2	M_{span} / M_1 q_{ult}	$M_{support}$ / M_3 Stage 2	$M_{support}$ / M_3 q_{ult}	M_1	M_3	$\alpha_{design,g}$*	$\alpha_{design,g}M_3$	$\bar{\lambda}_{cs,-ve}$	Method 1		Method 2		Method 3	
														$q_{1,g}$	$q_{1,g}$ /$q_{FE,u}$	$q_{2,g}$	$q_{2,g}$ /$q_{FE,g}$	$q_{3,g}$	$q_{2,g}$ /$q_{FE,g}$
	(m)	(kN/m)	(kNm)	(kNm)					(kNm)	(kNm)		(kNm)		(kN/m)		(kN/m)		(kN/m)	
1/150_50	4	23.603	29.272 29.272	-39.955 -39.955	0.889	0.889	1.078	1.078	32.914	-37.066	1.000	-37.066	0.455	18.533	0.785	24.860	1.053	24.860	1.053
	6	11.615	33.354 33.666	-40.978 -40.891	1.013	1.023	1.089	1.087	32.914	-37.616	1.000	-37.616	0.455	8.359	0.720	11.100	0.956	11.100	0.956
	8	6.451	31.981 33.754	-39.720 -38.995	0.972	1.026	1.054	1.035	32.914	-37.673	1.000	-37.673	0.455	4.709	0.730	6.247	0.968	6.247	0.968
1/150_40	4	20.966	26.884 26.884	-33.142 -33.142	1.012	1.012	1.097	1.097	26.576	-30.209	1.000	-30.209	0.528	15.105	0.720	20.132	0.960	20.132	0.960
	6	9.175	25.541 26.792	-32.068 -31.760	0.961	1.008	1.080	1.069	26.576	-29.698	1.000	-29.698	0.528	6.599	0.719	8.900	0.970	8.900	0.970
	8	5.020	23.692 26.928	-30.571 -28.455	0.891	1.013	1.070	0.996	26.576	-28.560	0.935	-28.560	0.528	3.570	0.711	4.946	0.985	4.946	0.985
1/150_30	4	15.289	19.280 19.747	-23.868 -23.786	0.973	0.997	1.105	1.102	19.806	-21.591	0.932	-21.591	0.631	10.795	0.706	14.809	0.969	14.809	0.969
	6	6.627	16.944 19.721	-22.721 -21.960	0.855	0.996	1.071	1.035	19.806	-21.221	0.851	-21.221	0.631	4.716	0.712	6.547	0.988	6.547	0.988
	8	3.598	14.608 19.460	-21.837 -20.061	0.738	0.983	1.020	0.937	19.806	-21.411	0.767	-19.920	0.631	2.676	0.744	3.693	1.026	3.620	1.006
1/125_20	4	6.951	8.741 8.827	-11.221 -11.217	0.975	0.985	1.117	1.117	8.965	-10.044	0.854	-10.044	0.664	5.022	0.722	6.760	0.973	6.760	0.973
	6	2.933	7.44 8.90	-10.54 -9.05	0.830	0.993	1.086	0.933	8.965	-9.704	0.758	-8.762	0.664	2.157	0.735	2.973	1.014	2.880	0.982
	8	1.576	6.874 8.800	-10.234 -8.018	0.767	0.982	1.041	0.815	8.965	-9.833	0.658	-7.480	0.664	1.229	0.780	1.679	1.065	1.555	0.986

Table A.1: *Bare Zeta I 2-span gravity FE and design methods 1, 2 and 3 results (continued)*

Section #	Span	$q_{FE,g}$	M_{span}	$M_{support}$	M_{span} / M_1 Stage 2	M_{span} / M_1 q_{ult}	$M_{support}$ / M_3 Stage 2	$M_{support}$ / M_3 q_{ult}	M_1	M_3	$\alpha_{design,g}$*	$\alpha_{design,g}M_3$	$\bar{\lambda}_{cs,-ve}$	Method 1		Method 2		Method 3	
														$q_{1,g}$	$q_{1,g}$ /$q_{FE,u}$	$q_{2,g}$	$q_{2,g}$ /$q_{FE,g}$	$q_{3,g}$	$q_{2,g}$ /$q_{FE,g}$
	(m)	(kN/m)	(kNm)	(kNm)					(kNm)	(kNm)		(kNm)		(kN/m)		(kN/m)		(kN/m)	
1/200_25	4	18.535	23.288 24.190	-28.481 -28.170	0.966	1.004	1.083	1.071	24.096	-26.309	0.855	-26.309	0.716	13.154	0.710	18.025	0.972	17.986	0.970
	6	7.767	19.47 23.87	-27.57 -23.39	0.808	0.991	1.050	0.891	24.096	-26.247	0.800	-24.554	0.716	5.833	0.751	8.005	1.031	7.840	1.009
	8	4.165	18.080 23.782	-26.632 -19.450	0.750	0.987	1.027	0.750	24.096	-25.930	0.743	-22.275	0.716	3.241	0.778	4.486	1.077	4.298	1.032
1/125_13	4	4.030	4.601 5.305	-6.504 -5.993	0.855	0.986	1.117	1.029	5.383	-5.823	0.660	-4.083	0.849	2.911	0.722	4.015	0.996	3.613	0.896
	6	1.725	3.860 5.310	-6.220 -5.250	0.718	0.986	1.045	0.881	5.383	-5.958	0.579	-3.587	0.849	1.324	0.768	1.797	1.042	1.565	0.907
	8	0.913	3.648 5.302	-6.125 -4.127	0.678	0.985	1.048	0.706	5.383	-5.842	0.497	-2.929	0.849	0.730	0.800	1.005	1.100	0.847	0.927
1/175_16	4	8.694	9.947 11.410	-13.477 -13.046	0.863	0.990	1.096	1.061	11.524	-12.300	0.648	-8.170	0.923	6.150	0.707	8.561	0.985	7.617	0.876
	6	3.759	8.760 11.56	-13.58 -11.47	0.760	1.003	1.073	0.907	11.524	-12.652	0.594	-7.605	0.923	2.812	0.748	3.838	1.021	3.347	0.890
	8	2.007	8.260 11.539	-13.301 -9.371	0.717	1.001	1.048	0.738	11.524	-12.696	0.539	-6.825	0.923	1.587	0.791	2.161	1.077	1.845	0.919
1/200_16	4	9.965	11.315 13.442	-15.306 -13.973	0.817	0.970	1.003	0.915	13.852	-15.264	0.657	-10.259	0.930	7.632	0.766	10.392	1.043	9.251	0.928
	6	4.227	11.003 13.849	-16.332 -9.698	0.794	1.000	1.086	0.645	13.852	-15.042	0.609	-9.288	0.930	3.343	0.791	4.598	1.088	4.039	0.955
	8	2.327	10.648 13.769	-16.548 -9.822	0.769	0.994	1.104	0.655	13.852	-14.985	0.562	-8.430	0.930	1.873	0.805	2.583	1.110	2.231	0.959
1/200_13	4	7.020	7.849 9.857	-11.256 -8.785	0.744	0.935	0.946	0.738	10.544	-11.900	0.583	-6.656	1.046	5.950	0.848	7.969	1.135	6.788	0.967
	6	3.092	7.950 10.370	-11.06 -7.130	0.754	0.984	0.934	0.601	10.544	-11.851	0.539	-6.068	1.046	2.634	0.852	3.537	1.144	2.975	0.962
	8	1.763	7.535 10.701	-12.394 -6.723	0.715	1.015	1.051	0.570	10.544	-11.791	0.496	-5.481	1.046	1.474	0.836	1.987	1.127	1.646	0.934
														STD	0.044		0.059		0.042
														MEAN	0.758		1.032		0.960
														COV	0.059		0.057		0.043

* $\alpha_{design,g} = \left[0.7 - 0.0045\left(\frac{L}{h}\right)\right]\bar{\lambda}_{cs,-ve}^{\left[-0.003\left(\frac{L}{h}\right)-1.4\right]}$

Table A.2: *Bare Zeta II 2-span gravity FE and design methods 1, 2 and 3 results*

Section #	Span	$q_{FE,g}$	M_{span}	$M_{support}$	M_{span} / M_1 Stage 2	M_{span} / M_1 q_{ult}	$M_{support}$ / M_3 Stage 2	$M_{support}$ / M_3 q_{ult}	M_1	M_3	$\alpha_{design,g}$*	$\alpha_{design,g}M_3$	$\bar{\lambda}_{cs,-ve}$	Method 1		Method 2		Method 3	
														$q_{1,g}$	$q_{1,g}$ /$q_{FE,u}$	$q_{2,g}$	$q_{2,g}$ /$q_{FE,g}$	$q_{3,g}$	$q_{2,g}$ /$q_{FE,g}$
	(m)	(kN/m)	(kNm)	(kNm)					(kNm)	(kNm)		(kNm)		(kN/m)		(kN/m)		(kN/m)	
2/225_50	4	17.78	55.376 58.003	-67.503 -64.951	0.988	1.035	1.135	1.093	56.021	-59.450	1.000	-59.450	0.541	29.725	0.676	41.544	0.945	41.544	0.945
	6	26.67	53.225 55.612	-66.893 -62.907	0.950	0.993	1.127	1.060	56.021	-59.360	1.000	-59.360	0.541	13.191	0.698	18.455	0.977	18.455	0.977
	8	35.56	48.333 55.734	-63.607 -55.851	0.863	0.995	1.072	0.941	56.021	-59.328	1.000	-59.328	0.541	7.416	0.724	10.379	1.013	10.379	1.013
2/225_40	4	17.78	42.679 46.179	-52.311 -48.810	0.974	1.054	1.023	0.954	43.828	-51.141	1.000	-51.141	0.634	25.571	0.743	33.479	0.972	33.479	0.972
	6	26.67	37.414 44.190	-49.834 -42.975	0.854	1.008	1.032	0.890	43.828	-48.279	1.000	-48.279	0.634	10.729	0.750	14.612	1.022	14.612	1.022
	8	35.56	35.531 44.283	-49.043 -39.873	0.811	1.010	1.044	0.848	43.828	-46.994	1.000	-46.994	0.634	5.874	0.743	8.151	1.031	8.151	1.031
2/225_35	4	17.78	36.442 40.148	-45.631 -42.164	0.946	1.043	1.033	0.955	38.505	-44.169	1.000	-44.169	0.694	22.085	0.740	29.253	0.980	29.253	0.980
	6	26.67	30.874 38.110	-43.028 -35.922	0.802	0.990	1.030	0.860	38.505	-41.777	0.996	-41.600	0.694	9.284	0.759	12.777	1.045	12.760	1.043
	8	35.56	28.161 37.504	-41.514 -32.320	0.731	0.974	0.988	0.770	38.505	-41.997	0.936	-39.317	0.694	5.250	0.793	7.199	1.088	7.057	1.066
2/225_30	4	17.78	28.636 33.409	-37.693 -33.753	0.887	1.035	1.014	0.908	32.289	-37.181	0.909	-33.810	0.768	18.591	0.756	24.560	0.999	23.848	0.970
	6	26.67	23.592 32.634	-35.078 -28.788	0.731	1.011	0.996	0.817	32.289	-35.226	0.857	-30.177	0.768	7.828	0.774	10.733	1.061	10.254	1.014
	8	35.56	23.127 31.557	-35.187 -26.959	0.716	0.977	0.998	0.764	32.289	-35.266	0.803	-28.326	0.768	4.408	0.793	6.039	1.087	5.668	1.020
2/285_30	4	14.04	34.457 44.021	-49.545 -44.341	0.765	0.977	1.002	0.897	45.035	-49.459	0.851	-42.092	0.818	24.729	0.765	33.750	1.043	32.180	0.995
	6	21.05	30.395 44.092	-45.554 -35.518	0.675	0.979	0.917	0.715	45.035	-49.656	0.812	-40.335	0.818	11.035	0.811	15.018	1.104	14.134	1.039
	8	28.07	29.474 44.107	-45.401 -32.025	0.654	0.979	0.919	0.649	45.035	-49.376	0.773	-38.176	0.818	6.172	0.825	8.433	1.127	7.834	1.047
2/225_25	4	19.606	21.600 26.632	-29.196 -26.951	0.828	1.021	0.970	0.895	26.096	-30.102	0.768	-23.110	0.863	15.051	0.768	19.861	1.013	18.372	0.937
	6	7.962	18.710 25.933	-28.777 -20.420	0.717	0.994	0.986	0.700	26.096	-29.176	0.721	-21.036	0.863	6.484	0.814	8.740	1.098	7.965	1.000
	8	4.423	17.911 25.901	-27.814 -19.383	0.686	0.993	0.977	0.681	26.096	-28.481	0.674	-19.194	0.863	3.560	0.805	4.880	1.103	4.380	0.990

Table A.2: *Bare Zeta II 2-span gravity FE and design methods 1, 2 and 3 results (continued)*

Section #	Span	$q_{FE,g}$	M_{span}	$M_{support}$	M_{span} / M_1 Stage 2	M_{span} / M_1 q_{ult}	$M_{support}$ / M_3 Stage 2	$M_{support}$ / M_3 q_{ult}	M_1	M_3	$\alpha_{design,g}$*	$\alpha_{design,g}M_3$	$\bar{\lambda}_{cs,-ve}$	Method 1		Method 2		Method 3	
														$q_{1,g}$	$q_{1,g}$ /$q_{FE,u}$	$q_{2,g}$	$q_{2,g}$ /$q_{FE,g}$	$q_{3,g}$	$q_{2,g}$ /$q_{FE,g}$
	(m)	(kN/m)	(kNm)	(kNm)					(kNm)	(kNm)		(kNm)		(kN/m)		(kN/m)		(kN/m)	
2/285_25	4	25.193	23.914 34.870	-35.765 -32.978	0.659	0.961	0.882	0.813	36.278	-40.567	0.691	-28.034	0.945	20.283	0.805	27.340	1.085	24.649	0.978
	6	10.868	22.834 35.719	-36.170 -27.012	0.629	0.985	0.862	0.644	36.278	-41.971	0.658	-27.599	0.945	9.327	0.858	12.283	1.130	10.913	1.004
	8	5.995	22.184 35.532	-36.967 -25.134	0.612	0.979	0.918	0.624	36.278	-40.250	0.624	-25.117	0.945	5.031	0.839	6.818	1.137	6.002	1.001
2/285_20	4	17.570	15.517 25.442	-24.657 -20.004	0.564	0.925	0.857	0.695	27.499	-28.770	0.565	-16.246	1.087	14.385	0.819	20.305	1.156	17.577	1.000
	6	8.079	15.980 26.724	-26.723 -19.624	0.581	0.972	0.937	0.688	27.499	-28.510	0.536	-15.274	1.087	6.336	0.784	9.000	1.114	7.715	0.955
	8	4.414	16.143 26.781	-26.751 -16.860	0.587	0.974	0.940	0.592	27.499	-28.462	0.507	-14.428	1.087	3.558	0.806	5.060	1.146	4.292	0.972
2/225_14	4	7.860	7.083 11.084	-12.323 -9.741	0.593	0.928	0.877	0.694	11.939	-14.045	0.479	-6.725	1.195	7.022	0.893	9.144	1.163	7.557	0.962
	6	3.543	7.100 11.551	-13.322 -9.058	0.595	0.968	0.974	0.662	11.939	-13.682	0.446	-6.100	1.195	3.041	0.858	4.030	1.137	3.296	0.930
	8	1.936	7.951 11.569	-13.530 -7.870	0.666	0.969	1.020	0.593	11.939	-13.270	0.413	-5.482	1.195	1.659	0.857	2.245	1.160	1.819	0.939
2/245_15	4	9.741	7.100 14.105	-15.202 -11.590	0.479	0.952	0.885	0.674	14.814	-17.186	0.467	-8.026	1.225	8.593	0.882	11.295	1.160	9.305	0.955
	6	4.334	8.716 14.293	-16.320 -10.647	0.588	0.965	0.965	0.630	14.814	-16.910	0.437	-7.397	1.225	3.758	0.867	4.994	1.152	4.072	0.940
	8	2.368	9.237 14.346	-14.962 -9.100	0.624	0.968	0.889	0.541	14.814	-16.825	0.408	-6.868	1.225	2.103	0.888	2.805	1.185	2.261	0.955
2/265_15	4	10.106	9.443 14.675	-15.383 -11.394	0.573	0.890	0.904	0.670	16.481	-17.012	0.457	-7.772	1.252	8.506	0.842	12.121	1.199	10.090	0.998
	6	4.719	9.586 15.571	-15.012 -11.573	0.582	0.945	0.842	0.649	16.481	-17.833	0.430	-7.670	1.252	3.963	0.840	5.464	1.158	4.474	0.948
	8	2.569	9.647 15.711	-16.544 -9.485	0.585	0.953	0.934	0.535	16.481	-17.716	0.404	-7.151	1.252	2.215	0.862	3.068	1.194	2.487	0.968
														STD	0.055		0.070		0.036
														MEAN	0.801		1.090		0.987
														COV	0.069		0.064		0.036

* $\alpha_{design,g} = \left[0.7 - 0.0045\left(\frac{L}{h}\right)\right]^{\bar{\lambda}_{cs,-ve}^{\left[-0.003\left(\frac{L}{h}\right)-1.4\right]}}$

Table A.3: *Bare Zed 2-span gravity FE and design methods 1, 2 and 3 results*

Section #	Span	$q_{FE,g}$	M_{span}	$M_{support}$	M_{span} / M_1 Stage 2	M_{span} / M_1 q_{ult}	$M_{support}$ / M_3 Stage 2	$M_{support}$ / M_3 q_{ult}	M_1	M_3	$\alpha_{design,g}$*	$\alpha_{design,g}M_3$	$\bar{\lambda}_{cs,-ve}$	Method 1		Method 2		Method 3	
														$q_{1,g}$	$q_{1,g}$ /$q_{FE,u}$	$q_{2,g}$	$q_{2,g}$ /$q_{FE,g}$	$q_{3,g}$	$q_{2,g}$ /$q_{FE,g}$
	(m)	(kN/m)	(kNm)	(kNm)					(kNm)	(kNm)		(kNm)		(kN/m)		(kN/m)		(kN/m)	
Z/125_20	4	5.109	4.822 6.949	-8.771 -7.139	0.644	0.928	1.040	0.846	7.485	-8.434	0.947	-7.988	0.700	4.217	0.825	5.655	1.107	5.560	1.088
	6	2.171	4.656 6.770	-8.820 -6.503	0.622	0.904	1.063	0.784	7.485	-8.296	0.839	-6.958	0.700	1.844	0.849	2.500	1.152	2.374	1.093
	8	1.177	4.307 6.691	-8.313 -5.698	0.575	0.894	1.001	0.686	7.485	-8.305	0.726	-6.032	0.700	1.038	0.882	1.407	1.195	1.285	1.092
Z/200_25	4	12.780	11.623 17.622	-19.551 -16.519	0.631	0.956	0.982	0.830	18.428	-19.903	0.911	-18.128	0.760	9.952	0.779	13.739	1.075	13.362	1.046
	6	5.666	12.375 17.702	-20.096 -16.160	0.672	0.961	1.010	0.812	18.428	-19.892	0.851	-16.920	0.760	4.420	0.780	6.105	1.078	5.823	1.028
	8	3.041	11.657 17.544	-20.096 -14.539	0.633	0.952	1.011	0.731	18.428	-19.887	0.789	-15.697	0.760	2.486	0.817	3.434	1.129	3.210	1.055
Z/125_14	4	3.188	2.800 4.593	-5.136 -3.814	0.578	0.948	0.957	0.710	4.844	-5.368	0.691	-3.708	0.865	2.684	0.842	3.640	1.142	3.284	1.030
	6	1.351	2.797 4.434	-5.354 -3.406	0.577	0.915	0.995	0.633	4.844	-5.379	0.606	-3.257	0.865	1.195	0.885	1.619	1.198	1.415	1.047
	8	0.767	2.852 4.370	-5.352 -3.594	0.589	0.902	1.010	0.678	4.844	-5.300	0.519	-2.751	0.865	0.663	0.864	0.906	1.182	0.768	1.001

Table A.3: *Bare Zed 2-span gravity FE and design methods 1, 2 and 3 results (continued)*

Section #	Span	$q_{FE,g}$	M_{span}	$M_{support}$	M_{span} / M_1 Stage 2	M_{span} / M_1 q_{ult}	$M_{support}$ / M_3 Stage 2	$M_{support}$ / M_3 q_{ult}	M_1	M_3	$\alpha_{design,g}$*	$\alpha_{design,g}M_3$	$\bar{\lambda}_{cs,-ve}$	Method 1		Method 2		Method 3	
														$q_{1,g}$	$q_{1,g}$ /$q_{FE,u}$	$q_{2,g}$	$q_{2,g}$ /$q_{FE,g}$	$q_{3,g}$	$q_{2,g}$ /$q_{FE,g}$
	(m)	(kN/m)	(kNm)	(kNm)					(kNm)	(kNm)		(kNm)		(kN/m)		(kN/m)		(kN/m)	
Z155_15	4	4.760	4.307 7.200	-7.231 -4.602	0.601	1.004	0.932	0.593	7.169	-7.756	0.646	-5.008	0.934	3.878	0.815	5.348	1.123	4.754	0.999
	6	1.994	4.048 6.983	-7.183 -3.807	0.565	0.974	0.931	0.494	7.169	-7.713	0.583	-4.497	0.934	1.714	0.860	2.373	1.190	2.063	1.035
	8	1.074	4.115 6.807	-7.401 -3.319	0.574	0.949	0.965	0.433	7.169	-7.670	0.520	-3.989	0.934	0.959	0.893	1.332	1.241	1.132	1.054
Z/170_14	4	4.855	3.822 7.424	-6.461 -4.476	0.528	1.025	0.828	0.574	7.241	-7.804	0.587	-4.577	1.009	3.902	0.804	5.395	1.111	4.695	0.967
	6	2.009	3.627 7.102	-7.006 -3.664	0.501	0.981	0.908	0.475	7.241	-7.716	0.534	-4.121	1.009	1.715	0.853	2.389	1.189	2.041	1.016
	8	1.148	4.363 7.022	-7.507 -4.239	0.603	0.970	0.980	0.554	7.241	-7.657	0.482	-3.688	1.009	0.957	0.834	1.341	1.168	1.124	0.979
Z/200_13	4	5.449	4.591 8.220	-7.032 -5.324	0.598	1.070	0.842	0.638	7.681	-8.351	0.504	-4.209	1.140	4.176	0.766	5.738	1.053	4.836	0.887
	6	2.160	4.151 7.707	-6.914 -3.744	0.540	1.003	0.822	0.445	7.681	-8.416	0.465	-3.913	1.140	1.870	0.866	2.557	1.184	2.119	0.981
	8	1.184	4.396 7.505	-7.401 -3.659	0.572	0.977	0.890	0.440	7.681	-8.320	0.722	-3.547	1.140	1.040	0.879	1.433	1.211	1.171	0.990
														STD	0.039		0.052		0.051
														MEAN	0.838		1.152		1.022
														COV	0.046		0.046		0.050

* $\alpha_{design,g} = \left[0.7 - 0.0045\left(\frac{L}{h}\right)\right]\bar{\lambda}_{cs,-ve}^{\left[-0.003\left(\frac{L}{h}\right)-1.4\right]}$

Table A.4: *Bare channel 2-span gravity FE and design methods 1, 2 and 3 results*

Section #	Span	$q_{FE,g}$	M_{span}	$M_{support}$	M_{span} / M_1 Stage 2	M_{span} / M_1 q_{ult}	$M_{support}$ / M_3 Stage 2	$M_{support}$ / M_3 q_{ult}	M_1	M_3	$\alpha_{design,g}$*	$\alpha_{design,g}M_3$	$\bar{\lambda}_{cs,-ve}$	Method 1		Method 2		Method 3	
														$q_{1,g}$	$q_{1,g}$ /$q_{FE,u}$	$q_{2,g}$	$q_{2,g}$ /$q_{FE,g}$	$q_{3,g}$	$q_{2,g}$ /$q_{FE,g}$
	(m)	(kN/m)	(kNm)	(kNm)					(kNm)	(kNm)		(kNm)		(kN/m)		(kN/m)		(kN/m)	
C/127_20	4	5.569	5.735 8.050	-9.123 -6.372	0.678	0.952	0.934	0.652	8.460	-9.768	0.649	-6.340	0.866	4.884	0.877	6.440	1.157	5.798	1.041
	6	2.403	5.901 8.187	-9.492 -5.201	0.698	0.968	1.020	0.559	8.460	-9.308	0.571	-5.311	0.866	2.069	0.861	2.819	1.173	2.470	1.028
	8	1.314	5.081 8.222	-8.716 -4.358	0.601	0.972	0.941	0.471	8.460	-9.258	0.491	-4.546	0.866	1.157	0.881	1.583	1.205	1.344	1.022
C/127_18	4	4.790	5.013 7.014	-8.154 -5.239	0.677	0.948	0.962	0.618	7.401	-8.474	0.609	-5.163	0.920	4.237	0.885	5.620	1.173	4.950	1.033
	6	2.070	4.649 7.152	-7.886 -4.215	0.628	0.966	0.967	0.517	7.401	-8.159	0.534	-4.357	0.920	1.813	0.876	2.468	1.192	2.118	1.023
	8	1.056	4.892 4.913	-8.062 -8.023	0.661	0.664	0.987	0.982	7.401	-8.166	0.458	-3.741	0.920	1.021	0.966	1.389	1.315	1.155	1.094
C/200_20	4	9.396	8.357 13.415	-13.559 -11.203	0.550	0.883	0.819	0.676	15.193	-16.564	0.626	-10.369	0.975	8.282	0.881	11.360	1.209	10.048	1.069
	6	4.100	8.670 14.125	-14.639 -8.459	0.571	0.930	0.883	0.510	15.193	-16.578	0.580	-9.619	0.975	3.684	0.898	5.050	1.232	4.391	1.071
	8	2.258	8.739 14.212	-15.055 -7.268	0.575	0.935	0.933	0.450	15.193	-16.137	0.534	-8.625	0.975	2.017	0.893	2.817	1.248	2.414	1.069
C/170_18	4	6.746	6.676 9.669	-10.877 -7.931	0.617	0.893	0.903	0.659	10.824	-12.043	0.602	-7.246	0.988	6.022	0.893	8.144	1.207	7.117	1.055
	6	2.910	6.506 9.980	-11.022 -6.125	0.601	0.922	0.948	0.527	10.824	-11.632	0.548	-6.378	0.988	2.585	0.888	3.581	1.230	3.077	1.057
	8	1.633	6.227 10.334	-10.695 -5.107	0.575	0.955	0.921	0.440	10.824	-11.613	0.495	-5.747	0.988	1.452	0.889	2.013	1.233	1.695	1.038

Table A.4: Bare channel 2-span gravity FE and design methods 1, 2 and 3 results *(continued)*

Section #	Span	$q_{FE,g}$	M_{span}	$M_{support}$	M_{span} / M_1 Stage 2	M_{span} / M_1 q_{ult}	$M_{support}$ / M_3 Stage 2	$M_{support}$ / M_3 q_{ult}	M_1	M_3	$\alpha_{design,g}$*	$\alpha_{design,g}M_3$	$\bar{\lambda}_{cs,-ve}$	Method 1		Method 2		Method 3	
														$q_{1,g}$	$q_{1,g}$ /$q_{FE,u}$	$q_{2,g}$	$q_{2,g}$ /$q_{FE,g}$	$q_{3,g}$	$q_{2,g}$ /$q_{FE,g}$
	(m)	(kN/m)	(kNm)	(kNm)					(kNm)	(kNm)		(kNm)		(kN/m)		(kN/m)		(kN/m)	
C/140_16	4	4.423	4.349 6.438	-7.358 -4.949	0.610	0.903	0.930	0.625	7.130	-7.914	0.568	-4.494	1.006	3.957	0.895	5.361	1.212	4.618	1.044
	6	1.899	4.255 6.546	-7.321 -3.906	0.597	0.918	0.944	0.504	7.130	-7.755	0.504	-3.907	1.006	1.723	0.908	2.368	1.247	1.994	1.050
	8	1.074	4.144 6.836	-7.156 -3.251	0.581	0.959	0.925	0.420	7.130	-7.738	0.440	-3.404	1.006	0.967	0.901	1.331	1.239	1.093	1.018
C/127_15	4	3.552	3.432 5.194	-5.817 -3.910	0.601	0.910	0.924	0.621	5.706	-6.294	0.547	-3.441	1.020	3.147	0.886	4.282	1.205	3.656	1.029
	6	1.600	3.714 5.406	-6.276 -5.529	0.651	0.947	0.987	0.870	5.706	-6.357	0.477	-3.032	1.020	1.413	0.883	1.909	1.193	1.584	0.990
	8	0.881	3.528 5.493	-6.066 -2.975	0.618	0.963	0.998	0.489	5.706	-6.080	0.407	-2.476	1.020	0.760	0.863	1.059	1.202	0.860	0.976
C/155_15	4	4.478	3.991 6.418	-6.807 -5.260	0.542	0.872	0.752	0.581	7.358	-9.057	0.545	-4.932	1.070	4.529	1.011	5.719	1.277	4.800	1.072
	6	1.994	4.475 6.741	-7.611 -4.458	0.608	0.916	0.848	0.496	7.358	-8.979	0.489	-4.392	1.070	1.995	1.001	2.535	1.271	2.081	1.044
	8	1.077	4.203 6.848	-7.306 -3.287	0.571	0.931	0.950	0.428	7.358	-7.687	0.434	-3.336	1.070	0.961	0.892	1.358	1.260	1.113	1.033
C/185_15	4	5.478	5.195 7.814	-8.285 -6.556	0.563	0.846	0.832	0.659	9.234	-9.953	0.534	-5.319	1.126	4.976	0.908	6.880	1.256	5.810	1.060
	6	2.407	4.923 8.371	-8.375 -4.760	0.533	0.907	0.831	0.472	9.234	-10.075	0.489	-4.931	1.126	2.239	0.930	3.069	1.275	2.545	1.057
	8	1.372	5.235 8.689	-9.001 -4.188	0.567	0.941	0.905	0.421	9.234	-9.942	0.445	-4.422	1.126	1.243	0.906	1.720	1.253	1.404	1.023
C/200_15	4	5.925	4.966 8.389	-7.983 -7.254	0.494	0.835	0.738	0.671	10.047	-10.813	0.527	-5.701	1.155	5.406	0.912	7.482	1.263	6.288	1.061
	6	2.637	5.812 8.928	-9.590 -5.857	0.578	0.889	0.883	0.540	10.047	-10.855	0.486	-5.278	1.155	2.412	0.915	3.329	1.263	2.755	1.045
	8	1.477	5.745 9.296	-9.758 -4.753	0.572	0.925	0.916	0.446	10.047	-10.648	0.446	-4.744	1.155	1.331	0.901	1.862	1.260	1.521	1.030
														STD	0.036		0.038		0.025
														MEAN	0.904		1.232		1.032
														COV	0.040		0.031		0.025

* $\alpha_{design,g} = \left[0.7 - 0.0045\left(\frac{L}{h}\right)\right]\bar{\lambda}_{cs,-ve}^{\left[-0.003\left(\frac{L}{h}\right)-1.4\right]}$

APPENDIX B: FLOW DIAGRAM TO CALCULATE THE CRITICAL LATERAL BUCKLING MOMENT USING EUROCODE 3: PART 1-3 SECTION 10

1 Calculate effective widths for section

W_{eff}	Effective section modulus of cross-section for bending about the y-y axis

2 Consider 1/5 h (Zeta II, C and Zed) or 1/6h (Zeta I) of the free flange including contributing part of the web

y_g		Position of N.A axis
I_{fz}		Second moment of area of the free flange
A_{fz}		Cross-sectional area the free flange
W_{fz}		Gross elastic section modulus of the free flange
i_{fz}	$= \sqrt{(I_{fz}/A_{fz})}$	Radius of gyration of the gross-section of the free flange

3 Try initial small load

4 Calculate lateral load $q_{h,ED}$ due to torsion and lateral bending

$q_{h,Ed}$	$= k_h\ q_{Ed}$	Equivalent lateral load	
	kh	= f (k_{h0}, loading direction, a, e or f)	Equivalent lateral load factor
		k_{h0} $= (I_{yz}/I_y)\ (g_s/h)$	Factor for lateral load on free bottom flange (at shear centre)

5 Calculate lateral spring stiffness

K	$= 1 / (1/K_A + 1/K_B + 1/K_C)$	Total lateral spring stiffness per unit length				
	K_A	$= C_D / h^2$	Lateral stiffness corresponding to the rotational stiff of the joint between the sheeting and purlin			
		C_D	$= 1/ (1/C_{D,A} + 1/C_{D,C})$	Total rotational spring stiffness 10.1.5.2(1)		
			$C_{D,A}$	$= C_{100}.\ k_{ba}.\ k_t.\ k_{bR}.\ k_A.\ k_{bT}$		Rotational stiffness of the connection between sheeting and the purlin
				A	k_{ba}	$= f (b_a)$
						b_a Width of purlin flange
					k_t	$= f (t_{nom})$
					k_{bR}	$= f (b_R)$
						b_R Corrugation width (mm)
					k_A	$= 1$ for uplift load
						$= f (t_{nom}, A(kN/m))$ for gravity load
						A Loading introduced from sheeting to the beam
						t_{nom} Nominal thickness of purlin
					k_{bT}	$= \sqrt{b_{T,max}} / b_T$
						b_T Width of the sheeting flange through which purlin is fastened to the purlin
						$b_{T,max}$ Maximum width of the sheeting flange
					C_{100}	Table (10.3) Rotation coefficient, representing the value of $C_{D,A}$ if b_a = 100 mm
				= 130 p		
				B	p	Number of sheet-to-purlin fasteners per metre length of purlin
						Providing: b < 120 mm ; $t_{sheeting}$ > 0.66 mm ; a or b-a > 25 mm
				$= h^2 / I_A / (1/K_A + 1/ K_B) - 4(1-v^2)\ h^2\ (h_d + b_{mod}) / (Et^3\ I_B)$		
				C	b_{mod}	$= a$ Providing the purlin and sheeting contact force is at the purlin web
						$= 2a-+b$ Providing the purlin and sheeting contact force is at the flange tip
						a Distance from the sheet-to-purlin fastener to the purlin web
						b Width of the purlin flange connected to the sheeting
					h	Overall height of purlin
					h_d	Developed height of the purlin web
					l_A	Modular width of tested sheeting
					l_B	Length of tested beam
			$C_{D,C}$	$= m / \theta$		
				A	m	Applied moment per unit width of sheeting
					θ	Resulting rotation
				$= k\ E\ I_{eff} / s$		10.1.5.2 (4)
				B	k	Numerical coefficient
					I_{eff}	Effective second moment of area per unit width of the sheeting
					s	spacing of purlins
				= 0		
				C		Providing: The effects of cross-section distortion have been taken into account

	K_B	$= 4(1-v^2)\, h^2\, (h_d + b_{mod}) / Et^3$		Lateral stiffness due to distortion of the cross-section of the purlin
		b_{mod}	$= a$	Lateral force brings purlin into contact with sheeting at the purlin web
			$= 2a-+b$	Lateral force brings purlin into contact with sheeting at the flange tip
			a	Distance from the sheet-to-purlin fastener to the purlin web
			b	Width of the purlin flange connected to the sheeting
		h	Overall height of purlin	
		h_d	Developed height of the purlin web	
		t	Thickness of the purlin	
	K_C	$= \infty$		Lateral stiffness due to the flexural stiffness of the sheeting
		Providing: The assumption KC is very large compared to KA and KB holds		

6 Calculate lateral bending moment				
$M_{fz,Ed}$	$= \kappa_R M_{0,fz,Ed}$			Lateral bending moment
	$M_{0,fz,Ed}$	= f (Relevant position, $q_{h,Ed}$, L_a)		Initial lateral bending moment in the free flange without any spring support
		L_a	Distance between sag-bars (L_a=L if none are present)	
		$q_{h,Ed}$	Equivalent lateral load	
	κ_R	=f (R)		Correction factor for the effective spring support
		R	$= K L_a^4 / (\pi^4 E I_{fz})$	
			I_{fz}	Second moment of area of the free flange
			K	Lateral spring stiffness per unit length
			L_a	Distance between sag-bars (L_a=L if none are present)

7 Calculate relative slenderness for flexural buckling of the free flange				
$\bar{\lambda}_{fz}$	$= (l_{fz} / i_{fz}) / \lambda_1$			
	λ_1	$= \pi [E / f_{yb}]^{0.5}$		
	i_{fz}	$= \sqrt{(I_{fz}/A_{fz})}$		Radius of gyration of the gross-section of the free flange
	l_{fz}	$= \eta_1 L_a (1 + \eta_2 R^{\eta 3})^{\eta 4}$		
		$\eta_1\, \eta_2\, \eta_3\, \eta_4$ = f (loading, no. sagbars)		Coefficients
			Table 10.2a	for down load
			Table 10.2b	for uplift load
			Providing: Spans are equal, uniformly loaded without sleeve and overlaps $0 \le R \le 200$	
		L_a	= f(loading, no. sagbars)	
			$L_a = L/3$	Providing: Gravity loading, equally spaced sagbar > 3 10.1.4.2 (4)
		$=0.7L_0(1 + 13.1\, R_0^{1.6})^{-0.125}$		Providing: Uplift loading, equally spaced sagbar =0 and $0 \le R_0 \le 200$
			L_0	Modified span length as per Fig 10.5
			R_0	$= K L_0^4 / (\pi^4 E I_{fz})$ Modified coefficient of the spring support

8 Reduction factor for lateral torsional buckling (flexural buckling of the free flange)				
χ_{LT}	$= 1 / (\varphi_{LT} + (\varphi_{LT}^2 - \beta\, \varphi_{LT}^2)^{0.5}$			Reduction factor for lateral torsional buckling
	β	$= 0.75$		
	φ_{LT}	$= 0.5 [1 + \alpha_{LT} (\lambda_{LT} - \lambda_{LT,0}) + \beta \lambda_{LT}^2]$		
		α_{LT}	$= 0.34$	(curve b)
		$\lambda_{LT,0}$	$= 0.4$	
		β	$= 0.75$	
		λ_{LT}	$=\lambda_{fz}$	

9 Check Buckling resistance			
$1 / \chi_{LT} (M_{y,Ed} / W_{eff,y}) + M_{fz,Ed} / W_{fz}$			10.1.4.2 (1)
	χ_{LT}	Reduction factor for lateral torsional buckling	
	$M_{y,Ed}$	Design bending moment y-y axis	
		Largest sagging bending moment	
	$W_{eff,y}$	Effective section modulus of cross-section for bending about the y-y axis	
	$M_{fz,Ed}$	Lateral bending moment	
	W_{fz}	Gross elastic section modulus of the free flange	
If $1 / \chi LT (My,Ed / Weff,y) + Mfz, Ed / Wfz \le fyb / \gamma M1$			
	Increase load q_{Fd}	Repeat process 3	
else			
	$M_{fz,Ed} = M_{fz,Ed\,(i)}$		

Figure B.1: *Flow diagram to calculate the critical lateral buckling moment using Eurocode 3: Part 1-3 section 10*

APPENDIX C: WORKED EXAMPLE – DETERMINATION OF THE CRITICAL LATERAL BUCKLING MOMENT USING EUROCODE 3: PART 1-3 SECTION 10

The purlin shown in Figure C.1 is continuous over 2 spans with a distance between main frames of 8.00 m. Determine the largest uplift load of the system.

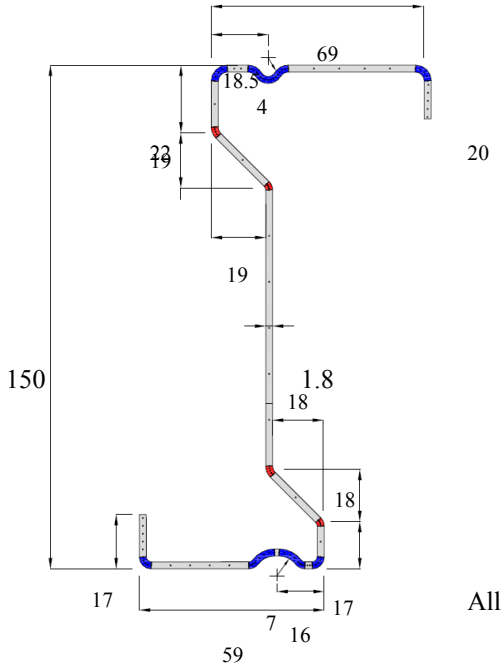


Figure C.1: *Geometrical dimensions of the Zeta IC section*

Step 1 - Calculate effective widths for section

The design thickness is taken as the core thickness:

$t=t_{nom} - t_{galv} = 1.8\text{-}0.04 = 1.76$ mm

Check geometrical proportions (Clause 3.4)

$0.2 < c/b = 20/69 < 0.6$

maximum $b/t = 69/1.76 < 60$

$h/t = 150/1.76 < 500$

Gross transversal section characteristics

$I_{xx}= 1955258$ mm^4; $Z_g =79.35$ mm; $W_g = 1955258/150\text{-}79.35 = 27675$ mm^3

$\lambda_{pb} = (b_{c2}/t)(1/(28.4\cdot\varepsilon\cdot\sqrt{k_\sigma}) = (69\text{-}22.5/1.76)(1/28.4\cdot0.819\cdot\sqrt{2}) = 0.568$

$\rho=\min[\lambda_{pb} -0.055(3+\psi)/ \lambda_{pb}^2,1] = 1$

All compression elements in the web are smaller and work under lesser stress that those in the flange, so they are also fully effective. In general if the whole section is not fully effective, a new position of the neutral axis and new value of the stress $\sigma_{com,ED}$ have to be calculated.

$W_{eff} = 27675\ mm^3$

Step 2 – Gross properties of the free flange

A $1/6^{th}$ part of the purlin height is considered (clause 10.1.4.1)

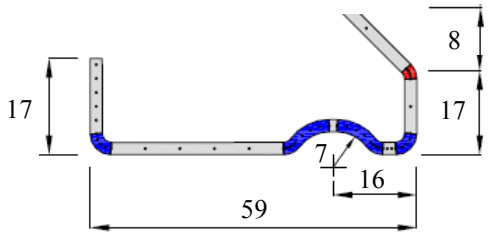


Figure C.2: *Gross properties of the free flange including the contributing web*

$y_G = 6.36\ mm$; $x_G = 31.7\ mm$; $I_{fz} = 79895 mm^4$

$A_{fz} = 176.2\ mm^2$; $W_{fz} = 2926.557\ mm^3$; $i_{fz} = 21.29 mm$

Step 3 – Try initial small load

$q_{(i)} = q_{(1)} = 1.5\ kN/m$; $M_{y,SD} = 9 \cdot 1.5 \cdot 8^2/128 = 6.75 kNm$

4 Calculate lateral load $q_{h,ED}$ due to torsion and lateral bending

Lateral load (to be calculated with gross section):

$k_{h0} = I_{yz} / I_y \cdot g_s /h = 0.120$

$k_h = k_{h0} -(f/h) = 0.120 – (-8.219/150) = 0.175$

$q_{h,Fd(i)} = {}^{q}{}_{h,Fd(1)} = 0.175 \cdot 1.5 = 0.262\ kN/m$

5 Calculate lateral spring stiffness

$1/K_A = h^2 / C_D = 150^2/ 3739 = 6.017$ mm·mm/N ($C_D = C_{DA} = 3739$ Nmm/mm)

$1/K_B = 4(1-\nu^2)\cdot h^2\cdot(h_d+e) / (E\cdot t^3) = 15.85$ mm·mm/N ($h_d = 187.03$ mm; e = 34.5 mm)

$K = 1/ (6.02 + 15.85) = 0.046$ N/mm^2

6 Calculate lateral bending moment

$R = K\cdot L_a^4/ (\pi^4\cdot E\cdot I_{fz}) = 114.62$ (L_a= 8000 mm)

$\kappa_r = (1-0.0141R)/(0+0.416R) = 0.030$ (case 'm' for fixed-pinned case)

$M_{0,fz,SD} = 9q_{h,FD}\cdot L_a^2 / 128 = 1.233$ KNm

$M_{fz,ED} = 9q_{h,FD}\cdot L_a^2 / 128 = 0.0156$ KNm

7 Calculate relative slenderness for flexural buckling of the free flange

Refer to table 10.2(b) - intermediate span with no anti-sagbars

$l_{fz} = \eta_1\cdot L_a(1+\eta_2 R^{\eta 3})^{\eta 4} = 0.306\cdot L_a(1+0.232\cdot 114.62^{0.742})^{-0.279} = 1333.41$ mm

8 Reduction factor for lateral torsional buckling

$\lambda_1 = \pi\cdot(E/f_{yb})^{0.5} = \pi\cdot(210000/390)^{0.5} = 72.900$

$\bar{\lambda}_{fz} = (l_{fz}/ i_{fz})/ \lambda_1 = (1333.41/ 21.29) / 72.900 = 0.859$

$$\Phi_{LT} = 0.5\left[1 + \alpha_{LT}(\bar{\lambda}_{LT} - \bar{\lambda}_{LT,0}) + \beta\cdot\bar{\lambda}_{LT}^{\,2}\right] = 0.5[1+0.34(0.859-0.4) + .75*0.859^2] = 0.8548$$

$$\chi_{LT} = \frac{1}{\Phi_{LT} + \sqrt{\Phi_{LT}^2 - \beta\cdot\bar{\lambda}_{LT}^2}} = \frac{1}{0.8548 + \sqrt{0.8548^2 - 0.75\cdot 0.8591^2}} = 0.784$$

9 Check buckling resistance

$$\frac{1}{\chi_{LT}}\frac{M_{y,Sd}}{W_{eff,y}} + \frac{M_{fz,Sd}}{W_{fz}} = \frac{1}{0.784}\frac{6.75\cdot 10^6}{27675} + \frac{15600}{2926.557} = 316.43 < f_y = 390\text{N/mm}$$

Increase trial load and repeat steps 4-9 again.

Maximum load = 1.7670 kN/m

APPENDIX D: RAW DATA FOR BARE SECTION PARAMETRIC STUDY – UPLIFT LOADING

Table D.1: Bare Zeta I 2-span uplift FE and design methods 1, 2 and 3 results

Section #	Span	$q_{FE,u}$	M_{span}	$M_{support}$	M_{span} /$\chi_{LT}M_2$ Stage 2	M_{span} /$\chi_{LT}M_2$ q_{ult}	$M_{support}$ / M_4 Stage 2	$M_{support}$ / M_4 q_{ult}	M_2	M_4	$\alpha_{design,u}$*	$\alpha_{design,u}M_4$	$\bar{\lambda}_{cs,+ve}$	Method 1		Method 2		Method 3	
														$q_{1,u}$	$q_{1,u}$ /$q_{FE,u}$	$q_{2,u}$	$q_{2,u}$ /$q_{FE,u}$	$q_{3,g}$	$q_{2,u}$ /$q_{FE,u}$
	(m)	(kN/m)	(kNm)	(kNm)					(kNm)	(kNm)		(kNm)		(kN/m)		(kN/m)		(kN/m)	
1/150_30	4	14.545	-17.495 -18.829	22.994 22.490	0.968	1.042	1.038	1.015	-19.659	22.160	0.951	21.078	0.617	11.080	0.762	14.195	0.976	13.800	0.949
	6	6.425	-17.095 -18.905	22.980 21.854	1.008	1.114	1.069	1.017	-19.659	21.488	0.873	18.749	0.617	4.775	0.743	6.107	0.951	5.662	0.881
	8	3.373	-14.039 -18.312	21.451 18.615	0.861	1.124	1.011	0.877	-19.659	21.226	0.793	16.827	0.617	2.653	0.787	3.256	0.965	2.997	0.888
	10	2.125	-13.804 -18.231	21.449 17.786	0.871	1.151	1.028	0.853	-19.659	20.862	0.712	14.853	0.617	1.669	0.785	2.009	0.945	1.813	0.853
1/125_20	4	6.748	-7.497 -8.852	10.551 10.126	0.942	1.112	1.050	1.007	-8.977	10.052	0.795	7.992	0.811	5.026	0.745	6.265	0.928	5.808	0.861
	6	2.837	-7.050 -8.272	10.498 9.858	0.939	1.102	1.083	1.017	-8.977	9.695	0.710	6.881	0.811	2.154	0.759	2.545	0.897	2.371	0.836
	8	1.479	-6.229 -8.109	9.857 7.964	0.861	1.121	1.007	0.814	-8.977	9.789	0.624	6.108	0.811	1.224	0.827	1.369	0.925	1.257	0.850
	10	0.955	-6.458 -8.112	10.140 8.214	0.918	1.153	1.062	0.860	-8.977	9.548	0.537	5.132	0.811	0.764	0.800	0.842	0.881	0.754	0.790
1/200_25	4	15.348	-17.905 -18.965	27.322 25.272	0.855	0.906	1.055	0.976	-23.463	25.890	0.847	21.931	0.832	12.945	0.843	14.445	0.941	15.461	1.007
	6	6.877	-17.400 -20.706	26.797 21.790	0.922	1.098	1.040	0.845	-23.463	25.774	0.795	20.481	0.832	5.728	0.833	6.683	0.972	6.261	0.910
	8	3.801	-16.674 -21.143	26.387 19.589	0.948	1.201	1.025	0.761	-23.463	25.742	0.742	19.100	0.832	3.218	0.847	3.741	0.984	3.285	0.864
	10	2.553	-17.294 -20.517	26.431 25.084	1.032	1.225	1.032	0.979	-23.463	25.621	0.689	17.656	0.832	2.050	0.803	2.293	0.898	1.984	0.777

Table D.1: *Bare Zeta I 2-span uplift FE and design methods 1, 2 and 3 results (continued)*

Section #	Span	$q_{FE,u}$	M_{span}	$M_{support}$	M_{span} $/\chi_{LT}M_2$ Stage 2	M_{span} $/\chi_{LT}M_2$ q_{ult}	$M_{support}$ $/ M_4$ Stage 2	$M_{support}$ $/ M_4$ q_{ult}	M_2	M_4	$\alpha_{design,u}$*	$\alpha_{design,u}M_4$	$\bar{\lambda}_{cs,+ve}$	Method 1		Method 2		Method 3	
														$q_{1,u}$	$q_{1,u}$ $/q_{FE,u}$	$q_{2,u}$	$q_{2,u}$ $/q_{FE,u}$	$q_{3,g}$	$q_{2,u}$ $/q_{FE,u}$
	(m)	(kN/m)	(kNm)	(kNm)					(kNm)	(kNm)		(kNm)		(kN/m)		(kN/m)		(kN/m)	
1/175_20	4	10.113	-11.187 -12.580	17.672 16.994	0.816	0.918	1.037	0.997	-15.176	17.044	0.776	13.233	0.950	8.522	0.843	9.304	0.920	9.883	0.977
	6	4.680	-10.886 -13.789	17.301 15.789	0.870	1.101	1.038	0.948	-15.176	16.663	0.719	11.985	0.950	3.703	0.791	4.293	0.917	4.003	0.855
	8	2.426	-10.121 -14.030	16.887 11.093	0.859	1.191	1.036	0.681	-15.176	16.293	0.662	10.788	0.950	2.037	0.839	2.380	0.981	2.092	0.862
	10	1.472	-9.827 -13.373	16.539 10.346	0.872	1.186	0.996	0.623	-15.176	16.602	0.605	10.043	0.950	1.328	0.902	1.444	0.980	1.272	0.864
1/150_19	4	7.879	-8.059 -10.474	13.264 11.071	0.757	0.984	1.020	0.851	-11.626	13.003	0.747	9.709	0.976	6.502	0.825	7.467	0.948	7.557	0.959
	6	3.523	-7.783 -11.343	12.921 9.242	0.787	1.146	1.017	0.728	-11.626	12.700	0.681	8.645	0.976	2.822	0.801	3.414	0.969	3.084	0.876
	8	1.857	-7.565 -10.612	12.838 8.851	0.801	1.124	1.036	0.714	-11.626	12.391	0.615	7.617	0.976	1.549	0.834	1.771	0.953	1.621	0.873
	10	1.254	-7.775 -10.596	12.836 10.917	0.852	1.161	1.010	0.859	-11.626	12.709	0.549	6.974	0.976	1.017	0.811	1.109	0.885	0.989	0.789
1/12513	4	3.689	-3.779 -4.951	6.244 5.076	0.808	1.059	1.032	0.839	-5.407	6.053	0.696	4.212	1.042	3.026	0.820	3.448	0.935	3.308	0.897
	6	1.573	-3.537 -4.951	5.981 4.495	0.822	1.150	1.001	0.752	-5.407	5.976	0.619	3.698	1.042	1.328	0.844	1.483	0.942	1.336	0.849
	8	0.874	-3.667 -4.755	6.113 4.724	0.898	1.165	1.047	0.809	-5.407	5.841	0.542	3.164	1.042	0.730	0.835	0.780	0.892	0.694	0.794
	10	0.504	-3.389 -4.640	5.795 3.388	0.862	1.180	0.989	0.578	-5.407	5.862	0.465	2.725	1.042	0.469	0.930	0.474	0.940	0.416	0.826

Table D.1: *Bare Zeta I 2-span uplift FE and design methods 1, 2 and 3 results (continued)*

Section #	Span	$q_{FE,u}$	M_{span}	$M_{support}$	M_{span} $/\chi_{LT}M_2$ Stage 2	M_{span} $/\chi_{LT}M_2$ q_{ult}	$M_{support}$ $/ M_4$ Stage 2	$M_{support}$ $/ M_4$ q_{ult}	M_2	M_4	$\alpha_{design,u}$*	$\alpha_{design,u}M_4$	$\bar{\lambda}_{cs,+ve}$	Method 1		Method 2		Method 3	
														$q_{1,u}$	$q_{1,u}$ $/q_{FE,u}$	$q_{2,u}$	$q_{2,u}$ $/q_{FE,u}$	$q_{3,g}$	$q_{2,u}$ $/q_{FE,u}$
	(m)	(kN/m)	(kNm)	(kNm)					(kNm)	(kNm)		(kNm)		(kN/m)		(kN/m)		(kN/m)	
1/175_16	4	7.123	-7.651 -9.223	13.123 10.501	0.738	0.890	1.011	0.809	-11.525	12.976	0.725	9.410	1.083	6.488	0.911	6.759	0.949	7.345	1.031
	6	3.178	-7.474 -9.920	12.813 9.104	0.802	1.064	1.013	0.720	-11.525	12.643	0.671	8.482	1.083	2.810	0.884	3.075	0.968	2.939	0.925
	8	1.863	-7.721 -10.499	13.263 9.222	0.891	1.211	1.072	0.746	-11.525	12.367	0.617	7.626	1.083	1.546	0.830	1.757	0.943	1.523	0.817
	10	1.155	-7.524 -10.279	12.790 8.678	0.913	1.247	1.051	0.713	-11.525	12.167	0.563	6.844	1.083	0.973	0.843	1.079	0.934	0.912	0.790
1/200_16	4	8.030	-8.645 -10.058	15.190 12.655	0.708	0.824	0.997	0.831	-13.779	15.230	0.738	11.245	1.084	7.615	0.948	7.580	0.944	8.688	1.082
	6	3.780	-9.074 -10.569	15.601 13.773	0.844	0.983	1.032	0.911	-13.779	15.118	0.691	10.444	1.084	3.360	0.889	3.410	0.902	3.451	0.913
	8	1.996	-8.729 -11.210	15.171 9.936	0.893	1.147	1.024	0.671	-13.779	14.813	0.643	9.530	1.084	1.852	0.928	1.951	0.978	1.767	0.885
	10	1.251	-8.553 -11.322	14.793 8.881	0.936	1.239	0.955	0.573	-13.779	15.489	0.596	9.231	1.084	1.239	0.991	1.248	0.998	1.068	0.854
1/200_13	4	5.886	-6.331 -7.392	11.572 8.867	0.688	0.804	1.003	0.768	-10.427	11.540	0.695	8.015	1.220	5.770	0.980	5.518	0.937	6.446	1.095
	6	2.591	-6.667 -7.465	11.231 8.001	0.839	0.940	0.994	0.708	-10.427	11.300	0.649	7.334	1.220	2.511	0.969	2.405	0.928	2.515	0.970
	8	1.500	-6.748 -7.839	12.002 7.774	0.953	1.107	1.028	0.666	-10.427	11.679	0.604	7.050	1.220	1.460	0.973	1.385	0.924	1.288	0.859
	10	0.944	-6.160 -6.660	11.749 11.747	0.944	1.020	1.071	1.071	-10.427	10.970	1.000	10.970	1.220	0.878	0.930	0.919	0.974	0.908	0.962
														STD	0.069		0.030		0.079
														MEAN	0.852		0.942		0.891
														COV	0.081		0.032		0.089

* $\alpha_{design,u} = \left[0.868 - 0.0049\left(\frac{L}{h}\right)\right]\bar{\lambda}_{cs,+ve}^{\left[-0.001\left(\frac{L}{h}\right)-0.5\right]}$

Table D.2: *Bare Zeta II 2-span uplift FE and design methods 1, 2 and 3 results*

Section #	Span	$q_{FE,u}$	M_{span}	$M_{support}$	M_{span} /$\chi_{LT}M_2$ Stage 2	M_{span} /$\chi_{LT}M_2$ q_{ult}	$M_{support}$ / M_4 Stage 2	$M_{support}$ / M_4 q_{ult}	M_2	M_4	$\alpha_{design,u}$*	$\alpha_{design,u}M_4$	$\bar{\lambda}_{cs,+ve}$	Method 1		Method 2		Method 3	
														$q_{1,u}$	$q_{1,u}$ /$q_{FE,u}$	$q_{2,u}$	$q_{2,u}$ /$q_{FE,u}$	$q_{3,g}$	$q_{2,u}$ /$q_{FE,u}$
	(m)	(kN/m)	(kNm)	(kNm)					(kNm)	(kNm)		(kNm)		(kN/m)		(kN/m)		(kN/m)	
2/225_30	4	20.517	-23.241 -25.952	36.327 31.557	0.783	0.874	0.959	0.834	-32.42	37.86	0.899	34.033	0.762	18.931	0.923	20.606	1.004	22.554	1.099
	6	9.549	-24.377 -28.113	37.517 31.259	0.907	1.046	1.034	0.861	-32.42	36.29	0.851	30.878	0.762	8.065	0.845	9.364	0.981	9.079	0.951
	8	5.189	-22.367 -29.272	35.871 25.473	0.896	1.173	0.968	0.688	-32.42	37.04	0.802	29.724	0.762	4.630	0.892	5.356	1.032	4.798	0.925
	10	3.265	-23.454 -28.882	36.501 24.995	0.988	1.217	1.010	0.691	-32.42	36.15	0.754	27.257	0.762	2.892	0.886	3.311	1.014	2.886	0.884
2/285_30	4	26.785	-31.031 -31.762	49.582 49.176	0.791	0.810	0.948	0.940	-43.18	52.31	0.878	45.945	0.832	26.153	0.976	26.104	0.975	29.991	1.120
	6	11.672	-29.541 -33.895	49.069 38.078	0.857	0.984	0.960	0.745	-43.18	51.11	0.842	43.022	0.832	11.358	0.973	11.830	1.013	11.960	1.025
	8	6.674	-30.471 -36.775	49.683 34.976	0.983	1.186	0.992	0.698	-43.18	50.08	0.805	40.311	0.832	6.260	0.938	6.886	1.032	6.136	0.919
	10	4.181	-29.970 -37.055	49.017 31.689	1.045	1.292	0.977	0.632	-43.18	50.17	0.768	38.534	0.832	4.014	0.960	4.370	1.045	3.673	0.879
2/225_25	4	16.047	-17.541 -20.261	29.290 25.643	0.736	0.851	0.987	0.864	-25.98	29.69	0.847	25.145	0.855	14.845	0.925	15.791	0.984	17.637	1.099
	6	7.066	-17.302 -21.375	29.152 21.055	0.805	0.995	0.966	0.697	-25.98	30.19	0.801	24.177	0.855	6.709	0.949	7.185	1.017	7.210	1.020
	8	4.035	-17.590 -22.895	29.290 19.314	0.884	1.151	1.015	0.669	-25.98	28.85	0.755	21.771	0.855	3.607	0.894	4.110	1.019	3.724	0.923
	10	2.521	-17.366 -23.047	28.790 17.285	0.921	1.222	0.988	0.593	-25.98	29.15	0.708	20.645	0.855	2.332	0.925	2.604	1.033	2.259	0.896
2_28525	4	20.417	-23.382 -23.475	39.501 39.484	0.752	0.755	1.061	1.060	-34.25	37.25	0.827	30.805	0.936	18.624	0.912	18.644	0.913	22.594	1.107
	6	9.126	-23.016 -25.305	40.168 31.620	0.844	0.928	0.960	0.756	-34.25	41.82	0.792	33.117	0.936	9.294	1.018	8.924	0.978	9.377	1.028
	8	5.115	-23.283 -27.601	39.845 26.742	0.955	1.132	0.995	0.668	-34.25	40.05	0.757	30.299	0.936	5.006	0.979	5.170	1.011	4.753	0.929
	10	3.208	-22.783 -28.487	38.905 24.062	1.014	1.268	0.991	0.613	-34.25	39.25	0.721	28.309	0.936	3.140	0.979	3.315	1.033	2.816	0.878

Table D.2: *Bare Zeta II 2-span uplift FE and design methods 1, 2 and 3 results (continued)*

Section #	Span	$q_{FE,u}$	M_{span}	$M_{support}$	M_{span} /$\chi_{LT}M_2$ Stage 2	M_{span} /$\chi_{LT}M_2$ q_{ult}	$M_{support}$ / M_4 Stage 2	$M_{support}$ / M_4 q_{ult}	M_2	M_4	$\alpha_{design,u}$*	$\alpha_{design,u}M_4$	$\bar{\lambda}_{cs,+ve}$	Method 1		Method 2		Method 3	
														$q_{1,u}$	$q_{1,u}$ /$q_{FE,u}$	$q_{2,u}$	$q_{2,u}$ /$q_{FE,u}$	$q_{3,g}$	$q_{2,u}$ /$q_{FE,u}$
	(m)	(kN/m)	(kNm)	(kNm)					(kNm)	(kNm)		(kNm)		(kN/m)		(kN/m)		(kN/m)	
2/285_20	4	13.950	-15.109 -15.391	28.909 28.694	0.655	0.667	1.204	1.195	-25.40	24.02	0.777	18.669	1.056	12.011	0.861	11.906	0.853	15.857	1.137
	6	6.314	-15.581 -17.460	29.095 21.146	0.776	0.870	0.936	0.680	-25.40	31.09	0.743	23.114	1.056	6.908	1.094	6.181	0.979	6.785	1.075
	8	3.728	-16.591 -18.563	30.060 17.844	0.937	1.048	1.024	0.608	-25.40	29.36	0.710	20.842	1.056	3.670	0.985	3.502	0.939	3.391	0.910
	10	2.411	-17.061 -19.859	29.849 19.968	1.059	1.233	0.986	0.660	-25.40	30.27	0.676	20.466	1.056	2.422	1.004	2.336	0.969	2.024	0.840
2/225_14	4	6.816	-7.585 -8.151	13.444 12.052	0.697	0.749	1.018	0.912	-11.93	13.21	0.709	9.367	1.205	6.605	0.969	6.196	0.909	7.604	1.116
	6	3.550	-7.412 -11.699	13.482 8.747	0.776	1.225	1.036	0.672	-11.93	13.01	0.668	8.695	1.205	2.891	0.814	3.499	0.986	3.010	0.848
	8	1.679	-7.057 -8.989	11.938 8.918	0.827	1.053	0.920	0.687	-11.93	12.98	0.628	8.150	1.205	1.623	0.966	1.592	0.948	1.534	0.913
	10	1.050	-6.982 -9.348	12.596 7.824	0.890	1.192	0.998	0.620	-11.93	12.62	0.587	7.411	1.205	1.009	0.961	1.023	0.974	0.899	0.857
2/245_15	4	8.076	-8.960 -8.997	16.396 16.386	0.674	0.677	0.992	0.992	-14.60	16.53	0.719	11.880	1.195	8.263	1.023	7.160	0.887	9.377	1.161
	6	3.502	-8.662 -9.704	16.114 12.795	0.747	0.837	0.977	0.775	-14.60	16.50	0.681	11.243	1.195	3.667	1.047	3.287	0.939	3.720	1.062
	8	2.001	-9.007 -10.542	15.540 11.388	0.878	1.027	0.963	0.706	-14.60	16.14	0.644	10.395	1.195	2.018	1.008	1.912	0.956	1.876	0.938
	10	1.239	-8.628 -10.794	15.711 9.448	0.921	1.152	1.015	0.610	-14.60	15.48	0.607	9.392	1.195	1.238	0.999	1.210	0.977	1.093	0.882
2/265_15	4	8.536	-9.280 -9.311	17.923 17.001	0.643	0.646	0.970	0.920	-15.88	18.47	0.713	13.168	1.233	9.235	1.082	7.590	0.889	10.238	1.199
	6	3.775	-9.234 -10.285	17.665 13.930	0.741	0.825	0.960	0.757	-15.88	18.40	0.679	12.486	1.233	4.089	1.083	3.537	0.937	4.039	1.070
	8	2.226	-9.970 -10.913	17.709 12.950	0.916	1.003	0.983	0.719	-15.88	18.01	0.644	11.606	1.233	2.251	1.011	2.025	0.910	2.020	0.908
	10	1.374	-9.519 -9.523	17.562 17.544	0.971	0.972	1.019	1.018	-15.88	17.24	1.000	17.242	1.233	1.379	1.004	1.364	0.993	1.388	1.010
														STD	0.067		0.049		0.106
														MEAN	0.965		0.973		0.988
														COV	0.070		0.051		0.107

* $\alpha_{design,u} = \left[0.868 - 0.0049\left(\frac{L}{h}\right)\right]\bar{\lambda}_{cs,+ve}^{\left[-0.001\left(\frac{L}{h}\right)-0.5\right]}$

Table D.3: *Bare Zed 2-span uplift FE and design methods 1, 2 and 3 results*

Section #	Span	$q_{FE,u}$	M_{span}	$M_{support}$	M_{span} /$\chi_{LT}M_2$ Stage 2	M_{span} /$\chi_{LT}M_2$ q_{ult}	$M_{support}$ / M_4 Stage 2	$M_{support}$ / M_4 q_{ult}	M_2	M_4	$\alpha_{design,u}$*	$\alpha_{design,u}M_4$	$\bar{\lambda}_{cs,+ve}$	Method 1		Method 2		Method 3	
														$q_{1,u}$	$q_{1,u}$ /$q_{FE,u}$	$q_{2,u}$	$q_{2,u}$ /$q_{FE,u}$	$q_{3,g}$	$q_{2,u}$ /$q_{FE,u}$
	(m)	(kN/m)	(kNm)	(kNm)					(kNm)	(kNm)		(kNm)		(kN/m)		(kN/m)		(kN/m)	
Z/125_20	4	5.064	-5.840 -6.702	9.223 7.341	0.889	1.020	1.081	0.860	-7.38	8.53	0.813	6.936	0.778	4.265	0.842	4.933	0.974	4.864	0.960
	6	2.171	-5.670 -6.975	8.952 5.796	0.909	1.118	1.051	0.680	-7.38	8.52	0.726	6.188	0.778	1.893	0.872	2.184	1.006	2.015	0.928
	8	1.198	-5.470 -6.956	8.701 5.391	0.906	1.152	1.049	0.650	-7.38	8.30	0.639	5.300	0.778	1.037	0.866	1.177	0.983	1.060	0.885
	10	0.729	-5.008 -6.898	8.319 4.372	0.850	1.171	1.014	0.533	-7.38	8.20	0.551	4.517	0.778	0.656	0.900	0.721	0.990	0.639	0.877
Z/200_25	4	11.342	-13.077 -13.567	21.338 20.378	0.872	0.905	0.995	0.951	-17.56	21.44	0.861	18.463	0.806	10.719	0.945	10.911	0.962	11.657	1.028
	6	5.206	-13.074 -15.537	20.848 17.020	0.968	1.151	0.993	0.810	-17.56	21.00	0.808	16.973	0.806	4.667	0.896	5.166	0.992	4.697	0.902
	8	2.738	-12.449 -15.144	20.359 14.384	0.986	1.199	1.007	0.711	-17.56	20.22	0.755	15.263	0.806	2.527	0.923	2.765	1.010	2.439	0.891
	10	1.684	-12.271 -14.788	20.102 13.307	1.019	1.228	1.001	0.662	-17.56	20.09	0.701	14.091	0.806	1.607	0.954	1.700	1.009	1.473	0.875
Z125_14	4	3.304	-3.618 -4.557	6.412 4.361	1.108	1.396	1.184	0.805	-4.73	5.41	0.728	3.943	0.957	2.707	0.819	3.188	0.965	2.522	0.763
	6	1.374	-2.944 -4.125	6.832 4.448	0.781	1.094	1.309	0.852	-4.73	5.22	0.648	3.383	0.957	1.160	0.844	1.265	0.920	1.184	0.862
	8	0.817	-2.748 -4.643	7.683 3.657	0.678	1.147	1.469	0.699	-4.73	5.23	0.568	2.974	0.957	0.654	0.801	0.755	0.924	0.679	0.832
	10	0.463	-3.011 -4.423	5.483 2.391	0.709	1.042	1.066	0.465	-4.73	5.14	0.488	2.512	0.957	0.411	0.888	0.449	0.969	0.434	0.937

Table D.3: *Bare Zed 2-span uplift FE and design methods 1, 2 and 3 results (continued)*

Section #	Span	$q_{FE,u}$	M_{span}	$M_{support}$	M_{span} /$\chi_{LT}M_2$ Stage 2	M_{span} /$\chi_{LT}M_2$ q_{ult}	$M_{support}$ / M_4 Stage 2	$M_{support}$ / M_4 q_{ult}	M_2	M_4	$\alpha_{design,u}$*	$\alpha_{design,u}M_4$	$\bar{\lambda}_{cs,+ve}$	Method 1		Method 2		Method 3	
														$q_{1,u}$	$q_{1,u}$ /$q_{FE,u}$	$q_{2,u}$	$q_{2,u}$ /$q_{FE,u}$	$q_{3,g}$	$q_{2,u}$ /$q_{FE,u}$
	(m)	(kN/m)	(kNm)	(kNm)					(kNm)	(kNm)		(kNm)		(kN/m)		(kN/m)		(kN/m)	
1/155_15	4	4.023	-4.456 -5.611	8.158 5.121	0.747	0.940	1.006	0.631	-6.87	8.11	0.735	5.965	1.016	4.057	1.008	4.163	1.035	4.347	1.081
	6	1.825	-4.511 -5.940	7.992 4.679	0.827	1.089	1.021	0.598	-6.87	7.83	0.672	5.263	1.016	1.740	0.953	1.859	1.019	1.748	0.958
	8	1.030	-4.412 -6.135	7.752 4.238	0.857	1.191	0.990	0.541	-6.87	7.83	0.610	4.775	1.016	0.979	0.951	1.044	1.014	0.918	0.891
	10	0.641	-4.284 -6.166	7.573 3.598	0.866	1.247	0.975	0.463	-6.87	7.77	0.547	4.248	1.016	0.622	0.969	0.652	1.017	0.552	0.861
1/170_14	4	3.779	-4.145 -4.871	7.791 5.791	0.698	0.820	0.994	0.739	-6.95	7.84	0.720	5.648	1.087	3.920	1.037	3.714	0.983	4.266	1.129
	6	1.758	-4.289 -5.576	7.760 4.902	0.808	1.050	1.023	0.646	-6.95	7.59	0.665	5.041	1.087	1.686	0.959	1.755	0.998	1.694	0.964
	8	1.004	-4.328 -5.896	7.667 4.349	0.876	1.193	1.004	0.570	-6.95	7.63	0.609	4.648	1.087	0.954	0.950	1.007	1.002	0.884	0.881
	10	0.638	-4.205 -5.916	7.662 3.798	0.896	1.261	1.024	0.507	-6.95	7.49	0.553	4.142	1.087	0.599	0.939	0.628	0.985	0.528	0.828
1/200_13	4	3.756	-4.017 -5.109	8.066 5.054	0.640	0.815	0.977	0.612	-7.51	8.26	0.700	5.779	1.202	4.130	1.100	3.864	1.029	4.464	1.189
	6	1.750	-4.336 -5.636	8.063 4.840	0.808	1.051	1.005	0.603	-7.51	8.02	0.654	5.245	1.202	1.782	1.018	1.788	1.021	1.725	0.986
	8	0.995	-4.452 -5.752	7.957 4.757	0.925	1.195	0.988	0.590	-7.51	8.06	0.608	4.901	1.202	1.007	1.012	1.002	1.007	0.882	0.886
	10	0.637	-4.424 -4.424	8.000 8.000	0.987	0.987	1.011	1.011	-7.51	7.91	1.000	7.914	1.202	0.633	0.994	0.631	0.991	0.636	0.999
														STD	0.074		0.029		0.098
														MEAN	0.935		0.992		0.933
														COV	0.079		0.029		0.105

* $\alpha_{design,u} = \left[0.868 - 0.0049\left(\frac{L}{h}\right)\right]\bar{\lambda}_{cs,+ve}^{\left[-0.001\left(\frac{L}{h}\right)-0.5\right]}$

Table D.4: *Bare channel 2-span uplift FE and design methods 1, 2 and 3 results*

Section #	Span	$q_{FE,u}$	M_{span}	$M_{support}$	M_{span} /$\chi_{LT}M_2$ Stage 2	M_{span} /$\chi_{LT}M_2$ q_{ult}	$M_{support}$ / M_4 Stage 2	$M_{support}$ / M_4 q_{ult}	M_2	M_4	$\alpha_{design,u}$*	$\alpha_{design,u}M_4$	$\bar{\lambda}_{cs,+ve}$	Method 1		Method 2		Method 3	
														$q_{1,u}$	$q_{1,u}$ /$q_{FE,u}$	$q_{2,u}$	$q_{2,u}$ /$q_{FE,u}$	$q_{3,g}$	$q_{2,u}$ /$q_{FE,u}$
	(m)	(kN/m)	(kNm)	(kNm)					(kNm)	(kNm)		(kNm)		(kN/m)		(kN/m)		(kN/m)	
C/127_20	4	5.430	-6.015 -7.530	10.081 6.959	0.773	0.968	1.027	0.709	-8.30	9.82	0.775	7.607	0.857	4.910	0.904	5.503	1.013	5.632	1.037
	6	2.413	-5.894 -7.995	9.854 5.800	0.796	1.079	1.038	0.611	-8.30	9.50	0.693	6.578	0.857	2.111	0.875	2.453	1.017	2.319	0.961
	8	1.282	-5.338 -7.691	9.237 5.136	0.742	1.070	0.991	0.551	-8.30	9.32	0.610	5.687	0.857	1.165	0.909	1.292	1.008	1.229	0.958
	10	0.806	-5.481 -7.706	9.298 4.634	0.779	1.096	1.002	0.499	-8.30	9.28	0.527	4.893	0.857	0.742	0.921	0.800	0.993	0.746	0.925
C/127_18	4	4.639	-5.032 -6.476	8.734 5.877	0.744	0.958	1.024	0.689	-7.23	8.53	0.750	6.398	0.911	4.266	0.919	4.701	1.013	4.849	1.045
	6	2.081	-4.991 -6.981	8.554 4.777	0.777	1.087	1.032	0.576	-7.23	8.29	0.670	5.550	0.911	1.841	0.885	2.123	1.020	1.996	0.959
	8	1.130	-4.739 -6.881	8.235 4.257	0.762	1.106	1.012	0.523	-7.23	8.14	0.589	4.799	0.911	1.018	0.900	1.140	1.009	1.056	0.934
	10	0.658	-4.684 -6.184	8.083 4.083	0.770	1.017	1.012	0.511	-7.23	7.99	0.509	4.066	0.911	0.639	0.971	0.647	0.983	0.639	0.971
C/200_20	4	8.299	-9.256 -10.656	16.716 13.216	0.714	0.822	0.978	0.773	-14.27	17.10	0.783	13.392	0.968	8.550	1.030	8.340	1.005	9.534	1.149
	6	3.924	-9.600 -12.671	16.902 10.350	0.817	1.079	0.995	0.609	-14.27	16.99	0.734	12.462	0.968	3.775	0.962	4.083	1.041	3.871	0.987
	8	2.248	-9.163 -13.441	16.023 9.126	0.834	1.223	0.963	0.548	-14.27	16.64	0.684	11.379	0.968	2.080	0.925	2.337	1.039	2.022	0.899
	10	1.419	-9.211 -12.610	16.022 10.732	0.879	1.204	0.983	0.659	-14.27	16.29	0.634	10.333	0.968	1.303	0.918	1.391	0.980	1.216	0.857
C/127_15	4	3.455	-3.647 -4.810	6.598 4.449	0.684	0.902	1.036	0.699	-5.73	6.37	0.710	4.520	1.010	3.183	0.921	3.442	0.996	3.711	1.074
	6	1.576	-3.617 -5.349	6.483 3.463	0.719	1.064	1.019	0.544	-5.73	6.36	0.633	4.029	1.010	1.414	0.897	1.605	1.018	1.533	0.972
	8	0.885	-3.542 -5.484	6.271 3.067	0.730	1.130	1.027	0.503	-5.73	6.10	0.556	3.395	1.010	0.763	0.863	0.885	1.000	0.805	0.910
	10	0.542	-3.451 -5.302	6.098 2.804	0.730	1.121	0.985	0.453	-5.73	6.19	0.479	2.967	1.010	0.495	0.913	0.536	0.989	0.490	0.904

Table D.4: *Bare channel 2-span uplift FE and design methods 1, 2 and 3 results (continued)*

Section #	Span	$q_{FE,u}$	M_{span}	$M_{support}$	M_{span} /$\chi_{LT}M_2$ Stage 2	M_{span} /$\chi_{LT}M_2$ q_{ult}	$M_{support}$ / M_4 Stage 2	$M_{support}$ / M_4 q_{ult}	M_2	M_4	$\alpha_{design,u}$*	$\alpha_{design,u}M_4$	$\bar{\lambda}_{cs,+ve}$	Method 1		Method 2		Method 3	
														$q_{1,u}$	$q_{1,u}$ /$q_{FE,u}$	$q_{2,u}$	$q_{2,u}$ /$q_{FE,u}$	$q_{3,g}$	$q_{2,u}$ /$q_{FE,u}$
	(m)	(kN/m)	(kNm)	(kNm)					(kNm)	(kNm)		(kNm)		(kN/m)		(kN/m)		(kN/m)	
C/155_15	4	4.115	-4.346 -5.384	8.002 6.212	0.672	0.833	0.981	0.761	-7.05	8.16	0.719	5.866	1.061	4.080	0.991	4.025	0.978	4.581	1.113
	6	1.920	-4.374 -6.328	7.933 4.725	0.733	1.060	0.982	0.585	-7.05	8.08	0.657	5.306	1.061	1.795	0.935	1.951	1.016	1.870	0.974
	8	1.101	-4.354 -6.701	7.783 4.146	0.768	1.182	0.989	0.527	-7.05	7.87	0.595	4.687	1.061	0.984	0.894	1.111	1.010	0.979	0.890
	10	0.678	-4.307 -6.535	7.651 3.762	0.788	1.196	0.965	0.474	-7.05	7.93	0.534	4.234	1.061	0.635	0.936	0.682	1.005	0.594	0.877
C/185_15	4	4.855	-5.273 -6.913	10.183 6.073	0.655	0.859	0.988	0.589	-8.87	10.30	0.719	7.413	1.117	5.152	1.061	5.143	1.059	5.726	1.179
	6	2.208	-5.323 -7.064	9.811 6.007	0.734	0.974	0.973	0.596	-8.87	10.08	0.669	6.741	1.117	2.241	1.015	2.257	1.022	2.300	1.042
	8	1.285	-5.402 -7.681	9.720 5.211	0.800	1.138	0.962	0.516	-8.87	10.10	0.618	6.242	1.117	1.263	0.983	1.321	1.029	1.202	0.936
	10	0.900	-5.175 -7.213	12.053 7.709	0.808	1.126	1.220	0.780	-8.87	9.88	0.567	5.603	1.117	0.790	0.878	0.785	0.873	0.719	0.799
C/200_15	4	5.057	-5.453 -6.242	10.390 8.565	0.624	0.714	0.929	0.766	-9.68	11.18	0.717	8.017	1.147	5.591	1.105	4.921	0.973	6.214	1.229
	6	2.376	-5.593 -7.220	10.385 7.418	0.718	0.926	0.932	0.666	-9.68	11.14	0.670	7.469	1.147	2.476	1.042	2.361	0.994	2.493	1.049
	8	1.368	-5.885 -8.041	10.616 5.912	0.821	1.122	0.987	0.550	-9.68	10.75	0.624	6.709	1.147	1.344	0.983	1.393	1.018	1.281	0.936
	10	0.882	-5.803 -8.335	10.347 5.348	0.860	1.235	0.955	0.494	-9.68	10.83	0.578	6.257	1.147	0.866	0.982	0.900	1.020	0.770	0.872
														STD	0.061		0.032		0.102
														MEAN	0.947		1.004		0.980
														COV	0.065		0.032		0.104

* $\alpha_{design,u} = \left[0.868 - 0.0049\left(\frac{L}{h}\right)\right]\bar{\lambda}_{cs,+ve}^{\left[-0.001\left(\frac{L}{h}\right)-0.5\right]}$

APPENDIX E: END SUPPORT REACTION DERIVATION FOR 2-SPAN SLEEVED SYSTEMS

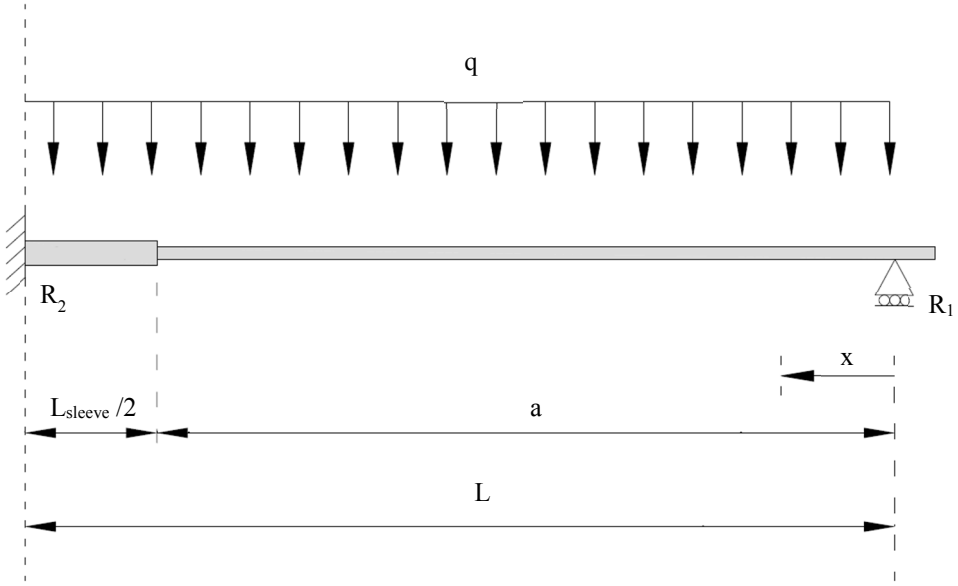


Figure E.1: Non-prismatic 2-span system schematic

Let the distance from the end support to the edge of the sleeve:

$$a = L - \frac{L_{sleeve}}{2} \tag{E.1}$$

Let the end support reaction R take the form:

$$R_1 = C_1 q L \tag{E.2}$$

For $0 \le x \le a$

$$EIv'' = R_1 x - \frac{qx^2}{2} \tag{E.3}$$

$$EIv' = \frac{R_1 x^2}{2} - \frac{qx^3}{6} + A_1 \tag{E.4}$$

$$EIv = \frac{R_1 x^3}{6} - \frac{qx^4}{24} + A_1 x + B_1 \tag{E.5}$$

For $a \le x \le L$

$$EI_s v = R_1 x - \frac{qx^2}{2} \tag{E.6}$$

$$EI_s v' = \frac{R_1 x^2}{2} - \frac{qx^3}{6} + A_2 \tag{E.7}$$

$$EI_s v'' = \frac{R_1 x^3}{6} - \frac{qx^4}{24} + A_2 x + B_2 \tag{E.8}$$

Apply boundary conditions to find constants A_1, A_2, B_1, B_2 and C_1:

i) $v(x = 0) = 0$ $\quad \therefore B_1 = 0$

ii) $v'(x = L) = 0$ $\quad \therefore A_2 = \frac{qL^3}{6} - \frac{C_1 qL^3}{2}$

iii) $v(x = L) = 0$ $\quad \therefore B_2 = \frac{C_1 qL^4}{3} - \frac{qL^4}{8}$

iv) $v'(x = a)$ using (E.5) = $v'(x = a)$ using (E.8)

$$\therefore A_1 = \frac{C_1 qLa^2 I}{2I_s} - \frac{qa^3 I}{6I_s} + \frac{qL^3 I}{6I_s} - \frac{C_1 qL^3 I}{2I_s} + \frac{qa^3}{6} - \frac{C_1 qLa^2}{2}$$

v) $v'(x = a)$ using (E.5) = $v'(x = a)$ using (E.8)

$$\therefore C_1 = \frac{3}{8}\left[\frac{I(a/L) - I\left(L^3/a^3\right) - I_s(a/L)}{I - I_s - I\left(L^3/a^3\right)}\right]$$

APPENDIX F: RAW DATA FOR SLEEVED SECTION PARAMETRIC STUDY – GRAVITY LOADING

Table F.1: *Sleeved Zeta I 2-span gravity FE and design methods 1, 2 and 3 results*

Sleeve Section #	Span	$q_{FE,gs}$	M_{span}	$M_{support}$	M_{span}/M_1 Stage 2	M_{span}/M_1 q_{ult}	$M_{support}/M_{3sleeve}$ Stage 2	$M_{support}/M_{3sleeve}$ q_{ult}	M_1	$M_{3sleeve}$	$\alpha_{design,g,s}$*	$\alpha_{design,gs}$ $M_{3sleeve}$	$-\lambda_{cs,s,-ve}$	Method 1		Method 2		Method 3	
														$q_{1,gs}$	$q_{1,gs}/q_{FE,gs}$	$q_{2,gs}$	$q_{2,gs}/q_{FE,gs}$	$q_{3,gs}$	$q_{2,gs}/q_{FE,gs}$
	(m)	(kN/m)	(kNm)	(kNm)					(kNm)	(kNm)		(kNm)		(kN/m)		(kN/m)		(kN/m)	
1/125_20	4	6.381	8.665 8.665	-9.435 -9.435	0.967	0.967	1.012	1.012	8.965	-9.319	1.000	-9.319	0.469	4.660	0.730	6.607	1.036	6.607	1.036
	6	2.891	8.737 8.737	-8.880 -8.880	0.975	0.975	0.972	0.972	8.965	-9.137	1.000	-9.137	0.469	2.030	0.702	2.919	1.010	2.919	1.010
	8	1.647	8.710 8.712	-9.398 -9.389	0.972	0.972	1.032	1.031	8.965	-9.111	1.000	-9.111	0.469	1.139	0.691	1.641	0.996	1.641	0.996
1/125_16	4	4.915	6.793 6.793	-7.151 -7.151	0.977	0.977	1.088	1.088	6.950	-6.574	1.000	-6.574	0.508	3.287	0.669	4.983	1.014	4.983	1.014
	6	2.174	6.663 6.663	-6.405 -6.405	0.959	0.959	0.973	0.973	6.950	-6.59	1.000	-6.585	0.508	1.463	0.673	2.216	1.019	2.216	1.019
	8	1.242	6.699 6.713	-6.718 -6.713	0.964	0.966	1.032	1.032	6.950	-6.507	1.000	-6.507	0.508	0.813	0.655	1.242	1.000	1.242	1.000
1/125_13	4	3.723	5.184 5.184	-4.549 -4.543	0.963	0.963	0.942	0.941	5.383	-4.828	1.000	-4.828	0.600	2.414	0.649	3.803	1.022	3.803	1.022
	6	1.659	5.139 5.149	-4.731 -4.714	0.955	0.957	0.992	0.988	5.383	-4.769	1.000	-4.769	0.600	1.060	0.639	1.684	1.015	1.684	1.015
	8	0.946	5.196 5.200	-4.837 -4.831	0.965	0.966	1.023	1.021	5.383	-4.731	0.928	-4.392	0.600	0.591	0.625	0.945	0.999	0.927	0.980
1/175_16	4	8.337	11.016 11.017	-11.914 -11.908	0.956	0.956	0.916	0.916	11.524	-12.999	1.000	-12.999	0.653	6.500	0.780	8.709	1.045	8.709	1.045
	6	3.871	11.444 11.457	-12.630 -12.605	0.993	0.994	0.977	0.975	11.524	-12.928	1.000	-12.928	0.653	2.873	0.742	3.864	0.998	3.864	0.998
	8	2.152	11.262 11.262	-12.138 -12.138	0.977	0.977	0.940	0.940	11.524	-12.912	0.952	-12.298	0.653	1.614	0.750	2.173	1.010	2.140	0.994

Table F.1: *Sleeved Zeta I 2-span gravity FE and design methods 1, 2 and 3 results (continued)*

Sleeve Section #	Span	$q_{FE,gs}$	M_{span}	$M_{support}$	M_{span}/M_1 Stage 2	M_{span}/M_1 q_{ult}	$M_{support}/M_{3sleeve}$ Stage 2	$M_{support}/M_{3sleeve}$ q_{ult}	M_1	$M_{3sleeve}$	$\alpha_{design,g,s}$*	$\alpha_{design,gs}$ $M_{3sleeve}$	$\bar{\lambda}_{cs,s,-ve}$	Method 1		Method 2		Method 3	
														$q_{1,gs}$	$q_{1,gs}/q_{FE,gs}$	$q_{2,gs}$	$q_{2,gs}/q_{FE,gs}$	$q_{3,gs}$	$q_{2,gs}/q_{FE,gs}$
	(m)	(kN/m)	(kNm)	(kNm)					(kNm)	(kNm)		(kNm)		(kN/m)		(kN/m)		(kN/m)	
1/200_16	4	9.804	11.409 12.956	-14.392 -14.000	0.824	0.935	0.904	0.879	13.852	-15.920	1.000	-15.920	0.657	7.960	0.812	10.530	1.074	10.530	1.074
	6	4.535	12.148 13.487	-15.734 -14.577	0.877	0.974	0.986	0.913	13.852	-15.958	1.000	-15.958	0.657	3.546	0.782	4.684	1.033	4.684	1.033
	8	2.458	11.902 13.310	-15.936 -13.133	0.859	0.961	0.999	0.823	13.852	-15.952	0.984	-15.691	0.657	1.994	0.811	2.634	1.072	2.620	1.066
1/150_15	4	6.321	6.982 8.592	-8.948 -8.468	0.805	0.991	0.998	0.944	8.669	-8.968	1.000	-8.968	0.672	4.484	0.709	6.379	1.009	6.379	1.009
	6	2.827	8.518 8.523	-8.762 -8.750	0.983	0.983	0.987	0.985	8.669	-8.880	0.951	-8.444	0.672	1.973	0.698	2.827	1.000	2.786	0.985
	8	1.599	8.496 8.496	-9.012 -9.010	0.980	0.980	1.024	1.024	8.669	-8.800	0.855	-7.521	0.672	1.100	0.688	1.586	0.992	1.517	0.949
1/200_13	4	7.260	8.655 9.535	-10.895 -10.539	0.821	0.904	0.939	0.909	10.544	-11.599	0.948	-10.994	0.739	5.800	0.799	7.906	1.089	7.778	1.071
	6	3.464	8.950 10.530	-11.483 -10.463	0.849	0.999	0.986	0.899	10.544	-11.642	0.886	-10.314	0.739	2.587	0.747	3.518	1.016	3.392	0.979
	8	1.863	9.299 10.439	-11.460 -9.425	0.882	0.990	0.989	0.813	10.544	-11.593	0.823	-9.539	0.739	1.449	0.778	1.976	1.061	1.867	1.002
1/175_10	4	4.101	5.365 5.365	-6.020 -6.020	0.933	0.933	0.937	0.937	5.747	-6.424	0.761	-4.888	0.848	3.212	0.783	4.331	1.056	4.002	0.976
	6	1.944	5.750 5.750	-6.338 -6.338	1.001	1.001	0.976	0.976	5.747	-6.495	0.699	-4.542	0.848	1.443	0.742	1.931	0.993	1.745	0.898
	8	1.074	5.638 5.639	-6.244 -6.243	0.981	0.981	0.975	0.975	5.747	-6.404	0.637	-4.080	0.848	0.801	0.745	1.082	1.007	0.956	0.891
														STD	0.056		0.028		0.045
														MEAN	0.725		1.024		1.003
														COV	0.078		0.028		0.045

* $\alpha_{design,u} = \left[0.7 - 0.0045\left(\frac{L}{h}\right)\right]\bar{\lambda}_{cs,s,+ve}^{\left[-0.003\left(\frac{L}{h}\right)-1.4\right]}$

Table F.2: *Sleeved Zeta II 2-span gravity FE and design methods 1, 2 and 3 results*

Sleeve Section #	Span	$q_{FE,gs}$	M_{span}	$M_{support}$	M_{span}/M_1 Stage 2	M_{span}/M_1 q_{ult}	$M_{support}/M_{3sleeve}$ Stage 2	$M_{support}/M_{3sleeve}$ q_{ult}	M_1	$M_{3sleeve}$	$\alpha_{design,g,s}$*	$\alpha_{design,gs}$ $M_{3sleeve}$	$-\lambda_{cs,s,-ve}$	Method 1		Method 2		Method 3	
														$q_{1,gs}$	$q_{1,gs}/q_{FE,gs}$	$q_{2,gs}$	$q_{2,gs}/q_{FE,gs}$	$q_{3,gs}$	$q_{2,gs}/q_{FE,gs}$
	(m)	(kN/m)	(kNm)	(kNm)					(kNm)	(kNm)		(kNm)		(kN/m)		(kN/m)		(kN/m)	
2/225_25	6	9.102	26.373 26.932	-29.927 -29.634	1.011	1.032	1.190	1.178	26.096	-25.154	1.000	-25.154	0.610	5.590	0.614	8.360	0.919	8.360	0.919
	8	4.824	22.962 27.024	-28.162 -22.982	0.880	1.036	1.120	0.914	26.096	-25.154	1.000	-25.154	0.610	3.144	0.652	4.703	0.975	4.703	0.975
	10	2.972	18.826 25.959	-32.588 -22.439	0.721	0.995	1.296	0.892	26.096	-25.154	1.000	-25.154	0.610	2.012	0.677	3.010	1.013	3.010	1.013
	12	1.978	21.296 26.013	-28.904 -18.189	0.816	0.997	1.149	0.723	26.096	-25.154	0.994	-25.003	0.610	1.397	0.706	2.090	1.057	2.087	1.055
2/285_25	6	11.797	32.617 36.439	-38.775 -33.956	0.899	1.004	1.091	0.956	36.278	-35.532	1.000	-35.532	0.668	7.896	0.669	11.676	0.990	11.676	0.990
	8	6.450	30.724 36.033	-37.645 -31.219	0.847	0.993	1.059	0.879	36.278	-35.532	1.000	-35.532	0.668	4.442	0.689	6.568	1.018	6.568	1.018
	10	4.117	27.634 36.000	-38.581 -30.760	0.762	0.992	1.086	0.866	36.278	-35.532	0.995	-35.339	0.668	2.843	0.690	4.203	1.021	4.197	1.019
	12	2.674	23.476 35.492	-32.985 -23.628	0.647	0.978	0.928	0.665	36.278	-35.532	0.945	-33.564	0.668	1.974	0.738	2.919	1.092	2.872	1.074
2/28520	6	8.843	26.005 26.005	-29.256 -29.256	0.946	0.946	1.233	1.233	27.499	-23.724	0.890	-21.104	0.769	5.272	0.596	8.544	0.966	8.290	0.938
	8	4.787	22.812 27.359	-26.332 -21.380	0.830	0.995	1.110	0.901	27.499	-23.724	0.848	-20.114	0.769	2.966	0.619	4.806	1.004	4.609	0.963
	10	2.859	18.928 26.592	-23.754 -16.848	0.688	0.967	1.001	0.710	27.499	-23.724	0.806	-19.112	0.769	1.898	0.664	3.076	1.076	2.914	1.019
	12	2.003	19.226 26.522	-33.793 -17.879	0.699	0.964	1.424	0.754	27.499	-23.724	0.763	-18.099	0.769	1.318	0.658	2.136	1.067	1.999	0.998

Table F.2: *Sleeved Zeta II 2-span gravity FE and design methods 1, 2 and 3 results (continued)*

Sleeve Section #	Span	$q_{FE,gs}$	M_{span}	$M_{support}$	M_{span}/M_1 Stage 2	M_{span}/M_1 q_{ult}	$M_{support}/M_{3sleeve}$ Stage 2	$M_{support}/M_{3sleeve}$ q_{ult}	M_1	$M_{3sleeve}$	$\alpha_{design,g,s}$*	$\alpha_{design,gs} M_{3sleeve}$	$\bar{\lambda}_{cs,s,-ve}$	Method 1		Method 2		Method 3	
														$q_{1,gs}$	$q_{1,gs}/q_{FE,gs}$	$q_{2,gs}$	$q_{2,gs}/q_{FE,gs}$	$q_{3,gs}$	$q_{2,gs}/q_{FE,gs}$
	(m)	(kN/m)	(kNm)	(kNm)					(kNm)	(kNm)		(kNm)		(kN/m)		(kN/m)		(kN/m)	
2/225_14	6	3.761	11.210 11.210	-12.008 -12.008	0.939	0.939	1.221	1.221	11.939	-9.835	0.744	-7.319	0.845	2.186	0.581	3.664	0.974	3.418	0.909
	8	2.047	10.277 11.616	-11.225 -9.468	0.861	0.973	1.141	0.963	11.939	-9.835	0.696	-6.845	0.845	1.229	0.601	2.061	1.007	1.896	0.926
	10	1.242	8.737 11.884	-10.285 -7.315	0.732	0.995	1.046	0.744	11.939	-9.835	0.647	-6.366	0.845	0.787	0.633	1.319	1.062	1.196	0.963
	12	0.850	8.124 11.681	-10.952 -7.398	0.680	0.978	1.114	0.752	11.939	-9.835	0.598	-5.884	0.845	0.546	0.643	0.916	1.078	0.819	0.963
2/245_15	6	4.616	13.740 13.740	-14.797 -14.797	0.927	0.927	1.214	1.214	14.814	-12.188	0.729	-8.882	0.866	2.708	0.587	4.545	0.985	4.221	0.914
	8	2.516	11.585 14.277	-13.189 -11.675	0.782	0.964	1.082	0.958	14.814	-12.188	0.686	-8.359	0.866	1.523	0.606	2.557	1.016	2.345	0.932
	10	1.499	10.431 13.995	-12.592 -8.862	0.704	0.945	1.033	0.727	14.814	-12.188	0.643	-7.831	0.866	0.975	0.650	1.636	1.092	1.482	0.989
	12	1.041	9.381 13.966	-11.886 -8.750	0.633	0.943	0.975	0.718	14.814	-12.188	0.599	-7.299	0.866	0.677	0.651	1.136	1.092	1.016	0.976
2/265_15	6	5.064	15.105 15.107	-16.133 -16.107	0.916	0.917	1.200	1.198	16.481	-13.448	0.715	-9.619	0.885	2.989	0.590	5.046	0.997	4.670	0.922
	8	2.875	13.242 16.535	-14.741 -12.516	0.803	1.003	1.096	0.931	16.481	-13.448	0.676	-9.098	0.885	1.681	0.585	2.838	0.987	2.598	0.904
	10	1.657	11.649 15.472	-13.903 -9.596	0.707	0.939	1.034	0.714	16.481	-13.448	0.638	-8.574	0.885	1.076	0.649	1.817	1.096	1.644	0.992
	12	1.145	10.349 15.483	-12.899 -9.435	0.628	0.939	0.959	0.702	16.481	-13.448	0.598	-8.047	0.885	0.747	0.653	1.262	1.102	1.128	0.986
														STD	0.051		0.051		0.047
														MEAN	0.642		1.029		0.973
														COV	0.065		0.050		0.048

* $\alpha_{design,u} = \left[0.7 - 0.0045\left(\frac{L}{h}\right)\right]\bar{\lambda}_{cs,s,+ve}^{\left[-0.003\left(\frac{L}{h}\right)-1.4\right]}$

Table F.3: *Sleeved Zed 2-span gravity FE and design methods 1, 2 and 3 results*

Sleeve Section #	Span	$q_{FE,gs}$	M_{span}	$M_{support}$	M_{span}/M_1 Stage 2	M_{span}/M_1 q_{ult}	$M_{support}/M_{3sleeve}$ Stage 2	$M_{support}/M_{3sleeve}$ q_{ult}	M_1	$M_{3sleeve}$	$\alpha_{design,g,s}$*	$\alpha_{design,gs} M_{3sleeve}$	$\bar{\lambda}_{cs,s,-ve}$	Method 1		Method 2		Method 3	
														$q_{1,gs}$	$q_{1,gs}/q_{FE,gs}$	$q_{2,gs}$	$q_{2,gs}/q_{FE,gs}$	$q_{3,gs}$	$q_{2,gs}/q_{FE,gs}$
	(m)	(kN/m)	(kNm)	(kNm)					(kNm)	(kNm)		(kNm)		(kN/m)		(kN/m)		(kN/m)	
Z/125_20	4	6.053	7.603 7.737	-9.540 -9.410	1.016	1.034	1.095	1.080	7.485	-8.715	1.000	-8.715	0.495	4.357	0.720	5.714	0.944	5.714	0.944
	6	2.425	6.158 7.512	-8.076 -6.922	0.823	1.004	0.927	0.794	7.485	-8.715	1.000	-8.715	0.495	1.937	0.798	2.539	1.047	2.539	1.047
	8	1.260	4.868 7.242	-7.171 -5.633	0.650	0.968	0.823	0.646	7.485	-8.715	1.000	-8.715	0.495	1.089	0.864	1.428	1.133	1.428	1.133
Z/20025	4	14.998	18.876 18.904	-24.168 -24.054	1.024	1.026	1.033	1.029	18.428	-23.385	1.000	-23.385	0.537	11.693	0.780	14.470	0.965	14.470	0.965
	6	6.225	17.518 17.550	-22.805 -22.792	0.951	0.952	0.975	0.975	18.428	-23.385	1.000	-23.385	0.537	5.197	0.835	6.431	1.033	6.431	1.033
	8	3.247	14.400 18.285	-20.231 -15.432	0.781	0.992	0.865	0.660	18.428	-23.385	1.000	-23.385	0.537	2.923	0.900	3.617	1.114	3.617	1.114
Z/12514	4	3.575	3.722 4.830	-4.906 -4.801	0.768	0.997	0.996	0.974	4.844	-4.928	1.000	-4.928	0.612	2.464	0.689	3.547	0.992	3.547	0.992
	6	1.463	3.229 4.690	-4.499 -3.714	0.667	0.968	0.913	0.754	4.844	-4.928	1.000	-4.928	0.612	1.095	0.748	1.576	1.077	1.576	1.077
	8	0.796	2.924 4.656	-4.317 -3.255	0.604	0.961	0.876	0.661	4.844	-4.928	0.901	-4.441	0.612	0.616	0.773	0.887	1.113	0.861	1.081

Table F.3: *Sleeved Zed 2-span gravity FE and design methods 1, 2 and 3 results (continued)*

Sleeve Section #	Span	$q_{FE,gs}$	M_{span}	$M_{support}$	M_{span}/M_1 Stage 2	M_{span}/M_1 q_{ult}	$M_{support}/M_{3sleeve}$ Stage 2	$M_{support}/M_{3sleeve}$ q_{ult}	M_1	$M_{3sleeve}$	$\alpha_{design,g,s}$*	$\alpha_{design,gs} M_{3sleeve}$	$\bar{\lambda}_{cs,s,-ve}$	Method 1		Method 2		Method 3	
														$q_{1,gs}$	$q_{1,gs}/q_{FE,gs}$	$q_{2,gs}$	$q_{2,gs}/q_{FE,gs}$	$q_{3,gs}$	$q_{2,gs}/q_{FE,gs}$
	(m)	(kN/m)	(kNm)	(kNm)					(kNm)	(kNm)		(kNm)		(kN/m)		(kN/m)		(kN/m)	
Z/155_15	4	5.291	6.541 7.107	-7.528 -7.241	0.912	0.991	1.037	0.998	7.169	-7.258	1.000	-7.258	0.661	3.629	0.686	5.242	0.991	5.242	0.991
	6	2.163	4.420 7.026	-6.042 -5.221	0.617	0.980	0.833	0.719	7.169	-7.258	0.986	-7.157	0.661	1.613	0.746	2.330	1.077	2.320	1.073
	8	1.145	3.999 6.795	-5.635 -4.356	0.558	0.948	0.776	0.600	7.169	-7.258	0.891	-6.470	0.661	0.907	0.793	1.310	1.145	1.268	1.108
Z/170_14	4	5.146	5.527 7.109	-6.580 -6.453	0.763	0.982	0.896	0.879	7.241	-7.344	0.976	-7.170	0.713	3.672	0.714	5.297	1.029	5.260	1.022
	6	2.165	4.436 7.080	-5.770 -5.086	0.613	0.978	0.786	0.693	7.241	-7.344	0.900	-6.610	0.713	1.632	0.754	2.354	1.088	2.284	1.055
	8	1.161	3.942 6.944	-5.476 -4.292	0.544	0.959	0.746	0.584	7.241	-7.344	0.822	-6.035	0.713	0.918	0.790	1.324	1.140	1.254	1.080
Z/200_13	4	5.689	6.879 7.687	-8.115 -7.632	0.896	1.001	1.065	1.001	7.681	-7.621	0.836	-6.371	0.806	3.811	0.670	5.583	0.982	5.314	0.934
	6	2.288	5.141 7.378	-6.601 -5.679	0.669	0.961	0.866	0.745	7.681	-7.621	0.779	-5.939	0.806	1.694	0.740	2.481	1.085	2.320	1.014
	8	1.249	4.971 7.436	-6.389 -4.700	0.647	0.968	0.838	0.617	7.681	-7.621	0.722	-5.501	0.806	0.953	0.763	1.396	1.118	1.281	1.026
														STD	0.061		0.064		0.058
														MEAN	0.765		1.060		1.038
														COV	0.080		0.061		0.056

* $\alpha_{design,u} = \left[0.7 - 0.0045\left(\frac{L}{h}\right)\right]\bar{\lambda}_{cs,s,+ve}^{\left[-0.003\left(\frac{L}{h}\right)-1.4\right]}$

APPENDIX G: RAW DATA FOR SLEEVED SECTION PARAMETRIC STUDY – UPLIFT LOADING

Table G.1: *Sleeved Zeta I 2-span uplift FE and design methods 1, 2, 3 and 4 results*

Sleeve Section #	Span	$q_{FE,us}$	M_{span}	$M_{support}$	M_{span} $/\chi_{LT}M_2$ Stage 2	M_{span} $/\chi_{LT}M_2$ q_{ult}	$M_{support}/$ $M_{4sleeve}$ Stage 2	$M_{support}/$ $M_{4sleeve}$ q_{ult}	M_2	$M_{4sleeve}$	$-\lambda_{cs,s,+ve}$	Method 1		Method 2		Method 3		Method 4	
												$q_{1,us}$	$q_{1,us}$ $/q_{FE,us}$	$q_{2,gs}$	$q_{2,gs}$ $/q_{FE,us}$	$q_{3,gs}$	$q_{2,gs}$ $/q_{FE,us}$	$q_{3,gs}$	$q_{2,gs}$ $/q_{FE,us}$
	(m)	(kN/m)	(kNm)	(kNm)					(kNm)	(kNm)		(kN/m)		(kN/m)		(kN/m)		(kN/m)	
1/150_19	4	7.879	-10.426 -10.426	11.190 11.190	0.979	0.979	0.871	0.871	-11.626	12.848	0.690	6.424	0.815	8.107	1.029	7.672	0.974	8.223	1.044
	6	3.684	-11.032 -11.032	11.603 11.614	1.115	1.115	0.917	0.918	-11.626	12.649	0.690	2.811	0.763	3.724	1.011	3.289	0.893	3.461	0.940
	8	2.017	-10.653 -10.653	11.452 11.452	1.128	1.128	0.915	0.915	-11.626	12.513	0.690	1.564	0.775	2.039	1.011	1.797	0.891	1.881	0.932
	10	1.282	-10.467 -10.468	11.781 11.777	1.147	1.147	0.947	0.947	-11.626	12.441	0.690	0.995	0.777	1.287	1.004	1.124	0.877	1.175	0.917
1/125_13	4	3.841	-4.914 -4.914	4.512 4.512	1.051	1.051	0.840	0.840	-5.407	5.372	0.737	2.686	0.699	3.678	0.958	3.302	0.860	3.555	0.926
	6	1.683	-5.225 -5.225	4.762 4.762	1.214	1.214	0.911	0.911	-5.407	5.228	0.737	1.162	0.690	1.692	1.006	1.398	0.831	1.480	0.880
	8	0.932	-5.031 -5.031	4.985 4.985	1.232	1.232	0.964	0.964	-5.407	5.172	0.737	0.646	0.694	0.924	0.991	0.759	0.815	0.801	0.859
	10	0.553	-4.614 -4.614	4.807 4.807	1.174	1.174	0.941	0.941	-5.407	5.107	0.737	0.409	0.739	0.555	1.003	0.471	0.852	0.498	0.900
1/175_16	4	7.310	-9.261 -9.261	11.605 11.605	0.894	0.894	0.876	0.876	-11.525	13.241	0.766	6.621	0.906	7.579	1.037	7.334	1.003	8.155	1.116
	6	3.408	-9.726 -9.726	12.092 12.092	1.043	1.043	0.927	0.927	-11.525	13.050	0.766	2.900	0.851	3.459	1.015	3.104	0.911	3.366	0.988
	8	2.003	-10.232 -10.232	12.438 12.438	1.181	1.181	0.962	0.962	-11.525	12.924	0.766	1.616	0.807	2.005	1.001	1.686	0.842	1.801	0.899
	10	1.412	-10.365 -11.227	14.491 13.886	1.258	1.362	1.134	1.087	-11.525	12.777	0.766	1.022	0.724	1.361	0.964	1.046	0.741	1.112	0.787

Table G.1: *Sleeved section Zeta I 2-span uplift FE and design methods 1, 2, 3 and 4 results (continued)*

Sleeve Section #	Span	$q_{FE,us}$	M_{span}	$M_{support}$	M_{span} /$\chi_{LT}M_2$ Stage 2	M_{span} /$\chi_{LT}M_2$ q_{ult}	$M_{support}$/ $M_{4sleeve}$ Stage 2	$M_{support}$/ $M_{4sleeve}$ q_{ult}	M_2	$M_{4sleeve}$	$\bar{\lambda}_{cs,s,+ve}$	Method 1		Method 2		Method 3		Method 4	
												$q_{1,us}$	$q_{1,us}$ /$q_{FE,us}$	$q_{2,gs}$	$q_{2,gs}$ /$q_{FE,us}$	$q_{3,gs}$	$q_{2,gs}$ /$q_{FE,us}$	$q_{3,gs}$	$q_{2,gs}$ /$q_{FE,us}$
	(m)	(kN/m)	(kNm)	(kNm)					(kNm)	(kNm)		(kN/m)		(kN/m)		(kN/m)		(kN/m)	
1/200_16	4	8.242	-10.165 -10.165	13.789 13.789	0.833	0.833	0.886	0.886	-13.779	15.561	0.767	7.781	0.944	8.529	1.035	8.379	1.017	9.600	1.165
	6	3.806	-10.485 -10.485	14.567 14.567	0.976	0.976	0.911	0.911	-13.779	15.997	0.767	3.555	0.934	3.905	1.026	3.568	0.937	3.967	1.042
	8	2.216	-10.940 -10.940	14.911 14.911	1.120	1.120	0.974	0.974	-13.779	15.307	0.767	1.913	0.863	2.221	1.002	1.901	0.858	2.067	0.933
	10	1.412	-10.365 -11.227	14.491 13.886	1.135	1.229	0.911	0.873	-13.779	15.911	0.767	1.273	0.901	1.465	1.038	1.199	0.849	1.289	0.912
1/200_13	4	6.153	-7.537 -7.537	10.475 10.475	0.820	0.820	0.850	0.850	-10.427	12.317	0.862	6.158	1.001	6.482	1.054	6.267	1.019	7.355	1.195
	6	2.746	-7.524 -7.524	10.641 10.641	0.947	0.947	0.899	0.899	-10.427	11.842	0.862	2.631	0.958	2.835	1.032	2.570	0.936	2.934	1.068
	8	1.574	-7.682 -7.682	10.829 10.829	1.085	1.085	0.897	0.897	-10.427	12.070	0.862	1.509	0.958	1.627	1.034	1.398	0.888	1.547	0.983
	10	1.032	-7.883 -7.883	11.031 11.031	1.208	1.208	0.938	0.938	-10.427	11.761	0.862	0.941	0.912	1.048	1.016	0.857	0.831	0.933	0.904
1/175_10	4	3.676	-4.535 -4.535	6.164 6.164	0.876	0.876	0.858	0.858	-5.867	7.187	0.997	3.594	0.978	3.855	1.049	3.443	0.937	4.192	1.140
	6	1.654	-4.506 -4.506	6.548 6.504	1.008	1.008	0.984	0.977	-5.867	6.656	0.997	1.479	0.894	1.659	1.003	1.356	0.820	1.650	0.998
	8	0.943	-4.615 -4.615	6.494 6.494	1.158	1.158	0.967	0.967	-5.867	6.713	0.997	0.839	0.890	0.950	1.008	0.731	0.775	0.867	0.919
	10	0.612	-4.691 -4.691	6.503 6.503	1.277	1.277	0.978	0.978	-5.867	6.647	0.997	0.532	0.868	0.612	1.000	0.450	0.735	0.526	0.859
												STD	0.097		0.023		0.078		0.105
												MEAN	0.848		1.013		0.879		0.971
												COV	0.114		0.023		0.089		0.108

Table G.2: *Sleeved section Zeta II 2-span uplift FE and design methods 1, 2, 3 and 4 results*

Sleeve Section #	Span	$q_{FE,us}$	M_{span}	$M_{support}$	M_{span} /$\chi_{LT}M_2$ Stage 2	M_{span} /$\chi_{LT}M_2$ q_{ult}	$M_{support}$/ $M_{4sleeve}$ Stage 2	$M_{support}$/ $M_{4sleeve}$ q_{ult}	M_2	$M_{4sleeve}$	$\bar{\lambda}_{cs,s,+ve}$	Method 1		Method 2		Method 3		Method 4	
												$q_{1,us}$	$q_{1,us}$ /$q_{FE,us}$	$q_{2,gs}$	$q_{2,gs}$ /$q_{FE,us}$	$q_{3,gs}$	$q_{2,gs}$ /$q_{FE,us}$	$q_{3,gs}$	$q_{2,gs}$ /$q_{FE,us}$
	(m)	(kN/m)	(kNm)	(kNm)					(kNm)	(kNm)		(kN/m)		(kN/m)		(kN/m)		(kN/m)	
2/285_20	4	13.625	-16.119 -16.119	24.277 24.277	0.699	0.699	0.800	0.800	-25.404	30.332	0.747	15.166	1.113	14.662	1.076	15.550	1.141	18.332	1.345
	6	6.674	-17.658 -17.658	27.789 27.789	0.880	0.880	0.920	0.920	-25.404	30.211	0.747	6.714	1.006	6.871	1.030	6.351	0.952	7.438	1.114
	8	4.012	-18.809 -18.809	29.865 29.865	1.062	1.062	0.974	0.974	-25.404	30.657	0.747	3.832	0.955	4.040	1.007	3.447	0.859	3.894	0.971
	10	2.649	-19.309 -19.309	30.982 30.982	1.199	1.199	1.031	1.031	-25.404	30.057	0.747	2.405	0.908	2.608	0.985	2.119	0.800	2.336	0.882
2/225_14	4	7.128	-8.502 -8.502	12.851 12.851	0.781	0.781	0.989	0.989	-11.935	12.990	0.852	6.495	0.911	7.128	1.000	7.164	1.005	8.375	1.175
	6	3.369	-9.015 -9.015	13.745 13.745	0.944	0.944	1.066	1.066	-11.935	12.893	0.852	2.865	0.850	3.279	0.973	2.948	0.875	3.404	1.010
	8	1.816	-8.939 -8.939	12.243 12.243	1.047	1.047	0.951	0.951	-11.935	12.874	0.852	1.609	0.886	1.834	1.010	1.591	0.876	1.780	0.980
	10	1.213	-9.030 -9.030	13.612 13.612	1.152	1.152	1.060	1.060	-11.935	12.840	0.852	1.027	0.847	1.180	0.973	0.985	0.812	1.080	0.890
2/245_15	4	8.148	-9.648 -9.703	14.897 14.718	0.726	0.730	0.919	0.908	-14.599	16.210	0.845	8.105	0.995	8.416	1.033	8.736	1.072	10.296	1.264
	6	4.006	-10.580 -10.580	16.782 16.782	0.913	0.913	1.041	1.041	-14.599	16.118	0.845	3.582	0.894	3.938	0.983	3.568	0.891	4.175	1.042
	8	2.193	-10.386 -10.651	15.541 15.231	1.012	1.038	0.955	0.936	-14.599	16.267	0.845	2.033	0.927	2.232	1.018	1.930	0.880	2.181	0.995
	10	1.431	-10.534 -10.542	16.484 16.479	1.124	1.125	1.030	1.029	-14.599	16.007	0.845	1.281	0.895	1.411	0.986	1.188	0.831	1.312	0.917

Table G.1: *Sleeved section Zeta II 2-span uplift FE and design methods 1, 2 and 3 results (continued)*

Sleeve Section #	Span	$q_{FE,us}$	M_{span}	$M_{support}$	M_{span} /$\chi_{LT}M_2$ Stage 2	M_{span} /$\chi_{LT}M_2$ q_{ult}	$M_{support}$/ $M_{4sleeve}$ Stage 2	$M_{support}$/ $M_{4sleeve}$ q_{ult}	M_2	$M_{4sleeve}$	$\bar{\lambda}_{cs,s,+ve}$	Method 1		Method 2		Method 3		Method 4	
												$q_{1,us}$	$q_{1,us}$ /$q_{FE,us}$	$q_{2,gs}$	$q_{2,gs}$ /$q_{FE,us}$	$q_{3,gs}$	$q_{2,gs}$ /$q_{FE,us}$	$q_{3,gs}$	$q_{2,gs}$ /$q_{FE,us}$
	(m)	(kN/m)	(kNm)	(kNm)					(kNm)	(kNm)		(kN/m)		(kN/m)		(kN/m)		(kN/m)	
2/265_15	4	8.538	-9.818 -9.818	15.774 15.774	0.681	0.681	0.861	0.861	-15.883	18.327	0.872	9.163	1.073	8.901	1.042	9.509	1.114	11.329	1.327
	6	4.142	-10.810 -10.810	17.689 17.689	0.867	0.867	0.984	0.984	-15.883	17.981	0.872	3.996	0.965	4.160	1.004	3.804	0.918	4.549	1.098
	8	2.373	-11.162 -11.162	17.638 17.638	1.026	1.026	0.969	0.969	-15.883	18.200	0.872	2.275	0.959	2.398	1.010	2.054	0.865	2.360	0.995
	10	1.524	-11.210 -11.210	17.626 17.626	1.144	1.144	0.968	0.968	-15.883	18.199	0.872	1.456	0.955	1.539	1.009	1.272	0.834	1.419	0.931
2/265_10	4	4.739	-5.291 -5.291	9.592 9.592	0.751	0.751	1.071	1.071	-7.788	8.956	1.195	4.478	0.945	4.613	0.973	4.533	0.956	5.537	1.168
	6	2.289	-5.570 -5.605	10.954 10.795	0.935	0.941	1.244	1.226	-7.788	8.809	1.195	1.957	0.855	2.111	0.922	1.702	0.743	2.194	0.958
	8	1.149	-5.031 -5.031	9.563 9.563	1.011	1.011	1.070	1.070	-7.788	8.935	1.195	1.117	0.972	1.118	0.973	0.906	0.788	1.110	0.967
	10	0.723	-4.908 -5.149	9.458 8.791	1.144	1.200	1.082	1.005	-7.788	8.743	1.195	0.699	0.967	0.719	0.995	0.552	0.764	0.646	0.893
												STD	0.069		0.032		0.112		0.143
												MEAN	0.944		1.000		0.899		1.046
												COV	0.073		0.032		0.124		0.137